



ESMRMB

European Society for Magnetic Resonance in Medicine and Biology



ESMRMB 2020 ONLINE

September 30 - October 2

Book of Abstracts

**Lightning Talks / Electronic Posters /
Clinical Review Posters / Software Exhibits**

DOI: 10.1007/s10334-020-00876-y

Lightning Talks

L01.01

Classification of Parkinson’s disease mild cognitive impairment with machine learning based on multimodal MRI biomarkers

B. Buz Yalug¹, O. Genc¹, D. B. Arslan¹, A. Kicik², B. Bilgic³, H. Hanagasi³, H. Gurvit³, T. Demiralp⁴, E. Ozturk-Isik¹

¹Bogazici University, Institute of Biomedical Engineering, Istanbul, Turkey, ²Demiroglu Bilim University, Department of Physiology, Faculty of Medicine, Istanbul, Turkey, ³Istanbul University, Behavioral Neurology and Movement Disorders Unit, Department of Neurology, Istanbul Faculty of Medicine, Istanbul, Turkey, ⁴Istanbul University, Department of Physiology, Istanbul Faculty of Medicine, Istanbul, Turkey

Introduction: Parkinson’s disease mild cognitive impairment (PD-MCI) is an intermediate condition between cognitively normal PD (PD-CN) and dementia [1]. Early diagnosis of PD-MCI has been challenging [2]. The aim of this study is to classify PD-MCI, PD-CN and healthy control (HC) groups with machine learning based on multimodal magnetic resonance imaging (MRI) biomarkers, and investigate the effect of oversampling methods in classification.

Subjects/Methods: Neuropsychological tests and MR examination of 74 participants, including 33 PD-MCI, 26 PD-CN and 15 HC, were performed after informed consent. The imaging protocol included T1-weighted MRI, T2-weighted MRI, arterial spin labeling MRI (ASL-MRI), diffusion tensor imaging (DTI) and proton MR spectroscopic imaging (1H-MRSI). MRI data were collected at a 3T Philips clinical MR scanner using a 32-channel head coil. Cerebral blood flow (CBF), fractional anisotropy (FA), and mean diffusivity (MD) maps were computed using in-house software. LCModel was used to estimate metabolite ratios, including choline (tCho) and N-acetyl aspartate (tNAA) over creatine (tCr). The resultant measures were evaluated at 100 different parcellations of the cerebral cortex defined by Schaefer et al. [3]. Random forest or k nearest neighbor machine learning methods were applied with 10 fold cross validation and false positive rate test based feature selection algorithm [4]. Additionally, synthetic data was generated using random oversampling or synthetic minority oversampling technique (SMOTE) [5] due to the small data size. The overall classification accuracy, precision and recall were evaluated.

Groups	Features	Brain Region
HC vs PD-CN	tCho/tCr	Left visual network - peripheral superior extrastriate cortex area 8
	tCho/tCr	Left visual network - peripheral superior extrastriate cortex area 7
HC vs PD-MCI	tCho/tCr	Left visual network - peripheral superior extrastriate cortex area 7
	tCho/tCr	Left default mode network - posterior cingulate cortex area 1
	CBF	Right default mode network - posterior cingulate cortex area 1
	CBF	Right default mode network - medial prefrontal cortex area 1
PD-CN vs PD-MCI	MD	Left uncinate fasciculus
	tCho/tCr	Left visual network - peripheral superior extrastriate cortex area 5
	tNAA/tCr	Left default mode network - posterior cingulate cortex area 1
	CBF	Left salience/ventral attention network - lateral prefrontal cortex area 1

Table 1. Most effective features for binary classifications.

Feature Selection	Accuracy	Precision	Recall	Feature Selection Method	Best Classification Method
HC vs PD-CN	0.81	0.82	0.95	Select K Best Features with False Positive Rate Test	k-Nearest Neighbor
HC vs PD-MCI	0.86	0.88	0.91	Select K Best Features with False Positive Rate Test	Random Forest
PD-CN vs PD-MCI	0.72	0.61	0.69	Select K Best Features with False Positive Rate Test	k-Nearest Neighbor
Feature Selection + Oversampling				Oversampling Method	
HC vs PD-CN	0.95	0.96	0.94	Random Over Sampling	Random Forest
HC vs PD-MCI	0.98	0.98	0.99	SMOTE	Random Forest
PD-CN vs PD-MCI	0.96	0.96	0.95	Random Over Sampling	Random Forest

Table 2. The classification performances of different approaches.

Results/Discussion: The most informative features included measures from all the MRI modalities, but tCho/tCr at visual network was selected in all binary classifications (Table 1). Oversampling increased the model performances with 98% accuracy (98% precision, 99% recall) for PD-MCI vs HC, 95% accuracy (96% precision, 94% recall) for PD-CN vs HC, and 96% accuracy (96% precision, 95% recall) for PD-MCI vs PD-CN classifications (Table 2). Future studies will explore the performance of machine learning algorithms in a larger patient cohort.

Grant Support: TUBITAK 115S219, Istanbul University BAP 1567/42362.

- References:** 1. Weil, R.S., et al., *Curr Neurol Neurosci Rep*, 2018. 18(4): p. 17.
 2. Poewe, W., et al., *Int J Clin Pract*, 2008. 62(10): p. 1581–7.
 3. Schaefer, A., et al., *Cereb Cortex*, 2018. 28(9): p. 3095–3114.
 4. Wang, H. and H. Zheng, *False Positive Rate*, in *Encyclopedia of Systems Biology*, W. Dubitzky, et al., Editors. 2013, Springer New York: New York, NY. p. 732–732.
 5. Chawla, N.V., et al., *Journal of artificial intelligence research*, 2002. 16: p. 321–357.

L01.02

Deep learning for reconstruction of undersampled low field MRI

R. Ayde, M. Fiorito, M. Yushchenko, N. Salameh, M. Sarracanie

Center for Adaptable MRI Technology (AMT Center), University of Basel, Department of Biomedical Engineering, Allschwil, Switzerland

Introduction: With promising benefits for a more accessible diagnosis, the impeded sensitivity in low field (LF) MRI translates into low SNR per unit time, challenging its relevance in the clinics. Undersampling k-space is an efficient way to accelerate acquisitions, and recent work has reported encouraging results when combined with deep learning approaches. However, training deep learning models requires large scale image databases (~thousands) with the same protocol that is difficult to achieve at LF. To address this issue, a transfer learning approach¹ was adopted which performance was evaluated first on simulated undersampled data before being tested on true LF MR acquisitions.

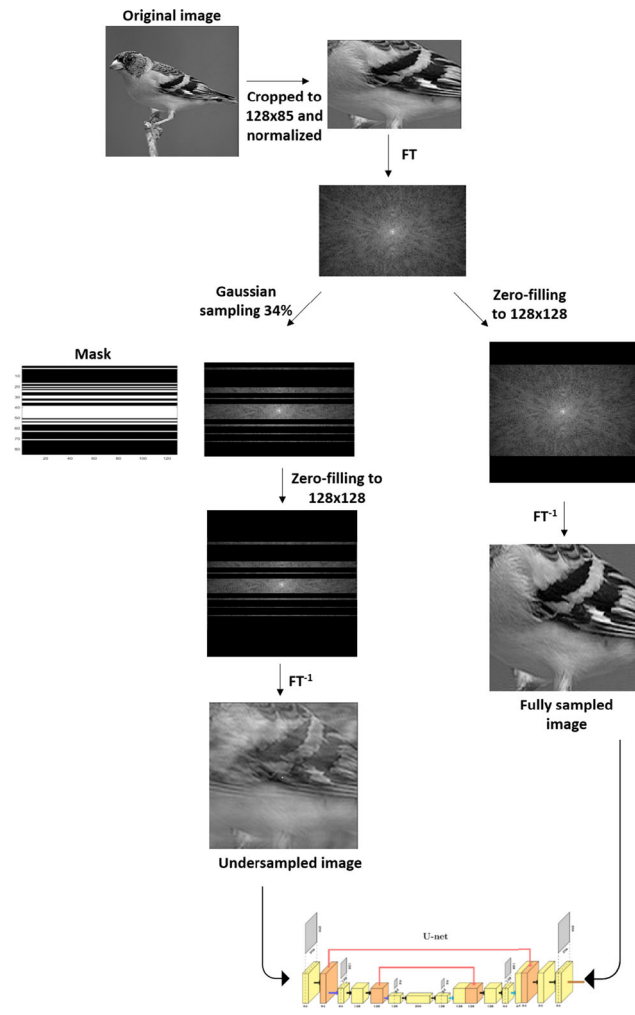
Subjects/Methods: We adopted a modified version of the Unet architecture (Fnet^{2,3}), as a supervised deep learning framework. To perform transfer learning from natural image domain to MR domain, the network was trained on 1500 natural images of ImageNet dataset⁴ that consisted in pairs of fully and under-sampled images. Images were normalized, resized to match our typical LF data size, and inverse Fourier transformed (FT). Undersampling was simulated by keeping 34% of k-space from a variable density Gaussian pattern

(Fig.1). To fit Fnet input/output dimensions, k-spaces were zero-filled to 128×128 before FT.

The trained Fnet network was then fine-tuned using 100 slice selective wrist images acquired at 0.1 T with a GRE sequence. Imaging parameters were: matrix = 128×85 , voxel size = $1.5 \times 1.5 \times 10 \text{ mm}^3$, TE/TR = 10.6/22 ms, NA = 125 (acquisition time = 4 min 23 s).

Simulated undersampled LF data used the same 34% variable density Gaussian coverage of k-space before being zero-filled to 128×128 before FT.

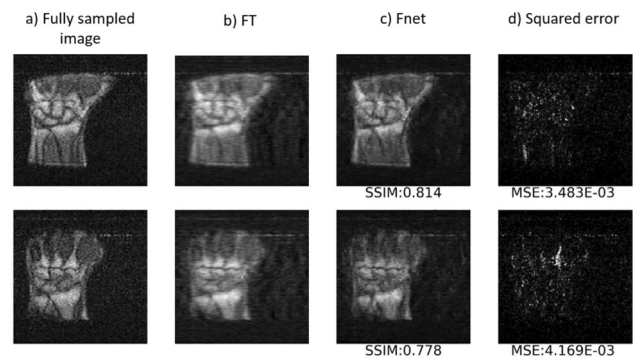
We used the RMSProp as an optimizer (learning rate 0.001, weight decay 0.9, and 2000 epochs); mini-batch sizes were 32 and 8 for trained and fine-tuned networks respectively.



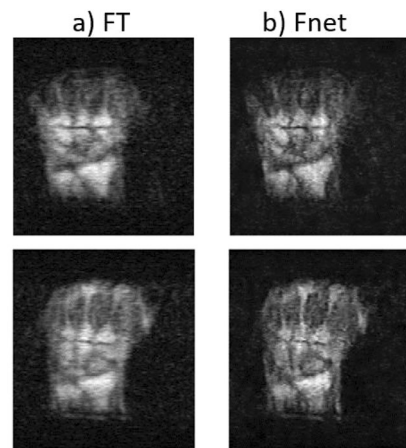
Final network performance was assessed on 4 test-data. Mean Squared Error (MSE), Structure Similarity Index (SSIM) and SNR were chosen as evaluation metrics. True undersampled images were

then acquired at 0.1 T with the protocol and sampling scheme (Fig1) described above; the total acquisition time was 1 min 29 s.

Results/Discussion: Fig.2 shows simulations output reconstruction using Fnet. Mean SSIM and MSE were 0.78 ± 0.01 and $3.6E-3 \pm 0.4E-3$, meaning that structures are mostly preserved. Mean SNR with Fnet is higher than fully-sampled data (~ 50 vs ~ 26.9). Fig. 3 shows output reconstructed results in acquired undersampled data, showing that our approach is able to maintain details and structure at reduced acquisition time. These preliminary results demonstrate the potential of transfer learning associated with the Fnet architecture at low field, without large training datasets.



Undersampling performance. a) Fully sampled image and corresponding simulated b) FT and c) Fnet reconstructions. d) Mean squared error of reconstructed images using Fnet versus fully sampled image.



Results of zero-filled (acquired) undersampled k-space reconstructed with a) FT and b) Fnet.

References: ¹Dar, Magnetic Resonance in Medicine, 2020
²Hyun, Phys. Med. Biol, 2018
³Zumar, <http://corey-zumar.github.io/submrine/>
⁴Deng, IEEE Conf. on Computer Vision and Pattern Recognition, 2009

L01.03

High-Fidelity Image Size Standardization using a Conditional Generative Adversarial Network (CGAN)

C. Kulkarni¹, R. Patil¹, D. M. Siddu¹, A. Dekker², L. Wee²

¹Philips Healthcare, Research India, Bengaluru, India, ²Maastricht University, Department of Radiation Oncology (MAASTRO), GROW – School for Oncology and Developmental Biology, Maastricht, The Netherlands

Introduction: One of the major hurdles of reusing retrospective Magnetic Resonance (MR) images for deep learning is variation in image resolution, image size and lack of fixed intensity calibration, even though deep neural network can handle low quality MR images which are resized the size of the network needs to be increased therefore increasing training and inference time. In this paper, we test if a CGAN has added value in restoring content fidelity in up-sampled FLuid-Attenuated Inversion Recovery (FLAIR) images.

Subjects/Methods: We used whole human brain images from an open source dataset that were stripped of non-brain tissues. Original images (566 in total) measuring 240 × 156 pixels were taken as ground truth; this is also the target image size. Training data (n = 448) was generated by initially down-sizing a random subset to 60 × 39 pixels. Our training procedure was : (i) offsetting the median intensity of whole brain tissue to zero, (ii) crudely up-sampling a 60 × 39 image to the target size by bicubic interpolation (BI), and (iii) training a CGAN that removes interpolation noise and reconstructs a high-fidelity FLAIR image relative to the original. The CGAN architecture has been based on a Super-Resolution GAN (SR-GAN) [1] but initial up-sampling layers on the generator were removed. The generator loss function was mean squared error (MSE) and discriminator loss, and the discriminator loss function was binary cross-entropy. The quality of reconstruction was measured using MSE and content loss, comparing the CGAN with bicubic interpolation alone. The validation was performed on 112 Brain MR images quarantined separately from the training set.

Results/Discussion: Table 1 reports the relative reduction of MSE (42%) and of content loss (80%) between (CGAN+BI) versus BI only, in the validation subset. There was significant added improvement with the CGAN. Figure 1 illustrates three example patients (columns) and the comparative results relative to the original image (rows). We chose to handle the up-sampling outside the neural network so that arbitrary image sizes can be combined together for training, which is not the case in the original SR-GAN network. This work is presently limited by small sample size, assumed constancy of the input image dimension (60x39) and lack of paired FLAIR images of the same human subject scanned at two different image dimensions. We have validated a prototype CGAN for standardizing FLAIR images to a fixed target image size with improved fidelity compared to bicubic interpolation alone. Future work will generalize the standardizing CGAN with variable input image sizes, and test this with a larger number of patients.

	BI only	BI + CGAN	Difference
Mean squared error	0.0003274	0.0001903	-0.0001371 (-42%)
Content loss	0.0104	0.00203	-0.00837 (-80%)

Table 1: Comparison of mean square error and content loss for the standardizing CGAN and ordinary bicubic interpolation (BI), in the validation subset of 112 images, using unaltered Brain MR Images as the ground truth.

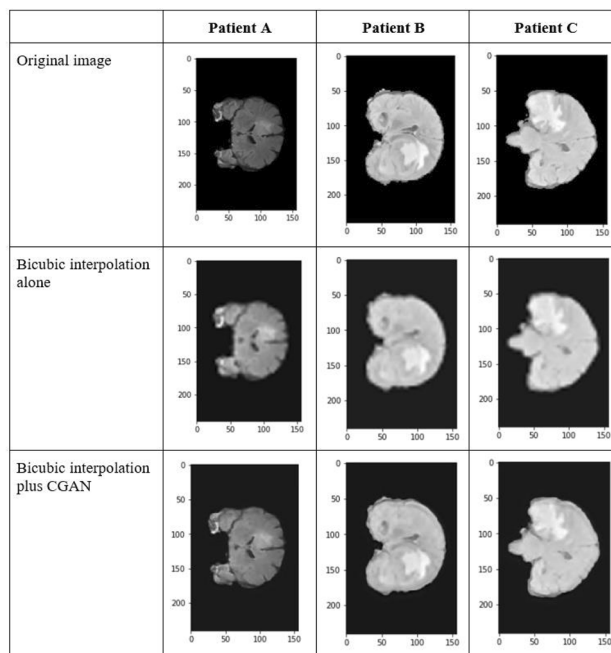


Figure 1: Comparison of three example subjects ordered as columns. The top row shows the original images, the middle row shows the result of upsampling with BI, and the bottom row is the result of BI combined with standardizing CGAN.

References: [1] C. Ledig, L. Theis, F. Huszar, J. Caballero, A. Cunningham, A. Acosta, A. Aitken, A. and Tejani, J. Totz, Z. Wang, and W. Shi. Photo-realistic single image super-resolution using a generative adversarial network. arXiv:1609.04802, 2016.

L01.04

Improving the image quality of cardiac T1 maps via a residual dense network

T. Ferreira da Silva¹, C. Galan-Arriola², P. Montesinos¹, V. Vicente-Palacios¹, M. Veta³, M. Breeuwer³, B. Ibañez², J. Sánchez-González¹

¹Philips Healthcare Iberia, Madrid, Spain, ²Centro Nacional de Investigaciones Cardiovasculares Carlos III, Madrid, Spain, ³Eindhoven University of Technology, Biomedical Engineering Department, Eindhoven, The Netherlands

Introduction: Recently, a novel fast MR imaging sequence was developed to acquire cardiac 3D T1 maps in a single-breath hold – 3D saturation recovery compressed SENSE rapid acquisition (3D SACORA) [1]. Although this sequence is capable of acquiring T1 maps with good image quality, we hypothesize that the cardiac T1 maps can be further improved using artificial intelligence techniques. A new residual dense network (RDN) has been proposed to improve the resolution and quality of real-world images [2, 3]. In this work, we aim to test the RDN on cardiac T1 maps. Here, we evaluate the improvement in image quality of applying the RDN on the 3D T1 maps obtained with 3D SACORA and the potential effect on quantitative T1 values.

Subjects/Methods: For the RDN training, several different 3D high-resolution acquisitions were performed on pigs to obtain a robust

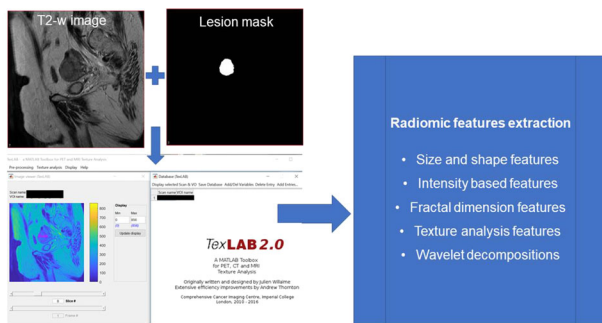


Figure 1. A T2-weighted MR image (top left) and manually-segmented whole-tumour volume (top right) are put through the pre-processing and radiomic pipeline using TexLAB 2.0 (bottom).

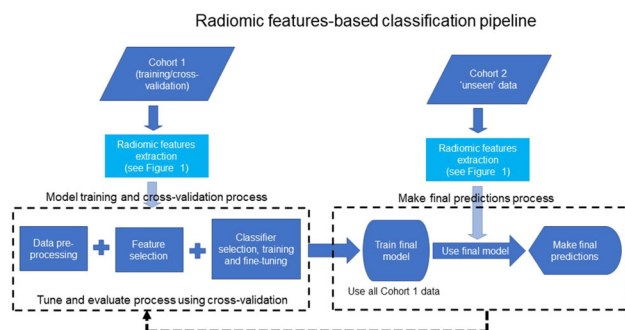


Figure 2. The entire radiomic features-based classification pipeline.

Results/Discussion: In this preliminary study involving 60 patients, 24 had aggressive tumours. In total, 656 features were extracted. Classification of features was based on a random forest wrapper, which identified the five most informative features using a minimum redundancy, maximum relevance method. The classifier reached an accuracy of 72% in the training/cross-validation testing.

Following our initial data-curation, we are currently completing segmentations, exploring pre-processing steps and refining the case stratification based on tumour pathology, grade, lymphovascular space invasion and overall stage. We also will test against patient outcomes.

It is hoped that the radiomic analysis may allow prediction of tumour behaviour that could assist with optimal treatment selection.

References: None.

L01.06

Measurement of bicipital groove depth with MRI and evaluation of its relationship with the long head of the biceps tendon

O. Turkoglu¹, E. Karatay²

¹Health Science University Sultan Abdulhamid Han Educational Research Hospital, Istanbul, Turkey, Department of Radiology, Istanbul, Turkey, ²Health Science University Kartal Lütfi Kırdar Educational Research Hospital, Istanbul, Turkey, Department of Radiology, Istanbul, Turkey

Introduction: The disorder of the long head of the biceps tendon (LHBT) is a well known source of anterior shoulder pain and instability. The bicipital groove is an important anatomic location which plays a role in the stability of the LHBT. There has been a few literature about LHBT pathologies. MRI is useful in demonstrating the position of LHBTs in the bicipital groove.

We aimed to investigate the relationship between bicipital groove bony morphology and LHBT instability and to determine the values

of the depth of the bicipital groove, the medial wall angle and the total opening angle.

Subjects/Methods: The depth of the bicipital groove (DBG), the medial wall angle (MWA) and the total opening angle (TOA) were measured on the shoulder MRI of 200 patients with anterior shoulder pain. 135 patients with a normally-located LHBT determined stable LHBT, 65 patients with subluxation or dislocation of the LHBT determined unstable LHBT. We assessed the relationship between measurements and LHBT stability and analyzed the cut-off values of the measurements to identify the long head of the biceps tendon instability.

Results/Discussion: The incidence of partial rotator cuff rupture, total rotator cuff tear, tendinosis and superior labral lesions were significantly higher in patients with unstable LHBT ($p < 0.05$). In patients with unstable LHBT, DBG was shallower, medial wall angle was narrower and TOA was higher compared to those with stable LHBT. We recorded high sensitivity and specificities for the cut-off values for DBG, MWA, TOA to determine the presence of the unstable LHBT.

DBG, MWA and TOA can be used as stability criteria for LHBT.

References: 1. Baggio M, Martinelli F, Netto MB, Martins RO, da Cunha RC, Stipp WN. Evaluation of the results from arthroscopic tenodesis of the long head of the biceps brachii on the tendon of the subscapularis muscle. *Rev Bras Ortop* 2016;51:157–62.

2. Szabó I, Boileau P, Walch G. The proximal biceps as a pain generator and results of tenotomy. *Sports Med Arthrosc Rev* 2008;16:180–6.

3. Abboud JA, Bartolozzi AR, Widmer BJ, DeMola PM. Bicipital groove morphology on MRI has no correlation to intra-articular biceps tendon pathology. *J Shoulder Elbow Surgery* 2010;19:790–4.

4. Lee HI, Shon MS, Koh KH, Lim TK, Heo J, Yoo JC. Clinical and radiologic results of arthroscopic biceps tenodesis with suture anchor in the setting of rotator cuff tear. *J Shoulder Elbow Surg* 2014;23:e53–e60.

5. Houtz CG, Schwartzberg RS, Barry JA, Reuss BL, Papa L. Shoulder MRI accuracy in the community setting. *J Shoulder Elbow Surg* 2011;20:537–42

L01.07

MRI-based classification of neuropsychiatric systemic lupus erythematosus patients with self-supervised contrastive learning

M. Kim¹, F. Inglese², G. M. Steup-Beekman³, T. W. Huizinga³, J. de Bresser², D. Kim¹, I. Ronen²

¹Korea Advanced Institute of Science and Technology, Daejeon, SOUTH KOREA, ²Leiden University Medical Center, Department of Radiology, Leiden, The Netherlands, ³Leiden University Medical Center, Department of Rheumatology, Leiden, The Netherlands

Introduction: Systemic lupus erythematosus (SLE) is a chronic autoimmune disease with a broad spectrum of clinical presentations, including heterogeneous and uncommon neuropsychiatric (NP) syndromes. NP-SLE diagnosis is challenging due to the lack of clinically useful biomarkers. So far, structural brain alterations on MRI have failed in contributing to NPSLE diagnosis¹. Deep learning has proven useful in classification tasks of clinical MRI data^{2, 3}. Self-supervised contrastive learning algorithms⁴ do not require labels, therefore it is possible to use them in rare diseases with limited datasets⁵. The aim of our study was to apply self-supervised contrastive learning on T₁-weighted images to distinguish between SLE patients with NP symptoms due to the disease (NP-SLE) or not SLE-related (non-NP-SLE).

Subjects/Methods: 120 patients were included. We used T₁-weighted images (3T Philips Achieva, voxel size = 1.17 × 1.17 × 1.2 mm³; TR/TE = 9.8/4.6 ms) registered to the MNI152 template. The training set comprised 68 non-NP-SLE and 34 NP-SLE patients. During the training procedure, we applied random geometric transformations

(cropping, left-right flipping and rotations) between iterations (figure 1a). Our ML pipeline consisted of convolutional base encoder and linear projector (1b). To test the classification task, the projector was removed and one linear layer was measured (1c). We trained the encoder and projector with the loss function *NT-xent*⁴, which maximizes the similarity between each transformed sample as contrastive learning (1d). We performed 5 validations, each using a random selection of 13% of samples from each group.

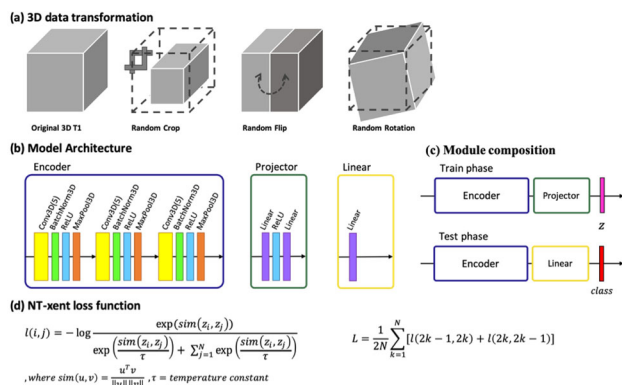


Figure 1. (a) Geometric transformations used between iterations of the training procedure (b) ML model architecture (c) Module composition for training and testing (d) Expression for the NT-xent loss function we used for contrastive learning

	1 trial	2 trial	3 trial	4 trial	5 trial	Avg (sd)
Ours	67.65	75.97	74.99	70.59	82.35	74.31 ± 5.02

Table 1. Accuracy of the classification in percent of the total test group (n = 18)

Classification results are shown in Table 1: in 5 trials, about 74% of the patients were correctly classified. Gradient-weighted Class Activation Mapping (*grad cam*), a measure of the network representing the region important to classification prediction⁶, was examined voxel-wise. Figure 2 shows the results obtained by averaging the grad cam for all samples, and setting the threshold to 0.7 and 0.8. We are currently independently evaluating the meaning of the grad cam results with respect to tissue loss or lesions.

To conclude, a self-supervised contrastive learning model was effective in capturing diagnostic brain MRI features from a small cohort of SLE patients with NP symptoms. Using additional image types may help to improve the accuracy of the classification and to better identify brain MRI features useful for NP-SLE diagnosis.

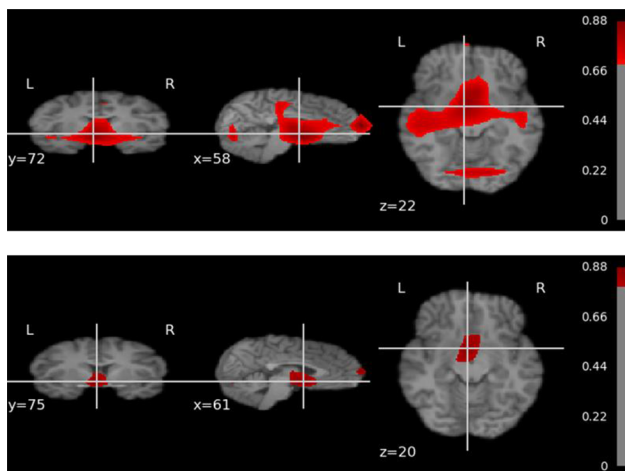


Figure 2. Grad-cam maps, representing regions significant to classification prediction results. Top: threshold set at 0.7; bottom: threshold at 0.8.

References: 1. Magro-Checa C, et al. *Front Med* (2018)
 2. S. Liu et al., *IEEE 11th ISBI*, 2014, pp. 1015–1018
 3. Daniel Durstewitz et al. *Molecular Psychiatry* (2019) 24, 1583–1598
 4. Chen, Ting, et al. (2020) arXiv:2002.05709.
 5. Kiyasseh, et al. (2020) arXiv:2005.13249.
 6. Selvaraju et al., (2019) arXiv:1610.02391v4

L01.08
Outcome Prediction from MR Images after Mild Traumatic Brain Injury via Support Vector Machine: Results from the CENTER-TBI Study

M. Siqueira Pinto¹, S. Winzeck², E. N. Kornaropoulos³, B. Glocker², P. Van Dyck¹, P.-J. Guns⁴, D. K. Menon³, M. M. Correia⁵, V. F. J. Newcombe³

¹Antwerp University Hospital, Radiology Department, Antwerp, Belgium, ²BioMedIA Group, Department of Computing, Imperial College London, London, UK, ³Division of Anaesthesia, Department of Medicine, University of Cambridge, Cambridge, UK, ⁴Physiopharmacology, University of Antwerp, Antwerp, Belgium, ⁵MRC Cognition and Brain Sciences Unit, University of Cambridge, Cambridge, UK

Introduction: Traumatic brain injuries (TBI) are caused by an external force to the head, and have a varied presentation and outcome [1]. Mild TBI (mTBI) cases often recover, but some patients show persistent functional impairment for months. MRI in the acute phase can differentiate patients from controls, and help classify patients with different outcomes [2]. One approach to such classification, used support vector machines (SVM) [3], however, this was with a limited number of subjects. We present results of SVM-based outcome prediction after mTBI based on structural and diffusion MRI from multiple sources, including the large-scale, multi-site CENTER-TBI study [4].

Subjects/Methods: We included 284 mTBI patients (Glasgow Coma Scale: 13–15) with acute MRI (≤ 50 days post-injury) and 97 controls. Patients were dichotomized according to their extended Glasgow Outcome Scale (GOSE) score at six months in a group with good (GOSE=8) and poor (GOSE< 8) outcome. FLAIR, FA and MD maps were non-linearly registered to a common space. Site-specific Z-scores of image intensities were used to train an SVM to predict the outcome between controls, mTBI with good outcome and mTBI with poor outcome. Recursive feature elimination was performed to identify the top 5% most discriminative voxels using 4 folds in a cross-validation workflow. For each image map, the voxels selected for outcome prediction were defined as all the selected voxels along the 4 folds, and were mapped onto anatomy on the JHU ICBM-DTI-81 or Harvard-Oxford sub-/cortical atlas.

Results/Discussion: SVMs performed better when trained on FLAIR or FA than on MD, with FLAIR being superior overall (Tab 1). The SVMs predicted controls vs mTBI with precision of 85% for FA, 70% for MD and 91% for FLAIR, and between good and poor outcome with precision of 75% for FA and FLAIR and 72% for MD. Locating the selected voxels revealed various regions with a high number of predictive voxels, such as the fornix or temporal fusiform cortex (Fig 1 and 2).

	Accuracy	Precision	Recall	F1 Score
FA	77.1 ± 2.9	77.3 ± 2.7	77.1 ± 2.9	76.7 ± 3.1
MD	70.9 ± 7.3	71.7 ± 5.8	70.9 ± 7.3	70.0 ± 7.7
FLAIR	79.0 ± 1.9	79.2 ± 1.6	79.0 ± 1.9	78.7 ± 1.9

Table 1. Performance of Outcome Prediction, Metrics displayed in % as mean ± standard deviation.

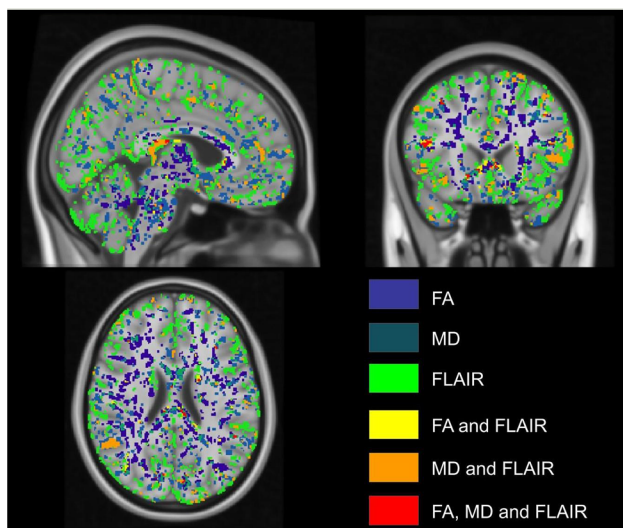


Figure 1. Selected voxels for outcome prediction. Color-coding according to the image modalities from which each voxel was selected. Radiological orientation.

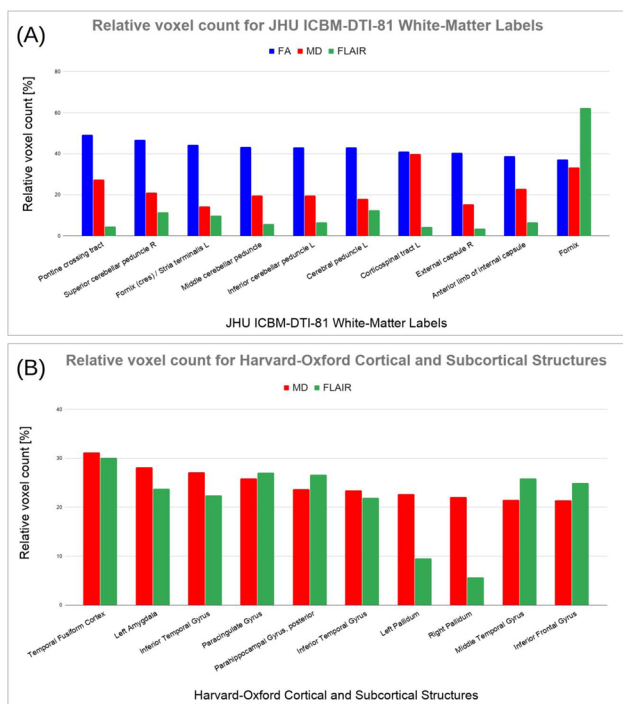


Figure 2. Representation of the relative voxels count for the most relevant white-matter (A), cortical and subcortical regions (B) for the outcome prediction using FA, MD and FLAIR.

FA voxels associated with outcome were predominantly sited in white-matter regions, such as the cerebellar peduncles, while FLAIR voxels were mainly located in cortical areas e.g. parahippocampal gyri. Predictive MD voxels were spread across the whole brain e.g. corticospinal tract or amygdala. Many regions identified using this

approach have been associated with mTBI outcome in previous single site studies [5]. We replicate these findings in a multicenter, multi-sequence study, and demonstrate the potential utility of voxel-wise mTBI diagnosis and outcome prediction using SVM-based approaches.

Research Grants: B-Q MINDED (EU H2020 764513) and CENTER-TBI (EC 602150)

References: 1-Galgano et al., Cell Transplantation. 2017;26(7):1118–1130

2-Vergara et al., Neuroimage Clin. 2018;19:30–37

3-Yuh et al., Journal of Neurotrauma. 2014;31(17):1457–1477

4-Maas et al., Neurosurgery. 2015;76(1):67–80

5-Narayana, Concussion. 2017;2(2):CNC35

L01.09

Prediction of Multiple Sclerosis Disability using Machine Learning Ensemble of Boosting Methods based on structural brain connectivity

B. Barile¹, A. Marzullo², C. Stamile³, F. Durand-Dubief⁴, D. Sappey-Marini⁵

¹Université Claude Bernard Lyon 1, CREATIS (UMR 5220 CNRS & U1206 INSERM), Lyon, France, ²University of Calabria, Department of Mathematics and Computer Science, Rende, Italy, ³R&D Department CGnal, Milan, Italy, ⁴Hôpital Neurologique, Hospices Civils de Lyon, Bron, France, ⁵CERMEP - Imagerie du Vivant, Université de Lyon, Bron, France

Introduction: Multiple Sclerosis (MS) is an inflammatory, demyelinating and neurodegenerative disease that gradually disrupts communication in the central nervous system and leads to an increased disability, measured using the Expanded Disability Status Scale (EDSS) [1]. Based on DTI to extract white matter (WM) fiber-bundles and graph theory to model the structural brain connectivity [2], Machine Learning (ML) techniques can be used for the classification of MS clinical forms [3]. In this study, a meta-model based on a Stacked Generalization approach is proposed for the prediction of patients' disability status [4].

Subjects/Methods: 476 patients distributed in four clinical forms were used in this study: Clinical Isolated Syndrome (CIS), Relapsing-Remitting (RRMS), Secondary-Progressive (SPMS) and Primary-Progressive (PPMS). Disability was assessed by EDSS (median 4, range 0-8). The model proposed is an ensemble of four boosting methods, organized in a meta-model by a Stacked Generalization approach [5] (GBM [6], XGBoost [7], CatBoost [8], LightBoost [9]), where linear regression is used as the higher-level model. In order to evaluate the model performance, a 10-folds cross-validation strategy was used.

Results/Discussion: The proposed meta-model achieved promising levels of accuracy with an average Mean Squared Error (MSE) of 0.95 (± 0.19). The absolute error was obtained for the prediction of the EDSS in patients separated into 3 groups of disability levels and by clinical forms (Fig. 1). The highest error is obtained for the CIS group corresponding to the patients with the lowest disability status. This result is expected since the disability evaluation at the primary stage of MS is highly variable due to the skewness of the EDSS.

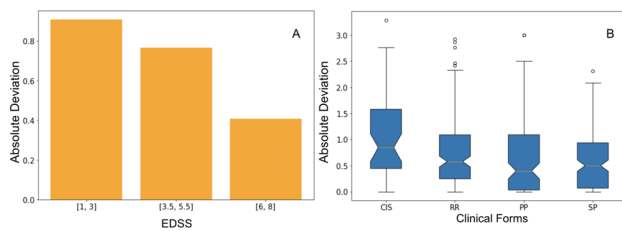
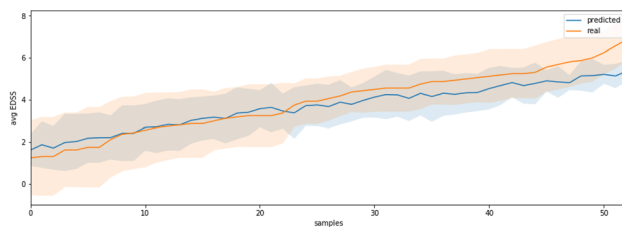


Fig. 1: A - Absolute Deviation between True and Predicted EDSS score by level of disability; B - Absolute Deviation between True and Predicted EDSS score by clinical forms; Absolute deviation between True and Predicted EDSS in MS patients separated in 3 groups of disability level (A) and four clinical forms (B)

Fig. 2 depicts the real and the predicted EDSS score for each patient at different levels of disability. It is possible to notice that the true and predicted line are very closed and the standard deviations almost always overlap.



Comparison between real (orange) and predicted (blue) EDSS score for each sample in the test set.

In this study, an implementation of ML models is developed to predict the MS patient disability based on the global graph representation of structural brain connectivity. These preliminary results demonstrated the feasibility to predict the EDSS score and open interesting perspectives for further clinical applications and future developments to extend the model by incorporating clinical as well as longitudinal information.

- References:** [1] Kurtzke J.F. et al. *Neurology*, 2011;33(11):1444–144
 [2] Rubinov M. et al. *Neuroimage*, 2010;52:1059–1069
 [3] Kocevcar G. et al. *Frontiers in neuroscience*. 2016;10
 [4] Marzullo et al., *IEEE Eng. Med. Biol. Soc.*, 2019
 [5] Wolpert D.H. *Pergamon Press*. 1992; 5: 241–259
 [6] Friedman J.H. *Ann. Statist.* 2001; 5:1189–1232
 [7] Chen T. et al. *SIGKDD*, 2016:785–794
 [8] Veronika A. et al. *arXiv*, 2018.
 [9] Ke G. et al. *ANIPS*, 2017, 30:3146–3154

L01.10

PrognosisAI: Simultaneous segmentation and prediction of genetic status and grade in glioma

S. van der Voort¹, F. Incekar¹, M. Wijnenga¹, G. Lycklama², A. Vincent¹, M. van den Bent¹, W. Niessen¹, M. Smits¹, S. Klein¹

¹Erasmus MC, Rotterdam, The Netherlands, ²Haaglanden MC, The Hague, The Netherlands

Introduction: The rising popularity and easier accessibility of machine learning methods and biomedical imaging data have caused a rapid increase in research on radiological-imaging based prediction methods. Convolutional neural networks (CNNs) have become especially popular for the prediction of genetic markers and tumour segmentation. However, most CNNs use patches instead of the full

MRI scan because of hardware constraints. By using the full scan instead of patches, the network has a larger field of view and location information, which may improve performance. Also, most CNNs perform a single prediction task, for example only segmenting the tumour or predicting a single genetic marker. Alternatively, a multi-task CNN can be used which can replace multiple single-task CNNs and can leverage common information between the different tasks to learn a more general representation. In view of these considerations, we developed a single CNN that takes the full 3D scan as input, automatically segments the tumour, while simultaneously predicting the IDH mutation, 1p/19q codeletion, and tumour grade (grade 2, 3, or 4).

Subjects/Methods: We included 1437 glioma subjects originating from 8 different data sources to develop our method. Subjects were included if pre-operative pre- and post-contrast T1-weighted, T2-weighted, and T2-weighted FLAIR scans were available. Subjects were not excluded based on image quality, radiological findings, or patient characteristics. All scans were registered to an atlas and skull stripped. The image size was $145 \times 181 \times 155$ voxels with a voxel size of 1 mm^3 . We used a UNet¹ inspired network, with the first downsampling block replaced by a strided convolution. Global average pooling (GAP) layers were added at each depth of the downsampling path, concatenated, and then split into three paths and connected to dense layers to predict the genetic tumour status (IDH mutation, 1p/19q codeletion) and grade. The upsampling path of the UNet was used for the segmentation. We tested our method in an independent test set of 236 subjects from the TCGA-LGG and TCGA-GBM data collections, using the same inclusion criteria as for the train set. For the test set, the ground truth labels of the genetic markers and segmentations were obtained from the TCGA and TCIA web sites, respectively.

Results/Discussion: In the independent test set, we achieved an IDH mutation-AUC of 0.90, 1p/19q codeletion-AUC of 0.85, grade-AUC of 0.86 (multi-class) and DICE score of 0.87 (whole tumour). Our model was trained on the largest, most diverse glioma dataset to date and contained scans with different visual appearances from multiple scanners. In conclusion, we have developed a method that can predict multiple genetic markers while simultaneously segmenting the tumour, that generalises well to unseen data.

References: O. Ronneberger et al. “U-net: convolutional networks for biomedical image segmentation” (2015)

L01.11

Relevance Analysis of MRI Sequences for MS Lesion Detection

A.-K. Schnurr¹, M. Schöben¹, I. Hermann¹, R. Schmidt¹, G. Chlebus², L. R. Schad¹, A. Gass³, F. G. Zöllner¹

¹Heidelberg University, Computer Assisted Clinical Medicine - Mannheim Institute for Intelligent Systems in Medicine - Medical Faculty Mannheim, Mannheim, Germany, ²Fraunhofer Institute for Digital Medicine MEVIS, Bremen, Germany, ³Heidelberg University, Department of Neurology, Medical Faculty Mannheim, Mannheim, Germany

Introduction: The benefit of novel MRI sequences can often only be rated subjectively or after a long clinical trial. We employ a layer-wise relevance propagation (LRP) on a convolutional neural network (CNN) for segmentation to rate the relevance of MRI sequences for the detection of multiple sclerosis (MS) white matter lesions.

Subjects/Methods: Sixteen MS patients were examined on a 3T scanner using novel magnetic resonance fingerprinting [1]. Reconstructed T1 and T2* maps were of size 240 × 240 × 60 voxels. Additionally, clinical FLAIR and quantified T2 sequences were acquired and registered to the maps. Parameters for all sequences are listed in Table 1. MS lesions were identified and manually outlined by a trained reader.

	T1 Map	T2* Map	T2 Map	FLAIR
FOV	240x240 mm	240x240 mm	256x256 mm	256x256 mm
matrix size	240x240	240x240	256x256	256x256
# slices	60	60	60	60
slice thickness	2 mm	2 mm	2 mm	2 mm
TE	varying	varying	35,105,187 ms	10 ms
TR	varying	varying	7600 ms	8500 ms
bandwidth	998 Hz/px	998 Hz/px	185 Hz/px	258 Hz/px
flip angle	varying	varying	180°	150°
GRAPPA R	2	2	-	-
partial fourier	5/8	5/8	-	-

Table 1: Parameters for the four MRI sequences. The quantitative T2 maps were reconstructed using a 2 parameter fit.

LRP [2] allows the calculation of voxel-wise contribution to the decision of a CNN and can thus be used to provide interpretability for CNNs. The relevance is computed layer-wise for each neuron starting from the class probability and then propagated to the network input. Analysis of sequence relevances for semantic segmentation using the investigate toolbox [3] has previously been proposed for liver tumor segmentation [4].

We trained a U-Net [5] to segment white matter lesions based on the four given contrasts using 8-Fold-Cross-Validation. A relevance map was then calculated individually for each true positive voxel (correctly detected lesion) and normalized by its sum. Patient maps were then combined by addition. For the sequence comparison each map was normalized to sum up to 1 to make them comparable. The same process was repeated for true negative (correctly classified non-lesion) white matter voxels.

Results/Discussion: The relevance maps resulting from the analysis of the correctly segmented lesions show which adjacent regions influence the detection and the high relevance of the lesion center voxels as can be seen in Fig. 2.

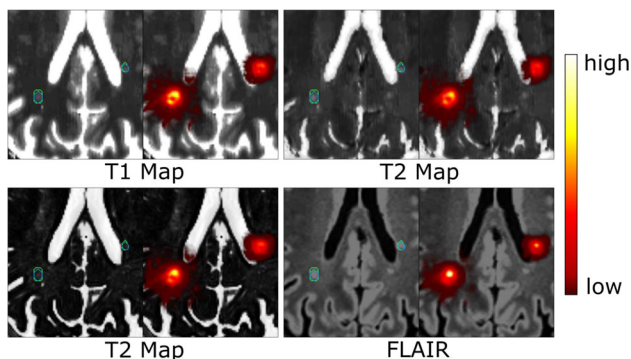


Figure 2: Example of a relevance map for the four contrasts of a correctly detected lesions. Relevance is superimposed on each of the images. The manually annotated lesion boundary is shown in green and the network prediction is shown in yellow.

Fig. 3 shows the sequence relevance distributions for true positives and true negatives. The FLAIR sequence had the significantly ($p < 0.01$, paired t-test) highest relevance for the lesion detection, which is to be expected as it is the clinical gold standard. The networks focused significantly on the T2* map to correctly identify non-lesion voxels. In both cases, the quantitative maps both scored higher relevance than the T2 map images. No sequence had zero relevance.

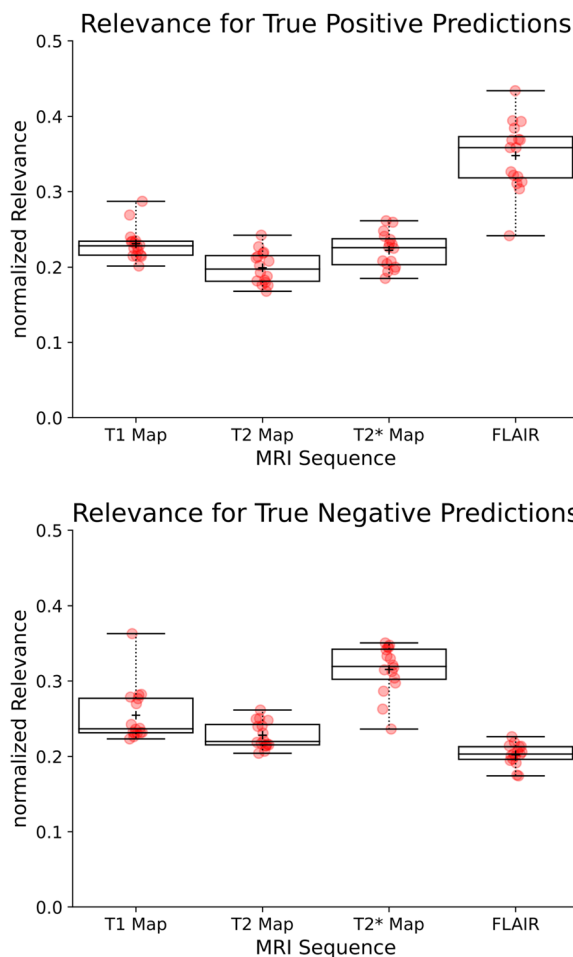


Figure 3: For each sequence the relevance distribution is shown as boxplots (black) and the individual patient values (red).

We can therefore conclude that the quantitative maps provide additional relevant information to the clinical contrasts for the detection of MS lesions. This information can potentially be used to optimized scanning protocols or the selection of sequences for deep learning approaches.

References: [1] B. Rieger et al., *Magn Reson Med* 78, 1724–1733, 2016.

[2] S. Bachet et al. *PLOS ONE* 10(7): e0130140, 2015.

[3] M. Alber et al., *arXiv preprint arXiv:1808.04260*, 2018.

[4] G. Chlebus et al., *In Proc. MIDL*, 2019.

[5] O. Ronneberger et al. *In Proc. MICCAI*, 234–241, 2015.

L01.12

Survival Time Prediction of Brain Tumor Patients by an end-to-end Attention-based multi-task 3D CNN

G. Karami¹, C. Del Gratta¹, M. J. P. van Osch², M. Caulo¹, M. Giussippe Orlando¹, S. Yousefi²

¹Gabriele D’Annunzio University, Department Neuroscience, Imaging, and Clinical Science, Chieti-Pescara, Italy, ²Leiden University Medical Center, Department of Radiology, Leiden, The Netherlands

Introduction: Presurgical prognosis prediction of gliomas is desired in clinical practice for better treatment planning but is still challenging due to variability in interpretation and sampling errors of biopsies. In [1], for this goal, we designed handcrafted features based on clinical knowledge. However, extracting handcrafted features is

time-consuming, biased, and subjective to human interference [2]. Therefore, we propose the use of an attention-based multi-task 3D convolutional neural network (CNN). To the best of our knowledge, this is the first study that deploys an end-to-end CNN for presurgical prognosis prediction. Also, different from previous works, we deploy quantitative imaging data reflecting intra-tumor habitats and tumor microenvironment.

Subjects/Methods: This study includes the neuroimaging and clinical data of 57 brain tumor patients with survival time from 100 to 3500 days. Patients received optimized treatment including surgery to remove most of the tumor. Overall survival was defined as the duration from the date when the patients received surgery. The brain tumor was delineated on T1 post-contrast and T2 images by a neuroradiologist. Two single- and multi-task CNNs were implemented. Features were extracted from T1-Gd, mean diffusivity (MD), and cerebral blood volume (CBV) maps. Fig. 1 shows the structures of the CNNs. The attention block was added to help the network to extract saliency information from deep and coarse layers. Multiple patches of size $64 \times 64 \times 5$ were extracted from each subject in a way that the relative volume of the tumor is similar for all patches. Rotation was applied as an augmentation to prevent overfitting. Cross-entropy was used as the loss function. The output of the network classifies the patients into short (< 1 year) vs. Long (>1 year) survival. The CNN models were implemented with the Tensorflow backend using Keras library in python. Fig. 2 shows the curves of the validation and training loss during training.

Results/Discussion: Table 1 tabulates the results for the proposed method compare to the handcrafted features approach. We achieved an overall accuracy of 64.7% and 68.5% by the single- and multi-task CNNs, respectively. Although the proposed approaches have less accuracy compare to the hand-crafted method (that included also FA and CBF), it could learn useful features from imaging data automatically.

This study demonstrated that CNN is promising for classifying the patients' survival which avoids being subjective, and is able to explore hard to design features. The results showed that multi-task CNN performs better than single-task CNN. The next step of this study is enriching the dataset with additional patients as well as multi-center data to increase the accuracy and applicability.

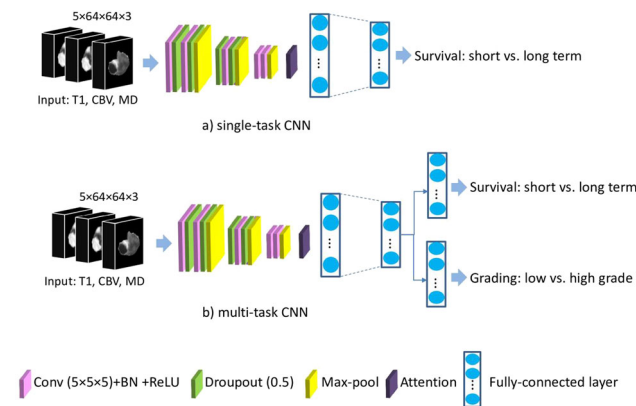


Figure 1- The 3D deep single task multi-channel CNN architecture

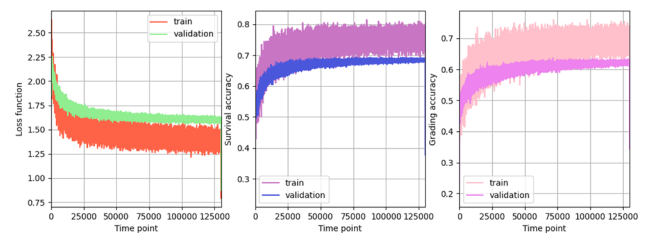


Figure 2- Loss and accuracy plots for the proposed multi-task CNN

Method	Survival accuracy%
Handcrafted classification [2]	86.5
Single-task CNN	64.7
Multi-task CNN	68.5

Table 1- Results

References: [1] Karami et al. ESMRMB, S368, 2019
[2] Nie et al. Scientific reports, 2019

L01.13

Towards Accurate Estimation of Microstructural Properties From Large-scale Light Microscopy Images Using Deep Learning: Validation by Electron Microscopy

L. Mordhorst¹, M. Morozova², S. Papazoglou¹, J. M. Oeschger¹, C. Jäger², H. Rusch³, N. Weiskopf², M. Morawski³, S. Mohammadi¹

¹University Medical Center Hamburg-Eppendorf, Department of Systems Neurosciences, Hamburg, Germany, ²Max Planck Institute for Human Cognitive and Brain Sciences, Department of Neurophysics, Leipzig, Germany, ³Paul Flechsig Institute of Brain Research, University of Leipzig, Leipzig, Germany

Introduction: Recent developments in deep learning (DL)-based 2D histology have enabled the automatic assessment of microstructural properties in WM tissue samples such as the axonal distribution or tissue volume fractions¹. Although large-scale light microscopy (lsLM) has limited capability of resolving small axons, its larger field of view covers 2-3 orders of magnitude more axons than manually labelled electron microscopy (mEM) data²⁻⁵. Thus, lsLM can help validating in-vivo histology using MRI (hMRI)⁶ by providing a more representative ensemble of axons than mEM. Here, we trained a DL-network on lsLM data and tested it against mEM data.

Subjects/Methods: Dataset: Human brain tissue samples from the corpus callosum (CC), the corticospinal tract (CST), and the optic chiasm (OC) were obtained at autopsy. lsLM and EM images were acquired and processed (Table 1).

Purpose	Sample	Images	FoV [mm ²]	Labeled	Modality	Pixel Size [μm/px]	Slice Thickness [μm ²]	Device
Training / Validation	OC	3	0.023	✓	LM	0.11	0.5	Zeiss AxioScan.Z1
	CST	2	0.007					
	CC	4	0.012					
Test (vs LM)	CST	1	0.017					
	CC	2	0.012					
Test (vs EM)	CC	6	2.638 to 9.142	✓	EM	0.0043	0.05	Zeiss EM 912 Omega
	CC	6	0.003 to 0.007					

Table 1: For training and evaluation of the DL algorithm, IsLM subimages were pixel-wisely labeled as axon, myelin or background. Similarly, consecutive EM subsections were annotated to compare microstructural properties estimated from IsLM slices.

Segmentation: Axon instances were segmented using a U-Net⁷ variant (patch size: 512²; batch normalization) and subsequent connected-component labeling (Figure 1).

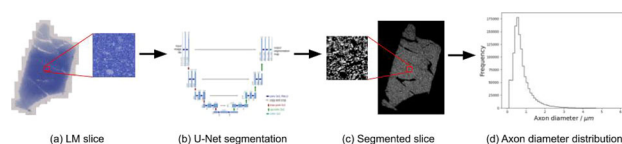


Figure 1: LM (a) segmentation using a U-Net (b). After identification of axon instances through connected-component labeling in the pixel-wise classifications (c), microstructural properties such as the axon diameter distribution (d) were computed.

Preprocessing: Patches were normalized to channel-wise zero mean and unit variance with respect to the training dataset.

Augmentation: Stain augmentation⁸ was applied prior to training (20/sample) and rotation, translation, scaling, flipping, Gaussian blurring, saturation and brightness transformations were employed on-the-fly.

Training and Validation: Adam was used to optimize hyperparameters (network parameters; learning rate and decay) using cross entropy loss. The best model was identified considering mainly the averaged dice score for axon and myelin using 5-fold cross-validation.

Testing: The best model was trained on the full training/validation dataset and tested using segmentation metrics on manually labeled IsLM and comparison of microstructural properties on mLEM data (Table 2).

Results/Discussion:

Sample	Tissue	Mean Diameter [μm] (LM EM)		Axon Volume Fraction (LM EM)		Myelin Volume Fraction (LM EM)		Axon Count (LM EM)	
CC	Anterior Genu	1.05	1.11	0.22	0.27	0.30	0.25	4.7*10 ⁵	1062
CC	Anterior Genu	0.98	0.84	0.21	0.27	0.28	0.30	7.5*10 ⁵	1151
CC	Posterior Genu	1.00	0.95	0.18	0.17	0.27	0.25	6.4*10 ⁵	1058
CC	Isthmus	0.99	0.84	0.18	0.20	0.24	0.30	5.0*10 ⁵	1670
CC	Midbody	0.96	0.81	0.18	0.18	0.28	0.24	4.8*10 ⁵	1054
CC	Splenium	0.76	0.69	0.15	0.19	0.35	0.32	2.1*10 ⁶	1021
Coefficient of Variation (CoV)		0.09		0.12		0.14			
Bias		0.11		-0.11		0.04			

Table 2: Microstructural properties estimated from IsLM images and consecutive mLEM images. Axons were approximated as circles with equivalent areas.

The dice similarity for axon/myelin (0.83/0.73), recall (0.85/0.85), precision (0.80/0.64) and pixel-wise accuracy (0.82), were comparable to the associated metrics of previously applied DL-segmentation algorithms on human large-scale SEM data. Cross-microscopy testing against mLEM revealed that axon diameters were overestimated by about 11%, axonal- and myelin-volume-fractions were under-/over-estimated by -11% and 4%, respectively (CoVs were 9, 11, and 14%, Table 2). Here, we successfully trained a DL-network to segment ~ 5*10⁶ axons in IsLM, which can be used to validate hMRI parameters⁹.

References: 1. Zaimi, A. *et al. Sci. Rep.* 8, 3816 (2018)
 2. Graf von Keyserlingk, D. *et al. Anat. Anz.* 157, 97 (1984)
 3. Aboitiz, F. *et al. Brain Res.* 598, 143 (1992)
 4. Caminiti, R. *et al. Proc. Natl. Acad. Sci. U. S. A.* 106, 19551 (2009)
 5. Liewald, D. *et al. Biol. Cybern.* 108, 541 (2014)
 6. Weiskopf, N. *et al. Curr. Opin. Neurol.* 28, 313 (2015)
 7. Ronneberger, O. *et al. MICCAI* 234 (2015)
 8. Macenko, M. *et al. IEEE Int. Symp. Biomed. Imaging Nano Macro* 1107 (2009)
 9. Mordhorst, L. *et al.*, at this ESMRMB (2020)

L01.14

PNS stimulation studies with broadband pulses up to 12 kHz

D. Grau-Ruiz¹, M. Murbach², E. Pallas³, J. P. Rigla¹, J. Alonso³, A. Rios¹, J. M. Benlloch³

¹Tesoro Imaging SL, Valencia, Spain, ²itis, Zurich, Switzerland, ³Institute for Instrumentation in Molecular Imaging (i3M), Spanish National Research Council (CSIC), Valencia, Spain

Introduction: Peripheral Nerve Stimulation (PNS) due to gradient switching is a main safety limitation in Magnetic Resonance Imaging (MRI). The International Electrotechnical Commission (IEC), in order 60601-2-33, sets out the essential safety and performance requirements for MRI equipment. However, the models used [1, 2] have been verified experimentally only in a very limited range of parameters and configurations. Here we present preliminary PNS simulations and experimental measurements in regimes beyond currently available data.

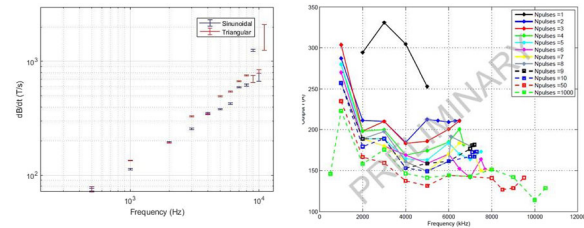
Subjects/Methods: We have designed and manufactured an experimental setup consisting of a coil system ([3]), which can generate both magnetic gradients and homogeneous fields. The system is driven by an IECO GPA-175/400 broadband gradient amplifier, operating from 250 Hz to 12 kHz and generating up to 43.5 mT for the homogeneous configuration.



PNS experimental setup with volunteer forearm

As opposed to previous experiments [2, 4], the broadband character of the amplifier and the load allows for testing magnetic pulses of different time characteristics, rather than just sinusoidal oscillations. In particular, we have exposed 10 healthy volunteers to sinusoidal, triangular and trapezoidal excitations, for different frequencies, pulse train lengths and amplitudes, and determined their PNS thresholds around the wrist/forearm.

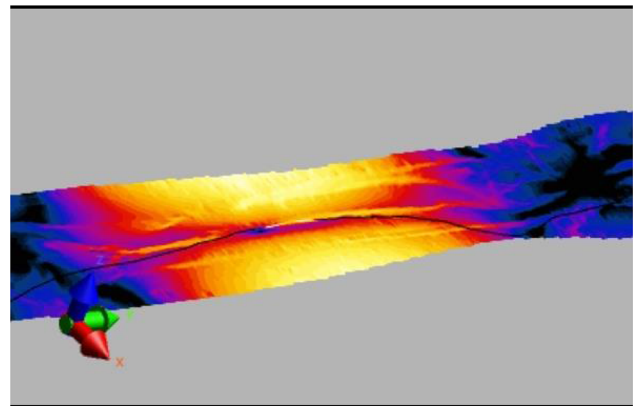
Results/Discussion: The following tests



Left: Average of PNS thresholds for 10 volunteers and triangular and sinusoidal pulse trains (1000 pulses). Right: Threshold dependence on the pulse train length (sinusoidal oscillations).

) have been performed only on 10 subjects and the results are hence still preliminary. The observed PNS threshold dependence on the excitation frequency (left) is compatible with classical models [1], which predict a $1/f$ dependence. Ref. [4], however, discusses potential deviations beyond 100 kHz. Although we have not reached this regime, the measurements in the right plot show that the pulse train length is a critical parameter and should be taken into account in studies of such deviations.

Besides, we have performed simulations of the magnetic and electric field distributions during the experiments, and started to incorporate neural models to benchmark their PNS prediction power.



Electric field generated on the forearm during the waveform at a given instant in time.

References: [1] J.P. Reilly et al., *IEEE Trans BioMed Eng* **12** (1985) 1001–1011.

[2] E.U. Saritas et al., *IEEE Trans Med Imaging* **32** (2013) 1600–1610.

[3] Grau-Ruiz D., Ultra-fast and intense magnetic fields for MRI and Peripheral Nervous System stimulation studies. 36th Annual ESMRMB Scientific Meeting. Rotterdam, October 3rd 2109.

[4] Weinberg, I. N. et al. *Medical physics*, 39(5), (2012) 2578–2583.

L01.15

The effect of PGH synthetase inhibitors on the intensity of BOLD signal and glutamate metabolism in the brain visual cortex during video stimulation. Functional MRI

M. Ublinskiy¹, A. Manzhurtsev², A. Yakovlev², N. Semenova², T. Akhadov²

¹Clinical and Research Institute of Urgent Pediatric Surgery and Trauma, Radiology, Moscow, Russian Federation, ²Clinical and Research Institute of Emergency Pediatric Surgery and Trauma, Radiology, Moscow, Russian Federation

Introduction: Aim of this study is to investigate the mechanisms of action of anti-inflammatory non-steroid drugs on the regulation of local cerebral blood flow during neuroactivation. It is proposed in vivo to reveal the participation of astrocytes in the formation of a hemodynamic response to a stimulus (BOLD effect) in the human brain by evaluating the effect of inhibitors of the synthesis of arachidonic acid derivatives (AA) on the intensity of the BOLD (blood oxygen level dependent) signal in the visual cortex of a human brain during video stimulation.

We propose to inhibit the prostaglandin synthesis enzyme—PGH synthetase, inactivate the formation of vasodilators synthesized by astrocytes and measure the intensity of BOLD in the visual cortex during neuroactivation before and after inhibition of PGH synthetase.

Subjects/Methods: fMRI study for each participant consisted of several stages: 1) conducting fMRI studies several times (to determine the adaptation effect of brain structures to video stimulation (determination of brain areas with change of BOLD intensity after repetition of video stimulation); 2) the inhibition of PGH synthetase by consuming an adequate dose of acetylsalicylic acid; 3) repeated fMRI study in an hour to determine the effect of the inhibitor. All fMRI data were processed in the Statistical Parametric Mapping (SPM) software package.

An intergroup analysis (before/after pill) was estimated using paired t-test in SPM package.

Results/Discussion: All participants showed significant fMRI activation in area of visual cortex.

However, we didn't reveal any changes in BOLD intensity in this area after pill. We found increases ($p < 0,1$) of BOLD signal after PGH-synthetase inhibition in following brain areas: left and right thalamus, left and right precentral gyrus, left postcentral gyrus, left inferior parietal lobule, right superior frontal gyrus, left putamen, left pallidum.

Among the above areas, we identified those, which are not marked in the adaptation effect: left and right thalamus.

References: As it is widely known, thalamus believed to act as a hub, relaying information between different subcortical areas and the cerebral cortex. That's why the changes we have discovered may indicate violations in transmission of visual information in human brain during the inhibition of one of the main ways of vasodilation. The obtained result will have not only fundamental, but also practical significance, since BOLD indirectly characterizes neural activity. So observed changes are very important for understanding of biological functions regulation in normal and pathological conditions.

L01.16

Characterisation of the Multiple Sclerosis Drug Siponimod for Fluorine 19 MRI

C. Prinz¹, F. Sherazi¹, L. Starke¹, P. Ramos Delgado¹, A. Kuehne², T. Niendorf¹, S. Waiczies¹

¹Max Delbrück Center for Molecular Medicine in the Helmholtz Association, Berlin Ultrahigh Field Facility (B.U.F.F.), Berlin, Germany, ²MRI.TOOLS GmbH, Berlin, Germany

Introduction: Siponimod is a trifluorinated anti-inflammatory drug indicated for multiple sclerosis¹ that has the potential to be monitored by fluorine-19 (¹⁹F) MR techniques² to support therapeutic decisions. In this study, we investigated the ¹⁹F MR properties of siponimod and its dependency on environmental factors for achieving best SNR efficiency *in vivo*.

Subjects/Methods: Phantoms were prepared in 2ml syringes. Siponimod (Sigma) was dissolved in DMSO and human serum to model an *in vivo* situation, and measured at both 20°C (RT) and 37°C. MR experiments were performed on a 9.4T MR scanner (Bruker Biospec) using a dual-tunable ¹⁹F/¹H mouse head RF coil³. Global

single pulse MR spectroscopy was used for ¹⁹F signal detection and T₁ measurements. A CPMG sequence was used for measuring T₂. T₁ mapping was performed using a saturation based RARE technique and T₂ mapping using a multi-slice multi-echo technique. We optimized RARE⁴, FLASH⁴, UTE⁴ and bSSFP⁵ sequences to compare SNR efficiencies (SNR/√time) for imaging siponimod in DMSO and in serum. Image processing and spectral analysis were performed in MATLAB R2018a and using ImageJ⁶.

Results/Discussion: Siponimod showed a single peak ¹⁹F MR spectrum. We found a temperature dependence of the T₁ and T₂ relaxation times and identified a T₂-drop by more than one order of magnitude in the presence of human serum which might be related to the environmental change.

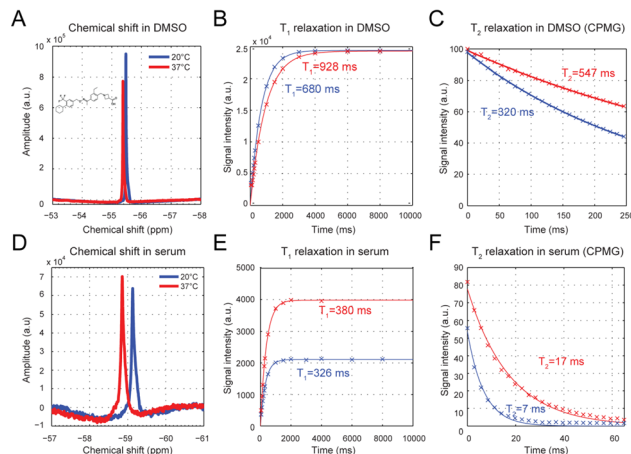


Figure 1. Characterisation of the ¹⁹F MR properties (MR Spectrum, T₁, T₂) of siponimod dissolved in DMSO (A-C) and serum (D-F), at RT (blue) and at 37°C (red)

We identified UTE as the most SNR-efficient MR pulse sequence to study siponimod *in vivo* and demonstrate the necessity of investigating MR properties under physiological conditions.

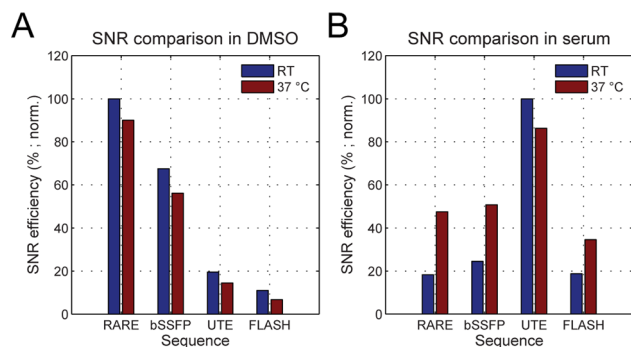


Figure 2. Comparison of the SNR efficiencies of different optimized sequences for imaging siponimod dissolved in DMSO (A) and in human serum (B), at RT (blue) and at 37°C (red)

The goal of ¹⁹F MR detection is to enable ¹⁹F MR imaging of low drug concentrations in different tissues for non-invasively informing clinical studies and aiding patient-tailored drug dose modifications.

Acknowledgements

This study is funded by Novartis as well as the Deutsche Forschungsgemeinschaft to S.W. (DFG-WA2804)

- References:** 1. Rommer, P. S. et al. *Front Immunol* (2019)
 2. Reid, D. G. & Murphy, P. S. *Drug discovery today* (2008)
 3. Waiczies, H. et al. *Scientific reports* (2013)
 4. Faber, C. & Schmid, F. in *Fluorine Magnetic Resonance Imaging* (2016)
 5. Scheffler, K. & Lehnardt, S. *European radiology* (2003)

6. Schindelin, J. et al. Nature methods (2012)
7. Prinz, C. et al. Magnetic Resonance Materials in Physics, Biology and Medicine (2018)
8. Waiczies, S. et al. Scientific reports (2017).
9. Waiczies, S. et al. Magnetic Resonance Materials in Physics, Biology and Medicine (2018)

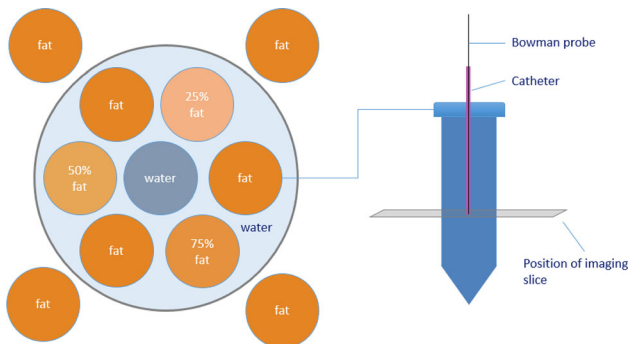
L01.17

Comparative study of different Gradient-Echo sequences for PRFS MR Thermometry

T. Feddersen¹, S. Curto², D. Poot³, K. Sumser², G. van Rhoon², M. Paulides⁴, J. Hernandez Tamames³

¹Erasmus MC, Department of Radiology and Nuclear Medicine & Department of Radiation Oncology, Rotterdam, The Netherlands, ²Erasmus MC, Department of Radiation Oncology, Rotterdam, The Netherlands, ³Erasmus MC, Department of Radiology and Nuclear Medicine, Rotterdam, The Netherlands, ⁴Eindhoven University of Technology, Department of Electrical Engineering, Eindhoven, The Netherlands

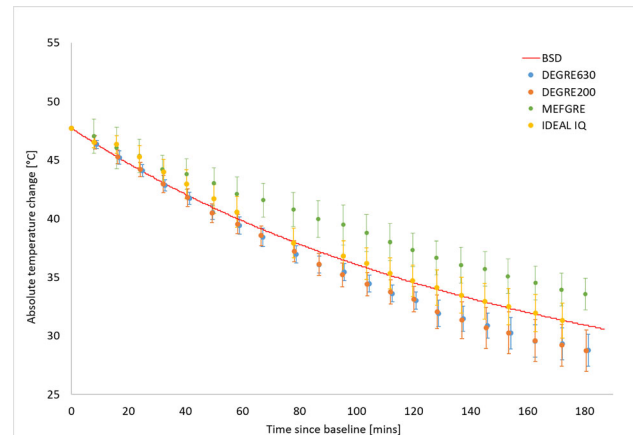
Introduction: MR thermometry (MRT) provides a non-invasive way to assess the temperature distribution during thermal therapies and provides crucial input for both dosimetry and treatment optimization. In the clinic, gradient echo (GRE) sequences are used but thermometry takes long (> 1 min) and stable and accurate MRT (< 0.5 °C) for the 60–90 min treatment is currently not available for most tumor sites. We compared different gradient echo sequences for PRFS MR thermometry on a 1.5T GE scanner (Signa MR450, GE Healthcare). **Subjects/Methods:**



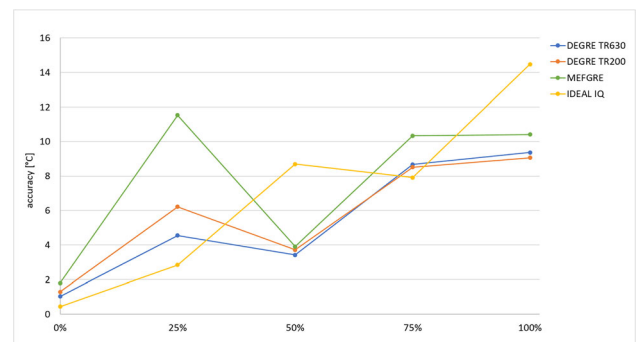
Schematic of the phantom.

The MR sequence used during clinical thermal treatments, DEGRE [1], was assessed for its MRT performance and compared against standard ME-FGRE [2] and the novel IDEAL IQ sequence [3] in a cooling-down experiment, covering a range of 51–30 °C. The protocols were tested in an in-house developed phantom contains vials of different fat percentages (0, 25, 50, 75, 100%) and their performance was compared to thermistor probe measurements. The temperature changes were calculated for a ROI near the tip of the probe in each vial. For DEGRE, phases were directly subtracted from the baseline measurement. For the ME-FGRE and IDEAL IQ measurements, a water+multipeak fat model was fitted to obtain both water&fat maps and offresonance frequency [4]. Temperature change was obtained from the change in offresonance frequency after applying drift correction using the fatmap differences. By comparing the MRT measurements to the temperature measured by the thermistor probes, accuracy, precision and bias of each sequence for the different fat percentages was established.

Results/Discussion:



Temperature change in the water vial measured with the MRT sequences as well as the ground truth thermistor probe measurement. The error bars result from the s.d. in the selected ROI of the temperature map.



MRT accuracy for different fat percentages for different thermometry methods. An overall decrease in accuracy with increase in fat percentages can be observed.

Figure 2 shows the MRT changes measured during cooling down and the temperature from the thermistor probe for the vial filled with water only. The average of MRT accuracy in different fat percentages are summarized in Figure 3. In water IDEAL IQ achieved the highest accuracy (< 0.5°C) when averaged over all measured temperatures. When shortening TR, DEGREs accuracy is identical despite the big improvement in scan time. All MRT methods are performing consistently worse when measuring in higher fat percentages. We found the performance of the IDEAL IQ sequence very promising in its application for MRT. Hence, we consider that there is untapped potential in already available sequences for their application in MR temperature mapping.

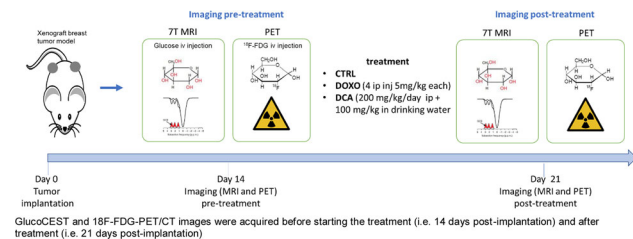
References: [1] Gellermann, J., et al. “Comparison of MR-thermography and planning calculations in phantoms.” (2006)
 [2] Todd, Nick, et al. “In vivo evaluation of multi-echo hybrid PRF/T1 approach for temperature monitoring during breast MR-guided focused ultrasound surgery treatments.” (2014)
 [3] Yu, Huanzhou, et al. “Combination of complex-based and magnitude based multiecho water fat separation for accurate quantification of fat-fraction.” (2011)
 [4] Salim, G., “Multipeak multiecho modeling for improved PRF-based thermometry”, ESMRMB 2015.

L01.18**Comparison between GlucoCEST MRI and ¹⁸F-FDG PET in monitoring therapy response in murine breast cancer 4T1 models**

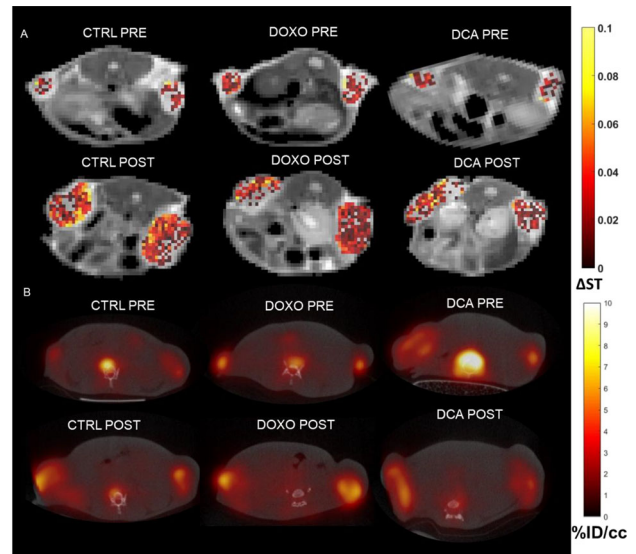
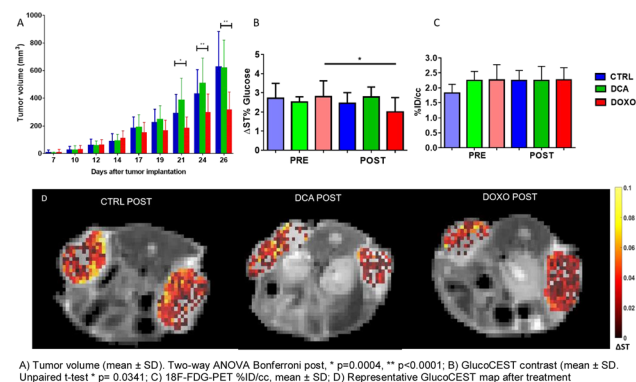
M. Capozza¹, A. Anemone², M. Della Peruta¹, S. Zullino², D. Villano², C. Dhakan³, E. Terreno², S. Aime², D. Longo³

¹University of Turin, Collettero Giacosa, Italy, ²University of Turin, Turin, Italy, ³Italian National Research Council (CNR), Turin, Italy

Introduction: New approaches for the early monitoring of treatment response are needed for the selection of the optimal therapeutic strategy in cancer patients. Sequential ¹⁸F-FDG-PET/CT acquisitions are the gold standard at clinical level for assessing early response as a decrease of tumor metabolic activity in several tumors¹. GlucoCEST MRI relies on the use of unlabelled D-glucose and it may be applied on ordinary MRI scanners available at research and clinical settings. It has been proposed as an alternative to the radiolabelled FDG. This work aims at validating the potential of MRI-GlucoCEST methodology in monitoring the response to two different treatment regimens based on doxorubicin (DOXO) and dichloroacetate (DCA) in breast tumor (4T1) bearing mice.

Subjects/Methods:

Balb/C female mice (n= 12 for each group) were inoculated with 4×10^4 4T1 murine breast cancer cells at both mice flanks. The two therapeutic treatments were based on DOXO³ (dose 5 mg/kg, 4 ip in 1 week) and on DCA⁴ (ip 200 mg/kg/day + 100 mg/kg water ad libitum). GlucoCEST MR images of control and treated groups were acquired before and after 1-week of treatment and compared with the analogous groups undergone to the ¹⁸F-FDG-PET/CT imaging. CEST protocol was performed on a Bruker 7T MRI scanner. Z-spectra before and after glucose (3g/kg) iv injection were acquired and CEST contrast was calculated between POST and PRE images. For PET, animals were fasted overnight before the iv ¹⁸F-FDG injection (5.48 ± 0.19 MBq/mouse). PET static acquisition was performed for 30 minutes starting 45 minutes after ¹⁸F-FDG administration.

Results/Discussion:

A) Representative GlucoCEST map overlaid on the anatomical image after i.v. injection of D-glucose (3 g/kg); B) Representative fused PET/CT axial view images after ¹⁸F-FDG injection (5.48 ± 0.19 MBq/mouse)

Doxo treated mice showed a marked decrease in tumor growth, being statistically significant from day 21 (after the last doxorubicin treatment), compared to the control group (Figure 1A). The FDG-PET technique showed no difference in mean %ID/cc values between the control and the treated groups (Figure 1C). Conversely, the calculated average GlucoCEST values between pre- and post-treatment highlighted a significant decrease of the metabolic activity (Figure 1B and D). When mice were treated with DCA any difference was observed in the tumor growth rates between the two groups. Both glucoCEST MRI and ¹⁸F-FDG PET did not observe any difference in glucose uptake between the treated and control groups following DCA treatment

In conclusion, for assessing the response to doxorubicin treated mice, GlucoCEST MRI appears more sensitive than ¹⁸F-FDG-PET in reporting the therapy response. These findings suggest that glucoCEST may be a sensitive technique in monitoring therapeutic effects but more work appears necessary to identify cancer types and specific treatments where the methodology can be effective.

References: 1. Avril S, *J Nucl Med.* 2016;57 Suppl 1:34S–39S.

2. van Zijl PC, *Magn Reson Med.* 2011;65:927–948.

3. Thorn CF. *Pharmacogenet Genomics.* 2011;21:440–446.

4. Kankotia S, *Biochim Biophys Acta.* 2014;1846:617–629.

L01.19**Guidewire Tracking Based on Passive MRI Markers for MR-Guided Endovascular Interventions**

D. C. Hoinkiss¹, H. Nijsink², P. Borm³, T. Hussain⁴, J. Greer⁴, S. Haase¹, J. Futterer², T. Pätz¹

¹Fraunhofer MEVIS, Bremen, Germany, ²Radboud University Medical Centre (Radboudumc), Nijmegen, The Netherlands, ³Nano4imaging GmbH, Aachen, Germany, ⁴UT Southwestern Medical Center, Dallas, USA

Introduction: Percutaneous Transluminal Angioplasty (PTA) is commonly performed under X-ray guidance [1-2]. MR-guidance, however, would allow this widely distributed therapy to be performed without radiation. To support this, we present a guidewire tracking functionality that allows monitoring of the guidewire position during intervention.

Subjects/Methods: For monitoring, we use a fast gradient echo sequence acquiring three parallel slices at ~ 2 Hz frame rate (TE/TR 1.7ms/3.4ms). The guidewire is equipped with distinct markers (Nano4Imaging GmbH, Germany) that produce negative MR artefacts. Marker position and concentration (iron oxide nanoparticles) are shown in Fig. 1.

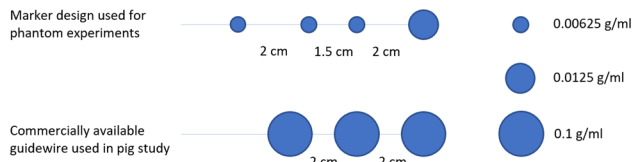


Figure 1: Guidewire design used for the performed experiments in MRI phantoms (top) and a pig study (bottom).

The tracking algorithm is shown in Fig. 2. A distinct front marker is used to locate the wire tip by utilizing Circle Hough Transforms with segmentation based on Connected Components. The search radius is then limited to represent the guidewire geometry before segmenting the smaller markers. Detected marker candidates are used to iteratively reconstruct the guidewire based on the angle between consecutive markers and the distances between markers (one-dimensional registration with a reference wire). Multimodal rigid image registration is used to align the images of the monitoring MRI sequence with a previously acquired volume scan.

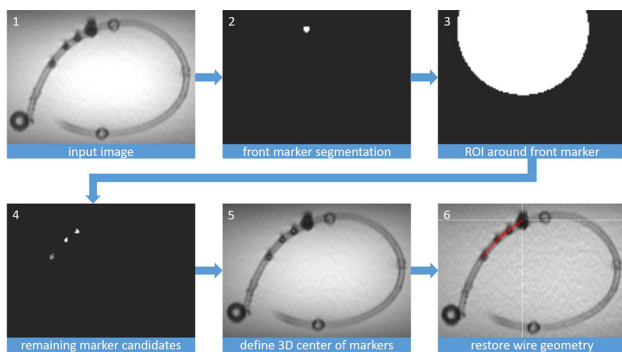


Figure 2: Overview of the wire reconstruction: (1) input image, (2) front marker segmentation, (3) limit search radius for subsequent algorithms, (4) segmentation of remaining markers, (5) define centers of gravity and (6) find best approximation.

Tracking performance was evaluated retrospectively using four different datasets; two phantom measurements mimicking vessels with different complexity (235 and 499 timepoints, three slices) and two time-series of a pig study, performed at the UT Southwestern Dallas (37 and 136 timepoints, single slice) using a commercially available guidewire with 3 equal markers at the tip (EmeryGlide, Nano4Imaging). Evaluation of image registration accuracy was conducted using in vivo datasets of the upper leg arteries with deliberate subject motion.

Results/Discussion: Fig. 3 shows the reconstructed guidewire in all four datasets, exemplary for a single slice and timepoint. Overall performance showed 98.1 % detection rate in phantom data with 0.4 % false positives; and 88.6 % detection rate with 1.1 % false positives in the animal datasets, only considering timepoints in which all markers were visible. The image registration decreased misalignments due to motion by 40 %, estimated by the Euclidean distances between manually annotated landmarks.

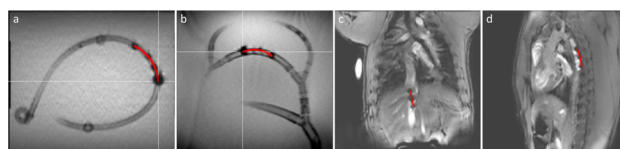


Figure 3: Image datasets used for validation of the wire tracking algorithms: (a, b) MRI phantoms mimicking vessel structures with different complexity and (c, d) animal (pig) data in two orientations.

We presented a tracking workflow able to detect passive MRI markers in a monitoring MRI sequence with high accuracy. It can ultimately be used to adjust the imaging slice during interventions to follow endovascular devices. This will enable more precise device positioning during MR-guided PTA, eliminating harmful ionizing radiation.

References: [1] Chambers et al. JACC; 2015;8:628–30.

[2] Picano et al. BioMed Central; 2011;9:35.

Acknowledgements: Funding from the Eurostars-2 joint programme with co-funding from the EU Horizon 2020 research and innovation programme (Eurostars E! 11263 - SPECTRE)

L01.20

The effect of glyceic control on renal triglyceride content assessed by proton-spectroscopy in patients with type 2 diabetes mellitus: a single-center parallel-group trial

I. Dekkers^{1, 2}, M. Bizino³, E. Paiman³, J. Smit⁴, I. Jazet⁵, A. de Vries⁶, H. Lamb²

¹Leiden University Medical Center, Radiology, Voorburg, The Netherlands, ²Leiden University Medical Center, Radiology, Leiden, The Netherlands, ³Leiden University Medical Center, Leiden, The Netherlands, ⁴Radboud University Medical Center, Internal Medicine, Nijmegen, The Netherlands, ⁵Leiden University Medical Center, Endocrinology, Leiden, The Netherlands, ⁶Leiden University Medical Center, Nephrology and Transplant Medicine, Leiden, The Netherlands

Introduction: Renal steatosis is a potential driver of diabetic kidney disease, and tight glyceic control can reduce risk of diabetic nephropathy. Recent technical developments have enabled non-invasive measurement of renal triglyceride content (RTGC) using Magnetic resonance spectroscopy (¹H-MRS)^{1,2}. In this clinical trial we assessed whether glyceic control influences RTGC measured by ¹H-MRS. Furthermore, we compared the treatment effects of GLP-1 receptor agonist liraglutide versus standard glucose-lowering therapy on RTGC.

Subjects/Methods:

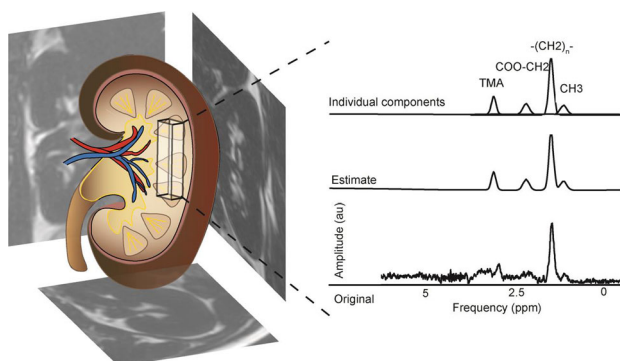


Figure 1: Planning of single voxel ¹H-MRS in the kidney (left), and corresponding spectra with methylene $-(CH_2)-$ and methyl CH_3 peak (right).

In this single-center parallel-group trial T2DM patients were randomized to liraglutide or placebo added to standard care (metformin/sulfonylurea-derivative/insulin). Change in RTGC after 26 weeks of glycemic control measured by proton-spectroscopy and difference in RTGC between treatment groups was analyzed.

All participants underwent baseline and follow-up MRI and ¹H-MRS using a 3T MR system (Philips Medical Systems, Best, the The Netherlands). Single voxel Point Resolved Spectroscopy (PRESS) unsuppressed spectra (ET 40ms; unsuppressed TR 8s; averages 8) and suppressed spectra using Multiply Optimized Insensitive Suppression Train (MOIST) (TE 40 ms; TR 3s; NSA 64) were acquired. Spectra were acquired during free-breathing at end-expiration with pencil beam navigator-based respiratory triggering.

Results/Discussion:

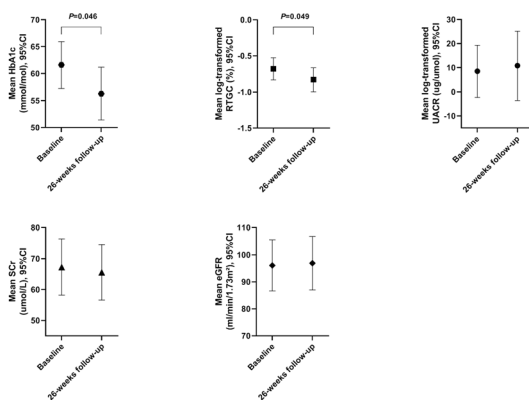


Figure 2. Treatment effect of glycemic control on Glycated haemoglobin A1c (HbA1c), renal triglyceride content (RTGC), urine-albumin-creatinine ratio (UACR), serum creatinine (SCR), and estimated glomerular filtration rate (eGFR) irrespective of rand

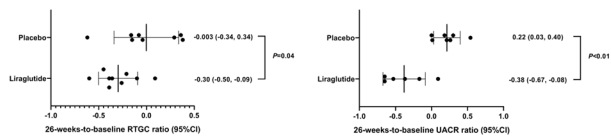


Figure 3. Treatment effect of liraglutide (n=9) versus placebo (n=8) on renal triglyceride content (RTGC) and urinary albumin-creatinine ratio (UACR).

Fifty T2DM patients were included in the baseline analysis (mean age of 56.5 ± 9.1 years; range 33–73 years; 46% males). Seventeen patients had baseline and follow-up measurements. Mean HbA1c was 61.6 ± 8.4 mmol/mol, which changed to 56.3 ± 9.5 mmol/mol after 26-weeks of glycemic control irrespective of treatment group ($p = 0.046$). Log-transformed RTGC was $-0.68 \pm 0.30\%$, and changed to $-0.83 \pm 0.32\%$ after 26-weeks of glycemic control irrespective of treatment group ($p = 0.049$). 26-weeks -to -baseline RTGC ratio (95%CI) was significantly different between liraglutide (-0.30

$[-0.50, -0.09]$) and placebo added to standard care ($-0.003 [-0.34, 0.34]$) ($P = 0.04$).

In conclusion, in this exploratory study we found that twenty-six weeks of glycemic control resulted in lower RTGC, in particular for liraglutide, however larger clinical studies are needed to assess whether these changes reflect a true effect of glycemic control on renal steatosis.

References: 1. Dekkers IA, de Heer P, Bizino MB, de Vries APJ, Lamb HJ. ¹H-MRS for the assessment of renal triglyceride content in humans at 3T: A primer and reproducibility study. *J Magn Reson Imaging*. 2018;48(2):507-513. doi:10.1002/jmri.26003
2. Jonker JT, de Heer P, Engelse MA, et al. Metabolic imaging of fatty kidney in diabetes: validation and dietary intervention. *Nephrol Dial Transplant*. 2018;33(2):224-230. doi:10.1093/ndt/gfx243

L01.21

Gadolinium retention in a Multiple Sclerosis murine model

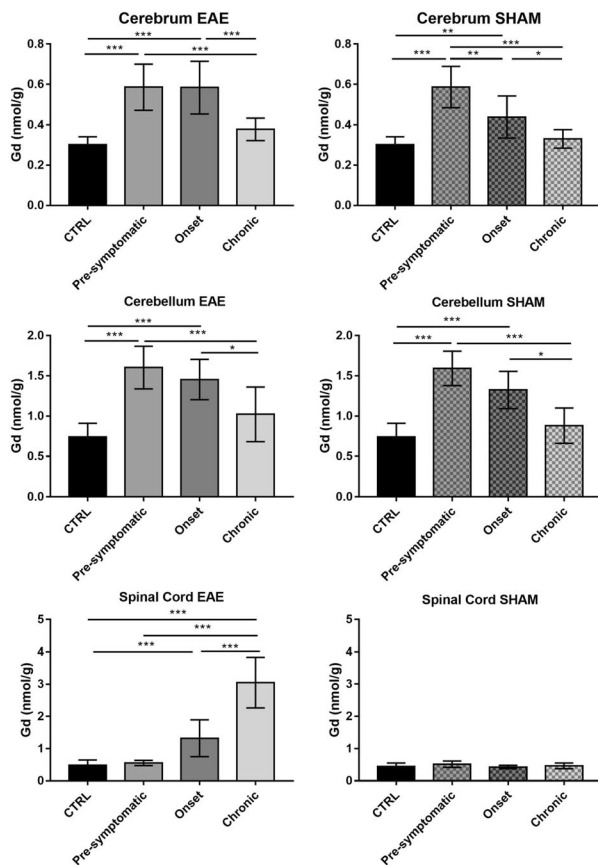
C. Furlan¹, E. Di Gregorio¹, S. Atlante¹, F. Montarolo², R. Parolisi³, A. Buffo³, A. Bertolotto⁴, S. Aime¹, E. Gianolio¹

¹University of Turin, Department of Molecular Biotechnology and Health Sciences, Torino, Italy, ²Neuroscience Institute Cavalieri Ottolenghi (NICO), Orbassano, Italy, ³University of Turin, Department of Neuroscience Rita Levi Montalcini, Torino, Italy, ⁴Neurobiology Unit, Neurology – CreSM (Regional Referring Center of Multiple Sclerosis), AOU San Luigi Gonzaga, Orbassano, Italy

Introduction: MRI is an important tool in the diagnosis of Multiple sclerosis (MS) as well as in the monitoring of disease. MS is an autoimmune inflammatory disease in which immune cells infiltrate the central nervous system (CNS) parenchyma leading demyelination. In MS, blood-brain barrier (BBB) permeability is detected as parenchymal leakage of gadolinium (Gd) based contrast agents (GBCA), thus enhanced MRI is commonly used for diagnostic purposes and MS patients are commonly exposed to multiple lifetime doses within routine clinical care.¹ Herein, our purpose is to quantitatively investigate, at the preclinical level, the issue of Gd retention in the CNS of immune-mediated murine models of MS, Experimental Autoimmune Encephalomyelitis (EAE), compared to control animals.²

Subjects/Methods: EAE was induced in C57BL/6 female mice. Mice were then administered intravenously with three doses (1.2 mmol/kg each) of Gadodiamide and sacrificed after 21 or 40 days. To evaluate the Gd retention during the different phases of the EAE, the Gd injections were performed at three different time points: in the pre-symptomatic, the onset and the chronic phases of the disease development. Two groups of mice were included in the study as control groups: C57BL/6 sham-immunized mice (SHAM) representing the inflammatory not-demyelinated group, and not-treated healthy mice (NT). After sacrifice, cerebrum, cerebellum and spinal cord was collected, mineralized and the amount of Gd was quantified through ICP-MS.

Results/Discussion:



Amounts of retained gadolinium in cerebrum, cerebellum and spinal cord of EAE (left) and Sham (right) mice administered with three doses of gadodiamide in pre-symptomatic, onset and chronic phases.

The Gd retention in cerebrum and cerebellum showed an analogous behavior in EAE and SHAM mice. Specifically, for both experimental groups, a significantly higher retention of Gd was observed with respect to NT mice when animals were injected with the GBCA in the pre-symptomatic phase and in the onset of the disease course. This results suggest that Gd retention in brain is influenced by the demyelinating process and the inflammatory state occurring in both EAE and in SHAM mice.

Conversely, a completely different retention behavior between EAE and SHAM mice was observed in the spinal cord. While in the SHAM group, the Gd retention is not significantly different from that of NT mice for GBCA injection, in EAE group a significantly higher and progressive accumulation of Gd is detected. A marked decrease in Gd retention is observed in the spinal cord of EAE mice 40 days after GBCA injection, indicating an efficient washout mechanism.

The detection of significant amounts of Gd in the damaged nervous system of EAE mice demonstrated that the metal is able to cross the BBB; this behavior is better observed in the spinal cord, where, in this animal model, the demyelinating plaques are localized.

References: 1. E. Di Gregorio, G. Ferrauto, C. Furlan, S. Lanzardo, R. Nuzzi, E. Gianolio and S. Aime Invest. Radiol. 2018, 53, 167-172. 2. Montarolo F, Perga S, Martire S, Bertolotto Inflamm Res. 2015;64(11):841-844.

L01.22

Helping hands for anti-PD-1 immunotherapy monitoring: an oscillatory pattern sampled by MRSI could act as immune system efficiency biomarker

S. Wu¹, P. Calero-Pérez¹, C. Arús¹, A. P. Candiota²

¹Universitat Autònoma de Barcelona (UAB), Department of Biochemistry and Molecular Biology, Cerdanyola Del Valles, Spain, ²Centro de Investigación Biomédica en Red en Bioingeniería, Biomateriales y Nanomedicina (CIBER-BBN), Cerdanyola Del Valles, Spain

Introduction: Glioblastomas (GB) are malignant brain tumours with poor prognosis even after aggressive therapy. Programmed cell death-1 (PD-1) immune checkpoint blockade is a promising strategy in many types of cancer, but therapeutic effects in GB remain low and associated with immune infiltration (1). In previous work (2), an oscillatory pattern of response sampled by MRSI-based nosological images was found after temozolomide (TMZ) administration in an Immune-Enhancing Metronomic Schedule (IMS). Experimental data suggest this oscillation could act as a biomarker of immune system attack onto GB. The presence of oscillations with other monotherapies such as anti-PD-1 would reinforce its monitoring potential.

Subjects/Methods: GL261 GB tumours were induced in C57BL/6j mice and divided into two groups. The anti-PD-1/ TMZ combined therapy group (n=7) received TMZ 60 mg/kg as in (2) and anti-PD-1 100 µg /dose (as in (3)) with IMS (every 6d) from day 11 post-implantation (p.i.). In the anti-PD-1 monotherapy group (n=5), anti-PD-1 was administered from day 6 p.i. (500 µg/dose) followed by repeated injections (250 µg/dose) with IMS (adapted from (4)). Mice were analysed by multi-slice 3D MRSI and/or MRI every two days. Nosological maps (5) and tumour responding index (TRI) (6) were calculated.

Results/Discussion: TRI oscillation (9 ± 1.4 days, n = 2) was observed in both groups. After therapy administration, TRI increased from near-zero to high values (85.3 ± 11.0 %, n = 2) and decayed two days after the TRI peak, while tumour volume decreased, probably due to immune system attack (figure 1). Such decrease prevented assessment of further TRI cycles. Animals in the combination therapy group survived 178 ± 76 days, while with anti-PD-1 monotherapy survived 146 ± 113 days. Although average survival is not significantly different from IMS-TMZ in the same time frame (163 ± 103 days) (2), the cured rate changed from 61.5 % in IMS-TMZ to 60% in IMS-anti-PD-1 and 100% in IMS-TMZ/anti-PD-1 therapy. Moreover, several cured mice presented immune memory upon re-challenge (100% in IMS-anti-PD-1 and 50% in IMS-TMZ/anti-PD-1 therapy). Preliminary TRI oscillation frequency seems slightly longer than in (2,6). Such oscillations could be at least partially due to local metabolic changes resulting from immune system action (2). Moreover, with anti-PD-1 monotherapy, the observed pattern changes should be essentially due to the action of the host immune system alone, without the confounding effect of chemotherapy. The oscillation mode reinforces the translational potential of the MRSI-based biomarker for patient-tailored GB therapy, including immunotherapy.

References: 1. Zhao J et al Nat Med. 2019;25:462–9. 2. Wu S et al NMR Biomed. 2020;e4229. 3. Garg A D et al Oncoimmunology. 2017;6:e1295903. 4. Reardon D A et al Cancer immunol res. 2016;4:124-35. 5. Delgado-Goñi T et al NMR Biomed. 2016;29:732–43. 6. Arias-Ramos N et al Metabolites. 2017;7:20.

L01.23

Neurodegenerative changes in the brain of Alzheimer’s mice model investigated by high-field 1H-31P MRS and segmentation on high-resolution MRI

C.-H. Yoo¹, H.-M. Baek², B.-Y. Choe¹

¹The Catholic University of Korea, Seoul, SOUTH KOREA, ²Gachon University, Department of Health Sciences and Technology, Incheon, SOUTH KOREA

Introduction: The aim of this study was to investigate morphological and metabolic changes in the brain of model mice with Alzheimer’s disease (AD) by using combined 1H-31P magnetic resonance spectroscopy (MRS) and 3D T2 MRI in an integrated way. By integrating quantification of metabolites with multi-nuclei MRS and volumetric analysis, pathophysiological insights into AD-related changes can be clearly elucidated.

Subjects/Methods: All MRI/MRS scans of WT control mice (n = 8) and 5 × FAD AD-model mice (n = 7) with age of 9 months were acquired with Bruker BioSpec® 94/20 scanner with a 72-mm linear transmit coil, and 4-channel phased-array surface coil. High-resolution 3D T2-weighted images and *in vivo* 1H and 31P MRS spectra were acquired with the sequence and parameters listed in Table 1.

Table 1. Acquisition protocols for high-resolution 3D T2-weighted images and 1H and 31P MRS.

Protocol	Sequence	TR/TE (ms)	FOV (mm)	Matrix size	Resolution	RARE factor	Averages
high-resolution 3D T2WI	T2 TurboRARE	2000 / 33	12 × 12 × 15.6 mm ³	120 × 120 × 156	100 μm isotropic	16	2
	Sequence	TR/TE (ms)	RF pulses	Voxel sizes	Data points	Spectral bandwidth	Averages
High-field short-TE 1H MRS	PRESS	4000/ 15.016	90°-Sinc3 pulse (12420 Hz, 0.5 ms) 180°-Sinc 3 pulses (4650 Hz, 1.0 ms)	2 × 1.5 × 1.2 mm ³ (PFC) 2 × 1.2 × 2 mm ³ (hippocampus)	2048	5000 Hz	16 × 20
	Sequence	TR/TE (ms)	RF pulses	Voxel sizes	Data points	Spectral bandwidth	Averages
Localized 31P MRS	ISIS	4000/-	bp32 excitation pulse (16000 Hz, 0.08 ms)	7 × 4 × 7 mm ³ (whole brain)	4096	16025.64 Hz	128 (1024)

Table 2. Mean concentrations and CRLB values for the 5x FAD AD-model mouse and WT control mouse obtained from the hippocampus and PFC.

		Metabolites										
		GABA	Gln	Glx	GSH	mIns	Tau	tCho	NAA	sCr	Glx	
Concentration (μmol/g)	PFC	5x FAD	3.27 ± 1.21	5.09 ± 1.17	12.83 ± 1.39	1.88 ± 0.43	6.91 ± 0.41	13.78 ± 1.39	2.22 ± 0.51	10.19 ± 0.69	9.61 ± 0.86	17.94 ± 1.43
		WT	3.30 ± 0.84	5.35 ± 1.08	13.66 ± 1.55	2.56 ± 0.46	7.24 ± 1.01	15.68 ± 1.05	2.46 ± 0.20	11.57 ± 1.08	10.76 ± 0.98	19.01 ± 1.87
	Hippocampus	5x FAD	2.80 ± 0.88	4.27 ± 0.99	8.38 ± 0.81	1.74 ± 0.55	6.92 ± 0.86	11.83 ± 1.71	1.52 ± 0.34	8.27 ± 0.64	10.03 ± 0.70	12.75 ± 1.53
		WT	3.74 ± 0.93	4.06 ± 0.67	8.74 ± 0.93	1.93 ± 0.34	6.16 ± 0.41	11.75 ± 0.95	1.71 ± 0.13	8.94 ± 0.68	9.36 ± 0.71	12.81 ± 1.25
	PFC	5x FAD	18.71 ± 16.13	9.14 ± 2.48	3.29 ± 0.49	12.14 ± 2.61	4.71 ± 0.49	2.86 ± 0.38	3.57 ± 0.79	3.43 ± 0.53	3.00 ± 0.00	3.57 ± 0.53
		WT	17.71 ± 6.26	9.71 ± 2.50	3.43 ± 0.53	9.84 ± 2.12	5.43 ± 0.53	3.00 ± 0.49	3.29 ± 0.49	3.29 ± 0.34	3.14 ± 0.38	3.71 ± 0.49
CRLB (%SD)	Hippocampus	5x FAD	12.29 ± 2.81	7.14 ± 1.35	3.43 ± 0.53	10.37 ± 4.65	3.57 ± 0.53	2.43 ± 0.53	3.43 ± 0.53	3.00 ± 0.58	2.00 ± 0.00	3.29 ± 0.49
		WT	10.13 ± 2.03	8.38 ± 1.30	3.88 ± 0.64	9.38 ± 2.00	4.38 ± 0.74	2.75 ± 0.46	3.50 ± 0.53	3.25 ± 0.71	2.25 ± 0.46	3.88 ± 0.64

Table 3. Mean /PCr ratio and CRLB values the 5x FAD AD-model mouse and WT control mouse.

PCr relative ratio (/PCr)		Metabolites												
		β-ATP	NADP	α-ATP	γ-ATP	PCr	GPC	GPE	PDE	Pi	PCbo	PE	PME	α-ATP
5x FAD	5x FAD	0.33 ± 0.08	0.54 ± 0.14	0.83 ± 0.19	0.66 ± 0.06	-	0.24 ± 0.07	0.15 ± 0.07	0.36 ± 0.07	0.40 ± 0.13	0.11 ± 0.08	0.55 ± 0.12	0.66 ± 0.07	1.88 ± 0.22
	WT	0.38 ± 0.11	0.81 ± 0.11	0.70 ± 0.11	0.70 ± 0.07	-	0.19 ± 0.10	0.14 ± 0.08	0.26 ± 0.06	0.45 ± 0.08	0.20 ± 0.11	0.56 ± 0.11	0.76 ± 0.03	1.78 ± 0.15
CRLB (%SD)	5x FAD	1.37 ± 6.54	5.50 ± 9.56	2.29 ± 7.75	0.59 ± 3.45	0.20 ± 1.47	1.17 ± 8.71	7.22 ± 13.39	-	6.89 ± 1.78	30.03 ± 11.83	12.23 ± 4.82	12.23 ± 4.82	-
	WT	2.11 ± 3.47	1.97 ± 1.97	0.26 ± 0.26	0.13 ± 0.13	0.07 ± 0.07	2.07 ± 4.03	-	-	-	-	-	-	-

Table 1, 2, and 3

Before the quantification, a series of preprocessing steps was performed to the acquired spectra using the FID Appliance (FID-A) package. The processed spectra were quantified by the LCModel and jMRUI, respectively. The acquired 3D T2WI scans were segmented into the brain regions using Atlas-based imaging data analysis (AIDAmri) pipeline. To investigate the AD-related metabolic changes, mean concentrations and /PCr relative ratios were compared between the groups for all major metabolites. In addition, a volumetric analysis was conducted on the voxel size of hippocampus, entorhinal cortex, and PFC between the groups.

Results/Discussion:

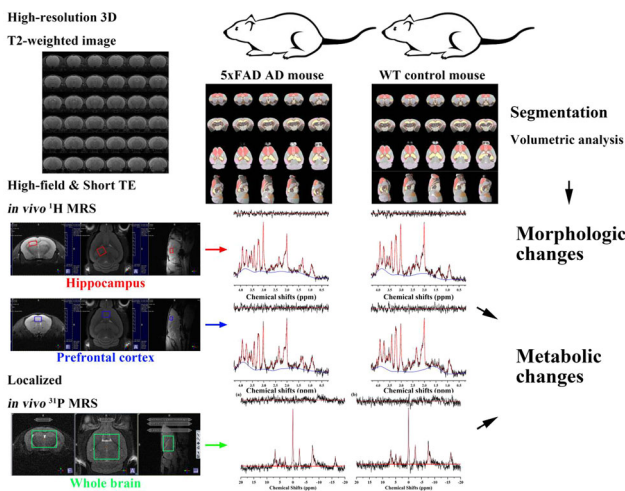


Figure 1. A schematic diagram of the experimental protocol of this study.

Figure 1 illustrates the experiment protocols of this study.

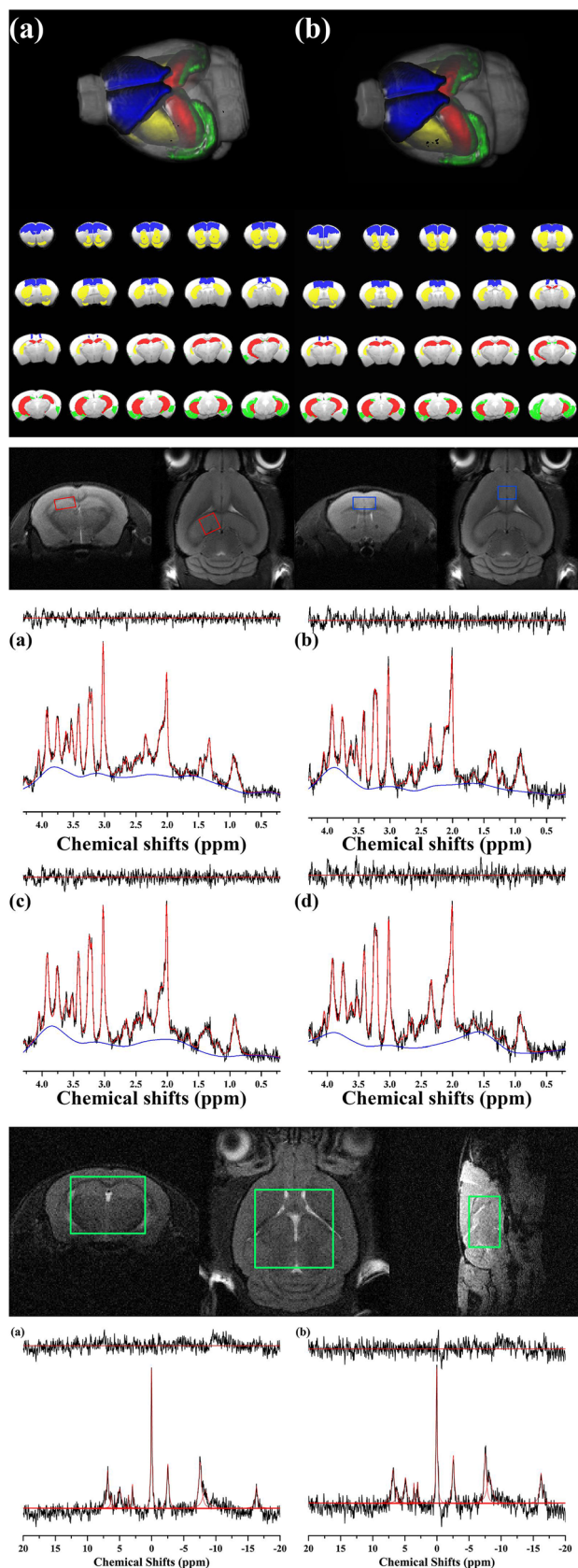


Figure 2 illustrates high-resolution 3D T2 MRI of the (a) 5xFAD and (b) WT with the hippocampus (red), PFC (blue), striatum (yellow) and entorhinal cortex (green). Figure 3-4 illustrates representative ^1H and ^{31}P MRS scans of the (a) 5xFAD and (b) WT, respectively. Table 2-3 lists the quantification results of MRS scans. Nearly significant reduction of GABA, tNAA, and tCr, or increase of mIns was observed in the hippocampus of the 5xFAD, compared to the WT. Significantly reduced GSH, Tau, tNAA, and tCr was observed in the PFC of the 5xFAD, compared to the WT. Statistically significant reduction of NADP and PME, or increase of PDE was observed in the 5xFAD, compared to the WT. Significant decreases in the volumes were not observed in any regions of the (a) 5xFAD, compared to the WT. In this study, the AD-related metabolic and morphologic changes in the brain, consistent with previous findings, can be investigated in an integrated way by high-resolution T2WI and high-field ^1H and ^{31}P MRS.

References: 1. Niklas Pallast et al. Processing Pipeline for Atlas-Based Imaging Data Analysis of Structural and Functional Mouse Brain MRI (AIDAmri). *Front Neuroinform*, 2019;13:42.
2. Robin Simpson et al. Advanced Processing and Simulation of MRS Data Using the FID Appliance (FID-A)-An Open Source, MATLAB-based Toolkit. *Magn Reson Med*, 2017;77:23-33.

L01.24

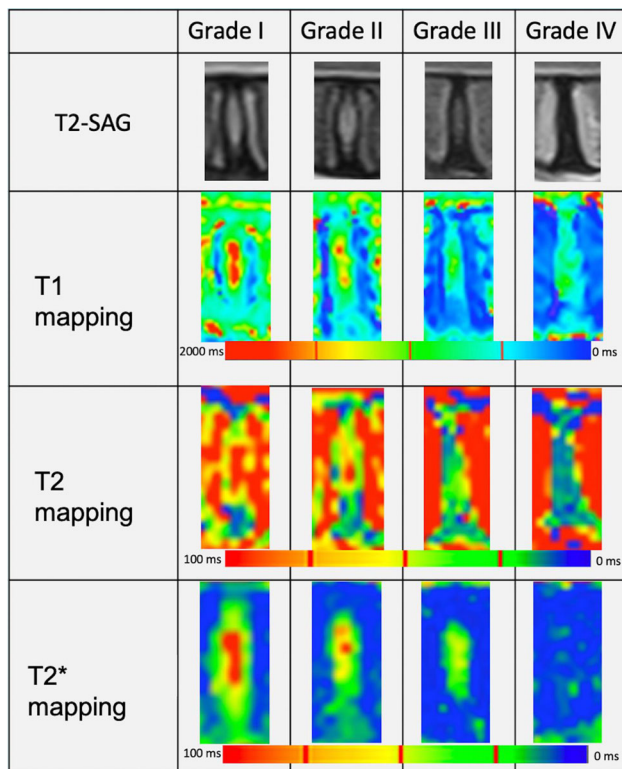
Comparison of three MRI quantitative sequences (T1, T2 and T2* mapping) and two drawing approaches for the assessment of lumbar disc degeneration in an ovine model

N. Bouhsina¹, J.-B. Hardel², C. Decante¹, D. Rouleau²,
C. Le Visage¹, J. Lesoeur¹, J. Guicheux¹, J. Clouet¹, M. Fusellier¹

¹INSERM, UMR 1229, Regenerative Medicine and Skeleton (RMes), Université de Nantes, ONIRIS, Nantes, France, ²ONIRIS College of Veterinary Medicine, Food Science and Engineering, Diagnosis Imaging, Nantes, France

Introduction: Recently, quantitative MRI have been developed to detect in vivo early lumbar intervertebral disc (IVD) degeneration in human and in various animal models such as sheep. Numerous human and animal studies using different approaches have shown the interest of T2 and T2* relaxation time measurements^{1,2} but only few have evaluated the T1 mapping method³. A standardized method of acquisition which can be applied in preclinical as well as in clinical studies is needed. It should be easy, reproducible and not time-consuming. Our objective was to compare MRI T1, T2 and T2* mapping methods using different region-of-interest (ROI). These ROI were defined by two drawing methods in the lumbar ovine IVD to determine the most suitable and applicable approach that can be used in pre- and clinical studies.

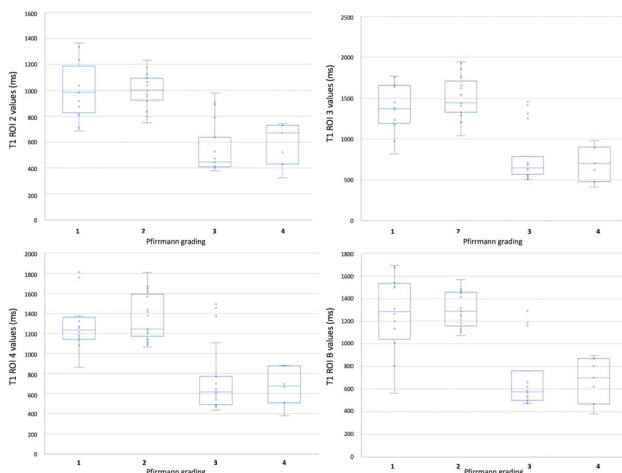
Subjects/Methods: 66 lumbar IVD of 12 sheep were analyzed using T1 and T2-weighted 1.5 T MRI for qualitative grading, variable-flip-angle T1 mapping and multi-echo T2 and T2* mapping.



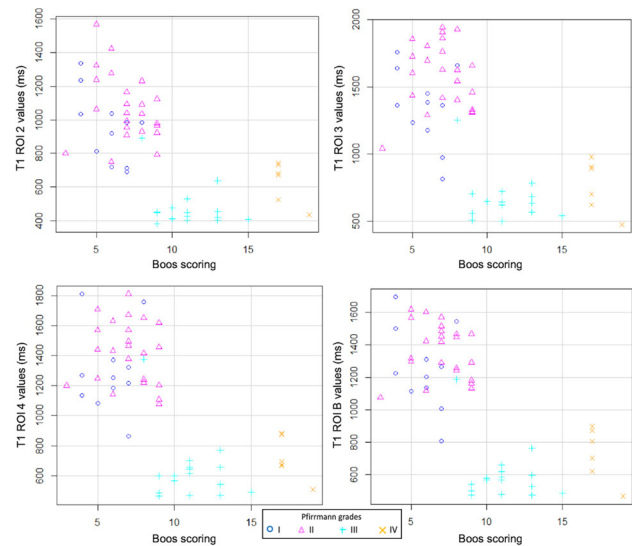
Evolution of the T2-Sag, T1, T2 and T2* mapping aspect of the lumbar ovine IVD according to the Pfirrmann grades

3 manual-drawn ROI and 5 squared-ROI methods were used five times on each IVD to delineate the *Nucleus pulposus*(NP) and the *Annulus fibrosus*(AF) by two independent observers. Spearman correlations of imaging data with histological data were finally assessed in 56 IVD.

Results/Discussion: NP ROI showed strong intra- and interrater agreement. T1, T2 and T2* mapping showed a good correlation with Pfirrmann, modified Pfirrmann grading and Boos scoring ($p < 0,05$) except for the T2 ventral AF ROI.



Mean T1 values variations with Pfirrmann grading for the NP ROI



Mean T1 values variations with Boos grading for the NP ROI according to the Pfirrmann grades

Correlations were excellent for all T1 ROI ($p < 0,01$) and T2* NP ROI ($p < 0,01$). Differences in T1 values were highly significant between all Pfirrmann grades except between grades I and II and grades III/IV. T2 and T2* values showed significant differences between all grades ($p < 0,05$) except between grades I and III.

Overall, our data indicate that mapping MRI is an efficient tool to evaluate the IVD degeneration with an excellent repeatability and a strong correlation with histology. Both ROI drawing methods can be used to quantify different degrees of IVD degeneration, especially in the NP and at the junction with the AF. While T2 and T2* mapping are well described to characterize IVD degeneration, our data also highlight that T1 mapping using the variable-flip-angle deserve to be further considered notably to assess the early events of IVD degeneration in preclinical and clinical studies.

References: ¹Stelzener et al. Quantitative T2 evaluation at 3.0 T compared to morphological grading of the lumbar intervertebral disc: A standardized evaluation approach in patients with low back pain. Eur. J. Radiol 2012;81:324–330.

²Kolf et al. T2* mapping of ovine intervertebral discs: Normative data for cervical and lumbar spine. J Orthop Res 2016;34:717-724

³Galley J et al. Real T1 relaxation time measurement and diurnal variation analysis of intervertebral discs in a healthy population of 50 volunteers. Eur J Radiol 2017;87:13–9.

L01.25

Fatty acids and cholesterol peaks found in MRS are biomarkers of Niemann-Pick C disease diagnosis

A. Xavier¹, F. Zacconi², J. E. Oyarzún¹, S. Zanlungo³, M. Andia¹

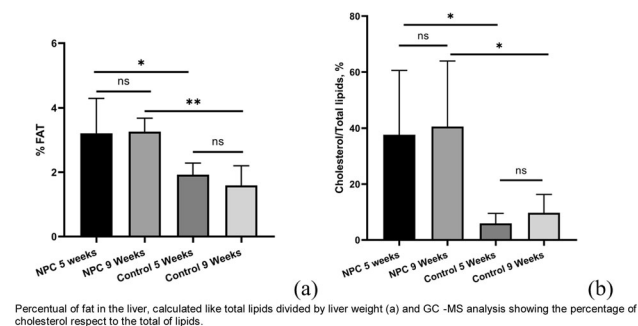
¹Pontificia Universidad Católica de Chile, Millennium Nucleus for Cardiovascular Magnetic Resonance, Santiago, Chile, ²Pontificia Universidad Católica de Chile, Faculty of Chemistry and of Pharmacy, Santiago, Chile, ³Pontificia Universidad Católica de Chile, School of medicine, Santiago, Chile

Introduction: Niemann-Pick is a genetic and rare group of diseases that affect many body organs. NP patients have an abnormal lipid metabolism that causes an accumulation of lipids in the liver, spleen, brain, and bone marrow. NP patients develop cirrhosis very fast¹. The purpose of this study is to characterize the liver lipids composition using ex vivo spectroscopy in a mice model of NP type C (NPC) and compare with wild-type (WT) mice with the aim of

providing a non-invasive technique to follow-up these patients and provide new hypothesis about the bad progression of NAFLD in some patients.

Subjects/Methods: A group of 12 mice was genetically modified to have NP type C. Those mice were euthanized with 5 weeks (n=6) and 9 weeks (n=6), to obtain their livers. We also obtained livers from wild type mice with 5 weeks (n=6) and 9 weeks (n=6). We made a lipid extraction from all those livers², and we analyzed it with Gas Chromatography-Mass spectrometer (GC-MS) and Magnetic Resonance Spectroscopy (MRS).

Results/Discussion: After lipids extraction, the percentage of fat was calculated as the total lipids divided by liver weight (Figure 1a). **GC-MS results:** We quantified 7 main fatty acids and 2 peaks of cholesterol. We calculated the percentage of cholesterol respect to total lipids (Figure 1b).



MRS results: We identified 5 metabolites peaks that correspond to the FA only, 3 peaks that correspond to cholesterol only, and 2 peaks correspond to FA and Cholesterol³. Figure 2 shows a comparison between the spectrum correspondent to the control group (red) and the NPC group (blue). The peaks in black are the fatty acids peaks; in orange are a mixture of FA and cholesterol and, in green, are only cholesterol.

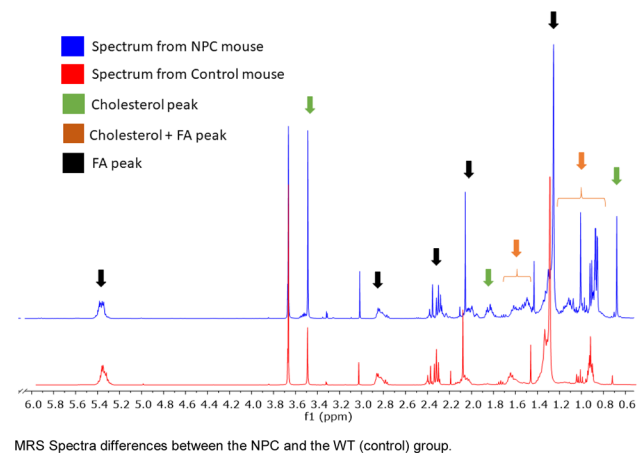
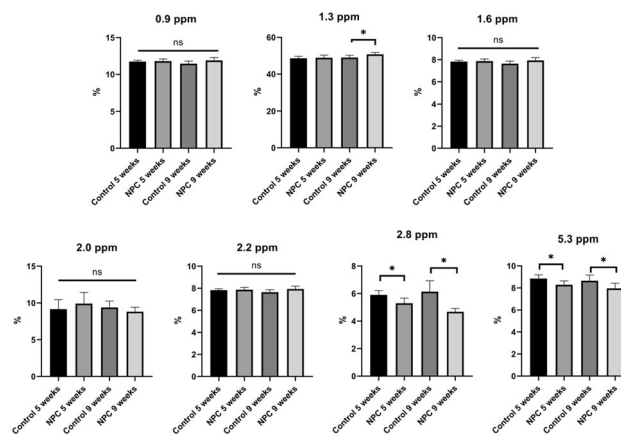


Figure 3 shows the FA profile MRS. The peak of 2.8 ppm and 5.3 ppm decrease in accordance with the disease progression⁴.



MRS Analysis. *p<0.05, **p<0.01, ***p<0.001 (significant differences between groups) and NS (No significant difference between groups).

Our results showed that the increase in liver cholesterol concentration is the main difference in NPC liver manifestation, and it has been associated with the bad liver prognosis since cholesterol promotes liver inflammation⁵. Also, there is a different pool of fatty acids stored in the NPC and WT liver, and the different MR liver spectra would provide biomarkers for non-invasive follow-up of these patients.

It is strongly possible that the accumulation of cholesterol in the liver and the decrease in 2.8 ppm and 5.3 ppm peaks could be a biomarker of bad prognosis in NAFLD.

References: Beltray e. et al. *Hepatology*. 2005.
 Folch et al. *The Jour Bio Chem*. 226(1). 1957.
 Oostendorp et al. *Clinical Chemistry*. 52 (7). 2006.
 Xavier, A. et al. *RSC Advances*, 9(72). 2019
 Hebbard, L. et al. *Nature reviews Gastroenterology & hepatology*, 8(1), 35. 2011.

Acknowledgements

This publication has received funding from Millennium Science Initiative of the Ministry of Economy, Development and Tourism, grant Nucleus for Cardiovascular Magnetic Resonance. CONICYT-PCHA/Doctorado Nacional/2016-21160835 and FONDECYT 1180525.

L01.26

A web application for computerised neuropsychological assessments for studying brain activation during fMRI

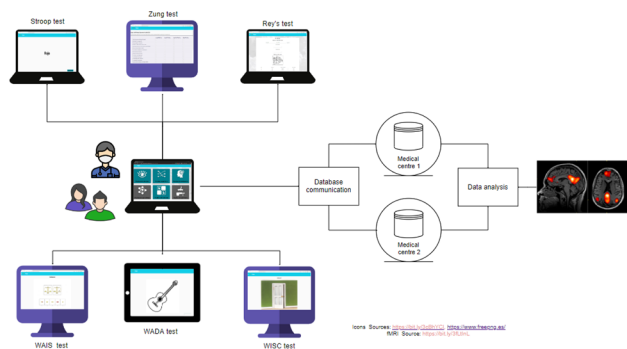
D. Diaz¹, S. Cadena¹, J. Gil¹, J. Bernal², M. Trujillo¹

¹Universidad del Valle, Valle del Cauca, Cali, Colombia, ²University of Edinburgh, Edinburgh, UK

Introduction: Neuropsychological tests permit diagnosing neurodegenerative diseases and evaluating potential cognitive repercussions caused during brain surgery. The lack of computerised neuropsychological assessment solutions of low cost and low hardware requirements makes these assessments time-consuming and error-prone, prevents storing results digitally, analysing them immediately, and sharing them among medical centres. We propose a web application called Psique, a tool that allows performing computerised neuropsychological assessments, provides storage and analysis methods, and supports decision making for diagnosis and treatment selection. Furthermore, our application enables medical centres to share such data among them as needed.

Subjects/Methods: We implemented six computerised neuropsychological tests comprising the Wechsler Intelligence Scales (WAIS and WISC), the Zung Anxiety Scale, the Rey’s Complex Figure Test, the Stroop Color and Word Test and the WADA test. This last one is

used in brain surgery and is controlled by the neuropsychologist from a remote device connected to the app. Additionally, we developed a patient-neuropsychologist voice recording and communication system for use during surgery assessment and also implemented a system to hold the tablet. Each test provides instructions to ease the assessment process. We used questionnaires, buttons, a voice recogniser and a keyboard to collect patient’s responses and a computer screen and a tablet with internet access to present the test stimuli. We evaluated our web application by consulting neuropsychologists about user experience and test functionality, taking into account that the user interface had to be as simple as possible to avoid distracting patients during the assessments. The evaluation was focused on user satisfaction on the graphic interface, functionality, right-scoring of tests and compliance with users needs. Test results are stored in a database that serves as a source for subsequent data analyses and cognition studies. We use a subset of the HL7 communication standard to ensure that these results can be shared among medical centres.



General overview of the Psique web application and their characteristics of analytics and communication between medical centres.

Results/Discussion: Five out of the six tests have been validated by the neuropsychologists and are ready to be used. The graphic user interface of our application was also well-accepted by them. We have identified a delay in the voice recogniser that hinders the Stroop test. We plan to tackle this issue by changing the stimuli when the voice recogniser does not recognise the right answer on time. In the future, we plan to carry out user experience tests with end-users and consider methodologies to use our web application in an MRI acquisition environment. Such an aim would permit studying brain activation in fMRI due to the stimuli in the neuropsychological assessment.

References: No References

L01.27

Brain Tumor Detection and Classification using Under Sampled k-Space Signals

S. Tania¹, S. Kurosaki¹, Y. Jitsumatsu¹, S. Kuhara², J. Takeuchi¹

¹Kyushu University, Graduate School of Information Science and Electrical Engineering, Fukuoka City, Japan, ²Kyorin University, Dept. of Medical Radiological Technology, Tokyo, Japan

Introduction: Magnetic Resonance Imaging (MRI) is an essential technique in medical diagnosis. In MRI, the key issue is to reduce observation time with assuring remarkable anatomical details. In this regard, Kitazaki et al. [1] introduced a new deep learning based method named multi-resolution CNN (MRCNN). The primary pur-

pose of MRCNN is to reconstruct good quality MR images from under sampled k-space data. They assessed its efficiency with respect to Peak Signal to Noise Ratio (PSNR). The key objective of this research is to measure the performance of MRCNN in the vital domain of brain tumor detection and classification using the VGG16 transfer learning model. This paper focuses on the brain tumor detection and classification accuracy based on MRCNN is considerably higher than zero-filling.

Subjects/Methods: In this work, we employ MRCNN to accelerate MRI using T1-contrast enhanced (CE) brain tumor detection and classification dataset –Figshare [2]. MRCNN, consists of three deep learning based super resolution (SRCNN) methods to restore all frequency components. Owing to MRCNN, the average PSNR (dB) of 20% acquisition rate is higher than that of 10% acquisition rate. In our experiment, we apply pre-trained VGG16 transfer learning model to MRI restored by MRCNN in order to detect and classify of brain tumors. However, the earlier feature extractor layer extracts more general features whereas later layers provide high level object specific features. In our case, we freeze feature extractor layers of VGG16 which is trained by large dataset such as ImageNet and then fine tune [3] remaining fully connected layers using brain tumor dataset – Figshare. We modify the last softmax layer, which has 1000 classes into that with three classes since Figshare dataset has three classes. We set categorical cross entropy as a loss function and use Adam optimizer. The value of mini batch size is 32 and the maximum number of epochs is 10. We use 80% data for training whereas 20% data for test purpose.

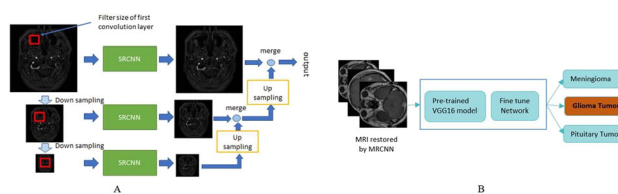


Figure.1 MRCNN framework (A) and proposed model architecture (B).

Results/Discussion: We conduct our experiments on GPU Tesla V100 PCIE × 2 with 16GB memory and CUDA version is 10.1. We implement our method using Keras with Tensorflow backend. In our study, we compare the accuracy of brain tumor detection and classification using MRCNN and Zero-filling. According to Table 1, the classification accuracy using MRCNN is around 91±1.3% and Zero-filling is only around 80±3.2%, for 10% acquisition rate. This tendency is similar for 20% acquisition rate. This means that MRCNN significantly improves the accuracy of DNN based tumor detection methods.

Brain tumor dataset -Figshare	Accuracy
Zero-filling (10% acquisition rate)	80.1%
Zero-filling (20% acquisition rate)	83.1%
MRCNN (10% acquisition rate)	91.2%
MRCNN (20% acquisition rate)	92.5%
Full-sampled	95.1%

Table.1 Results of VGG16 with fine tune using brain tumor dataset -Figshare.

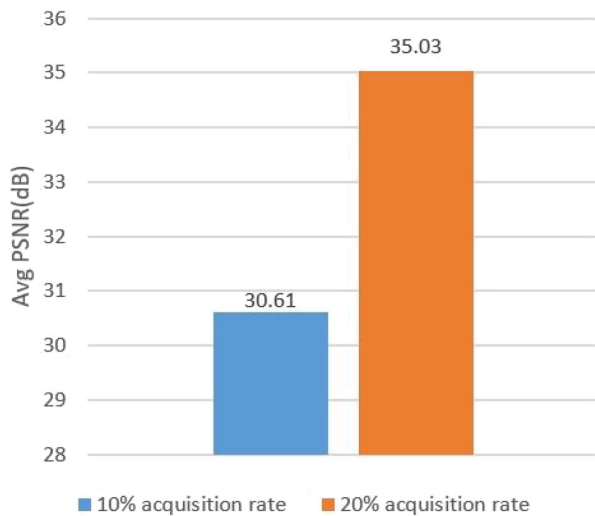


Figure 2 Average PSNR (dB) of MRI reconstructed by MRCNN for 10% as well as 20% acquisition rate.

References: 1. S. Kitazaki, M. Kawakita, Y. Jitsumatsu, S. Kuhara, and J. Takeuchi, “MRI Acceleration by Super Resolution,” Proc. of the ESMRMB congress, 2019.
 2. https://figshare.com/articles/brain_tumor_dataset/1512427.
 3. N. Tajbakhsh *et al.*, “Convolutional Neural Networks for Medical Image Analysis: Full Training or Fine Tuning?,” *IEEE Trans. Med. Imaging*, 2016.

L01.28

Effect of intravoxel incoherent motion on post mortem diffusion parameters

M. Bauer, C. Berger, E. Scheurer, C. Lenz

Institute of Forensic Medicine, Department of Biomedical Engineering, University of Basel, Basel, Switzerland

Introduction: Intravoxel incoherent motion (IVIM) magnetic resonance imaging (MRI) allows quantification of different diffusive processes according to varying molecule speeds. Its signal decay depends on the perfusion fraction (*f*) and coefficients for diffusion (*D*) and pseudo-diffusion (*D**) [1,2]. To consider the non-Gaussian behavior of the diffusion, several models, e.g. the kurtosis (*K*) model, exist [2,3]. In this study, the effect of brain IVIM on post mortem (PM) diffusion parameters was analyzed to enhance the insight into the underlying properties and to validate its temperature dependency.

Subjects/Methods: For this study, 5 deceased and 2 living volunteers underwent 3T MRI scans. An overview of the subject characteristics is given in Table 1. The IVIM sequence consisted of a diffusion-weighted single-shot-echo-planar imaging sequence with 6 isotropically distributed directions acquired at 16 *b*-values (0, 20, 40, 60, 80, 100, 120, 140, 160, 180, 200, 500, 1000, 1500, 2000, 2500 s/mm²). A two-step kurtosis model was applied for IVIM analysis: *D* and *K* were determined for high *b*-values (> 200 s/mm²) at first and thereafter kept constant to calculate *f* and *D** for all *b*-values. The calculations were performed after automatic segmentation into white matter (WM) and gray matter (GM) separately.

Subject	Age (y)	Forehead temperature (°C)	PMI (h)	Cooling time (h)	Cause of death
PM 1	35	8.0	65.5	42.0	Cardiac failure
PM 2	53	6.8	41.0	26.5	Intoxication
PM 3	60	18.8	19.5	5.0	Cerebral hemorrhage
PM 4	66	9.5	38.5	27.5	Cardiac failure
PM 5	69	7.5	35.3	27.0	Pulmonary embolism
Mean PM	56.6 ± 13.54	10.1 ± 4.95	27.4 ± 11.14	25.6 ± 13.23	-
Control 1	23	31.0	-	-	-
Control 2	30	31.8	-	-	-
Mean Control	26.5 ± 4.95	31.4 ± 0.57	-	-	-

Table 1. Subjects parameters.

Results/Discussion: Lower values for *f* and *D* were obtained for the PM cases than for the controls and they are higher in the gray matter than in the white matter (see Table 2). *D** is in a similar range for dead and living people. The fits for the PM cases show a slower decay than those for the volunteers with good intra-group congruence and a clear inter-group difference (see Figure 1). Although PM 4 was scanned with a higher forehead temperature compared to the other PM cases, only a slight difference to the other deceased is visible in the white matter fit. The product of *D*, *K* and *b*-value is less than 3 in all cases, indicating a successful fitting with the kurtosis model [2]. The IVIM parameter results for the volunteers correspond well to the already published results [4]. Though expected due to the missing blood flow in PM subjects, *f* does not level to 0 %, but approximates the value of the less perfused WM of living people. The steeper curve for PM 3 regarding the WM can be explained by its higher forehead temperature of 18.8 °C (mean of other deceased: 8.0 °C) as diffusion imaging is temperature dependent. The intoxication of PM 2 followed by a fatal cytotoxic cerebral edema causes an increased *D** (see high standard deviation for *D** in Table 3) because of the edema clearance via capillaries.

In conclusion, it was verified that the IVIM parameters *f* and *D* depend on the blood flow and the temperature, respectively.

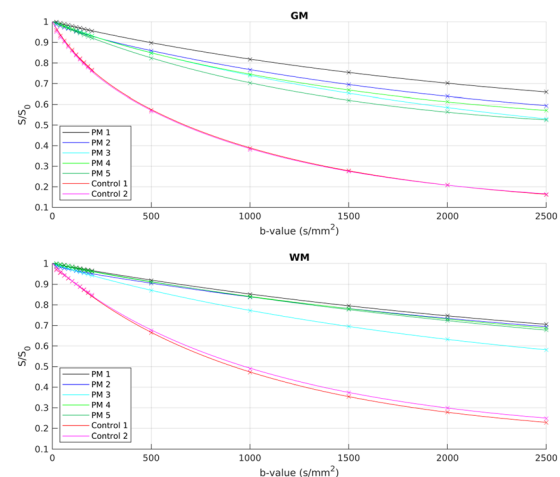


Figure 1. IVIM fits for gray (top) and white (bottom) matter for all investigated subjects. In addition, data points are illustrated with their standard deviations.

Region	<i>f</i> (%)		<i>D</i> · 10 ⁻⁴ (mm ² /s)		<i>D*</i> · 10 ⁻³ (mm ² /s)	
	PM	Control	PM	Control	PM	Control
GM	1.7 ± 0.50	11.0 ± 0.45	3.0 ± 0.69	9.3 ± 0.20	4.6 ± 1.02	6.8 ± 0.27
WM	1.1 ± 0.24	1.9 ± 0.10	1.9 ± 0.44	8.0 ± 0.30	5.5 ± 4.15	2.4 ± 0.24

Table 2. Mean values and standard deviations of determined coefficients.

References: [1] Le Bihan *et al.*, *Radiology*, 1986, 401-407. [2] Le Bihan, *NeuroImage*, 2019, 56-67. [3] Chabert *et al.*, *Proceedings Annual Meeting ISMRM*, 2004, 1238. [4] Vieni *et al.*, *NeuroImage*, 2020, 116228.

L01.29**Evaluation of disturbance of hemo- and cerebrospinal fluid dynamics in patients with “overcrowded posterior cranial fossa” syndrome according to MRI**

O. Bogomyakova¹, V. Kim², Y. Stankevich¹, L. Vasilkiv¹, A. Tulupov¹

¹International Tomography Center, MRI Technology, Novosibirsk, Russian Federation, ²Novosibirsk State University, Novosibirsk, Russian Federation

Introduction: “Overcrowded posterior cranial fossa” syndrome is a violation of the craniovertebral junction anatomical structure and characterized a cisterna magnum narrowing, as well as the cerebellar tonsils ectopia [1]. The clinical manifestations of this pathology vary widely from asymptomatic course to disabling lesions. In this case, CSF flow disorders can modify or accelerate clinical manifestation [2].

The study aim: To reveal the most momentous disturbances of hemo- and cerebrospinal fluid dynamics in patients with “overcrowded posterior cranial fossa” syndrome using phase-contrast MRI.

Subjects/Methods: The study involved 15 control patients and 6 patients with radiological signs of cerebellar tonsils ectopia (on 1-5 mm lower than the foramen magnum level), narrowing of the cisterna magnum and subarachnoid space at the level of foramen magnum. All this patients had such clinical signs as headaches and neck pain, visual disturbances without any organic lesions of the brain. All patients underwent routine MR imaging and phase-contrast MRI on the 3.0T “Inginia” Philips. We observed velocity values of blood and CSF flows at the some intracranial, foramen magnum and C2-C3 cervical levels. The received parameters were compared using the Mann-Whitney test.

Results/Discussion: Analysis of differences has shown that in patients group the maximal mean and flux velocity values of caudal flow were significantly higher than the cranial flow ($p < 0.05$). Mean velocity values of the CSF flow at the subarachnoid spaces of foramen magnum and C2-C3 cervical level significantly higher than in control group ($p < 0.05$). No significant differences were found at the brain aqueduct level. Arterial blood flow rates did not significantly differ in the control and patients groups. There was a tendency to increased venous outflow along the straight and superior sagittal sinuses in the patient group.

The data obtained indicate a significant influence of the anatomical features of the craniovertebral junction level and the posterior cranial fossa on disturbances in the movement of CSF flow. A change in the speed characteristics in the group of patients indicates an increase in the CSF outflow from the cranial cavity and the development of intracranial hypertension syndrome.

Acknowledgments: We thanks the Ministry of Science and Higher Education of the Russian Federation for access to MRI equipment, the Russian Science Foundation (project No. 19-75-20093) for MRI studies.

References: 1. Zabbarova A.T., Bogdanov E.I., Khusainova D.K., Fatkheeva L.S. Comorbidities in chronic «overcrowded posterior cranial fossa» syndrome. Kazanskiĭ meditsinskiĭ zhurnal, 2013; 94(2):221–227.

2. Wang C., Wang X., Fu C-H., Wei L., Zhou D., Lin J. Analysis of cerebrospinal fluid flow dynamics and morphology in Chiari I malformation with cine phase-contrast magnetic resonance imaging. Acta Neurochirurgica, 2014; 156:707–713.

L01.30**Evaluation of IVIM-MRI acquisition parameters for clinical protocol optimization in high-grade glioma patients**

A. M. Paschoal¹, L. M. Costa², A. C. dos Santos³, R. F. Leoni²

¹University of Sao Paulo, InBrain lab - Medical School of Ribeirao Preto, Ribeirao Preto, Brazil, ²InBrain Lab - University of Sao Paulo, Department of Physics, Ribeirao Preto, Brazil, ³University of Sao Paulo, Medical School of Ribeirao Preto, Ribeirao Preto, Brazil

Introduction: Intravoxel incoherent motion (IVIM), a diffusion-weighted (DWI) MRI method, explores the moving water molecules in blood flow using different diffusion b-values (1). Data fitting is a key point for obtaining IVIM output values of perfusion and diffusion. Mathematically, the fitting is better for higher number of points. However, increasing the number of points means increasing the scan time, restricting the clinical use. Moreover, an open question regards the maximal b-value, since a low maximal b may not be optimal for fitting the data, and a very high b may introduce non-Gaussian noise (2). Therefore, we aimed to evaluate the number of b-values and its maximal value to balance data fitting results and scan duration.

Subjects/Methods: For simulation, IVIM signals were generated in MATLAB, setting D and D* values (2). The amplitudes f and f* randomly varied between 0 and 1, respecting the constraint that $f + f^* = 1$ (2). Two sets of b-values were used, with 10 and 20 values, ranging from 0 to 1000 s/mm² and 0 to 2000 s/mm² respectively. Each configuration was analyzed without and with noise by using a Gaussian distribution with standard deviation estimated from typical real data measured in a 3T MRI system. In vivo DWI of 5 healthy subjects and 5 patients with high-grade glioma were acquired in a 3T MRI system using $b=(0\ 4\ 8\ 16\ 30\ 60\ 120\ 250\ 500\ 1000\ 1200\ 1400\ 1600\ 1800\ 2000)$. Both simulated and in vivo data were analyzed using the non-negative least square fitting model(3). In vivo data were processed using all 15 b-values and 2 different sets of 8 b-values (0 4 16 60 250 1000 1400 2000), (0 8 30 120 250 500 1000 1600). An inter-class correlation (ICC) was performed to compare the results between the 3 sets of b-values. The residue ($S_{fit} - S$) was calculated in the whole brain for controls and in a tumor ROI for patients.

Results/Discussion:

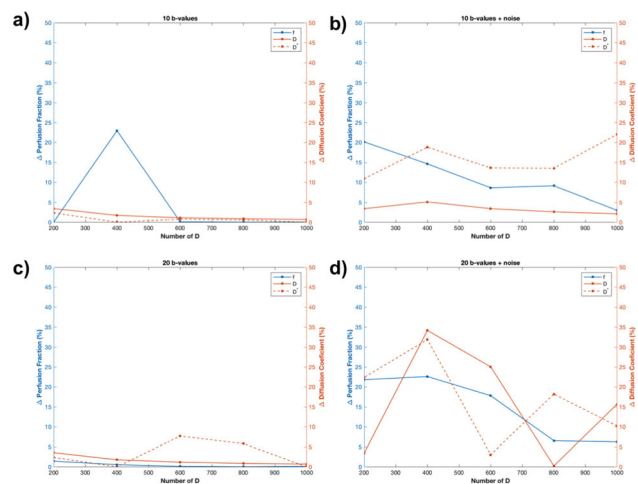


Figure 1 - IVIM fitting errors for the simulation experiment

For the simulation, Fig1 shows that a higher number of points does not necessarily represent a better fitting, since the addition of higher b-values could introduce additional noise, which may hamper the fitting. Fig2a-c shows the perfusion fraction (f) maps of a representative healthy subject for the 3 sets of b-values. For the control group (fig 2d), the set of b prioritizing lower b values showed lower residues, since higher b values may add higher noise contribution, even when using 15 b. However, for the tumor ROI, the signal intensity is higher, which increases the SNR even for higher b-values, resulting in lower residue distribution when compared to the sets of 8 b (fig 2e). The ICC (table 1) for f showed a better correlation when comparing the set of 15 b-values to the set of 8 b-values that prioritized lower b-values. Therefore, we may conclude that an optimal combination of smaller dataset can be used to reduce scan time without compromising the analysis.

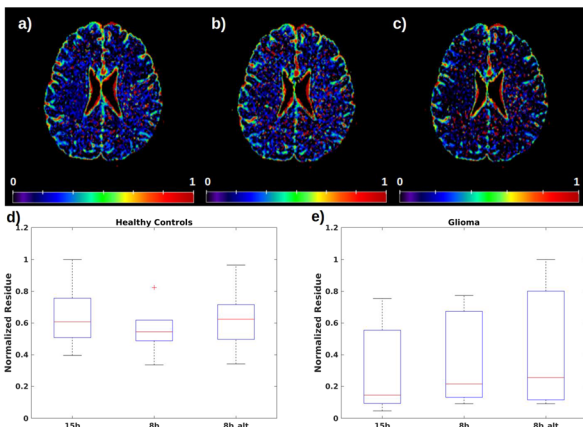


Figure 2 - a-c) Example of perfusion fraction maps for the 3 sets of b-values. d) Residue of the 3 sets of b-values for healthy controls. e) Residue of the 3 sets of b-values for glioma patients.

Subject	R 15x8	LB 15x8	UB 15x8	R 15x8*	LB 15x8*	UB 15x8*	R 8x8*	LB 8x8*	UB 8x8*
Subject 1	0.6296	0.6287	0.6287	0.6225	0.6216	0.6234	0.6225	0.6216	0.6234
Subject 2	0.6882	0.6874	0.689	0.6182	0.6173	0.6192	0.6182	0.6173	0.6192
Subject 3	0.63	0.6291	0.6309	0.5635	0.5624	0.5645	0.5635	0.5624	0.5645
Subject 4	0.6846	0.6838	0.6854	0.5896	0.5886	0.5906	0.5896	0.5886	0.5906
Subject 5	0.6618	0.661	0.6627	0.6479	0.647	0.6488	0.6479	0.647	0.6488
Average	0.65884	0.658	0.65934	0.60834	0.60738	0.6093	0.60834	0.60738	0.6093

Table 1 - Inter-class correlation among the three sets of b-values for each subject. R = correlation coefficients; LB = lower base; UB = upper base. Sets of 15, 8 and 8* b-values.

- References:** 1 LeBihan et al, Radiology 1986.
 2 LeBihan. Neuroimage 2017.
 3 Keil et al, JMRI 2017.

L01.31

Longitudinal changes in white matter tissue microstructure in patients with newly diagnosed Systemic Lupus Erythematosus assessed by diffusion tensor imaging

F. Inglese¹, E. Silvagni², A. Bortoluzzi², M. Borrelli³, I. Ronen¹, J. de Bresser¹, E. Fainardi⁴, M. Govoni², E. Ercan¹

¹Leiden University Medical Center, Department of radiology, Leiden, The Netherlands, ²University of Ferrara and Azienda Ospedaliero-Universitaria S. Anna, Rheumatology Unit, Department of Medical Sciences, Cona (Ferrara), Italy, ³Azienda Ospedaliero-Universitaria Sant’Anna, Neuroradiology Unit, Department of Neuroscience and

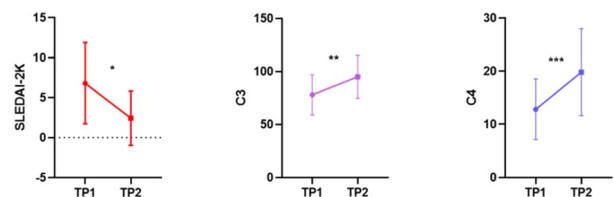
Rehabilitation, Cona (Ferrara), Italy, ⁴University of Florence, Neuroradiology Unit, Department of Experimental and Clinical Biomedical Sciences, Florence, Italy

Introduction: Systemic lupus erythematosus (SLE) is an autoimmune disease characterized by the multi-organ involvement and a broad spectrum of clinical manifestations, including Neuro-Psychiatric (NP) syndromes¹. NP syndromes occur in 12-95% of SLE patients and decrease their quality of life¹. Conventional brain MRI is the method of choice to evaluate SLE patients experiencing NP events². However, MRI findings, such as white matter (WM) lesions, are not specific to NP-SLE³. Furthermore, the absence of reliable outcome measures prevents an effective monitoring of the disease and impacts therapy efficiency. The aim of our study was to evaluate longitudinal variations in the brain WM of newly diagnosed SLE patients using diffusion tensor imaging (DTI) and to assess whether DTI changes relate to changes in clinical evaluations over time.

Subjects/Methods: 17 newly diagnosed SLE patients (19-55 years) were included within 24 months from their diagnosis. All patients underwent brain MRI (1.5 T Philips-Achieva), clinical, and serological evaluations at baseline and after at least 12 months (Figure 1).

	TP1	TP2
Demographics		
Female, N (%)	14 (82.35)	
Age, mean (sd)	37.84 (12.36)	
Serology and clinimetrics		
C3 (mg/dl), mean (sd)	80.65 (21.46)	95.00 (20.32)
C4 (mg/dl), mean (sd)	14.12 (7.73)	19.81 (8.20)
SLEDAI-2K, mean (sd)	6.53 (1.23)	2.44 (3.41)
SDI, mean (sd)	0.47 (0.87)	0.47 (0.87)

SLE: systemic lupus erythematosus; TP1: time-point 1; TP2: time-point 2; sd: standard deviation; SLEDAI-2K: Systemic lupus erythematosus disease activity index 2000; SDI: Systemic Lupus International collaborating clinics American College of Rheumatology Damage index.



*: p value < 0.05; **: p value < 0.01; ***: p value < 0.001.

Figure 1. Clinical characteristics of newly diagnosed SLE patients (N=17) across the follow-up.

Fractional anisotropy (FA), mean (MD), radial (RD) and axial diffusivity (AD) values were calculated in 21 normal-appearing WM (NAWM) tracts (Figure 2).

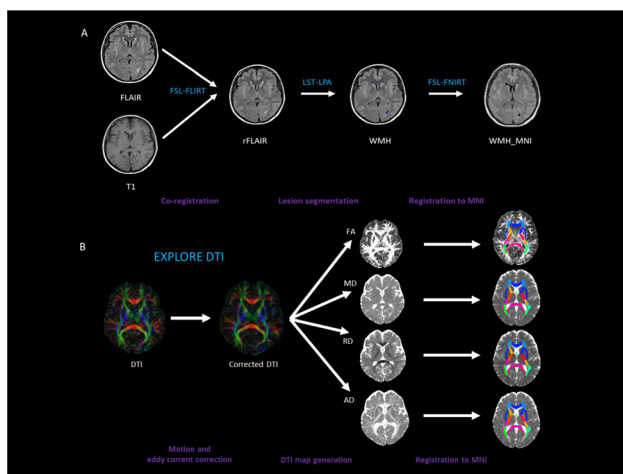
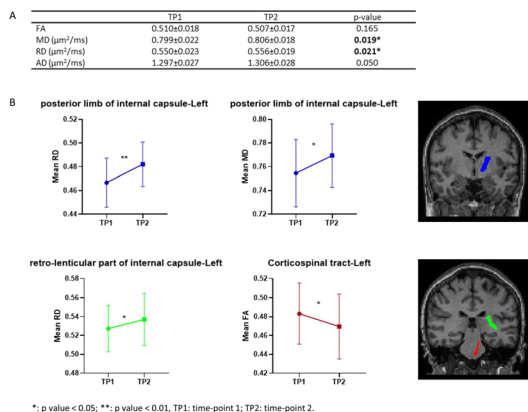


Figure 2. Lesion segmentation and registration to a standard brain template (A). Calculation of fractional anisotropy (FA), mean diffusivity (MD), radial diffusivity (RD) and axial diffusivity (AD) maps and segmentation of white matter tracts (B).

Longitudinal variations in DTI metrics were analyzed by repeated measure ANOVA analysis. Longitudinal DTI changes in 21 WM tracts were separately assessed by paired t-test statistics and were corrected using a permutation-based multiple comparison method. Associations between longitudinal variation of DTI metrics and clinical measures (SLEDAI-2K, complement levels) were evaluated through adjusted Spearman correlation analysis.

Results/Discussion: Mean MD and RD values from the NAWM significantly increased over time ($p = 0.019$ and $p = 0.021$, respectively). A significant increase in RD ($p = 0.005$) and MD ($p = 0.012$) was found in the left posterior limb of the internal capsule; RD significantly increased in the left retro-lenticular part of the internal capsule ($p = 0.013$) and FA significantly decreased in the left corticospinal tract ($p = 0.029$). No significant correlation was found between the longitudinal change in DTI metrics and the change in clinical measures (Figure 3)



*: p value < 0.05; **: p value < 0.01, TP1: time-point 1; TP2: time-point 2.

Figure 3. DTI results expressed as mean ± standard deviation and calculated through repeated measures ANOVA (corrected for gender and age at baseline)(A). Longitudinal changes in RD, MD and FA from 3 selected normal appearing white matter tracts (B).

Our results show evidence of longitudinal microstructural changes in NAWM of the newly-diagnosed SLE patients. Despite the improvement of the systemic disease activity, the increase in

diffusivity indicates a compromised WM tissue microstructure in early phases of SLE disease course, even in absence of overt NP syndromes. This understanding may help to restructure the treatment strategy in newly SLE to prevent progression of WM damage and the future occurrence of NP symptoms.

- References:** 1. Ainiola H, et al. *Neurology* (2001)
2. Bertias GK, et al. *Annals of the Rheumatic Diseases* (2010)
3. Magro-Checa C, et al *Front Med* (2018)

L01.32

Magnetic resonance angiography of intracerebral arteries in prognosis of risk of post-operation and peri-infarction cerebral stroke in patients with extensive atherosclerosis

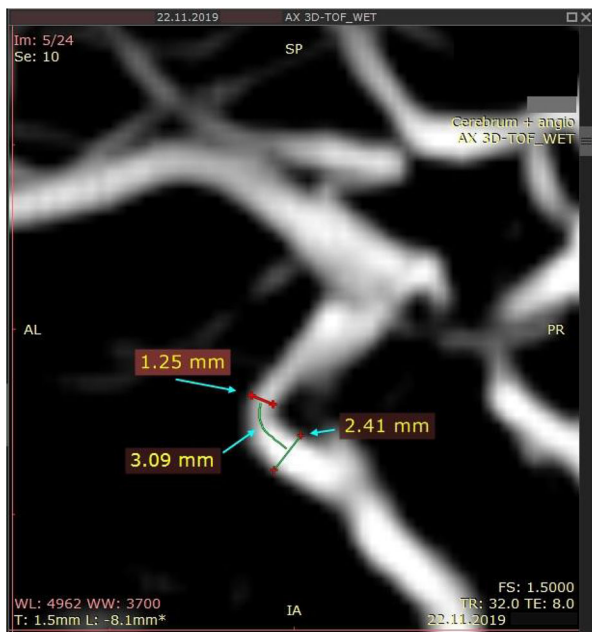
W.-Y. Ussov¹, E.-E. Bobrikova², T.-A. Bergen², A.-S. Maksimova¹, A.-M. Chemiavsky³, A.-A. Tulupov², V. E. Sinitsyn⁴

¹Tomsk Medical Research Center/ Institute of Cardiology, Lab of Tomography, Tomsk, Russian Federation, ²E.N. Meshalkin State Research Institute of Circulation Pathology, Diagnostic Radiology, Novosibirsk, Russian Federation, ³E.N. Meshalkin State Research Institute of Circulation Pathology, Novosibirsk, Russian Federation, ⁴M.V.Lomonosov Moscow State University, Moscow, Russian Federation

Introduction: The role of intracerebral stenosis of brain arteries for development of postoperative strokes in patients with extensive atherosclerosis remains unclear, and in clinical practice, the MR-angiography of the cerebral arteries is not carried out routinely to predict the risk of postoperative cerebrovascular disorders. We tried to identify factors of MRA of intracerebral arteries for prognosis of ischemic strokes in post-surgical period and acute myocardial infarction (AMI), from the quantitative processing of brain MRA.

Subjects/Methods: The results of brain MRA in 195 patients with extensive atherosclerosis carried out before cardio - or angio-surgical interventions were analyzed. Of these, three had an ischemic stroke after carotid endarterectomy, three — after CABG operations, and five — after surgical treatment of thoracic aortic aneurysms., on the second — fifth day after surgery. We also studied the results of brain MRA in five patients who developed an episode of ischemic brain stroke in the acute period of acute myocardial infarction. In all cases of circulatory disorders were localized in the region of the middle cerebral artery (MCA). Everyone was given a time-of-flight MRA with reconstruction of the three-dimensional anatomical picture of the cerebral arteries. The index of the gradient of narrowing of the arterial lumen (GNL) was calculated as the ratio of the difference in the area of the artery at the stenosis and at nearest proximal non-stenosed level, to the distance between them, along the course of the vessel:

$$GNL = \{(S_{norm} - S_{stenosis}) / D_{norm - stenosis}\}, \text{ mm}^2/\text{mm} [1] - \text{fig.1.}$$



Calculating the GNL index for the ICA, stenosed in C5 segment. The diameter in non-stenosed part is 2.41 mm, the diameter at stenosis is 1.25 mm, distance between them is 3.09 mm. $GNL = 3.14 \times (1.20^2 - 0.63^2) / 3.09 = 1.09 \text{ mm}^2/\text{mm}$. 3.14 is π value

Results/Discussion: When analyzing the brain MRA in our patients, the sign of stenosis of MCA for $> 50\%$ was observed in all five patients with acute ischemic stroke concomitant with acute myocardial infarction. In all 11 patients who developed postoperative stroke, the MCA stenosis was bilateral, more pronounced on the side of the ischemic disorder after the operation. When using the GNL index, it was obvious that ischemic stroke developed only when the stenosis GSP was $> 1.05 \text{ mm}^2/\text{mm}$. Of the five patients who showed MCA stenosis but did not have postoperative stroke, four took doses of 250 mg/day or more of ethylmethylhydroxypyridine succinate (mexidol) for more than a month. The sensitivity of MRA preoperative sign of MCA stenosis in relation to postoperative ischemic stroke was 100% in all groups, the specificity and diagnostic accuracy was 97.5%, the prognosticity of a positive conclusion was 62.5–75%, and the prognosticity of a negative conclusion was 97–99%. Thus the GNL index for atherosclerotic middle cerebral artery over $1.05 \text{ mm}^2/\text{mm}$ in patients with extensive atherosclerosis predicts increased risk of strokes in the postoperative period, or as a complication of acute myocardial infarction.

References: 1. Ussov W., e.a. Russ.J.of Cardiol. 2019;24(12):62–69. doi:10.15829/1560-4071-2019-12-62-69.

L01.33

Partial least squares regression differentiates cognitive and non-cognitive functional connectivity traits in Parkinson's disease

V. J. Ferrer Gallardo¹, T. Bolton², M. Delgado³, P. M. Paz-Alonso¹, M. C. Rodriguez-Oroz⁴, C. Caballero-Gaudes¹

¹Basque Center On Cognition Brain and language, San Sebastian-Donostia, Spain, ²ATR Computational Neuroscience Laboratories, Department of Decoded Neurofeedback, Kioto, Japan, ³Sierrallana Hospital, Neurology Department, Torrelavega, Spain, ⁴Clinica Universidad de Navarra, Servicio de Neurologia, Pamplona, Spain

Introduction: We performed partial least squares (PLS) regression analysis to study the relationship between subject-specific anthropometric and cognitive variables and independent functional connectomes (FC) derived with connICA [1] from resting-state (RS) fMRI data in Parkinson's Disease (PD).

Subjects/Methods: Participants: 23 PD patients with mild cognitive impairment (PD-MCI), 21 PD patients cognitively normal (PD-CN), and 21 healthy controls (HC) formed the final study sample (22 subjects (10 PD-MCIs, 5 PD-CN, 7 HCs) excluded due to excessive head motion). A battery of cognitive tests was taken per individual to diagnose PD-MCI (MDS task force guidelines Level II). PD patients were under anti-parkinsonian medication during the study. **MRI acquisition:** Siemens Trio 3T with 32-channel head coil, T1-w & T2-w images ($1 \times 1 \times 1 \text{ mm}^3$), two 10-min eyes-open RS-fMRI runs (TE/TR=28/2000ms, matrix= 64×64 , voxel= $3 \times 3 \times 3 \text{ mm}^3$, 33 slices) with (MB=3) and without multiband (MB = 1). **Preprocessing:** Despiking, slice timing, distortion correction, realignment and warping to MNI, and nuisance regression. **Data analysis:** Subject-specific FCs (Pearson's correlation) were computed between cortical and subcortical ROIs [2,3], and input to connICA to obtain 65 independent FC traits. Individual weights of FC traits and anthropometric and PD-MCI diagnostic cognitive variables were input to PLS [4]. Permutation ($n = 1000$) testing was used to determine statistical significance (corrected $p = 0.05$), and the robustness of FC traits and score saliences was evaluated using bootstrapping (500 random samples with replacement).

Results/Discussion:

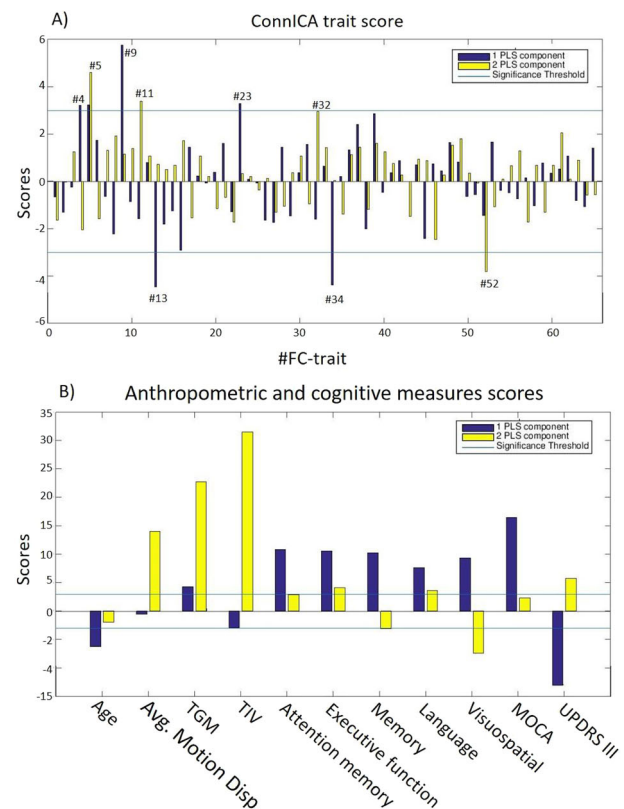


Figure 1. Results of PLS regression analysis revealed 2 significant components. A) Scores of connICA FC traits; B) Scores of anthropometric and cognitive measures. Exceeding the threshold indicates statistical significance.

Two PLS components (PLSc) were found significant (Fig. 1).

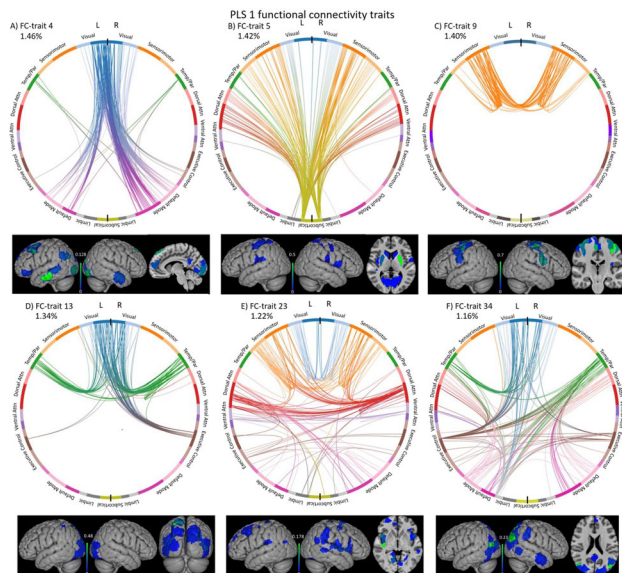


Figure 2. Significant connICA FC traits associated with PLS 1 (shown in blue in Figure 1); circular plots and nodal strength brain maps of each ROI ordered by total explained variance. Mainly related to age, cognitive tests and motor disability.

PLSc 1 was significantly linked to age, cognitive tests and motor disability, in turn showing associations with 6 connICA FC traits (Fig. 2) with the highest scores for #9 (sensorimotor), #13 (secondary visual and temporo-parietal, and executive control) and #34 (default mode network with hubs in bilateral parietal).

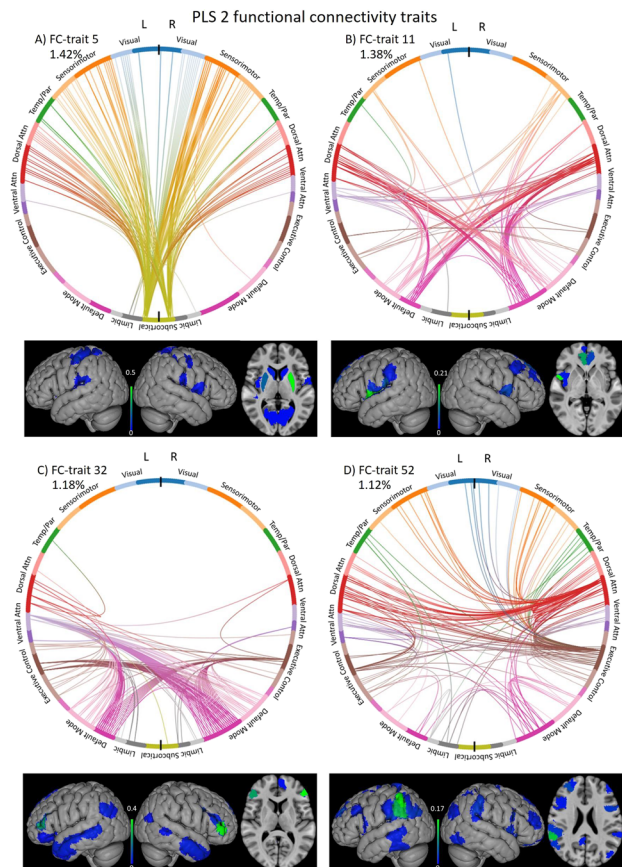


Figure 3. ConnICA FC traits associated with PLS 2 (shown in yellow in Figure 1); circular plots and nodal strength brain maps of each ROI ordered by total explained variance. Mainly related to anthropometric measures.

PLSc 2 was mainly associated with average motion displacement, total GM and intracranial volumes, as well as visuospatial skills and motor disability, and was significantly related to 4 FC traits, with the highest scores in #5 showing subcortical functional hubs (bilateral putamen and caudate nucleus) that connect with attention, visual and motor regions. Notably, FC trait #5 was revealed significant in both PLSc, proving the relevance of subcortical-cortical circuits in PD. In conclusion, our results demonstrate that PLS enables to reveal independent FC traits selectively related to cognition and more anthropometric scores with relevance for cognitive decline in PD.

References: 1. Amico E., et al (2017) doi:10.1016/j.neuroimage.2017.01.020 2. Schaefer A., et al (2018) doi: 10.1016/j.neuroimage.2010.06.010 3. Destrieux C., et al (2010) doi: 10.1016/j.neuroimage.2010.06.010 4. McIntosh A.R., et al (2004) doi:10.1016/j.neuroimage.2004.07.020

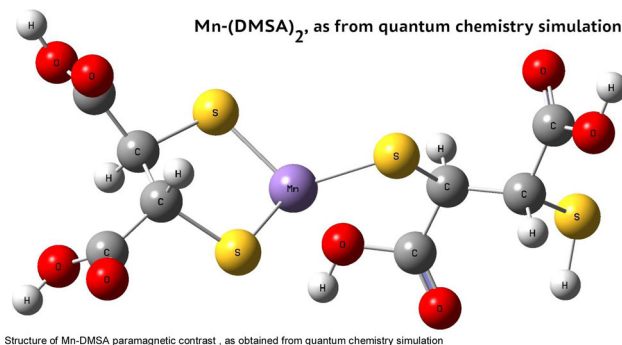
L01.34

Pre-clinical study of paramagnetic contrast enhancement with Mn(II)-dimercaptosuccinate complex in magnetic resonance imaging of primary tumor and metastatic spread of breast cancer

W.-Y. Ussov¹, M.-L. Belyanin², A.-I. Bezlepkin³, M. A. Lucic⁴, V.-D. Filimonov², N.-L. Shimanovskiy⁵

¹Tomsk Medical Research Center/ Institute of Cardiology, Lab of Tomography, Tomsk, Russian Federation, ²Tomsk National Research Polytechnic University, Organic Chemistry, Tomsk, Russian Federation, ³Aldan-Vet Veterinary Clinic, Tomsk, Russian Federation, ⁴Medical Faculty Novi Sad, University of Novi Sad, Diagnostic Imaging Center, Novi Sad, Serbia, ⁵N I Pirogov Moscow National Medical Research University, Molecular Pharmacology, Moscow, Russian Federation

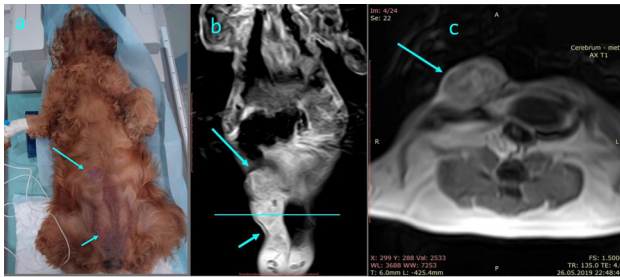
Introduction: We have studied the possibility of imaging of malignant breast tumors in dogs by magnetic resonance imaging with paramagnetic contrast enhancement using recently proposed and produced [1] complex Mn-dimercaptosuccinate (Mn-DMSA₂, TMSuccinang - structure shown on image01), in dogs.



Subjects/Methods: In seven animals (all – veterinary patients) with newly revealed breast cancer the MRI study had been carried out, when sleeping (slow infusion of propofol), with paramagnetic contrast enhancement using Mn-DMSA₂, (local synthesis in the Department of Organic Chemistry and Biotechnology of the National Research Tomsk Polytechnic University) injected slowly as 0,5M solution, in the dose as high as 0,1 mM /Kg of BW, in T1-weighted mode. The MRI scans were acquired in T1-w. mode, before, and in 12-17 min after the injection of paramagnetic. The parameters of the study were : TR = 450–600 ms, TE = 12-15 ms, to the matrix as large as 256 × 256 or 256 × 392 with the field of view as large as 250 mm × 380 mm and slice thickness 2,5 — 4 mm. All the studies have been

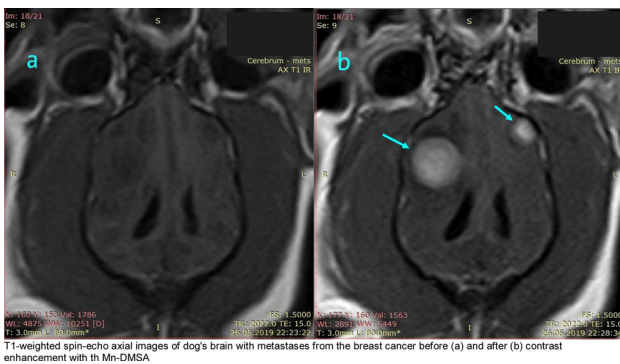
carried out using MR-scanners Toshiba Titan Vantage (Toshiba Medical, field strength 1,5 T, in five animals) and Magnetom Open (Siemens Medical, field strength 0,2 T, in two animals). The uptake of paramagnetic to the tumor was quantified using the Index of Enhancement which is ratio of intensity per per voxel of the post-contrast image to the intensity of the pre-contrast initial image. Venous blood samples were taken before and in 10 min, 30 min, 1 h, 5 h and 24 h after injection in order to control the possible blood toxic effects.

Results/Discussion: In all cases the uptake of paramagnetic contrast agent has been seen in the areas of both primary tumor (please see image02)



Breast tumor in a Cocker Spaniel (obvious on visual inspection - a, marked with arrows), enhanced with Mn-DMSA, as seen on frontal - b, and axial - c, T1-w, slices. Straight line on image02b shows the level of axial slice image02c.

and of metastatic spread to lymph nodes and to the brain (image03)



T1-weighted spin-echo axial images of dog's brain with metastases from the breast cancer before (a) and after (b) contrast enhancement with Mn-DMSA

, depicting visually the real extent of the tumor process by eye. The values of index of enhancement of the T1-w MRI were, respectively, as high as: for the primary tumor (n = 7) - $1,52 \pm 0,19$ (border values 1,35; 1,83), for the metastases to the lymph nodes (n = 12) - $1,37 \pm 0,14$ (1,12; 1,64), for the peripheral zone of the metastases to the brain (n = 11) - $1,48 \pm 0,15$ (1,29; 2,37), and for the central zone of the metastases to the brain (n = 11) - $2,76 \pm 0,12$ (1,48; 3,21). No any case demonstrated any complicationm blood toxic or concomitant effect.

Therefore, the complex Mn-DMSA₂ is an perspective non-gadolinium paramagnetic contrast agent useful for both diagnosis of primary tumor as well as of metastatic lymphogenic and haematogenic metastases in breast cancer.

References: 1. Ussov W.Y., Filimonov V.D., Belyanin M.L., Lucic M., Bezlepkin A.I., Rogovskaya Yu., Shimanovskiy N.L. Synthesis, quantum chemistry analysis and pre-clinical in vivo evaluation of paramagnetic manganese complex with 2,3-dimercaptosuccinate. *Medical Visualization*. 2019;(3):133-143. (In Russ.) <https://doi.org/10.24835/1607-0763-2019-3-133-143>

L01.35

Influence of image artifacts on image-based electrophysiological simulations using simulated XCAT phantom MR images

E. Kruihof¹, S. Amirrajab¹, M. Cluitmans², K. Lau³, M. Breeuwer⁴

¹Eindhoven University of Technology, Biomedical Engineering, Eindhoven, The Netherlands, ²Maastricht University Medical Center, Maastricht, The Netherlands, ³Philips Research Eindhoven, Digital Twin, Eindhoven, The Netherlands, ⁴Philips Healthcare Best, MR R&D Clinical Science, Best, The Netherlands

Introduction: Myocardial infarct (MI) patients have an increased risk of scar-based ventricular tachycardia (VT) and therefore sudden cardiac death [3]. Late gadolinium enhancement (LGE) magnetic resonance (MR) imaging provides the geometric extent of MI scar, but lacks functional information to assess VT risks. Image-based electrophysiological (EP) models provide a personalized solution to understand the functional relationship between MI and VT emergence [3, 4].

The geometry of the enhanced scar can be reconstructed by thresholding and interpolation of the LGE image. However, scan parameters and image artifacts can affect the reconstructed result and therefore the EP simulation outcome. To our knowledge, the effect of slice thickness and slice alignment artifacts on detected scar geometry and EP simulation remains uncharacterized. We investigated these effects by simulating LGE images on the XCAT anatomical phantom with different slice thickness and slice alignment artifacts.

Subjects/Methods: Deng [3] reports that conduction channels (CC), which are channels of remodeled living tissue through the dead scar core, sustain 63% of the induced VTs. Rhinoceros modeling software [5] is used to design a cylindrically shaped scar with inner layers for CC, which is added around the right coronary artery in the left ventricle (LV) wall of the XCAT heart model (Fig. 1).

Numerical Bloch-based MR image simulation is performed to generate inversion recovery LGE images as introduced by [1] with slice thickness of 5 and 1 mm. Slice alignment artifacts are simulated by combining slices of 10 images created at slightly different time points across two breath cycles in the parameterized XCAT model (Fig. 1).

The simulated images are segmented and interpolated to create a volumetric LV mesh with infarct regions. EP simulations are performed in CARPentry [2] using the Ten Tusscher ionic model, which is adapted to account for the remodeled CC tissue properties [3, 4]. Baseline pacing is performed in six locations, followed by a premature stimulus to induce VT (Fig. 1). For each model, a vulnerable window (VW) is identified that defines the time intervals at which VTs are induced (Fig. 2).

Results/Discussion: Table 1 shows small changes in scar volume measurements for images with variable slice thickness compared to the initial ground truth. However, these minor changes significantly affected EP simulation results, reflected by a shift in VW (Fig. 2).

Low-res image partial volume effects enlarge the reconstructed CC width compared to the high-res image result. This reduces the delay in CC repolarization and the low-res model is therefore more vulnerable to premature stimuli entry at shorter time intervals.

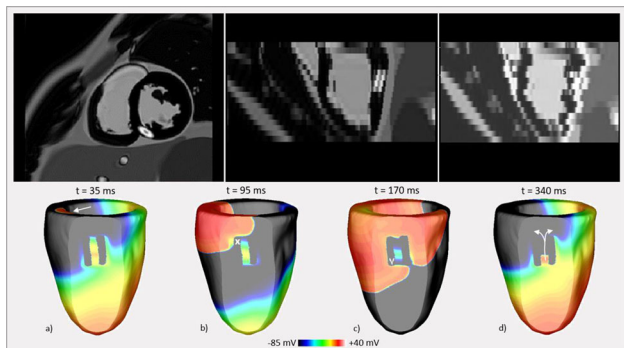


Fig. 1 Top) Phantom simulated MR image aligned (middle) and misaligned (right). Bottom) EP model with a) premature stimulus, b) EP wave block at entrance of depolarized CC, c) EP wave enters repolarized CC and d) EP re-entering tissue via CC.

	XCAT	Low-res	High-res
LV [ml]	115.56	108.27	115.62
Total scar [ml]	2.24	2.40	2.42
Core [ml]	1.24	1.38	1.45
CC [ml]	1.00	1.02	0.97

Table 1 Volumes of XCAT ground truth and image-based reconstructions.

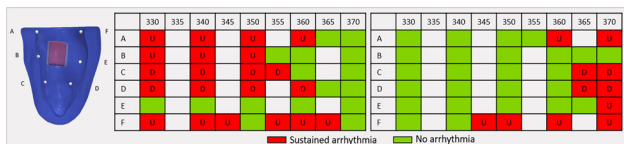


Fig. 2 Pacing locations (left) and their vulnerable windows for models based on low-res (middle) and high-res (right) XCAT phantom MR images. 'U' and 'D' type VTs are sustained by EP waves propagating upwards or down through the CC.

- References:** [1] Amirrajab (2020). *ESMRMB 2020* (Under review).
 [2] <https://carpentry.medunigraz.at/carputils>
 [3] Deng (2019). *Biophysical J.*, 117(12), 2287-2294.
 [4] Lau (2019). *CinC* (pp. P1). IEEE.
 [5] <https://www.rhino3d.com>

L01.36

Bone imaging of the spine and pelvis using an improved 3D adiabatic inversion recovery-prepared ultrashort TE sequence at 3T

M. Zamskiy¹, S. Kronthaler¹, D. Weidlich¹, I. Ball², A. S. Gersing¹, M. R. Makowski¹, J. Herzen³, D. Karampinos¹

¹Technical University of Munich, Department of Radiology, Klinikum rechts der Isar, School of Medicine, Munich, Germany, ²Phillips Australia & New Zealand, North Ryde, Australia, ³Technical University of Munich, Department of Physics, Garching, Germany

Introduction: MR-based radiation-free imaging is gaining clinical relevance for the diagnosis of multiple different bone pathologies, including osteoporosis screening¹. Different MRI techniques have been proposed to measure the short T2 components of bone, including UTE techniques². An inversion recovery (IR) prepared 3D UTE imaging sequence acquiring multiple spokes per TR has been recently introduced³. However, UTE techniques have been primarily applied to the extremities. The present work shows an improved UTE

technique for direct bone imaging of the spine and pelvis, addressing the presence of long T2 signals and occurring artifacts.

Subjects/Methods: Bloch simulations

An IR UTE sequence (Fig.1A) with 2 different adiabatic pulses was simulated with 30 repetitions to achieve a magnetization steady-state. First, the standard vendor’s 20ms offset independent trapezoid (sOIT) pulse with an amplitude of 5.32uT and frequency sweep (FS) of 635Hz and second, an improved 15ms OIT (iOIT) with an amplitude of 9.22uT and FS of 1100Hz (Fig.1B) was simulated. Fat, water and bone signals were simulated for different B0 and B1 values.

In vivo measurements

A sagittal IR 3D UTE sequence was performed with a stack-of stars center-out radial readout (Fig.1C) on a 3T MR system (Ingenia Elation, Philips Healthcare, Best, The The Netherlands) in the lower lumbar spine and pelvis. The first scan was performed with the sOIT and nonselective excitation (TE = 0.14 ms, duration = 4 m 10 s), the second scan was performed with the sOIT and selective excitation (TE = 0.21 ms, duration = 5 m 9 s) (Fig.1C) and the third one with the iOIT and selective excitation (TE = 0.21 ms, duration = 10 m 6 s). In all scans, 13 spokes were acquired after the IR pulse with max flip angle = 16, FOV = 250 × 250 × 321 mm³, resolution = 3 × 3 × 3 mm³.

Results/Discussion: The simulation showed that the iOIT has wider off-resonance profiles and a higher B₁ insensitivity compared to the sOIT (Fig.2).

The sequence with selective excitation was able to resolve folding arms artifacts compared to the non-selective excitation (Fig.3, orange arrows). Sequences with the sOIT regardless of the excitation were sensitive to B0 inhomogeneities leading to image artifacts. The implementation of the iOIT pulse removed the B0 artifacts due to the incomplete inversion (Fig.3, red arrows). In conclusion, the combination of iOIT and selective excitation in a 3D IR-prepared UTE allowed direct bone imaging of the spine and pelvis, while reducing B0 sensitivity and folding artifacts.

References: ¹Wehrli, et al. “Quantitative MRI for the assessment of bone structure and function” *NMR Biomed*(2006), DOI: 10.1002/nbm.1066

²Du, Jiang, et al. “Short T2 contrast with three-dimensional ultrashort echo time imaging” *MRI*(2011), DOI: 10.1016/j.mri.2010.11.003

³Carl, et al. “UTE imaging with simultaneous water and fat signal suppression using a time-efficient multispoke inversion recovery pulse sequence” *MRM*(2016), DOI:10.1002/mrm.25823

L01.37

Single-shot multi-point stimulated echo imaging for analysis of spontaneous muscular activities

M. Schwartz¹, P. Martirosian¹, G. Steidle¹, B. Yang², F. Schick¹

¹University Hospital of Tübingen, Section on Experimental Radiology, Tübingen, Germany, ²University of Stuttgart, Institute of Signal Processing and System Theory, Stuttgart, Germany

Introduction: Acquisition of physiological properties of unique spontaneous muscular activities (SMAMs) [1] is limited with common imaging sequences. A multi-point diffusion-weighted stimulated echo (mp-dw-STE) EPI sequence is introduced to image SMAMs at different points in time. Furthermore, a controllable incoherent motion phantom was developed to prove the feasibility of the mp-dw-STE EPI sequence.

Subjects/Methods: MR imaging sequence: The mp-dw-STE EPI scheme is illustrated in Fig. 1A. The stored longitudinal magnetization (after second 90° RF pulse) is deflected by multiple RF pulses with varying low flip angles. This leads to a series of DW images with an increasing diffusion-sensitizing time [2]. Number of RF pulses and time between the RF pulses (T_{RF}) are adjustable. Therefore, it can be

used to sample SMAMs at different points in time. To avoid signal interference, the transverse magnetization is fully spoiled after each readout. The mp-dw-STE EPI was implemented with Pulseseq [3] and tested on a 3T MR scanner (MAGNETOM Prisma^{fit}, Siemens Healthcare).

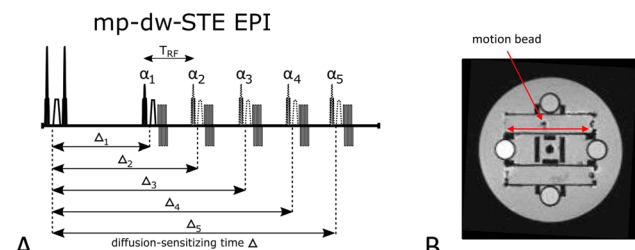


Figure 1: A. Scheme of the mp-dw-STE EPI sequence with five RF pulses leading to five different diffusion-sensitizing times Δ . B. Water-filled incoherent motion phantom with small beads which can be moved by external motor devices.

Incoherent motion phantom: Small beads in several tubes in the water-filled phantom are utilized to induce turbulences leading to signal voids in DWI [4] (Fig. 1B). The position and velocity is controlled by an external microcontroller and motor devices allowing arbitrary motion patterns. Furthermore, the imaging sequence can be triggered to synchronize the motion and data acquisition. **Evaluation:** Signal intensity was corrected before detection and segmentation of SMAMs [5]. Motion bead position was visualized and verified by additional bSSFP imaging.

Results/Discussion: An exemplary phantom and sequence control scheme is illustrated in Fig. 2A.

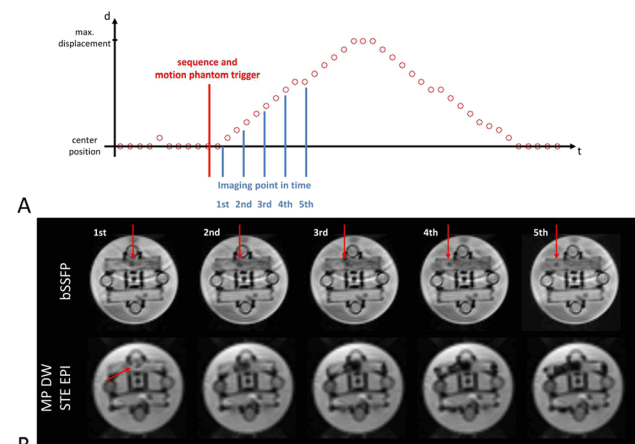


Figure 2: A. Triangular motion bead pattern with imaging points in time (derived from bSSFP images). B. bSSFP (TE=0.97ms, TR=130.57ms) and mp-dw-STE EPI images (TM=145ms, TRF=200ms, TE=60ms, b=100s/mm²) with incoherent motion (interpolated images).

The sequence is triggered by the controller just before start of motion. Corresponding bSSFP images and mp-dw-STE EPI images are shown in Fig. 2B. It is visible from the image series that the signal void is growing according to the motion bead position. MP images from the right calf of a volunteer are depicted in Fig. 3A.

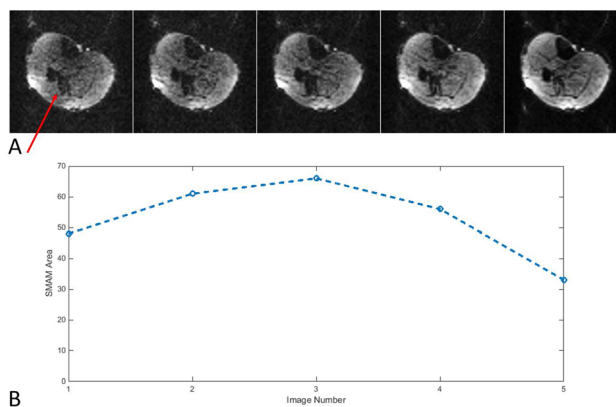


Figure 3: A. Exemplary mp-dw-STE EPI images ($\alpha=12^\circ, 16^\circ, 23^\circ, 33^\circ, 90^\circ$; TM=60ms; TRF=60ms; TE=60ms, b=100s/mm²) with visible SMAM at each point in time (MR images are interpolated). B. Corresponding SMAM area showing a section of contraction and relaxation.

The SMAM is visible in the m. soleus in all 5 images. The muscular contraction relaxes after the third image (Fig. 3B). 37.5% of all repetitions with an SMAM have shown activities in all 5 MP images.

Conclusion

Feasibility of the mp-dw-STE EPI sequence as well as the incoherent motion phantom was investigated. To reduce varying signal intensity due to T1 related effects and to improve the SNR, the flip angle series have to be optimized. Further studies have to be conducted to measure 1) physiological parameters from spontaneous muscular activities, 2) restricted diffusion properties and 3) myoelectrical activity triggered images by synchronizing the muscular contraction and the data acquisition [6-8].

References: 1:Steidle,NMR,2015.

2:Merboldt,MRM,1992.

3:Layton,MRM,2016.

4:Schwartz,NMR,2018.

5:Schwartz,ESMRMB,2019.

6:Schwartz,ESMRMB,2017.

7:Schwartz,EMBC,2018.

8: Schwartz,ISMRM,2020.

L01.38

Effects of Vitamin D on cerebral blood flow of children with adrenoleukodystrophy disease

M. Zhao^{1, 2}, N. Jimenez Ramirez³, K. Van Haren⁴

¹Stanford University, The Richard M. Lucas Center for Imaging, Stanford, USA, ²Stanford University, Department of Radiology, Stanford, USA, ³Stanford University School of Medicine, Stanford, USA, ⁴Stanford University, Department of Neurology and Neurological Sciences, Stanford, USA

Introduction: Adrenoleukodystrophy (ALD) is caused by mutations in a gene involved in the metabolism of fatty acids in the brain and blood [1]. Among children with ALD, 30% develop inflammatory demyelinating brain lesions originating at the splenium. Demyelinating brain lesions in ALD share many similarities with multiple sclerosis (MS), including links to vitamin D deficiency and cerebral hypoperfusion [2].

We hypothesized that vitamin D supplementation in ALD boys would increase cerebral blood flow (CBF). We used pseudo-continuous arterial spin labeling (PCASL) data, collected as part of a pilot study of vitamin D supplementation in ALD boys, to measure the perfusion changes of the whole brain and splenium.

Subjects/Methods: ALD boys (N = 16, aged 1.8–22 years) were enrolled in a single-arm, 12 month, dose-escalation study of oral vitamin D. Imaging data were collected on a 3T MRI scanner (GE

SIGNA, Waukesha, WI, USA) at baseline, 6 months, and 12 months. The scanning parameter of the ASL data followed the pseudo-continuous ASL sequence of GE’s product (PLD = 1.525s, bolus duration = 1.45 s, NEX = 3). A T1-weighted structural image was collected from each patient using GE’s BRAVO sequence. A mask for splenium was defined using the atlas in the MNI152-2mm standard space. CBF was quantified by fitting the ASL data to the general kinetic model using the BASIL tool [3], and it was transformed to the standard space using FLIRT and FNIRT [4]. Mean CBF of the whole brain and splenium were compared between the 6 months results and baseline and the 12 months results and baseline using paired t-tests.

Results/Discussion: Figure 1 shows the CBF of 3 example subjects at baseline, 6 months, and 12 months. Figure 2 shows the mean CBF of the whole brain and splenium. Mean CBF increased modestly by 4% ($p = 0.054$) after 6 months and 7% ($p = 0.067$) after 12 months. Figure 3 shows the correlation between vitamin D and CBF changes. Mean vitamin D level increased by 80% at 6 months and 108% at 12 months. In this small sample, we found a weak, non-significant correlation between vitamin D levels and CBF at 12 months (Figure 3). Limitations include lack of normal CBF reference values for this population, and imperfections in registration, which are areas of ongoing investigation.

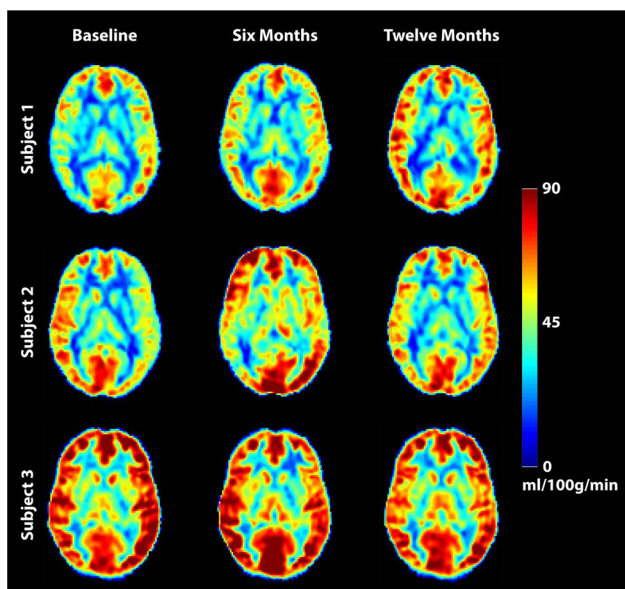


Figure 1: Estimated CBF maps of three example subjects at baseline, 6 months, and 12 months.

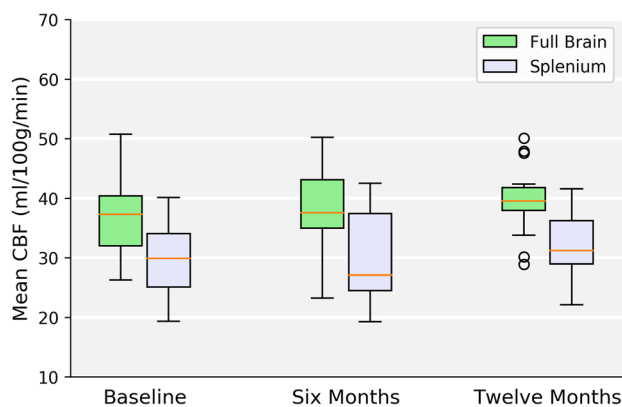


Figure 2: Mean perfusion of the full brain and splenium of all patients. No significant CBF differences were identified.

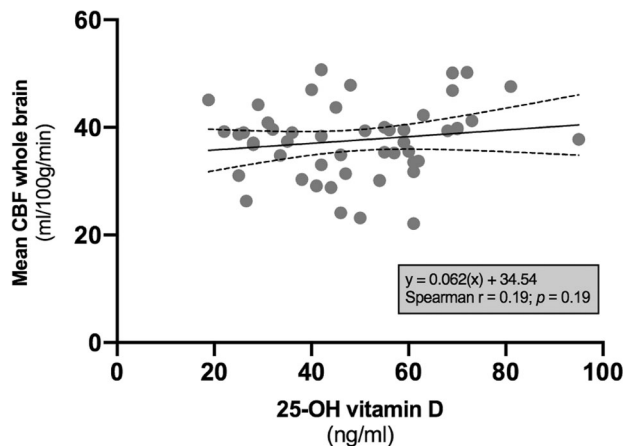


Figure 3: Correlation between CBF and vitamin D after 12 months. A weak correlation was found.

References: 1 Van Haren, et al, *Neurology*, vol. 2013
 2 Lauer, et al, *Brain J. Neurol.*, 2017
 3 Chappell, et al, *IEEE Trans. Signal Process*, 2009
 4 Jenkinson, et al, *NeuroImage*, 2002

L01.39

Insights into the development of white matter microstructure using voxel-based and fixel-based analysis methods

M. Toneva, D. Jones, E. Raven, M. Chamberland, S. Genc

Cardiff University Brain Research Imaging Centre (CUBRIC), Cardiff, UK

Introduction: The human brain white matter undergoes significant changes throughout childhood and adolescence¹. Advances in diffusion magnetic resonance imaging (dMRI) have allowed us to study these changes *in vivo*. Here we compare the performance of two dMRI analysis approaches: a voxel-based and a fixel-based analysis, in characterizing microstructural development in relation to chronological age and pubertal maturation. Our primary aim is to compare the sensitivity of microstructural measures such as fractional anisotropy (FA) and apparent fibre density (AFD) metrics to developmental patterns.

Subjects/Methods: dMRI data were acquired from a group of typically developing children aged 8-18 years (n=93) using a Siemens 3T Connectom Scanner (14 x b = 0, 30 x b = 500, 1200 s/mm², 60 x b = 2400, 4000, 6000 s/mm², TE/TR: 59/3000 ms) and pre-processed (denoising, corrections for signal drift, eddy distortions, susceptibility-induced distortions, gradient non-linearities, Gibbs ringing artefacts). Voxel-wise analysis of FA was carried out using Tract-Based Spatial Statistics (TBSS)² and fixel-wise analysis of AFD was carried out using fixel-based analysis (FBA)³. Pubertal development stage was determined using the Pubertal Development Scale (PDS)⁴. Statistical significance was set at $p < .05$.

Results/Discussion: TBSS revealed widespread age-related increases in FA in tracts spanning the entire brain, including bilateral ATR, IFOF, ILF, SLF, UF, cingulum, corticospinal tract, and the corpus callosum (Fig. 1A). In contrast, FBA revealed age-related increases in AFD in a smaller cluster of regions, including the bilateral ATR, left cingulum and corpus callosum (Fig. 2A). Tracts where FA significantly correlated with pubertal status include bilateral ATR, IFOF, SLF, the corticospinal tract, and the right ILF, UF and cingulum (Fig. 1B). Puberty-related increases in AFD were limited to bilateral ATR, left cingulum and corpus callosum (Fig. 2B). Mean FA and

AFD values were extracted from significant voxels/fixels and plotted to illustrate the strength of the associations (Fig. 3).

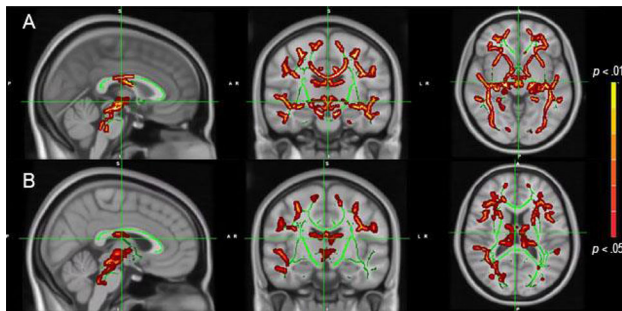


Figure 1. Sagittal, coronal and axial view of TBSS analysis of age (A, top) and pubertal development scores (B, bottom). Voxels where FA values significantly correlated with age/pubertal status are presented in red-yellow, $p_{FWE} < .05$.

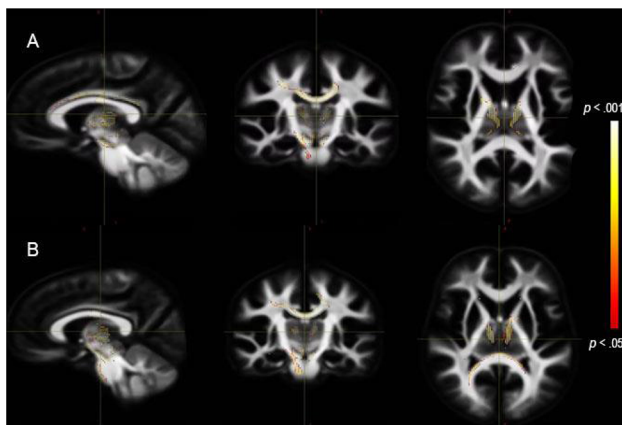


Figure 2. Sagittal, coronal, and axial view of FBA analysis of age (A, top) and pubertal development scores (B, bottom). Fixels where AFD values significantly correlated with age/pubertal status are presented in red-yellow, $p_{FWE} < .05$.

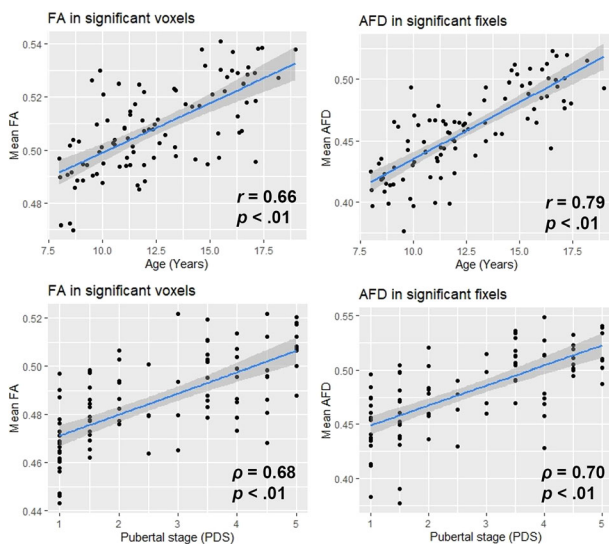


Figure 3. Associations between age, pubertal development scores, and mean participant FA/AFD values extracted from significant clusters. Pearson (r) and Spearman (ρ) correlation coefficients have been reported.

Our findings suggest that differences in analysis approaches can lead to varied results in the context of regional development of white matter microstructure. These discrepancies may be due to the inherent differences in sensitivity to microstructural attributes, as FA is sensitive to multiple properties such as axon density, organization and crossing fibres, whereas AFD is more specific to the intra-axonal signal fraction⁵. Future work will incorporate additional dMRI metrics and directly compare age-effects between analysis approaches in specific single- and crossing-fibre pathways.

References: 1. Lebel et al, NeuroImage, 2008.

2. Smith et al, NeuroImage, 2006.

3. Raffelt et al, NeuroImage, 2017.

4. Petersen et al, J Youth Adol, 1988.

5. Genc et al, HBM, 2020.

L01.40

Quantitative MRI assessment of bone marrow in children with leukaemia

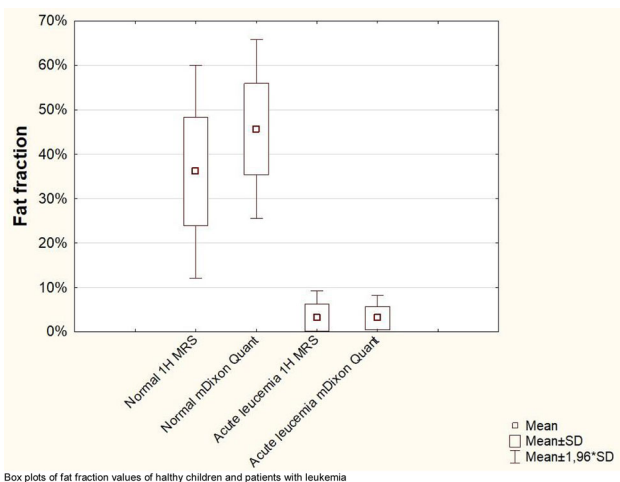
N. Strumila¹, D. Kupriyanov², P. Menshchikov², D. Litvinov¹, A. Maschan¹, G. Novichkova¹, G. Tereshchenko¹

¹Dmitry Rogachev National Research Center of Pediatric Hematology, Oncology and Immunology, Moscow, Russian Federation, ²Philips Healthcare, Moscow, Russia, Moscow, Russian Federation

Introduction: By statistics, 39,7 children per 1 million annually are diagnosed with leukaemia in Russian Federation. The diagnosis is verified using bone marrow puncture—a painful procedure of red bone marrow sampling from the iliac bones. There are some evidence that fat fraction (FF) quantified in vivo using MRI may be a non-invasive method to provide important information about the state of the bone marrow [1]. Normally, the red bone marrow contains 40% fat, 40% water and 20% protein [2]. The aim of this study was to establish a normal bone marrow FF values in healthy children and changes in this parameter in patients with acute leukemia (AL).

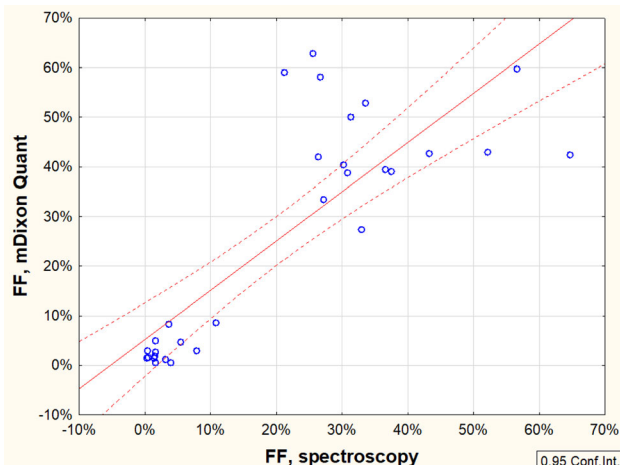
Subjects/Methods: Our research contained 16 healthy volunteers from 7 to 16 years (median of age 13.1 ± 2.9 years) and 17 patients with acute leukemia from 4 to 17 years (median of age 11.5 ± 2.7 years). The study was performed using Philips Achieva 3T MRI scanner. FF values in both patient and control groups were evaluated using 2 methods: mDixon-Quant (TR = 6.5 ms, 6 echo times starting from TE = 1.2 ms with 0.8 ms increment, coronal slices which include Ilium) and proton single-voxel MR spectroscopy (PRESS, TE/TR = 39/2000 ms). Spectroscopic voxels in size of $10 \times 10 \times 10$ mm were located in the right Ilium bone. FF values were quantified using built-in Philips console programs for both methods.

Results/Discussion: The FF in the bone marrow of healthy volunteers by the method of mDixon-Quant was $45.66\% \pm 10.27\%$, and by spectroscopy – $36.07\% \pm 12.22\%$. In children with the AL the content of fat decreases sharply to $3.08\% \pm 2.6\%$ in mDixon-Quant and to $3.14\% \pm 3.0\%$ in spectroscopy.



Box plots of fat fraction values of healthy children and patients with leukemia

Difference between the parameters of healthy volunteers and patients with leukemia according to each method was statistical significance by T-test ($p < 0.01$). Two methods had a strong correlation (Pearson's $r = 0,82, p < 0,05$).



Pearson correlation analysis results for fat fraction quantification by mDixon-Quant and MR-spectroscopy

References: 1.Ruschke, S., et al., Measurement of vertebral bone marrow proton density fat fraction in children using quantitative water-fat MRI. *Magnetic Resonance Materials in Physics Biology and Medicine*, 2017. 30(5): p. 449-460.
2.Chan, B.Y., et al., MR Imaging of Pediatric Bone Marrow. *Radiographics*, 2016. 36(6): p. 1911-1930.

L01.41
Determination of Cognitive Impairment in Parkinson’s Disease Using Proton Magnetic Resonance Spectroscopic Imaging Based Biomarkers

S. Azamat¹, S. Cengiz¹, E. Erdođdu², B. Bilgic³, H. Hanagasi³, H. Gurvit³, T. Demiralp⁴, E. Ozturk-Isik¹

¹Bogazici University, Institute of Biomedical Engineering, Istanbul, Turkey, ²Isik University, Faculty of Arts and Sciences, Department of Psychology, Istanbul, Turkey, ³Istanbul University, Istanbul Faculty of Medicine, Department of Neurology, Behavioral Neurology and Movement Disorders Unit, Istanbul, Turkey, ⁴Istanbul University,

Istanbul Faculty of Medicine, Department of Physiology, Istanbul, Turkey

Introduction: Proton magnetic resonance spectroscopic imaging (¹H-MRSI) is a noninvasive technique that provides information about the metabolism of the brain. In this study, metabolite concentrations and ratios estimated using ¹H-MRSI were compared in several brain regions of Parkinson’s disease patients with normal cognition (PD-CN), mild cognitive impairment (PD-MCI), and dementia (PDD) to identify significant metabolite-based biomarkers across the spectrum of cognitive decline.

Subjects/Methods: ¹H-MRSI data of 21 PDD, 30 PD-MCI, and 24 PD-CN patients were prospectively evaluated. The research protocol was approved by the Institutional Review Board, and all subjects provided written informed consent. ¹H-MRSI data were acquired at multiple slices using point resolved spectroscopy (PRESS) sequence at 3T (TR/TE=1000/52 ms). LCModel software was used for estimating N-acetyl-aspartate (NAA), total creatine (Cr), choline (Cho), and glutamate/glutamine complex (Glx) metabolite intensities and their ratios over Cr. An in-house software was used for creating spectral frequency images, and overlay them onto the reference T2-weighted MRI. Then, these overlaid metabolite images were registered onto the MNI152 brain atlas using FMRIB Software Library (FSL). Afterwards, the mean metabolite intensities and ratios were calculated at 400 different functional parcellations of the cerebral cortex defined by Schaefer et al [1]. Metabolic differences between the three different cognitive states were examined by a covariance analysis followed by post-hoc Dunn’s tests at each parcellation.

Results/Discussion: The mean age of PD-CN, PD-MCI and PDD patients were 60 ± 9, 63 ± 8, and 71 ± 6, respectively. Table 1 shows the metabolic ratios at the regions that were statistically significantly different between the three cognitive groups. PDD and PD-MCI patients had statistically significantly higher Cho/Cr at the medial part of the salience/ventral attention network than that of PD-CN ($P = 0.001$ for PDD vs PDCN, $P = 0.018$ for PDMCI vs PDCN). On the other hand, PDD patients had higher Glx/Cr than PD-MCI at the lateral prefrontal cortex part of the frontoparietal control network ($P = 0.002$). NAA/Cr had a progressive decline going from PD-CN to PDD at right visual network ($P = 0.0005$) (Table 2). This study indicated that metabolic intensities varied between different cognitive stages of PD. Decreased NAA/Cr may be associated with reduced neuronal viability at visual network, whereas increased Cho/Cr and Glx/Cr might be associated with membrane breakdown and cellular turnover in salience/ventral attention and frontoparietal control networks.

Brain Regions and Metabolites	Ratios		
	PDD	PD-MCI	PD-CN
Cho/Cr			
Left salience/ventral attention network, medial part	0.43±0.04	0.42±0.07	0.42±0.08
Right salience/ventral attention network, medial part	0.41±0.05	0.41±0.07	0.41±0.08
Glx/Cr			
Left frontoparietal control network, lateral prefrontal cortex	4.67±3.47	2.80±1.37	3.10±1.21
NAA/Cr			
Right visual network	1.45±0.17	1.70±0.97	2.66±0.18

Table 1. Mean (±std) metabolite ratios at regions differing between the cognitive stages in PD.

Brain Regions and Metabolites	p			
	Main	PDD vs PD-MCI	PDD vs PD-CN	PD-MCI vs PD-CN
Cho/Cr				
Left salience/ventral attention network, medial part	0.0008	0.382	0.001	0.018
Right salience/ventral attention network, medial part	0.0002	0.382	0.0007	0.004
Glx/Cr				
Left frontoparietal control network, lateral prefrontal cortex	0.003	0.002	0.054	0.252
NAA/Cr				
Right visual network	0.0005	0.775	0.031	0.0005

Table 2. Comparison of metabolite ratios between different cognitive stages of PD by ANCOVA.

Grant Support: Bogazici University BAP 15222, TUBITAK 115S219, Istanbul University BAP 1567/42362

References: 1. Schaefer, A., et al., *Local-Global Parcellation of the Human Cerebral Cortex from Intrinsic Functional Connectivity MRI*. Cereb Cortex, 2018. 28(9): p. 3095-3114.

L01.42

Functional MEGA-PRESS study of NAA and NAAG in visual cortex at 3T

A. Manzhurtsev¹, P. Menshchikov², A. Yakovlev³, M. Ublinskiy³, I. Melnikov³, T. Akhadov³, N. Semenova¹

¹Emanuel Institute of Biochemical Physics of the Russian Academy of Sciences, Moscow, Russian Federation, ²Philips Healthcare, Moscow, Russian Federation, ³Clinical and Research Institute of Emergency Pediatric Surgery and Trauma, Moscow, Russian Federation

Introduction: The role of NAA and NAAG in neuronal activation is unclear. The decrease in NAA and increase in NAAG were reported [1, 2] at 3 T. At 7T, NAAG decreased [3] and remained constant [4, 5] during visual stimulation. However, relatively low accuracy of NAAG estimation creates difficulties in evaluation of NAAG response to video stimulation even at 7T. The aim of this study is to obtain separate NAA and NAAG signals in resting state and during continuous visual stimulation using a 3T scanner with MEGA-PRESS pulse sequence and spectral averaging over subjects.

Subjects/Methods: Twelve healthy subjects aged 21-29 participated in the study. Philips Achieva dStream 3T, Head-Neck SENSE receive coil, InVivo Sensavue monitor, the mirror and home-made 8 Hz flashing checkerboard video were used. The spectroscopy voxel sized 20x40x30 mm was positioned in visual cortex (fig.1).

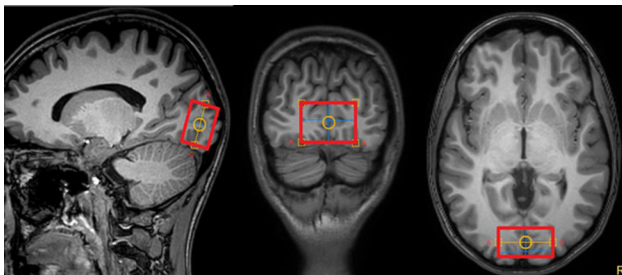


Figure 1. Voxel location in visual cortex

NAAG and NAA spectra were obtained using MEGA-PRESS sequence (PS) with parameters defined in [6]: TE = 140 ms, TR = 2000 ms, NSA = 576, 35 ms editing pulses applied at $\delta_{On} = 4.61$ ppm and $\delta_{Off} = 4.15$ ppm for NAAG, and $\delta_{On} = 4.38$ ppm and $\delta_{Off} = 4.84$ ppm for NAA. For the first half of PS the monitor was switched off, in the last the video was demonstrated. There was a 5 min break separating NAAG and NAA parts of the study.

Preprocessing was performed in FID-A: rest and activation spectra were separated, bad dynamics were rejected, spectral averages were aligned, and spectral between-subject aligning and averaging were

performed. Integral intensities of NAA, NAAG and lactate+macro-molecules (from NAAG spectra) signals in averaged resting and activation spectra were calculated by integrating. Noise integrals were used as error values.

Results/Discussion:

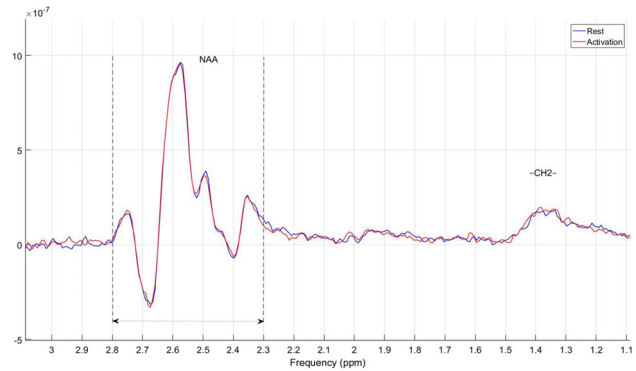


Figure 2. Averaged (over 14 subjects) NAA MEGA-PRESS spectra of visual cortex in resting and activated state

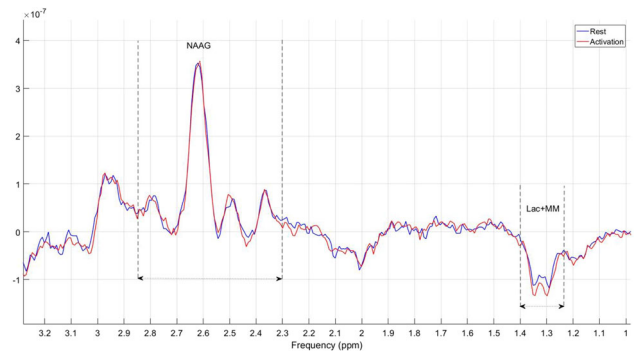


Figure 3. Averaged (over 14 subjects) NAAG MEGA-PRESS spectra of visual cortex in resting and activated state

Figures 2 and 3 represent NAA and NAAG spectra, respectively, in resting and activation states averaged from all subjects. Averaged NAA spectra in rest and activation are practically equal. The integral of the unbroadened spectra calculated from 2.1 to 2.8 ppm were $(2.03 \pm 0.07) \times 10^{-5}$ in rest and $(2.00 \pm 0.07) \times 10^{-5}$ in activation. NAAG resonance lines (fig. 3) are very similar in rest and activation, the integrals of 2.3–2.85 ppm were, respectively, $(5.28 \pm 0.53) \times 10^{-6}$ and $(5.29 \pm 0.45) \times 10^{-6}$. The increase in lactate is observable, its integral (1.24–1.4 ppm) increased from $(1.56 \pm 0.13) \times 10^{-6}$ to $(1.84 \pm 0.12) \times 10^{-6}$ upon activation.

The results of this study contradict with [2]. Spectral averaging over all subjects allowed to demonstrate that neither NAA nor NAAG change during continuous visual stimulation. This may mean that these metabolites do not participate in neuroactivation process. The increase in Lac is in good agreement with literature, e.g. [3–5].

References: 1. Castellano G et al. Braz J Med Biol Res. 2012; 45:1031–6.

2. doi:10.1016/j.mri.2015.10.038

3. doi: 10.1038/jcbfm.2014.233

4. Mangia et al. JCBFM. 2007 May;27(5):1055-63.

5. Schaller et al. J. Neurosci. Res. 91:1076–1083 (2013)

6. Edden et al. MRM 57:977–982 (2007)

L01.43**Neurometabolic white matter changes after single concussion**

P. Menshchikov¹, A. Ivantsova², A. Manzhurtsev², M. Ublinskiy², D. Kupriyanov¹, I. Melnikov², T. Akhadov², N. Semenova²

¹LLC Philips Healthcare, Moscow, Russian Federation, ²Clinical and Research Institute of Emergency Pediatric Surgery and Traumatology, Moscow, Russian Federation

Introduction: Majority of the MRS studies report reduced total NAA and NAAG (tNAA) white matter (WM) concentrations in the acute phase of mild Traumatic brain injury (mTBI). In about 25–30% of WM tNAA signal is determined by NAAG contamination. Therefore, reduced WM tNAA signal intensity might be associated both with NAA and NAAG. Main aim of this study was to determine WM NAA and NAAG as well as Asp, Glu (which are involved in NAAG and NAA synthesis) concentrations in acute mTBI.

Subjects/Methods: 24 patients with acute mTBI and 29 healthy controls (age range 13–18 years) were enrolled in the current study. 12 patients/15 controls underwent the following MRI-protocol: NAA-edited MEGA-PRESS (TE/TR = 140/2000 ms; NSA = 288; 35-ms editing pulses applied at $\delta_{ON} = 4.84$ ppm and $\delta_{OFF} = 4.38$ ppm) and an NAAG-edited spectrum (TE/TR = 140/2000 ms; NSA = 288; 35-ms editing pulses applied at $\delta_{ON} = 4.61$ ppm and $\delta_{OFF} = 4.15$ ppm). For other 12 patients/14 controls Asp-edited MEGA-PRESS (TE/TR = 90/2000 ms; NSA = 288; 25-ms editing pulses applied at $\delta_{ON} = 4.84$ ppm and $\delta_{OFF} = 4.38$ ppm) and TE-averaged PRESS (for glutamate quantification, TE from 35 ms to 185 ms with 2.5-ms increments; TR=2 s). All ¹H MRS voxels 50 × 17 × 29 mm in size were placed in the normal-appearing brain tissue of the dorsolateral pre-frontal area (fig.1).

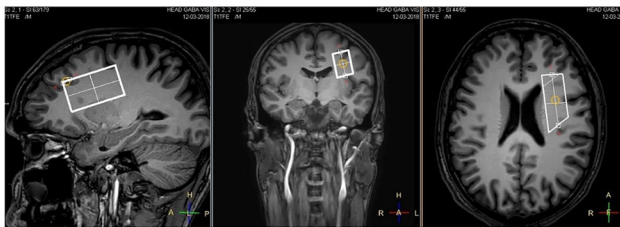


Fig.1. Voxel localization in white matter

For all subjects research protocol also contain PRESS spectra with the same size (TE/TR = 35/2000 ms).

Results/Discussion: The results are presented in the table below.

Metabolites	mTBI patients			Controls			P values
	Mean	SD	Number of spectra	Mean	SD	Number of spectra	
NAAG	1.84	0.27	10	2.30	0.25	15	0.001
NAA	8.99	0.47	10	9.06	0.68	15	n.s.
tNAA	10.99	0.69	24	11.48	0.71	29	0.026
Glu	6.91	0.41	12	7.08	0.52	14	n.s.
GLX	10.32	0.80	24	10.21	0.80	29	n.s.
Asp	0.83	0.13	11	0.95	0.12	14	0.005
mI	4.58	0.44	24	4.25	0.59	29	0.043
tCho	1.98	0.19	24	1.96	0.20	29	n.s.
tCr	7.08	0.43	24	6.98	0.48	29	n.s.

Quantification results

Statistical analysis revealed significant 4% reduction in both tNAA concentration in patients with mTBI compared to controls, respectively. The reductions were associated with a reduction in NAAG, the concentration of which, according to our data, significantly decreased in the acute mTBI phase against a constant concentration of NAA. This highlights the importance of the separate quantification of NAA and NAAG for accurate interpretation of the results. NAAG reduction might be the result of different processes, which occurs after mTBI: 1) increased NAAG consumption for binding with metabotropic Glu receptors (GluRs). Thus, damage due to excitotoxicity might be reduced, supporting a neuroprotective function of NAAG [54]; 2) NAAG might be involved in a local hyperaemic response [60]. This response increases the supply of neurons with the necessary high-energy compounds. The mI increase after mTBI in WM might be associated with microglial activation, to modulate excitatory neurotransmission by recruiting astrocytes. Glu concentration was found to be unchanged. Reduced Asp concentrations might be associated with activation of the malate–aspartate shuttle (MAS) and enables mitochondrial oxidation of the cytosolic reduced form of nicotinamide adenine dinucleotide (NADH), which is known to be important in providing energy for neurons in the CNS.

This work was supported by grants RFBR 19-29-10040.

References: 1) Moffett 2014.

2) Baslow 2016.

L01.44**Pediatric acute mTBI study of GABA and Glu levels in posterior cingulate cortex**

A. Manzhurtsev¹, P. Menshchikov², A. Yakovlev³, M. Ublinskiy³, O. Bozhko³, T. Akhadov³, N. Semenova¹

¹Emanuel Institute of Biochemical Physics of the Russian Academy of Sciences, Moscow, Russian Federation, ²Philips Healthcare, Moscow, Russian Federation, ³Clinical and Research Institute of Emergency Pediatric Surgery and Trauma, Moscow, Russian Federation

Introduction: The mechanisms underlying functional disorders in the central nervous system (CNS) caused by mild traumatic brain injury (mTBI) require intensive research. In 10–25% of mTBI patients, post-concussion symptoms persist over several month, impairing the quality of life. The balance between major neurotransmitters (excitatory – glutamate (Glu), and inhibitory – γ -aminobutyric acid, GABA), is crucial for the normal functioning of CNS. In this study, [GABA] and Glu are measured in the posterior cingulate cortex (PCC) of children with acute mTBI.

Subjects/Methods: Nineteen patients with acute mTBI (12–70 hours since injury, aged 16.7±2.2) and seventeen healthy subjects (aged 19.3±1.7) participated in the study. MRI scanner Philips Achieva dStream 3.0T was used. MRI revealed no pathological lesions in brain tissue of any subject. MRS voxels were located in the area of posterior cingulate cortex (fig. 1).

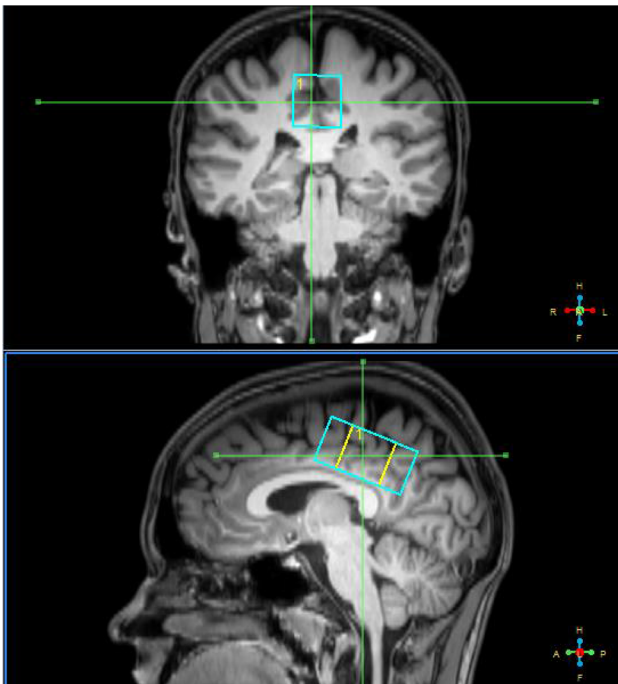


Figure 1. Voxel location in posterior cingulate cortex

MEGA-PRESS pulse sequence was used to obtain GABA signal without macromolecules [1]: TR = 2 s, TE = 80 ms, 20 ms editing pulses on $\delta_{On} = 1.9$ ppm, $\delta_{Off} = 1.5$ ppm, NSA = 288. TE averaged PRESS spectrum [2] was acquired for Glu: TR = 2 s, TE from 35 ms up to 185 ms with the 2.5 ms step, NSA for each TE=4, (acq time ~4.5 min). Standard PRESS spectrum (TE = 35 ms, TR = 2000 ms, NSA = 128) and water reference scan (TE = 28 ms, TR = 10 s, NSA = 4) were collected. GABA spectra were processed in Gannet, PRESS spectra and TE averaged PRESS – in LCModel. For basis set, TE averaged PRESS spectra of cerebral metabolites were simulated in FID-A. Absolute concentrations were calculated. Normalized (Cr) values were analyzed as well.

Statistical analysis was performed in STATISTICA 12. The Mann-Whitney criterion was used to reveal the significance of between-group differences.

Results/Discussion: Typical GABA spectrum processing in Gannet is demonstrated on figure 2. Values of [GABA] in PCC in mTBI group and in the norm were equal. No difference in GABA/Cr and GABA/Glx was found as well. TEavg spectrum processing is shown on figure 3. Glu/Cr from TE averaged PRESS decreased by 6% ($p < 0.05$) in mTBI group. The absolute concentrations of standard PRESS metabolites were equal in both groups.

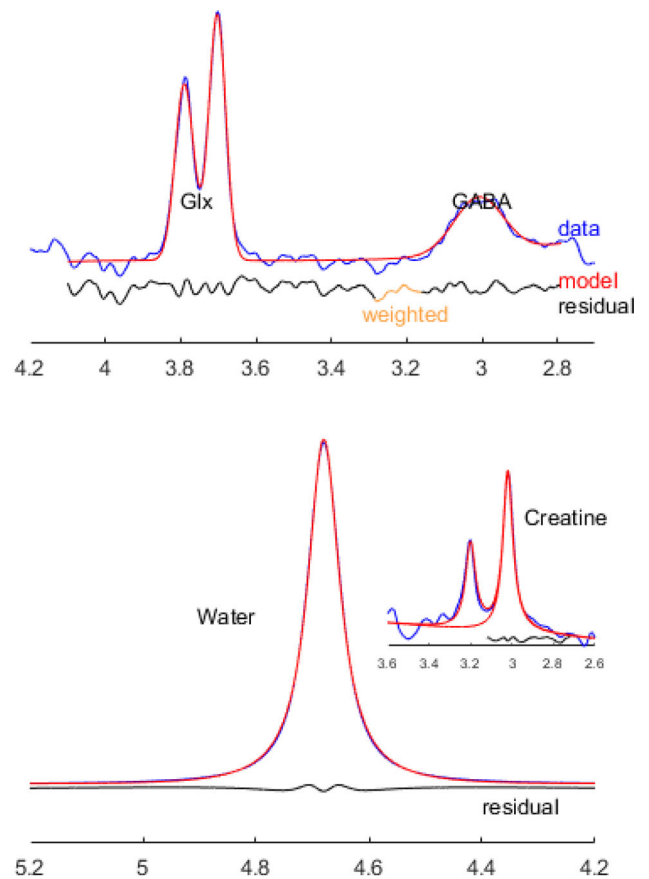


Figure 2. MEGA-PRESS GABA- spectrum processing in Gannet

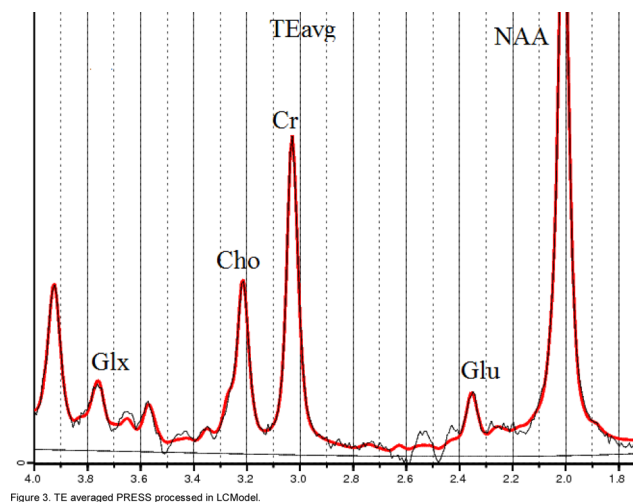


Figure 3. TE averaged PRESS processed in LCModel.

To our knowledge, this is the first measurement of pure GABA concentration in the PCC of children with mild TBI in the acute phase. The result obtained disagrees with our previous study, where [GABA] was increased ($p < 0.01$) in the anterior cingulate cortex (ACC) of children with mTBI [3]. The revealed decrease in Glu is indicative of the inactivation of excitatory processes. These findings point at the necessity of further data collecting (e.g. in different regions) in order to discover [GABA] and [Glu] alterations in various cerebral loci. This would help to identify the cases of an inhibition/excitation imbalance.

References: 1. 10.1002/mrm.24391
2. 10.1002/mrm.20007
3. 10.1134/S0006350917060161

L01.45

The use of magnetic resonance spectroscopy and principal component analysis in order to identify the progression of NAFLD

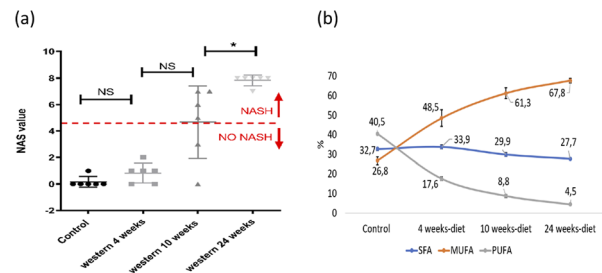
A. Xavier¹, F. Zacconi², C. Gainza³, D. Cabrera⁴, M. Arrese⁵, S. Uribe¹, C. Sing-Long¹, M. Andia¹

¹Pontificia Universidad Catolica de Chile, Millennium Nucleus for Cardiovascular Magnetic Resonance, Santiago, Chile, ²Pontificia Universidad Catolica de Chile, Faculty of Chemistry and of Pharmacy, Santiago, Chile, ³Pontificia Universidad Catolica de Chile, Institute for Mathematical and Computational Engineering, Santiago, Chile, ⁴Universidad Bernardo O'higgins, Faculty of Medical Sciences, Santiago, Chile, ⁵Pontificia Universidad Catolica de Chile, Gastroenterology Department, Santiago, Chile

Introduction: Nonalcoholic fatty liver disease (NAFLD) is characterized by the accumulation of intracellular fatty acids in the liver. The only method to confirm the stage of this disease is the biopsy, but it is invasive and risky for the patients¹. Currently, the methods for NAFLD diagnosis are based on the total amount estimation of fat infiltration in the liver², but they do not consider the differences in its composition (i.e., fatty acids profile), which has been proposed as a better method to discriminate between this group of diseases³. The purpose of this study is to investigate the liver fatty acids composition in a NAFLD mice model and to use principal component analysis (PCA) with a clustering method to group the mice according to the stage of the disease.

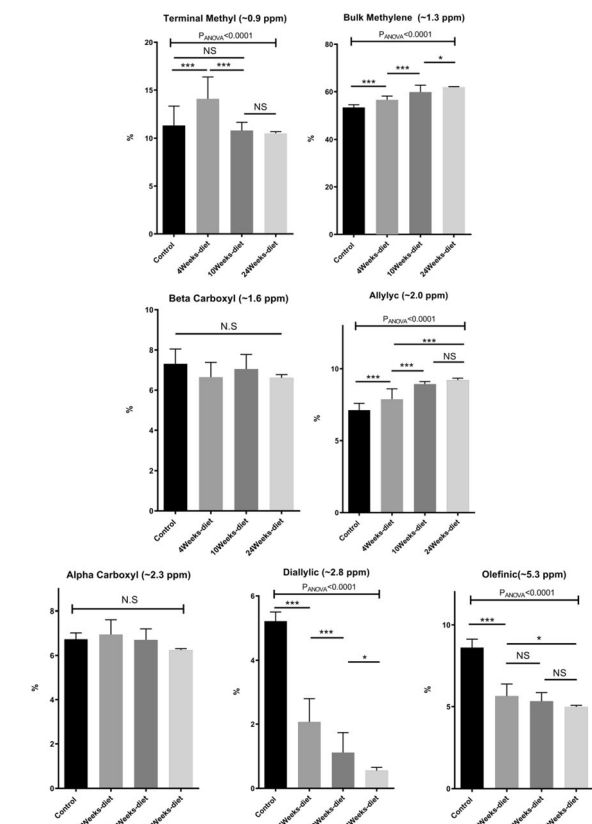
Subjects/Methods: We fed a group of C57BL/6 male mice with a Western diet for 4 weeks ($n = 6$), 10 weeks ($n = 6$) and 24 weeks ($n = 6$); and a control group ($n = 6$). A portion of the liver was used for histology and the remaining liver was analyzed with a 9.4T MRS and gas chromatography with mass spectrometer (GC-MS). The PCA for the FA composition, measured with GC-MS and metabolites identified in the MRS, were computed separately.

Results/Discussion: The mice's weight and the amount of fat stored in the hepatocytes during the Western-diet intervention increased. Histological analysis confirmed the progression of NAFLD (Fig. 1a). PUFA liver content decreased (from 40.5% in controls to 4.4% at 24 weeks-diet, $p < 0.05$) and MUFA increased (from 26.8% in controls to 67.8% at 24 weeks-diet $p < 0.05$) (Fig. 1b).



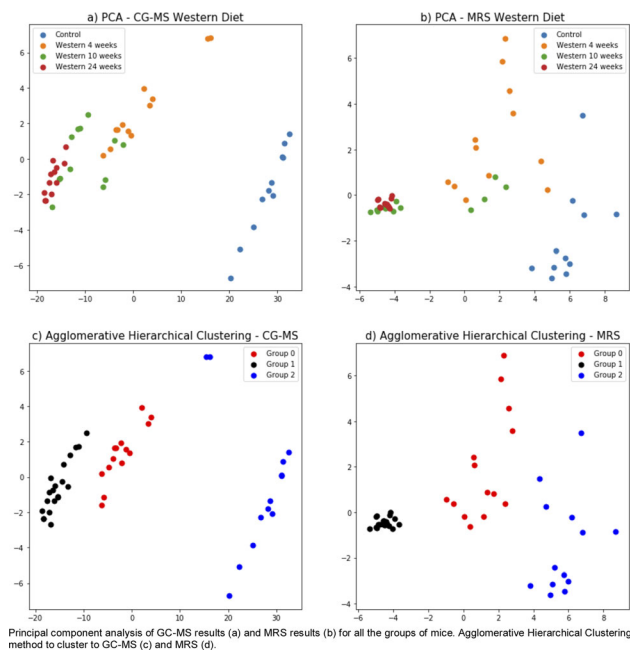
(a) Boxplot of NAS value and value for each mouse individually. (b) The relative contribution of each group of fatty acids: Saturated fatty acids (SFA), monounsaturated fatty acids (MUFA) and Polyunsaturated fatty acids (PUFA).

We have identified seven metabolite peaks in the MRS spectra. Four of them (diallylic, olefinic, allylic and bulk methylene) showed significant differences between control, 4 weeks-diet, 10 weeks-diet and 24 weeks-diet (Fig. 2).



Change in the AUC of the 7 peaks measured in the MRS for the four different groups of mice (control or chow diet, 4 weeks of Western diet, 10 weeks of Western diet and 24 weeks of Western diet).

With PCA, it was possible to identify changes in the GC-MS measurements as the time of diet intervention increases and the disease progresses (Fig. 3a). This behavior is replicated for the MRS measurements (Fig. 3b) indicating the potential for MRS to be used both as a biomarker for the progression of the disease and as a surrogate for GC-MS. By using agglomerative hierarchical clustering, it was possible to identify the 3 most relevant clinical groups: normal, steatosis, and NASH (Fig 3c,d).



Our results, as evidenced by PCA, showed that the liver fatty acid composition changes as NAFLD progresses and it was possible to identify the 3 most relevant clinical groups: normal, steatosis and NASH.

References: Friedman et al. (2018). *Nature medicine*, 24(7)
 McClain, C. J. et al. (2007). *Hepatology*, 45(6)
 Araya, J. et al. (2004). *Clinical science*, 106(6)

Acknowledgments

This publication has received funding from Millennium Science Initiative of the Ministry of Economy, Development and Tourism, grant Nucleus for Cardiovascular Magnetic Resonance, from CONICYT-PCHA/Doctorado Nacional/2016-21160835 and FONDECYT 1180525.

L01.46

Radiological and clinical analysis of dural sac diameter in lumbar spinal stenosis

E. Karatay¹, O. Turkoglu²

¹Health Science University Kartal Lütfi Kırdar Educational Research Hospital, Istanbul, Turkey, Department of Radiology, Istanbul, Turkey, ²Health Science University Sultan Abdulhamid Han Educational Research Hospital, Istanbul, Turkey, Department of Radiology, Istanbul, Turkey

Introduction: Magnetic resonance imaging (MRI) has an important role in the diagnosis of spinal stenosis. Lumbar spinal stenosis (LSS) is a very serious degenerative disease that affects the human spine. Degenerative lumbar canal stenosis often occurs with disc bulging, ligamentum flavum thickness, and facet joint hypertrophies. In many studies today, the dural sac cross-sectional area (DSA) 70–80 mm² is used as a marker of stenosis. The limit value in which the neurological signs of central spinal stenosis occur is 75 mm² for DSA. We demonstrated the relationship between the clinical symptoms of the patients and the DSA values measured in MRI as well as the states of the patients undergoing surgery.

Subjects/Methods: A total of 120 patients included in the study. All patients were divided into two groups (group A- the level of the dural sac diameter < 70 mm² and group B- the level of the dural sac

diameter >70 mm²). Clinical signs as the estimated walking distance (EWD), visual analog scale (VAS) and Oswestry disability index (ODI).

Results/Discussion: MRI data, and types of surgery recorded for each patient. Decompressive laminectomy and fusion (DL+F) or unilateral laminotomy bilateral decompression (ULBD) preferred in 48 patients of this group.

Magnetic resonance imaging (MRI) has an essential role in the diagnosis of LSS. Our study showed a positive correlation between dural sac diameter and EWS, VAS and ODI values on axial T2-weighted MR images of patients undergoing surgery.

References: 1.Malmivaara A, Slaten P, Heliövaara M. Surgical or nonoperative treatment for lumbar spinal stenosis? A randomized controlled trial. *Spine* 2007;32:1–8.

2. Marawar SV, Ordway NR, Madam IA, Tallarico RA, Palumbo M, Metkar U, Wang D, Huang D, Lavelle WF: Comparison of SurgeonRating of Severity of Stenosis Using Magnetic Resonance Imaging, Dural Cross-Sectional Area, and Functional Outcome Scores. *World Neurosurg* 2016;96:165–170.

3. Park CH, Lee SH, Jung JY: Dural sac cross-sectional area does not correlate with efficacy of percutaneous adhesiolysis in a single level lumbar spinal stenosis. *Pain Physician* 14:377–382, 2011 23-Park HJ, Kim SS, Lee SY, Park NH, Rho MH, Hong HP, Kwag HJ, Kook SH, Choi SH: Clinical correlation of a new MR imaging method for assessing lumbar foraminal stenosis. *AJNR Am J Neurorad* 2012;33:818–22.

4. Zheng F, Farmer JC, Sandhu HS, O’Leary PF: A novel method for the quantitative evaluation of lumbar spinal stenosis. *HSS* 2006;J2:136–40.

L01.47

Complementarity of T2-weighted and contrast-enhanced T1-weighted MR radiomic features for characterization of lung cancers

M. Lacroix¹, F. Orhac², I. Buvat², C. Nioche², J.-F. Bernaudin³, F. Frouin², P.-Y. Brillet¹

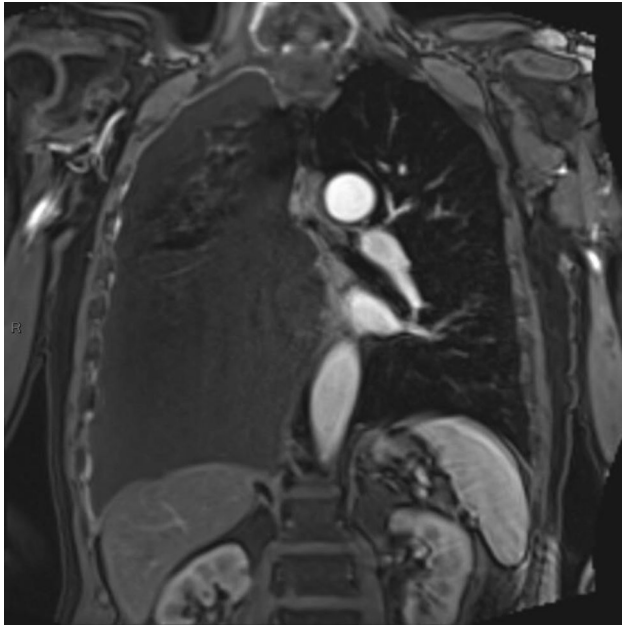
¹Hospital Avicenne, Radiology, Bobigny, France, ²Institut Curie. Inserm. U1288 LITO, Orsay, France, ³INSERM UMR 1272 Hypoxie et Poumon, Bobigny, France

Introduction: Radiomic features from MR T2-weighted (T2) images of lung cancers provide promising classification performance to predict the tumor histological type [1]. Our goal was to assess the complementarity of contrast-enhanced T1-weighted (ceT1) and T2 radiomic features to distinguish adenocarcinomas from the other histological types of lung cancers.

Subjects/Methods: 68 patients with advanced lung cancer underwent a pretreatment thoracic MR at 3T, including ceT1 and T2 Propeller sequences. The tumor was segmented using the LIFEX software [2] with a surrounding region manually defined and then refined using an intensity threshold. The images were corrected for inhomogeneity (N4ITK algorithm) and voxel intensities were normalized using fat as a reference region for T2 [1] and aorta lumen for ceT1. Radiomic features were then computed in 3D and in 2D (independently for each slice of the volume) both for T2 and ceT1 MR images providing 46 features in 3D and 44 features in 2D (choosing the median value over all slices of each patient). A screening procedure based on leave-one-out cross-validation (LOOCV) was used to identify radiomic models able to distinguish adenocarcinoma from the other histological types. The procedure involved: 1) Selection of all features with a p-value of univariate Wilcoxon test lower than 0.005, 0.01, 0.05 or 0.10 for (n-1) learning patients, 2) Based on these features, selection of only one feature among correlated features using a Pearson correlation cut-off (Rco) varying from 0.95 to 0.50, 3) Building of a radiomic signature

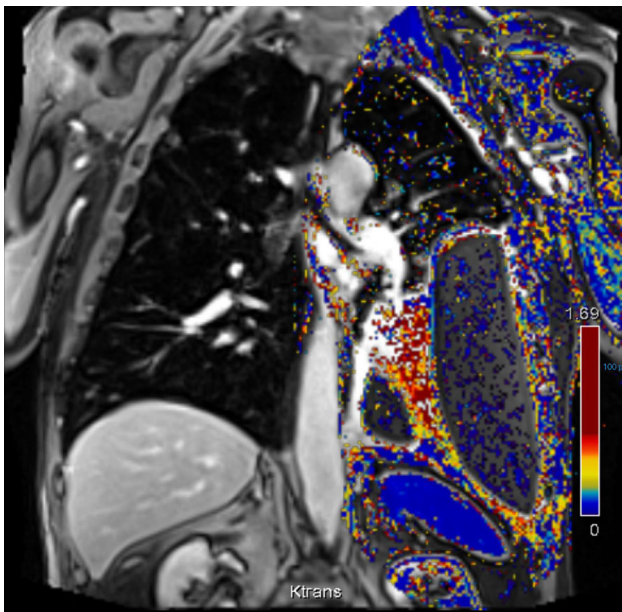
MRI to diagnose pleural malignancy (PM) in a range of patients suspected of having small volume PM.

Subjects/Methods: 60 consecutive patients with suspected PM underwent contrast-enhanced 3T MRI followed by confirmatory pleural biopsy. In 47 eligible cases, blinded placement of multiple regions of interest (ROI) per case were made on T1-weighted coronal images



A coronal T1-weighted, fat saturated and contrast enhanced image of the thorax demonstrating a large right pleural effusion and parietal pleural enhancement.

obtained 4.5 minutes post gadolinium-based contrast agent administration. K^{trans} , K^{ep} , V^e and AUC values were obtained per ROI from the parietal pleura.



A Ktrans parametric map is superimposed on a contrast enhanced T1-weighted coronal image. A moderate left pleural effusion and lateral pleural thickening is observed.

Using a threshold mean value calculated from the K^{trans} , K^{ep} , V^e

and AUC values of 6 cases of overt pleural malignancy, cases were designated as benign or malignant. A two step diagnostic process was then evaluated, with Early Contrast Enhancement (ECE) the primary diagnostic marker combined with one of the 4 pharmacokinetic analyses as the secondary marker. The case was designated as malignant if either of these markers were individually defined as malignant.

Results/Discussion: 61.7% (29/47) patients had pleural malignancy. Of the pharmacokinetic analyses, peak sensitivity was K^{ep} with 83% (95% CI 64–93%), specificity 6% (95% CI 0–29%), positive predictive value (PPV) 59% (95% CI 42–73%) and negative predictive value (NPV) 17% (95% CI 1–64%). Using the two step process, peak sensitivity was achieved with combinations of ECE plus V^e (sensitivity 100% (95% CI 85–100%), specificity 17% (95% CI 4–42%), PPV 66% (95% CI 50–79%), NPV 100% (95% CI 31–100%)) and ECE plus AUC (sensitivity 100% (95% CI 85–100%), specificity 22% (95% CI 7–48%), PPV 67% (95% CI 51–80%), NPV 100% (95% CI 40–100%)).

Combining quantitative pharmacokinetic analyses with the semi-objective perfusion biomarker ECE generally improves test performance, with particular benefit in excluding pleural malignancy in patients with small volume thickening. Further study is warranted.

References: 1. Bibby A, Tsim S, Kanellakis N et al. Malignant pleural mesothelioma: an update on investigation, diagnosis and treatment. *European Respiratory Review* 2016 25: 472-486; DOI: 10.1183/16000617.0063-2016

2. Giesel FL, Bischoff H, von Tengg-Kobligk H et al. Dynamic contrast-enhanced MRI of malignant pleural mesothelioma: a feasibility study of noninvasive assessment, therapeutic follow-up, and possible predictor of improved outcome. *Chest*. 2006;129(6):1570–1576; DOI: 10.1378/chest.129.6.1570.

L01.49

WB-MRI detection of primary lung cancer in the MALIBO study using machine learning: preliminary results of radiology clinical validation

A. Fagan¹, A. Rockall¹, S. Taylor², N. Bharwani¹, N. Johnson³, X. Li³, Q. Dou³, B. Glocker³, M. Investigators³

¹Imperial College Healthcare NHS trust, Department of Radiology, London, UK, ²University College London, Department of Radiology, London, UK, ³Imperial College London, London, UK

Introduction: Whole body MRI (WB-MRI) as part of the staging pathway for lung and colon cancer has been shown to have similar accuracy to standard pathways and to reduce the staging time and costs (1). The MALIBO study (Machine Learning in Body Oncology) investigates the application of machine learning (ML) to identify cancer lesions on WB-MRI in both lung and colon cancer. In this abstract, we present the preliminary results of a sub-set of data for the detection of the primary lung cancer by expert MRI readers with or without machine learning output.

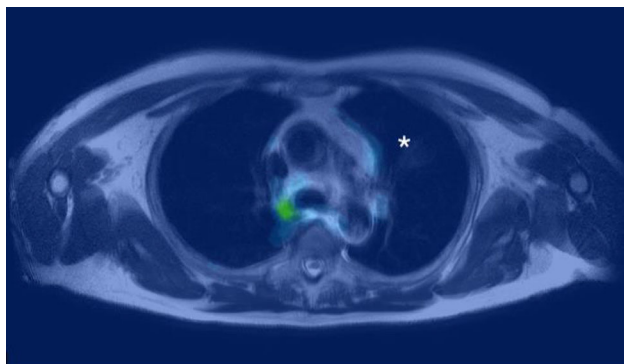
Subjects/Methods: Prospectively acquired WB-MRI scans from the NIHR STREAMLINE study were available for development (n = 226) and testing (n = 192 evaluable scans, 71 subjects with confirmed lung cancer). Ground truth findings in the training set were segmented by expert readers, using the consensus reference standard from the STREAMLINE study. DeepMedic, a 3D CNN-based deep learning approach was trained on 181 subjects to detect and segment cancer lesions and 17 normal anatomical structures. Internal validation was performed on 45 subjects. For clinical testing, all available sequences, in addition to stitched volumes of T2, b900 diffusion, and ADC maps, were provided on PACS. These were read by expert (experienced WB-MRI radiologists) and non-expert readers. These cases were allocated randomly, and were read twice, once with and

once without ML output, at least 4 weeks apart. The ML detection of the tumour and metastases was recorded based on a probability map. **Results/Discussion:** Based on the STREAMLINE consensus reference standard, there were 71 confirmed primary lung cancers. Of those, 70 were detected by expert readers both on the reads with and those without machine learning support, sensitivity of 98.6% (see table).

	Expert	Non-expert
Number of readers	17	7
Number of cases (primary tumour confirmed)	71	20
Number of pickups without ML output	70 (sensitivity 98.6%)	20 (sensitivity 100%)
Number of pickups with ML output	70 (sensitivity 98.6%)	20 (sensitivity 100%)
Number of pickups with maximum confidence without ML output	58 (81.7%)	15 (75%)
Number of pickups with maximum confidence with ML output	59 (83.1%)	18 (90%)

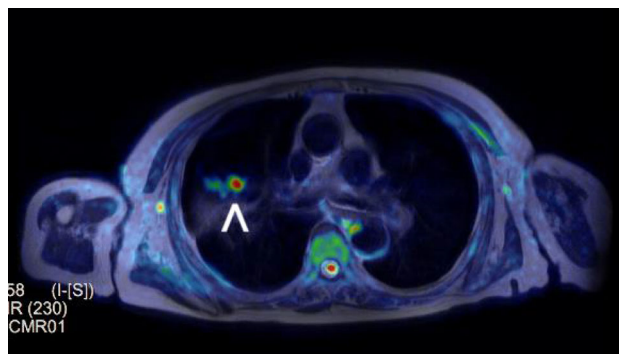
Table outlining the sensitivity of expert and non-expert reads with and without ML output

Review of the case that was missed demonstrated tumour in the left upper lobe (image A)



Axial MRI with ML output demonstrating a tumour (*) which was missed by expert readers and ML

with final stage T1b which had a ground glass appearance (*), with no evidence of restricted diffusion. Image B



Axial MRI with ML output demonstrates a right sided tumour (^) which was identified with high confidence by ML.

demonstrates a right sided tumour (^) which was correctly identified by ML.

Our findings demonstrate a high detection rate for the primary lung cancer in WB-MRI either with or without ML support. ML performance was very encouraging in view of the challenges presented by a data set from 16 different hospitals from different MR vendors and a significant heterogeneity of scan appearance, despite the prospective acquisition protocol used.

References: (1) Taylor SA, Mallett S, Ball S and Streamline investigators. Diagnostic accuracy of whole-body MRI versus standard imaging pathways for metastatic disease in newly diagnosed non-small-cell lung cancer: the prospective Streamline L trial. *Lancet Respir Med.* 2019 Jun;7(6):523–532.

L01.50

Channel compression for multiple receiver coil data in MRI

M. Arshad, M. Qureshi, O. Inam, H. Omer

COMSATS University, Medical Image Processing Research Group (MIPRG), Electrical and Computer Engineering, Islamabad, Pakistan

Introduction: Parallel Imaging (PI)[1] accelerates the data acquisition process using multi-channel receiver coil arrays. A large number of receiver coil arrays in MRI enables fast data acquisition at the cost of increase in computational complexity, memory requirement and image reconstruction time[2]. Recently, Principal Component Analysis (PCA)[2] has been used to compress multiple physical channels to a few virtual channels. However, the results showed a degradation in the image quality [2]. We propose a novel deep learning framework to compress a large number of physical channels into a few virtual channels.

Subjects/Methods: A customized U-Net[3] is used to compress the 30 receiver coil images into 8 virtual coil images. For training purpose, 1.5T T2-weighted fully sampled 30 receiver coil Cartesian human head dataset [3] is given as an input and fully sampled 8 receiver coil Cartesian human head dataset is used as label. The input and label multi-receiver coil images have been simulated from the acquired single coil images by using the 30 and 8 receiver coil sensitivities estimated by Biot Savart Law [4]. 200 datasets were used for training and 20 datasets were used for testing purpose.

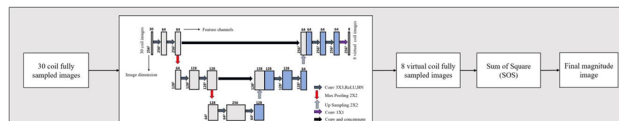


Figure 1: Block diagram of the proposed method. U-Net is used to compress 30 coil fully sampled data into 8 virtual coil fully sampled data. SOS of these virtual coil images generates the final reconstructed image.

For training purpose, all the weights of the convolutional layers

were initialized by a zero-centered normal distribution with standard deviation 0.05 without a bias term. The loss function of Mean Square Error was minimized by using the RMSPropOptimizer with learning rate of 0.001, mini-batch size 2, and 500 epochs. Training was performed on Python 3.7.1 by Keras using TensorFlow as a backend on Intel(R) core (TM) i7-4790 CPU, clock frequency 3.6GHz, 16 GB RAM and GPU NVIDIA GeForce GTX 780 for approximately three hours.

After compression, the square root Sum of Square (SOS) of the 8 virtual coil images estimated from U-Net provides the final image. The results are compared against the SOS of PCA-based 8 virtual coil [2] images.

Results/Discussion: Figure 1 shows a block diagram of the proposed method. Figure 2 shows the SOS of the compressed 8 virtual coil images obtained from the proposed method and PCA respectively. Figure 3 shows the central line profiles of the reference image (SOS of 30 receiver coil fully sampled images) and SOS of the 8 virtual coil images obtained from the proposed method and PCA[2].

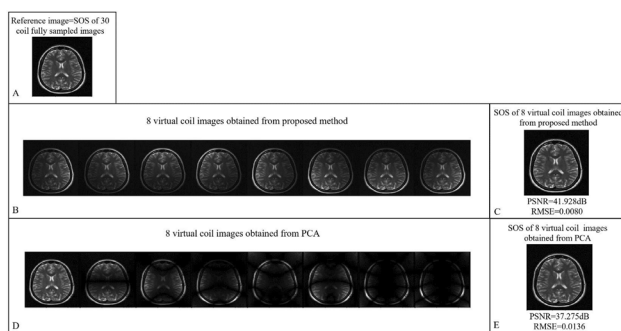


Figure 2: Image A is the reference image. (B & D) show the 8 virtual coil images obtained from the proposed method and PCA respectively, (C & E) show the SOS of 8 virtual coil images obtained from the proposed method and PCA respectively.

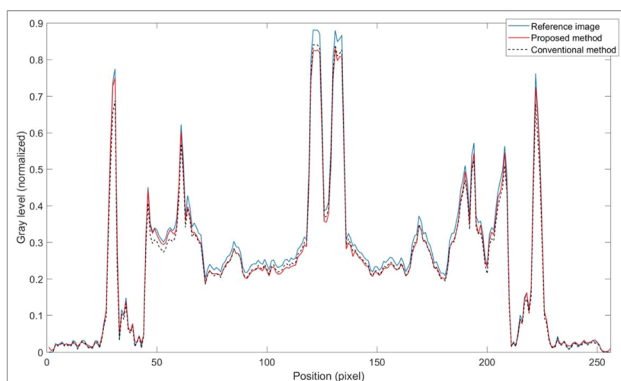


Figure 3: Central line profiles of the reference image and SOS images of the compressed 8 virtual coil images obtained from the proposed and conventional (PCA) methods.

The virtual coil images obtained from the proposed method retain the sensitivity information better as compared to virtual coil images obtained from PCA. An improvement of 12.48% and 41.17% is seen in the PSNR and RMSE respectively of SOS of virtual coil images obtained from the proposed method as compared to PCA in our experiments.

References: [1] Hamilton J et al., *Prog Nucl Magn Reson Spectrosc*, 2017

[2] Inam O et al., *Biomed Res Int*, 2017

[3] Hyun CM et al., *Phys Med Biol*, 2018

[4] Guerquin-Kern M, *Matlab code for MRI simulation and reconstruction*, 2012

L01.51

CS based p -thresholding with pMRI for the Reconstruction of Radial MRI data

F. Aamir¹, H. J. Bhatti¹, I. Aslam^{1, 2}, H. Omer¹

¹COMSATS University Islamabad, Electrical and Computer Engineering, Islamabad, Pakistan, ²University Of Geneva, Department of Radiology and Medical Informatics, Geneva, Switzerland

Introduction: Accelerated non-Cartesian trajectories are used to speed up MRI scan time, but it results in artifacts. In this paper, Compressed Sensing with parallel MRI (CS-pMRI) based p -thresholding with GRAPPA operator gridding (GROG) is proposed to recover the un-aliased MR images from the under-sampled radial k -space data. The proposed method is compared with CS-pMRI based soft and hard thresholding techniques. The proposed method provides better images in terms of quantifying parameters (AP, RMSE & PSNR) e.g. 10.8% and 10.9% improvement in AP, 0.3% and 0.6% improvement in RMSE, 1.26 % and 1.27% improvement in PSNR than CS-pMRI based soft and hard thresholding techniques at AF = 4 for 3T short-axis radial data.

Subjects/Methods: Compressed Sensing (CS)[1] is an advanced MR image reconstruction method that requires lesser k -space samples, noisy artifacts and an efficient non-linear method to recover the solution MR images. p -thresholding[2] is a variant of iterative soft thresholding (ISTA) that is used for CS to minimize the l_1 -constrained problem iteratively and recovers the unaliased MR images from the variable density Cartesian under-sampled k -space data[1]. This paper proposes a new method i.e. ‘CS-pMRI based p -thresholding with GROG’ to get the un-aliased MR images from the radial k -space data. In the proposed method initially, GROG[3] uses self-calibrated coil-by-coil weight sets and maps the acquired radial data to the Cartesian grid. In the next stage, the receiver coil sensitivity maps are estimated via Auto-calibration[4] approach from the center of the GROG gridded data. In the final stage, estimated receiver coil sensitivity maps are incorporated with the p -thresholding to model CS with pMRI to recover the un-aliased image. Figure 1 shows the schematic diagram of the proposed scheme.

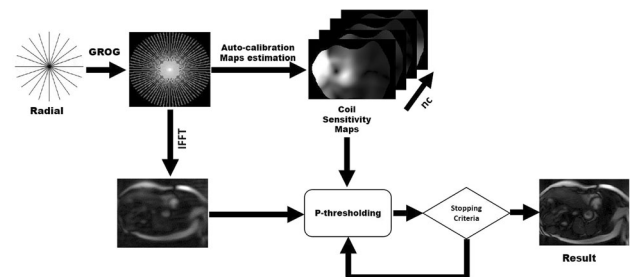


Figure 1: Schematic diagram of the proposed method (CS-pMRI based p -thresholding)

In this research work, the value of p ($p = -0.05$), λ ($\lambda = 0.3 \times 10^{-3}$) are chosen empirically and the number of iterations ($\text{iter} = 100$) is used as a stopping criterion.

Results/Discussion: The proposed method is validated on 3T short-axis radial data. Figure 2 shows the reconstruction results of the proposed method (CS-pMRI based p -thresholding), CS-pMRI based soft and hard thresholding (Column A, B & C) at AF = 4, 6, and 9 respectively.

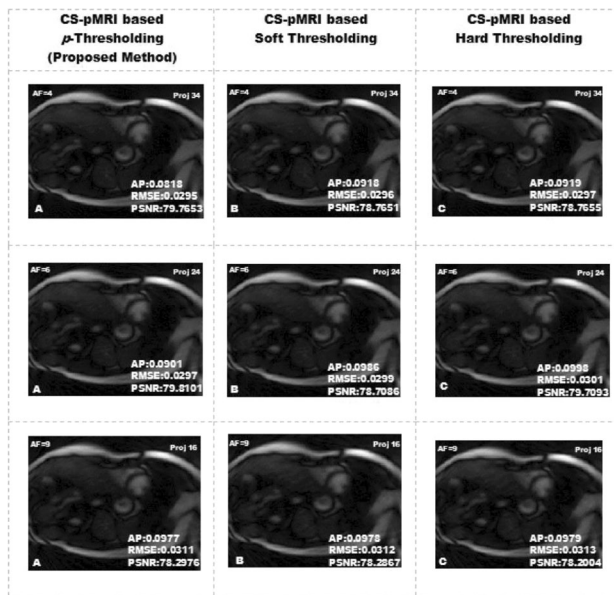


Figure 2: Reconstruction results of 3T short-axis radial data, proposed method compared with CS-pMRI based soft and hard thresholding techniques for the radially sampled k-space data at AF = 4, 6 and 9, respectively

Table 1 provides a comparison in terms of quantifying parameters. Table 1 shows an improvement of 10.8% & 10.9% in AP, 0.3% & 0.6% in RMSE, 1.26% & 1.27% in PSNR as compared to CS-pMRI based soft and hard thresholding for the cardiac radial data, respectively.

Proposed Method w.r.t CS-pMRI based Soft Thresholding (% improvement)				Proposed Method w.r.t CS-pMRI based Hard Thresholding (% improvement)		
Acceleration Factor	AP	RMSE	PSNR	AP	RMSE	PSNR
AF = 4	10.8%	0.3%	1.26%	10.9%	0.6%	1.27%
AF = 6	8.6%	0.6%	2.3%	9.70%	1.3%	1.39%
AF = 9	0.1%	0.3%	0.01%	0.20%	0.6%	0.12%

Table 1: Reconstruction results of 3T short-axis radial data, proposed method compared with CS-pMRI based soft and hard thresholding at AF 4, 6 and 9, respectively.

Results show that the CS-pMRI based iterative p -thresholding successfully recovers the un-aliased MR images from the GROG gridded data and iteratively removes the noisy artifacts while converging to the solution.

- References:** 1. M. Lustig et.al. MRM, 58, 1182–1195, 2007
 2. S. Elahi et.al. JMR, 286, 91–98, 2018
 3. N. Seiberlich et.al. MRM, 59, 1127–1137, 2008
 4. M. A. Griswold et al. NMR Biomed, 19,316–324, 2006

L01.52

Deep-learning based super-resolution reconstruction for sub-millimeter 3D isotropic coronary MR angiography

T. Kuestner¹, N. Fuin¹, A. Bustin², H. Qi¹, C. Munoz¹, R. Neji³, K. Kunze³, R. Botnar¹, C. Prieto¹

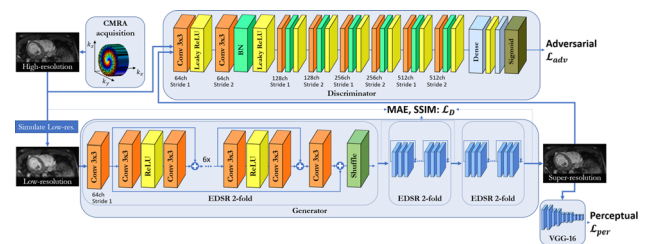
¹King’s College London, London, UK, ²LIRYC, Electrophysiology and Heart Modeling Institute, Bordeaux, France, ³MR Research Collaborations, Siemens Healthcare Limited, Frimley, UK

Introduction: 3D whole-heart coronary magnetic resonance angiography (CMRA) has shown significant potential for diagnosis and

characterization of coronary artery disease (CAD). A non-rigid motion compensated reconstruction and 2D respiratory image navigator has been recently proposed to enable free-breathing 0.9 mm³ CMRA in ~ 10 min^{1,2}. However, spatial resolution is still limited compared to coronary computed tomography angiography and scan time remains relatively long.

To further accelerate the acquisition time, we propose in this work a deep-learning based super-resolution (SR) framework combined with non-rigid respiratory motion compensation. In this retrospective study, we analyse the possibility of an 8-fold increase in resolution of a retrospectively downsampled dataset from 0.6mm³ to low-resolution (LR)=1.2 × 4.8 × 4.8 mm (FHxLRxAP) in a cohort of 50 CMRA patients with suspected CAD. This reflects an ~ 8x faster acquisition of ~ 1 min to reconstruct a high-resolution (HR) target of 0.6mm³.

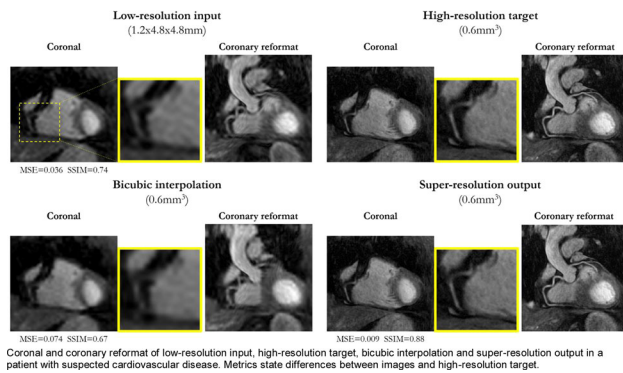
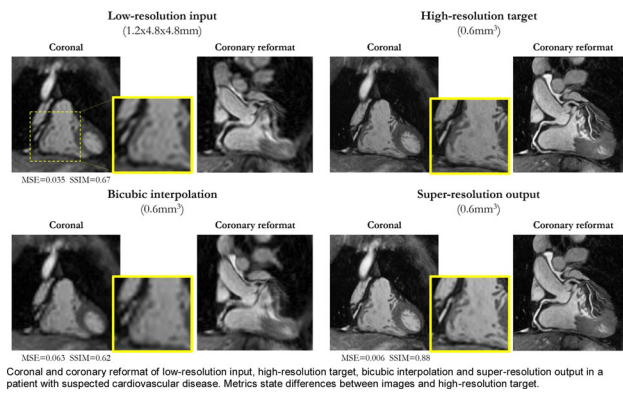
Subjects/Methods: The proposed SR framework is depicted in Fig. 1. We propose a generative adversarial network which consists of three cascaded Enhanced Deep Residual Network for SR³ generator and a trainable discriminator⁴. The input of the network is an LR CMRA whereas the output is the corresponding SR image (0.6mm³). The network is trained in a supervised manner on 22600 axial sliced HR images from 47 patients while testing is done on 780 axial images from 3 patients. In total, the network consists of ~2.4m trainable parameters optimized under mean absolute error (MAE), structural similarity index (SSIM), adversarial and perceptual (VGG-16⁵) loss by an Adam optimizer (batch size=16, 60 epochs).



Proposed generative adversarial super-resolution (SR) framework with cascaded Enhanced Deep Residual Network for SR (EDSR) generator and discriminator network.

ECG-triggered 3D whole-heart Cartesian bSSFP CMRA was acquired under free-breathing in coronal orientation in patients with suspected CAD. Imaging parameters are stated in². Data was acquired in ~7min with an isotropic resolution of 1.2mm³ and reconstructed with a non-rigid PROST² to 0.6mm³ serving as HR target. Retrospectively simulating a 12.5% phase and slice resolution provides the LR input (readout resolution was not affected). This will result in an expected acquisition time of ~1min, when prospectively acquired.

Results/Discussion: The low-resolution input, high-resolution target, commonly used bicubic interpolation and SR output of two test patients is shown in Fig. 2+3. Qualitatively and quantitatively (MAE, SSIM) SR showed significant improvement in edge sharpness and vessel delineation. The SR framework required ~ 110 h for training but only 3 s for inference.



In conclusion, the proposed SR framework has the potential to provide an 8-fold upsampling with comparable image quality than the high-resolution CMRA image. In a future study, we will investigate its applicability to prospectively accelerate CMRA in clinical practice.

- References:** 1.Cruz MRM 2017
 2.Bustin JCMR 2020
 3.Lim CVPR 2017
 4.Ledig CVPR 2017
 5.Russakovsky IJCV 2015

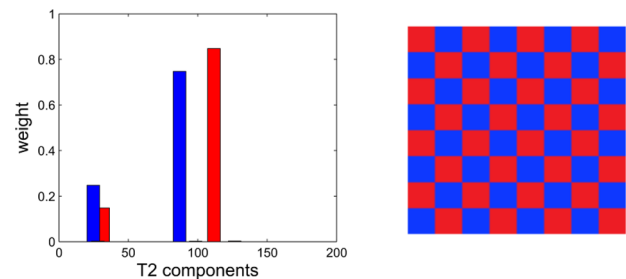
L01.53
Faster Myelin water mapping from highly undersampled 3D-GRASE acquisitions using the subspace constrained reconstruction

R. Byanju, S. Klein, A. Cristobal-Huerta, J. A. Hernandez-Tamames, D. H. J. Poot

Erasmus MC, Department of Radiology and Nuclear Medicine, Erasmus MC, Rotterdam, The Netherlands

Introduction: For Myelin water mapping (MWF) the GRASE sequence has been combined with parallel imaging to reduce scan time¹. However, further reduction is preferable. Recent works have shown that multi-echo acquisitions can be accelerated by exploiting redundancy across the temporal dimension². Model-based techniques predict undersampled k-space data from parameter maps, which can be iteratively matched to the measured k-space². However, for MWF mapping, constrained multi-exponential fitting is required³, Application of such voxel-wise constraints during model-based estimation from the k-space domain is challenging.

Previously, a subspace constrained image reconstruction technique was proposed where instead of explicitly using a model, a subspace containing most of the signal variations of the model was used for fitting. It was demonstrated to accelerate a Multi Spin Echo (MSE) acquisition⁵. Here, we show that such subspace-based reconstruction can be applied to 3D GRASE, allowing even higher acceleration. **Subjects/Methods:** A Monte Carlo simulation was performed with the ground truth shown in Figure 1.



In a multi-exponential model, the signal from a single voxel in GRASE scan can be modeled as,

$$S_{j,x} = \sum_{t \in [1, \dots, nT2]} s_{t,x} eTE_j / T_{2,t} G_{j,x}, \quad (1)$$

where $nT2$ is logarithmically spaced T_2 times indexed by $t \in [1, \dots, nT2]$, s_t is the unknown amplitude of the spectral component at relaxation time $T_{2,t}$, TE_j is the echo time and $G_{j,x}$ is compensation for gradient echoes. $G_{j,x} = e^{-i\Delta_j R_2^{sup} + i\Delta B_0 \Delta_j}$ where Δ_j is the offset of echo j from the spin echo, ΔB_0 is the local offset in the magnetic field, R_2' is the component of R_2^* accounting for the de-phasing of magnetization.

The k-space signal was obtained by adding a Complex Gaussian noise to the signal model:

$$\mu_{j,k,c} = U_{j,k} \sum_x e^{-ikx} C_{x,c} S_{j,x}, \quad (2)$$

where \mathbf{k} is k-space index, $C_{x,c}$ is coil map with coil index c , $U_{j,k} \in \{0,1\}$ is the undersampling mask generated with a Halton sequence as proposed in Byanju et. al⁶. The main acquisition settings were taken from Prasloski et. al¹. The decays shown by $nT2$ components were computed by:

$$D_{j,t} = d S_{j,x} / d s_{t,x} eTE_j / T_{2,t} G_{j,x}, \quad (3)$$

The set of decays $D_{j,t}$ were decomposed using SVD, and $d = 1$ to 25 components were used for reconstruction of $S_{j,x}$. Finally, the MWF maps were obtained with Non-Negative Least Square fitting on spin echoes⁴.

Results/Discussion: Figure 2 shows for the best d , the RMSE of the MWF map for acceleration factors up to 24, and SNR between 10 and 150.

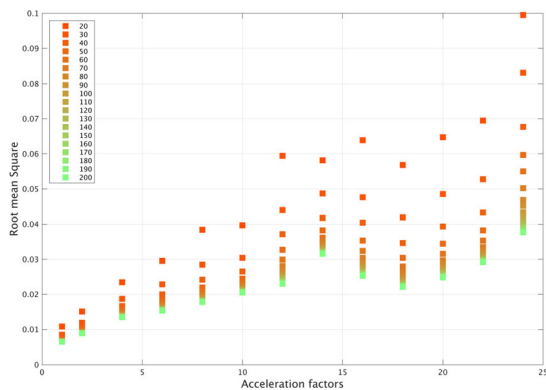


Figure 2: The minimum Root mean square error observed in monte-carlo simulation for various SNR cases represented by different colour for different acceleration factors.

Observe that for the acceleration factor of 20 the error is less than 0.03 for SNR > 70. This is more than three times higher than what was reported for MSE.

- References:** 1 Prasloski et. al, NeuroImage 2012: 533-539
 2 Zhao et. al, TMI 33 2014: 1832 1844
 3 Mackay et. al, JMR 84 1989: 134-152
 4 Prasloski et al, MRM 67 2012: 1803–1814
 5 Byanju et. al, proc.ISMRM Benelux 2020
 6 Byanju et. al, proc.ISMRM 2019: 4540



The project B-Q MINDED has received funding from the European Union's Horizon 2020 research and innovation programme under the Marie Skłodowska-Curie grant agreement No 764513.

L01.54
Further studies and acceleration of Fast Model-based Acceleration of Parameter mapping algorithm

M. Staniszewski¹, U. Klose²

¹Silesian University of Technology, Department of Computer Graphics, Vision and Digital Systems, Gliwice, POLAND, ²Eberhard Karls University, Department of Diagnostic and Interventional Neuroradiology, Tübingen, Germany

Introduction: Quantitative studies such as T1 mapping, in contrast to qualitative images, can give much better comparison and direct scanner-independent properties of tissues. The long conventional way of T1 maps acquisition, however, was recently shortened due to application of the Inverse Recovery Look-Locker sequence [1] into even 4 seconds [2]. Thus, T1 mapping finds its application in a wide variety of scientific and clinical fields. Parallel to the short acquisition time, there is a long reconstruction time, from minutes up to hours. In our preliminary work [3] we introduced the FIR-MAP method by using a 2-step fitting procedure and a coil sensitivity factor, which shortened the computational time in the best case in about 6,5 minutes for single slice. In this work we report deeper analysis of the entire reconstruction process, which ultimately led us to shortening the calculation time to 3 minutes.

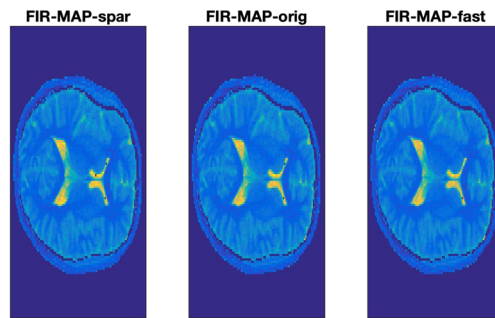


Figure 1. The FIR-MAP algorithm tested by application of sparsity (spar – calculated in faster case in 6,5 minutes), original projections (orig – calculated in the best case in 5 minutes) and without sparsity (fast – calculated in 3 minutes).

Subjects/Methods: The FIR-MAP algorithm was presented with two initial models – more accurate results are given for the interpolated version. The FIR-MAP in these studies (Figure 1) was verified with a) the use of sparsity in the interpolation process followed by iterations (FIR-MAP-spar), b) the use of original projections in the interpolation process (FIR-MAP-orig) and c) without sparsity and additional calculations (FIR-MAP-fast). The ROI analysis for the number of iterations is shown in Figure 2 compared to the referenced IR-MAP method [1]. In addition, in Figure 3 we conducted a pixel-wise analysis of all tested variants compared to the IR-MAP for image quality parameters i.e. normalized absolute error, the universal image quality index and the SSIM index [4]. The applied data is available online [1] and consists of seven volunteers obtained for single slice.

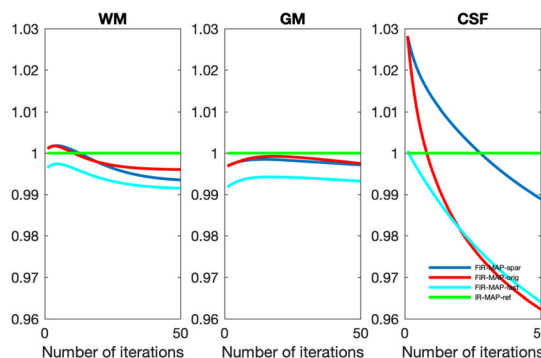


Figure 2. The selected region of interest (ROI) analysis for white matter (WM), grey matter (GM) and CSF presented in relation to the reference value with respect to the number of iterations of reconstruction.

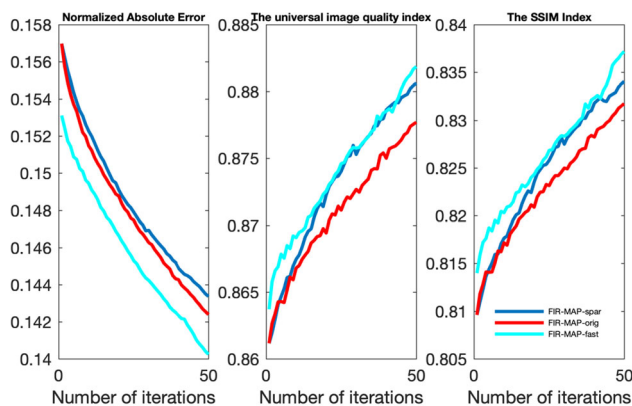


Figure 3. The image quality parameters with respect to the number of iterations of reconstruction.

Results/Discussion: The main benefit of basic IR-MAP relied on first reconstruction of interpolated projections meeting the sparsity

condition, requiring more calculations. In our research, we showed that without calculation of sparsity, no significant changes can be seen - in values after 50 iterations it differs up to 3% in the worst case of the selected ROI. In total, without additional calculations, we were able to reduce the calculations time into 3 minutes for single slice for 5 iterations. We showed also that image quality parameters can be used as an alternative in verifying the effectiveness of the reconstruction.

References: 1. Tran-Gia, J.; et. al. Model-based acceleration of look-locker T1 mapping. *PLoS ONE* **2015**, *10*.

2. Wang, X.; et. al. Model-based T1 mapping with sparsity constraints using single-shot inversion-recovery radial FLASH. *Magn. Reson. Med.* **2018**, *79*, 730–740.

3. Staniszewski, M.; Klose, U. Improvement of Fast Model-Based Acceleration of Parameter Look-Locker T₁ Mapping. *Sensors* **2019**, *19*, 5371.

4. Staniszewski, M. Image quality parameters in application of compressed sensing for MRI data. *AIP Conf. Proc.* **1978**, 110002 (2018).

L01.55

Improved GROG based Sparse-SENSE Reconstruction using Iterative Estimation of Receiver Coils Sensitivity Maps

R. Rani¹, F. Aamir¹, I. Aslam^{1, 2}, H. Omer¹

¹COMSATS University Islamabad, Electrical and Computer Engineering, Islamabad, Pakistan, ²University of Geneva, Department of Radiology and Medical Informatics, Geneva, Switzerland

Introduction: Parallel imaging with undersampled non-Cartesian trajectories enables effective k -space coverage but provides complex artifacts in the image. This work presents an improved GROG based Sparse-SENSE reconstruction using iterative estimation of receiver coil sensitivity maps for radial MRI.

The proposed method is evaluated using 3T human head data and compared with both conventional GROG based Sparse-SENSE[1] and JSENSE[2] approach. The results show that the proposed method provides up to 43%, 24%, and 3%, 90%, 69%, and 14.6% improvement than conventional GROG based Sparse-SENSE and JSENSE method in terms of AP, RMSE, and PSNR for AF=9 in our experiments.

Subjects/Methods: Conventionally, GROG based Sparse-SENSE technique[1] has been used to reconstruct MR image from the under-sampled radial data; where the receiver coil sensitivity maps obtained from the GROG gridded data are combined with the Sparse-SENSE reconstruction[6] to get the solution image. Another non-linear reconstruction method called JSENSE[2] simultaneously estimates the coil sensitivities and performs an iterative reconstruction to get the final image.

This work presents an improved GROG based Sparse-SENSE reconstruction using iterative estimation of receiver coil sensitivity maps for radial MRI. In proposed work, firstly, GROG[3] is applied to map the radial data points to the adjacent Cartesian locations using self-calibrated coil-by-coil weights sets and then the receiver coil sensitivity maps are estimated from the center of the GROG gridded data by using the auto-calibration technique[4]. Finally, these maps are used with Sparse-SENSE reconstruction to get the final image. In the proposed method, estimates of the solution image and the coil sensitivities are updated at each iteration as shown in Figure 1.

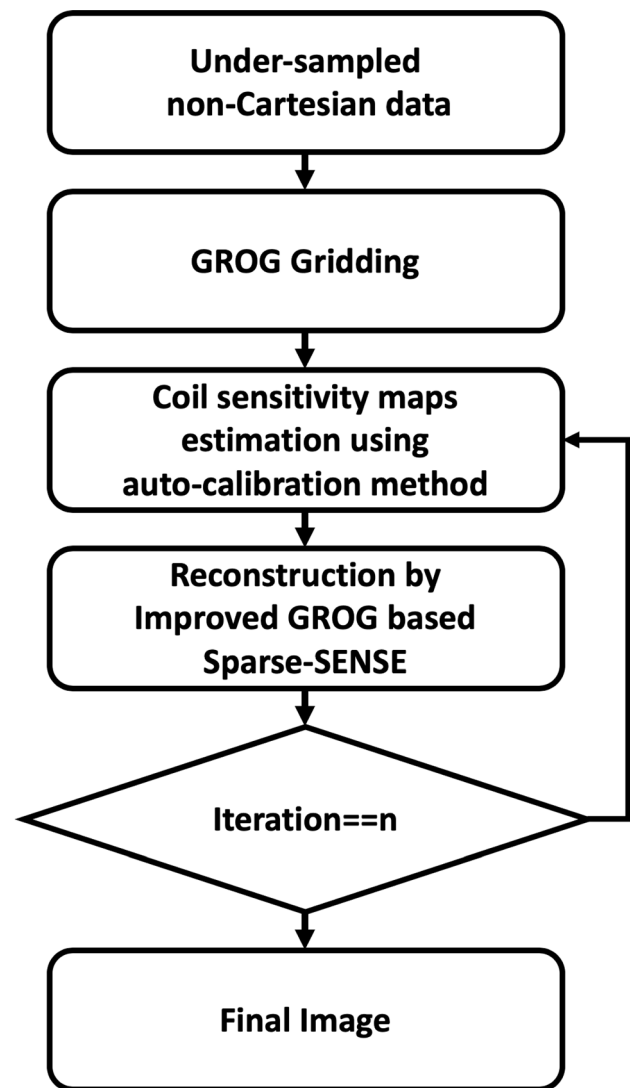


Figure 1: Block diagram of the proposed method (Improved GROG based Sparse-SENSE technique)

Results/Discussion: The proposed method is validated on 3T human head data using MATLAB (Math Works, R2019a).

Figure 2 shows the final images obtained with the proposed GROG based Sparse-SENSE (Row A), conventional GROG based Sparse-SENSE (Row B) and the JSENSE (Row C) method at acceleration factors 4, 6, and 9 with 101, 67, and 45 radial spokes, respectively.

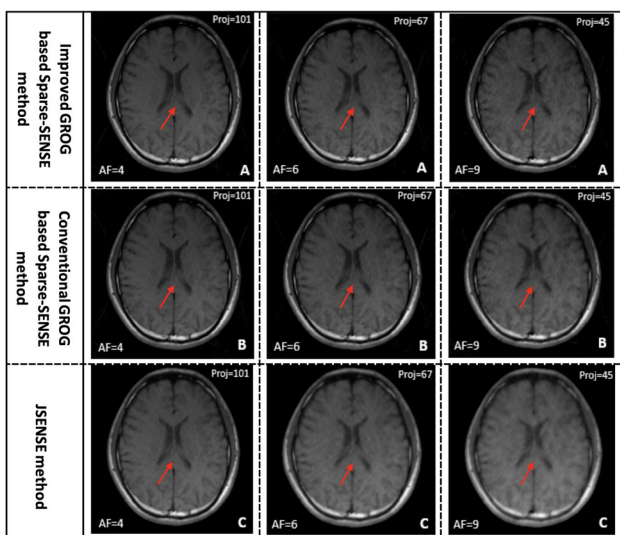


Figure 2. Reconstruction results of 3T human head data, comparing the proposed method (Row A) with the conventional GROG based Sparse-SENSE method (Row B) and the JSENSE method (Row C). The arrows indicate corpus callosum.

Table 1 shows the reconstruction results in terms of AP, RMSE, and PSNR values. Table 1 shows that the proposed method provides good improvement than the conventional GROG based Sparse-SENSE and JSENSE method e.g. 43% & 90%, 24% & 69% and 3% & 14.6% in terms of AP, RMSE and PSNR at AF = 9, respectively.

Acceleration Factor (AF)	Improved GROG based Sparse-SENSE method			GROG based Sparse-SENSE method			JSENSE method			% improvement w.r.t the GROG based Sparse-SENSE method			% improvement w.r.t the JSENSE method		
	AP	RMSE	PSNR	AP	RMSE	PSNR	AP	RMSE	PSNR	AP	RMSE	PSNR	AP	RMSE	PSNR
4	0.0085	0.0187	82.7180	0.0087	0.0189	82.6333	0.0369	0.0389	76.3598	2%	1%	0.1%	77%	52%	8%
6	0.0109	0.0211	81.6674	0.0127	0.0229	80.9768	0.0847	0.0590	72.7464	14%	7.8%	0.85%	87%	64%	12.3%
9	0.0151	0.0249	80.2430	0.0264	0.0229	77.8124	0.1587	0.0807	70.0233	43%	24%	3%	90%	69%	14.6%

Table 1. The reconstruction results of the proposed technique compared with the conventional GROG based Sparse-SENSE and JSENSE approach in terms of AP, RMSE, and PSNR at AF = 4, 6, and 9, respectively.

The proposed method provides better results both visually and in terms of quantifying parameters for highly under-sampled radially encoded data than the conventional GROG based Sparse-SENSE and the JSENSE methods.

- References:** 1. K. Afsar et al. in proceeding of 27th ISMRM Annual Meeting & Exhibition, 11-16 May 2019, Montreal, Canada.
 2. L. Ying et al. *MRM*. 1196–1202 (2007)
 3. I. Aslam et al. *APMR*. 107–124(2018)
 4. M. A. Griswold et al. *NMR Biomed*. 316–324 (2006).

L01.56

A novel methodology of confident habitats in quantitative diffusion: a use-case to classify neuroblastic tumours

L. Cerdá Alberich¹, A. Alberich-Bayarri², L. Marti-Bonmati³

¹Health Research Institute La Fe, Biomedical Imaging Research Group, Valencia, Spain, ²Quantitative Imaging Biomarkers in Medicine, QUIBIM S.L., Valencia, Spain, ³Hospital Universitario y Politécnico La Fe, Valencia, Spain

Introduction: The standard-of-care voxel-by-voxel ADC calculation is usually biased by several factors, such as the b-values used in acquisition, the eddy currents, the echo-planar imaging factor that has an influence in geometry distortion, and the level of noise. There exists no source region and signal definition standardization and, therefore, values are heavily dispersed between different centres and machines.

Prior detections of habitats as similar clusters in the tumour may help to minimize the level of noise in the extraction of ADC values when comparing to a voxel-wise analysis, generating ‘confidence habitats’, that is, regions in which stability of ADC quantification is guaranteed in terms of biases.

There is a clear need to explore how to evaluate the degree of uncertainty in the calculation of ADC values, related to the voxel vs region signal input, and provide the related statistics towards a more robust ADC quantification.

Our focus is to explore the utility of a novel approach to identify data clusters or habitats based on the minimization of uncertainty as signal inputs in the computational analysis of DW images. As a use-case in paediatric cancer, this approach will be evaluated and compared with the standard one, for classifying neuroblastic tumours as benign and malignant [1]. If proven useful, this method may help using DW derived metrics as diagnostic imaging biomarkers.

Subjects/Methods: The study included 33 consecutive paediatric oncology patients available within the H2020 PRIMAGE project. Each patient had been diagnosed with a neuroblastic tumour and had an MR study performed at diagnosis. A novel automated methodology based on histogram analysis and clustering algorithms was used to determine the ADC values from diffusion-weighted MR images. This methodology, referred to as *Fit-Cluster-Fit*, accounts for the benefits of performing a voxel-wise dual cluster parcellation, incorporating a smearing process to predict the expected cluster assignment with a high accuracy (less than 5% statistical error) and applying an uncertainty exclusion strategy to identify and remove noise and low-quality lesion voxels (Figure 1).

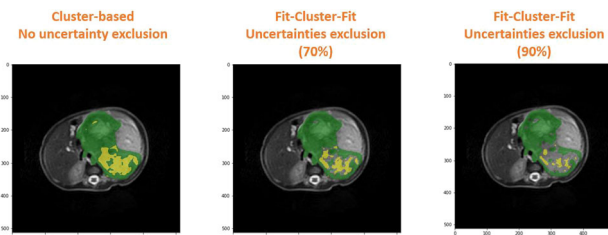


Figure 1. Representative map of ADC values per tumor malignancy, using the cluster-based and Fit-Cluster-Fit methodologies.

Results/Discussion: A significant improvement (sensitivity = 100%, specificity = 87%, p<0.001) in the differentiation between benign and malignant neuroblastic tumours with respect to state-of-the-art voxel-by-voxel methodologies has been observed (Table 1). Three visualization algorithms have been developed to account for different symbolic representation levels of the tumor heterogeneity: parametric maps, confidence maps and representative maps. Their combination with other sources of data opens the door to new possibilities for the discovery of new insights into a high-accuracy definition of tumor heterogeneity.

Strategies	ADC cut-off value	ADC value		Sensitivity (%)	Specificity (%)	Accuracy (%)	Precision (%)	AUC
		Benign	Malignant					
Voxel-based	1.56	1.89±0.55	1.23±0.34	0.78	0.87	0.84	0.70	0.877
Cluster-based	0.75	1.22±0.38	0.50±0.23	1.0	0.87	0.91	0.75	0.976
FCF	0.77	1.25±0.38	0.53±0.24	1.0	0.87	0.91	0.75	0.967
FCF (60%)	0.75	1.24±0.38	0.51±0.24	1.0	0.83	0.88	0.69	0.961
FCF (70%)	0.77	1.21±0.39	0.48±0.24	0.89	0.91	0.91	0.80	0.959
FCF (80%)	0.68	1.07±0.34	0.45±0.22	1.0	0.87	0.91	0.75	0.967
FCF (90%)	0.60	0.98±0.33	0.41±0.20	1.0	0.83	0.88	0.69	0.967
FCF (95%)	0.57	0.94±0.32	0.39±0.19	1.0	0.83	0.88	0.69	0.964

Table 1. Apparent Diffusion Coefficient (ADC) per tumour malignancy, using the voxel-based, cluster-based and Fit-Cluster-Fit methodologies.

- References:** [1] Meeus E, et al. Diffusion-weighted MRI and

intravoxel incoherent motion model for diagnosis of pediatric solid abdominal tumors. *JMRI*. 2017 Nov 21

L01.57

Axon-diameter index mapping with extra-strong diffusion-weighted MRI: the impact of intra-axonal axial diffusivity

M. Ashtarayeh¹, U. K. E. Consortium², B. U. F. Consortium³, P. F. Consortium⁴, M. P. Consortium⁵, W. i. a. s. Consortium⁶, S. Mohammadi¹

¹Department of Systems Neurosciences, University Medical Center Hamburg-Eppendorf, Hamburg, Germany, ²Jan-Malte Oeschger, Tobias Streubel, Department of Systems Neurosciences, University Medical Center Hamburg-Eppendorf, Hamburg, Germany, ³Joao Periquito, Andreas Pohlmann, Thoralf Niendorf, Berlin Ultrahigh Field Facility (B.U.F.F.), Max-Delbrueck-Center for Molecular Medicine in the Helmholtz Association, Berlin, Germany, ⁴Maria Morozova, Henriette Rusch, Markus Morawski, Paul Flechsig Institute, Leipzig, Germany, ⁵Carsten Jäger, Nikolaus Weiskop, Department of Neurophysics, Max Planck Institute for Human Cognitive and Brain Sciences, Leipzig, Germany, ⁶Karsten Tabelow, Weierstrass Institute Applied Stochastics, Berlin, Germany

Introduction: A recently proposed MRI-based method for axon diameter index (ADI) estimation using extra-strong diffusion-weighted MRI (esDWI) showed good agreement with its histological counterpart¹. Hereby, the intra-axonal axial diffusivity, D_a , is a parameter of this ADI-model that can be either fixed or measured. Here, we test the impact on ADI estimation when using a fixed literature value for D_a as compared to measuring it using two different models^{2, 3}.

Subjects/Methods: Sample: Here, we analyzed one *in vivo* brain, one *ex vivo* corpus callosum and one *ex vivo* human medulla oblongata.

Effective axon diameter from histology (ADI_{Hist}) was calculated from histological axon diameter distribution^{6–9} as proposed in¹⁰.

Results/Discussion: All measured *ex vivo* D_a values in Table 1 were smaller than $D_{a,fix}$, which might be due to the deviating fixative used in⁴ and ours.

We found that ADI_{MRI} was 16% larger than ADI_{Hist} when $D_{a,fix}$ was used. ADI_{MRI} was closest to ADI_{Hist} when measuring D_a with JESP+ (10% overestimation) and farthest apart when measuring it with JESP- (15% underestimation) and WMTI(30% underestimation). JESP+ was also favored by Jespersen et al.² when investigating the diffusion-time dependence.

We showed that ADI_{MRI} strongly depends on D_a . By comparing ADI_{MRI} against gold standard the best approach to measure D_a can be identified. However, the data used here as reference might be inappropriate because they are based on classical electron microscopy data, where large-diameter axons are underrepresented (for more details see Mordhorst et al. at this ESMRMB).

ROI	Genu [mm ² /s]	Anterior Body [mm ² /s]	Mid Body [mm ² /s]	Posterior Body [mm ² /s]	Splenium [mm ² /s]	All [mm ² /s]	
<i>ex vivo</i>	JESP+	0.43±0.17	0.46±0.2	0.49±0.21	0.51±0.10	0.56±0.09	0.49±0.05
	JESP-	0.21±0.13	0.18±0.08	0.16±0.08	0.20±0.08	0.18±0.11	0.18±0.02
	WMTI	0.12±0.02	0.12±0.02	0.05±0.02	0.07±0.02	0.07±0.01	0.09±0.03
<i>in vivo</i>	JESP+	3.06±0.44	3.13±0.19	3.11±0.31	2.86±0.23	2.89±0.25	3±0.12
	JESP-	0.86±0.39	1.14±0.31	1.63±0.66	1.98±0.51	1.60±0.63	1.44±0.44
	WMTI	1.10±0.13	1.07±0.11	1.21±0.15	1.15±0.12	0.95±0.16	1.09±0.09

Table 1: The mean and standard deviation of measured D_a^I using JESP+, JESP- and WMTI models within ROIs of human *ex vivo* and *in vivo* corpus callosum. ROIs: genu, anterior body, mid body, posterior body and splenium.

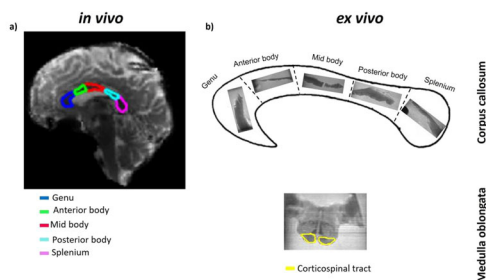


Fig. 1 (a): Non-diffusion weighted image of *in vivo* human brain including the region of interests in corpus callosum. (b): Non-diffusion weighted image of *ex vivo* human corpus callosum (Genu, Anterior body, Mid body, Posterior body and Splenium) and medulla oblongata. Note that the *ex vivo* samples were obtained at autopsy with prior informed consent (24 hrs postmortem) and approved by the responsible authorities. Following standard brain bank procedures, the samples were immersion-fixed 3% paraformaldehyde + 1% glutaraldehyde.

MRI: *Ex vivo* diffusion MRI was performed on a small bore 9.4T MR system (Bruker Biospin, Ettlingen, Germany) with 6 shells from 50k s/mm^2 to 100k s/mm^2 (esDWI) and 3 shells up to 7.5k s/mm^2 (low diffusion-weighted MRI, IDWI).

In vivo diffusion MRI was measured on a 3T MR system (Siemens, Prisma Fit) with 3 shells up to 2500 s/mm^2 .

Parameter estimation: The effective axon diameter from MRI (ADI_{MRI}) was estimated according to the approach introduced in¹.

For intra-axonal axial diffusivity estimation the fixed value $D_a=0.6 mm^2/s$ as suggested by⁴ was used (denoted as: $D_{a,fix}$). The measured D_a was estimated for each sample from the IDWI data using (a) an in-house implementation of the model introduced by Jespersen et al.² including both branches (JESP+ and JESP-), and (b) the white matter tissue integrity (WMTI) model³ as implemented in⁵.

ROI	Genu [μm]	Anterior Body [μm]	Mid Body [μm]	Posterior Body [μm]	Splenium [μm]	CST [μm]	All [μm]
Method							
Fixed D_a^I	4.16±0.36	3.97±0.16	3.78±0.17	3.74±0.14	2.98±0.23	3.88±0.22	3.75±0.37
JESP +	3.84±0.37	3.72±0.14	3.6±0.16	3.58±0.14	2.93±0.23	3.92±0.23	3.59±0.32
JESP -	3.12±0.12	2.97±0.10	2.71±0.13	2.85±0.10	2.2±0.18	2.73±0.19	2.76±0.28
WMTI	2.72±0.11	2.65±0.11	2.12±0.10	2.17±0.08	1.74±0.14	2.14±0.19	2.25±0.33
Histology	2.2±0.32	3.7±0.98	3.23±1.54	4±0	2.7±0.75	4.1±1.13	3.24±0.75

Table 2: The mean and standard deviation of estimated axon diameters using fixed D_a^I and measured D_a^I with JESP+, JESP- and WMTI models across different ROIs: Genu, Anterior body, Mid body, Posterior body, Splenium and corticospinal tract. Last row: effective axon diameters from literature using published histological axon-diameter distribution.

- References:** 1.Veraart, J. *et al. eLife* **9**, e49855 (2020).
 2.Jespersen, S.N. *et al. NI* **182**, 329 (2018).
 3.Fieremans, E. *et al. NI* **58**, 177 (2011).
 4.Alexander, D.C. *et al. NI* **52**, 1374 (2010).
 5.<https://github.com/NYU-DiffusionMRI/DESIGNER>
 6.Aboitiz, F. *et al. Brain Res.* **598**, 143 (1992).
 7.Caminiti, R. *et al. PNAS* . **106**, 19551 (2009).
 8.Graf von Keyserlingk, D. *et al. Anat. Anz.* **157**, 97 (1984).
 9.Liewald, D. *et al. Biol. Cybern.* **108**, 541 (2014).
 10.Burcaw, L.M. *et al. NI* **114**,18(2015)

L01.58**Comparison of NODDI parameter estimates in staggered versus non-staggered 2-shell acquisitions**

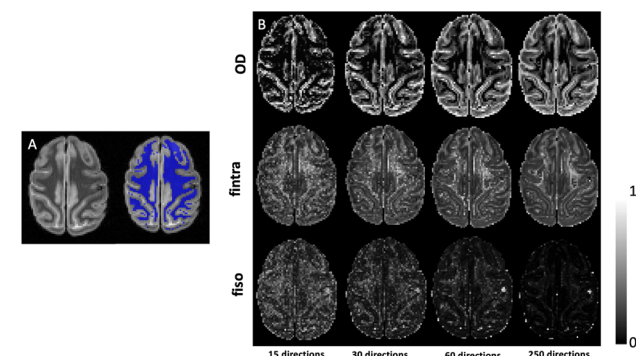
C. Tisca, A. F. D. Howard, S. Jbabdi, A. Martins-Bach, K. L. Miller

University of Oxford, Nuffield Department of Clinical Neurosciences, Oxford, UK

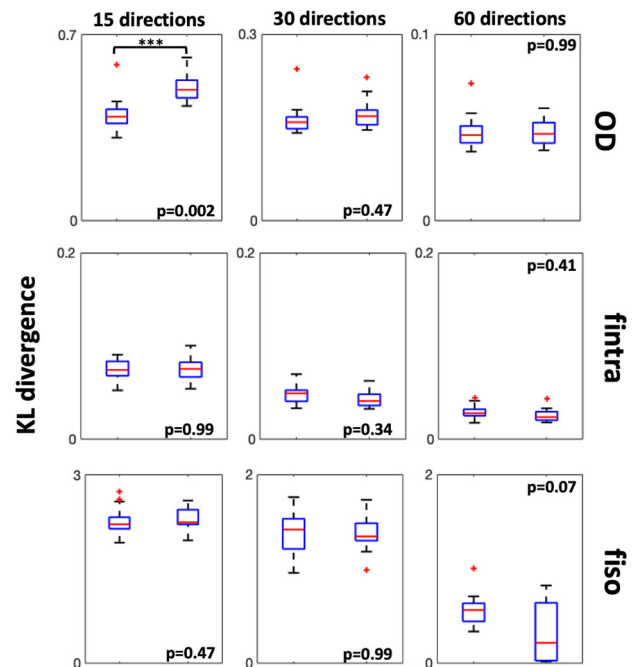
Introduction: NODDI¹, a DW-MRI model, examines 3 non-exchanging water compartments in the brain: intra-neurite (axons/dendrites), extra-neurite and CSF. It estimates maps of the orientation dispersion index (OD), describing the dispersion of neurite structures, the intra-cellular volume fraction (fintra) and the free water volume fraction (fiso). At least two shells are needed for accurate parameter estimates, but it is not clear if using different (staggered) directions in each shell would improve the accuracy of the results due to increased angular resolution. Here, we analysed if staggered (sg) directions improve estimates of OD, fintra and fiso, compared to using the same directions for both shells (non-staggered, n-sg). We used a unique dataset acquired at ultra-high resolution from a whole post-mortem macaque brain². NODDI parameters in white matter (WM) were compared between sg and n-sg approaches in subsets with 15, 30 and 60 directions in each shell.

Subjects/Methods: Images were acquired on an Agilent 7T scanner (spin echo multi slice acquisition, single line readout, TR/TE = 3.5 s/42.5 ms, d/D = 14/24 ms, 1mm isotropic resolution). Each shell (b = 7000, 10000 s/mm²) has 1000 uniformly distributed gradient directions and 40 interleaved b = 0 volumes. They were linearly registered together using FLIRT³ and corrected for signal drift. NODDI fitting (16 distinct subsets of 15, 30 and 60 directions for sg and n-sg) was done using FSL cuDIMOT⁴ ($d_l = 5.6 \times 10^{-4}$, $d_{iso} = 10^{-4}$ mm²/s) to obtain maps of OD, fintra and fiso. A WM mask was created from a T1-w image using FSL FAST⁵. Kullback-Leibler divergence (KLDiv) was used to compare the distribution of parameter values within the WM mask to the pseudo ground-truth, estimated using 250 directions (n-sg) per shell.

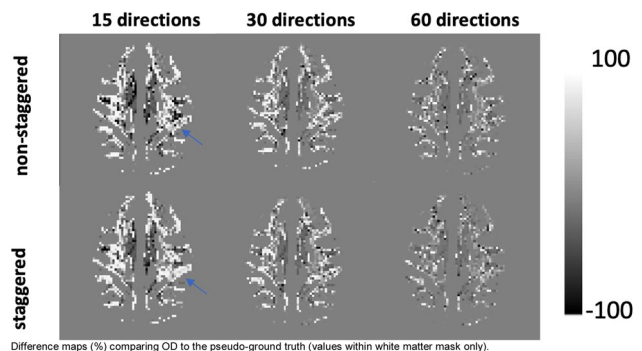
Results/Discussion: The dissimilarity to pseudo-ground truth maps increased as the number of directions was reduced, prominently in the OD and fiso maps (Figure 1B). For OD estimates, KLDiv was higher for sg acquisitions in the 15-direction protocol (two sample t-test, p = 0.0002, FDR-corrected; Figure 2). Figure 3 illustrates the difference maps for sg and n-sg acquisitions when compared to the pseudo-ground truth. The differences observed across fiso, fintra and OD in the 30- and 60- direction protocols were not significant, but fiso estimates tended improve in the sg approach at higher direction numbers. To conclude, NODDI parameter estimates are differentially affected depending on the number and choice of directions across each shell. Particularly, when the number of directions is low, staggering directions impairs OD estimates.



A. structural (T1-weighted) image at 0.3mm isotropic resolution with and without with white matter mask overlaid. B. Example NODDI parameter maps.



Boxplots (each summarising output from 16 distinct gradient subsets) of KLDiv in sg and n-sg protocols for 15, 30 and 60 directions for OD, fintra, fiso maps. Identical distributions at KLDiv=0. Note the change of scale on the y-axis.



Difference maps (%) comparing OD to the pseudo-ground truth (values within white matter mask only).

- References:** 1. Zhang et al, NeuroImage, 2012.
2. Howard et al, ISMRM, 2019.
3. Jenkinson et al, NeuroImage, 2002.
4. Hernandez-Fernandez et al, NeuroImage 2019.
5. Zhang et al, IEEE Trans. Med. Imag., 2001.

L01.59**Does water diffusion increase or decrease following stimulation?**

W. Olszowy, I. Jelescu

École Polytechnique Fédérale de Lausanne, Center for Biomedical Imaging, Lausanne, Switzerland

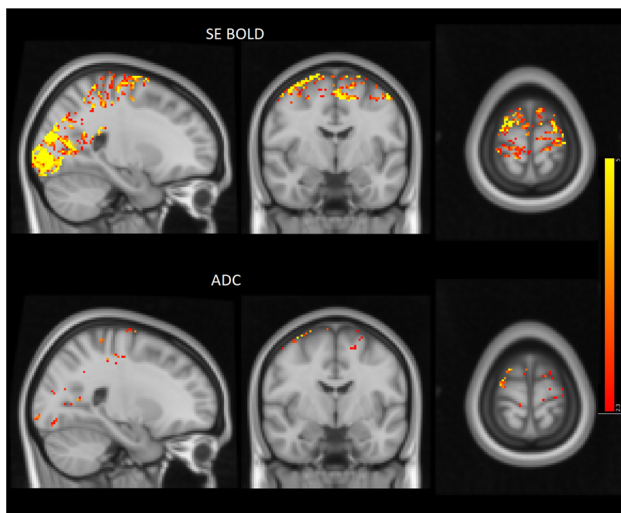
Introduction: Functional MRI is mainly performed with the BOLD contrast, which means that the signal relies on neurovascular coupling. That is why fMRI-BOLD suffers from poor spatial and temporal specificity to neuronal activation. Diffusion fMRI (dfMRI) was proposed to overcome these limitations: it relies on dynamic microstructural changes driven by neural activity, such as cell

swelling, to induce changes in the diffusivity of water molecules on-site. While some studies show water diffusion decreases following stimulation [1,2], some point to increases [3]. A recent study performed in rats suggests diffusion might first decrease and then increase [4]. The first component might reflect rapid microstructural changes, while the latter component could be due to BOLD contamination.

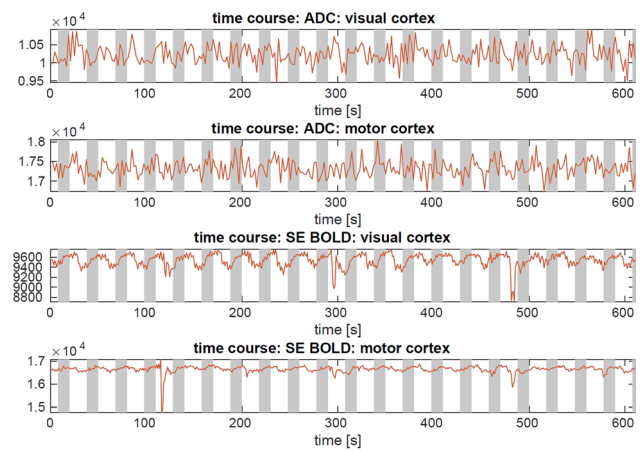
Subjects/Methods: The preliminary data are from one human subject scanned at a Siemens Magnetom 7T scanner. Two fMRI runs were acquired: one SE-EPI yielding T_2 BOLD contrast and one DW TRSE-EPI with alternating b-values of 0 and 1000 s/mm^2 , from which a quantitative apparent diffusion coefficient (ADC) time-course was calculated. Other sequence parameters were: TE/TR = 65 ms/1035 ms, 2-mm isotropic resolution, matrix size 116×116 , GRAPPA x2, Multiband x2 [5], 600 volumes total. 16 slices were acquired for DW TRSE-EPI, and 14 slices for SE-EPI. The temporal resolution of the ADC map was $2 \times 1.035s = 2.07s$.

The subject was viewing a flashing checkerboard and concurrently finger-tapping for 12s following 18s of rest (x20). Data pre-processing included denoising [6] and corrections for susceptibility distortion, motion and slice-timing. We estimated the response functions with the help of the Finite Impulse Response method in SPM, which averaged the signal across trials using 14 bins (width 2.07s).

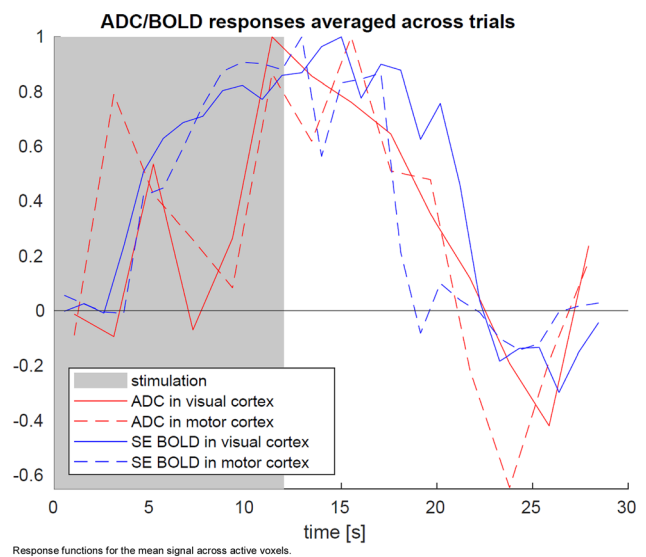
Results/Discussion:



The voxels used for the estimation of the response functions. In the SE BOLD map, 1537 and 985 voxels were active ($z_{stat} > 2.3$) in visual cortex and motor cortex, respectively. Using the ADC map, we found 54 and 96 active voxels in the visual and motor cortices.



Time courses for the mean signal across active voxels.



Response functions for the mean signal across active voxels.

Visual and motor stimulation produced a brief positive peak in ADC prior to a more durable increase that followed the BOLD response. Increased blood oxygenation reduces background gradients and results in higher ADC, in spite of using a bipolar gradient scheme to mitigate this effect. Perfusion changes could also contribute to this effect and could be suppressed by choosing all b-values $> 200 s/mm^2$ [7].

The initial fluctuation in ADC deserves further investigation to shed light on potential mechanisms: neuromorphological changes during activation are expected to decrease the ADC, but increased trans-membrane water fluxes during neural firing could potentially also transiently increase the ADC.

In our future work we will scan more subjects and will also scan with reduced TR.

- References:** 1 Darquié ea. *PNAS* 98.16 (2001): 9391-9395
 2 Tsurugizawa ea. *PNAS* 110.28 (2013): 11636-11641
 3 De Luca ea. *HBM* 40.17 (2019): 5069-5082
 4 Nunes ea. *arXiv preprint arXiv:2001.08508* (2020)
 5 Uğurbil ea. *Neuroimage* 80 (2013): 80-104
 6 Veraart ea. *Neuroimage* 142 (2016): 394-406
 7 Jin and Kim *Neuroimage* 41.3 (2008): 801-812

L01.60**Frequency and b-value dependence of the diffusion tensor in the human brain using enhanced oscillating gradient spin-echo (OGSE) sequences with 250 mT/m gradients**

E. S. Michael, F. Hennel, K. P. Pruessmann

Institute for Biomedical Engineering, ETH Zurich and University of Zurich, Zurich, Switzerland

Introduction: OGSE sequences can be used to study the dependence of the diffusion tensor on frequency ω . This relation is associated with properties of tissue microstructure² and can be captured in the spectra of tensor-based metrics, such as mean diffusivity (MD). As such, a characterization of these spectra may permit discovery of microstructural abnormalities in cases where spectral anomalies exist. In human brain OGSE experiments, the ability to probe such spectra with sufficient diffusion weighting (i.e., relative insensitivity to perfusion³) and at high ω is limited by gradient amplitudes, which typically reach only 80 mT/m in modern clinical scanners. In this work, this limitation was overcome by utilizing a high-performance gradient system⁴ with gradient amplitudes up to 250 mT/m and slew rates up to 600 mT/m/ms. OGSE DTI sequences were applied in the in-vivo human brain at higher ω and b-values than have been previously achieved, thereby revealing diffusion metric trends over a wider spectral range and permitting less microcirculatory bias than past studies. Furthermore, a modified trapezoidal-cosine OGSE waveform was developed for and used in these experiments to attain stronger diffusion sensitization and improved spectral selectivity.

Subjects/Methods: Two adult male volunteers were scanned using a 3T Philips system equipped with the aforementioned gradient system. For each subject, the scanning protocol comprised three PGSE DTI and twelve modified OGSE DTI scans, measuring diffusion at $b = 450, 685, \text{ and } 975 \text{ s/mm}^2$ with maximum ω of 125, 100, and 75 Hz, respectively; additional information is given in Table 1.

Scan	$b \text{ (s/mm}^2\text{)}$	Sampled frequency (Hz)	Periods	Gradient amplitude (mT/m)
OGSE	450	125	10.5	248.55
OGSE	450	100	8.5	196.10
OGSE	450	75	6.5	144.40
OGSE	450	50	4.5	93.50
OGSE	450	30	2.5	57.90
PGSE	450	0	–	9.00
OGSE	685	100	8.5	244.30
OGSE	685	75	6.5	179.30
OGSE	685	50	4.5	115.95
OGSE	685	30	2.5	71.70
PGSE	685	0	–	10.10
OGSE	975	75	6.5	214.60
OGSE	975	50	4.5	138.50
OGSE	975	30	2.5	85.60
PGSE	975	0	–	13.10

Table 1. Scanning protocol for both subjects. The number of periods corresponds to the entire OGSE waveform (i.e., considering both pulses and the gap between pulses). The slew rate used for all ramps in all OGSE sequences was 600 mT/m/ms.

Each DTI sequence consisted of two $b = 0 \text{ s/mm}^2$ acquisitions, 32 diffusion directions at the designated b-value, and EPI readouts. After scanning, field monitoring was performed for each scan to record spatiotemporal field dynamics fit to third-order spherical harmonics⁵; images were reconstructed by an algorithm accounting for these higher order field terms⁶. Diffusion metrics (namely, MD) were computed voxel-wise for each scan and plotted against ω .

Results/Discussion: In a white matter region in one subject, MD increases with ω for all b-values, as shown in Figure 1. Also, MD decreases with rising b-value, likely due to perfusion. Similar results were observed for several regions in both subjects.

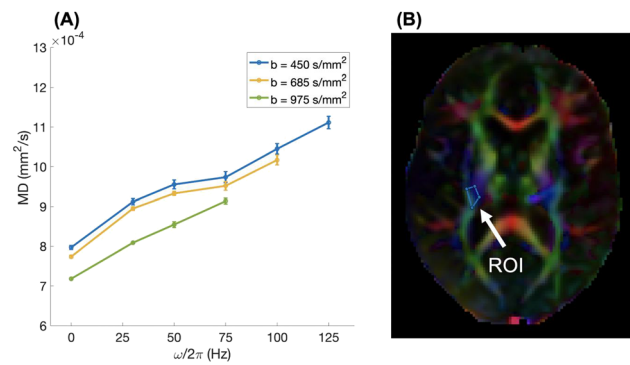


Figure 1. MD vs. frequency for all three b-values (A) for a white matter region of one subject (B). MD is seen to increase with ω and decrease with b-value.

Compared to the standard trapezoidal-cosine OGSE waveform, the altered sequence produces a higher b-value (by up to 21%, which occurs for the 30 Hz waveform) and, in the gradient moment power spectrum, higher peaks at the desired ω and smaller side lobes. These changes, shown in Figure 2, allow for more precise diffusion encoding at any given ω .

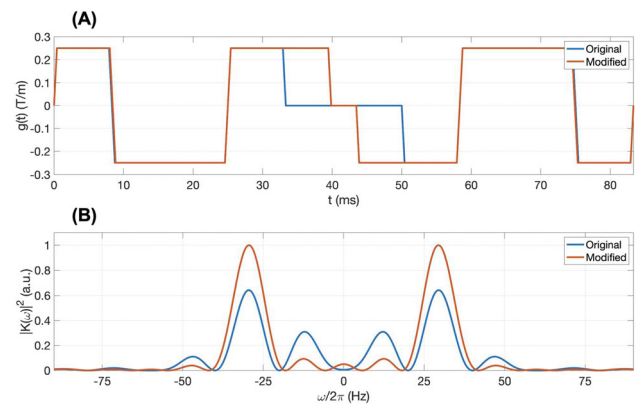


Figure 2. Gradient waveforms (A) and gradient moment power spectra (B) for 30 Hz trapezoidal-cosine OGSE sequences (250 mT/m amplitude) with and without proposed modifications. Note the reduced dead time between pulses in the modified sequence.

- References:** 1. Does et al., *MRM* 2003;49:206–15.
 2. Novikov et al., *PNAS* 2014;111:5088–93.
 3. Le Bihan et al., *Radiology* 1988;168:497–505.
 4. Weiger et al., *MRM* 2018;79:3256–66.
 5. Dietrich et al., *MRM* 2016;75:1831–40.
 6. Wilm et al., *MRM* 2011;65:1690–1701.

L01.61**Impact of sub-sampling an existing DWI multi-shell acquisition scheme on the estimation of DTI and DKI scalar metrics**A. R. Fouto¹, R. G. Nunes¹, M. Golub¹, A. Ruiz-Tagle¹, I. Esteves¹, N. A. Silva², P. Figueiredo¹

¹Instituto Superior Técnico, Universidade de Lisboa, Institute for Systems and Robotics/LARSyS, Department of Bioengineering, Lisbon, Portugal, ²Hospital da Luz, Learning Health, Lisbon, Portugal

Introduction: DWI is widely used to probe brain microstructure, with a multitude of models developed to extract various metrics such as DTI and DKI[1]. More complex models typically need increasing numbers of diffusion directions and b-values (multi-shell), leading to long acquisition times. To enable deciding on protocol duration depending on subject tolerance, while preserving cross-exam

comparability, we evaluated the impact of optimal data subsampling of DWI multi-shell acquisitions on diffusion metrics based on DTI (FA, MD, AD, and RD) and DKI (MK, AK, and RK).

Subjects/Methods: Ten DWI datasets from 7 participants (34±8yrs), were acquired on a 3T Siemens Vida system with a 64-channel RF-receive head coil: DWI-EPI(TR/TE=6800/89 ms, 66 slices, SMS factor 3, 2mm isotropic resolution; 3 shells with b = 400, 1000, 2000 s/mm² along 32, 32, 60 directions respectively, with 8 b = 0 volumes). Six optimal subsets were generated by uniformly discarding a fraction of the total directions[2] per shell with MATLAB(mathworks.com): 5, 10, 20, 30, 40 and 50% (Table 1). Data preprocessing followed the DESIGNER pipeline[3]: denoising and Gibbs ringing correction with MRTrix [4]; Rician bias correction [5]; geometric, eddy-current distortions and motion correction with FS(fsl.fmrib.ox.ac.uk/fs); and bias field correction with MRTrix. Tensor-fitting was performed with DIPY’s(dipy.org). A skeleton representing the major white-matter tracts was obtained by FSL’s tract-based spatial statistics (TBSS). We computed the voxelwise relative difference between the value of the metric obtained from each subset and the full dataset (taken as ground truth). Results were compared by repeated-measures ANOVA (Bonferroni correction, p < 0.05).

Results/Discussion: Fig.1 illustrates examples of the relative difference skeleton maps for each diffusion metric obtained with subset50. Fig.2 shows the median across the skeleton of the metric values and corresponding relative differences, for each metric and subset, across all datasets. Sub-sampled data provided biased estimates of all diffusion metrics, particularly DKI metrics: FA, MD, AD and AK were overestimated up to a maximum error of 3%, while RD, RK and MK were underestimated, up to 5% (RD, MK) and 10% (RK). Our results indicate that, although subsampling DWI acquisitions has a significant impact on diffusion metrics, in line with previous reports[6], the errors compared to a full acquisition are mostly under 5%. In general, DKI was more sensitive to undersampling than DTI. Accordingly, if shortening the acquisition of a DWI multi-shell protocol is needed, these errors should be considered with care when comparing with fully-sampled data.

Data set	b=400	b=1000	b=2000	Number of non-DWI volumes	Total acquisition time (min.)
original	32	32	60	8	14:96
subset5	30	30	57	8	14:17
subset10	29	29	54	8	13:60
subset20	26	26	48	8	12:24
subset30	22	22	42	8	10:65
subset40	19	19	36	8	8:84
subset50	16	16	30	8	7:93

Table1-Description of original (full) dataset and derived subsets: number of DWI volumes for each shell (b=400, b=1000, and b=2000 s/mm²), and corresponding total acquisition time.

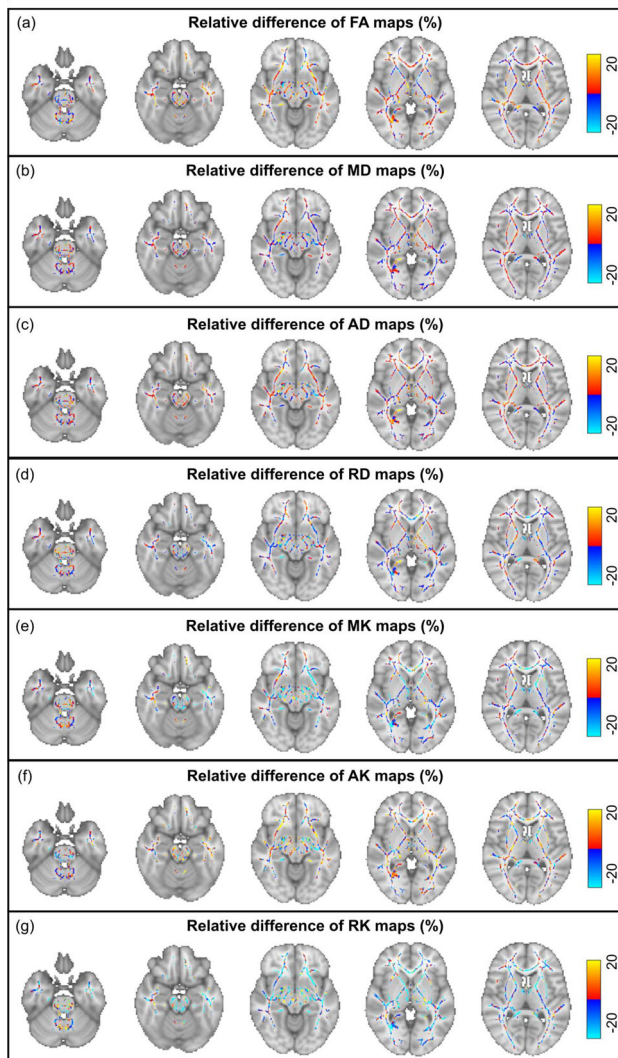


Fig.1-Illustrative examples of the spatial distribution of the relative difference (in percentage) between each diffusion parameter extracted from the subset50 and the corresponding original map using the TBSS mask overlaid on the MNI template.

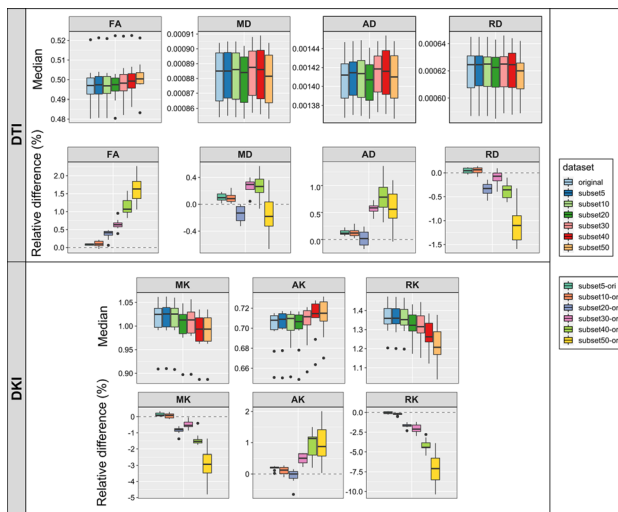


Fig.2-Distribution across datasets of the median values over the TBSS mask of each diffusion metric and corresponding relative difference (in percentage) from the ground truth for both diffusion models: DTI (upper panel) and DKI (lower panel).

References: [1]Jelescu IO, et al. *Front Phys*(2017);
 [2]Cheng J, et al. *Lect Notes Comput Sci*(2014);
 [3]Ades-Aron B, et al. *Neuroimage*(2018);
 [4]Veraart J, et al. *Magn Reson Med*(2016)
 [5]Koay CG, et al. *J Magn Reson*(2006);
 [6]Zhuo J, et al. *ISMRM 20th Annu Meet*(2012);

L01.62
Optimising frequency-constrained gradient waveforms for imaging axon diameter

M. Drakesmith, C. M. W. Tax, M. Afzali, M. Molendowska, D. K. Jones

Cardiff University, CUBRIC, Cardiff, UK

Introduction: Beyond the classic Stejskal-Tanner gradients, general, multi-dimensional, gradient waveforms can improve sensitivity to fine complex geometries [1-3]. A notable development is the strategy of optimising waveforms that maximises b , constrained to desired \mathbf{B} -tensor shape and other constraints [4]. We propose to modify this framework to optimise gradients for axon diameters by considering the resolution limit [1]:

$$r_{\min} = (1536/7) (\sigma D_0 / b V)^{1/4}$$

where V is the spectral encoding variance, which can conveniently be expressed in both time and frequency domain:

$$bV = \gamma^2 \int_{-\infty}^{\infty} \mathbf{g}^T(t)\mathbf{g}(t) dt = (1/2\pi) \int_{-\infty}^{\infty} \mathbf{q}^T(\omega)\mathbf{q}(\omega) d\omega$$

We propose to: (1) generate gradient waveforms that maximises the denominator bV instead of b , thereby optimising the resolution limit; (2) generate waveforms constrained to specific values of V , to tune the frequency profile of the gradient, which in turn, selectively tunes sensitivity to specific axon diameters [2], with $V^{1/2}$ representing the desired characteristic frequency. We demonstrate optimised waveforms generated with these modifications and simulate diffusion MRI signals for a simplified axon-like geometry.

Subjects/Methods: We modified the Numerical Optimization of gradient Waveforms (NOW) toolbox [4] to implement two separate modifications: (1) the objective function maximises bV instead of b , (2) an additional constraint on V :

$$\int_{\text{TE}} \mathbf{g}^T(t)\mathbf{g}(t) dt = \mathbf{B}V_{\text{target}}$$

where V_{target} is the target value for V . Five values of V_{target} were tested, on a reciprocal scale from the b - and bV -optimised values for V from modification (1). Optimised gradient waveforms were generated for linear, planar and spherical \mathbf{B} -tensors. Optimisation was performed using constraints appropriate for a 9.4T Bruker system ($G_{\max} = 340$ mT/m, $[dG/dt]_{\max} = 2500$ T/(s.m)). Monte Carlo simulations of diffusion signals in cylindrical geometries of radii in range of 0.05-11.4 μm were generated in Camino [5] for the optimised gradients.

Results/Discussion:

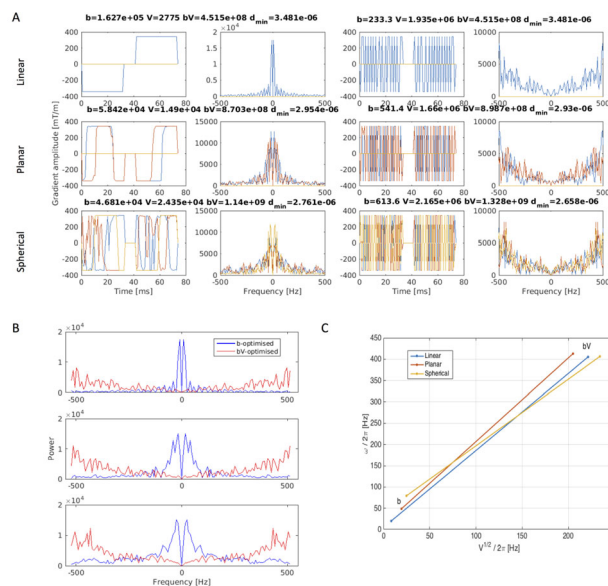


Fig. 1: (A) Optimised gradient waveforms for the 3 B-tensor encodings, optimised for b (left) and bV (right) in time and frequency domain. (B) Combined spectral power for the 3 B-tensor encodings (C) Relationship between V and v .

bV -optimised gradients do not provide any improvement for imaging axons below the resolution limit compared to b -optimised gradients (Fig. 1). The product bV is roughly equal, with the diameter limits ~ 3.5 μm for linear and ~ 2.9 μm for planar \mathbf{B} -tensors.

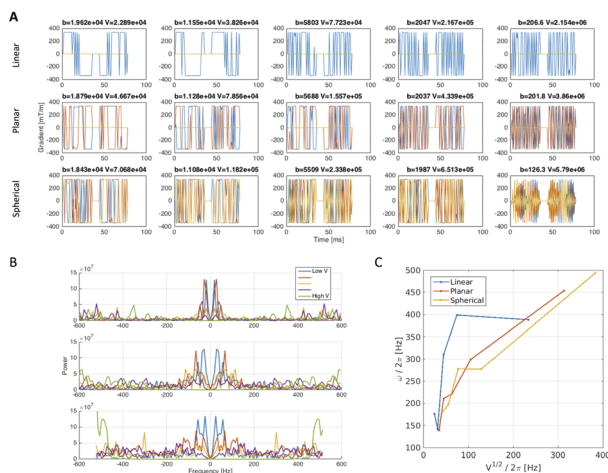


Fig. 2: (A) Optimised gradient waveforms for the B-tensor encodings, constrained to different values of V . (B) Combined spectral power for the 3 B-tensor encodings (C) Relationship between V and v .

Varying V has the effect of increasing power in higher frequency components while also decreasing b and bV remaining approximately constant (Fig. 2).

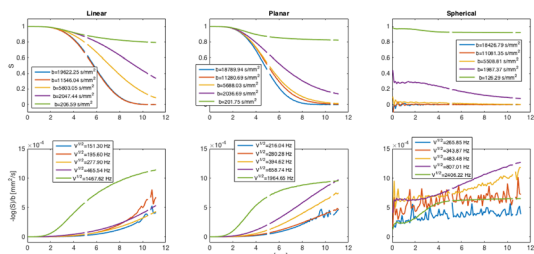


Fig. 3: Signal amplitude S (top row) and b -normalised attenuation, $-\log(S)/b$ (bottom row) obtained from Monte-Carlo simulations of diffusion in cylinders of varying radii r for the optimised gradient waveforms constrained to different values of V .

Simulations show increased selectivity of axon radii across V , particularly for the planar \mathbf{B} -tensor (Fig. 3). This suggests improved characterisation of axon diameter distributions can be achieved by combining optimised planar \mathbf{B} -tensor gradients with different values of V .

- References:** [1] M. Nilsson, et al (2017), *NMR in Biomed.*, 30, e3711.
 [2] I. Drobnjak, et al (2013), *Micropor. Mesp. Mat.*, 178, 11–14.
 [3] D. Topgaard (2017), *J. of Mag. Reson.*, 275, 98–113.
 [4] J. Sjölund et al (2015), *J. of Mag. Reson.* 261, 157–168.
 [5] P. A. Cook, et al, (2006), *Proc. Intl. Soc. Mag. Reson. Med.*, 14, 2759

L01.63
Reducing Rician Noise Bias In Axial Symmetric Diffusion Kurtosis Imaging – A Simulation Study

J. M. Oeschger¹, K. Tabelow², S. Mohammadi¹

¹University Medical Center Hamburg-Eppendorf, Institute of Systems Neuroscience, Hamburg, Germany, ²Weierstrass Institute for Applied Analysis and Stochastics, Berlin, Germany

Introduction: Diffusion kurtosis imaging (DKI) has recently attracted additional attention in form of the axial symmetric DKI signal model¹ (DKIax) and its relation to biological tissue parameters such as axon water fraction and fiber dispersion^{2,3}. MRI data is contaminated with noise. While the influence of the resulting Rician bias⁴ and its correction was investigated within the standard DKI model^{5,6}, it is currently unknown how Rician noise bias correction can help to improve parameter estimation in DKIax. Here, based upon a simulation study, the efficacy of a newly implemented Rician bias correction algorithm (RBCA) on DKIax parameter estimation was investigated.

Subjects/Methods: We correct for the Rician bias in MRI magnitude data by solving the optimization problem⁷ using a non-linear Gauss-Newton algorithm:

$$\text{argmin}_W \sum_i \text{Meas}_i - \mu(S_{b,gi}(W), \sigma)^2$$
 where $\mu(S_{b,gi}(W), \sigma)$ is the expectation value of the Rician distribution depending on the predicted noise-free signal $S_{b,gi}(W)$ and noise level σ^7 , $W = \{D_{||}, D_{\perp}, W_{||}, W_{\perp}, MW, S_0, c\}$ is the model parameter set. The implementation is Matlab-based and freely available online within the ACID Toolbox (<http://www.diffusiontools.com/>). Noise-free diffusion weighted MRI image data sets were simulated based upon the DKIax-signal model $S_{b,gi}(W)^1$ using two ground truth (GT) parameter sets⁸ associated with white matter with highly aligned fibers (HF) and disperse fibers (DF). Simulated noise-free image data were contaminated with noise for varying SNRs (5000 noise samples drawn from a complex Gaussian with varying standard deviation σ) and MRI magnitude images were computed. From the noisy data W was estimated using the method above. The W estimates were then compared to the GT. For each SNR and estimated parameter, the mean and standard deviation was computed. Figure 1 shows the results for the mean kurtosis MW in HF.

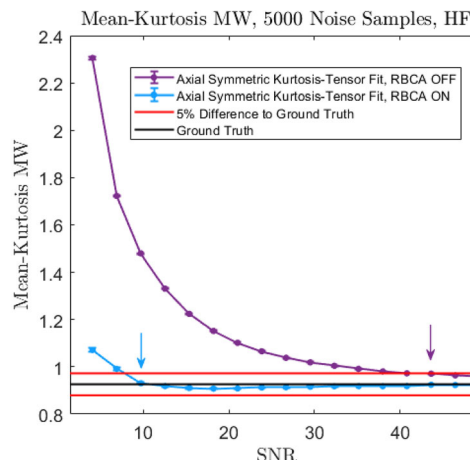


Figure 1: Estimation of MW in HF. Plotted are the mean and standard error of the mean for the results obtained from each of the 5000 random noise samples per SNR. The arrows indicate reaching the $\pm 5\%$ threshold for each method.

The GT was assumed to be correctly reproduced if the computed mean reached its 5% vicinity. Table 1 summarizes the SNR needed to reach the 5% vicinity with or without RBCA.

Parameter	SNR (RBCA ON) HF	SNR (RBCA OFF) HF	SNR (RBCA ON) DF	SNR (RBCA OFF) DF
MW	10	44	7	7
$W_{ }$	10	32	12.5	10
W_{\perp}	12.5	>50	12.5	18
DE	10	10	10	12.5
DE	7	12.5	12.5	7
S0	4	7	4	4
c	4	4	>50	>50
Average	8.2	>22.8	>15.5	>15.5

Table 1: SNRs required for reaching the $\pm 5\%$ threshold for DKIax parameters in HF and DF with and without RBCA.

Results/Discussion: RBCA succeeds in lowering the required SNR for accurate estimation of the GT parameters in DKIax for HF white matter (RBCA ON: SNR=8.2, RBCA OFF: SNR>22.8, see Table 1). The SNR requirements vary for HF and DF and are lowest for HF: HF exhibits a strong signal decay due to its anisotropy (see Figure 2) causing a pronounced Rician bias within the diffusion dataset that can be corrected. DF is highly isotropic and exhibits a less strong and more uniform signal decay (see Figure 2) causing a less pronounced Rician bias.

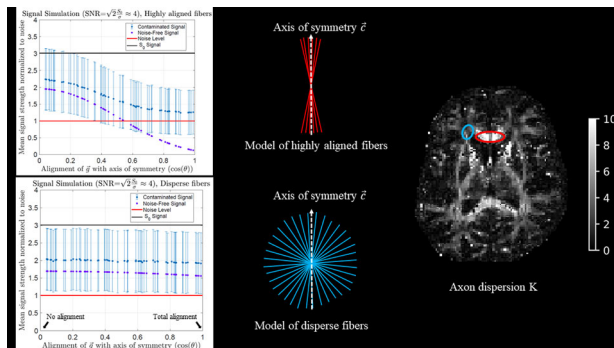


Figure 2: DKI signal for the $b=2500/\text{mm}^2$ shell as a function of alignment between diffusion gradient g with axis of symmetry c for a fixed SNR=4 (left), stick model of corresponding fiber arrangement (middle) and map of axon dispersion K (right).

- References:** 1. Hansen, B. et al. *NI* 142, 381 (2016).
 2. Firemans, E. et al. *NI* 58, 177 (2011).
 3. Jespersen, S.N. et al. *NI* 182, 329 (2018).

4. Gudbjartsson, H. *et al. MRM* **34**, 910 (1995).
5. Veraart, J. *et al. MRM* **66**, 678 (2011).
6. André, E.D. *et al. PLoS ONE* **9**, 1480 (2014).
7. Polzehl, J. *et al. JASA* **111**, 1480 (2016).
8. Coelho, S. *et al. MRM* **82**, 395 (2019).

L01.64

Spherical diffusion encoding with varying frequency-content can improve the characterisation of isotropic restricted compartments

M. Molendowska, M. Drakesmith, D. K. Jones, C. M. W. Tax

Cardiff University Brain Research Imaging Centre (CUBRIC), Cardiff, UK

Introduction: Spherical tensor encoding (STE) at very high b-values allows to suppress the signal from anisotropic components and reveal isotropic restricted compartments^{1,2}. We aim to explore whether varying frequency-content of STE waveforms can lead to a better characterisation of the isotropic restricted compartment (e.g. the sphere radius, r_s , or diffusivity, D_s).

Subjects/Methods: STE waveforms were repeatedly generated using optimisation^{3,4} with settings¹: 35.48 ms (first encoding), 25.63 ms (second encoding), and 6.9 ms (pause), $G_{\max} = 250$ mT/m, SR = 60 T/m/s, and the max-norm to achieve the highest possible b-value. We employed the implementation in the MISST toolbox^{5–7} to generate signals for arbitrary STE waveforms from a spherical compartment. Gaussian noise was added in 50 noise-realizations. Two acquisition protocols were generated, *protocol 1*: a single waveform shape (FWF12) and 16 b-values $(10:0.3:15) \cdot 10^3$, and *protocol 2*: 4 waveforms with different frequency-characteristics (FWF5, 12, 15, 21) and 4 b-values $(10.5:1.5:15) \cdot 10^3$, to match total number of acquisitions. Signals were generated and estimates of r_s were obtained using a nonlinear least-squares trust-region-reflective algorithm in Matlab, D_s was fixed.

Results/Discussion: Fig.1A shows 4 of the 25 waveforms and their encoding spectra, which show differences in their spectral characteristics. Fig.1B shows simulated signal decays for exemplary STE waveforms (FWF 1), for spherical compartments with different D_s and radii r_s and a cylinder and zeppelin reflecting intra- and extra-axonal space. At high b-values, the signal arising from a cylindrical compartment is largely compressed, while for low D_s and small r_s the signal of a spherical compartment still remains. Fig.2A shows the signal at high b-values for different waveforms, varying r_s and D_s , SNR = 50, and it reveals an impact of the waveform on the signal evolution exceeding the noise. Fig.2B suggests that the estimation precision can be increased with waveforms of different frequency characteristics.

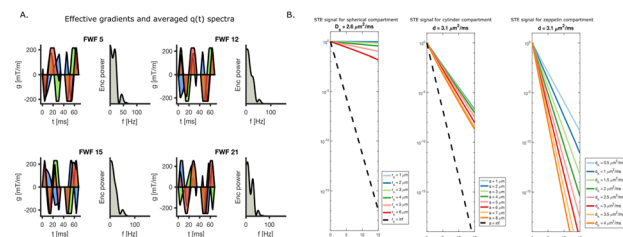


Fig. 1. A. STE waveforms and their spectrum averaged across the axes, revealing differences in frequency content. B. Signal evolution for spherical (fixed diffusivity and radius), cylindrical and zeppelin compartments as a function of b-value

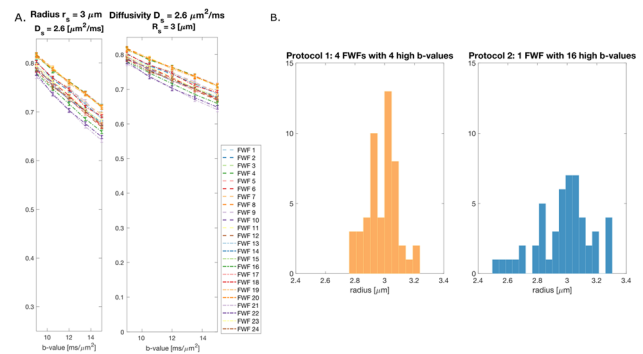


Fig. 2A. Signal as a function of b-value for a spherical compartment (fixed radius and diffusivity), for different STE waveforms. EBs represent EBs across 50 noise realisations. B. Distributions of estimates, ground truth radius of 3 μm.

We applied STE at high b-values to study the regime in which remaining signal arises from the isotropic restricted domain; a strategy being used to study the intra-axonal signal at high b-values^{8–10}. Varying the waveform frequency content can provide an independent dimension to study tissue microstructure¹¹. Our results show a dependence of the signal on the waveform used, suggesting that varying the frequency content can improve isotropic compartment characterisation. Future work will focus on optimisation of STE waveforms to enhance estimation accuracy of the spherical compartment.

References: ¹Tax et al. NI 2020; ²Dhital et al. NI 2017; ³Sjölund et al. JMR 2015; ⁴Szczepankiewicz et al. MRM 2019; ⁵Drobnjak et al. JMR 2010; ⁶Drobnjak et al. JMR 2011; ⁷Ianuș et al. JMR 2013; ⁸Veraart et al. NI 2019; ⁹Kleban E et al. ISMRM 2019; ¹⁰McKinnon et al. MRM 2019; ¹¹Lundell et al. ScieReps. 2019

L01.65

The effect of computation strategy on fiber tractography metrics: A focus on fractional anisotropy and corpus callosum

A. Zhyłka¹, A. Leemans², J. Pluim¹, A. De Luca²

¹Eindhoven University of Technology, Biomedical Engineering, Eindhoven, The Netherlands, ²University Medical Center Utrecht, Image Sciences Institute, Utrecht, The Netherlands

Introduction: The analysis of diffusion MRI metrics along pathways reconstructed with fiber tractography¹ (FT) (tractometry²) is becoming increasingly popular and reaching clinical application³. This kind of analysis requires, however, several computational steps and user choices, whose effect on the analysis step remains unknown.

In this work, we showcase the effect of two interpolation approaches (Fig. 1a) and of three ways of assigning metrics to the points along a pathway on the reconstruction and quantitative analysis of the corpus callosum (CC).

Subjects/Methods: Thirty subjects from the Human Connectome Project⁴ were used for the analysis consisting of 18 volumes at $b = 0$ s/mm² and 90 volumes at $b = 1000$ s/mm².

Deterministic whole-brain DT-based FT was performed with a range of FA thresholds {0.1, 0.15, 0.2, 0.25, 0.3}, 1mm step size, 45° angle threshold, then the CC was delineated⁵. For each setting, FT was performed twice, calculating the FA at each point with DT- and FA-based interpolation. The FA was computed by averaging the FA values of each of pathways' points (denoted as "plain"), and by calculating the average and the weighted average FA on a voxel-basis. In the latter case, the weights were defined as the numbers of the unique pathways visiting each voxel, and the voxel assignment was performed both directly and using a Bresenham-like discretization algorithm⁶ ("Bresenham map", Fig. 1b). Statistical testing was performed using the two-tailed Wilcoxon test with confidence level $\alpha=0.05$.

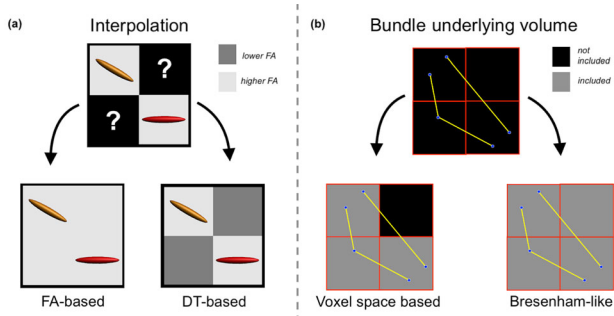
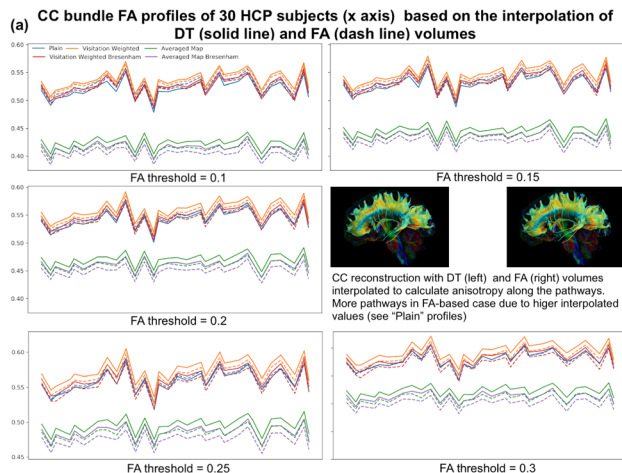


Fig. 1 (a) Using either FA or DT volume for FA calculation along the pathway might lead to different results. (b) Using Bresenham-like approach voxels passed by pathways, but not containing their points are included into the bundle-wise computation.

Results/Discussion: From the FA profiles (Fig. 2a) it can be seen that different approaches to averaging FA values as well as using a different interpolation strategy (DT vs FA) provide different results. Fig. 2b shows that DT-interpolated FA values significantly differ from FA-interpolated FA values in most cases. The correlation between all the approaches is high (Fig. 2c), which is in line with the observed similarity in shape for the FA profiles (despite the offset).



(b) P-values from the two-tailed Wilcoxon test (confidence level 0.05)

Bundle	CC				
FA Threshold	0.1	0.15	0.2	0.25	0.3
[DT]Plain Average vs [FA]Plain Average	0.000002	0.000002	0.000002	0.000002	0.021823
[DT]Plain Average vs [FA]Visitation Weighted Average	0.000002	0.000002	0.000002	0.000002	0.000002
[DT]Plain Average vs [FA]Averaged Map	0.000002	0.000002	0.000002	0.000002	0.000002
[DT]Plain Average vs [FA]Visitation Weighted Bresenham Map	0.000359	0.029235	0.484350	0.000345	0.000002
[DT]Plain Average vs [FA]Averaged Bresenham Map	0.000002	0.000002	0.000002	0.000002	0.000002

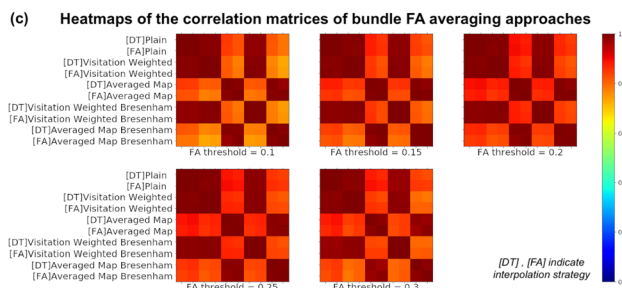


Fig. 2 Despite similar shapes of the bundle FA profiles (a) mainly significant difference was reported by the Wilcoxon test (b). However, the bundle FA correlation is high (c) which is in conformity with the profiles' shapes.

When zero-centering each bundle FA set, we did not observe

significant differences between any pair of bundle FA sets, independently from the choice of the averaging and interpolation approaches (Tab. 1).

Our results suggest that FA values computed with different interpolation methods have near-identical sensitivity to physiological changes along the reconstructed pathways. However, the presence of an offset between the methods hampers the comparability of the results obtained with different settings and suggests the need to report the chosen interpolation method along with other user-defined settings of FT.

FA Threshold	0.1	0.15	0.2	0.25	0.3
[DT] Plain Average vs [FA] Visitation Weighted Averaged Map	0,9181	0,8693	0,9672	0,8050	0,9344
[DT] Plain Average vs [FA] Averaged Map	0,8855	0,9836	1,0000	0,9836	0,9181
[DT] Plain Average vs [FA] Visitation Weighted Bresenham Map	1,0000	0,9672	0,9018	0,7892	0,5372
[DT] Plain Average vs [FA] Averaged Bresenham Map	0,9508	1,0000	0,9836	0,8855	0,9018
[DT] Visitation Weighted Averaged Map vs [FA] Averaged Map	0,9181	0,9836	0,9508	0,9508	1,0000
[DT] Visitation Weighted vs [FA] Visitation Weighted Bresenham Map	0,8855	0,8531	0,6658	0,9672	0,9508
[DT] Visitation Weighted Averaged Map vs [FA] Averaged Bresenham Map	0,9836	0,9672	0,9672	0,9836	0,9344
[DT] Averaged Map vs [FA] Visitation Weighted Bresenham Map	0,9836	0,9836	0,8693	1,0000	0,9836
[DT] Averaged Map vs [FA] Averaged Map	0,9836	1,0000	0,8531	0,8693	0,9672
Averaged Bresenham Map					

Tab. 1 Two-tailed Wilcoxon test results (p-values) on centered bundle averages of a subset of compared pairs of bundles where one is tracked with FA values inferred from DT and FA ([DT]/[FA]-marked) volumes, showing insignificant differences ($\alpha=0.05$).

- References:** 1.Jeurissen, et al. *NMRBiomed*2019
 2.Bells, et al *ISMRM*2011
 3.Cousineau, et al. *NeuroImage*2017
 4.Van Essen, et al, *NeuroImage*2013
 5.Wasserman, et al. *BrainStructFunct*2016
 6.Rheault, et al. *FrontNeuroinform*2017

L01.66

Comparison of individual alpha band features in simultaneous EEG-fMRI relative to EEG acquired outside the MR scanner

I. Esteves, A. Vourvopoulos, A. R. Fouto, A. Ruiz-Tagle, A. Rosa, P. Figueiredo

Institute for Systems and Robotics - Lisboa and Department of Bioengineering, Instituto Superior Técnico, Universidade de Lisboa, Lisboa, Portugal

Introduction: The correction of MR artifacts from EEG acquired simultaneously with fMRI comes with a trade-off between artifact removal and physiological signal preservation. A possible concern is

the preservation of the commonly studied alpha band, which is essential for its correct interpretation¹. Our goal was to investigate changes in the individual alpha band (IAB) during simultaneous EEG-fMRI recordings, relative to EEG only recordings, either due to contamination by MR-induced artifacts or other factors linked to the MR environment.

Subjects/Methods: Data was acquired from 5 volunteers undergoing a paradigm with 1min eyes open (EO) facing a fixation cross and 1min eyes closed (EC). This was performed: outside the scanner room, in a seated position with normal room light, without fMRI (EEG-Outside); and inside the scanner, in a supine position in dim light, simultaneously with fMRI (EEG-fMRI). fMRI was acquired on a 3T Siemens Vida with a 64-channel RF coil using 2D EPI with SMS 3, 60 slices, TR = 1260 ms. EEG was acquired with a 32-channels MR-compatible EEG system (Brain Products) including ECG. The FMRIB plugin² was used for gradient artifact (GA) correction. For comparison, several pulse artifact (PA) correction methods were applied: FMRIB (OBS and AAS) and PROJIC-AAS³ optimized for physiological weights $w_{bkg}=0.5,0.7,1.0$. The corrected signals were bandpass filtered to 0.5-40Hz, and EO/EC periods were extracted. The frequency power spectrum was computed using Welch's method. The IAB was defined using the frequency of the peak closest to 10Hz for EC and the bounds set according to the peak frequency, ensuring a bandwidth of 4Hz.⁴

Results/Discussion: Based on the analysis of the EEG-fMRI obtained after GA and PA correction (Fig.1), we chose PROJIC-AAS with $w_{bkg} = 0.5$ as the best compromise between PA reduction and physiological signal preservation.

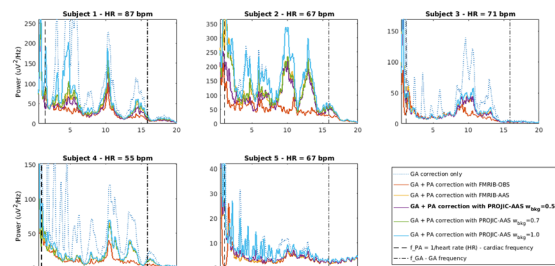


Fig. 1: EEG-fMRI power spectra for channel O2 following GA correction only and GA + PA correction with different methods for each subject.

When compared with the EEG-Outside (Fig.2), the IAB peak frequency and bounds are similar, but the IAB power is higher in both conditions, specially EO, resulting in a much reduced EC/EO ratio, mostly in the occipital area (Fig.3).

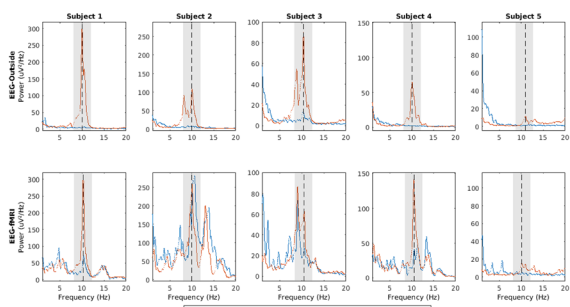


Fig. 2: Comparison of EO (blue) and EC (red) power spectra for channel O2 during EEG-Outside (top) and EEG-fMRI (bottom) acquisitions, for each subject, showing the respective IAB (shaded area).

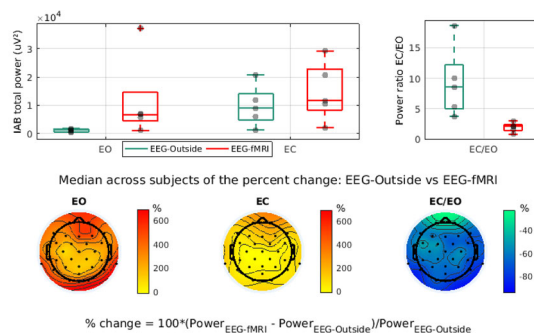


Fig. 3: Comparison of IAB power during EEG-Outside and EEG-fMRI: distribution of EO, EC and EC/EO power across subjects, for channel O2 (top); topographic maps of the median across subjects of the percent change of EEG-fMRI relative to EEG-Outside

Our results suggest that MR-related artifacts were adequately removed, and hence changes relative to EEG-Outside may be attributed to a physiological source. Possible explanations should be further investigated, and include the difference in lighting conditions (dimmer in the scanner) and the supine position adopted in the scanner (relative to the seated position outside). Overall, our findings highlight the need to account for and/or minimize the impact on EEG measurements if being performed simultaneously with fMRI.

- References:** 1. J. Jorge, W. van der Zwaag, P. Figueiredo, *NeuroImage*. 102, 24–34 (2014).
 2. R. K. Niazy, C. F. Beckmann, G. D. Iannetti, J. M. Brady, S. M. Smith, *NeuroImage*. 28, 720–737 (2005).
 3. R. Abreu et al., *NeuroImage*. 135, 45–63 (2016).
 4. J. Sousa, thesis, Universidade de Lisboa, Instituto Superior Técnico (2019).

L01.67

Evaluating multi-echo based denoising strategies for breath-hold induced cerebrovascular reactivity mapping

S. Moia¹, M. Termenon¹, E. Uruñuela¹, R. C. Stickland², M. G. Bright², C. Caballero-Gaudes¹

¹Basque Center on Cognition, Brain and Language, Donostia, Spain, ²Northwestern University, Department of Biomedical Engineering and Department of Physical Therapy and Human Movement Science, Chicago, IL, USA

Introduction: Cerebrovascular reactivity (CVR) is the ability of brain vessels to respond to vasoactive substances such as endogenous CO₂. It can be induced with Breath-Holds (BH) and measured with BOLD fMRI [1]. However, BH is a task intrinsically time-locked with motion-related artefacts, potentially biasing CVR estimation and reducing its reliability. Multi-echo (ME) fMRI can improve reliability and repeatability of BH-induced CVR via optimal combination (optcom) [2], and denoising with ME Independent Component Analysis (ME-ICA) [3]. This work evaluates the performance of single echo, optcom and ME-ICA preprocessing to diminish task-correlated artefacts and obtain more reliable CVR mapping.

Subjects/Methods:

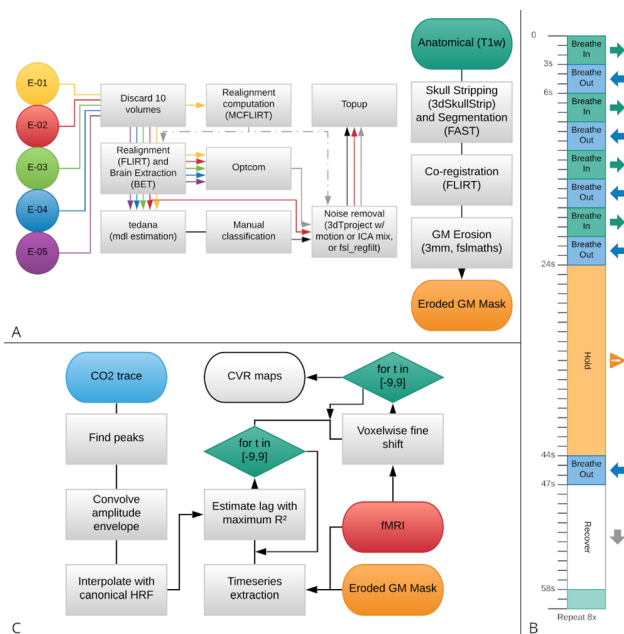


Figure 1: (A) Preprocessing and data analysis. (B) A BH trial. Note that subjects were instructed to exhale before and after the breath-hold to estimate PETCO2 changes. The BH task was composed of 8 trials. (C) CVR and lag data analysis.

Seven healthy volunteers underwent 10 weekly MRI sessions (3T Siemens PrismaFit, 64 channel head coil). A BH task [4] was administered in each session (Fig. 1B) while collecting ME-fMRI data (340 scans, TR = 1.5 s, TEs = 10.6/28.69/46.78/64.87/82.96 ms, FA = 70°, MB = 4, GRAPPA = 2, 52 slices, PF = 6/8, FoV = 211 × 211 mm², voxel size = 2.4 × 2.4 × 3 mm³). CO2 levels were measured using a nasal cannula, a gas analyzer (ADInstruments), and a BIO-PAC MP150 system. After data preprocessing (Fig. 1A), CVR and lag maps were first obtained in the second TE (echo-2) and optcom data (GLM with lagged HRF-convolved PETCO2 timeseries as covariate of interest; 12 motion parameters and Legendre polynomials as nuisance regressors [5], Fig. 1C). Optcom was decomposed using ME-ICA [6]. Noise and signal ICs were manually labelled, and three additional extended GLMs were created: adding the noise ICs timeseries directly as additional nuisance regressors (meica-agg); orthogonalized w.r.t. the PETCO2 trace (meica-ort); or orthogonalized w.r.t. the PETCO2 trace and signal ICs timeseries (meica-con). FD and DVARS were computed before realignment (pre) and after removal of the fitted nuisance regressors from echo-2 and optcom data. ICC(2,1) [7] was computed on the CVR and lag maps in MNI space to assess their reliability across sessions.

Results/Discussion:

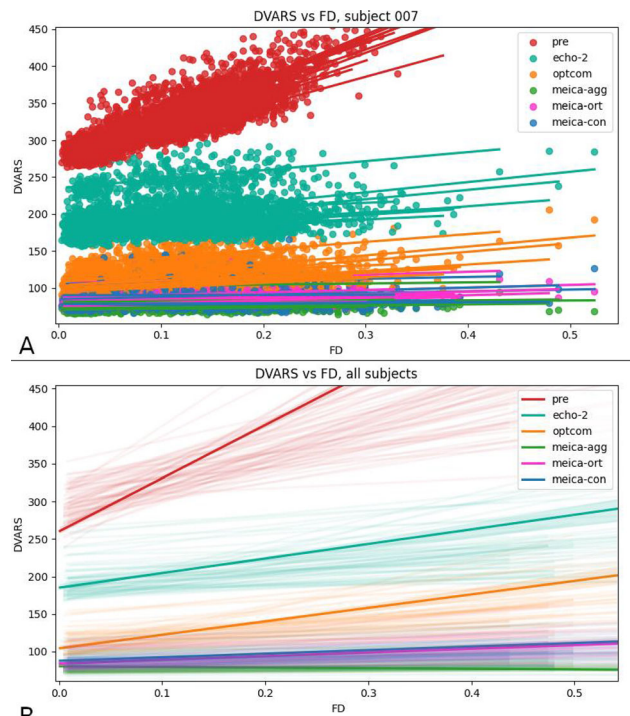


Figure 2: (A) FD vs DVARS correlation for a representative subject, and (B) for all subjects for all of the analysis approaches. A lower slope in the correlation means lower residual motion effects and better motion denoising.

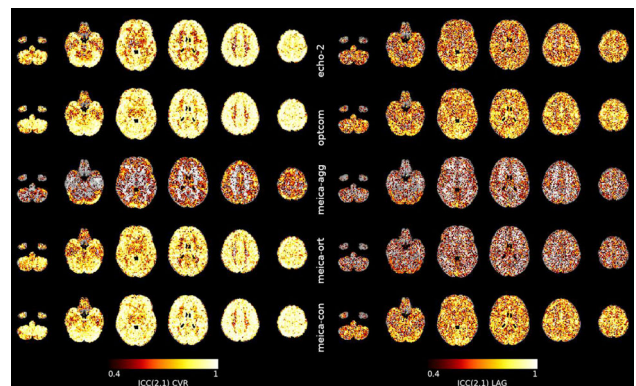


Figure 3: Thresholded (>0.4) voxelwise ICC(2,1) of CVR and lag in MNI space. Note how optcom and meica-con have the best reliability for both CVR and lag maps, while meica-agg has the lowest in both. ICC below 0.4 indicates poor reliability.

Considering the relationship between FD and DVARS (Fig. 2) and the ICC analysis (Fig. 3), a conservative ME-ICA denoising approach is the best way to reduce impact of motion without compromising

reliability in CVR mapping. Otherwise, a conventional optcom approach is recommended, but with less reduction of motion effects. Further studies should extend these results to other fMRI with substantial collinear artefacts

- References:** 1. Kastrup A, et al (2001) doi:10.1016/S0730-725X(01)00227-2
 2. Cohen AD, Wang Y (2019) doi:10.1038/s41598-019-41199-w
 3. Kundu P, et al (2017) doi:10.1016/j.neuroimage.2017.03.033
 4. Bright MG, Murphy K. (2013) doi:10.1016/j.neuroimage.2013.07.007
 5. Moia S, Stickland R, et al (2020), Proc. 42nd Ann. Int. Conf. IEEE Engineering Medicine and Biology Society (EMBC), Montreal, Canada
 6. DuPre E, et al (2019) doi:10.5281/ZENODO.2558498
 7. Chen G, et al (2018) doi:10.1002/hbm.23909

L01.68

Fiber-based ratiometric fluorescence recordings can be performed simultaneously with MR measurements

H. Lambers, D. Thomas, P. Zheng, L. Wachsmuth, C. Faber

University Hospital Muenster, Clinical Radiology, Muenster, Germany

Introduction: The combination of fiber-based calcium recordings and functional magnetic resonance imaging enables the direct readout of neuronal activity during functional neuroimaging. However, with standard single-wavelength sensors (such as OGB and GCaMP) the quantification of the fluorescence signal is difficult, since the signal depends on fluctuations in excitation light source, the expression of the sensor and bleaching. This problem might be solved by applying fluorescence resonance energy transfer (FRET) based ratiometric sensors, which consist of a donor fluorophore and a respective acceptor. In its basic state, the donor emits light; after binding of calcium, light is emitted by the acceptor (figure 1A). The calcium signal corresponds to the ratio of the fluorescence light of donor and acceptor. We show first in vivo fiber-based calcium recordings using the sensor Twitch 2B¹.

Subjects/Methods: AAVs encoding Twitch 2B under synapsin-promoter were injected in the forelimb regions (S1F1) of two Fischer rats. After at least 5 weeks, fiber-based ratiometric calcium-recordings were performed under medetomidine sedation upon electrical paw stimulation (paradigm: 10 s on, 20 s off, 1ms-pulses, amplitude: 1.5 mA, frequency: 2 Hz, 6 Hz or 9 Hz). The twitch expressing region was constantly illuminated (458 nm) using an optical fiber (200 μ m or 400 μ m diameter). The emitted fluorescence light was separated into the light of donor and acceptor fluorophores (figure 1B). The resulting fluorescence signals were analyzed using MATLAB: linear trends were removed, data were normalized to the baseline and a low pass filter was used. The FRET ratio (acceptor signal/ donor signal) was calculated and the amplitudes of the calcium responses were determined.

RARE and single shot GE-EPI measurements were performed at 9.4 T using a phase array coil after the implemented 400 μ m fiber was glued to the skull of a Fischer rat.

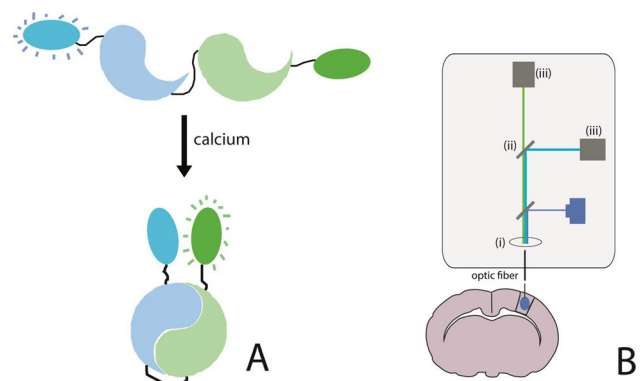


figure1: (A) FRET sensor principle: Without calcium, the donor emits light; after calcium binding, light is emitted by the acceptor. (B) Fluorescence setup: Light is coupled into a fiber (i). Fluorescent light is separated (ii) and detected (iii).

Results/Discussion: Results

Ratiometric calcium recordings were successfully performed in both rats. Figure 2 shows an exemplary ratiometric calcium profile. Amplitudes of the calcium responses detected with the 400 μ m fiber were examined exemplarily: Stimulation frequency at 2 Hz, 6 Hz and 9 Hz resulted in amplitudes of (0.8 ± 0.2), (1.6 ± 0.3) % and (1.0 ± 0.2) %, respectively.

RARE and EPI measurements showed a small artefact at the fiber position (figure 3).

Discussion

We have successfully performed fiber-based ratiometric calcium recordings. Several studies have shown that despite the fiber artefact in the MR measurements, simultaneous fluorescence recordings and MR measurements can be performed.^{2,3} We postulate that fiber-based ratiometric fluorescence recordings can be performed simultaneously with MR measurements.

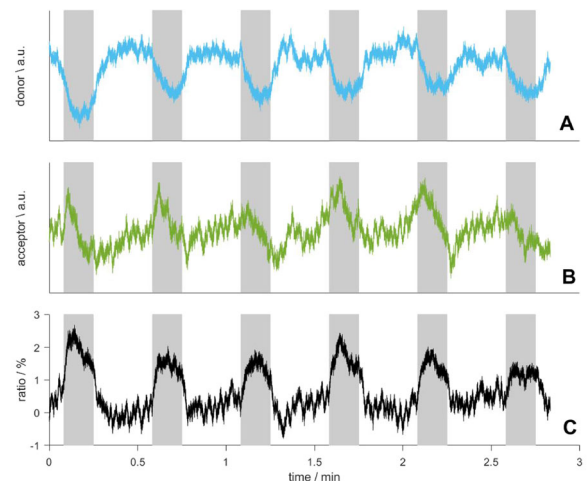


figure2: Donor (A) and acceptor (B) fluorescence signals upon 6 Hz electrical paw stimulation. The ratiometric calcium signal corresponds to the ratio of acceptor and donor signal (C). Stimulation periods are shaded grey.

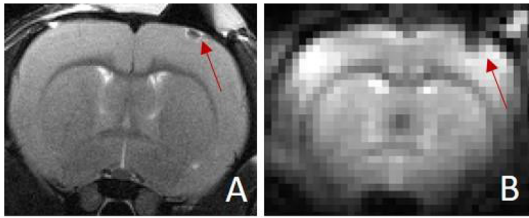


Figure 3. RARE (A) and single shot GE-EPI (B) axial images of a rat brain with implanted 400 µm optic fiber. Red arrows mark the artifact caused by the fiber.

- References:** ¹ Thestrup, T. et al., *Nat Methods* **11**, 175–182 (2014)
² Schulz, K. et al., *Nat Methods* **9**, 597–602 (2012)
³ Schwalm et al., *Elife* **6**, e27602 (2017)

L01.69

Increased connectivity in default mode and salience networks in video game players: A rsfMRI Study on task-based (tfMRI) Data

G. Fu, M. Noseworthy

McMaster University, Electrical and Computer Engineering, Hamilton, Canada

Introduction: Video games have become an increasingly popular past time and with its growing popularity it's important to study the long-term impacts of video game play on our brains. While previous works have shown that habitual game play leads to changes in the Default Mode Network (DMN) and Salience Network (SN) [1], our study aims to expand this scope to include 165 brain networks and atlases to determine how the brain connectivity of gamers compare to control groups. Changes in the connectivity can indicate functional differences in the brain and can be used to explain why video game players perform better at certain tasks.

Subjects/Methods: Data was acquired from freely available online databases containing 3 studies using task-based fMRI (tfMRI) and resting state fMRI (rsfMRI). Data was categorized into 4 groups:

- (1) gamers: 10 sets of tfMRI data [2]
- (2) non-gamers: 10 sets of tfMRI data [2]
- (3) rs-control: 10 sets of rsfMRI data [3]
- (4) t-control: 8 sets of bilateral left/right hand alternating finger tapping

The mean subject age was 25 years. MRI data was acquired in each study using similar acquisition protocols and a 3T MRI system [2,3]. CONN: Functional Connectivity Toolbox v.19.C was used for data analysis and preprocessing. Using the default preprocessing pipeline, first and second level analysis was performed for seed-based (SBC) and ROI-to-ROI (RRC) connectivity metrics to examine patterns in the 4 groups.

Results/Discussion:

Figure 1A: SEED-BASED ANALYSIS OF DEFAULT MODE NETWORK (SEED # MPFC) FOR GAMERS, NON-GAMERS AND THE TWO CONTROL GROUPS

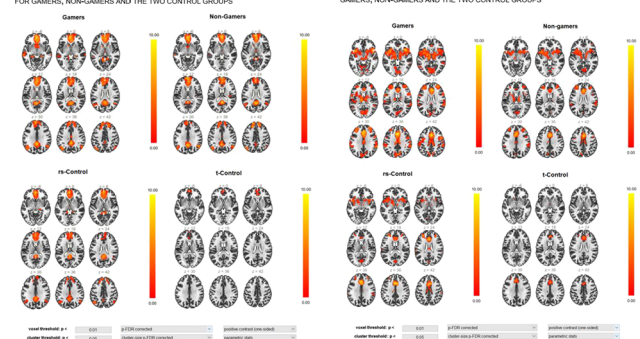


Figure 1B: SEED-BASED ANALYSIS OF SALENT NETWORK (SEED # ACC) FOR GAMERS, NON-GAMERS AND THE TWO CONTROL GROUPS

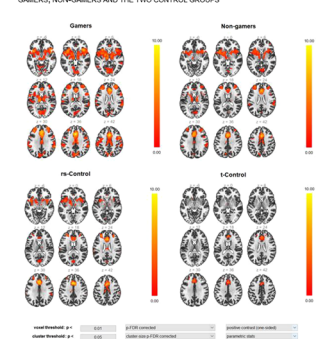


Figure 2A: ROI-TO-ROI CONNECTIVITY OF DEFAULT MODE NETWORK FOR GAMERS, NON GAMERS AND THE TWO CONTROL GROUPS

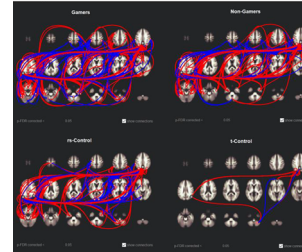


Figure 2B: ROI-TO-ROI CONNECTIVITY OF SALENT NETWORK FOR GAMERS, NON GAMERS AND THE TWO CONTROL GROUPS



To the best of our knowledge, freely available fMRI scans of gamers only contain elaborate task-based data. We performed resting state-based analysis knowing differentiation of groups would still be possible. **Figures 1(a)** and **1(b)** show the SBC map of the correlation coefficients for the DMN and SN, respectively, and the connectivity pattern of each seed. The DMN for gamers, non-gamers and the rsfMRI-based control group show similar patterns of connectivity compared to the tfMRI-based control group which shows lower activity levels. The SN of gamers showed greater connectivity compared to non-gamers and the two control groups, with the tfMRI-control group showing the least activation of all groups. Using a FDR corrected p-level of 0.05, we show that gamers have increased connectivity in both the DMN (**Fig.2a**) and SN (**Fig.2b**) relative to other atlases and networks in the brain, which may result in functional differences including faster response times and greater cognitive control. By using rsfMRI techniques such as SBC and RRC analysis for both resting state and task-based data, rsfMRI analysis is a versatile and powerful technique to examine connectivity in the brain.

- References:** [1] Ding WN, et al. (2013). *PloS one*, 8(3). <https://doi.org/10.1371/journal.pone.0059902>
[2] Gorbet DJ, Sergio LE. (2018). *PloS one*, 13(1). <https://doi.org/10.1371/journal.pone.0189110>
[3] Power JD, et al. (2017). *PloS one*, 12(9). <https://doi.org/10.1371/journal.pone.0182939>

L01.70**Ultra-high field resting-state fMRI biomarkers in an Alzheimer mouse model**R. Golgolab¹, T. Tsurugizawa¹, M. Simonneau², L. Ciobanu¹¹CEA, NeuroSpin, Gif-sur-Yvette, France, ²Ecole Normale Supérieure Paris-Saclay, Département de Biologie, Gif-sur-Yvette, France

Introduction: Resting-state fMRI (rs-fMRI) investigates brain functional connectivity (FC) in a non-invasive manner. Improvements in sensitivity and spatial resolution provided by the ultra-high fields (UHF) available today make rs-fMRI a well-suited candidate for early detection of neurodegenerative diseases such as Alzheimer's Disease (AD). To assess the potential of UHF rs-fMRI to provide early biomarkers of AD, we conducted a longitudinal study in which we compared control and transgenic mice overexpressing BIN1 at three timepoints.

Subjects/Methods: Two mice groups were scanned at 6, 12 and 18 months of age: 11 controls (WT) and 10 transgenic overexpressing human BIN1, the second most strongly Alzheimer-associated gene after APOE [1] (hBIN1). The rs-fMRI data were acquired on a 17.2T preclinical scanner using a 2D GE-EPI sequence with the following parameters: TE/TR=10/2000 ms, 12 slices, 300 repetitions, resolution 200 × 200 × 400 mm. After data preprocessing, ROI-to-ROI connectivity matrices were computed with the CONN toolbox [2], using 17 ROIs. NBS Connectome [3] was used to conduct statistical inferences.

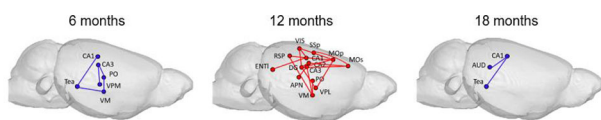
Results/Discussion:

Figure 1: Networks of altered connectivity revealed by NBS in the hBIN1 group compared to the WT group. Lines are colored according to contrast hBIN1 > WT (blue: hypoconnectivity in hBIN1. Red: hyperconnectivity in hBIN1).

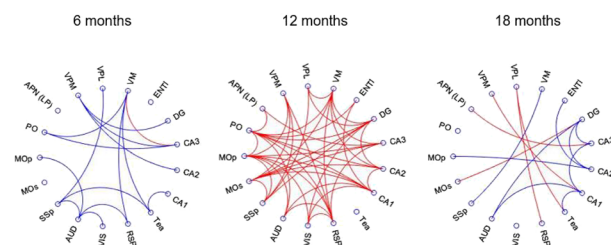


Figure 2: Large effect size (Cohen's $d > 0.7$) group differences are shown at 6, 12 and 18 months for hypoconnectivity in hBIN1 compared to WT. Red: hyperconnectivity in hBIN1 compared to WT). contrast hBIN1 > WT (blue: hypoconnectivity in hBIN1 compared to WT. Red: hyperconnectivity in hBIN1 compared to WT).

At each timepoint, NBS reveals a significant network of altered FC in the hBIN1 group compared to the WT group (Fig. 1). The earliest affected regions include the hippocampus (CA1, CA3), the thalamus (PO, VPM, VM) and temporal association areas (Tea) with a decrease of connectivity at 6 months. A spreading of the abnormalities is observed at 12 months in the hBIN1 group, with a network of

hyperconnectivity comprising the hippocampus, the thalamus, the lateral entorhinal cortex (ENT1), the retrosplenial cortex (RSP), the visual cortex (VIS), the somatosensory cortex (SSp) and the motor cortex (MOp, MOs). At 18 months, a significant network of hypoconnectivity is observed in the hBIN1 group, comprising the CA1, auditory areas (AUD) and Tea. Cohen's d shows that there is also a large effect of hyperconnectivity in some regions at 18 months, although larger sample size is required to infer statistical significance (Fig. 2, right most panel).

Conclusion and Perspectives: Using UHF rs-fMRI we report early FC alterations in AD hBIN1 mice and track them over time. Our results are in agreement with hypoconnectivity found in APPS1 and APOE mice at 18 months [4][5]; however, as opposed to [5], we find a network of hyperconnectivity at 12 months. Future work includes the combination of rs-fMRI and diffusion MRI data for a better characterization of the hBIN1 model.

References: ¹ Harold et al., Nature Genetics, 41, 2009

² Whitfield-Gabrieli, S., & Nieto-Castanon, A., Brain Connectivity, 2(3), 2012

³ Zalesky et al., NeuroImage, 53(4), 2010

⁴ Shah et al., PLOS One, 2013

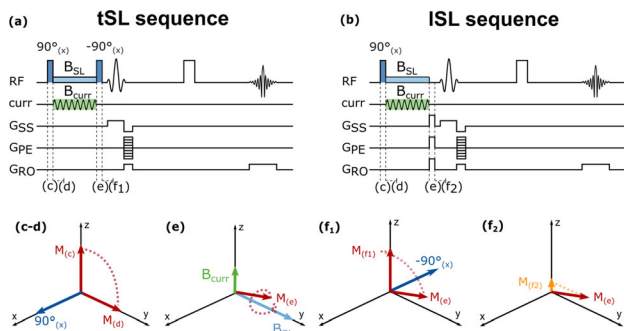
⁵ Zerbi et al., Journal of Neuroscience, 34(42), 2014

L01.71**Understanding limitations of neuronal-current MRI for functional imaging of brain activation: A simulation study**C. Coletti¹, S. Domsch¹, F. Vos², S. Weingärtner¹

¹TU Delft, Faculty of Applied Sciences, Department of Imaging Physics, Magnetic Resonance Systems Lab, Delft, The Netherlands, ²TU Delft, Faculty of Applied Sciences, Department of Imaging Physics, Delft, The Netherlands

Introduction: Functional MRI (fMRI) is one of the most important tools for the study of brain activity in vivo, enabling non-invasive imaging with high spatial resolution and whole-brain coverage. Conventionally, fMRI is based on the blood-oxygen-level-dependent (BOLD) effect¹. However, this contrast has intrinsic limitations due to the temporal delay of the hemodynamic response, and provides only an indirect measure for neuronal activity². Direct detection of the magnetic fields elicited by neuronal activity in MRI has been a long-standing research goal³. Recent studies demonstrated that MRI signals can be sensitized to concerted voltage fluctuation, the local field potentials (LFP), using spin-lock preparations^{3,4}. However, compromised sensitivity in the presence of system imperfections has so far hindered widespread use.

In this work we sought to investigate the performance of recent methods for direct neuronal current MRI in the presence of system imperfections in silico.

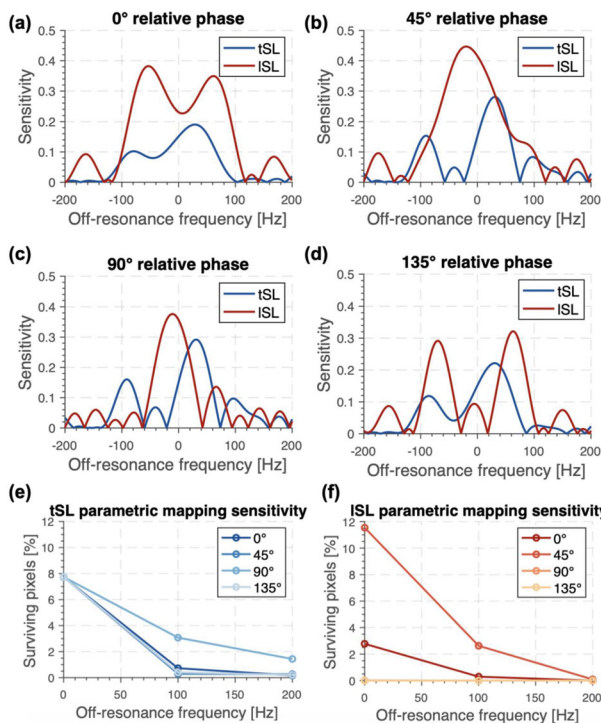


Pulse sequences for tSL (a) and ISL (b) sequences. After excitation (c-d), M is locked by the SL field on y, where it nutates due to resonant neuronal currents (e). Either transverse or longitudinal magnetization are retained with tSL and ISL (f1-2).

Subjects/Methods: Two techniques based on spin-lock preparations, in resonance with oscillating currents at a target frequency, were studied. In the methods the currents' strength is encoded in the transverse (tSL) and longitudinal (ISL) magnetization, respectively (Fig. 1).

Bloch-simulations were performed to assess the sensitivity of the methods in the presence of system imperfections^{3,4}.

Synthetic neuro-current data was generated by using BOLD response as a rough proxy for LFP activation⁵. BOLD-fMRI data from 6 healthy subjects (24 ± 3 y/o, 3 females) were acquired at 3T (resolution = $1 \times 1 \times 3$ mm³, TE/TR = 35 ms/2.7 s) during a bilateral fingertapping block-paradigm. Off-resonances were simulated based on a representative 3D field map⁶. Time series were modulated to account for off-resonances and relative phase between the current and spin-lock field. Activation maps were quantitatively assessed using statistical parametric mapping (SPM12). Additionally, sensitivity of parameter mapping was quantified by applying off-resonances to a simulated data-set with full activation.

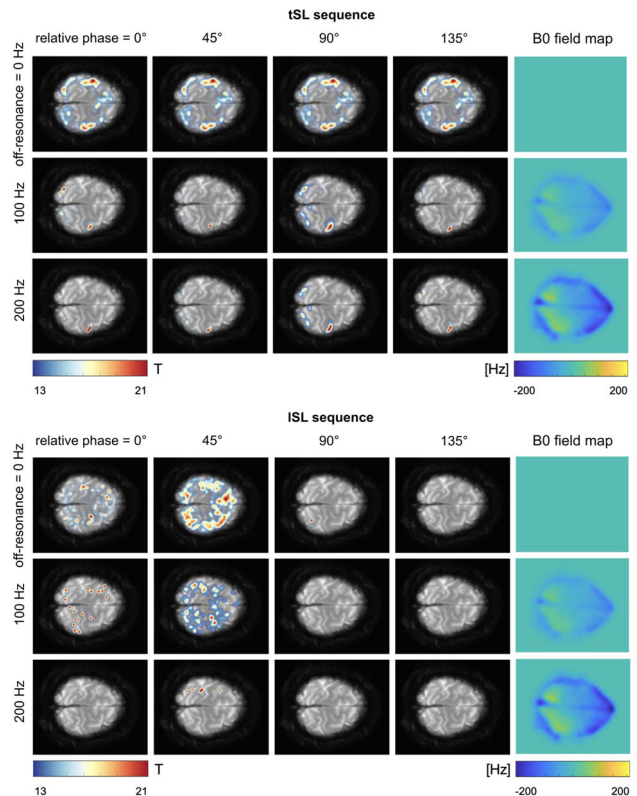


Sensitivity curves for ISL and tSL sequences on a 400 Hz range of off-resonance for different relative phase values (a,b,c,d). Ratio of voxels that survive after SPM analysis of ISL (e) and tSL (f) synthetic data with respect to full activation.

Results/Discussion: Substantial variation of the sensitivity was found over a range of 400 Hz off-resonance and 0-180° of initial relative phase (fig 2a). For the tSL sequence the relative phase only affects the contrast in the presence of field inhomogeneity.

The quantification of signal loss on activation maps shows a significant degradation in presence of imperfections (fig 2b, fig 3), down to 0% surviving pixels.

Our results show that both methods incur important loss in sensitivity in the presence of system imperfections. Thus, more robust MRI sequences are essential for the effective use of neuro-oscillating current MRI in the study of brain activity.



T maps (z=63mm) obtained from the SPM analysis on tSL (a) and ISL (b) synthetic data, in presence of different scaling of B0 inhomogeneity maps and initial relative phase between SL and currents field.

References: 1. Ogawa S et al., MRM.14(1990)
 2. Menon RS et al., TiCS.13(1999)
 3. Halpern-Manners NW et al., PNAS.107(2010)
 4. Truong TK et al., MRM.81(2019)
 5. Logothetis N et al., Nature.412(2001)
 6. Friston KJ et al., HBM.2(1994)

L01.72
Correcting image distortions caused by gradient nonlinearities in low-field MRI using a neural network

M. de Leeuw den Bouter¹, M. van Gijzen¹, R. Remis²

¹Delft Institute of Applied Mathematics, Delft, The Netherlands,
²Delft University of Technology, Circuits and Systems, Delft, The Netherlands

Introduction: The introduction of low-field, portable MRI scanners [1,2] is of great clinical relevance, especially for low-income countries. In low-field MRI, with background field strengths in the range of

50–80 mT, the background field is often not sufficiently homogeneous nor can the gradients always be assumed to be linear, leading to distortions and intensity variations in the resulting images. Many methods exist that correct for such distortions, but in general they require either multiple images of the same object, or accurate field and gradient maps. Usually, in practice, neither of these conditions are met. Here, we present a deep learning approach with the goal of eliminating the distortions in a single simple MR image without exact knowledge of the magnetic field maps.

Subjects/Methods: *Experimental setup:* A 3D-printed version of the Shepp-Logan phantom (Fig. 1) was imaged using the low-field MRI scanner described in [1]. A spin-echo sequence was used with the following parameters: bandwidth 50 kHz, $T_R/T_E = 1000$ ms/10 ms, 128×128 data points, FoV 12 cm x 12 cm.



Shepp-Logan phantom

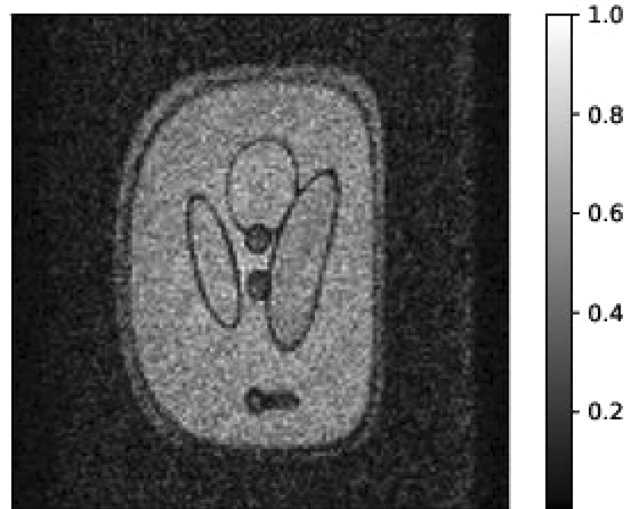
Training set simulation:

A training set of 100,000 2D images was generated using simulations. In these images, it was assumed that the phantoms consist of a number of superimposed large and small ellipses of varying intensities. Both gradient fields were perturbed using spherical harmonics of the second and third order. These perturbations varied from sample to sample. The corresponding signals were generated and an inverse FFT was applied, leading to distorted images. To each of the distorted images, noise was added with varying SNRs.

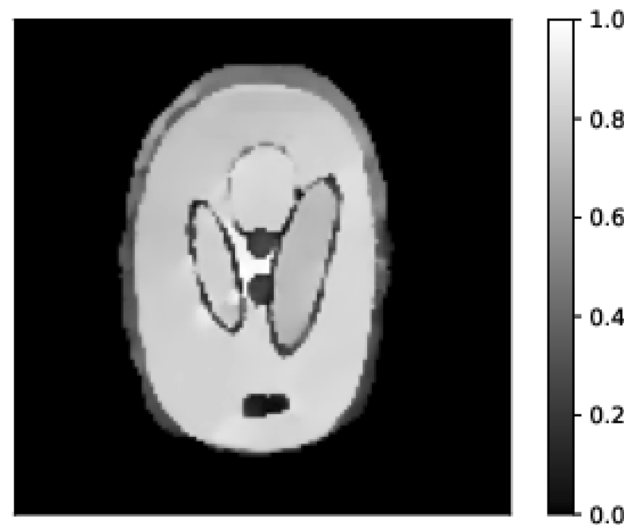
Neural network: A neural network with the U-Net architecture [3] was trained using the distorted images as input and the undistorted images as output. The loss function was defined as L1-loss. For training, the Adam optimizer was used on a training set of 90,000 samples, with a validation set of 10,000 samples.

Results/Discussion: Applying the trained neural network on the distorted image (Fig. 2) yields the result shown in Fig. 3. Clearly, the network manages to eliminate most of the distortions. Additionally, it

successfully denoises the image. Future work should focus on extending this approach to (3D) brain images.



Initial distorted reconstruction



Neural network reconstruction

References: [1] O'Reilly, T., Teeuwisse, W. M., & Webb, A. G. (2019). Three-dimensional MRI in a homogenous 27 cm diameter bore Halbach array magnet. *Journal of Magnetic Resonance*, 307, 106578.

[2] Cooley, C. Z., Stockmann, J. P., Armstrong, B. D., Sarracanie, M., Lev, M. H., Rosen, M. S., & Wald, L. L. (2015). Two-dimensional imaging in a lightweight portable MRI scanner without gradient coils. *Magnetic resonance in medicine*, 73(2), 872–883.

[3] Ronneberger, O., Fischer, P., & Brox, T. (2015, October). U-net: Convolutional networks for biomedical image segmentation. In *International Conference on Medical image computing and computer-assisted intervention* (pp. 234–241). Springer, Cham.

L01.73

Efficient Early Stopping algorithm for Quantitative Susceptibility Mapping (QSM)

C. Milovic, A. Karsa, K. Shmueli

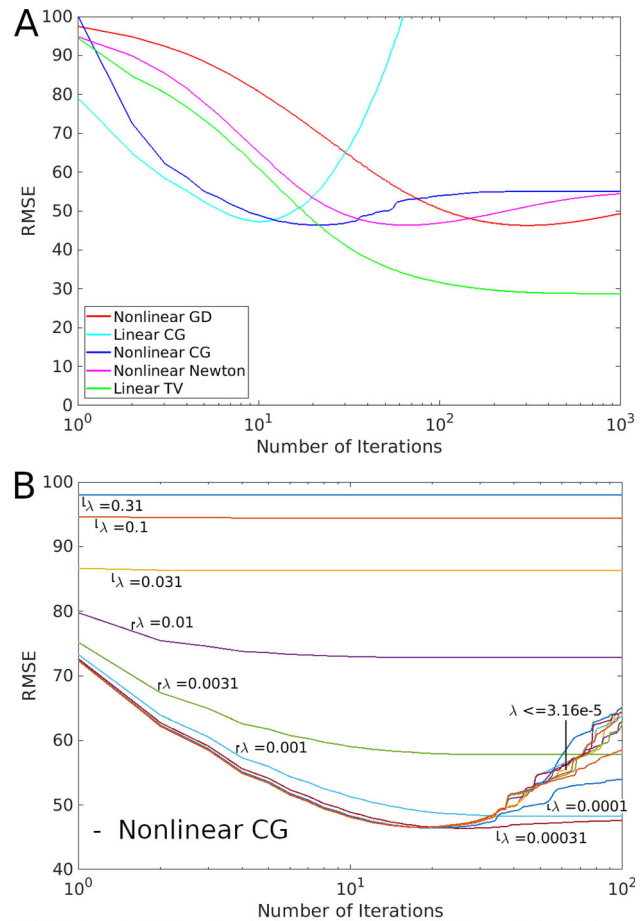
University College London, Department of Medical Physics and Biomedical Engineering, London, UK

Introduction: Susceptibility maps are calculated from local magnetic field maps estimated from the phase of Gradient Echo MRI acquisitions by solving an ill-posed inverse problem. Most inversion methods rely on minimizing a functional until it converges¹. This is time-consuming and requires fine-tuning of one or more parameters by performing the inversion many times. A recent nonlinear gradient descent (GD) algorithm² may lead to results comparable to state-of-the-art MEDI³ and FANSI⁴ by stopping the algorithm before it diverges from the true solution². The algorithm was stabilized by a Tikhonov term largely independent of its weight. In this new framework, the number of iterations becomes the main parameter that controls the results. Nevertheless, GD algorithms typically require hundreds of iterations (albeit fast) to achieve optimal results, and manual supervision is needed as there are no available automatic methods to reliably stop these algorithms. Here, we propose an efficient nonlinear conjugate gradient method to achieve optimal results in significantly fewer iterations than other GD methods.

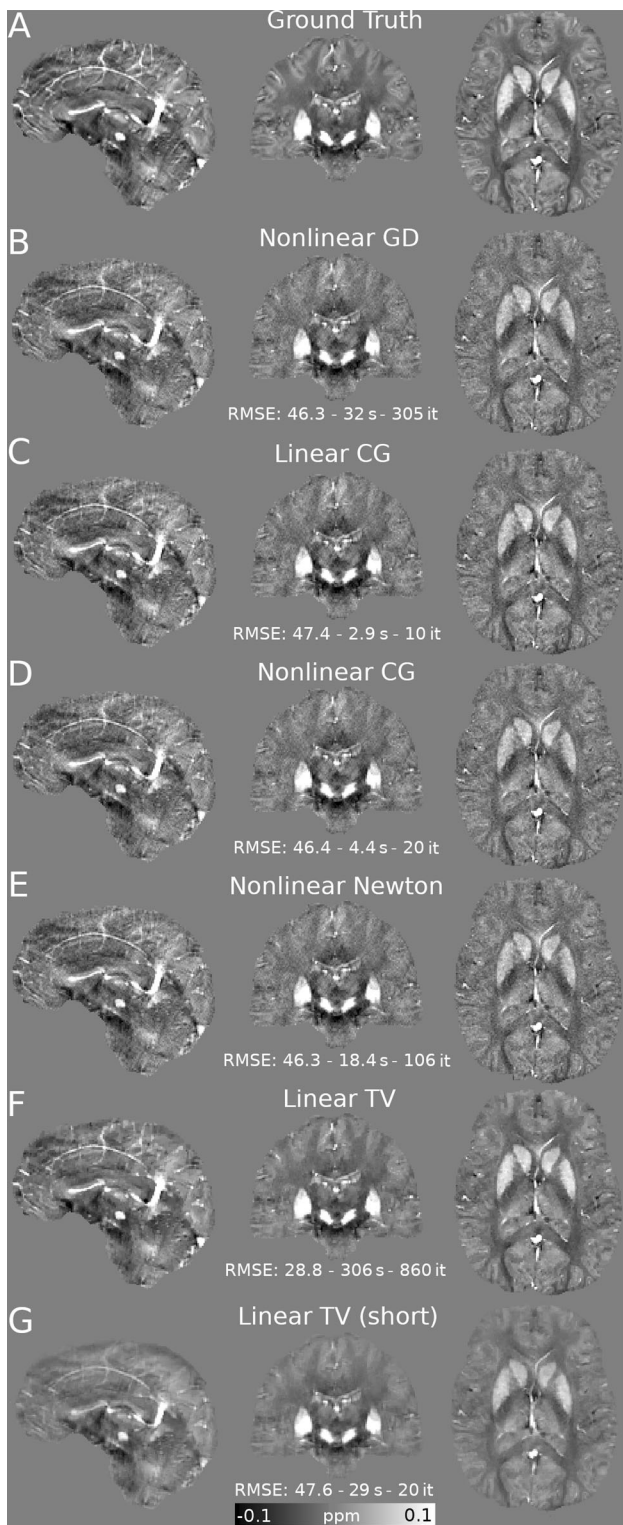
Subjects/Methods: We used a brain dataset from the 2016 QSM challenge as a susceptibility ground-truth⁵ to forward simulate the local magnetic field, and to test different QSM optimization strategies: Nonlinear GD, linear⁶ and nonlinear conjugate gradient (CG), dampened Newton methods, and a linear total variation (TV) regularized solver⁷ (FANSI Toolbox⁴). Reconstructions were compared in terms of root mean squared error (RMSE), computation time (i7-9750H @4.5GHz with 32Gb RAM), and the number of iterations. All strategies were also tested on a challenging in-vivo Head and Neck dataset⁶.

Results/Discussion: Unless large dampening terms are used, Newton methods diverged quickly. However, these required fine-tuning to achieve fewer iterations than GD methods. Nonlinear GD and CG methods were more robust, with the CG methods achieving results in the least iterations (Figure 1A). Optimal GD solutions were largely insensitive to the Tikhonov term (Figure 1B). All early stopping methods had similar RMSE, with a slight advantage for nonlinear methods (Figure 2). The linear TV method had a lower RMSE but required the most iterations to converge. TV with early stopping resulted in blurring and susceptibility attenuation (Figure 2G).

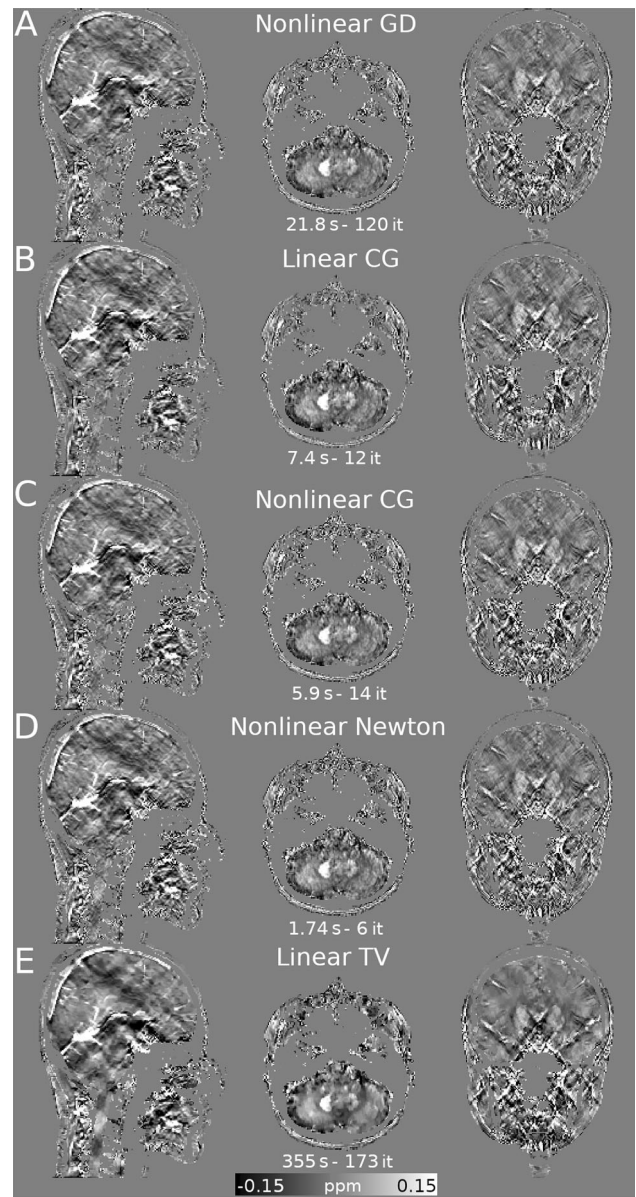
In vivo, CG reconstructions showed a good compromise between image quality and number of iterations (Figure 3). In conclusion, CG methods stopped at 10–20 iterations provide sharp and robust results but may contain moderate streaking artifacts compared to TV methods. Nonlinear CG may be preferable due to better noise management.



Synthetic phantom results. A) RMSE scores for each method vs the number of iterations. B) RMSE scores vs iteration number for different regularization weights using the nonlinear CG method. Similar behaviour was found for the other GD methods.



Sagittal, coronal and axial slices of the synthetic phantom (A) and optimal results (B-F). (G) Represents the TV solution for 20 iterations, the optimal number of iterations for the nonlinear CG method (and similar RMSE scores).



Sagittal, axial and coronal slices of the in-vivo results. The number of iterations for (A-D) and regularization weight of (E) was determined by visual inspection. (E) used a stopping criterion of < 0.1% change rate between iterations.

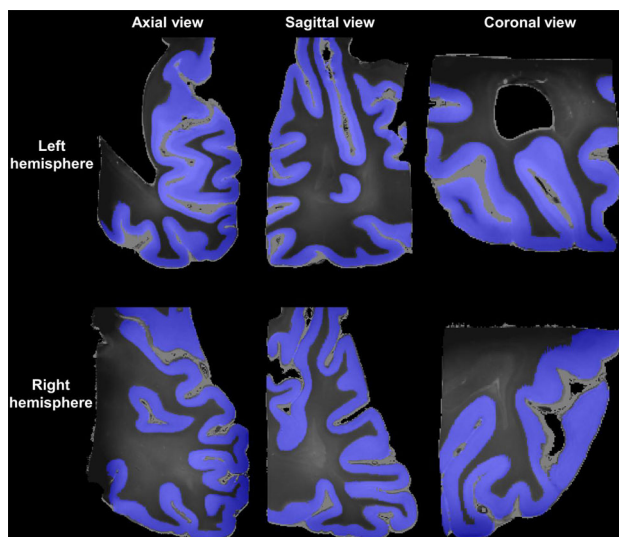
References: 1. Kee IEEE TBE 2017; 2. Polak et al., NMR Biomed 2020. 3. Liu et al MRM 2013. 4. Milovic et al, MRM 2018. 5. Langkammer, MRM 2018. 6. Karsa et al., MRM 2020; 7. Bilgic SPIE 2015

L01.74***Ex vivo* mapping of the cyto- and the myeloarchitecture of the human cerebral cortex using ultra-high field MRI (7T and 11.7T)**

R. Yebga Hot¹, A. Popov¹, J. Beaujain¹, G. Perez¹, F. Poupon¹, J.-F. Mangin¹, I. Lima Maldonado², C. Destrieux², C. Poupon¹

¹NeuroSpin - CEA, Gif-sur-Yvette, France, ²Université de Tours, INSERM, Imaging and Brain laboratory (iBrain), UMR 1253, Tours, France

Introduction: Imaging the cortical thickness has become a well-known approach to investigate neuropathologies¹. Segmentation of its laminar structure at a mesoscopic scale would allow to better identify slight cortical damage in pathological cases. Ultra-high field (UHF) MRI is a suitable candidate to probe the cortex laminar structure² of the occipital lobe that we propose to investigate here using quantitative MRI related to myelination³ and diffusion MRI related to cytoarchitecture⁴ at the mesoscopic scale.

Subjects/Methods:

Cortex masks (in blue) superimposed on the quantitative T1 maps of both hemispheres in the axial (left column), sagittal (middle column) and coronal (right column) views. Cortices' masks obtained from the qT1 and the p maps

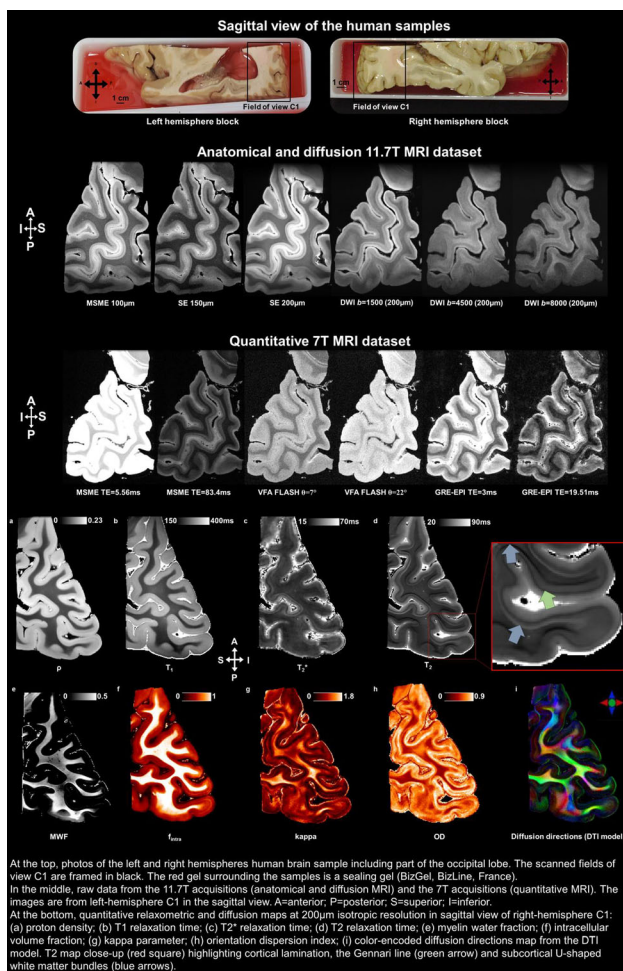
Two occipital samples of an *ex vivo* human brain were scanned using preclinical Bruker 11.7T/7T MRI systems, and ¹H 60mm volume coils.

The 11.7T MRI protocol focused on anatomical and diffusion MRI (dMRI) including a 100 μ m isotropic 3D T₂-weighted MSME sequence, a 150 μ m isotropic 2D T₂-weighted SE sequence and 200 μ m isotropic 3D segmented EPI PGSE sequences ($b = 1500/4500/8000$ s/mm²; 25/60/90 directions).

The 7T MRI protocol targeted quantitative MRI (qMRI) at 200 μ m isotropic resolution including 3D variable flip angle FLASH sequences⁵, a 3D T₂-weighted MSME sequence, a 3D T₂*-weighted multi-GRE EPI sequence and a dual flip-angle 3D EPI B₁ mapping sequence⁶.

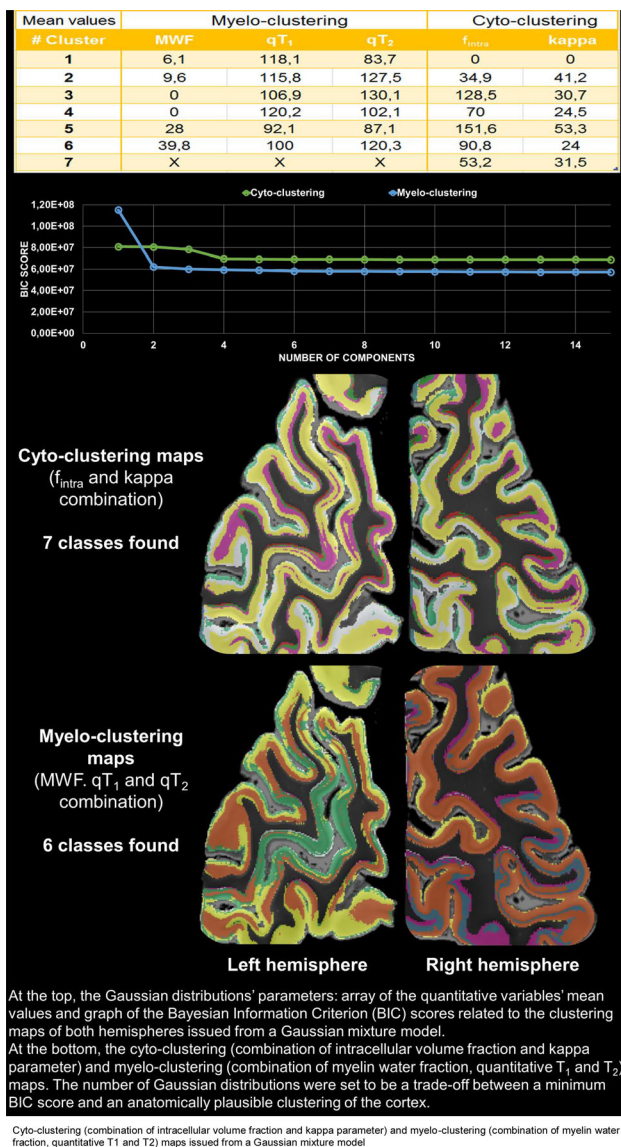
All data were denoised using a non-local means filter⁷. Quantitative T₁ (qT₁), T₂ (qT₂) and T₂* maps were computed using a fit of the T₁w and T₂w signal equations. The myelin water fraction map was computed from the 7T qMRI data as proposed in⁸. The NODDI model⁹ was computed from the 11.7T dMRI data.

Quantitative maps were combined using a multidimensional Gaussian mixture model to obtain clusters and their associated probability maps optimized using a Bayesian Information Criterion (BIC).

Results/Discussion:

At the top, photos of the left and right hemispheres human brain sample including part of the occipital lobe. The scanned fields of view C1 are framed in black. The red gel surrounding the samples is a sealing gel (BizGel, BizLine, France). In the middle, raw data from the 11.7T acquisitions (anatomical and diffusion MRI) and the 7T acquisitions (quantitative MRI). The images are from left-hemisphere C1 in the sagittal view. A=anterior, P=posterior, S=superior, I=inferior. At the bottom, quantitative relaxometric and diffusion maps at 200 μ m isotropic resolution in sagittal view of right-hemisphere C1: (a) proton density; (b) T₁ relaxation time; (c) T₂* relaxation time; (d) T₂ relaxation time; (e) myelin water fraction; (f) intracellular volume fraction; (g) kappa parameter; (h) orientation dispersion index; (i) color-encoded diffusion directions map from the DTI model; T₂ map close-up (red square) highlighting cortical lamination, the Gennari line (green arrow) and subcortical U-shaped white matter bundles (blue arrows).

Photos of the two human brain samples showing the scanned fields of view which include part of the occipital lobe, followed by the 11.7T and 7T raw datasets as well as the quantitative relaxometric and diffusion maps at 200 μ m isotropic resolution



The two samples present similar contrasts and quantitative values, both being coherent with literature¹⁰. Differences in myelination appear within the calcarine sulcus where sub-clusters are found for the left-hemisphere sample. These discrepancies may implicate a hemispherical

specificity of the myelinated components and even ocular dominance¹¹. The cyto-clustering map displays one more cluster/layer than the myelo-clustering one which needs to be further investigated. As for U-shaped white matter bundles, they exhibit a clear contrast from qT₂ mapping.

References: 1. Thompson & Toga. *Cerebral Cortex Diseases and Cortical Localization*. e LS. (2001)
2. Roebroeck *et al.* *NMR in Biomed.* 32(4), e3941. (2019)
3. Lifshits *et al.* *NeuroImage* 164, 112–120. (2018)
4. Beaujoin *et al.* Oral communication. Abstract #0654, ISMRM 2019
5. Trzasko *et al.* *Magnetic resonance in medicine* 69(6), 1787–1794. (2013)
6. Boudreau *et al.* *J. Magn. Reson. Imaging* 46(6), 1673–1682. (2017)
7. Buades *et al.* *Image Processing On Line* 1, 208–212. (2011)
8. Kulikova *et al.* *PLoS one* 11, e0163143. (2016)
9. Zhang *et al.* *NeuroImage* 61(4), 1000–1016. (2012)

10. Sengupta *et al.* *NeuroImage* 168, 162–171. (2018)

11. Menon *et al.* *Journal of neurophysiology* 77(5), 2780–2787. (1997)

L01.75

Harmonization of DTI and cortical thickness measurements of healthy subjects imaged on two different scanners

S. Tecelão¹, P. Selnes¹, T. Fladby¹, A. Bjørnerud²

¹Akershus University Hospital, Department of Neurology, Lørenskog, Norway, ²University of Oslo, Department of Physics, Oslo, Norway

Introduction: The harmonization tool ComBat¹, traditionally used for batch-effect correction in genomics data, has shown promising results to correct for scanner effect on DTI² and cortical thickness (CT) data³. The aim of this study was to test the ComBat tool using structural and DTI data from subjects scanned on two different scanners within a short time-span.

Subjects/Methods: 10 healthy subjects (7 male, mean age: 63.4) from the Dementia Disease Initiation project⁴, were scanned on a Philips Ingenia 3T and Siemens Prisma 3T scanner (2/4 days between scans). Ingenia DTI acquisition parameters were: b = 1000, 32 directions, 1b0/slice, TR/TE = 13549/64 ms, 60 slices, voxel resolution = 2 × 2 × 2 mm³. Prisma DTI acquisition parameters were: b = 1000, 2 × 30 directions, 1b0/slice, TR/TE = 5600/54 ms, 60 slices, voxel resolution = 2 × 2 × 2 mm³. Fractional anisotropy (FA) was computed using the TBSS tool from FSL 6.0.1 software. The 20 WM tracts from the JHU white-matter tractography atlas were analysed. CT was computed using Freesurfer 6.0.0. ComBat harmonization was performed using an R algorithm⁵, with age, gender and Abeta42 as covariates. A Wilcoxon signed-rank test was used to compare the DTI parameters and CT between scanners (an uncorrected p-value for multiple corrections lower than 0.05 was considered statistically significant). In order to check if the ComBat harmonization preserved the biological information, the correlation between DTI parameters, as well as CT, and age were computed before and after harmonization.

Results/Discussion: The Prisma's mean FA was found to be 9.2% ± 3.6% higher than Ingenia's and a statistically significant difference (p = 0.05) between scanners was found in 100% of the WM tracts. After harmonization, Prisma FA was 0.12% ± 1.1% smaller than Ingenia FA (10% WM tracts, p < 0.05). The correlation between mean FA and age shows that, before harmonization, 27.6% of Ingenia FA and 24.2% of Prisma FA were explained by age. After harmonization these values increased to 28.0% and 25.1% respectively. Regarding structural data, CT from Prisma was 2.95% ± 5.7% higher than from Ingenia. A statistically significant difference between scanners was found in 54% of the CT ROIs. After harmonization, CT from Prisma was 0.15% ± 1.4% smaller than from Ingenia (1.5% ROIs, p < 0.05). Before harmonization, 55.5% of Ingenia CT and 31.0% of Prisma CT were explained by age. After harmonization these values increased to 56.4% and 34.0% respectively. This analysis corroborates previous studies by showing that ComBat harmonization is an efficient tool to correct for scanner variations, while preserving the biological information.

References: ¹ *Biostatistics* 2007;8(1):118–127

² *NeuroImage* 2017;161:149–170

³ *NeuroImage* 2018;167:104–120

⁴ *JAlzheimersDis* 2017;60(1):97–105

⁵ <https://github.com/Jfortin1/ComBatHarmonization>

L01.76**Importance of applying ComBat besides image standardisation in multicentre Breast MRI radiomics: A phantom study**M.-J. Saint Martin¹, F. Orhac¹, P. Akl², F. Khalid¹, C. Nioche¹, C. Malhaire³, F. Frouin¹¹Université Paris-Saclay, Inserm, Institut Curie, Laboratoire d'Imagerie Translationnelle en Oncologie (LITO), Orsay, France, ²HCL, Radiologie du groupement hospitalier Est, Hôpital Femme Mère enfant, Unité Fonctionnelle: imagerie de la femme, Lyon, France, ³Institut Curie, Service de Radiodiagnostic, Paris, France

Introduction: The large number of images required to perform relevant radiomic analyses often calls for the use of multicentre and retrospective data. Still, MR images are quantified in arbitrary units that vary between patients, acquisitions, coils and scanners of imaging centres and suffer from bias field inhomogeneity. This results in inter and intra patient differences as well as centre effects. This study uses breast phantoms to assess the performance of standardisation pipelines in correcting retrospectively bias field inhomogeneity and reducing the centre effect affecting radiomic features.

Subjects/Methods: Two identical breast phantoms (CIRS, model 073) were simultaneously scanned twice using three sequences (T1, T2 and T1-weighted DCE) in three settings: GE Optima MR450w (1.5T) with 8-channel coil, Siemens MAGNETOM Aera (1.5T) with 18-channel coil and with 16-channel Sentinelle Breast Coil. Fifteen identical 3D spherical regions (600 voxels) were drawn in the phantoms' neutral inner layer on every image.

Images were corrected for bias field inhomogeneity with the N4ITK algorithm using breast specific parameters [1]. In T1 and DCE, the outer layer of the phantom, emulating the skin and subcutaneous fat of the patient, was segmented to be used as a reference tissue to conduct White Stripe (WS) normalisation while in T2, Z-score normalisation was performed using a mask of the phantom to compute the intensity mean and standard deviation.

On the raw, the N4 corrected and the N4 corrected and normalised images, the impact of the correction on intra and inter patient inhomogeneities was assessed by computing the coefficient of variation of the intensity means over the 15 regions inside every image and by extracting 42 radiomic features from the regions using the LIFEx software v5.79 [2]. The differences in the statistical distributions of radiomic features between settings were appraised using the Kruskal-Wallis test at every standardisation step and also after applying the non-parametric ComBat method [3].

Results/Discussion: N4 correction decreased the coefficient of variation of the intensity means over the regions and improved signal homogeneity inside phantoms (Fig. 1).

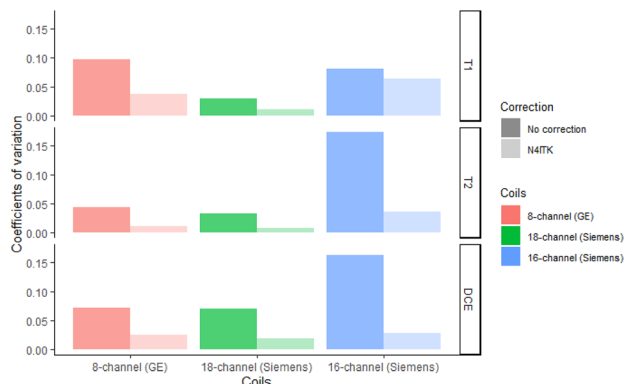


Fig. 1 Coefficients of variation of the intensity means over the regions across settings and sequences without any correction and when using the N4 correction (N4ITK)

In T1, T2 and DCE, the statistical distributions were significantly

different ($p < 0.05$) between settings for almost all radiomic features in raw images. N4 correction and normalisation both reduced the number of significant features but applying ComBat remained essential to fully correct for setting differences (Fig. 2).

Sequence	P value	Pipeline steps			
		Raw images	After N4	N4 & WS	N4 & WS & ComBat
T1	$p < 10^{-5}$	37	38	24	0
	$10^{-5} \leq p < 10^{-3}$	3	1	7	0
	$10^{-3} \leq p < 0.01$	1	0	2	0
	$0.01 \leq p < 0.05$	1	2	5	0
	$0.05 \leq p$	0	1	4	42
T2	$p < 10^{-5}$	38	32	24	0
	$10^{-5} \leq p < 10^{-3}$	4	6	8	0
	$10^{-3} \leq p < 0.01$	0	3	2	1
	$0.01 \leq p < 0.05$	0	1	3	0
	$0.05 \leq p$	0	0	5	41
T1 weighted DCE	$p < 10^{-5}$	39	39	39	0
	$10^{-5} \leq p < 10^{-3}$	1	0	0	0
	$10^{-3} \leq p < 0.01$	1	0	1	1
	$0.01 \leq p < 0.05$	0	0	0	0
	$0.05 \leq p$	1	3	2	41

Fig 2 Distribution of the features in ranges according to their p-values from Kruskal-Wallis tests between settings across sequences and pipeline steps. In raw T1 images, 1 feature out of 42 was different between settings with $0.01 \leq p < 0.05$ (pink cell)

References: [1] Khalid et al. ECR, 2020.

[2] Nioche et al. Cancer Res, 2018.

[3] Orhac et al. Radiology, 2019.

L01.77**Improving CEST-MRI contrast quantification in 3T in vivo data**F. Romdhane¹, D. Villano¹, L. Consolino¹, D. L. Longo²¹Molecular Imaging Center, Department of Molecular Biotechnology and Health Sciences, University of Torino, Turin, Italy, ²Institute of Biostructures and Bioimaging (IBB), National Research Council of Italy (CNR), Torino, Italy

Introduction: Chemical exchange saturation transfer (CEST) imaging is a sensitive approach to microenvironment properties [1] and has been increasingly applied in vivo. However, in clinical scanners operating at 3T the acquired MRI-CEST images suffer from low SNR that emphasizes noise in the images and consequently affect accurate CEST contrast quantification. The aim of this work is to investigate and validated novel denoising methods to improve the CEST contrast quantification at 3T.

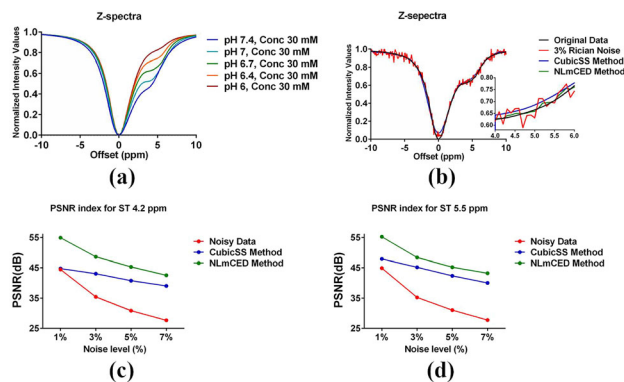
Subjects/Methods: A proposed combination between the NL-mean filter and anisotropic diffusion tensor (NLmCED) [2] was implemented and adapted for MRI-CEST images and compared to the Cubic Smoothing Spline (Cubic SS) [3] approach. Both methods were evaluated on simulated Z-spectra at 3T containing iopamidol at several pH value and 30mM concentration (Conc) (Fig1 a) and corrupted by different level of Rician noise. Preclinical data acquired on tumor bearing mice ($n = 8$) following iopamidol injection, collected on a 3T scanner, were exploited to validate the proposed approach.

Results/Discussion: NLmCED method shows a greater reduction of noise, illustrated by the lower oscillation in the Z-spectra (Fig1 b) compared to CubicSS method and provided better PSNR values for denoising CEST images surpassing CubicSS method (Fig1 c-d). For in vivo data, the NLmCED method achieved the best results (Fig2) by improving the contrast detection and by increasing the detectability of the contrast agent (fraction of pixels).

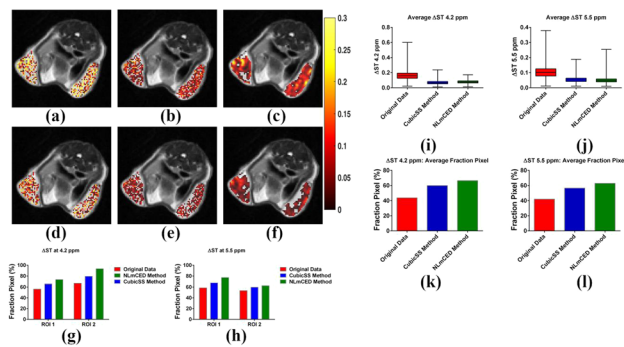
References: [1] P. Zijl van and N. Yadav, "Chemical exchange saturation transfer (CEST): what is in a name and what isn't?", Magn Reson Med, 2011.

[2] F. Romdhane, F. Benzarti and H. Amiri, "A new method for three-dimensional magnetic resonance images denoising", Int. J. Comput Vis Robots, 2018.

[3] J. Stancanello, E. Terreno, D. Castelli, et al., “Development and validation of a smoothing-splines-based correction method for improving the analysis of CEST-MR images”, *Contrast Media Mol I*, 2008.



Denoising phantom data: (a) Simulated Z-spectra at several pH values and 30 mM Conc, (b) Denoising Z-spectra at 6.7 pH and 30 mM Conc with 3% of Rician noise by CubicSS and NLMCED method, (c-d) PSNR index for ST at 4.2 and 5.5 ppm, respectively.



Denoising in vivo data: ΔST for Original (a, d), CubicSS (b, e) and NLMCED (c, f), (g-h) fraction pixel, at 4.2 and 5.5 ppm respectively, for one patient. (i-j) Average ΔST (k -l) average fraction pixel, at 4.2 and 5.5, respectively, of 8 patients.

L01.78

Monitoring of TMZ therapy in murine GL261 glioblastoma by combining Radiomics, Convex-NMF and feature selection in MRI/MRSI data analysis

L. M. Nuñez Vivero¹, M. M. Julià-Sapè¹, E. Romero², C. Arús³, A. Vellido², A. P. Candiota¹

¹Centro de Investigación Biomédica en Red - Universitat Autònoma de Barcelona, Bioquímica i Biologia Molecular, Cerdanyola del Vallès, Spain, ²Universitat Politècnica de Catalunya, Dept. of Computer Science, IDEAI Research Center, Barcelona, Spain, ³Universitat Autònoma de Barcelona, Facultat de Biociències, Bioquímica i Biologia Molecular, Cerdanyola del Vallès, Spain

Introduction: Medical decision combines human expertise and medical evidence. Machine learning (ML) can help in the decision making process, but it must be interpretable [1]. We implemented an analytical pipeline for distinguishing between treated and control mice bearing GL261 glioblastoma (GB) using MRI and MRSI data. Previous research [2,3] proved that MRSI-derived metabolomics patterns could help in this distinction, but no attempt was made to investigate whether MRI data could improve results. Accordingly, our proposed pipeline now includes both MRI and MRSI.

Subjects/Methods: Data originates from $n = 30$ GL261 GB tumour-bearing mice ($n = 13$ controls, $n = 17$ treated) from [5]. TMZ administration schedule, MRI/MRSI acquisition and processing

parameters are described in [5]. Histopathological validation was performed at chosen time points. MRI was a T2-weighted acquisition of 256×256 pixels, while MRSI consisted of a 10×10 grid of 14ms TE spectra. For the Radiomics study, a manual segmentation of the tumor was performed in MRI; texture and Minkowski functions features were then extracted. MRSI sources were obtained using Convex-NMF [4] and only spectra completely representing the tumor region were selected. Feature selection consisted in a univariate filter t -test [6] and recursive feature elimination (RFE). Data were trained with leave-one-out or 10-fold cross-validation depending on the analysis.

Results/Discussion: Support vector machine (SVM) classifiers performed overall best. For Radiomics analysis, best results were obtained with 5-6 features with an accuracy of 96.7%. Transient response to TMZ in GL261 GB leads to the appearance of giant cells and acellular spaces and decrease of proliferation [2], impacting on MRI features. Amongst the features distinguishing treated from control tumours, we find GLRLM (coarseness) and GLSZM (gray level zones). Both measure aspects of tissue homogeneity which may change upon therapy (Fig. 1).

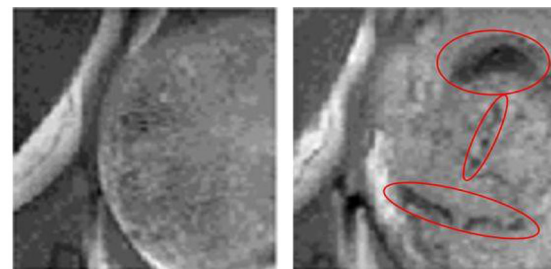


Fig. 1: Control (left, C583) and treated, transiently responding to TMZ (right, C574) murine GL261 GB. Hypointense zones (red circles) seen in T2w MRI from the treated mouse, while more homogeneous appearance is observed in the control case

For MRSI data, non-linear SVM achieved 97.7% accuracy with 14-17 sources. Previous work [2,5] described spectral features able to distinguish treated/responding and control cases, such as polyunsaturated fatty acids (2.8 ppm), lactate (1.3-4.1 ppm), mobile lipids (0.9 ppm) and myo-inositol/glycine (3.55 ppm), also noticeable in this work (Fig.2).

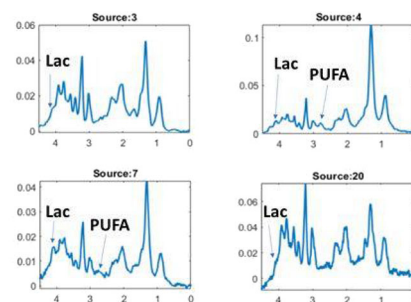


Fig. 2: Examples of convex-NMF sources selected by RFE. Y: arbitrary units; X: ppm. Lac: lactate; PUFA: Polyunsaturated Fatty Acids. Sources 4 and 7 are compatible with responding tumours as in [5], sources 3 and 20 are compatible with control tumours

In summary, the Radiomics-based approach could bear translational potential, since T2w MRI can be acquired at every clinical scanner and does not require contrast administration.

References: 1. Vellido, A *Neural Comput & Applic* (2019) doi.org/10.1007/s00521-019-04051-w

2. Arias-Ramos N et al, *Metabolites* (2017) 7: E20

3. Wu S et al, *NMR Biomed.* (2020) 33:e4229

4. Ding CH et al. *IEEE T. Pattern Anal.* (2008) 32:45-55

5. Delgado-Goni T et al. *NMR Biomed* (2016) 29:732-43

6. König CL et al. *BMC Bioinformatics* (2015) 16:314

L01.79

Quantitative texture analysis of prostate tumor heterogeneity from multi-parameter magnetic resonance images

S. Alanezi¹, F. Sullivan², C. Kleefeld³, J. Grealley⁴, M. Krašny³, D. Sheppard⁵, N. Colgan³

¹National University of Ireland Galway, School of Physics, College of Science and Engineering, Galway, Ireland, and Northern border University, School of Physics, Faculty of Science, Arar, Saudi Arabia, ²Department of Radiation Oncology, Galway Clinic, and National University of Ireland Galway, Faculty of Medicine, National University of Ireland Galway, Galway, Ireland, ³National University of Ireland Galway, School of Physics, College of Science and Engineering, Galway, Ireland, ⁴Galway Clinic, Department of Pathology, Galway, Ireland, ⁵University Hospital Galway, Department of Radiology, and Galway Clinic, Department of Radiology, Galway, Ireland

Introduction: The use of multiparametric magnetic resonance imaging (mp-MRI) has refined the diagnosis of prostate cancer in radiology [1]. Malignancy modified critical features in tissue composition such as heterogeneity which has been associated with adverse tumor biology [2]. Heterogeneity can be quantified through texture analysis, which is emerging as a fruitful technique for reviewing tumor images that are acquired in routine clinical practice [3-5]. This study focused on quantifying tumour heterogeneity from prostate multiparametric magnetic resonance images (mp-MRI) utilising texture analysis (TA).

Subjects/Methods: The cohort was involved with 18 men with presumed prostate cancer who acquired prostatic mp-MRI (Philips Ingenia 3T) before receiving prostatectomy. Patients scored as significant cancer ($\geq 3+4$) were estimated with reference to the Gleason grade and ISUP grade [7,8], then non-significant cancers were estimated based on the corresponding zone that was estimated for malignant with distinct regions. The ADC map, T₂ and T₁ weighted images segmented ROIs from the particular slice axial that included a non-significant tumour and a significant tumour where present underwent MRTA with in house developed MATLAB software and was verified using ImageJ software. MRTA consisted of image histogram interpretation based on first-order statistics of skewness, kurtosis, and entropy. The primary filtration stage emphasised ROIs of texture features extraction of designated filter sizes (3×3, 6×6, and 9×9 pixels) using (Joachim Walter's FFT Filter) [5]. The essential characteristic between a malignant and benign tumors ROIs was determined for every single textural parameter using the two-tailed Mann Whitney U test (p < 0.05).

Results/Discussion: mp-MRI with an exhibited malignant tumor in a specific zone of the prostate is presented in Fig. 1. Table 1 indicates textural parameters for skewness, kurtosis, and entropy form ADC map, T₂, T₁ weighted images. The ROC-AUC for notable univariate parameters that best demonstrated the enhanced specificity and sensitivity are indicated in Fig. 2.

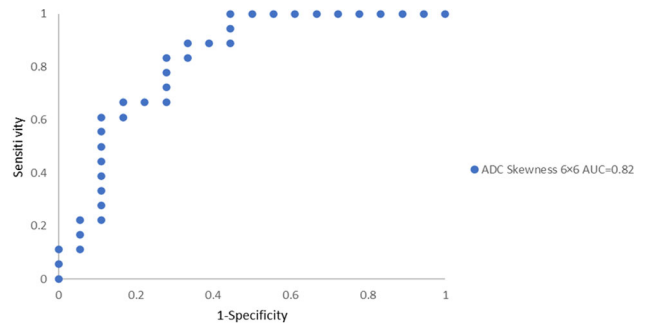


Figure 2 The foremost textural feature from ROC curves and distinguishing of ROIs comprising either significant tumors or non-significant tumors with AUC values as presented.

Sequence	Benign tumour median	Significant tumour median	p-value	ROC area undercurve (95%CI)
Skewness				
ADC 3×3	0.03	-0.32	0.94	0.66
T2 3×3	0.22	-0.03	0.54	0.31
T1 3×3	0.04	-0.09	0.29	0.39
ADC 6×6				
ADC 6×6	-0.19	0.41	0.001	0.82
T2 6×6	-0.03	0.03	0.8	0.47
T1 6×6	0.17	-0.08	0.2	0.37
ADC 9×9				
ADC 9×9	-0.09	0.25	0.08	0.66
T2 9×9	-0.005	-0.04	0.48	0.43
T1 9×9	0.04	0.07	0.5	0.56
Kurtosis				
ADC 3×3	-0.75	-0.71	0.37	0.58
T2 3×3	-0.71	0.26	0.6	0.55
T1 3×3	-0.09	-0.08	0.46	0.57
ADC 6×6				
ADC 6×6	-0.96	-0.70	0.22	0.61
T2 6×6	-0.70	-0.22	0.72	0.53
T1 6×6	-0.43	-0.40	0.65	0.54
ADC 9×9				
ADC 9×9	-0.9	-0.79	0.81	0.52
T2 9×9	-0.79	-0.22	0.82	0.47
T1 9×9	-0.55	-0.61	0.56	0.55
Entropy				
ADC 3×3	4.07	4.05	0.84	0.48
T2 3×3	6.31	6.36	0.75	0.46
T1 3×3	6.05	5.96	0.71	0.53
ADC 6×6				
ADC 6×6	4.14	4.15	0.64	0.54
T2 6×6	5.95	5.94	0.87	0.51
T1 6×6	5.31	5.04	0.68	0.54
ADC 9×9				
ADC 9×9	4.13	4.07	0.54	0.55
T2 9×9	5.80	5.64	0.56	0.55
T1 9×9	4.95	4.47	0.89	0.48

Table 1 Illustrating Median values of mp-MRI acquired from first-order statistical analysis of skewness, kurtosis and entropy for ROIs regions. P-values and ROC-AUC for MRTA parameters were calculated between ROIs.

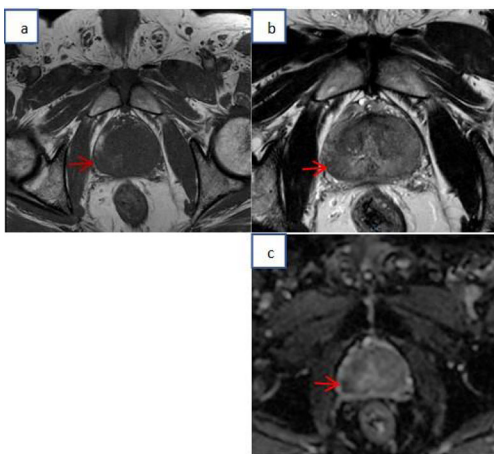


Figure 1 Prime tumour determined from a single slice axial (arrow images) (a) T1 weighted image. (b) T2 weighted image. (c) ADC map image. Images are from 58-year-old patient with significant tumor ($\geq 3+4$).

The results demonstrated that ADC skewness was the foremost classifying textural feature (ROC-AUC 0.82 on ADC 6×6 pixel filter image). In this cohort, the kurtosis and entropy of ADC, T₂ and T₁ weighted images for all filter sizes were not substantively associated with discriminating between benign and malignant. In summary, this study occupied mp-MRI obtained TA to quantify tumour heterogeneity with and without prostate tumours. The study evinced that mp-MRI originated TA may be utilised as a non-invasive procedure to evaluate the heterogeneity in prostate cancer.

- References:** [1] Delongchamps NB, BJU international 2011. [2] Colgan N, Frontiers in neuroscience 2017. [3] Ganeshan B, Cancer imaging 2013. [4] Davnall F, Insights into imaging 2012. [5] Miles KA, Cancer Imaging 2013. [6] Pierorazio PM, BJU international 2013.

L01.80**Simulating realistic appearing multiple contrast brain MRI**A. Ayaz¹, F. Wenzel², C. Lorenz², J. Weese², M. Breeuwer¹¹Eindhoven University of Technology, Biomedical Engineering Department, Eindhoven, The Netherlands, ²Philips Research Laboratories, Hamburg, Germany

Introduction: There is a lack of large sets of MRI data, needed for training and validating medical imaging analysis algorithms. Such data can be generated by MRI simulation and can be synthesized using AI methods such as generative adversarial networks¹. We propose a method to generate realistic brain MRI, which is based on creating a realistic phantom, performing k-space simulation, adding realistic noise, followed by FFT reconstruction. The steps followed resulted in more realistic appearing brain MRI images than our previous method².

Subjects/Methods: The complete methodology to generate brain MRI is shown in Figure 1.

A young healthy single subject structural brain MRI volume from the open source WU-Minn human connectome project³ is used to generate an anatomically plausible phantom. The data is fed to the Philips proprietary automated complete brain classification tool for 20 class brain labels. The tool is based on the fully convolutional network architecture that process images at multiple scales and different fields of view⁴. The labels generated covered the full brain and skull. The phantom generated is taken as a ground truth for contrast simulations.

Diverse tissue properties from literature⁵ are assigned to the generated phantom. Open source numerical Bloch-solver software JEMRIS⁶ is used as a simulation platform. Whole brain MRI is simulated consisting of multiple 2D gradient echo T1w (TE 10 ms, TR 400 ms and FA 90°) and spin echo T2w (TE 100 ms, TR 3000 ms and FA 90°–180°) axial slices. Cartesian k-space data is simulated at 1 mm³ isotropic resolution from a phantom resolution of 0.7 mm³. Variable complex noise (as per k-space frequency levels and for overall desired SNR) is generated and added to the raw k-space data. FFT reconstruction on the noise added k-space data is performed and resulting image volumes are stored in NIFTI format.

The simulated MR images are qualitatively evaluated for the preservation of anatomical details and for the overall realistic appearance for the desired SNR and image sharpness.

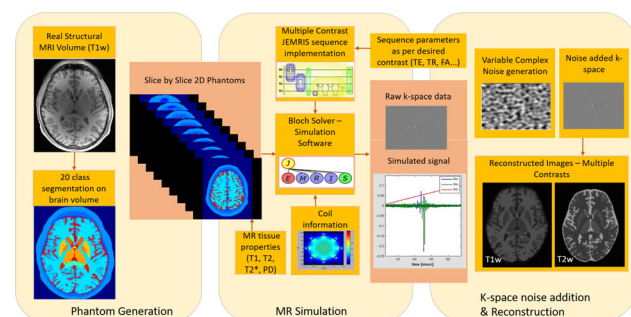


Figure 1: Overall methodology for generating brain MRI style database. Steps included for phantom generation, MR simulation and complex noise addition in raw k-space data followed by reconstruction.

Results/Discussion: Multiple axial slices of the simulated T1w and T2w brain MRI along with the ground truth are presented in Figure 2. The complex noise incorporated into the raw k-space simulated data resulted in more realistic overall image appearance, while the detailed set of phantom labels well preserved the anatomical details.

In the future, a larger database has to be generated over more ground truths with more images per set. As a direct application, such database will then be used to further generate MRI data, by synthesizing new

MRI examples with multiple styles using generative adversarial networks¹.

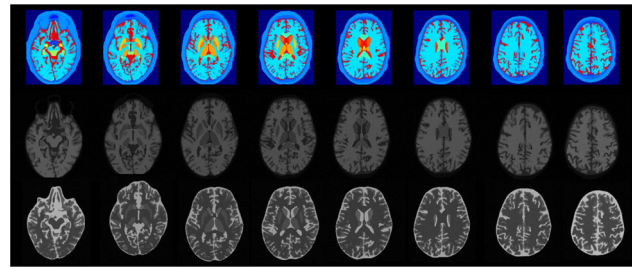


Figure 2: Multiple brain axial slices of generated Ground Truth (GT) (top row), simulated T1w (middle row) and T2w (bottom row). GT include 20 labels for skull and brain GM, WM, CSF, midbrain, deep gray structures, and ventricles.

References: 1. Park et al. CVPR 2019

2. Ayaz et al. ISMRM Benelux Chapter 2020

3. Van Essen et al. NeuroImage 2013; 80: 62-79

4. Brosch et al. SPIE Medical Imaging 2018; Image Processing. Vol. 10574

5. Bojorquez et al. JMRI 2017; 35: 69-80

6. Stöcker et al. MRM 2010; 64.1: 186-193

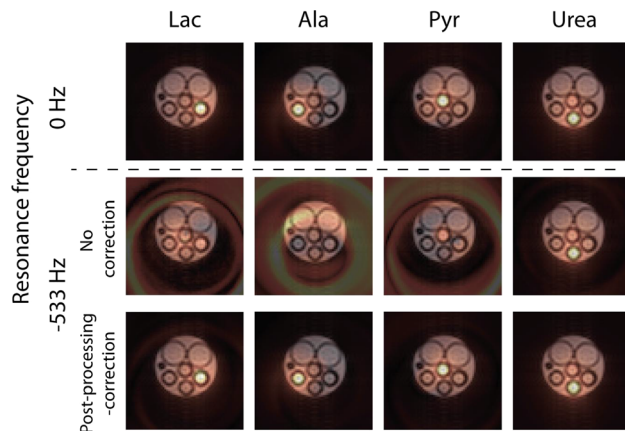
L01.81**Spurious phase correction in multi-shot MRSI**N. El Sabbagh¹, C. Chassain¹, H. Ratiney², G. Pages¹, J. M. Bonny¹¹INRAE, AgroResonance, UR QuaPA, F-63122 Saint-Gènes-Champanelle, France, ²University of Lyon, CNRS, Inserm, CREATIS UMR 5220, U1206, F-69621 Lyon, France

Introduction: Spectral multi-shot (MS) MRSI sequences are used essentially to decrease the scan time and enlarge the spectral width. Here, the spectral information is encoded by acquiring several experiments while shifting the readout position relative to the echo time (TE). These techniques are highly exposed to phase errors with the phase evolution being indirectly sampled through the different echo time increments. During this sampling, phase coherency is crucial. Nowadays, MS techniques can lead up to image distortion because of the loss of phase coherency between the shots. The purpose of this work is to present theoretically and experimentally how to overcome this phase problem.

Subjects/Methods: We demonstrated that during the extra delay to shift the echo time for a 2D slice selection, the phase evolves depending on the chemical shift with respect to the excitation frequency. The latter is generally significantly higher than the chemical shift, and the phase will mostly depend on it. This phase shift can be corrected on either the acquired signal or the reconstructed image by subtracting the additional frequency excitation applied when shifting the slice position. These methods were applied to rapid metabolic imaging (1) of a ¹³C phantom and on the particular case of **B**₀ mapping.

Results/Discussion: Results showed phase errors in MS MRSI, leading to image distortion, therefore incorrect and inefficient studies. However, applying one of the provided correction methods cancels the phase errors, improving the image quality.

Unwanted phase shifts are susceptible to be accumulated in MS techniques during different echo time increments, especially when the slice position is shifted from a null resonance frequency. We were able to correct the phase-shifting through post-processing in the k-space dimension, by image phase correction according to the Nyquist frequency rule or even during a particular experimental case. The three proposed correction approaches were able to discard the spurious phase and then to reconstruct parametric maps accurately.



Reconstruction of the metabolite maps of ^{13}C -labeled Lactate, Alanine, Pyruvic acid and Urea, for different slice positions: centred 0 Hz and shifted -533 Hz. For proper reconstruction, post-processing phase correction is critical for a shifted slice.

References: 1. Wiesinger F, Weidl E, Menzel M et al. IDEAL spiral CSI for dynamic metabolic MR imaging of hyperpolarized [^{1-13}C]pyruvate. *Magn Reson Med* 2012;68(1):8-16.

L01.82

The effect of oblique image slices on the accuracy of quantitative susceptibility mapping

O. C. Kiersnowski¹, J. S. Thornton², K. Shmueli¹

¹University College London, Department of Medical Physics and Biomedical Engineering, London, UK, ²University College London, UCL Queen Square Institute of Neurology, London, UK

Introduction: Susceptibility mapping (QSM) utilises phase to calculate tissue susceptibility (χ) differences and has increasing clinical applications. Acquiring oblique slices is a common clinical practice to facilitate radiological viewing, but gives incorrect χ estimates when not properly accounted for. Pilot studies have shown that the effect of tilted slices can be corrected by rotating unwrapped phase images before background field removal¹. A comprehensive analysis is required to disentangle the effect of slice tilting and correction on each step in the QSM pipeline: phase unwrapping, background field removal and χ calculation. Here, we use simulated local field maps² to investigate the effect of slice tilting and several correction methods on χ calculation.

Subjects/Methods: Local field maps from a numerical phantom² were used allowing investigation of the effects of slice tilt correction on χ calculation without confounds from background field removal. Five QSM tilt correction methods were compared for i) thresholded k -space division (TKD)³ (threshold = 2/3), and ii) iterative fitting with Tikhonov regularisation^{4,5} (regularisation parameter = 0.003) both corrected for χ underestimation⁶. Rotations (-45° to $+45^\circ$) about the x -axis were carried out using FSL Flirt⁷ with spline interpolation: *RotIm* – χ calculation with (axial) slices aligned with the scanner axes. No rotations were applied for this reference method. *RotImBNF* – field map rotated forward and backward before χ calculation to simulate rotating tilted slices into alignment with the scanner axes.

DipK – dipole defined in k -space and rotated to align with tilted image.

DipIm – dipole defined in image-space and rotated to align with tilted image. Both *DipK* and *DipIm* χ maps were rotated back to align with scanner axes for comparison.

UnRot – method to simulate mistakenly leaving the k -space dipole unaligned with the tilted image.

Mean χ values were calculated in five deep grey matter ROIs provided with the phantom².

Results/Discussion: The results from QSM with iterative Tikhonov regularisation (Figs 1&2), and TKD are similar. Figures 1-3 show that *RotImBNF* has very small χ errors relative to *RotIm* arising purely from rotation interpolations and is fairly constant over all angles. *DipK*, *DipIm* and *UnRot* all show increasing χ errors with angle with *DipIm* and *UnRot* giving the largest errors. In conclusion, the most accurate method to correct for tilted slices in QSM is to rotate the local field map to align it with the scanner axes prior to χ inversion with a k -space dipole defined in the scanner frame.

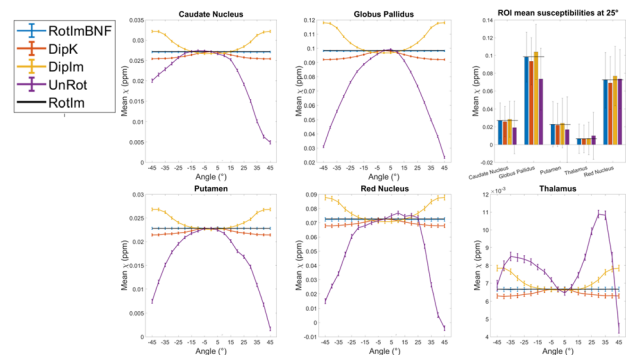


Figure 1: Mean χ for slices tilted by angles from -45° to 45° about the x -axis in five deep basal ganglia regions of interest for all five QSM tilt correction methods with iterative Tikhonov. Those from TKD (not shown) are similar.

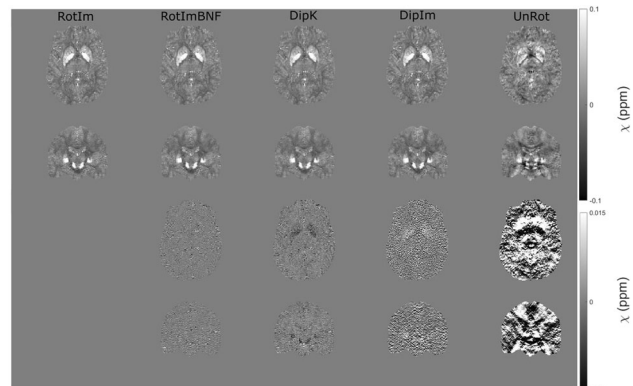


Figure 2: Axial and coronal slices showing QSM (iterative Tikhonov) with all five tilt correction methods (top two rows) and their difference images relative to *RotIm* (bottom two rows), all for a 25° tilt. Images from TKD (not shown) are similar.

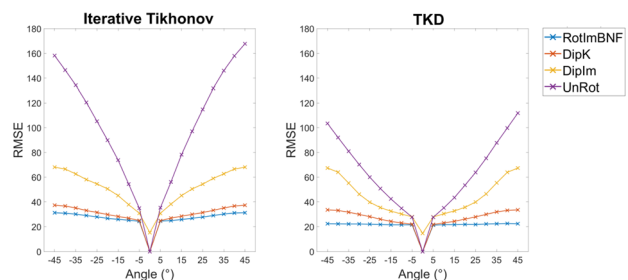


Figure 3: Root mean square error (RMSE) in susceptibility relative to *RotIm* throughout the brain across all tilt angles for QSM with iterative Tikhonov and TKD susceptibility calculation methods.

References: 1. Dixon EC. *UCL, London*. 2018
2. Marques J, et al. *In proc ISMRM2019:Canada*
3. Shmueli K, et al. *Magn Reson Med*. 2009;62(6):1510-1522

- 4.Kressler B, et al. *IEEE Trans Med Imaging*. 2010;29(2):273-281
 5.https://xip.uclb.com/i/software/mri_qsm_tkd.html
 6.Schweser F, et al. *Magn Reson Med*. 2013;69(6):1581-1593
 7.Jenkinson M, et al. *Neuroimage*. 2012;62:782-790

L01.83

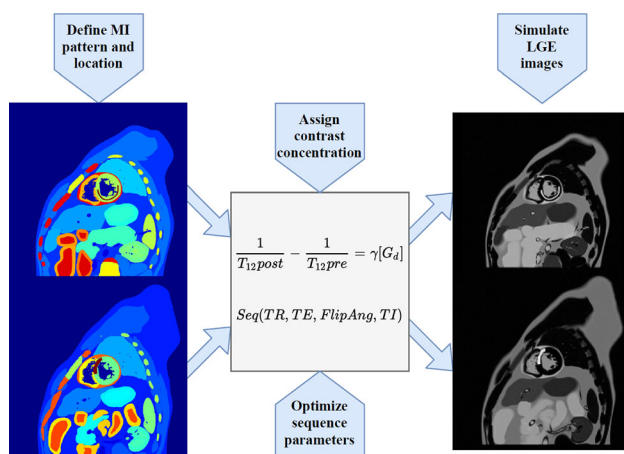
A multipurpose numerical simulation tool for late gadolinium enhancement cardiac MR imaging

S. Amirrajab¹, C. Lorenz², J. Weese², M. Breeuwer¹

¹Eindhoven University of Technology, Biomedical Engineering, Eindhoven, The Netherlands, ²Philips Research Laboratories, Hamburg, Germany

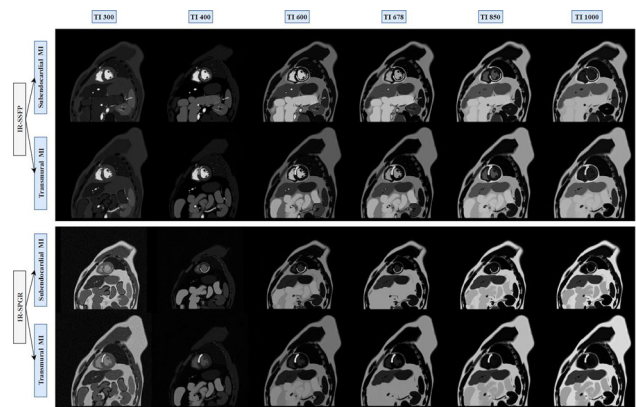
Introduction: Bloch equation-based numerical simulation tools for cardiac magnetic resonance (CMR) have provided great potential for various applications in medical imaging including myocardial first-pass perfusion quantification, fetal CMR imaging, and image database generation^{1–3}. The MRXCAT⁴ approach grounded on the XCAT⁵ anatomical phantom has shown remarkable utility for simulating cine and perfusion images. However, the application of late gadolinium enhancement MRI (LGE) for myocardial infarction imaging has not been investigated. In this work, we extend the MRXCAT tool for cardiac LGE image simulation by implementing two clinical sequences, defining relevant imaging parameters, contrast agent dynamics, and incorporating two patterns of myocardial infarctions (MI).

Subjects/Methods: To create virtual patients with MI, we utilize the modified version of the XCAT phantom with heart trabeculation⁶. We create two patients with transmural and subendocardial MI patterns associated with coronary artery disease and the extent of the infarct and its location corresponding to the area of the heart which is supplied by specific coronary arteries⁷. To simulate LGE images, we extend the MRXCAT with inversion recovery steady-state free precession (IR-SSFP) and inversion recovery gradient echo (IR-GRE) MR sequences for bright blood imaging⁸. The relaxation rate for the infarct area linearly depends on the contrast agent concentration and its relativity according to the formula shown in the pipeline depicted in



LGE image simulation overview for two MI patterns incorporated into the left ventricular myocardium (left). Parameterized tissue and sequence parameters to optimize the contrast (middle) and late gadolinium enhancement simulated images (right).

Results/Discussion: As shown in,



IR-SSFP and IR-SPGR sequences with variable inversion time for subendocardial (1st and 2nd rows) and transmural (3rd and 4th rows) MIs. Given the T1 relaxation time for the myocardium, the inversion time to null the myocardium signal is around 678ms

simulated images with variable inversion times demonstrate that MI visibility is sensitive to the inversion time and the scar-to-myocardium contrast is maximized when the signal of normal myocardium is nulled. The inversion time could be optimized to obtain adequate contrast between the blood pool and subendocardial MIs. Blood pool to normal myocardium contrast is higher in the IR-SSFP sequence compare to the IR-SPGR which is considered as one of the advantages of using a steady-state sequence in clinical routine. The sensitivity of the MI signal to the inversion time is lower in gradient echo sequence, which suggests robustness in detecting MIs.

In this paper, we extend the application of MRXCAT for LGE cardiac MRI simulation. This extension provides an opportunity to compare, estimate, and optimize sequences to achieve high contrast between the infarct region, normal myocardium, and blood pool. Moreover, a population of images with variable scar geometry and location could be generated to aid the development of deep learning-based cardiac disease classification algorithms.

- References:** 1. Wissmann L, et al. *JCMR*. 2017;
 2. Roy CW, et al. *JCMR*. 2019;
 3. Tobon-Gomez C, et al. *MRM*. 2011;
 4. Wissmann L, et al. *JCMR*. 2014;
 5. Segars WP, et al. *Med Phys*. 2010;
 6. Amirrajab, S, et al. *Proc. 28th ISMRM*. 2020;
 7. Vöhringer M, et al. *Herz*. 2007;
 8. Kellman P, et al. *JMRI*. 2012;

L01.84

Automated Segmentation of the Human Cranial Vault with Bone-Selective MRI as an alternative to radiative CT for Craniofacial Imaging

P. Khandelwal¹, C. E. Zimmerman², L. Xie³, H. Lee³, H. K. Song³, S. P. Bartlett², P. A. Yushkevich³, F. W. Wehrli³

¹University of Pennsylvania, Department of Bioengineering, Philadelphia, USA, ²University of Pennsylvania, Division of Plastic Surgery, Children's Hospital of Philadelphia, Philadelphia, USA, ³University of Pennsylvania, Department of Radiology, Philadelphia, USA

Introduction: Bone-selective solid-state Magnetic Resonance Imaging (MRI) sequence produced by a Dual Radiofrequency (RF), dual-echo 3D Ultrashort Echo Time (UTE) pulse sequence and bone-selective image reconstruction process provides a radiation-free imaging modality with high concordance to computed tomography (CT). Visualization of the human cranial vault anatomy on 3D rendered images is vital for craniofacial surgery. The aim of this study is to pilot the use and validation of an automated segmentation pipeline

on the bone-selective MR images with the goal of reducing time required for 3D segmentation.

Subjects/Methods: 30 healthy adult volunteers (Sex: n=15 male, n=15 female, Median age: 26.4 year). Dual-RF, dual-echo, 3D UTE pulse sequence MR using 3T (Siemens Medical Solutions) scanner at 1 mm^3 isotropic resolution, and low-dose research CT images at $0.47 \times 0.47 \times 0.75\text{ mm}^3$ were acquired and two MR images were constructed; I_1 =Bone-selective, I_2 =Longer echo time, which were subtracted to derive, I_{bone} =Subtraction image (I_1-I_2) as described in [1,2] (Fig. 1A). The CT images were thresholded and manually corrected by an expert to isolate the cranial vault. The CT images, and segmentations were then rigidly registered to I_1 . We thus obtained groundtruth segmentations of cranial vault as reference for MR images. Then, an automated multi-atlas (formed by I_2 and I_{bone} image pairs) segmentation pipeline (Fig. 1B [3]) was used to segment the cranial vault in I_{bone} images.

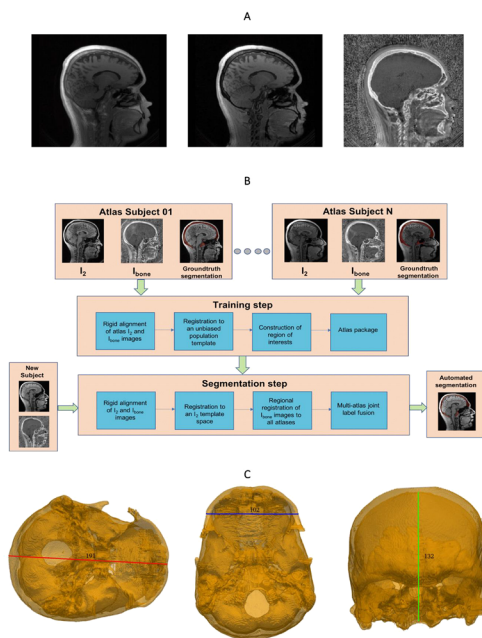


Fig. 1: (A) I_1 (left), I_2 (middle), I_{bone} (right) images. (B) Automated segmentation pipeline [3]. (C) 3D distance (mm) for landmarks: Left: Glabella-Opisthocranium (GO), Center: left and right frontozygomatic suture (FZ), Right: Vertex and Basion.

Results/Discussion: We evaluated the method using leave-one-out cross validation setting. The average Dice score was $90.86\% \pm 1.94$, and 95th percentile Hausdorff distance was $1.65\text{mm} \pm 0.44$ between groundtruth and corresponding automated segmentation (Fig. 2,3) across the cohort.

We also computed 3D Euclidean distance between six craniometric landmarks located on the cranial vault: vertex-basion (VB), left-right frontozygomatic suture (FZ) and glabella-opisthocranium (GO) (Fig.1C) for both CT thresholded, and MR-based automated segmentations. The mean distance on CT segmentations were VB: $140.3\text{mm} \pm 6.0$, FZ: $102.6\text{mm} \pm 5.8$, and GO: $182.1\text{mm} \pm 9.6$, and for automated MR segmentations VB: $141.5\text{mm} \pm 5.1$, FZ: $103.8\text{mm} \pm 5.0$, and GO: $181.4\text{mm} \pm 10.3$. Concordance correlation coefficient for distances between CT and MR-based landmarks were 0.906, 0.780, and 0.956 for the three measurements.

The segmentation results, and high concordance between gold standard CT and our novel imaging sequence for measured distances suggests that the automated method could be used to segment MR images to delineate the cranial vault, and be applicable to craniofacial surgeries.

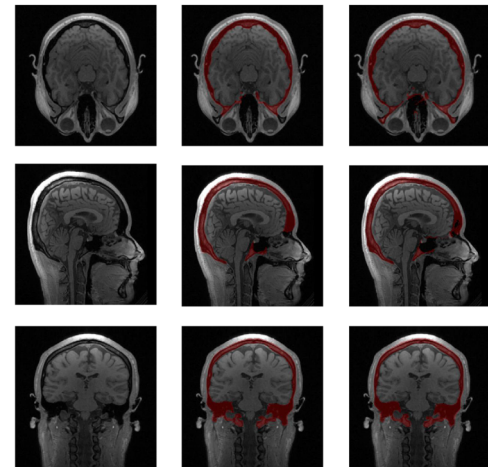


Fig. 2: Automated and groundtruth segmentations in 2D slices for axial (top row), sagittal (middle row), and coronal (bottom row) views. Segmentations overlaid in red for groundtruth (middle column) and automated segmentations (rightmost column).

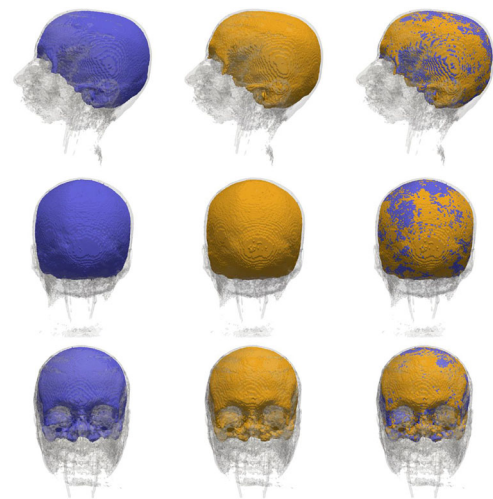


Fig. 3: Automated and groundtruth segmentations 3D renderings. Shown are three viewing planes: Rows: lateral (top), posterior (middle), and anterior (bottom). Columns: groundtruth (left), automated (middle), and automated overlaid over groundtruth.

References: [1] Lee et al. Rapid dual-RF, dual-echo, 3D ultrashort echo time craniofacial imaging. MRM 2019.

[2] Zhang et al. Bone-Selective MRI as Nonradiative Alternative to CT. Academic Radiology 2019.

[3] Yushkevich et al. Automated Volumetry, Regional Thickness Analysis of Hippocampal Subfields. HBM 2015.

L01.85

CEST signal at different magnetic fields and temperature conditions for three main brain metabolites

S. Bardin¹, H. Lambers², D. Schache², J. R. Krug³, V. Hoerr², C. Faber², F. Boumezeur¹, L. Ciobanu¹

¹CEA, Neurospin, Gif-sur-Yvette, France, ²Westfälische Wilhelms-Universität, Münster, Germany, ³Wageningen University & Research, Wageningen, The Netherlands

Introduction: Chemical Exchange Saturation Transfer (CEST) is based on the exchange between labile protons of metabolites with those of bulk water [1]. The optimization of *in vivo* CEST signal is not straightforward

as it depends on many experimental parameters such as static magnetic field B_0 , radiofrequency field B_1 applied for saturation as well as pH and temperature. For these reasons, the optimization is done *in vitro*, on samples with known physicochemical characteristics. In this study, we determined the optimal B_1 powers for three main brain metabolites at three different static fields and two temperatures.

Subjects/Methods: Three aqueous solutions were studied: 40mM Lactate, 20mM Glutamate and 20mM Glucose (pH 7.0). CEST PRESS measurements were performed on 9.4T, 11.7T, 17.2T scanners, with a saturation module consisting of 35 pulses of 50ms duration with chemical shift offsets from -10 to +10ppm, in a 2^*2^*4 mm³ voxel. The temperature dependence was investigated at 9.4T and 17.2T at RT ($20\pm 1^\circ\text{C}$) and at body temperature ($37\pm 1^\circ\text{C}$).

The $\text{CEST}_{\text{contrast}}$ was computed as: $\text{CEST}_{\text{contrast}}(\Delta\omega) = 100 * (S_{\text{sat}}(-\Delta\omega) - S_{\text{sat}}(\Delta\omega)) / S_0$ where $S_{\text{sat}}(\pm\Delta\omega)$ indicate the signals measured with saturation offsets at $\pm\Delta\omega$.

Results/Discussion: Table 1 shows the optimal B_1 power for all metabolites. As best compromise between obtaining a high $\text{CEST}_{\text{contrast}}$ and limiting the SAR, we selected the smallest B_1 that yields an increase in $\text{CEST}_{\text{contrast}}$ higher than a defined threshold 1.5% for a 0.5 μT increase in B_1 power. Overall, the optimal B_1 power is constant across B_0 fields and it does not change with the increase in temperature for any of the metabolites, unlike [2] which reports a higher optimal B_1 power at 37°C than at RT, for lactate.

Metabolites	Optimal B1 [μT]					
	9.4T		11.7T		17.2T	
	RT	37°C	RT	37°C	RT	37°C
Lactate (0.4ppm)	2.5	2.0	2.0		2.5	2.5
Glucose (1.2ppm)	4.0	4.0	4.0		4.5	5.0
Glutamate (2.8ppm)	8.0	8.0	7.5		8.0	8.0

Table 1. Optimal B1 power (μT) at three static fields (9.4T, 11.7T, 17.2T) at two temperatures (20°C and 37°C) for lactate, glucose and glutamate.

In Table 2, we report the $\text{CEST}_{\text{contrast}}$ obtained for the optimal B_1 . For all metabolites and for a given temperature, the increase in B_0 leads to an increase in the $\text{CEST}_{\text{contrast}}$. This is due not only to the increase in sensitivity but also to the condition of slow to intermediate exchange being better satisfied at higher fields. The example of glutamate is given in Fig 1A.

Metabolites	Maximum $\text{CEST}_{\text{contrast}}$ [%] at optimal B1					
	9.4T		11.7T		17.2T	
	RT	37°C	RT	37°C	RT	37°C
Lactate (0.4ppm)	8.6	9.5	9.5		10	11.7
Glucose (1.2ppm)	25.6	13.6	26.2		30.3	29.2
Glutamate (2.8ppm)	31.6	13.5	35.5		45	28.6

Table 2. $\text{CEST}_{\text{contrast}}$ (%) obtained with optimal B1 at three static fields (9.4T, 11.7T, 17.2T) at two temperatures (20°C and 37°C) for lactate, glucose and glutamate.

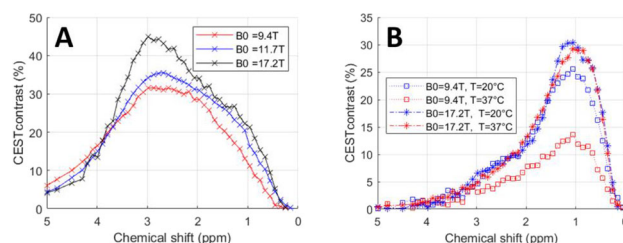


Figure 1. 1A) Glutamate CEST contrast at RT with three static fields: 9.4T, 11.7T, 17.2T with optimized B1 power. 1B) Glucose CEST contrast at 20°C and 37°C for two static fields: 9.4T, 17.2T with optimized B1 power.

For a given B_0 , the increase in temperature causes an increase in the lactate $\text{CEST}_{\text{contrast}}$ because the exchange rate is slow on the MR scale at the B_0 fields considered ($k_{\text{lactate}} = 350 \pm 50 \text{ s}^{-1}$ [2]). $\text{CEST}_{\text{contrast}}$ for glucose and glutamate decreases with temperature because the exchange is approaching the fast regime ($k_{\text{glucose}} = 3940 \pm 260 \text{ s}^{-1}$ and $k_{\text{glutamate}} = 7480 \pm 90 \text{ s}^{-1}$ [2,3]). This decrease, while certainly a challenge for *in vivo* acquisitions, is somewhat mitigated by the increase in B_0 : Glucose $\text{CEST}_{\text{contrast}}$ decreases by 47% at 9.4T vs 4% at 17.2T (Fig 1B).

To conclude, we have optimized the B_1 power for CEST detection of three brain metabolites. The decrease of $\text{CEST}_{\text{contrast}}$ at 37°C remains a challenge for *in vivo* glucose and glutamate detection even if it is mitigated by increasing B_0 .

References: [1] van Zijl 2012 [2] C. DeBrosse 2016 [3] Khlebnikov 2019

L01.86

Compressed sensing in hyperpolarized xenon (^{129}Xe) ventilation MRI

J. Tan¹, S. Svenningsen², N. Konyer³, P. Nair², M. Noseworthy¹

¹McMaster University, Electrical and Computer Engineering, Hamilton, Canada, ²McMaster University, Firestone Institute for Respiratory Health, St. Joseph's Healthcare and Department of Medicine, Division of Respiratory, Hamilton, Canada, ³St. Joseph's Healthcare, Imaging Research Centre, Hamilton, Canada

Introduction: Compressed sensing (CS) involves reconstructing a signal that has been undersampled relative to the requirements of traditional sampling methods. The advantage of this is reduced MRI acquisition times, that translates into reduced motion artefact for lung scans acquired under breath-hold conditions. There is a significant amount of literature exploring the application of CS within MRI [1]. However, use of CS with hyperpolarized ^{129}Xe MRI is limited. In this work, fully sampled hyperpolarized ^{129}Xe MRI ventilation images were pseudo-stochastically undersampled and CS reconstruction was applied. Our objective was to evaluate both undersampling schemes and CS algorithms on resultant image quality to inform an optimal plan for ^{129}Xe MRI CS-based acquisition.

Subjects/Methods: Hyperpolarized ^{129}Xe ventilation MR images were collected with a GE MR750 3T MRI and an elliptical quadrature ^{129}Xe birdcage coil. Following shimming on the proton signal the RF transmit power to produce a 90° RF pulse was calibrated using the Bloch-Siegert shift method [2]. Hyperpolarized ^{129}Xe gas was provided using a spin-exchange polarizer (Polarean 9800). ^{129}Xe ventilation images were acquired using a 3D fast gradient-echo pulse sequence (3.1x3.1x15mm resolution, 16 slices, 11s scan time) as previously described [3]. 100 masks each of 30%, 50% and 70% sampling (examples shown in Fig.1) were pseudo-randomly generated [4], applied to the fully sampled k-space, and images were reconstructed using the BART toolbox [5], specifically using the 11-wavelet reconstruction implementation. The effectiveness of undersampled image reconstruction was compared to the fully sampled images by calculating the SNR and RMSE of each image.

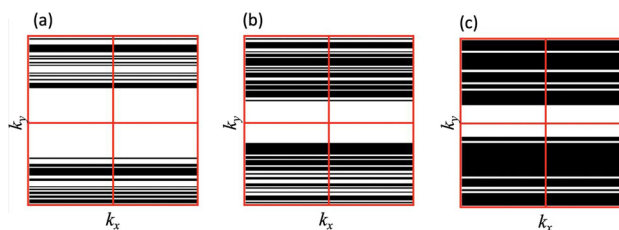


Figure 1. Masks used to undersample full k-space data, each with 50% centre rate. (a) shows 30% undersampling (b) shows 50% and (c) shows 70%. White rows are preserved. Phase encoding direction is superior to inferior.

Results/Discussion:

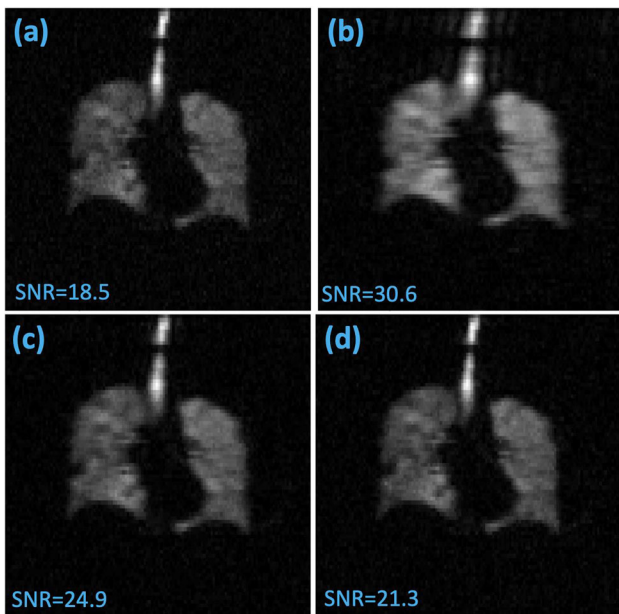


Figure 2. Images reconstructed using the 11-wavelet. (a) is fully sampled, (b) 30% sampled, (c) has 50% sampling, and (d) is 70% sampled.

Fig.2 shows the reconstruction of 30%, 50% and 70% sampling rates, compared to the fully sampled (100%) reconstruction. We found that reconstructing with 30% of the data, using the 11-wavelet algorithm, most often resulted in the highest SNR, compared to the fully sampled case. However, there is decreased high spatial frequency content with increased undersampling. The increased SNR is attributed to the reconstruction algorithm filtering out background noise present in the original k-space data, as previously described [1]. Interestingly, SNR varied according to mask features. **Fig.3** shows the variation in SNR for reconstruction using 100 random masks from each undersampling scheme. Further investigation revealed pseudo-stochastic sampling plays a vital role in both SNR and image spatial frequency content for CS reconstruction of undersampled ¹²⁹Xe ventilation images.

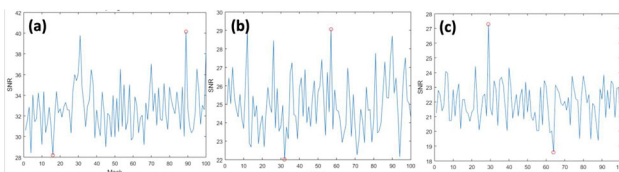


Figure 3. SNR for 100 random k-space undersampling schemes and subsequent reconstruction with (a) 30%, (b) 50% and (c) 70% of the full dataset. Considerable variation in SNR was noted (red circles = max and min), depending on undersampling mask.

- References:** [1] Lustig M et al. (2007) MRM 58(6):1182–1195. [2] Schulte RF et al. (2011) NMR Biomed 24(9):1068-1072. [3] Svenningsen S et al. (2013) JMRI 38(6):1521-1530. [4] Kojima S et al. (2018) Radiol. Phys. Tech. 11(3):303–319. [5] Uecker M et al. (2015) <http://indexsmart.miramsmart.com/ismrm2015/PDFfiles/2486.pdf>

L01.87
Effect of flip-angle selection on sub-millimetre resolution gradient-echo 3D-EPI at 7T

S. Kashyap, L. Huber, D. Ivanov, D. Kurban, D. A. Feinberg, B. A. Poser

Maastricht University, Cognitive Neuroscience, Maastricht, The Netherlands

Introduction: Sub-millimetre resolution is desirable for laminar fMRI studies to reduce partial voluming of grey matter (GM) voxels with neighbouring tissues such as cerebrospinal fluid (CSF) and white matter (WM). During activation, changes in blood volume (CBV) in tissue and/or pial vessels can affect the CSF volume fractions, thereby affecting the BOLD signal sampled at the uppermost layers. Therefore, minimising regional CSF contributions during acquisition can be advantageous. In this regard, the benefit of 3D-EPI readout as used for sub-millimetre fMRI is the inherently stronger suppression of CSF (long T₁, very short TR) relative to 2D-EPI¹. The degree of CSF suppression depends on the selected flip angle (FA, α). There has been no systematic study into this matter, so here we investigate the effect of FAs on the relative signal contributions of different tissue compartments and the resulting temporal SNR (tSNR).

Subjects/Methods: All data were acquired on a Siemens Magnetom 7T using the product 32ch head coil. Three healthy volunteers participated in the study and all procedures were followed as per institutional ethical guidelines. We developed a 3D-EPI sequence² with alternating FAs across TRs in a block-wise manner (50 volumes per FA), in order to remove confounds due to the re-acquisition of GRAPPA calibration scans, system adjustments, and inter-run subject motion. MP2RAGE anatomical reference was used. Two transition volumes at the start and end of each FA cycle were discarded. The data were motion- and distortion-corrected using ANTs and tSNR was calculated. A vein mask was obtained from the mean EPI by thresholding to very low intensities and were excluded from the CSF mask. In laminar fMRI acquisition the goal is to maximise the GM tSNR, without introducing a layer-dependent sensitivity bias. To this end, we computed the depth-dependent tSNR over the entire cortical ribbon. Laminar analyses were carried out using LAYNI.

3D-EPI[4]	TE	TR	Matrix	BW	Echo-spacing	GRAPPA
Resolution	22ms	3010ms	202x202x32	1126Hz/px	1.01ms	3
0.8mm iso						
PE	Flip-angles in order	Volumes per flip-angle	BWTP	PF(phase),PF(3De)	TA	
A>>P	5°,10°,15°,20°,15°,30°	50	25	6/8,8/8	13min	
MP2RAGE[5]						
Resolution	TE	TR	Matrix	BW	Echo-spacing	GRAPPA
0.8mm iso	1.96ms	5500ms	204x204x240	250Hz/px	5.8	3
TIs	Flip-angles	PE	PF(phase),PF(slice)	TA		
900,2750ms	5°,4°	A>>P	6/8,8/8	7,5min		

Imaging parameters used in the study

Results/Discussion:

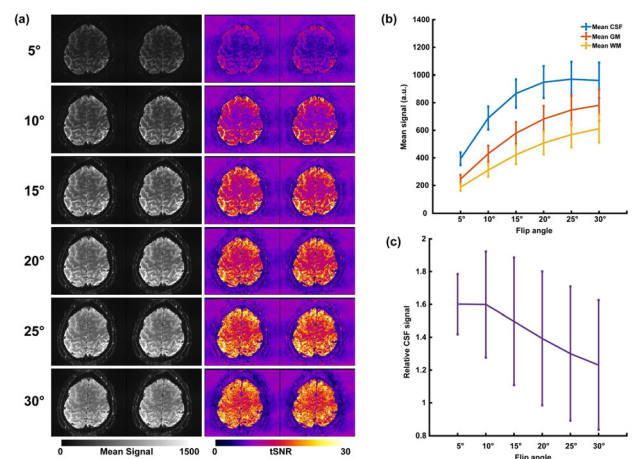


Fig1 (a) Single-subject mean EPI and tSNR maps for different FAs (b) Mean signal in different tissue compartments (c) relative CSF signal for different FAs. The variable CSF signal across FAs can affect the thermal and physiological noise interaction.

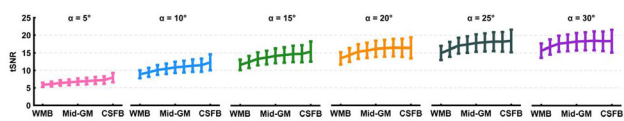


Fig2 Laminar profiles of the GM tSNR for the different flip angles. Note the different behaviour at the surface. While thermal-noise limited small FAs have largest tSNR in superficial layers, higher FAs are more flat.

To optimise the GM tSNR, the recommended FA is the Ernst angle³ (here $\sim 15^\circ$). Fig 2 shows that the GM tSNR is higher at higher FAs. Furthermore, the GM tSNR laminar profiles are stable across cortical depths indicating no baseline bias from the acquisition. For FAs higher than 15° , we observed GM tSNR decrease towards the cortical surface. This is consistent with suppressed relative CSF fractions as illustrated Fig 1c. These preliminary findings indicate that higher FAs than Ernst angle can be preferable and the SAR efficiency of the 3D-EPI readout allows for this. Next steps are to follow-up using a stimulus paradigm to evaluate the impact on BOLD activation profiles.

References: ¹W.van der Zwaag(2011)10.1002/mrm.23007

²L.Huber(2020)10.1016/j.pneurobio.2020.101835

³RR.Ernst(1966)10.1063/1.1719961

⁴BA.Poser(2010)10.1016/j.neuroimage.2010.01.108

⁵JP.Marques(2010)10.1016/j.neuroimage.2009.10.002

L01.88

Fast Steady-State Approach for 3D T1 and B1 Mapping with an Updated Optimization Merit Function for an Improved Accuracy and Precision

M. A. Zampini, R. Garipov

MR Solutions Ltd, Guildford, UK

Introduction: High field T1 mapping with 3D Gradient Echo sequences is still a challenging task due to the necessity of inhomogeneous RF excitation (B1) correction¹, which impacts on acquisition time and accuracy. VAFI sequence was proposed² as a simultaneous T1 and B1 mapping technique joining Variable Flip Angle and Actual Flip angle Imaging, and is now widely employed. Low flip angles are used for its VFA measurements, and the approach to steady state (SS) may require many dummy pulses, possibly rising SAR issues at high field. While preparation modules were proposed for VFA – but never implemented in VAFI – no AFI preparation has been proposed yet. Besides, for low TR/T1, VAFI shows no real improvement when several images acquired with different flip angles are included in map reconstruction.

The aim of this abstract is twofold: first, we propose a new preparatory module for a fast approach to SS signal in AFI sequences based on the approach by Busse³. Then, a straightforward modification of the processing algorithm which provides better accuracy and precision is disclosed.

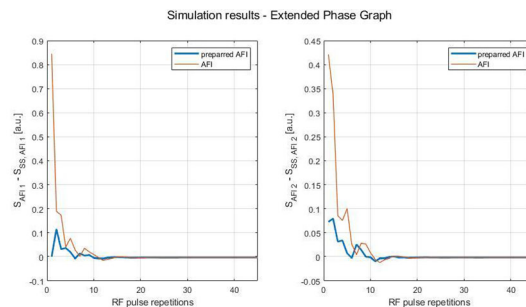
Subjects/Methods: Prior to the first AFI imaging pulse, we included a 90° adiabatic preparation pulse followed by a recovery time of $T_{rec} = TR(n + \cos\alpha)/(1 - \cos^2\alpha)$, which minimises T1-sensitivity for biological T1s at high field. Extended Phase Graph (EPG) simulations to test dependency on RF phase were performed considering variations

in T1, T2, TR, and spoiling gradient strength. Data were acquired with MR Solutions 4.7T preclinical scanner on an agar gelatin phantom. A prepared 3D VAFI (preVAFI) was tested with $\alpha=60^\circ$, $n=50ms/10ms$, matrix size= $128 \times 128 \times 32$, FOV= $40 \times 40 \times 40mm^3$, 6 VFA acquisitions (M), and optimized RF spoiling.

We used a preparation pulse for both AFI and VFA parts of the sequence. Data processing was performed via 2 optimization steps as for VAFI but with a new merit function: $RSS = M \sum_{i=1}^2 (S_{AFI} - \hat{S}_{AFI})^2 + \sum_{i=1}^M (S_{VFA} - \hat{S}_{VFA})^2 - S$ and \hat{S} being voxel-wise model and observed signal intensity, respectively.

Simulations for testing accuracy and precision were performed with a LM-BFGS optimization algorithm for $\alpha_{AFI} \in [40, 70]$, random distributions of $\alpha_{VFA} \in [5, 25]$, TR=10ms, and T1 $\in [1, 3]$ s.

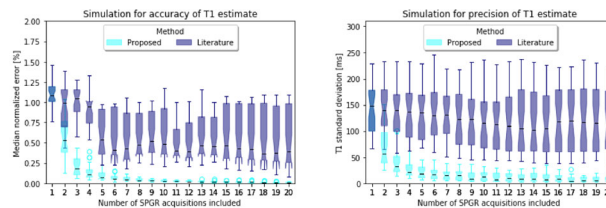
Results/Discussion: EPG simulations show a faster approach to SS signal, reducing variability in the very first RF pulses, which is noticeable in particular for short T2 values (<100ms).



Extended Phase Graph simulation results for the signal behavior of prepared AFI and AFI for both echo signals (T1 = 1.5s, T2 = 50ms, TR = 5ms, AFI $\alpha = 60deg$, RF phase increment = 50deg).

Agar phantom AFI and preAFI images have a median intensity difference <0.5%.

Optimization test with the proposed figure of merit show an increase in median precision and accuracy: literature method² systematically underestimated T1 (median $\Delta T1 > 2ms$) and showed non-decreasing std when more VFA acquisitions were included for the optimization.



Accuracy and precision trend for increasing number of spoiled GE acquisitions included in the optimization for the discussed methods. Data are overlapped when a single acquisition is used. Lower values within the boxplot corresponds to higher AFI α .

T1 values of agar gel with preVAFI were found to be $2.41 \pm 0.15s$ (literature method) and $2.49 \pm 0.16s$ (proposed) against a reference 12 points Inversion Recovery of 2.49s.

References: ¹Stikov, MRM.25135

²Hurley, MRM.23199

³Busse, MRM.1088

L01.89**Fluorescence recordings of optogenetic sensors have no detectable impact on simultaneously performed CEST measurements**

H. Lambers¹, D. Schache¹, S. Bardin², F. Boumezbaur², L. Ciobanu², V. Hoerr¹, C. Faber¹

¹University Hospital Muenster, Clinical Radiology, Muenster, Germany, ²NeuroSpin-CEA, Gif-Sur-Yvette, France

Introduction: To assess cell type-specific contributions to the Chemical Exchange Saturation Transfer (CEST) signal, the combination with simultaneous optogenetic fluorescence recordings offers a powerful approach. Recently, a method was presented which allows fCEST measurements with a high temporal resolution by alternating two saturation frequencies.¹ Fluorescence recordings require constant illumination of the investigated region.² Here, we investigate the impact of heat generated by illumination on the CEST contrast.

Subjects/Methods: CEST measurements were performed on two glucose samples (50 mM Glucose in 0.01 M PBS and in 0.01 M PBS with 1 % agarose) at 9.4 T (TR: 2.5 s, saturation: 35 block pulses, pulse duration: 50 ms). A CEST-PRESS (TE: 15.2 ms, VOI: 2³ mm³) and a CEST-EPI sequence (SE, TE: 25 ms, 350x325μm², 1 mm slice) were used. For laser light illumination (488 nm, 7 mW) a 200-μm optic fiber was inserted.

First, CEST-PRESS spectra (− 5 to 5 ppm) were acquired from the solution sample at different temperatures and the asymmetric magnetization transfer ratio ($MTR_a = (S(-\Delta\omega) - S(\Delta\omega)) / S(0) * 100$) was computed. The MTR_a at 1.5 ppm was plotted against the temperature and fitted with a linear function.

Second, PRESS and EPI measurements were performed for 5 min with alternating CEST saturation frequencies ($B_1 = 5$ or $6 \mu T$ and $\delta = 1.5$ or 2.75 ppm for the solution and the gel sample, respectively) The ratio $S(-\delta) / S(\delta)$ was computed for each pair of consecutive acquisitions. The resulting ratio time course was fitted with a linear function. Two conditions were examined: (i) decreasing sample temperature and (ii) constant sample temperature (37 °C) during illumination.

Results/Discussion: Results

The MTR_a was strongly temperature dependent. In solution, a temperature increase of 1 °C led to a decrease of the MTR_a of 1.7 % (figure 1).

Also the CEST ratio was strongly temperature dependent: A temperature increase of 1 °C led to a ratio decrease of 0.04 and 0.01 for the solution and the gel sample, respectively (figure 2).

However, illuminating for 5 minutes did not change the CEST ratio in either sample (figure 3). In addition, a u-test showed no significant differences between the signal change of the fiber area and a remote region.

Discussion

We postulate that the gel better reproduces optical properties of the brain than the solution. Therefore, results of the gel may allow inferences about in vivo measurements, suggesting only negligible effects of illumination. The light intensity used was 70 times stronger than in normal in vivo fluorescence recordings. Therefore, illumination is expected to have no influence on the CEST ratio in functional measurements. We conclude that fluorescence recordings of optogenetic sensors will not cause heat artefacts in functional CEST measurements.

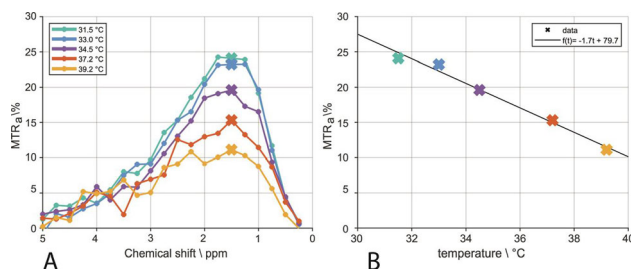


figure 1: (A) MTR_a of the solution sample for different temperatures. (B) The MTR_a at 1.5 ppm versus the temperature; a linear function was fitted to the data. A temperature increase of 1 °C leads to an MTR_a decrease of 1.7 %.

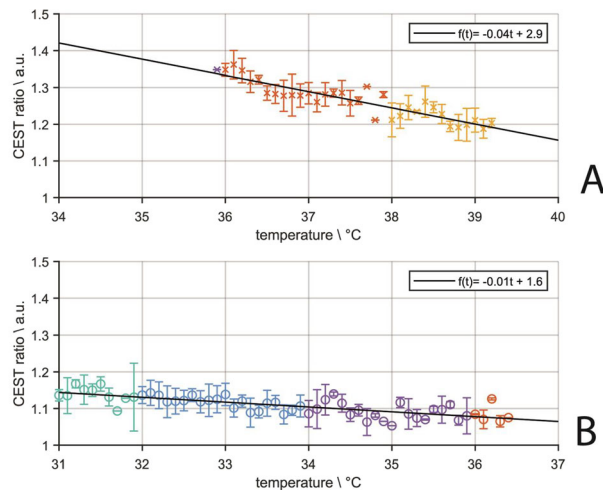


figure 2: CEST-PRESS ratio of the solution (A) and the gel (B) sample vs. temperature; a linear function was fitted to the data. If the temperature rises 1 °C, the ratio decreases 0.04 and 0.01 in the solution and the gel sample, respectively.

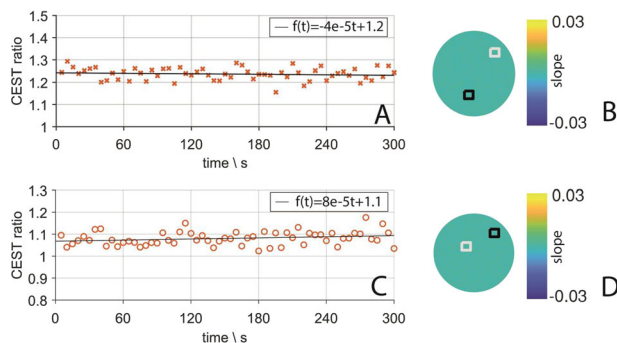


figure 3: PRESS time courses and slopes of a voxel-wise linear fit of EPI signal during illumination for solution (A, B) and gel sample (C, D). No significant differences were found between the region near the fiber (white) and a remote area (black).

References: ¹Roussel, T. et al., *Sci Rep* **9**, 4423 (2019)
²Albers, F. et al., *Mol Imaging Biol* **20**, 171–182 (2018)

L01.90**Interaction between fitting and analytical approaches to improve quantitative CEST analysis**

D. Schache¹, H. Lambers¹, S. Bardin², F. Boumezeur², L. Ciobanu², C. Faber¹, V. Hoerr¹

¹University Hospital Münster, Clinic of Radiology, Münster, Germany, ²Université Paris-Saclay, NeuroSpin, CEA, Gif-sur-Yvette, France

Introduction: CEST MRI allows measuring small molecules with enhanced sensitivity based on their chemical exchange with water protons [1].

To quantify dissolved solutes and metabolites in CEST data, Z-spectra can be fitted with Lorentzian functions [2]. Thereby, the choice of the number of Lorentzian functions representing the exchangeable pools as well as the starting and boundary conditions are crucial. Complementary, simulations based on Bloch-McConnell (BM) equations offer an analytical approach to evaluate the CEST data [1].

The aim of this study is to investigate whether analytical solutions can support optimization of fitting processes.

Subjects/Methods: 75mM glucose was dissolved in four buffer system (distilled water, 1 mM phosphate buffer, 10 mM phosphate buffer and 10 mM phosphate buffered saline (PBS)), pH was adjusted at 7.4.

CEST measurements were performed at 20 °C on a 9.4 T small animal MR Biospec system (Bruker) equipped with a 72 mm quadrature coil. Datasets were acquired with a CEST RARE sequence and corrected by WASSR [3].

To calculate the exchange rates, data were simulated based on BM-equations assuming a 5-pool model consisting of water and four glucose pools [1].

CEST data were fitted for individual components (exchangeable glucose pools, direct saturation) by Lorentzian functions.

Results/Discussion: The exchange rates of the different glucose pools were calculated in four different buffer systems with different ionic strength based on BM simulations (figure 1).

The exchange rates scaled with increasing ionic strength. As a consequence of the lower sensitivity of the CEST contrast for faster chemical exchange processes, not all exchangeable glucose pools could be detected in the Z-spectra of the different systems (figure 2).

However, the knowledge about the number of detectable sites has a strong impact on fitting analysis. Different numbers of the underlying Lorentzian functions led to fundamental differences in individual components of the global fit (figure 3). This makes it considerably more difficult to quantify the contributions of the spectrum.

Therefore, the detection limit in the Z-spectra for each exchange process must be critically examined. The exchange rate seems to be a suitable parameter to estimate the choice of an appropriate fitting model.

Additionally, a significant increase in peak width (FWHM) Γ of individual Lorentzian functions can be observed with faster exchange rate ($\Gamma_B(\text{distilled water}) = 250 \text{ Hz}$, $\Gamma_B(\text{PBS}) = 530 \text{ Hz}$; $\Gamma_E(\text{distilled water}) = 305 \text{ Hz}$, $\Gamma_E(\text{PBS}) = 502 \text{ Hz}$) representing ideal potential boundary condition.

Thus, by using additional analytical information, the fitting process can be regulated in order to enable a meaningful quantification.

References: [1] Zaiss M et al., NMR Biomed. 2019; 32(9): e4113.

[2] Zaiss M et al., J Magn. Reson. 2011; 2(211): 149-155.

[3] Kentrup D et al., Kidney Int. 2017; 3(92): 757-764.

buffer	exchange rate k_B [Hz]	k_C [Hz]	k_D [Hz]	k_E [Hz]	Ionic strength [M]
distilled water	252	276	367	980	$< 10^{-6}$
1mM phosphat buffer	913	1788	578	1788	0,004
10mM phosphat buffer	1703	3784	3852	4773	0,040
10mM PBS	1924	4516	2434	3945	0,165

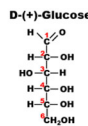


Fig. 1: Exchange rates and ionic strengths for different buffers (left), structural formula of D-(+)-glucose (right) with the following chemical shifts δ : 6C-OH: $\delta_E=0.66 \text{ ppm}$, 2,3,4C-OH: $\delta_B=1.29 \text{ ppm}$, 1C-OH (a): $\delta_F=2.08 \text{ ppm}$, 1C-OH (b): $\delta_D=2.88 \text{ ppm}$.

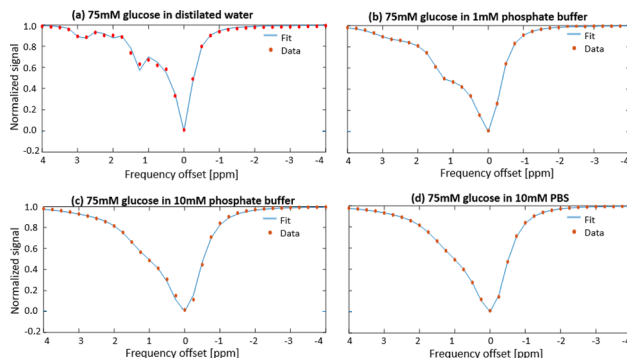


Fig. 2: Z-spectra for glucose in different buffer systems fitted by BM-simulation.

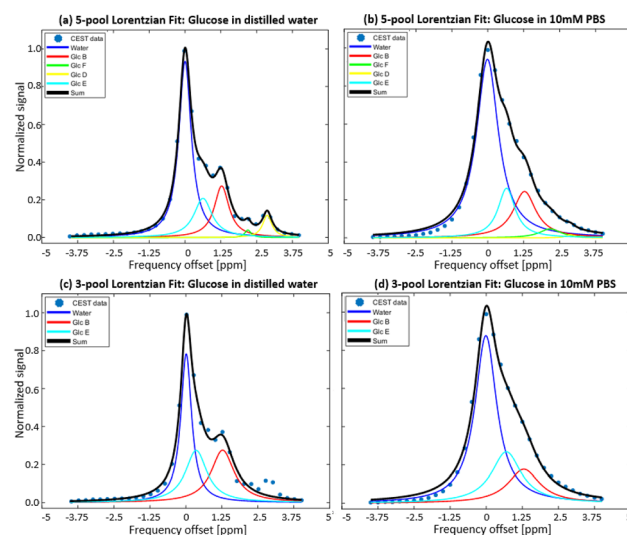


Fig. 3: Z-spectra for glucose in distilled water and 10 mM PBS. Lorentzian fitting assuming a 5- or a 3-pool model for each buffer showing fundamental differences for the individual Lorentzian functions in distilled water (a, c) and in PBS (b, d).

L01.91**Quantitative T_1 maps by multi-slice multi-shot inversion recovery EPI: correcting T_1 for MT effect of fat suppression.**

R. Sanchez Panchuelo, R. Turner, O. Mougin, S. Francis

University of Nottingham, Sir Peter Mansfield Imaging Centre, Nottingham, UK

Introduction: High spatial resolution quantitative T_1 maps can be obtained using 2D multi-slice multi-shot inversion recovery EPI (MS-IR-EPI) [1] combined with slice order shifting across multiple acquisitions [2]. This sequence provides high resolution T_1 maps which are homogeneous across slices, but magnetization transfer (MT) effects of the spectrally selective fat suppression (FS) pulses

shorten the fitted T_1 -values. Here, we proposed a model to correct for the MT effects due to the FS pulses in the T1 quantification.

Subjects/Methods: Three subjects were scanned on a 7T Philips Achieva scanner to measure 0.7mm isotropic resolution MS-IR-EPI relaxation rate, R_1 , maps at a range of nominal FS flip angles (FA) of 30,40,50,60,70°. An additional data set with no FS (0°) and a B_1 -map were also acquired. R_1 was modelled as a function of myelin density, m , and the B_1 field distribution, X : $R_1 = a \cdot m + b \cdot FA \cdot X \cdot m$, where a and b are constants. For each subject, a voxel-wise linear fit of R_1 versus $FA \cdot X$ was performed to estimate $a \cdot m$ and $b \cdot m$ from least squares regression, and thus evaluate (b/a) for each voxel. A corrected R_1 map ($R_{1,corr}$) was then computed for each FS of distinct FA from: $R_{1,corr} = R_1 / (1 + b/a \cdot FA \cdot X)$. R_1 maps were corrected (i) using a voxel specific (b/a) parameter (voxel-wise correction) or (ii) using a constant b/a value (defined by the mode of the histogram of (b/a) values) for each voxel (global correction).

Results/Discussion:

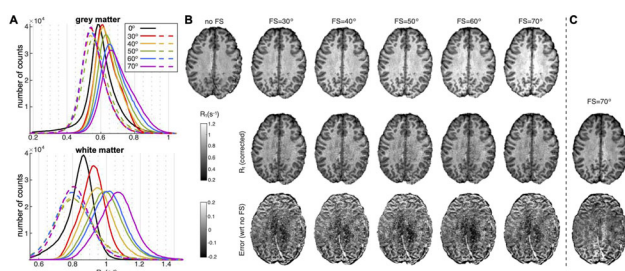


Figure 1: (A) R_1 histograms for different FS levels (black: no FS) before (solid) and after (dash) voxel-wise correction. (B) Original and corrected R_1 maps, and variance of corrected R_1 wrt no FS. (C) R_1 map (FA=70°) corrected using global method.

The fitted (b/a) parameter values were fairly constant across the brain (and subjects) of $0.0048 \pm 0.0004 \text{ degree}^{-1}$. Figure 1A shows spread of R_1 -histograms with no correction (solid colour lines) and the similarity of R_1 -histograms after voxel-wise (b/a) correction (dash color lines) for the different FS levels, and closer agreement to the R_1 -histogram without FS (black line). Figure 1B and C shows the similarity of the corrected R_1 -maps to those acquired with no fat suppression. T_1 values with both correction methods are similar but give longer T_1 -values than those using MS-IR-EPI with no FS (Table 1).

		Subject 1	Subject 2	Subject 3	Mean±std
FS=0° (no FS)	GM	1694	1697	1706	1699±5
	WM	1135	1063	1156	1118±40
FS=70° (no correction)	GM	1369	1436	1475	1426±44
	WM	917	880	934	910±23
Global (b/a) correction	GM	1814	1794	1846	1818±26
	WM	1207	1101	1189	1166±57
Voxel-wise (b/a) correction	GM	1814	1831	1806	1817±15
	WM	1283	1170	1238	1230±57

Table 1: T_1 values (given by mode of histogram) for data acquired with no fat suppression (no FS) and 70 degree FS flip angle with no correction and global correction using a constant (b/a) value and voxel-wise correction using (b/a) parameter map.

Discussion: A model has been described for correcting MT effects due to FS from estimated T_1 maps, and has been shown to remove the variation due to a specified FS flip angle. T_1 values after correction (1230/1818ms for WM/GM) were closer to those reported in the literature (Table 1 [3]), but shorter than T_1 values obtained with no FS. T_1 quantification is possible in the presence of spectrally selective fat suppression pulses using the proposed method to correct for MT effects. Our proposed method could be applied to other T_1 mapping methods once the (b/a) parameter (which is specific to each protocol, site and vendor) has been characterized.

- References:** 1. Sanchez Panchuelo et al. Proceedings ISMRM, 2018, 60.
 2. Ordidge et al. MRM, 1990;16:238-45.
 3. Caan et al. HBM, 2019: 40,1786-98.

L01.92

Selective Parity Diffusion-Weighted HASTE for High Field

A. Arbabi, V. Khlebnikov, J. P. Marques, D. G. Norris

Radboud university, Donders Centre for Cognitive Neuroimaging, Nijmegen, The Netherlands

Introduction: Fast spin echo sequence (FSE/RARE) is popular because of its high sensitivity and high immunity against B_0 inhomogeneity artifacts. However, a prerequisite for its successful application is the fulfillment of the Carr-Purcell-Meiboom-Gill (CPMG) condition, which is impossible, in diffusion-weighted imaging, in which any bulk motion can lead to an arbitrary phase shift. In this work, we describe an extension of the selective parity FSE approach introduced in [1]. This method offers a near full sensitivity, no image distortion, and no a priori restriction on the range of refocusing angles. It does not require dummy cycles for the echo amplitude stabilization, and benefits from a large reduction in the specific absorption rate (SAR), and is hence, suitable for imaging at 3T.

Subjects/Methods: In a centre-out phase-encoding scheme, central k-space lines are measured with near full signal intensity, and afterwards, the refocusing angle is reduced to a constant low value through TRAPS [2], when echo parities are equalized in amplitude (fig. 1A). Using recursive application of Bloch equations, the echo parity with the higher amplitude is selected, and the other parity is spoiled by a displacing gradient, as described in [1]. SLR refocusing pulses are employed for smooth signal decay during the echo train in order to obtain a narrow point spread function (fig. 1B). Furthermore, the excitation and refocusing slice profiles are included in the parity selection algorithm to ensure a correct determination of the parity of interest.

The reconstruction of alias free images was implemented as a three step process: (1) separation of the k-space data according to the echo parity and estimation of the missing lines on a per parity basis using SPIRIT reconstruction [3], (2) estimation of the phase difference between the acquired lines of one echo parity and the corresponding estimated lines of another echo parity, and (3) combination of the phase-corrected originally acquired data of both echo parities followed by FT reconstruction.

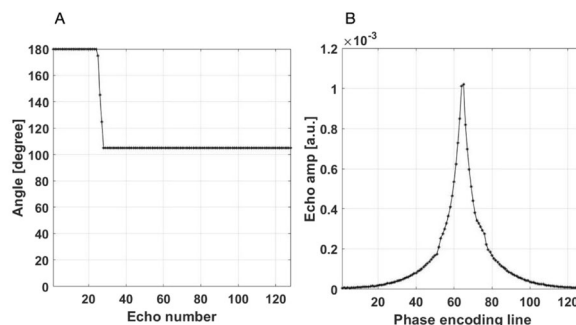


Fig 1. Selective parity FSE imaging of a water phantom: (A) Refocusing angles, and (B) T2-weighted signal decay

Results/Discussion: Methods developed so far for non-CPMG FSE imaging suffer mainly from low signal-to-noise ratio and high SAR values, and their application is commonly limited to the low field of 1.5T. The presented approach addresses these problems by using both parities of echoes in the image formation and applying high refocusing angles only for important echoes encoding for the k-space centre, it is independent of CPMG condition, and would have a broad range of applications in the 3T field.

- References:** [1] Norris D, MRM 58:643–649 (2007)
 [2] Hennig et. al., MRM 49:527–535 (2003)
 [3] Lustig M et. al., MRM 64:457-471 (2010)

L01.93**Simultaneous imaging of hard and soft biological tissues in a low-field MRI scanner**

J. M. Algarin¹, E. Díaz², P. Borreguero¹, F. Galve¹, D. Grau², J. P. Rigla², R. Bosch¹, J. M. Benlloch¹, J. Alonso¹

¹Institute for Instrumentation in Molecular Imaging (I3M), CSIC, MRI Group, Valencia, Spain, ²Tesoro Imaging S.L., Valencia, Spain

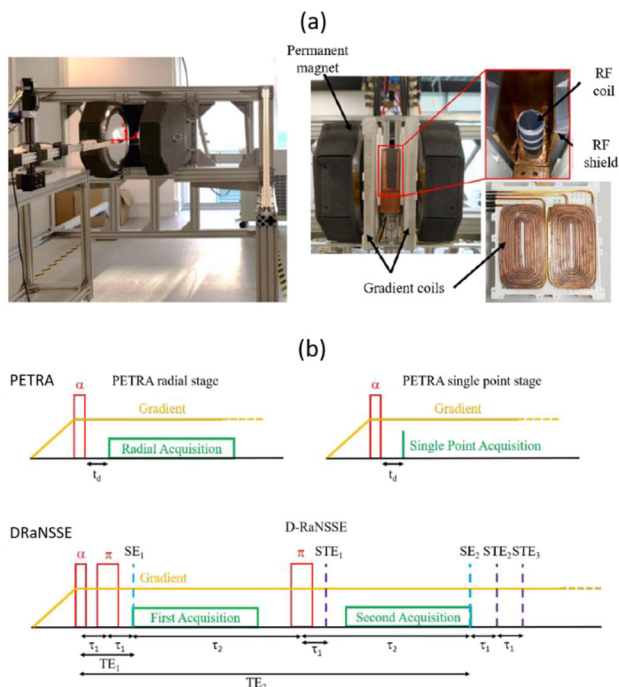
Introduction:

Figure 1. (a) Photographs of the “DentMRI – Gen I”, (b) Sequence diagram for a single repetition of PETRA (top) and DRaNSSE (bottom).

Here we present “DentMRI – Gen I” (Fig. 1(a)), a home-made special-purpose MRI scanner designed with the goal of demonstrating dental imaging at low field (260 mT). We use two variations of zero echo time (ZTE) pulse sequences (Fig. 1(b)): standard PETRA [1,2], and Double Radial Non Stop Spin Echo (DRaNSSE), which we have devised to address limitations we encounter with PETRA. We perform image reconstruction by Algebraic Reconstruction Techniques (ART, [3]).

Subjects/Methods: “DentMRI – Gen I” operates with a “C”-shaped permanent NdFeB magnet that provides 260 mT over a spherical region of 150 mm in diameter. The system is equipped with a gradient system capable of reaching strengths > 0.4 T/m along any spatial direction and a TxRx RF solenoid coil able to induce a flip angle of 90 degrees in a few microseconds.

Results/Discussion: Figure 2(c) contains selected slices from the full 3D ART reconstruction of a rabbit head employing a PETRA sequence with 0.5 mm isotropic resolution. We acquired two images: one with a short (90 μ s) dead time (Fig. 3(c) top) with a scan time of 61 minutes; and one with a long (1 ms) dead time (Fig. 2(c) middle) with a scan time of 31 minutes. The bottom image in Fig. 3(c) shows difference between both images to highlight hard tissues.

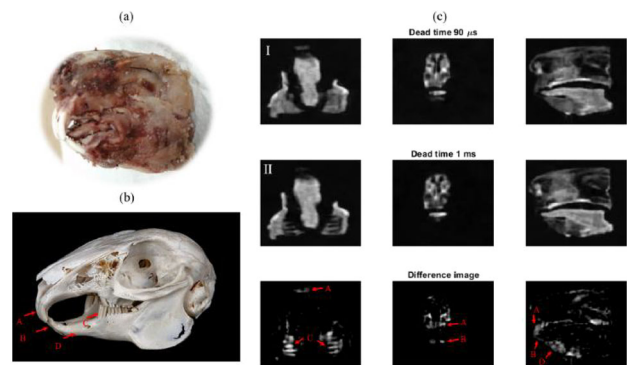


Figure 2. (a) Picture of the scanned rabbit head. (b) Picture of a rabbit skull, taken from Gabrielle Ochnik, Pinterest. (c) Top: single slices for 90 μ s dead time, middle: the same slices for 1 ms dead time, bottom: difference between the above images

Figure 3 shows ART reconstructions slices from DRaNSSE (top) and PETRA (bottom) acquisitions. Images were acquired with 1 mm isotropic resolution with a total scan time of 30 (15) minutes for DRaNSSE (PETRA). Due to the long echo time for the second echo (10 ms), tissue contrast is higher with DRaNSSE.

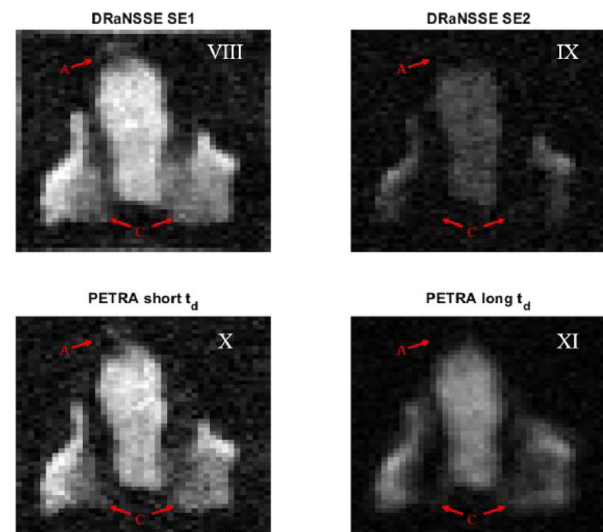


Figure 3. Rabbit image slices obtained with DRaNSSE (top) and PETRA (bottom) for short time parameters (left) and long time parameters (right).

In the present work we have demonstrated the capability of our new low-cost “DentMRI – Gen I” scanner to simultaneously image hard and soft biological tissues; we have devised a new pulse sequence (DRaNSSE) that, compared to standard sequences such as PETRA, yields higher SNR images and enhanced tissue contrast.

Acknowledgment

This work was supported by the European Commission under Grants 737180 (FET-OPEN: HISTO-MRI) and 481 (ATTRACT: DentMRI).

References: [1] M. Weiger, K. P. Pruessmann, A.-K. Bracher, S. Köhler, V. Lehmann, U. Wolfram, F. Hennel, and V. Rasche, “High-resolution ZTE imaging of human teeth,” *NMR in Biomedicine*, vol. 25, no. 10, pp. 1144–1151, oct 2012. [Online]. Available: <http://doi.wiley.com/10.1002/nbm.2783>.

[2] D. M. Grodzki, P. M. Jakob, and B. Heismann, “Ultrashort echo time imaging using pointwise encoding time reduction with radial acquisition (PETRA),” *Magnetic Resonance in Medicine*, vol. 67, no. 2, pp. 510–518, feb 2012.

[3] R. M. Gower and P. Richtarik, “Randomized iterative methods for linear systems,” *SIAM Journal on Matrix Analysis and Applications*, vol. 36, no. 4, pp. 1660–1690, 2015.

L01.94 **T_1 - and T_2 -prepared SSFP sequences for fast relaxometry at low field**D. Cicolari¹, M. Yushchenko², M. Fiorito², R. Ayde², M. Mariani¹, N. Salameh², M. Sarracanie²¹University of Pavia, Department of Physics, Pavia, Italy, ²Center for Adaptable MRI Technology (AMT Center), University of Basel, Department of Biomedical Engineering, Allschwil, Switzerland

Introduction: Low field approaches are gaining momentum for more accessible MRI-based diagnoses¹. Quantitative relaxometry is a critical step towards comparable metrics in MRI², despite being regrettably often set aside due to impractical acquisition times. Remarkably, low field relaxometry could be particularly compelling, benefitting from higher dispersion and potentially unveiling new contrasts³. With a further decreased sensitivity though, it becomes crucial to explore fast approaches for precise and accurate mapping of nuclei relaxation rates. The presented work reports on the use of magnetization prepared steady-state (SSFP) sequences tuned for fast T_1 and T_2 mapping at low field.

Subjects/Methods: An MRI phantom composed of nine vials filled with different $[\text{MnCl}_2]$ solutions was made, spanning a wide range of T_1 s and T_2 s. Ground-truth relaxation times were measured with a resistive biplanar 0.1 T MRI system (Bouhnik SAS, France), at room temperature, using standard spectroscopic sequences (IR and CPMG). Custom T_1 - and T_2 -prepared SSFP sequences were developed (PRIm, RS²D, France) that consist of three main blocks: 1) T_1 or T_2 magnetization preparation, 2) transient-state stabilization, 3) transient-state SSFP readouts with customized k-space centric ordering in 2D (projection)⁴. Validation of both magnetization preparation block was assessed spectroscopically (FIDs only) for each sample. Imaging parameters were: matrix size 64x47, TR/TE=5000/26 ms, FOV=153x154 mm, and NA=5 leading to 10 min total acquisition time for each series of T_1/T_2 weighted images. T_1 and T_2 maps were obtained through a pixel-wise fit using Matlab (Mathworks, USA).

Results/Discussion: The obtained relaxation maps are shown in Fig.1.

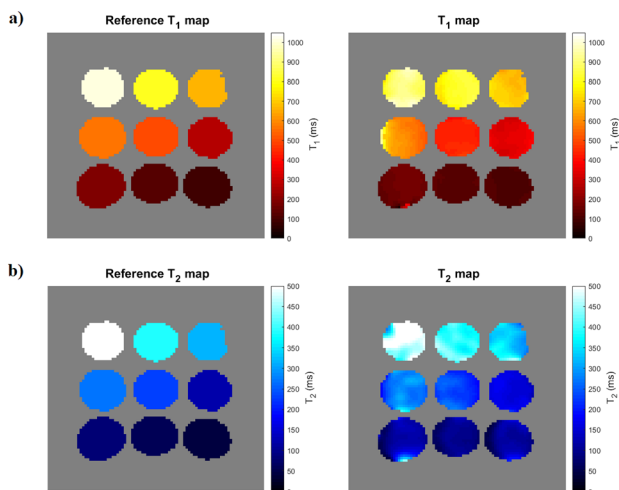


Fig. 1: a) NMR reference (left) and measured T_1 maps (right). Acquisition: 10 images with T_1 s in the range 5–5000 ms, NA=5; b) NMR reference (left) and measured T_2 maps (right). Acquisition: 10 images with T_2 s in the range 2–200 ms, NA=5.

The comparison of spectroscopic measurements with computed maps is reported in Fig. 2, with $R_1=1/T_1$ and $R_2=1/T_2$.

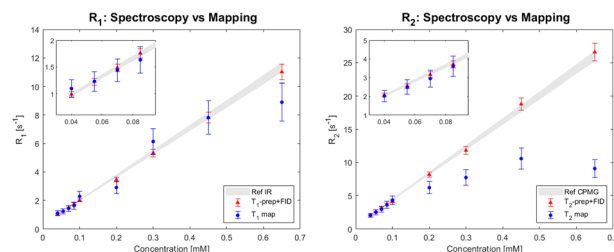


Fig. 2: Relaxation rates R_1 (left) and R_2 (right) as function of $[\text{MnCl}_2]$ for the different techniques used. An error of 15% is associated to all values obtained from the maps (3% for IR and CPMG results, 5% for T_1 and T_2 preparation+FID results).

As a reference, both the calibration curves from NMR spectroscopy (grey areas) and the values obtained from the validation of the magnetization preparation block are shown. A good correlation was found for high T_1 and T_2 values. Blurring artifacts (not shown) from intrinsic filtering of k-space and possible balancing issues critical in the approach to steady-state phase could explain the discrepancies observed at low T_1 and T_2 values. The sampling schemes of the recovery and decay curves could also affect the accuracy of the extracted maps, particularly over a broad range of relaxation rates. Introducing slice selection and adding undersampling strategies are possible solutions to reduce both artifacts and acquisition times. In conclusion, the proposed method returned very promising results both in terms of speed and accuracy for fast and reliable relaxometry of T_1 and T_2 at low field strength.

References: ¹Sarracanie, Salameh, *Front Phys*, 2020

²Cheng et al., *J Magn Reson Im*, 2012

³Broche et al., *Sci Rep*, 2019

⁴Huang et al., *Magn Reson Med*, 2007

L01.95**Advanced MRI for intra-operative MRI, an initial study of the impact of flex-coils and off-center imaging**

A. Tisell, P. Lundberg

Linköping University, Medical radiation physics, Linköping, Sweden

Introduction: Magnetic resonance imaging has been used in radiology for decades and the whole MR system is optimised for radiological diagnostics, ie coil design, sequences implementations. However, in recent years MR have made its way in to other fields of medicine e.g. intra operative tumor surgery.

Intra-operative MRI for tumor resections comes with a number of challenges. Besides, safety issues, there are a number of technical challenges including usage of flex coils placement of the head in off-center positions.

For high-grade tumors the main application in intra-operative MRI is to use a standard T1w-volume pre and post GD injections for detecting residual tumor. However, recent development for advanced MRI makes this methods desired to also use advanced MRI methods.

In this project the aim was to investigate the impact on image quality of using flex coils and off-center imaging for advanced MRI methods.

Subjects/Methods: All measurements was performed on a 3 T Skyra system (Siemens Healthcare). A standard fBIRN phantom was used [1]. Seven different examinations were performed on the BIRN phantom. One reference examination was performed using the standard 20 channel head coil and six examination was performed with the phantom fixated in the DORO LUCENT headrest (PMI) using titanium skull-pins figure 1.

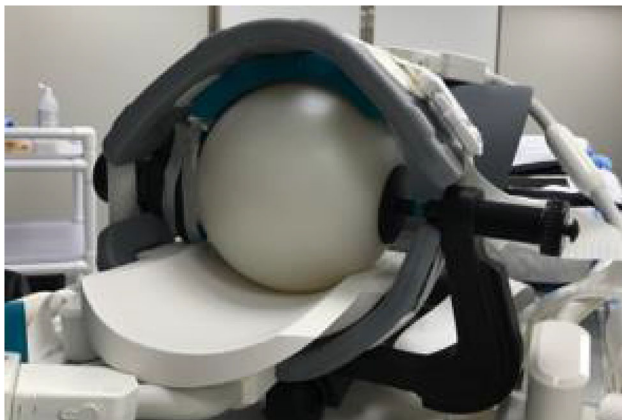


Figure 1. Placement of phantom in the headrest

To evaluate the effect of scanning off-center the phantom was scanned on six different locations. With the center of the phantom placed 4, 7, 10, 13, 16 and 17 cm off-center.

The examination protocol consisted of: Two identical T1 volumes MPRAGE, one diffusion based on EPI, one diffusion based on the resolve sequence and one qMRI was performed using QRAPMASTER sequence [2].

Results/Discussion: Comparing the SNR for the flex-coils compared to the standard head-coil show that the SNR were comparable close to the surface of the coils but lower in the central part of the phantoms (figure 2 and 3). No effect from the skull pins were seen in the SNR images.

For diffusion estimates of ADC the flex coil images were showing a higher degree of variation due to lower SNR. Off-center imaging showed a severe effect on distortion. Moreover, distortion due to the skull-pins was more severe for the EPI based diffusion.

The quantitative images showed that the distribution of estimated values were wider for the flex coil measurements. see figure 3. Moreover a strong variation in T1 estimate was observed

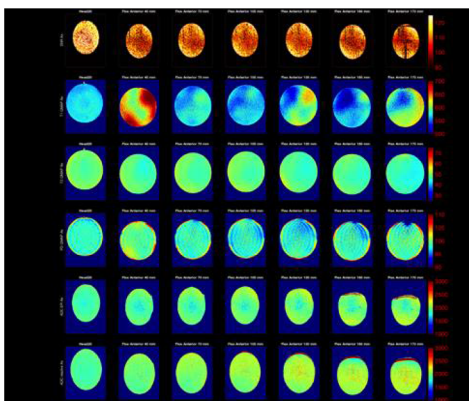


Figure 2. Axial images of SNR (row 1), T1-map (row 2), T2 (row 3), PD (row 4), ADC EPI base (row 5) and ADC resolve (row 6). Head 20 ch coil (column 1), Flex coil with distance to center 40, 70, 100, 130, 160 and 170 mm in column 2 to 6.

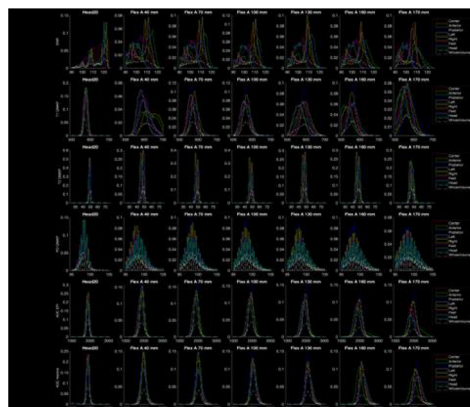


Figure 2. Histogram of SNR (row 1), T1-map (row 2), T2 (row 3), PD (row 4), ADC EPI base (row 5) and ADC resolve (row 6). Head 20 ch coil (column 1), Flex coil with distance to center 40, 70, 100, 130, 160 and 170 mm in column 2 to 6.

Conclusion: The SNR is affected for intra operative imaging. Resolved based diffusion mitigates distortion effects from the skull-pins. Effects of B1 inhomogeneity needs to be investigated for qMRI. **References:** 1. Friedman, Report on a multicenter... J MRI, 2006 2. Warntjes, J.B., et al., Rapid magnetic resonance MRM, 2008.

Acknowledgement

The qMRI sequence (QRAPMASTER) was provided by Tobias Granberg (Karolinska University Hospital), developed in collaboration with Frederik Testud, (Siemens Healthcare AB).

L01.96

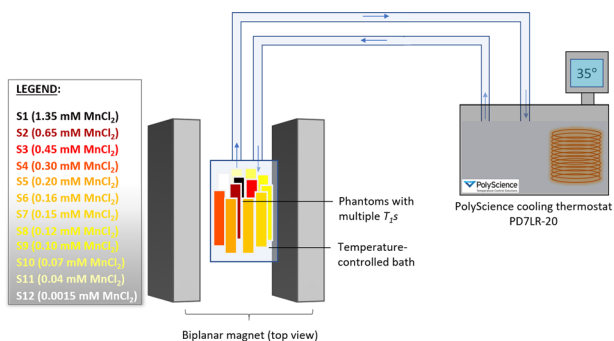
Fast, interleaved Look-Locker based T_1^* mapping for low field MR thermometry

M. Fiorito¹, M. Yushchenko¹, D. Cicolari², M. Sarracanie¹, N. Salameh¹

¹Center for Adaptable MRI Technology (AMT Center), University of Basel, Department of Biomedical Engineering, Allschwil, Switzerland, ²University of Pavia, Department of Physics, Pavia, Italy

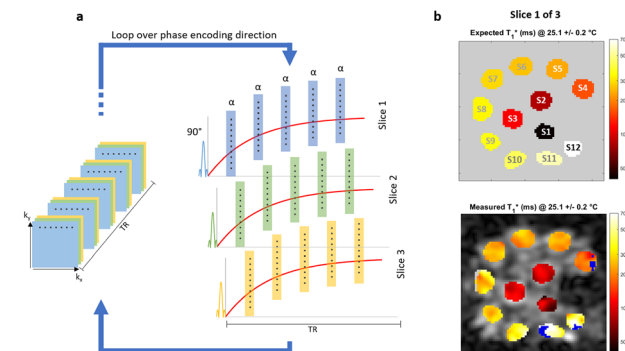
Introduction: Interventional MRI performed on high field scanners can suffer from limited access to the patient and MR incompatibility of surgical instruments and devices. MR systems operating at low field can overcome these constraints and naturally benefit from increased T_1 dispersion¹. T_1 was shown to correlate well with temperature at low field², yet fast T_1 mapping sequences for temperature mapping in thermotherapies have not been explored. Here we provide a proof-of-concept study to measure T_1^* dispersion at low field as a function of temperature using a fast, custom developed, Look-Locker-based FLASH sequence.

Subjects/Methods: A phantom made of 12 vials filled with solutions of different $[\text{MnCl}_2]$ was placed in a sealed container connected to a water tank. A higher MnCl_2 concentration associates to a lower T_1 at room temperature. Temperature was regulated and monitored using a water circulating system (Fig.1).



Experimental set up employed for the acquisition of temperature maps. MR images of 12 samples characterised by different T_1 s were acquired at 8 different temperatures, monitored through a thermal camera.

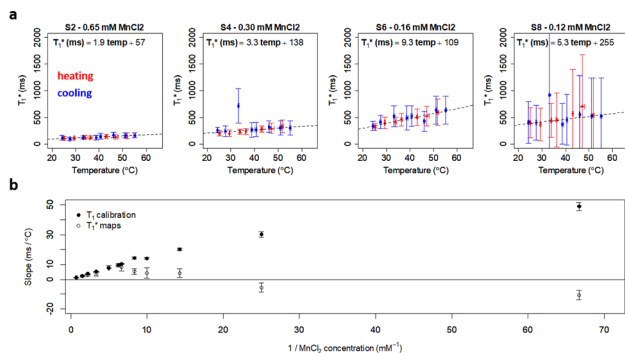
An interleaved, multi-slice sequence based on the Look-Locker approach³ (Fig.2a) was employed to acquire 52 stacks of images spaced by $TR_{\alpha} = 37.6$ ms (in-plane resolution = 3×3 mm², slice thickness = 20 mm, matrix = $40 \times 39 \times 3$, $TR/TE = 2000/7.2$ ms, $\alpha = 15^\circ$) using a resistive biplanar MRI system (Bouhnik S.A.S., France) at 0.1 T.



a) Schematics of the interleaved Look-Locker-based FLASH sequence. The saturation pulse allows not to wait for full T_1 recovery. b) Example of measured and expected T_1^* maps. The blue regions show where the model failed and were excluded.

The entire acquisition was carried out in 4 min. T_1^* maps of the phantom for 8 temperature points, monitored with a thermal camera, were reconstructed both when heating up and cooling down (Fig.2b). The extracted T_1^* s were compared with the calibration curves obtained from a spectroscopic saturation-recovery sequence.

Results/Discussion: Good correlation was found between the measured T_1^* maps and the calibration curves (Fig.2b). Our model struggles to accurately retrieve the short T_1^* of sample 1 due to a relatively long TR_{α} . Similarly, samples with long T_1 s lead to T_1^* overestimation because of the relatively short TR. In agreement with the literature, sample 1 to 7 display a linear relationship over the investigated temperature range², with increasing slopes associated to lower $[MnCl_2]$ (Fig.3a).



a) T_1^* linearly grows with temperature, with a higher slope as $[MnCl_2]$ decreases. The model fails to capture the trend for samples characterised by longer T_1 s. b) For the other samples, T_1^* dispersion follows T_1 dispersion from calibration.

For those cases, the slopes match the values expected from spectroscopic calibration of T_1 as a function of temperature (Fig.3b). Dispersion ranges from 1.01 ± 0.13 ms/°C of sample 1 to 8 ± 2 ms/°C of sample 7, characterised by a T_1 of ≈ 67 ms and ≈ 520 ms at $37^\circ C$, respectively. Such T_1 range is comparable with measurements found in the literature at magnetic fields close to ours⁵. Converting T_1^* into T_1 is a foreseen development with the acquisition of an accurate B_1 field map, which can be non-trivial at small flip angles. Nonetheless, these results propose T_1^* as a reliable indicator of temperature variation and offer a further step towards the application of thermotherapies at low field.

References: ¹Fischer H.W., MRM, 1990
²Nelson T.R. & Tung S.M., Magn Reson Imaging, 1987
³Deichmann R., MRM, 2005
⁴Bottomley P.A., Med Phys, 1984

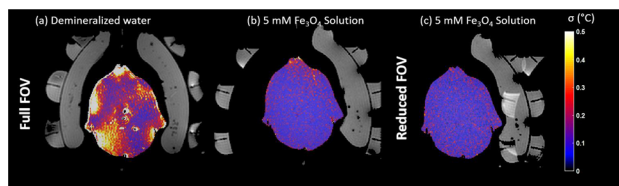
L01.97
The Benefits Of Using Fe₃O₄ nanoparticles doped water in water bolus of MR compatible RF hyperthermia devices

K. Sumser¹, G. Bellizzi¹, G. van Rhooon¹, M. Paulides²
¹Erasmus University Medical Center, Department of Radiotherapy, Rotterdam, The Netherlands, ²Eindhoven University of Technology, Department of Electrical Engineering, Eindhoven, The Netherlands

Introduction: MR thermometry (MRT) allows 3D non-invasive temperature monitoring during hyperthermia treatments. The water in water bolus (WB) of hyperthermia devices causes an unnecessary increase in the MRI field of view (FOV), creates flow artifacts and skews pre-scan calibrations, resulting in temperature errors and a longer scan time. Suppressing MRI signal of the WB may result in reduced MRT errors and scan time. This can be achieved by doping water with Fe₃O₄ nanoparticles without altering the electromagnetic properties needed for a proper operation of the RF hyperthermia device.

Subjects/Methods: We have compared WB filled with demineralized water to the one filled with 5mM Fe₃O₄ (Stock# US7568, US-Nano-Research, Houston, TX) doped solution. The dielectric properties of the 5mM Fe₃O₄ solution were measured with open-ended coaxial probe DAK-12 (v2.4; SPEAG, Zurich, Switzerland). The effect on hyperthermia treatment planning were investigated through multi-physics simulations¹. The MRT precision was tested in a 15minutes of no heating experiment using in MRcollar head and neck hyperthermia applicator and in house developed patient representative phantom². Also, feasibility of reducing FOV was tested.

Results/Discussion: The 5mM Fe₃O₄ solution was shown to have similar dielectric properties as the demineralized water. Thus, there was no effect in the SAR distribution, HTP parameters or power efficiency of the applicator. MRT precision maps are illustrated in Figure 1. MRT precision on average in the phantom when demineralized water was used in the WB was 0.39°C as opposed to. MRT precision improved to 0.10°C when 5mM Fe₃O₄ water-based solution was used. Finally, this allowed 20% reduction in FOV that improved the MRT precision to 0.09°C and also reduced the scan time by 20%.



MRT precision maps for three different cases: (a) demineralized water (b) 5mM Fe₃O₄ Solution (c) after 20% reduction in FOV.

Fe₃O₄ nanoparticles doped WB improves MRT precision with no performance tradeoffs. Therefore, it has great potential to improve MR-guided RF hyperthermia.

References: ¹ Sumser, K., et al. “Feasibility and relevance of discrete vasculature modeling in routine hyperthermia treatment planning.” *International Journal of Hyperthermia* 36.1 (2019): 800-810.

² Sumser, K., et al. “MR thermometry guided RF hyperthermia in the head and neck region – does the new MRcollar affect the imaging?” in *ISMRM 27th Annual Meeting & Exhibition, Montreal, Canada, 2019*.

L01.98

A new class of MRI contrast agent based on NMR Quadrupolar peak for monitoring tissue implants

E. Di Gregorio¹, V. Bitonto¹, S. Baroni¹, R. Stefania¹, S. Aime¹, D. Lurie², L. Broche², N. Senn², S. Geninatti Crich¹

¹University of Torino, Department of Molecular Biotechnology and Health Sciences, Torino, Italy, ²University of Aberdeen, The Institute of medical sciences, Aberdeen, UK

Introduction: One of the challenges of regenerative tissue therapy is represented by the possibility to noninvasively monitor cells-containing implants. The development of innovative biocompatible sensors reporting on the status of the implants is an urgent biomedical need. These sensors are aimed at reporting i) on the eventual degradation of the scaffold and ii) on the overall condition of transplanted cells. Herein, we reported an innovative biocompatible PLGA scaffold containing polyhistidine as a sensor detectable by Fast Field Cycling (FFC) MRI. The sensor triggers the generation of ¹⁴N-Quadrupolar Peaks (QPs) that cause a relaxation enhancement of water protons at a proper frequency (1.39 MHz) well distinguishable from the frequencies associated with QPs generated by endogenous proteins.

Subjects/Methods: Poly(lactic-co-glycolic acid) (PLGA) was conjugated with polyhistidine (n=15) and used for the preparation of porous biodegradable PLGA-scaffold. Polyhistidine-PLGA was dissolved in tetraglycol in presence of glucose to create pores in the solid matrix. Scaffolds were subcutaneously implanted in the scruff of 10-weeks male Balb/c mice. The degradation of scaffolds was monitored by acquiring T₂w and T₁w - MRI at 7T up to 25 days from the implantation. After the sacrifice, relaxometric dispersion profiles of scaffolds were acquired on a FFC relaxometer (Stelar S.r.l.) with 6mm microcoil (0.01-10MHz). Finally, scaffolds were processed for H/E histology to monitor the transplanted scaffold status and to evaluate the polymer degradation by immune cells system.

Results/Discussion: NMRD profiles of Polyhistidine PLGA scaffolds show a characteristic QP at 1.39 MHz due to the ¹⁴N nuclear quadrupole resonance frequency of the imidazole groups present on the polymeric histidine chains (Fig.1A). Also the classical QPs of amide protons of polypeptide backbone are present (2.1 and 2.7 MHz). These QPs are not distinguishable from those arising from endogenous proteins (Fig.1A). QP at 1.39MHz is very specific and polyhistidine can be used as a new class of frequency-encoded NMRD sensor. The QPs are detectable only when the contrast agent is in a solid-like form². MRI images (B₀=7T) of mice demonstrated a decrease of the scaffold size during days after the implantation due to degradation (from 150 to 20mm³). Scaffolds were excised at different time points and NMRD profiles acquired to detect QPs. A change of relaxivity proportional to the amount of cells was detected thus demonstrating cells colonization. Histology confirms the colonization and proliferation of murine cells on the implanted scaffolds (Fig.2). FFC-MRI of scaffold opens new avenues in biomedical imaging of regenerative therapy and it appears a promising approach to generate contrast in MR images without contrast agents.

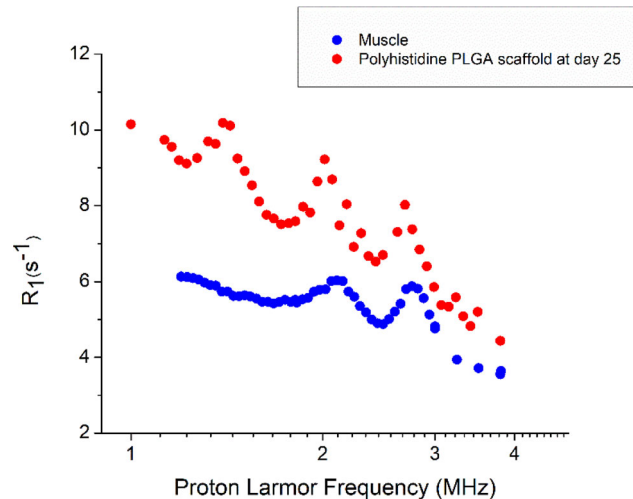


Fig.1 (A) Representative NMRD profiles of reference muscle and ex vivo scaffold at day 25 from implantation.

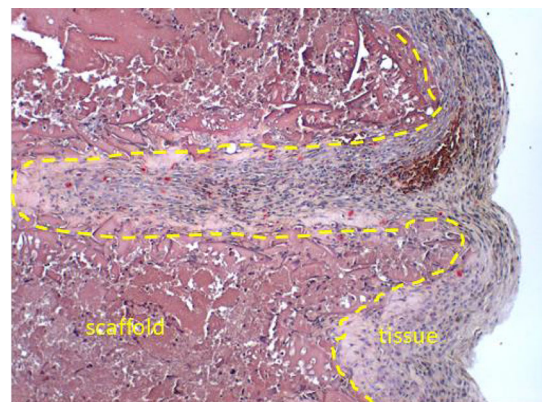


Fig.2 H/E histology of excised scaffold at day 25, showing the colonization of cells and the presence of immune system cells.

References: [1] C. Gosweiner et al. *Phys. Rev. X* 8, 021076. 1-20 (2018)

[2] S. Geninatti Crich et al., Patent n 102019000007647 (2019)

L01.99

CEST Simulations with JEMRIS

S. Akbey, T. Stöcker

German Center for Neurodegenerative Diseases (DZNE), Bonn, Germany

Introduction: The measurable chemical exchange saturation transfer (CEST) effect strongly depends on the saturation module used in the experiment. Extended by the Bloch McConnell (BMC) equations, the MRI simulation framework JEMRIS[1] allows to optimize the saturation and thus maximize this effect. BMC simulations were previously integrated into an older JEMRIS version in the context of MT simulations[2]. We updated and extended the approach to be usable with the newest JEMRIS version and developed a python user interface for CEST simulations.

In our proof-of-concept study, we compared a simple simulation experiment with the analytical solution and a numerical matrix

approach[3]. Moreover, the simulations were verified based on phantom measurements at 7T.

Subjects/Methods: Using JEMRIS, the z-magnetization directly after the saturation block was simulated. First, a two-pool experiment with a continuous wave saturation (Tab. 1a) was simulated and compared to the analytical and the matrix approach.

Afterwards, three different protocols with pulsed saturation trains were used (Tab. 1b).

Phantom data were acquired at a 7T Siemens scanner with a 32-channel Nova head coil applying a 3D-EPI sequence[4,5] with 2mm isotropic resolution.

Experiments were performed on an available, in-house made phantom, containing two brain metabolites Glutamate and GABA (ratio 2:1). As there is a broad discrepancy in reported CEST parameters, simulation parameters were manually adjusted to match the phantom data.

(a)	sample	$\delta\omega$ (ppm)	fraction	exchange rate (Hz)	T1/T2 (ms)
	water	0			2000/115
	glutamate	3	0.002	1000	1000/10
no. pulses					
	1	1000	1	1	
(b)	sample	$\delta\omega$ (ppm)	fraction	exchange rate (Hz)	T1/T2 (ms)
	water	0			2000/115
	glutamate	3	0.002	1000	1000/10
	GABA	2.75	0.001	2000	1000/10
no. pulses					
	10	100	1	2	50
	20	50	1	2	50
	40	25	1	2	50

Tab. 1: Parameters for multi pool samples and saturation modules. a) Used sample and saturation scheme to compare the BMC simulations of JEMRIS, matrix and analytical approach. b) Parameters for the three phantom experiments and the related simulation

Results/Discussion: Fig. 1 shows Z-spectra and MTR_{asym} analysis of the two-pool continuous wave simulation. As expected, the results of the three approaches are in excellent agreement. Small deviations to the analytical solution for both numerical approaches can be attributed to time discretization and limited floating-point precision. JEMRIS uses an adaptive step-size integrator for the solution of the BMC equation, which is typically less efficient than an optimized implementation of the matrix approach, but it provides greater flexibility for the simulation of arbitrary sequences.

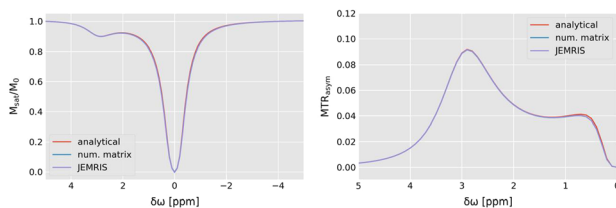


Fig. 1: Z-spectra and MTR_{asym} of the two-pool continuous wave simulations ($t_{pulse}=1s$, $B1=1\mu T$). The results of the simulations are in very good agreement.

Fig. 2 shows the Z-spectra of measured phantom data and related BMC simulations using different saturation modules. A short pulse duration results in strong side lobes of the frequency response, which generates wiggles in the Z-spectrum [6]. This is consistent in measured and simulated data. In order to accurately simulate CEST effects, the exact parameters are needed. These parameters can

potentially be extracted by iterative adapting the simulation parameters in a reference experiment.

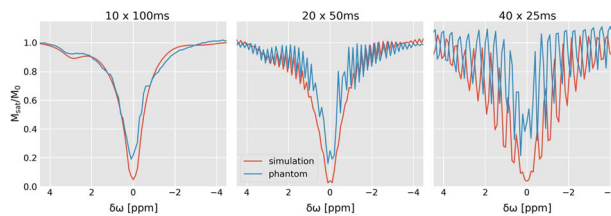


Fig. 2: Simulated and single voxel Z-spectra of the phantom for three pulsed saturation schemes with a total saturation time of 2s. The shorter the pulses, the stronger the side lobes.

Utilizing these values, JEMRIS enables simulations and optimization of arbitrary sequence building blocks for CEST labeling. Beyond, to simulate more realistic conditions, more features of JEMRIS could be included in the future.

References: 1. Stöcker.2010.MRM. www.jemris.org

2. Kubach.2010.ISMRM

3. Zaiss. www.cest-sources.org

4. Akbey.2019.MRM

5. Mueller.2020.MRM

6. Liu.2013.NMR Biomed

L01.100

First *in vivo* ^{19}F -MRI quantification of mouse brain inflammation using a cryogenic transceive surface RF probe and RARE MRI

P. Ramos Delgado¹, C. Prinz¹, J. M. Millward¹, H. Waiczies², L. Starke¹, J. S. Periquito¹, T. Niendorf¹, A. Pohlmann¹, S. Waiczies¹

¹Max-Delbrück-Center for Molecular Medicine, Berlin Ultrahigh Field Facility, Berlin, Germany, ²MRI.TOOLS GmbH, Berlin, Germany

Introduction: Cryogenically-cooled RF coils (CRP) in association with acquisition methods such as RARE are often necessary to boost the low SNR inherent to ^{19}F -MRI but the B_1 -field inhomogeneity of transceive surface CRP hampers quantification¹. We showed a B_1 correction method using 1H -MRI where RARE's signal intensity (SI) was modeled as a function of flip angle (FA) and T_1 ². Now we established a workflow to correct and quantify ^{19}F MR signals arising from inflammatory regions of the mouse brain using a ^{19}F -CRP.

Subjects/Methods: Experiments were performed on a Bruker 9.4T animal MR scanner. Four capillary tubes filled with perfluoro-15-crown-5-ether nanoparticles (NP) (10/10/25/50 mM) were embedded in a 15 mL-tube. Experimental autoimmune encephalomyelitis (EAE) was induced in $n = 4$ SJL/J mice³ and 10 μM of NP was administered *i.v.* for 12 days⁴. Mice were euthanized, fixed and the skull embedded in 15 mL-tubes ($n=3$).

T_1 values of 2 NP preparations (20-300mM in 2% agarose) and *ex vivo* samples were computed using non-localized spectroscopy (block pulse: 10TRs, 250–10,000 ms). T_1 values in the brain were achieved using localized spectroscopy (PRESS) *ex vivo* (12TRs, 250–15,000 ms) and *in vivo* ($n = 2$, 8TRs, 413–13,000 ms). T_1 measurements were done with a volume RF coil.

Anatomical images (FLASH: TE/TR = 3.72/120 ms, resolution=(260x260) μm^2 , 5 axial slices, 14min) were acquired with a 72mm-volume RF coil placed around the center tube of the ^{19}F -CRP using an in-house built system to keep positioning stable. ^{19}F MRI (RARE: TE/TR=5.08/1000ms, ETL=32, centric encoding, flipback, same geometry; 30/50min phantom/mouse) was acquired with the ^{19}F -CRP and a volume RF coil. A flexible reference containing 300mM NP in 2% agarose placed on top of the phantom/mouse was used for reference power adjustments and quantification.

B_1 correction: B_1 maps of the ^{19}F -CRP were computed. A SI model was calculated from RARE scans (same parameters, $\text{FA}=5^\circ$ - 165° , NMR tubes with $T_1=190$ – 2870ms) using a volume RF coil. Corrected images² were overlaid on the anatomy.

Results/Discussion: We show the first *in vivo* ^{19}F images of the inflamed EAE mouse brain using a ^{19}F -CRP in combination with RARE and report the first *in vivo* T_1 values for ^{19}F NP in the EAE brain. Using a capillary phantom, we showed a restoration in signal (relative to reference images) following a B_1 correction of the CRP images. We also computed concentration maps and established a workflow that enables ^{19}F and anatomical imaging with a single-tuned CRP. These results will be invaluable for spearheading future studies using a ^{19}F -CRP to quantify inflammation or ^{19}F compounds in *in vivo* longitudinal studies.

Acknowledgements

Deutsche Forschungsgemeinschaft WA2804 (S.W.) and PO1869. (A.P.).

References: 1. Axel L, Hayes C. *Arch. Int. Physiol. Biochim.* 1985;**93**(5):11-18

2. Delgado P, et al. *Magn Reson Med* 2020; 00:1-18

3. Waiczies H, et al. *Sci Rep* 2013; **3**:1280

4. Waiczies H, et al. *PLoS* 2011; **6**(7):e21981

L01.101

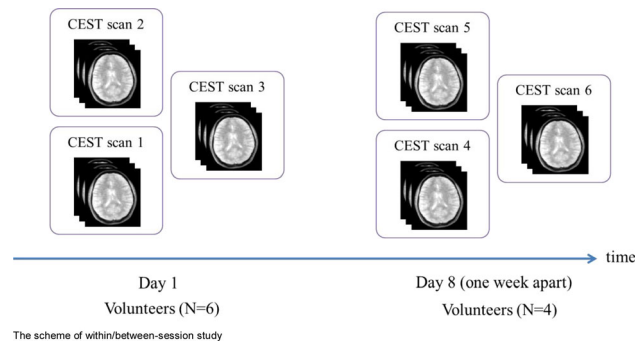
Reproducibility study of Chemical Exchange Saturation Transfer imaging in the human brain at 3 T

Y. Wu¹, T. Wood², J. A. Hernandez-Tamames¹, G. J. Barker², M. Smits¹, E. A. Warnert¹

¹Erasmus MC - University Medical Centre Rotterdam, Department of Radiology & Nuclear Medicine, Rotterdam, The Netherlands, ²King's College London, Department of Neuroimaging, London, UK

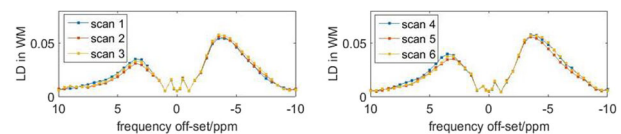
Introduction: Chemical Exchange Saturation Transfer (CEST) imaging is a novel MRI technique with great potential for early detection of tumor progression in low grade glioma. Amide Proton Transfer (APT) weighted imaging and assessing the Nuclear Overhauser Enhancement (NOE) effect are common CEST-based approaches¹⁻² for assessment of cancer and ischemic stroke *in vivo* at 3 T^{3-4} . However, in particular for between subject comparisons or longitudinal observations it is important to understand the reproducibility of CEST measurements to aid further clinical adoption. The goal of the current work was to measure reproducibility of APT-weighted and NOE CEST measurements in healthy volunteers.

Subjects/Methods: A 3 Tesla MRI scanner equipped with a 32-channel head coil (General Electric, Chicago, USA) was used for this project. CEST image acquisition parameters were: B_1 amplitude of $1\ \mu\text{T}$, 14 slices, voxel size $1.7 \times 1.7 \times 3\ \text{mm}^3$, 53 frequency offsets ($\Delta\omega$) distributed between -100 and 100 ppm, duration 4 minutes. An additional T_1 -weighted structural scan was acquired. The total scan duration of one session was approximately 20 minutes. To assess within-session reproducibility 6 healthy volunteers underwent the same CEST scan 3 times in one scan session. To assess between-session reproducibility, 4 volunteers underwent the same session one week later.



Z-spectra were normalized by one image acquired without saturation, followed by voxel-wise B_0 correction. After B_0 correction, two-pool Lorentzian fitting was performed to fit the direction water saturation (DS) and magnetization transfer (MT). Lorentzian Difference (LD) at 3.5 ppm was calculated to assess APT-weighted CEST. LD at -3.5 ppm was used for NOE CEST. White matter (WM) was used for regions of interest (ROI) and was segmented by FMRIB Software Library v6.0 based on the T_1 -weighted structural scan. Coefficient of variation (COV) was calculated to evaluate the within- and between-session reproducibility of each measure within each tissue type.

Results/Discussion: A high degree of within- and between-session reproducibility was found for both APT-weighted and NOE CEST MRI in WM (Table 1, group mean values <4%), which lays the groundwork for implementation in the clinic. During the summer of 2020 and for presentation at the annual meeting, further investigations are planned both to increase the number of volunteers and to include other three 3 Tesla scanners to assess between-scanner reproducibility.



Mean LD as a function of frequency off-sets in WM of one volunteer from the first 3 scans (left) and the other 3 scans one week apart (right)

volunteer	COV of LD amide in WM			COV of LD NOE in WM		
	within session 1	within session2	between-session	within session 1	within session2	between-session
1	2.64%	0.62%	0.31%	1.85%	1.31%	1.14%
2	4.95%	6.11%	6.29%	2.20%	1.28%	0.95%
3	1.81%	1.67%	2.08%	0.36%	0.87%	0.50%
4	3.51%	n.a.	n.a.	1.10%	n.a.	n.a.
5	1.35%	3.71%	6.93%	0.87%	2.53%	4.25%
6	4.09%	n.a.	n.a.	1.97%	n.a.	n.a.
group mean	3.06%	3.02%	3.90%	1.39%	1.50%	1.71%

Within-session COV computed based on the mean LD amide/NOE in WM from all scans per session, while between-session COV computed based on the average of the mean LD amide/NOE in WM from 3 scans in session 1 and 3 scans in session 2.

References: 1. Zhou J, et al. *Nat Med.* 2003;**9**:1085–90.

2. Zhou J, et al. *Nat Med.* 2011;**17**:130–4.

3. Togao O, et al. *Neuro Oncol.* 2014;**16**:441–8.

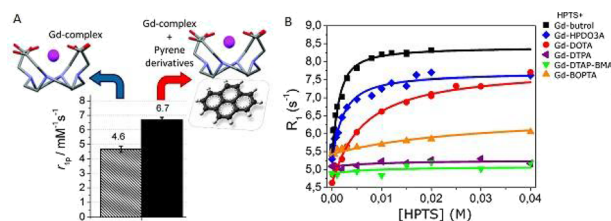
4. Wang M, et al. *Magn Reson Med.* 2015.

L01.102**Supramolecular adducts between macrocyclic Gd (III) complexes and polyaromatic systems: a route to enhance the relaxivity through the formation of hydrophobic interactions**E. Di Gregorio¹, L. Lattuada², A. Maiocchi², S. Aime¹, G. Ferrauto¹, E. Gianolio¹¹University of Torino, Department of Molecular Biotechnology and Health Sciences, Torino, Italy, ²Bracco Imaging Spa, Bracco Research Centre, Collettero Giacosa (TO), Italy

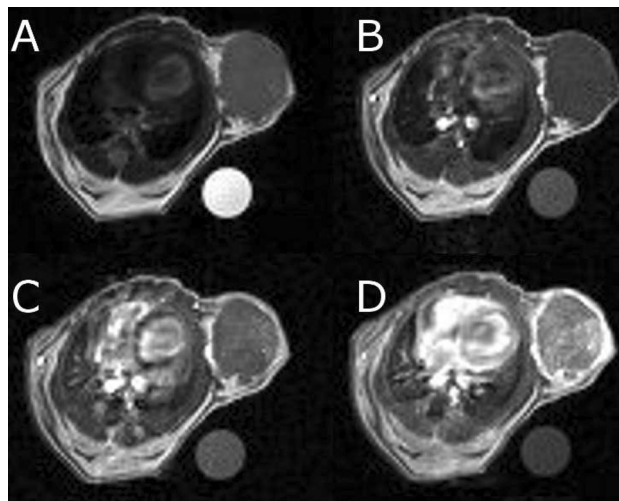
Introduction: MRI is the election imaging technique for the diagnosis and monitoring of numerous diseases. About 40–45% of MRI scans are performed with the use of Gadolinium based contrast agents (GBCAs). The recent findings related to NSF and Gd-retention strongly required caution in the use of GBCAs.¹ Chemistry becomes central in looking for i) more stable and ii) more efficient GBCAs (*i.e.* enhanced relaxivity). Different routes to enhance relaxivity were exploited as i) the *set-up* of non-covalent binding interactions with macromolecules present in solution (*e.g.* albumin), ii) the increase of the number of coordinated or second sphere water molecules, iii) the increasing of prototropic exchange rates.² Herein, we describe the increase of relaxivity attainable through reversible binding interactions between the hydrophobic region of macrocyclic GBCAs and SO³/OH containing pyrene derivatives (Fig.1A).

Subjects/Methods: Macrocyclic (ProHance, Gadovist, Dotarem) and linear (Magnevist, Omniscan, MultiHance) GBCAs were tested. The increase of relaxivity upon the addition of SO³/OH containing pyrene derivatives was assessed by ¹H-relaxometry and ¹H- / ¹⁷O-NMR. The binding parameters K_a (*association constant*) and R_b (*relaxivity of the adduct*) between GBCAs and the pyrene derivatives were calculated by using the PRE technique (0.5T). ¹H NMRD profiles were measured *w* or *w/o* of pyrene derivatives at variable B₀ (0.00024 to 1.5 T). Insights into the formation of the adduct were obtained by high resolution ¹H-NMR of YbHPDO3A complex *w* or *w/o* of pyrene derivatives (14 T). Finally, the *in vivo* proof of concept of the enhancement of contrast was obtained by MRI of tumor-bearing mice pre and post injection of GBCA (7T) upon injection of Gd-HPDO3A (0.15 mmol/Kg) or Gd-HPDO3A/HPTS adduct (0.15 and 0.45 mmol/Kg).

Results/Discussion: A high binding affinity of macrocyclic GBCAs toward pyrene derivatives was observed. The supramolecular adducts display a significant increase of relaxivity. No enhancement was observed for linear GBCAs (Fig.1B). This is due to the increase of the molecular reorientation time (τ_R) and second sphere water molecules (for the presence of SO³ and OH). NMR spectra of the Yb-HPDO3A/pyrene mixture support the formation of the supramolecular adduct. When HPTS/Gd-HPDO3A ratio is 3:1 (m/m), > 90% of Gd-HPDO3A is in the associated adduct and there is a 40% relaxation enhancement in respect to the value observed for Gd-HPDO3A alone (*i.e.* 6.5 mM⁻¹s⁻¹ vs. 9.2 mM⁻¹s⁻¹ in serum). In T_{1w}-MRI of tumor-bearing mice there is the increase of signal enhancement from 53% (upon *i.v.* of only Gd-HPDO3A) to 125% (upon *i.v.* of Gd-HPDO3A/HPTS adduct) (Fig.2). By concluding, the reported results show a novel tool to enhance the relaxivity of GBCAs through the formation of supramolecular adducts at clinical doses.



Enhancement of relaxivity upon supramolecular interaction with pyrene derivatives. (B) R1 of GBCAs (1mM) in the presence of HPTS at variable concentration (0–40mM)



Axial MRI of tumor region. (A) T2w MR image. (B) uncontrasted (pre) T1w MR image without Gd(III)-CA. (C) T1w MR image after 2 min from injection of Gd-HPDO3A (0.15 mmol/Kg) (D) T1w MR image after 2 min from the injection of Gd-HPDO3A and HPTS

References: 1) Aime S, *et al.* Magn Reson Imaging. 2009, 30, 1259; 2) Caravan P. *et al.* Chem. Soc. Rev. 2006, 35, 512;

L01.103**Use of osmolarity-responsive Gd- liposomes for the *in vitro* assessment of osmolarity of biological specimens**

E. Di Gregorio, S. Aime, G. Ferrauto

University of Torino, Department of Molecular Biotechnology and Health Sciences, Torino, Italy

Introduction: Liposomes have been largely exploited for the generation of *in vitro* analytical assays for quantification of diseases' biomarkers. Different kinds of responsive liposomes have been described, *e.g.* responsive to enzyme activity, to metal ion, to environmental pH, to temperature, to the presence of an analyte, etc...^{1,2} The presence of the biomarker to be assessed triggers detectable changes in liposomes structure or the release of the content or a modification of the chemical properties. These events can be quantified by using different approaches, depending on the liposomes formulation (*e.g.* measurement of fluorescence or of relaxivity, if they are filled with a fluorochromes or a paramagnetic Gd-complex, respectively).

Herein, we propose a new class of osmolarity-responsive paramagnetic liposomes, able to measure the osmolarity of the surrounding microenvironment, based on the use of ¹H-relaxometry.

Subjects/Methods: Small Unilamellar vesicles (SUVs) were prepared according to the classical thin lipid film hydration followed by extrusion and dialysis.² Different formulation were tested, all filled with Gd-HPDO3A (30mM, pH7.2, 30 mOsm/L). For testing the

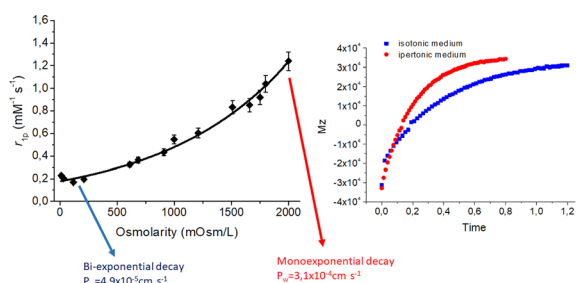
analytical assay, different specimens were analysed, both biological (*i.e.*: i) urine, ii) blood plasma, iii) splittle and iv) sweat) and pharmaceutical (*i.e.*: i) Iopamidol, ii) Iodixanol and iii) ibuprofen solutions). Liposomes (30 μL) were mixed with the specimen to be analysed (60 μL) and relaxivity (r_{1p}) measured at 21 MHz (Spin-Master relaxometer, Stelar). r_{1p} results were compared with calibration curve obtained by using standard solutions (0-2000 mOsm/L range, Fig.1).

Results/Discussion: Water permeability (P_w) and r_{1p} of different formulations of liposomes were measured. The best one was composed by 95% DPPC and 5% DSPE-PEG2000-methoxy. This formulation allows obtaining « *quenched liposomes* » displaying a very low relaxivity ($r_{1p}=0.2 \text{ mM}^{-1} \text{ s}^{-1}$). In presence of increased external osmolarities, there is a significant r_{1p} increases (up to $1.2 \text{ mM}^{-1} \text{ s}^{-1}$ for 2000mOsm/L), occurring for liposomes' shrinkage in ipertonic environment and increases of permeability. In fact, P_w moves from $4,9 \times 10^{-5}$ to $2.1 \times 10^{-4} \text{ cm}$ when liposomes are in isotonic or ipertonic environment, respectively (from biexponential to monoexponential decay of magnetization) (Fig.1 right).

Responsiveness to osmolality is maintained also when liposomes' surface is covered by proteins (*e.g.* Albumin or Streptavidin).

The assay has been tested for measuring osmolality of different biological and pharmaceutical specimens and results are in agreement with those ones obtained by using classical osmometer.

In conclusion, a novel class of responsive- paramagnetic liposomes has been described, able to be used as analytical assay for the measurement of osmolality of external medium.



(left) r_{1p} at different external osmolarities; (right) Magnetization vs. time when liposomes are placed in isotonic (blue points) or ipertonic (red points) environment.

References: (1) Ferrauto G. *et al* Angew Chem Int Ed Engl, 2017, 56, 12170.

(2) Terreno E. *et al*. Chem Biodivers. 2008, 5, 1901.

L01.104

Non-linear model to predict head motion using a magnetic field camera in a 7 T MRI scanner

L. Bortolotti, R. Bowtell

University of Nottingham, Nottingham, UK

Introduction: Motion artefacts resulting from head motion can be ameliorated by prospective and retrospective motion correction techniques based on real-time monitoring of head position. Widely used techniques for monitoring head position are MR image or marker based^{1,2}. Here, a new procedure, that neither requires use of a marker nor image sequence modification³, is tested. This technique predicts head motion parameters from measurements of extracranial magnetic field changes made using a magnetic field camera.

Subjects/Methods: The procedure involves a training phase, during which data for training a non-linear autoregressive exogenous model (NARX)⁴ are acquired and the regression method is trained, tested and validated, and a prediction phase where the model is applied

during the MRI data acquisition. The first part has been tested by performing a motion correction experiment that involves concurrent measurements of subject-specific, extra-cranial magnetic field variation (ΔB) and head movements using a field camera and an optical tracking system (Fig.1), while the subject executes a range of different head movements.

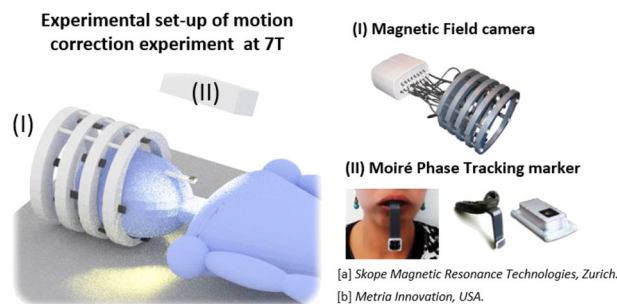


Figure 1: The experimental set-up consists of (I) Array of 16 NMR field probes displaced in four coaxial hard plastic rings mounted inside the head transmit coil (II) Moiré Phase Tracking marker rigidly coupled to the head via a dental mould.

This procedure was performed on a healthy adult subject able to control head movements and to hold the mouthpiece necessary for the optical tracking system. Training lasted 10-minutes, during which the subject was at rest (most common situation during MRI) or was instructed to alternate between rest and various head movements. We classified the position changes as large (one or more head movement parameters $> 3 \text{ mm}$ or 3°) or small. Changes were always small at rest, whilst during instructed movement position changes were small for 35% of measurements. Two NARX networks were trained. New data on 1-minute periods were then acquired at rest, holding a pose after a large head movement and dynamically performing large head movements to test the trained methods. The second phase was validated in post-processing. Physiological noise in ΔB was reduced by spatial filtering.

Results/Discussion:

Actual and predicted head movement parameters resulting from applying two different NARX architectures (top & bottom row) to data from three different movement conditions (first three columns)

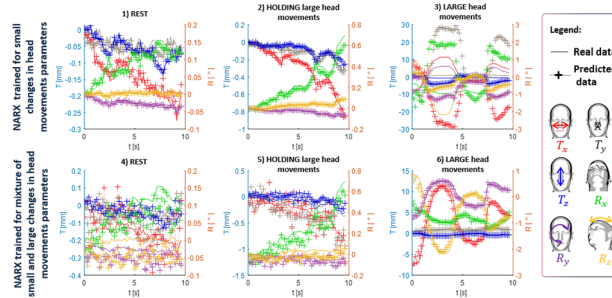


Figure 2: Plots represent a comparison between measurements and the results of applying NARX methods to various head movements. In general, the best predictions were obtained for data well represented in the training set (1, 2, 6).

Good predictions (Fig.2) of head position over a range of different movements result from applying the NARX method to both training sets. The accuracy of the predicted values (Tab.1) was evaluated by calculating the root mean squared (RMS) difference between estimated and actual movement parameters and comparing to the standard deviation (STD) of the measured parameters.

		Tx [mm]	Ty [mm]	Tz [mm]	Rx [o]	Ry [o]	Rz [o]
REST	STD	0.189	0.018	0.064	0.042	0.033	0.009
	(1) RMS	0.031	0.033	0.012	0.009	0.003	0.002
	(4) RMS	0.155	0.085	0.033	0.040	0.025	0.061
HOLDING	STD	0.514	0.190	0.326	0.558	0.037	0.071
	(2) RMS	0.044	0.094	0.206	0.345	0.057	0.008
	(5) RMS	0.594	0.672	0.269	0.190	0.041	0.068
LARGE	STD	3.924	0.213	0.337	0.559	0.298	0.650
	(3) RMS	14.404	10.248	1.398	1.241	0.741	0.495
	(6) RMS	0.772	0.160	0.080	0.113	0.056	0.115

Tab 1: Standard deviation (STD) of the executed movements and root mean squared (RMS) error between predicted and actual movements (numbers refer to plots in Fig.2). NARX trained on a larger span of movements do not well predict small head movements.

Better results were obtained on data best represented in the training set. This work provides a step forward towards a non-contact motion monitoring technique. Future improvements include fitting magnetic field probes around the RF receiver coil array, sending motion data to the scanner in real-time and using imaging methods for the training phase to remove the need for the optical camera and mouthpiece.

References: ¹McLaren J. et al, Mag.Res.Med, 2013; ²Aranovitch A. et al, Mag.Res.Med, 2019; ³Bortolotti L. et al, ESMRMB2019; ⁴Lin T. et al,IEEE,1996;

L01.105

The MRI cold head artifact is no longer a significant problem for simultaneous fMRI/EEG experiments

A. Amador¹, A. Harrison², M. D. Noseworthy³

¹McMaster University, School of Biomedical Engineering, Hamilton, Canada, ²Hamilton Health Sciences, Nuclear Medicine, Hamilton, Canada, ³McMaster University, Electrical and Computer Engineering, Hamilton, Canada

Introduction: Simultaneous studies of fMRI/EEG provide hemodynamic and electrophysiological information about brain function¹ with high spatial and temporal resolution. However, EEG recordings have always been thought to be contaminated by the cold head artifact generated by the helium pump of the MRI cooling system. The pump is commonly turned off when acquiring concurrent fMRI/EEG data² in order to avoid the artifact, at the cost of reducing the pump lifespan. The research objective was to characterize the cold head artifact present in EEG recordings, during simultaneous fMRI/EEG, and to design a filter to allow for its removal without requiring cold head shut-down.

Subjects/Methods: EEG data were acquired inside a GE Discovery MR750 3T MRI scanner and 32-channel RF receiver coil, using an MRI-compatible EEG amplifier and 64-channel cap with scalp electrodes following the International 10-20 system (Brain Products, Germany). Data were sampled at 5 kHz with 0.5 μV resolution, and referenced to position FCz. Electrode impedances were kept below 5 kΩ. EEG recordings were collected for 5 minutes from a spherical MRI phantom covered by a layer of EEG gel, with the MRI helium pump (model RDK-408A3, Sumitomo) turned on and off; and from 3 healthy volunteers with and without a gradient-echo EPI sequence (TE/TR = 35/2000 ms, 64 × 64 matrix, 4 mm thickness). Equipment that could be sources of other EMF electrical noise (e.g. MRI scanner

lighting and ventilation, MRI compatible projector) was turned off. EEG recordings were downsampled to 1024 Hz, band-pass filtered at 1–200 Hz and corrected for gradient, pulse and blink artifact using EEGLab³. Spectral analysis (Kaiser window, β = 6, overlap = 25%) was performed on the EEG phantom and volunteer data using Matlab (The MathWorks Inc., Natick, USA).

Results/Discussion: Phantom power spectrum showed cold head artifact peaks from 11 to 150 Hz (Fig.1, Table 1) with the highest peak at 12 Hz and a peak group at ~ 115 Hz. With phantom EEG data as reference, volunteer recordings only showed the peak group at ~ 115 Hz. Commonly studied EEG frequency bands include delta to gamma waves within 0.1-40 Hz, and this range is not affected by the cold head artifact in EEG volunteer recordings (Fig. 2). Moreover, artifact peaks above 40 Hz can be filtered with a low-pass filter which would attenuate the peak group at ~ 115 Hz.

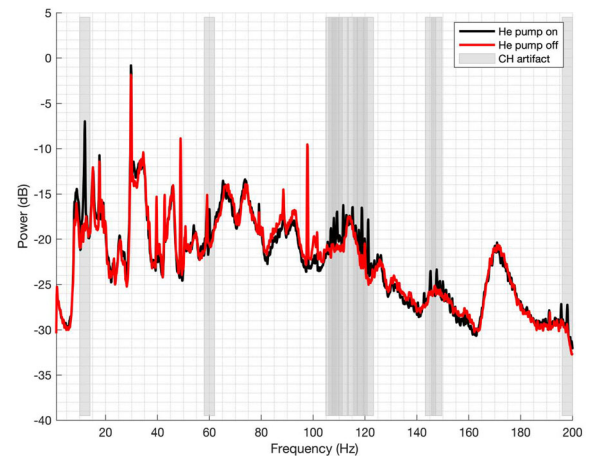


Figure 1. Average power spectra of EEG phantom recordings with the helium pump on (black) and off (red). Peaks with power difference greater than 2 dB between the pump on and off recordings were associated with the cold head artifact (shaded gray)

#	Frequency (Hz)	Power He pump on (dB)	Power He pump off (dB)	Absolute difference (dB)
1	12	-7.0	-18.9	11.9
2	121	-17.8	-24.8	7.0
3	119	-16.8	-22.5	5.7
4	112	-16.2	-21.2	5.0
5	60	-16.7	-20.6	3.9
6	109	-16.9	-20.6	3.6
7	108	-17.6	-21.0	3.4
8	107	-18.8	-22.0	3.3
9	118	-19.0	-21.6	2.6
10	145	-23.5	-26.1	2.6
11	198	-27.3	-29.7	2.4
12	115	-16.5	-18.9	2.4
13	148	-23.3	-25.6	2.2

Table 1. Cold head artifact peaks sorted by power difference between recordings with the helium pump on and off. As observed, the principal peak is at 12 Hz with a power difference of 11.9 dB.

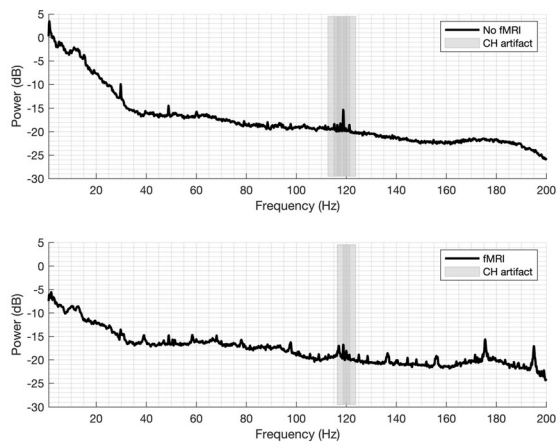


Figure 2. Average power spectra of EEG volunteer recordings with no fMRI sequence (top) and with fMRI sequence (bottom) at rest. Peaks associated with the cold head are at ~115 Hz (shaded gray).

This analysis suggests that with newer liquid helium recycling systems there is a decrease in the cold head artifact, compared to previous studies^{1,2}. We suggest turning the cold head off for simultaneous fMRI/EEG is not necessary. Nonetheless, characterization of this artifact should be carried out for each MRI system to conclude whether turning the helium pump off is necessary.

References: 1. Mulert, C. et al. (Springer Berlin Heidelberg, Berlin, Heidelberg, 2010)

2. Nierhaus, T. et al. *NeuroImage* **74**, 70–76 (2013)

3. Delorme, A. et al. *J. neuroscience methods* **134**, 9–21 (2004)

L01.106

Wavelet filtering of undersampled MRI using trainable wavelets and CNN

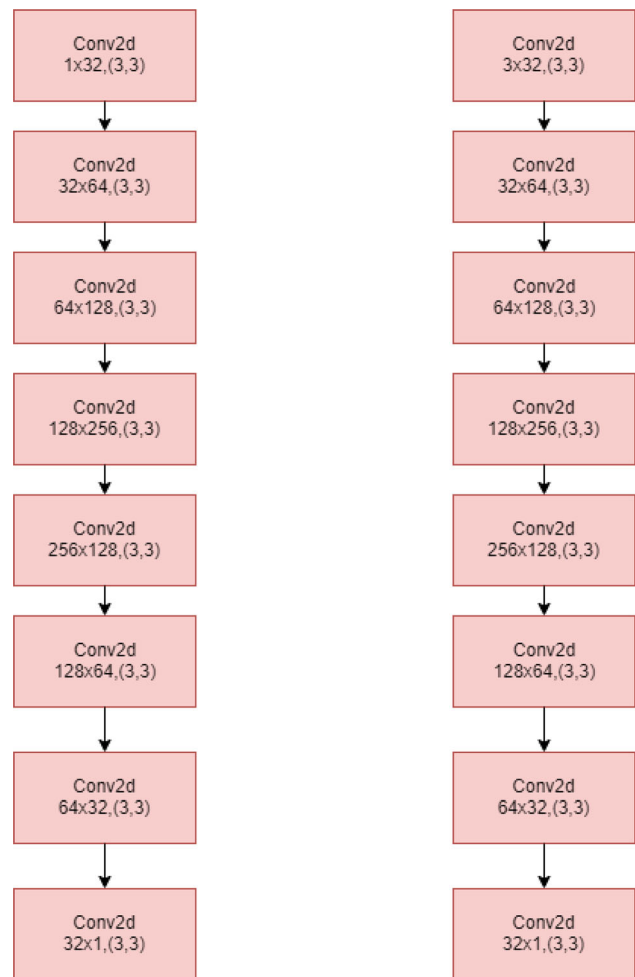
S. Chatterjee¹, P. Putti², A. Nürnberger³, O. Speck¹

¹Otto-von-Guericke University, Department of Biomedical Magnetic Resonance, Magdeburg, Germany, ²Otto-von-Guericke University, Faculty of Computer Science, Magdeburg, Germany, ³Otto-von-Guericke University, Data and Knowledge Engineering Group, Magdeburg, Germany

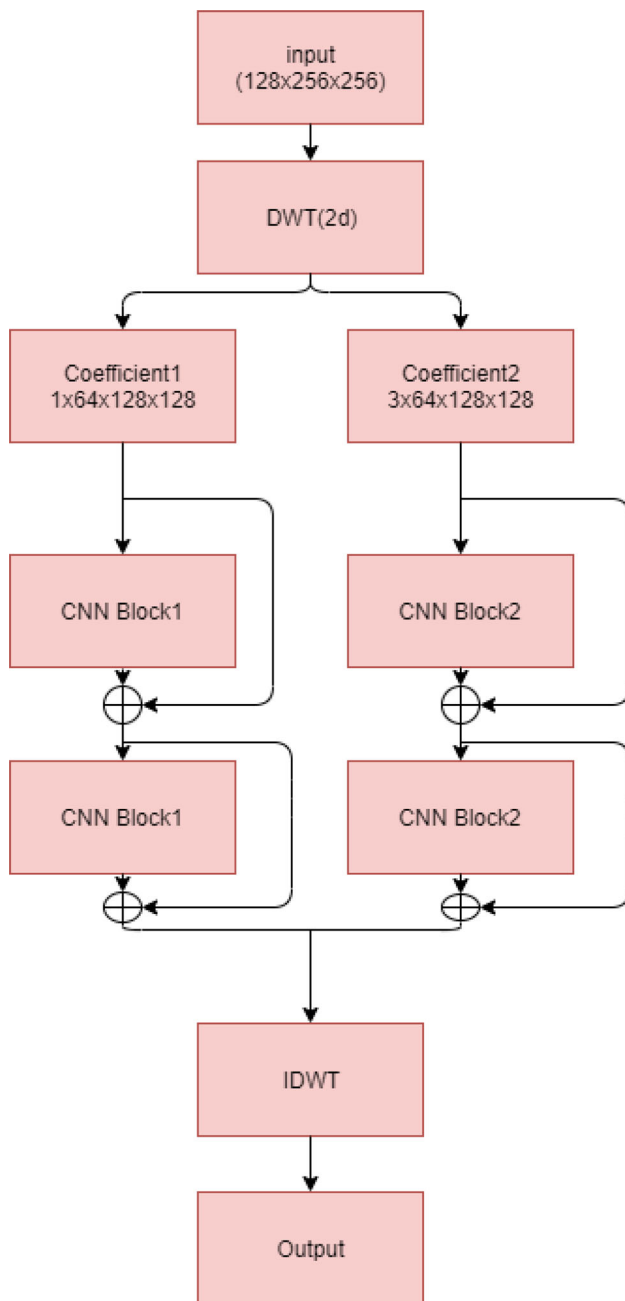
Introduction: Image processing for MRIs can be done in both Spatial and Frequency Domain. Wavelet is one of the frequency domain which can be used for such operations. The use of discrete wavelet transform (DWT) to remove the artifacts in the images are done in compressed sensing [1], where the image is thresholded iteratively in the wavelet domain, making it a time-consuming task. In this work, a Deep Learning approach has been proposed to work as the thresholding operator in the wavelet space. The idea is if a pattern for thresholding can be learned from the undersampled data itself, then for new unseen data thresholding can be performed using this and can be thresholded without the need of iterations, making the operation faster. Nonlinearity in deep learning can also help to find out other additional filtering patterns from the data.

Subjects/Methods: Fig1 illustrates the layers of the CNN blocks and Fig2 demonstrates the model architecture. Each of the convolution layers is followed by a PReLU with a number of parameters same as

the number of output feature maps in the preceding layer. Under-sampled 3D volumes were split into multiple 2D images and DWT [2] was applied, which resulted in two components; first with 1 channel and the second with 3; both with half of the size of the input image. These two components were sent to CNN Block1 and 2 respectively. The input of each of the blocks was added back with its output, to create a residual link [3]. Two of these residual blocks were stacked on top of another and the outputs of the second set of CNN Blocks were then merged to undergo an inverse DWT. IDWT brought the model output to the spatial domain and then the loss was calculated. The backpropagation lead to an update of the coefficients of DWT and learnt a thresholding pattern. In general, the filters (low pass and high pass) of the DWT are static and pre-computed. But in this implementation, they were made trainable, and were initialized with the default values [2] and then got updated over time during training - making it a trainable wavelet.

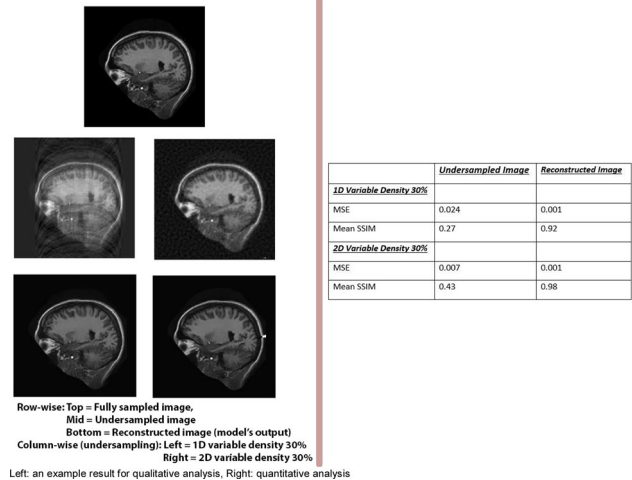


CNN Blocks with 1 and 3 channel input



Model Architecture

Results/Discussion: This approach uses only a few number of layers and has shown promising results by doing filtering in the wavelet domain. An example result has been shown in Fig3. Compressed sensing approaches only work for 2D variable density sampling, as the artefacts are noise-like. But this approach also performed well for 1D variable density sampling. Further tests must be performed for different patterns and levels of undersampling. Furthermore, the same strategy can be applied for removing the artifacts from EEG signals, and background noise during speech recognition.



References: [1] Lustig et al: "Sparse MRI: The Application of Compressed Sensing for Rapid MR Imaging". Magnetic Resonance in Medicine (2007)
 [2] https://github.com/fbcotter/pytorch_wavelets
 [3] Kaiming He et al: "Deep Residual Learning for Image Recognition". arxiv-1512.03385v1 (2015)

L01.107

From PCB to Simulation: a workflow instruction for designing birdcage models from production data

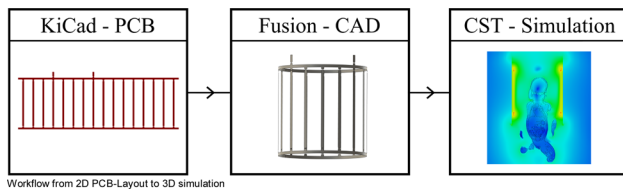
R. Kowal¹, M. Prier¹, E. Pannicke², R. Vick², O. Speck¹

¹Otto von Guericke University, Chair of Biomedical Magnetic Resonance, Magdeburg, Germany, ²Otto von Guericke University, Chair of Electromagnetic Compatibility, Magdeburg, Germany

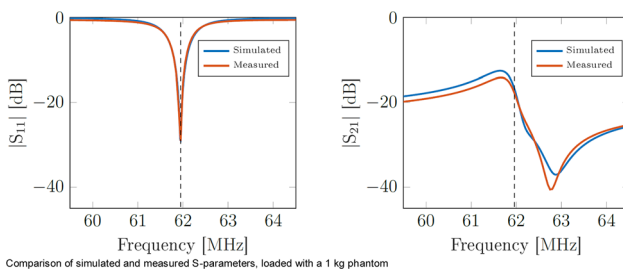
Introduction: Field simulations of birdcage coils in MRI permit the analysis of magnetic excitation fields and of safety relevant Specific Absorption Rate (SAR) distributions in human tissue [1]. The development of birdcage coils requires an in-depth analysis of the excitation fields to ensure safe usage of the MR system. However, the possibility to transfer simulation results to the real world depends on the quality of the underlying model. With continuously increasing computing power, more precise models can be simulated. A workflow is described for the development and evaluation of birdcage coils at 1.5 T. Using Printed Circuit Board (PCB) data, a one-to-one mapping of the coil's geometry into the simulation software is achieved. This assures that the simulated coil corresponds to the one built. Due to the flexible workflow, new design variations can be rapidly integrated and evaluated.

Subjects/Methods: The PCB production data are script generated and parameterizable designs. The geometric properties of the traces are adjustable, as well as the position and pads for the capacitors or further components. The created PCB is processed by an open source electronic design software (KiCad). Utilizing computer-aided design software (Fusion 360, Autodesk), the PCB-layout is used for structuring an unreel cylindrical structure, as is visualized in figure 1. The model can then be further imported to the field simulation software (CST, Dassault Systèmes). By filling it with lumped capacitors the desired resonant structure is created. Shown is the modeling of one of the designed 16-rung low-pass birdcage with a length and diameter of 26 cm. The scattering parameters of the resulting two port system were calculated in simulation and also measured for the real system using a vector network analyzer. Additionally the electric field

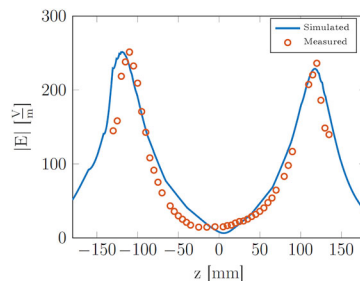
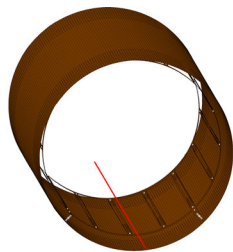
strength was measured with a field-probe (EASY6, Speag) along the z-axis and compared to the simulation.



Results/Discussion: The simulated coil's S-parameters match the measured ones (fig. 2), using the same coarse tuning capacitance values in the rungs. Measured and simulated electric field match each other as well, especially the strength of the end ring maxima (fig. 3). Together this verifies the modeling process and its precision. The workflow allowed for efficient testing of design variations, accelerating development iterations of the birdcage coil.



Comparison of simulated and measured S-parameters, loaded with a 1 kg phantom



Simulated and measured electric field along z-axis (red line), 1W per port

References: [1] Malik et al., NMR in Biomedicine 28.3, 2015, p. 344-352.

L01.108

High-input impedance preamplifiers for multi-channel strategies at low frequency

T. Quirin^{1, 2}, M. Yushchenko¹, N. Salameh¹, M. Sarracanie¹

¹Center for Adaptable MRI Technology (AMT Center), University of Basel, Department of Biomedical Engineering, Allschwil, Switzerland, ²Institute for Medical Engineering and Medical Informatics, University of Applied Sciences and Arts Northwestern Switzerland, School of Life Sciences, Muttenz, Switzerland

Introduction: Approaches to increase signal-to-noise ratio (SNR) per unit-time at a fixed static magnetic field [1-2] are crucial to maximize low field MRI potential [3]. At low frequency, the principal source of noise comes from the acquisition chain, hence reducing the latter is

key to enhancing SNR [4]. Multi-channel detection strategies could also exploit the non-coherence of noise sources (Johnson noise dominated regime) at low field to increase detection sensitivity. Here, we present a custom high-input impedance preamplifier for MRI at 4.25 MHz (0.1T) that shows good decoupling in multi-channel detectors, and high SNR performance.

Subjects/Methods: Multi-channel detection is used in MRI to extend spatial coverage, accelerate acquisitions via undersampling strategies and increase detection sensitivity [5]. To explore this approach at low frequency, we designed and built a set of two (identical) preamplifiers made of two amplification stages. The input stage is based on Junction Field Effect Transistors (JFETs) to provide high-input impedance and low noise floor. The second stage consists in a bipolar amplifying stage acting as a low-noise high-gain stage. At 4.25 MHz, simulations show an input-referred noise voltage density of 1.17 nV/Hz at 39.5-dB gain for a 1-M Ω output load. Decoupling performance was characterized on the bench with a weakly coupled double-loop probe and a vector network analyser (VNA), by connecting the preamplifier prototypes to in-house surface coils (4-cm diameter, 4-turn) [6] (Fig. 1).

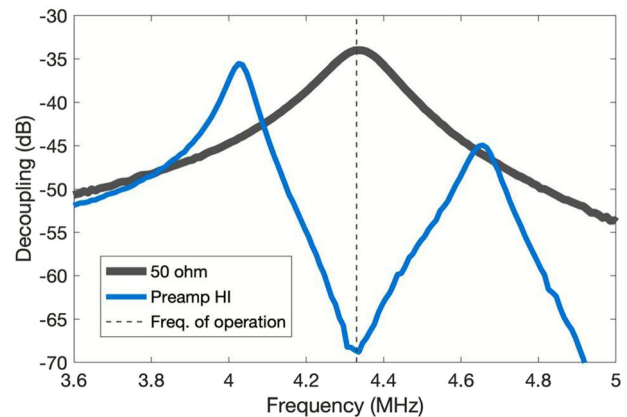


Fig 1: Preamplifier decoupling. The blue curve represents the configuration of 4-cm diameter surface coils connected to our high-input impedance preamplifiers. The dark grey curve represents the same coils connected to a 50 Ω load.

Decoupling was also assessed with MRI, imaging a 2-cm thick silicone phantom placed between two 4-cm, 4-turn surface coils, both detectors facing each other (Fig. 2).

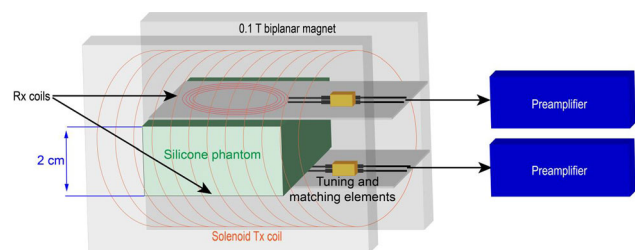


Fig 2: Experimental setup installed in the imager to assess the preamplifier decoupling performance with MRI.

Results/Discussion: We demonstrated proof-of-concept of a high-input impedance preamplifier design for low frequency NMR/MRI. Mean SNR measured in MR images was 36.1, compared to 33 with a commercial preamplifier (NMR Service GmbH, Germany). Decoupling observed with imaging is consistent with measurements realized on the bench.

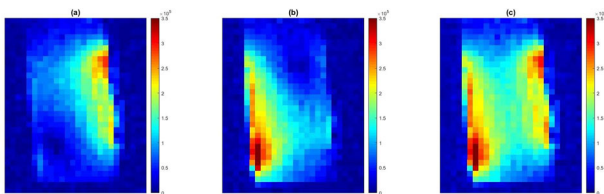


Fig 3: MR images (1 partition of 3D data) with two Rx coils connected to the high-input impedance preamplifiers. Separate images acquired with the first (a) and second coil (b), and (c) the composite image reconstructed from the two channels (a & b).

Fig. 3 shows that the sensitivity of each antenna is minimally influenced by the second one. These preliminary results are promising for future applications of multi-channel detection at low frequencies. Further improvements include minimizing noise with alternative topologies for the first amplifying stage, or increasing input impedance from higher performance components.

- References:** [1] P.B. Roemer *et al.*, *Magn. Reson. Med.*, 16:192–225, 1990
 [2] B.L. Sorgenfrei *et al.*, *Magn. Reson. Med.*, 36:104–110, 1996
 [3] M. Sarracanie *et al.*, *Front. Phys.*, 8:1–14, 2020
 [4] D.I. Hoult, *Rev. Sci. Instrum.*, 50:193–200, 1979
 [5] A. Deshmane *et al.*, *J. Magn. Reson. Imaging*, 36:55–72, 2012
 [6] J.D. Sanchez *et al.*, *Proc. ISMRM 25th Ann. Meeting*, 2017

L01.109

In-vivo imaging using an open biplanar volume coil at 0.1 T

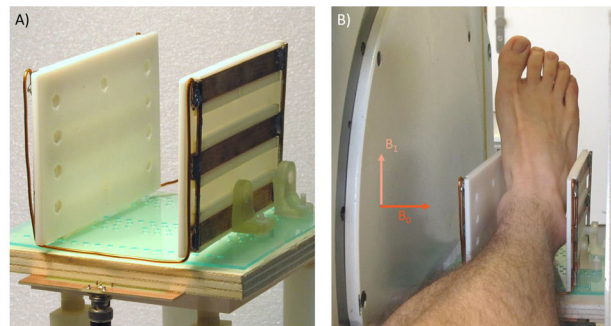
M. Yushchenko, M. Sarracanie, N. Salameh

Center for Adaptable MRI Technology (AMT Center), University of Basel, Department of Biomedical Engineering, Allschwil, Switzerland

Introduction: Low-field MRI systems often employ open, biplanar magnets to combine the advantages of low field with enhanced access to the patient. The proposed biplanar volume coil¹ follows the same philosophy, enabling simple positioning and comfortable patient scanning from its open access, while maintaining good B₁ homogeneity and filling factor. Such a geometry appears particularly handy for ankle imaging in various positions, as opposed to conventional volume coil geometries² (e.g. solenoids or Helmholtz) due to the foot’s peculiar shape and orientation with respect to the leg. Here, we demonstrate proof-of-concept of fast *in-vivo* acquisitions of a human ankle, relying on the proposed custom-built biplanar transceiver coil at 4.2 MHz (0.1 T).

Subjects/Methods: The coil’s side planes are made of three Cu bars (15 x 3 x 140 mm) connected in parallel via Ø 3 mm Cu rods (total inner volume: 85 x 100 x 140 mm). The planes are connected in series and tuned by a 3.28 nF capacitor to 4.2 MHz. Inductive coupling was used to interface the coil³ and reduce its bandwidth in undermatched condition (BW: 25 kHz, Q: 170). The inter-plane connecting wires are positioned so to leave three sides accessible from any angle (Fig 1A, B). MRI was performed on a resistive biplanar 0.1 T magnet (Bouhnik S.A.S., France) designed for imaging extremities, with the coil interfaced in transceive mode using a TR switch (NMR Service, Germany) and a custom preamplifier. A 3D bSSFP sequence (details in Fig 1C) was run on a Cameleon3 spectrometer (RS2D, France) with a variable Gaussian density k-space sampling pattern of 50% for phase-encoding. The k-space was filtered with a Tukey window

(cosine fraction 0.5) using MATLAB (Mathworks, USA), and zero-filled to double the matrix size in 3D.



C)

Data	FOV (mm ³)	Acquired matrix	Acq. voxel size (mm ³)	Reconstructed matrix	Rec. voxel size (mm ³)	TE/TR (ms)	NA	Acquisition time
1	160 x 160 x 68	100 x 100 x 9	1.6 x 1.6 x 7.5	200 x 200 x 19	0.8 x 0.8 x 3.6	4.5 / 8.7	120	7 min 52 s
2	160 x 160 x 57	100 x 100 x 15	1.6 x 1.6 x 3.8	200 x 200 x 31	0.8 x 0.8 x 1.8	4.5 / 8.7	160	17 min 29 s

Fig 1: Materials and methods: A) biplanar coil with the inductive coupler underneath; B) example of foot positioning in the biplanar coil within the 0.1 T magnet; C) sequence parameters of the acquired bSSFP scans (NA: number of averages).

Results/Discussion:

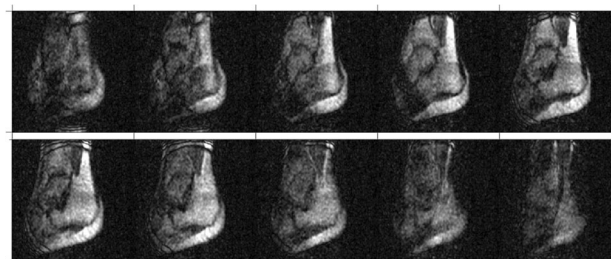


Fig 2: Results: reconstructed 3D bSSFP images acquired with our biplanar coil at 0.1 T, ankle of volunteer 1, sagittal view. Voxel size 0.8 x 0.8 x 3.6 mm, acq. time 7 min 52 s. Top: slices 5-9, bottom: sl. 10-14 out of 19.

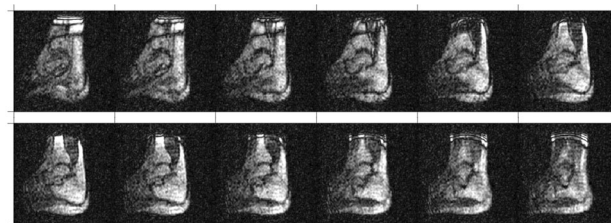


Fig 3: Results: reconstructed 3D bSSFP images acquired with biplanar coil at 0.1 T, flexed ankle of volunteer 2, sagittal view. Voxel size 0.8 x 0.8 x 1.8 mm, acq. time 17 min 29 s. Top: slices 6-11, bottom: sl. 12-17 out of 31.

Sagittal images from two healthy volunteers are shown in Fig 2 & 3. Good contrast is observed between bones/tendons (hypersignal) and muscles/joint interstitial space (hyposignal). Typical bSSFP banding artifacts appear on the edges of the field of view (FOV). The coil maintains good sensitivity over its entire volume, including towards the edges. Despite some limitations from a reduced inductance and sensitivity, e.g. in comparison with a solenoid, this coil allowed to perform *in-vivo* ankle imaging at low frequency with high

resolution within acceptable acquisition times. The coil's geometry can be scaled for optimal coverage and positioning of different body parts. Complementing the advantages of low-field with open access detectors shows great potential for a variety of MRI applications, such as standing and intra/post-operative MRI without artifacts from surgical instruments and orthopedic hardware.

References: 1. Roberts 1993 J Magn Res
2. Mispelter 2008 Comp Rend Chim
3. Hoult 2002 Conc Magn Res

L01.110

Transmit-/receive system for combined temperature sensitive proton-/fluorine-iimaging in a 7 T whole-body MRI system

C. Bruns, M. Plaumann, T. Herrmann, F. Euchner, J. Bernarding

Otto-von-Guericke University, Institute of Biometrics and Medical Informatics, Magdeburg, Germany

Introduction: ^{19}F MR research became more important during the past years¹. Topics are the development of MR contrast media and the detection of fluorine nuclei in living organisms, e.g. in metabolisms studies². The huge chemical shift range and the high MR sensitivity predestine ^{19}F for the determination of e.g. changes in temperature. Until now, there are only a few published data that described the influence of temperature changes on the ^{19}F signals. The low natural abundance of ^{19}F in living organisms leads to background-free ^{19}F images. These facts result to the idea of this study to develop new types of temperature sensitive contrast agent.

Here we present the development of a transmit-receive system for 7T whole-body MRI and its usage for ^{19}F imaging, spectroscopy and temperature detection.

Subjects/Methods: Several substances were selected as model compounds for temperature dependence ^{19}F NMR measurements. For preliminary investigation and calibration, these substances were measured with a Bruker WB300 NMR spectrometer between 300K and 330K.

Furthermore, same solutions were measured in a human whole-body 7T MR (MAGNETOM) system. Therefore, a 4-elements transmit-/receive coil and a transmit-/receive box based on Wilkinson power dividers and transmit-/receive switch was developed. Both, the RF-coil and the transmit-/receive box were broad banded optimized to the ^{19}F MR signal. This aims a sufficiently high gain of the ^{19}F MR signal. This aims a sufficiently high gain of the ^{19}F MR signal. This aims a sufficiently high gain of the ^{19}F MR signal. The samples in the 7T whole-body scanner were heated and ^{19}F MR spectra and images were obtained during the following cooling process.

Results/Discussion:

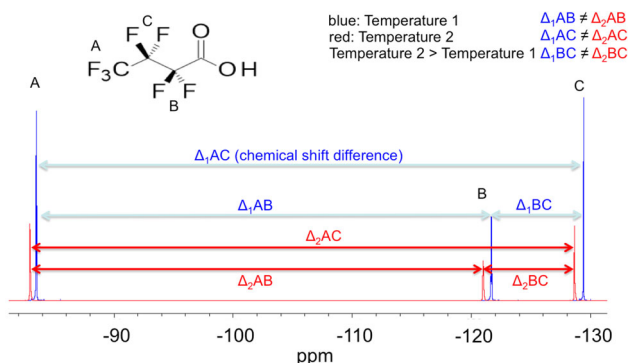


Fig. 1: Temperature dependency of the ^{19}F NMR signals of heptafluorobutyric acid in aqueous solution: Each signal of every group shows up a characteristic change of chemical shift to higher frequencies for higher temperatures and a loss of intensity.

An overlay of ^{19}F NMR spectra demonstrates in Fig. 1 that all signals shifted. The chemical shift differences determined by us vary between 1.4Hz/K (3-fluoropyridine) and 8.7Hz/K (2-fluoro-4-(trifluoromethyl)-pyridine-3-carboxylic acid). The temperatures can thus be determined from the distances between two signals of a molecule. The MRI experiments with the developed transmit-/receive system end up by a resolution of $0.3 \times 0.3 \times 1.00 \text{ mm}^3$ and concentrations beneath 40 mM (Fig. 2).

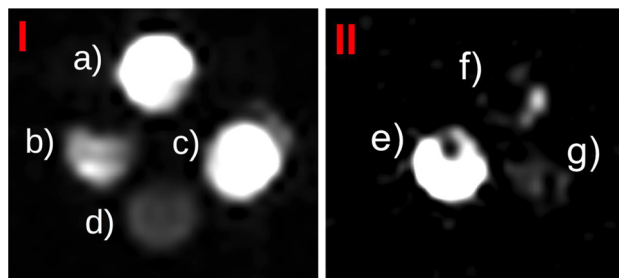


Fig. 2: ^{19}F imaging (I: UTE sequence, TE=8 ms, TR=200 ms; II: FLASH sequence, TE=4.8 ms, TR=2500 ms) of 15 ml falcon tubes with different concentrations of infuoroethanol: a) 926.9 mM, b) 231.7 mM, c) 463.4 mM, d)

A decrease of signal intensity like in the NMR experiments was detected for higher temperatures, leading to lower contrasts (Fig. 3).

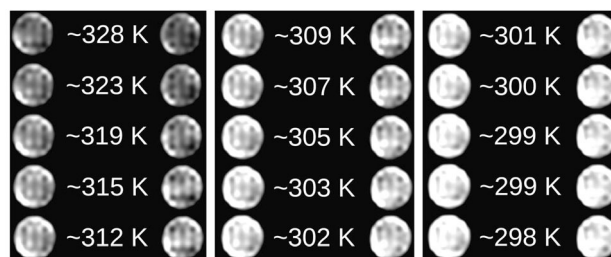


Fig. 3: The contrast in the ^{19}F MRI is temperature dependent. These images (FLASH-sequence) base on the two CF groups (one group on the left-hand side and one on the right-hand side) of heptafluorobutyric acid in aqueous solution.

Further experiments for a 3D temperature map are in investigation and the search for water soluble fluorinated molecules is going on. Another idea is to add paramagnetic ions to reduce relaxation times. If the ^{19}F signal intensity remains high enough, the gain is based on the shortening of the acquisition time.

These first comparable data on the relationship between molecular structure and ^{19}F chemical shifts at 7T are important for future studies in the field of development of temperature sensitive contrast agents.

References: 1 Waiczies, S *et al.* *MAGMA* **32**, 1–3 (2019).

2 Ruiz-Cabello J *et al.* *NMR Biomed.* **24**(2):114–129 (2011).

L01.111

Applying a direct spectral baseline parameterization method to short echo time proton magnetic resonance spectroscopy in different regions of rats

C.-H. Yoo¹, H.-M. Baek², D.-C. Woo³, B.-Y. Choe¹

¹The Catholic University of Korea, Seoul, South Korea, ²Gachon University, Department of Health Sciences and Technology, Incheon, South Korea, ³Asan Medical Center, Asan Institute for Life Sciences, Seoul, South Korea

Introduction: The effects of a spectral baseline mainly contributed by macromolecules (MM) of lipids signals have been increasingly investigated for high-field and short-echo-time (TE) proton magnetic resonance spectroscopy (MRS). Several studies have reported that the directly measured MM baseline can improve quantification accuracy and reliability compared to conventional baseline handlings. However, a direct measurement of the MM baseline requires an additional scan session, and can be affected by T1-weighting. Recently, a direct parameterization of spectral baseline from short TE MRS has been proposed, and suggested as feasible. The aim of this study was to apply the direct spectral baseline parameterization method to high-field and short-TE MRS, and to compare the results with conventional quantification methods.

Subjects/Methods: All the MRI/MRS scans of eight Sprague–Dawley rats and in vitro phantom were performed using a Bruker PharmaScan® 7T MRI system with a 72-mm linear transmit resonator, and surface coil. Multislice T2-weighted images and high-field short-TE MRS spectra were acquired with the sequence and parameters listed in Table 1.

Table 1. Acquisition protocols for T2-weighted images and high-field short-TE MRS.

Protocol	Sequence	TR/TE (ms)	FOV (mm)	Matrix size	Resolution	RARE factor	Averages
T2-weighted image	T2 TurboRARE	2000/33	12 × 12 × 15.6 mm ³	120 × 120 × 156	100 μm isotropic	16	2
	Sequence	TR/TE (ms)	RF pulses	Voxel sizes	Data points	Spectral bandwidth	Averages
High-field short-TE MRS	PRESS	4000/15.016	90°-excitation pulse (8400 Hz; 0.5 ms) 180°-refocusing pulses (3400 Hz; 1.0 ms)	2 × 1.5 × 1.2 mm ³ (PFC) 2 × 1.2 × 2.0 mm ³ (hippocampus)	2048	5000 Hz	192

Table 2. The initial line parameters of the metabolites basis sets. The linewidth of each peak was determined by the *in vitro* experiment.

Peak number	Metabolites	Chemical shifts (ppm)	Linewidth (Hz)
1	tNAA- ² CH ₃	2.01	12
2	Glx- ³ CH ₂	2.13	30
3	Glu- ⁴ CH ₂	2.35	19
4	Gln- ⁴ CH ₂ NAA- ³ CH ₂	2.46	34
5	NAA- ³ CH ₂	2.67	20
6	tCr-CH ₃	3.03	11
7	tCho-(CH ₃) ₃	3.19	9
8	Tau- ² CH ₂ mI- ⁵ CH	3.25	20
9	Tau- ¹ CH ₂	3.42	11
10	mI- ^{1,3} CH	3.52	19
11	mI- ^{4,6} CH	3.61	18
12	Glx- ² CH	3.75	16
13	tCr-CH ₂	3.92	10
14	mI- ³ CH	4.05	19
15	NAA- ² CH	4.38	37

Table 1 and 2

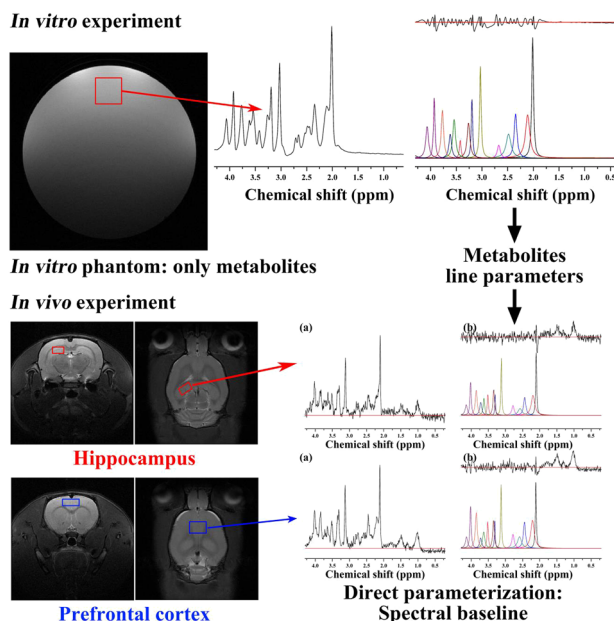


Figure 1. Schematic diagram of the experimental protocol of this study.

As illustrated in Figure 1, the direct parameterization of the spectral baseline was performed referring to the study of Kim et al. using the jMRUI software with the AMARES algorithm. Initial line parameters of the metabolites basis sets, used for the parameterization of the MM baseline, were acquired from the *in vitro* phantom. With the parameterized MM baseline included, the quantification of the acquired spectra in the hippocampus and prefrontal cortex was performed with the QUEST algorithm.

Results/Discussion:

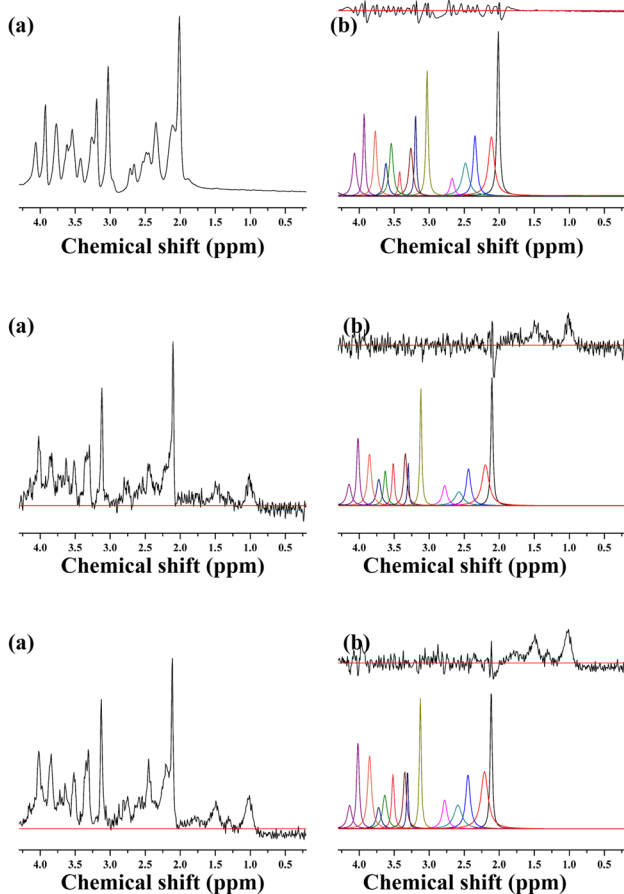


Figure 2. Representative *in vitro* 1H MRS spectra. Figure 3. Representative *in vivo* 1H MRS of the hippocampus. Figure 4. Representative *in vivo* 1H MRS of the prefrontal cortex.

Figure 2 shows the results of the *in vitro* experiments. As shown in Table 2, the initial line parameters of the 15 metabolites basis sets were acquired from the *in vitro* experiment. Figure 3-4 illustrates representative high-field and short-TE MRS scans of the hippocampus and prefrontal cortex of the rats. For the parameterization of the MM baseline, the *in vivo* scans were decomposed into 15 metabolites peaks with the acquired initial line parameters, with initially 20 Gaussian peaks for MM baseline. The number of peaks and line parameters of MM baseline were optimized with minimizing residual standard deviation in the spectra. Although, the IR-based MM measurement has suggested as a gold standard method, the application of direct parameterization may provide an improved insight into the

spectral baseline compared to the conventional mathematical approximation without any additional scans.

References: 1. Lee HH, Kim H. Parameterization of spectral baseline directly from short echo time full spectra in 1 H-MRS. *Magn Reson Med.* 2017;78(3):836-847. doi:10.1002/mrm.26502

L01.112

Investigating the partial volume effects in magnetic resonance spectroscopy localization using high-resolution 3D MRI and segmentation

C.-H. Yoo¹, H.-M. Baek², B.-Y. Choe¹

¹The Catholic University of Korea, Seoul, South Korea, ²Gachon University, Department of Health Sciences and Technology, Incheon, South Korea

Introduction: Previous studies have proposed the methods that can decompose the mouse brain MRI scans into various anatomical regions. By performing proper registration of the high-resolution MRI to a brain atlas, an advanced tissue compartmentalization can be achieved, instead a simple decomposition into white matter, gray matter, and cerebrospinal fluids (CSF). The aim of this study was to investigate partial volume effects on proton magnetic resonance spectroscopy (¹H MRS) voxels in the mouse brain, using high-resolution 3D MRI and segmentation.

Subjects/Methods: All MRI/MRS scans were acquired with Bruker BioSpec® 94/20 USR system with a 72-mm linear transmit resonator, and 4-channel phased-array surface coil. High-resolution 3D T2-weighted images and high-field short-TE MRS spectra were acquired with the sequence and parameters listed in Table 1.

Table 1. Acquisition protocols for high-resolution 3D T2-weighted images and high-field short-TE MRS.

Protocol	Sequence	TR/TE (ms)	FOV (mm)	Matrix size	Resolution	RARE factor	Averages
high-resolution 3D T2WI	T2 TurboRARE	2000 /33	12 × 12 × 15.6 mm ³	120 × 120 × 156	100 μm isotropic	16	2
	Sequence	TR/TE (ms)	RF pulses	Voxel sizes	Data points	Spectral bandwidth	Averages
High-field short-TE MRS	PRESS	4000/ 15.016	90°-excitation pulse (8400 Hz; 0.5 ms) 180°-refocusing pulses (3400 Hz; 1.0 ms)	2 × 1.5 × 1.2 mm ³ (PFC) 2 × 1.2 × 2.0 mm ³ (hippocampus) 1.5 × 1.5 × 2 mm ³ (striatum)	2048	5000 Hz	16 × 40

Table 2. Mean concentrations and CRLB values acquired by MRS from the three voxels.

		Metabolites									
		tCr	tNAA	tCho	Glu	Gln	Glx	mIns	Tau	GSH	GABA
Prefrontal cortex	Conc.	12.50	11.42	2.27	13.44	5.24	18.69	8.37	19.12	2.96	4.56
	(μmol/g)	±2.72	±1.48	±0.26	±0.59	±1.31	±1.76	±1.96	±2.50	±1.10	±1.02
	(%SD)	±0.55	±0.55	±0.55	±0.55	±2.00	±0.55	±0.71	±0.45	±2.17	±1.30
Hippocampus	Conc.	11.26	7.90	1.84	8.30	4.16	12.46	7.02	13.32	2.81	3.45
	(μmol/g)	±0.62	±0.94	±0.25	±0.91	±0.48	±1.32	±0.28	±0.51	±0.13	±0.80
	(%SD)	±0.55	±0.84	±0.84	±0.84	±1.79	±0.89	±0.71	±0.45	±0.71	±3.36
Striatum	Conc.	11.07	8.15	2.16	10.26	5.23	15.50	6.78	21.22	3.22	4.00
	(μmol/g)	±0.86	±1.23	±0.22	±1.64	±0.50	±1.97	±1.00	±3.00	±0.59	±0.69
	(%SD)	±0.86	±1.23	±0.22	±1.64	±0.50	±1.97	±1.00	±3.00	±0.59	±0.69

Table 1 and 2

The acquired 3D T2WI scans were segmented into the brain regions using Atlas-based imaging data analysis (AIDAmri) pipeline.

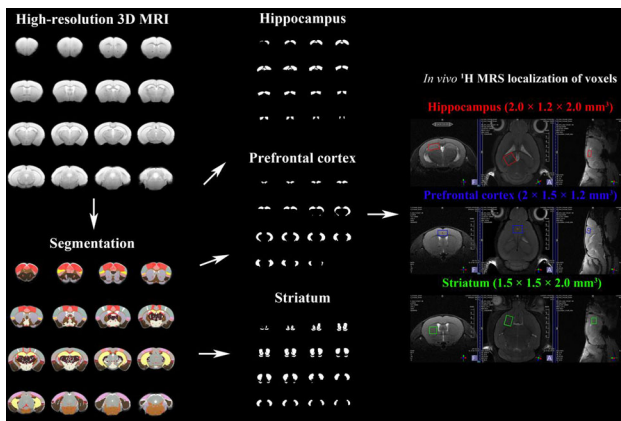


Figure 1. A schematic diagram of the experimental protocol of this study.

As described in the schematic diagram of Figure 1, a volumetric analysis on the localized voxel and anatomical regions was performed.

Results/Discussion:

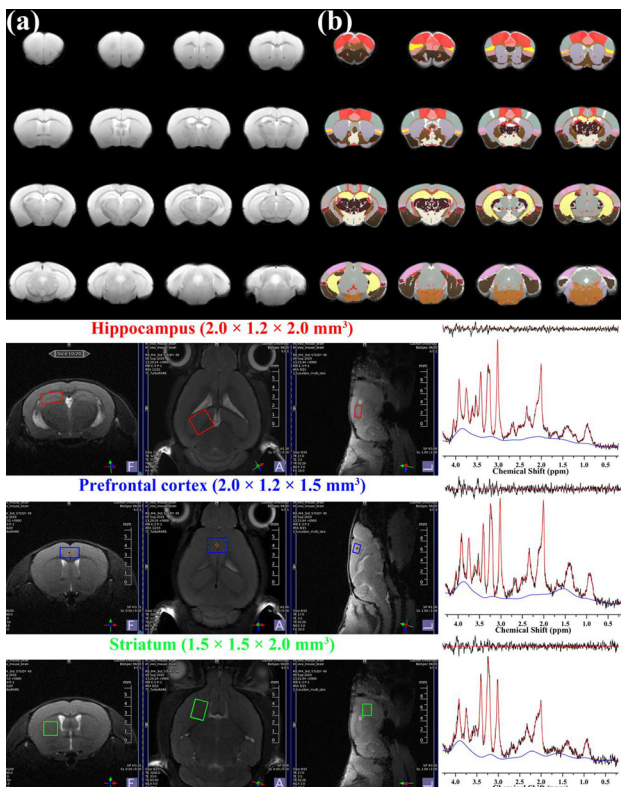


Figure 2. Representative (a) high-resolution 3D T2-weighted MRI scans obtained in the mouse brain with the TurboRARE sequence. Figure 3. Representative in vivo ^1H MRS spectra of the hippocampus (topside), PFC (middle), and striatum (bottom).

Figure 2 illustrates representative high-resolution 3D T2WIs. As visually inspected, the acquired MRI scans showed sufficient SNR for the whole brain region with the high spatial resolution (100 μm). In addition, the co-registration and segmentation was reliably performed without artifacts. Figure 3 illustrates representative MRS scans obtained in the (a) hippocampus, (b) prefrontal cortex, and (c) striatum with the localized voxel, respectively. Table 2 lists the mean concentrations and CRLB values. The CRLB values of the major metabolites were reliable for the voxels. In this study, the atlas-based automatic brain segmentation was applied to high-resolution 3D MRI of the mouse brain, and the brain was decomposed into various anatomical regions. By volumetrically analyzing binary masks of the tissue label and voxels, the true contribution of the intended tissue compartment in the localized voxel can be assessed. In addition, by analyzing the metabolite-specific volume masks, an agreement of the localization between major metabolites can be evaluated in conjugate with the chemical shifts displacements. By evaluating the true contribution of the intended region and metabolite-specific agreement of localization, localization reliability can be improved.

References: 1. Niklas Pallast et al. Processing Pipeline for Atlas-Based Imaging Data Analysis of Structural and Functional Mouse Brain MRI (AIDAmri). *Front Neuroinform*, 2019;13:42.
2. Robin Simpson et al. Advanced Processing and Simulation of MRS Data Using the FID Appliance (FID-A)-An Open Source, MATLAB-based Toolkit. *Magn Reson Med*, 2017;77:23-33.

L01.113

The lactate signal in postmortem skeletal muscle detected with non-water-suppressed proton MR spectroscopy

F. Riedel¹, D. Gascho², H. Richter³, S. Kozerke¹, N. Zoelch²

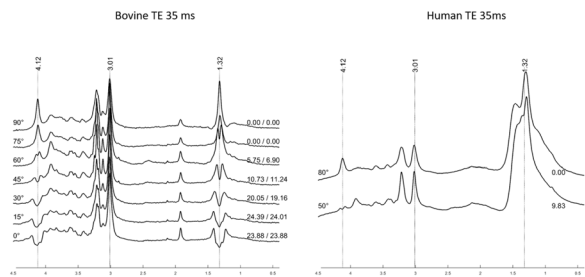
¹ETH Zurich, Institute for Biomedical Engineering, Zurich, Switzerland, ²University of Zurich, Institut for Forensic Medicine, Zurich, Switzerland, ³University of Zurich, Clinic of Diagnostic Imaging, Vetsuisse Faculty, Zurich, Switzerland

Introduction: The detection of lactate in human skeletal muscle by proton magnetic resonance spectroscopy (MRS) is hampered by interference from lipid signals and a relatively low concentration at rest. In addition, the appearance of the lactate resonances depends on the orientation of the muscle fibers relative to the main magnetic field (B_0) due to residual dipolar coupling¹. Therefore in vivo at rest the lactate signal is in general only detectable with spectral editing methods. In this work we used postmortem human and bovine muscle tissue to investigate the lactate methine (at 4.1 ppm) and methyl (at 1.31 ppm) resonances in situ by a simple PRESS based method. In postmortem tissue lactate levels are increased due to anaerobic glycolysis. The goal was to improve the understanding of the lactate resonance in muscle tissue and with that potentially the detection of lactate using basic MRS sequences.

Subjects/Methods: Experiments were performed in a human corpse (male, age: 21 y, postmortem interval (PMI): 55 hours, temperature: 13.5 °C) and a detached muscle from a bovine leg (stored for one month at 5°C, measured at 22°C). MRS spectra were acquired on a 3T whole-body MRI scanner (Achieva, Phillips Healthcare) in the musculus soleus (human corpse) and the rectus femoris (bovine leg).

Measurements were conducted at different angles of the muscle relative to the main magnetic field axis and at different echo times. All spectra were acquired with non-water-suppressed PRESS localization sequence using the metabolite cycling (MC) technique² (TR = 3000 ms, 128 averages, 14 × 17 × 14 mm³ effective voxel size). Simulations of the TE dependence were performed using VeSPA³.

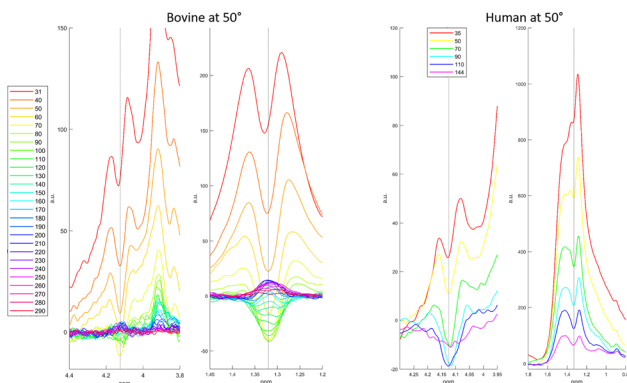
Results/Discussion: The MC PRESS sequence enables a robust in situ detection of the lactate methine peak in close vicinity to the water peak. This allows studying the orientation dependence of the lactate signal even in the human muscle where lipid resonances obscure the methine peak.



Orientation dependence of the lactate resonances due to residual dipolar coupling. On the left the measured splitting (in Hz) for the resonances at 4.1 and 1.3 ppm are given.

The frequency splitting observed for the methine and the methyl peaks is due to a combination of J-coupling and orientation dependent residual dipolar coupling ($\Delta f = J + 1.5 * D * (1 - 3 * \cos(\alpha)^2)$) with a minimal splitting for $\alpha \approx 75^\circ$. Our observations are in agreement with earlier results obtained from double quantum NMR spectra of the lactate methyl resonance in bovine muscle samples¹.

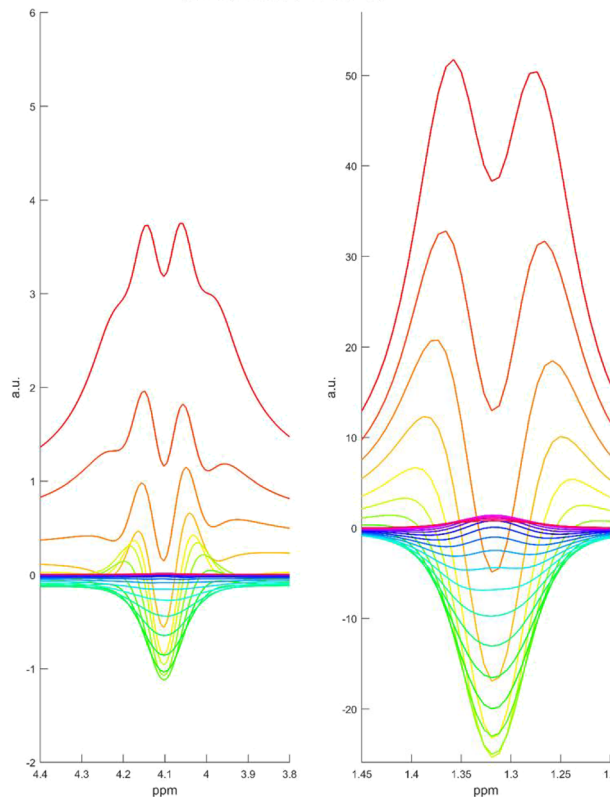
At smaller angles ($\alpha < 65^\circ$), the frequency splitting seems to increase with increasing TE.



Measured echo time dependence of the lactate resonances at 4.1 and 1.3 ppm. The frequency splitting appears to increase with increasing TE.

This has already been noted⁴ for the methine resonance measured with TE 100 and 140 ms after exercise at 7T. However, this behavior is simply explained by the different phase the two involved resonances are collecting as demonstrated by the simulated spectra.

Simulation at 50°



Simulated lactate peaks obtained for an ideal press localization, $\Delta f = 7$ Hz and using measured T2 of 50 and 30 ms for methyl and methine, respectively. The measured pattern in situ at 50 degree is well reproduced

At $\alpha \approx 75$ both resonances collect no phase, resulting in a higher signal and allowing pure T₂ measurements for lactate.

References: 1. Asllani I, *JMR* 1999
 2. Dreher W, *MRM* 2005
 3. Soher B, *ISMRM* 2011
 4. Ren J, *MRM* 2013

L01.114

A comparison of criteria for automatic detection of arterial input function in DSC-MRI

R. Sobhan, D. Cameron, G. Johnson

University of East Anglia, Norwich Medical School, Norwich, UK

Introduction: Perfusion quantification through dynamic susceptibility-contrast MRI (DSC-MRI) requires determination of the arterial input function (AIF)—the concentration time course (CTC) of the contrast agent (CA) in an arterial voxel (AV)¹. Automatic detection is faster, more objective, and reproducible than its manual variant, which involves visual assessment of the CTCs from prospective AVs. To discard soft tissue voxels, empirical thresholds are applied on criteria corresponding to several characteristics of an arterial bolus—

e.g. early arrival, narrow width, and high peak^{1,2}. Optimal thresholds for these criteria have not been studied systematically.

In this study, we compare the individual effectiveness of ten AV detection criteria and systematically determine the optimal threshold ranges for the effective criteria.

Subjects/Methods: DSC-MRI data were acquired from nine subjects at 1.5T (Siemens Vision/Symphony; Germany) with a gradient-echo echo-planar imaging sequence during the first pass of a 0.1 mmol/kg bolus of gadopentetate dimeglumine: TR/TE = 1000/47ms; acquisition time, 60s; flip angle = 30°; slice thickness = 5 mm; FOV = 220 × 220 mm; matrix = 128 × 128.

Signals were converted to CTCs. For each curve, values were extracted for eight previously proposed criteria: area under the curve (AUC); full width at half maximum (FWHM); peak concentration (PeakConc); first moment; time to peak (TTP); bolus arrival time; wash-in rate (MWI); and M_{peak} , which combines three criteria ($M_{\text{peak}} = \text{PeakConc} \div (\text{TTP} \times \text{FWHM})$)². Further, two novel criteria—duration of first pass and rate of concentration drop (MWO)—were explored. True AVs were obtained by a semi-automatic process that included visual inspection.

For each criterion, a receiver operating characteristic (ROC) curve was generated. The mean area under this curve (AUC_{ROC}) gave the discriminatory power of each criterion for separating AV from soft tissue voxels. The optimal threshold for each criterion was the point on the ROC curve with the highest Youden index³ and was presented as a percentage increase from the mean criterion value over all brain voxels.

Results/Discussion: AUC, PeakConc, M_{peak} and MWO showed $AUC_{\text{ROC}} > 0.97$ ($p > 0.01$, two-way ANOVA). All other criteria had $AUC_{\text{ROC}} < 0.5$ —failing to identify AVs. The mean (SD) of optimal thresholds were 64.23(22.54), 142.68(65.14), 118.90(69.85) and 9.11(27.46)-% above the overall means of AUC, PeakConc, M_{peak} and MWO, respectively.

In conclusion, AUC, PeakConc, M_{peak} and the proposed MWO are effective AV detection criteria. Combining them into one criterion could increase the AUC_{ROC} (i.e. effectiveness). The systematically obtained optimal thresholds will assist any future threshold-based AV detection.

References: 1. Calamante. *Prog Nucl Magn Reson Spectrosc*, 2013.74: p. 1-32 .

2. Yin. *J Magn Reson Imaging*, 2015. 41(4): p. 1071-8.

3. Krzanowski. 2009: ROC curves for continuous data.

L01.115

A comparison of impulse response functions for model-dependent deconvolution in Dynamic Susceptibility Contrast MRI

R. Sobhan, D. Cameron, G. Johnson

University of East Anglia, Norwich Medical School, Norwich, UK

Introduction: Model-dependent approaches to solving the central convolution equation of dynamic susceptibility-contrast MRI (DSC-MRI) involve assuming a parametric form for the tissue impulse response function—the product of a trial residue function, $R(t)$ and cerebral blood flow (CBF). The resultant estimated signal is then fitted to the data using least-squares fitting¹. Rather than creating a physiologically plausible model for R , it is simpler to find an analytical form for the transit time distribution (TTD), h , of the contrast agent and derive R using: $R(t) = 1 - \int h(t) dt$.

In this study, we compare two proposed forms of transit time distribution (TTD)—Weibull and gamma-variate—to two published forms: gamma¹ and skewed Gaussian².

Subjects/Methods: DSC-MRI data were acquired at 1.5T (Siemens Vision/Symphony; Germany) with a gradient-echo echo-planar imaging sequence during the first pass of a 0.1 mmol/kg bolus of

gadopentetate dimeglumine: TR/TE = 1000/47 ms; acquisition time, 60 s; flip angle = 30°; slice thickness = 5 mm; FOV = 220 × 220 mm; matrix = 128 × 128. Signals were collected from normal appearing white matter (WM) in the frontal and parietal lobes and grey matter (GM) in the caudate nucleus of nine glioma patients.

Parametric equations for small vessels (i.e. tissue microvasculature)³ with four different TTDs were fitted to the signals using non-linear least squares fitting. Curve fits were run for 100 random guesses of the free parameters that were uniformly distributed over their likely physiological ranges. CBF and TTD parameters were calculated from the fit with the lowest root mean square error (RMSE).

For each TTD, the goodness of fit was evaluated by RMSE. The fit stability was quantified as the percentage of total fits converging to the global minimum and yielding the lowest RMSE. The consistency of perfusion estimates and the computational complexity were evaluated through comparison to literature values and measurement of the computation times, respectively.

Results/Discussion: Curve fits—with all functions—were excellent, with similar RMSEs ($p > 0.008$, repeated measures ANOVA). Cerebral blood volume (CBV), CBF and mean transit time (MTT) were similar ($p > 0.008$) and congruent with previously reported values, with their GM to WM ratios between 1.82–1.90, 2.93–3.17 and 0.65–0.73, respectively. The proposed models showed a higher fit stability ($p < 0.008$), at the expense of longer computation time ($p < 0.008$).

In conclusion, the proposed TTDs provide more stable fits, with perfusion estimates being in line with literature values. Alongside usual perfusion parameters, those related to the width and shape of the TTDs can be calculated to distinguish normal and tumour vessels and inform the grading of tumours.

References: 1. Mouridsen. *Neuroimage*, 2006. 33(2): p. 570-9.

2. Koh. *Phys Med Biol*, 2001. 46(5): p. 1519-38.

3. Yablonskiy. *Magn Reson Med*, 1994. 32(6): p. 749-63.

L01.116

Advanced-Model DCE-MRI regularized by ASL

R. Jiřík¹, L. Krátká¹, O. Macíček¹, K. Souček², E. Dražanová¹, R. Fedr², A. Hampl³, Z. Starčuk, jr.¹

¹Institute of Scientific Instruments, Czech Academy of Sciences, Brno, Czech Republic, ²Institute of Biophysics, Czech Academy of Sciences, Brno, Czech Republic, ³Faculty of Medicine, Masaryk University, Brno, Czech Republic

Introduction: Dynamic contrast-enhanced (DCE) MRI can provide maps of perfusion parameters useful for diagnostics and treatment monitoring, mainly in oncology. DCE-MRI with advanced pharmacokinetic (PK) models leads to a more complete set of estimated perfusion parameters (including blood flow, F , and permeability-surface area, PS), but it is less reliable, especially in estimates of F , mean capillary transit time, T_c , and extraction fraction, E , due to ill-conditioning, see Fig.1. We suggest to use additional information regularizing the DCE estimation process by combining it with arterial spin labeling (ASL).

Subjects/Methods: The DCE image sequence (after baseline subtraction and normalization) is voxel-by-voxel fitted with the ATH model [1] by minimizing the squared differences between the measured and modeled signals. The criterial function is extended by a regularization term - squared difference between the actual estimate of F and its estimate from the separate ASL analysis.

Standard Bruker 2D FAIR RARE ASL is used, with flow quantification based on T1 estimates from the selective- and nonselective-IR experiments [2].

Due to the uncertainty in scaling of the DCE arterial input function and in the literature-based parameters of the ASL model (T1 of blood,

lambda), a global scaling factor between DCE and ASL is determined as the slope of their scatter plot (Fig. 2).

The regularization-term weight was set experimentally. Two tumor-bearing mice (SCID hairless, MiaPaCa mCherry luc2) were imaged on a 9.4T MR scanner (Bruker), 1 mm thick axial slice. 2D DCE-MRI was acquired using the golden-angle spoiled gradient echo sequence (TR/TE = 15/1.5 ms, flip angle 20 deg.), image sequence reconstruction based on total variation [3]. ASL acquisition: TR/TE = 7500/30 ms, TI = 30, 500, 800, 1000, 1100, 1300, 1500, 2000 ms, RARE factor 32.

Results/Discussion: Fig. 1 illustrates the ill-conditioning problem for some PK-parameter combinations and its solution by ASL regularization.

The flow maps of separate DCE-MRI and ASL analyses showed a decent correlation (Fig. 2) indicating that DCE-ASL analysis might be meaningful.

Fig. 3 shows that compared to DCE alone, DCE-ASL leads to more consistent flow maps (fewer outliers, high-flow regions align more precisely with the highly vascularized high-vp regions) and fewer outliers in the maps of E and Tc. The maps of vp and PS remained mostly unchanged as DCE-MRI alone is well-conditioned with respect to these parameters.

The proposed DCE-ASL combination exploits information of DCE-MRI and ASL that have been used separately so far. DCE-ASL provides more reliable perfusion analysis. The main challenge is the assumption of no motion between the DCE and ASL scans.

Acknowledgement: Supported by MEYS (CZ.02.1.01/0.0/0.0/16_013/0001775, LM2018129)

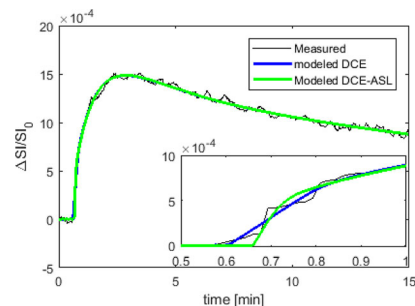


Fig. 1. Example DCE curve (black), its DCE (blue) and DCE-ASL fitting (green). Fitting difference visible in the magnified inset. Some PK parameters clearly different - DCE/DCE-ASL: F=0.4/1.1 ml/min/ml; E=0.5/0.2; ve=0.6/0.6 ml/ml; Tc=0.2/0.04 min

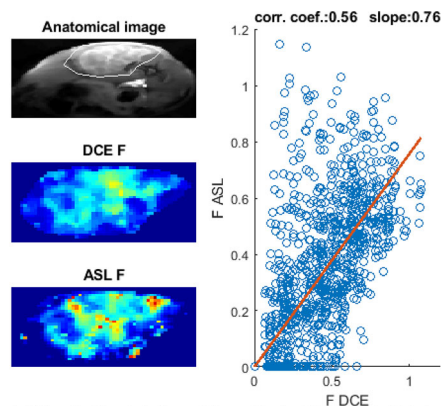


Fig. 2. Mouse 1, axial anatomical image with tumor delineation, DCE (3x3 median filtering) and ASL tumor flow maps and their scatter plot with the least-mean-squares estimate of the slope used for DCE-ASL scaling; correlation coefficient in the title.

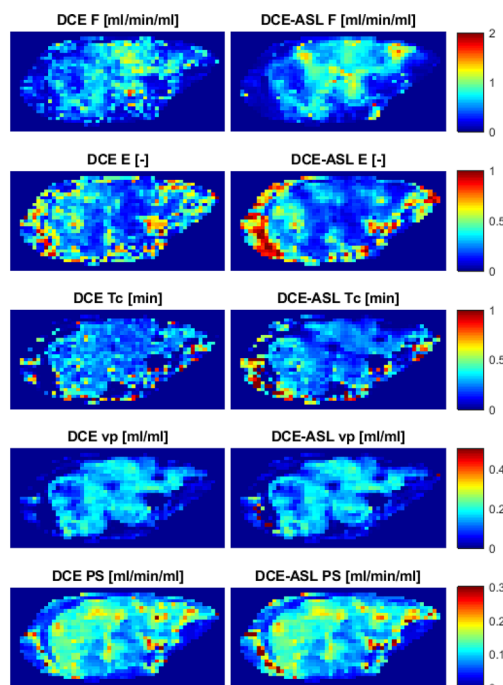


Fig. 3. Mouse 1, perfusion maps of selected PK parameters: F – blood flow, E – extraction fraction, Tc – mean capillary transit time, vp – blood plasma volume

References: [1] St Lawrence KS et al., *J Cereb Blood Flow Metab* 18(12):1365–77

[2] Kim SG, *Magn. Reson. Med.* 34(3), 293–301

[3] Tian Y. et al., *Med. Phys.*, 44:4025–4034

L01.117

Contrast agent and MR signal simulation for any MR pulse sequence on GE Scanners

K. Venugopal¹, D. Poot¹, D. van Dorth², M. van Osch², M. Smits¹, J. A. Hernandez-Tamames¹

¹Erasmus MC, Radiology and Nuclear Medicine, Rotterdam, The Netherlands, ²Leiden University Medical Center, Radiology, Leiden, The Netherlands

Introduction: MRI techniques that obtain information on microvasculature are important for diagnosis and monitoring of glioma. They exploit exogenous tracers by dynamically monitoring the passage of GBCA. For vascular signature mapping, accurate simulation of the sequence as well as the tissue is relevant. In this work we integrate MRI pulse sequences exactly as played out on the GE scanner, into the Bloch based DCE simulation tool¹, that also simulates contrast agent extravasation and diffusion. By starting from the exported sequence from the scanner, all sequence details (exact gradients, phase-cycling, RF-pulse shapes) are taken into account.

Subjects/Methods: As an example, we recorded the Hybrid(H) EPI sequence² on our GE-MR750, which was imported into the simulator¹. The HEPI combines gradient echo (GE; TE = 20ms) and spin echo (SE; TE = 70ms) images with a TR of 1s. The simulation is performed with 5 vessels of varying vessel radius (R) and permeability (k). The CA in the vessels and extravascular space as well as

the MR signals are recorded and compared for different R (ranging from 3µm to 20µm) and k, namely $k_0 = 0s^{-1}$, $k_1 = 1.83 \cdot 10^{-3}s^{-1}$ (for healthy tissue) and $k_2 = 4.83 \cdot 10^{-3}s^{-1}$ (for tumor tissue)³.

Results/Discussion: Fig 1 shows the results for different R. For increasing R, the GE signal decreases and the SE signal increases. Fig 2 shows the results for varying permeabilities: the concentration of CA (Fig 2a) and the corresponding signal intensity was higher for k2 and much lower for k1 and k0 in both GE (Fig 2b) and SE (Fig 2c) with the largest signal difference occurring at the maximum concentration of CA in the vessels. This demonstrates sensitivity to permeability, with the change in MR signal being dependent on R. Fig 3 shows the change in magnitude and phase distribution of the vessels and the extravascular space for varying permeabilities. The phase of the SE signal also provided information on the magnetic field inhomogeneities around the vessels (Fig 3j-l) due to the use of a 120° SE refocusing flip angle. Optimization of such a refocusing angle is easily performed with our current setup that allows loading the sequence details directly into the simulations. The results show dominance of the T1 shortening effect over T2 shortening, which is caused by the 1s TR and the fact that a pre-bolus was not included in the current simulations. Future studies will include this by either changing the baseline T1 of tissue accordingly or by expanding the time-axis and including the prebolus in the AIF.

In this work we demonstrated the simulation of MR signals from the microvasculature loading a sequence recorded on a MR scanner. This can be applied to optimize the assessment of microvascular properties by vascular fingerprinting⁴ with any sequence available at the GE scanner.

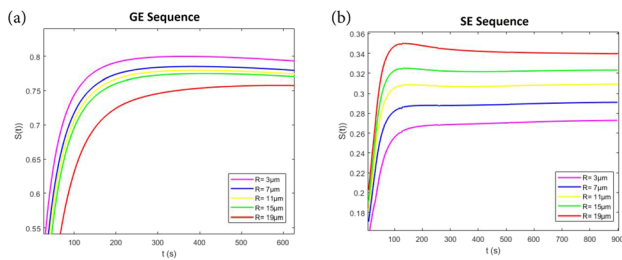


Fig 1: MR signal, S(t) obtained at different vessel radius (R) for (a) Gradient Echo (GE) and (b) Spin Echo (SE) sequence

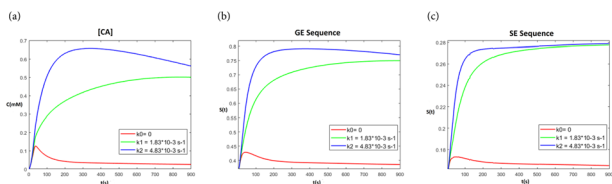


Fig 2: (a) CA concentration ([CA]) in the vessels for different permeabilities (k0(red), k1(green) and k2(blue)) and the corresponding MR signals S(t) for (b) GE and (c) SE sequence

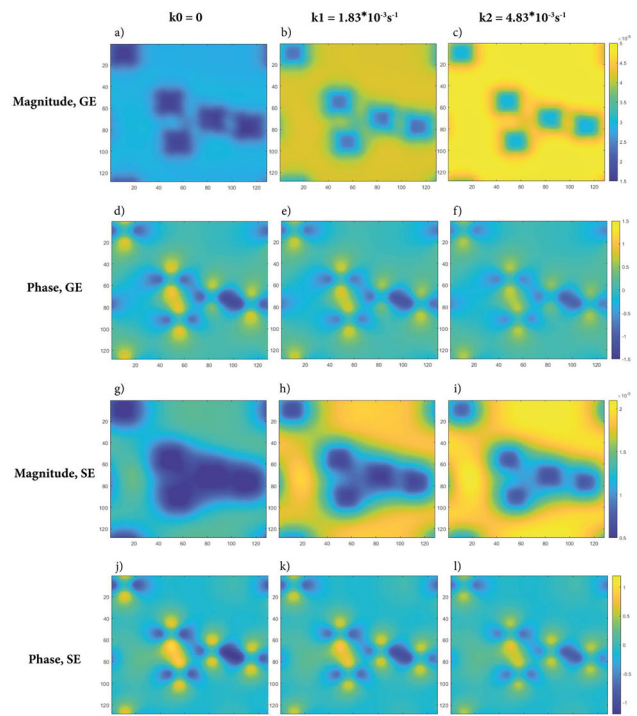


Fig 3: Magnitude distribution of GE for k0 (a), k1 (b), k2 (c) and SE for k0 (g), k1 (h), k2 (i) and Phase distribution of GE for k0 (d), k1 (e), k2 (f) and SE for k0 (j), k1 (k), k2 (l) simulated for 5 vessels acquired at time, t= 200s

References: ¹Pannetier et al, Plos One, 2013

²Cox et al, MRM, 2010

³Beaumont et al, JCBFM, 2009

⁴Christen et al, Neuroimage, 2014

L01.118

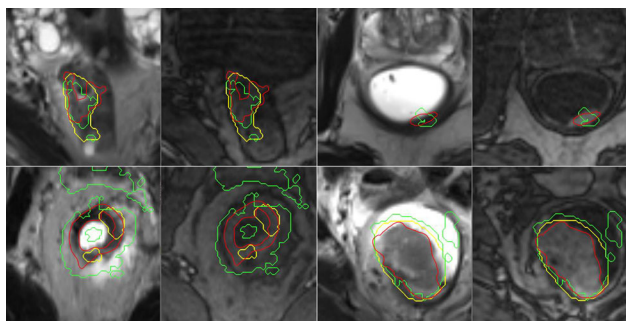
Exploration of deep learning approaches for the segmentation of colorectal cancer in DCE-MRI images

C. Tönnies¹, S. Janssen², A.-K. Schnurr¹, F. Zöllner¹, L. Schad¹

¹Mannheim Institute for Intelligent Systems in Medicine, Medical Faculty Mannheim, Heidelberg University, Chair in Computer Assisted Clinical Medicine, Mannheim, Germany, ²Medical Faculty Mannheim, University Heidelberg, Mannheim, Germany, Department for Clinical Radiology and Nuclear Medicine, Mannheim, Germany

Introduction: For the clinical assessment of colorectal cancer quantitative perfusion calculation on dynamic contrast enhanced MRI image is used. Because But this is difficult, due to the low contrast between tumor tissue and the surrounding, often inflamed, colon walls. Therefore, in clinical practice a radiologist additionally uses T2w images for tumor annotation (Figure 1). Manual annotation takes time and in current clinical practice is only performed on one slice and at one timestep.

We want to develop a deep learning system for fast and automatic segmentation of the tumor using the two modalities.



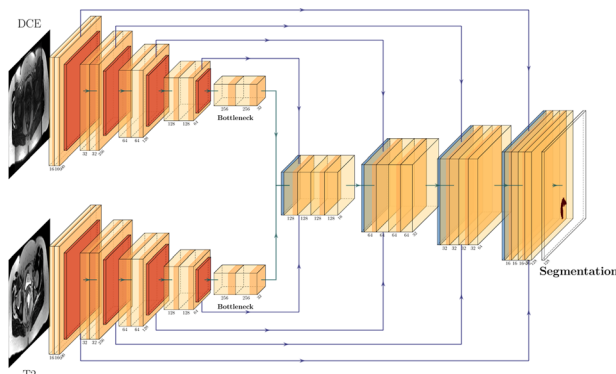
T2w and DCE images of four different tumors with annotations. For every pair of image: Left: cropped T2w, Right: cropped DCE image, Red: manual annotation, Yellow: Best Deeper UHUNet, Green: Best DeepVess

Subjects/Methods: We performed a retrospective study on 40 patients with colorectal cancer.

Patients received a DCE-MRI and T2w at 3T (Magnetom Trio/Magnetom Skyra, Siemens Healthineers).

DCE-MRI used a TWIST sequence with TR/TE/FA = 3.6 ms/1.44 ms/15, matrix size = 192 × 144, FOV = 260 × 158 mm², slice thickness = 3.6 mm, GRAPPA factor = 2. T2w used TR/TE/FA = 5800 ms/121 ms/120, matrix size = 320 × 207, FOV = 288 × 360mm², slice thickness=4mm, GRAPPA factor=2. For training we used only the annotated timestep, at the first intensity peak.

We developed a novel network architecture, depicted in Figure 2, based on the U-Net, by adding a second encoder branch, to encode two images independently. Then, the decoder combines both encoders to generate the segmentation result.



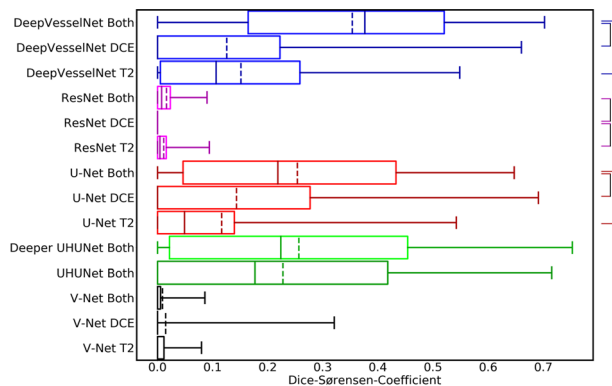
Network architecture for the UHUNet. Yellow blocks: convolution, red: down sampling, blue: upsampling with a concatenation. The last layer is a convolution with a 1x1 filter using a softmax activation for Dice/Tanimoto and sigmoid activation for cross

We trained several U-Nets[2], ResNets (U-Net with residual connections), V-Nets[1], DeepVesselNets[3] and our novel architecture. For each literature network architecture we trained three versions: one using only DCE images, only T2w images and both images in separate input channels.

Each was trained with with three losses functions (Dice, Tanimoto and Cross-Entropy) and 5-fold cross-validation.

The networks were evaluated using the Dice-Similarity-Coefficient.

Results/Discussion:



Box-Plot of the DSC for the trained architectures. Dashed lines is the mean value, solid line is the median, whiskers are min and max value. Brackets denote a significant (p<0.05) difference between versions of the same architecture.

Figure 3 shows, that networks trained with both, DCE and T2w images, perform significantly (p< 0.05, paired t-test) better than networks using only one image. But, even the best networks still perform poorly (mean DSC< 0.4). We trained one fully convolutional network (DeepVesselNet) which performed better than all auto-encoders.

Our novel architecture performed on par with the U-Net trained with both images and better than the all networks trained with only one image.

Our results show, that tumor segmentation solely on the DCE images is not possible and T2w images are required. Still, the overall performance is poor, probably due to the complexity of the problem: use the shape from T2w and adapt it to the deformed and moved tumor in the DCE image. The results could be improved by registering the T2w image onto the DCE image or better match the sequence parameters.

References: [1] Milletari, F et al: 2016 4th 3DV. pp 565–571
 [2] Ronneberger, O et al: MICCAI 2015. pp 234–241
 [3] Tetteh, G et al: Deepvesselnet: Vessel segmen-tation, centerline prediction, and bifurcation detection in 3-d angiographicvolumes (2018)

L01.119 Leakage correction of dynamic susceptibility contrast (DSC)-MRI on enhancing and nonenhancing glioma

F. Arzanforoosh¹, P. Croal², M. Chappell², M. Smits¹, E. Warnert¹
¹Erasmus MC, Department of Radiology & Nuclear Medicine, Rotterdam, The Netherlands, ²Precision Imaging Beacon & Sir Peter Mansfield Imaging Centre, School of Medicine, University of Nottingham, Nottingham, UK

Introduction: Relative cerebral blood volume (rCBV) is the most widely used parameter derived from DSC perfusion MR imaging for predicting brain tumor grade [1]. rCBV estimates for high-grade gliomas are artificially changed by contrast extravasation through a disrupted blood-brain barrier (BBB). Moreover, with an intact BBB in non-enhancing tumor, the DSC signal intensity would not recover to its baseline level due to steady-state agent distribution. In this study a thorough investigation of two different leakage correction algorithms and their effects on rCBV estimation for enhancing and non-enhancing tumors was conducted. These are: a unidirectional model-based algorithm [2] with flux of contrast agent from the intra- to the extravascular extracellular space (EES); a bidirectional model-based

algorithm [3] additionally including flow from EES to the intravascularly.

Subjects/Methods: Two datasets were used retrospectively in this study: 1. A publicly available TCIA [4] dataset (37 patients with enhancing and non-enhancing glial brain lesions); 2. The iGENE study [5] running at Erasmus MC (12 patients with non-enhancing gliomas) (See table 1 for more details).

In-house code developed in Python was used for image analysis. DSC signal–time curves were converted to concentration–time curves. Correction methods were applied on a voxel-wise basis. Trapezoidal integration between entrance and exit bolus time points was used to obtain rCBV. rCBV maps were normalized by dividing all intensities by the mean intensity of the contralateral normal-appearing white matter rCBV value.

Data	TCIA datasets	iGENE dataset
Patients	n=9 non-enhancing / n=28 enhancing gliomas	n=12 non-enhancing gliomas
Vendors	GE Healthcare, WI, USA Siemens, Erlangen, Germany 1.5T & 3T Field Strength	GE, Milwaukee, WI, USA 3T Field Strength
Preload bolus	0.05 mmol/kg of gadobenate dimeglumine (MultiHance, Bracco Diagnostics, Cranbury, NJ)	7.5 ml of gadolinium-based contrast agent (Gadovist, Bayer, Leverkusen, GE)
DSC MRI	120 time points with 0.1 mmol/kg of Gd injected 60 seconds into the scan voxel size: 0.85x0.85x6.4 mm3	120 time points with 7.5ml of gadolinium-based injected 40 seconds into the scan. voxel size: 1.88x1.88x4 mm3
T1W MRI	SPGR (Post contrast)	MPGR (Pre and Post contrast)
Tumor Mask	enhancing tumor: determined from deltaT1 maps non-enhancing tumor: determined manually	non-enhancing tumor: determined manually
NAWM* Mask	Provided with dataset determined manually Provided with dataset	determined automatically with in-house code

Table 1. Information of data acquisition. The NAWM* (Normal Appearing White Matter) mask is used as the whole-brain-non-enhancing reference tissue required by both leakage correction algorithms and for normalization of the rCBV.

Results/Discussion: In enhancing glioma applying leakage correction algorithms significantly decreased average tumor rCBV ($p < 0.001$ for bidirectional and $p = 0.002$ for unidirectional; Fig. 1a), indicating that either correction method alleviates the problem of overestimated rCBV even when preload has been applied. In non-enhancing glioma applying leakage correction made no significant difference to rCBV estimates compared to the uncorrected tumor rCBV (TCIA $p = 0.37$, iGENE $p = 0.03$, Fig. 1bc). This suggests that, with an intact BBB, the effect of using model-based correction is small and does not substantially affect rCBV measurements.

For clinical routine, this work recommends application of pre-bolus technique combined with either of correction methods in enhancing glioma for rCBV estimation, while eliminating the need for leakage correction for non-enhancing ones.

Acknowledgments: The study was funded by “Glioma MR Imaging 2.0, COST Action CA18206”.

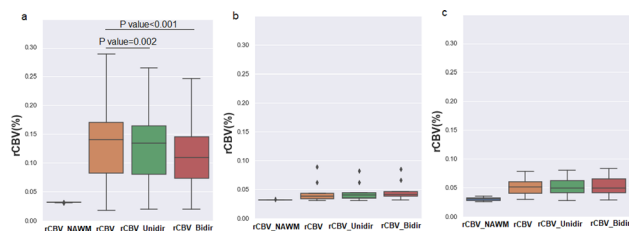


Figure 1: Patient averages of rCBV in tumor ROI for a) enhancing glioma from TCIA (n=28), b) non-enhancing glioma from TCIA (n=9), c) non-enhancing glioma from iGENE (n=12).

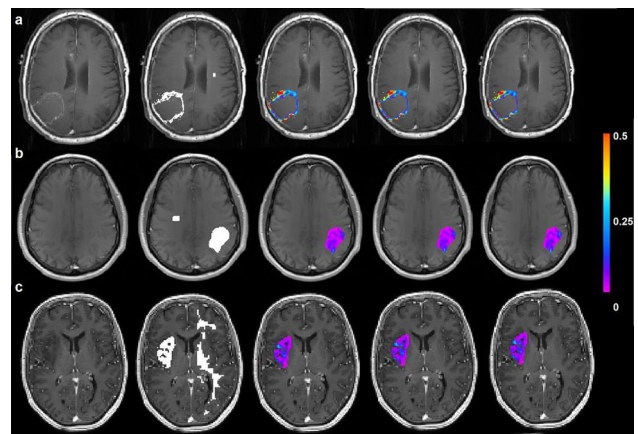


Figure 2: Single slice of exemplary post contrast T1W overlaid with tumor mask and NAWM: uncorrected, unidirectional corrected and bidirectional corrected rCBV maps. a) enhancing (TCIA) b) non-enhancing (TCIA), c) non-enhancing (iGENE).

References: [1] S. Kremer *et al.*, *J. Neuroradiol.*, 2002.
[2] J. L. Boxerman *et al.*, *J. Neuroradiol.*, 2006.
[3] K. Leu *et al.*, *J. Magn. Reson. Imaging*, 2016.
[4] K. M. Schmainda *et al.*, *J. Neuroradiol.*, 2018.
[5] S. R. van der Voort *et al.*, *Clin. Cancer Res.*, 2019.

L01.120

Perfusion imaging under hypercapnia: Single echo pCASL vs. Dual Echo pCASL

G. Hoffmann, J. Kufer, L. Schmitzer, C. Zimmer, C. Preibisch, S. Kaczmarz

Technical University of Munich (TUM), Klinikum rechts der Isar, Department of Neuroradiology, Munich, Germany

Introduction: Calibrated functional MRI (c-fMRI) is a highly promising technique to quantify changes in the cerebral oxygen metabolism.¹ However, it’s applicability is currently limited by long scan times of separate cerebral blood flow (CBF) and blood oxygenation level dependent (BOLD) acquisitions during hypercapnia (HC).^{2,3} A viable alternative with notably reduce scan time and also improved tolerability, due to shorter HC application, is Dual echo pCASL (DE-pCASL) with simultaneous CBF and BOLD acquisition. However, DE-pCASL acquisition under HC requires further evaluations.^{4,5}

The aim of this study was therefore to compare the data quality of previously applied single echo pseudo-continuous ASL (pCASL) vs. DE-pCASL under HC in 19 healthy participants. We hypothesized that DE-pCASL is suitable for perfusion imaging under HC.

Subjects/Methods: Nineteen healthy participants (23-49y) underwent MRI on a 3T Philips Elition. The imaging protocol and derived parameters are summarized in Fig.1. Two pCASL sequences were compared, single- and DE-pCASL, following the consensus recommendations.⁶ In a 3-minute block design, medical air (baseline) and 5% CO₂ (HC) were administered with an air-CO₂-mixer (Altitrainer, SMTec) and a sealed face mask. Evaluations were based on temporal SNR (tSNR), contrast to noise ratios (CNR) between baseline and HC⁵ and the corresponding perfusion increase under HC. Paired t-tests were considered statistically significant at $p < 0.05$.

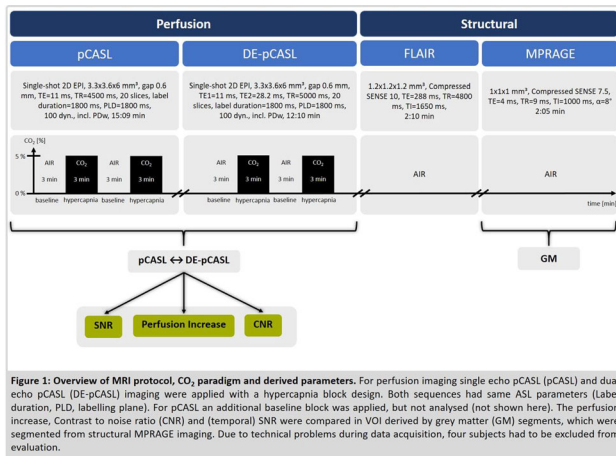


Figure 1: Overview of MRI protocol, CO₂ paradigm and derived parameters. For perfusion imaging single echo pCASL (pCASL) and dual echo pCASL (DE-pCASL) imaging were applied with a hypercapnic block design. Both sequences had same ASL parameters (Label duration, PLD, labelling plane). For pCASL an additional baseline block was applied, but not analysed (not shown here). The perfusion increase, Contrast to noise ratio (CNR) and (temporal) SNR were compared in VOI derived by grey matter (GM) segments, which were segmented from structural MPRAGE imaging. Due to technical problems during data acquisition, four subjects had to be excluded from evaluation.

Figure 1

Results/Discussion: As hypothesized, CBF-maps by DE-pCASL showed good data quality under HC. The perfusion increase was comparable between both perfusion sequences ($\sim 30\%$) and in good accordance with the literature.^{5,7} While single-echo pCASL performed better in terms of tSNR and CNR, measured values of both sequences were reasonable.⁵ Future background suppression optimization may further improve the DE-pCASL performance.⁵ To conclude, DE-pCASL is highly promising for combined BOLD-CBF imaging for HC calibration, which largely improves the tolerability for participants in clinical studies.

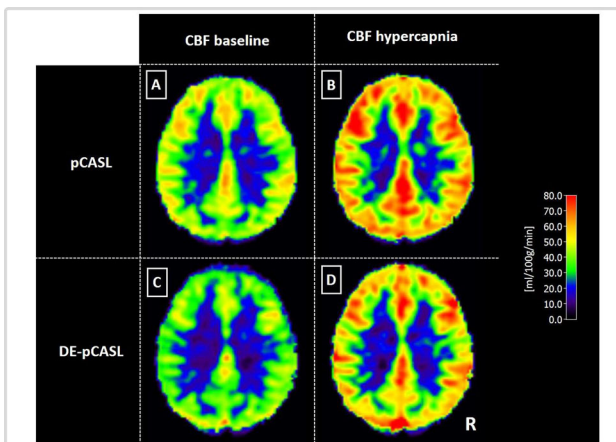


Figure 2: Exemplary data of hypercapnia effects on perfusion. CBF-maps of a young healthy subject are shown. Maps obtained with pCASL imaging at baseline (A) and hypercapnia (B) are compared to CBF-maps obtained with DE-pCASL at baseline (C) and hypercapnia (D) with the same colormap scaling. CBF maps are showing a similar perfusion increase between baseline (A & C) and hypercapnia state (B & D), with globally 16% larger CBF-values for pCASL imaging (A & B) compared to DE-pCASL (C & D).

Figure 2

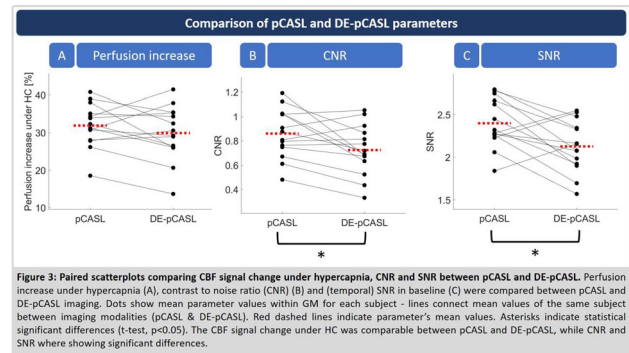


Figure 3: Paired scatterplots comparing CBF signal change under hypercapnia, CNR and SNR between pCASL and DE-pCASL. Perfusion increase under hypercapnia (A), contrast to noise ratio (CNR) (B) and (temporal) SNR in baseline (C) were compared between pCASL and DE-pCASL imaging. Dots show mean parameter values within GM for each subject - lines connect mean values of the same subject between imaging modalities (pCASL & DE-pCASL). Red dashed lines indicate parameter's mean values. Asterisks indicate statistical significant differences (t-test, $p < 0.05$). The CBF signal change under HC was comparable between pCASL and DE-pCASL, while CNR and SNR were where showing significant differences.

Figure 3

References: 1: Davis et al., ProcNAS, 1998

2: Blockley et al., NMRBiomed, 2013

3: Kaczmarz et al., ISMRM, 2020

4: Perthen et al., MRI, 2008

5: Ghariq et al., Neuroimage, 2014

6: Alsop et al., MRM, 2015

7: Liu et al., Neuroimage, 2020

L01.121

Study of changes in perfusion in the foci of demyelination in multiple sclerosis by perfusion MRI.

L. Vasilkiv, Y. Stankevich, O. Bogomyakova, A. Tulupov

International Tomography Center Siberian Branch of Russian Academy of Sciences, Novosibirsk, Russian Federation

Introduction: Multiple sclerosis is an immune-mediated disease of the central nervous system with disseminated foci of demyelination and progressive neurodegeneration; is a leading cause of disability of neurological patients of a young age, characterized by a wave-like course with alternating periods of remission and relapse. Currently, there is a discussion about the participation of vascular changes in the formation of neurological disorders and about the possibility of correction of therapeutic approaches in connection with the revealed microcirculatory disorders. Perfusion MRI allows you to evaluate hemodynamics at the capillary level in vivo. **Purpose.** To evaluate perfusion changes in foci of demyelination in multiple sclerosis using the method of dynamic susceptibility contrast (DSC).

Subjects/Methods: The MR study was carried out on a MR-scanner "Ingenia" ("Philips") 3 Tesla. The study included 30 healthy volunteers and 80 patients with demyelinating disease of the central nervous system (9 patients with CIS), 66 patients with RRMS and 5 patients with SPMS over the age of 18 up to 48 years (average age was 34.6 ± 8.02 years). Assessment of CBF, CBV, MTT, TTP in foci of demyelination was carried out.

Results/Discussion: On perfusion maps, "active" foci of demyelination are visualized as asymmetric hyperperfusion zones, and inactive foci as asymmetric hypoperfusion zones.

In foci of demyelination, a local dynamic change in perfusion was noted: at the initial stages, a significant increase in CBF and CBV was noted with their subsequent decrease. In active foci of demyelination, there is an increase in CBF and CBV, the most pronounced changes in patients with CIS: CBF by 65.2% and CBV by 78.1%, with a slight increase in MTT and TTP by 6%; in the group with RRMS in the acute stage, there is an increase in CBF and CBV in active foci of demyelination by 34.1% and 35.3%, respectively, with a decrease in MTT and TTP by 4.7%. In the group with the SPMS in the active foci, there was an increase in CBF by 12.3% and CBV by 8.6%, with a decrease in TTP by 5.9% and MTT by 5.4%; However, pronounced hypoperfusion is noted in inactive foci: CBF is reduced by 42.9% and

CBV by 34.7%, with an increase in time parameters: TTP by 14.8% and MTT by 12.7%. In the group with relapsing-relapsing course of multiple sclerosis in remission, a decrease in CBF by 33.5% and CBV by 21.1% was noted.

Conclusion: Evaluation of brain perfusion allows you to take a fresh look at the role of the vascular component in the formation of inflammatory focal changes in the brain in multiple sclerosis, which can determine a new direction for pathogenetic treatment.

References: We thank Ministry of Science and Higher Education of the RF for access to MRI equipment (AAAA-A16-116121510090-5). The work was supported by Russian Science Foundation (the project #19-75-00052).

L01.122

Data-based modeling of transfer function for single electrode straight leads

M. Hussain, J. Kreutner, G. Schaefers

Magnetic Resonance Institute for Safety, Technology and Research GmbH, Gelsenkirchen, Germany

Introduction: Long leads of active implantable medical devices (AIMD), when exposed to high frequency radio waves such as in MRI, converge the incident electric field in certain areas of the body, generating hotspots for tissue heating. These implants are often simulated to observe their electromagnetic behavior under high frequency radio waves. However, a complete 3D electromagnetic simulation of a sophisticated implant with long leads is often too time consuming and require extensive computing resources. In such case, the transfer function approach is employed to estimate the magnitude of the electric field at the end of the leads.

In this work, we have analyzed the simulation data of transfer functions of single electrode straight leads with various lengths. The objective is to develop an empirical model of the transfer function that can be used to estimate the transfer function of similar leads without experimental measurements and simulations.

Subjects/Methods: The transfer functions of single electrode leads of lengths 40cm, 60cm, 80cm and 100cm are computed by using reciprocity method [1]. Other parameters and properties of the leads are summarized in Table 1 (see also Fig. 1).

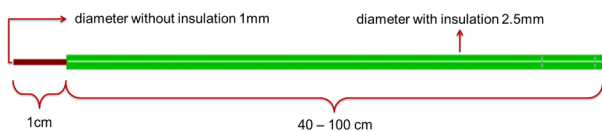


Figure 1. Dimensions of the investigated leads.

Sim #	Freq. [MHz]	Length [cm]	Dia. wire [mm]	Dia. Insulation [mm]	Insulation	Wire	Medium
Sim 1	64	40	1	2.5	Silicone	Titanium	Gel
Sim 2	64	60	1	2.5	Silicone	Titanium	Gel
Sim 3	64	80	1	2.5	Silicone	Titanium	Gel
Sim 4	64	100	1	2.5	Silicone	Titanium	Gel
Sim 5	128	40	1	2.5	Silicone	Titanium	Gel
Sim 6	128	60	1	2.5	Silicone	Titanium	Gel
Sim 7	128	80	1	2.5	Silicone	Titanium	Gel
Sim 8	128	100	1	2.5	Silicone	Titanium	Gel

Table 1. Lead parameters for simulations.

By analyzing the data of the real and imaginary parts of the complex transfer functions, it was found that the transfer function of single electrode straight leads computed by reciprocity method

behaves like a damped sinusoidal function. To verify our hypothesis, we defined a generalized damped sinusoidal function given as,

$$y(x) = a \cdot \exp(-\lambda x) \cdot \cos(\omega x + \varphi), \quad (1)$$

Where, a is the initial amplitude, λ is the decay constant, ω is the angular frequency, φ is the phase angle at $x=0$ and y is the real or imaginary part of the complex transfer function. To find the values of the parameters, we used the method of minimization of the sum of the squares of the residuals. The minimization function is given by,

$$\min_p \sum_{n=1}^N (y_{sim}^n - y^n)^2. \quad (2)$$

Here, N is the number of data points, and p is the vector consisting of all the fitting parameters $a, \lambda, \omega,$ and φ .

Results/Discussion: The optimization problem defined in (2) was solved for each simulation to find the optimal vales of the parameters. In Fig. 2, a comparison of the simulated and empirically fitted (eq. 1) complex transfer function for 80cm lead is compared. It can be observed from Fig. 2 that the empirical model (eq. 2) along with the optimal parametric values captured the magnitude as well as the phase of the complex transfer function with good accuracy. Small deviation in simulated and empirically modeled phase of the transfer function can be seen at the end of the lead which is due to the numerical inaccuracy in estimating extremely small values of the complex transfer function.

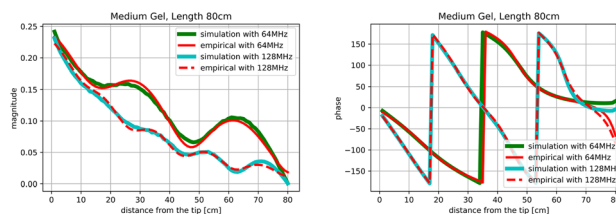


Figure 2. Comparison of simulated and empirically modeled magnitude (left) and phase (right) of the complex transfer function for 80cm lead.

References: [1] S. Feng, R. Qiang, W. Kainz, and J. Chen. A technique to evaluate mri-induced electric fields at the ends of practical implanted lead. IEEE Transactions on microwave theory and techniques, 63:305–313, 2015.

L01.123

Insights into structural differences of macrocyclic GBCAs affecting the transit and retention in the brain’s district

E. Gianolio¹, E. Di Gregorio¹, C. Furlan¹, S. Atlante¹, C. Carrera², S. Aime¹

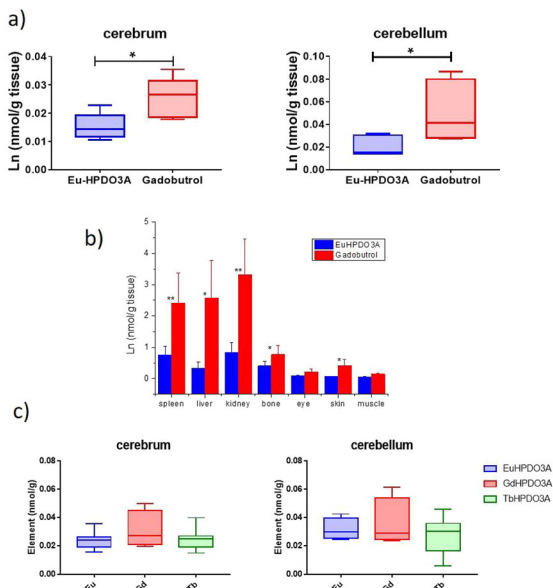
¹University of Torino, Molecular Biotechnologies and Health Science, Torino, Italy, ²National Research Council, Institute of Biostructures and Bioimaging, Torino, Italy

Introduction: In recent years, much attention has been devoted to observations reporting that tiny amounts of GBCAs evade the blood circulation bed being retained for long time in the body districts. Particular concerns is related to brain depositon.^{1–2} The aim of this preclinical study is to investigate whether minor structural changes can influence the biodistribution and retention of macrocyclic Ln(III)-complexes (Ln(III)= Gd, Eu or Tb) in the principal body districts. Insights on potential interactions between the Ln(III) complexes and components of the brain ECM have been gained by *in vitro* relaxometry.

Subjects/Methods: Two groups of healthy mice received 10 doses containing either Eu-HPDO3A and Gadobutrol (Gd-DO3A-butrol) – study 1, or Eu-HPDO3A, Tb-HPDO3A and Gadoteridol (Gd-HPDO3A)- study 2, in equimolar ratio (0.3 mmol/Kg of each complex) every second day. The mice were sacrificed by cervical dislocation 21 days after the last administration and cerebrum,

cerebellum, spleen, liver, kidney, eyes, bone, skin and muscle were recovered. Each specimen was weighted, mineralized and underwent ICP-MS analysis to determine their metal content. Proton longitudinal relaxation enhancement was used to investigate possible interactions with the brain ECM components.

Results/Discussion:



Lanthanides concentration determined in the mice tissues upon the administration of ten doses of a mixture of Eu-HPDO3A/Gadobutrol (a,b) or a mixture of Eu-HPDO3A/Gadoteridol/Tb-HPDO3A (c) (0.3 mmol/Kg each) 21 days after the last injection.

The first animal study dealt with the comparison between Eu-HPDO3A and Gadovist. 3 weeks after the last administration, the amount of Gadolinium found in all organs, except eye and muscle, was significantly higher than that of Europium, indicating that Gadovist is retained to a greater extent than Eu-HPDO3A.

The *in vitro* relaxometric study indicated that, in the presence of Hyaluronic acid, the increase in relaxation rate was in the order Gadobutrol > Gadoteridol > Gadoterate with significant differences between each other. The addition of Chondroitin and Heparan sulfate did not yield any significant increase in relaxivity of the three complexes.

The second animal study dealt with the comparison between Eu-HPDO3A, Gd-HPDO3A and Tb-HPDO3A. Eu-, Gd- and Tb-HPDO3A displayed a similar distribution in the different tissues/organs but liver and spleen, where the content of Tb-HPDO3A doubles the amounts of the corresponding Eu- and Gd-systems.

These results show how the use of different Ln(III)-complexes allows to get a direct comparison of the biodistribution of different GBCAs, ruling out the uncertainties associated to the variability of the animal model. The behavior here shown by the macrocyclic complexes points to indicate that minor structural differences are sufficient to generate changes in the molecular interactions with the macromolecules of the extracellular space.

References: 1) McDonald, R.J., Levine, D., Weinreb, J. et al. *Radiology*, 2018; 289:517–534.

2) Lancelot, E., Desché, P. *Invest Radiol.* 2020;55:20-24.

L01.124

Long-time stability of image quality in the German National Cohort (NAKO) Imaging Study Based on automatic image quality assessment

D. C. Hoinkiss¹, S. Struckmann², N. Werner², C. O. Schmidt², M. Günther¹, J. G. Hirsch¹

¹Fraunhofer MEVIS, Bremen, Germany, ²Institute of Community Medicine, SHIP/Clinical-Epidemiological Research, University Medicine Greifswald, Greifswald, Germany

Introduction: The German National Cohort (NAKO, [1]) includes a multi-center imaging study with 30,000 participants, each undergoing a 60-minute MRI protocol, performed with identical MRI hardware at five dedicated MRI sites across Germany [2]. In this abstract, we investigate the long-time stability of image quality, assessed by automatic algorithms that were part of the daily study workflow (QA). Algorithms and workflows were in detail presented in previous work [3].

Subjects/Methods: During MRI acquisition, DICOM data are securely transferred to a central storage where QA procedures are calculated within one hour, including image-based quality measures (e.g. signal-to-noise ratio (SNR) or sharpness) [3]. Results of the daily QA are furthermore integrated in a monthly data quality report [4]. In this abstract, we exemplarily focus on the T1-weighted neuro MPRAGE protocol to explore the stability of image quality and characterize deviating data points.

Results/Discussion: Fig. 1 shows a high stability of SNR and sharpness measures throughout the acquisition of the 30,000 subjects. A small number of outliers of ~1.5% and ~0.8% can be found for sharpness and SNR, respectively.

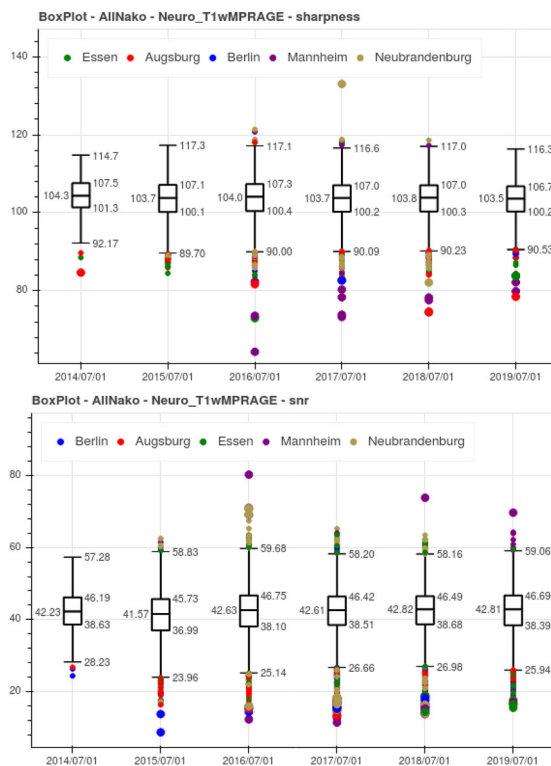


Figure 1: Box plots summarizing sharpness (top) and SNR (bottom) for each year between 2014 and 2020, covering all 30,000 subjects. The boxplots display the median with the 5% and 95% quantiles together with whiskers and outlying data points.

Despite the strong long-time stability shown, splitting the data into the different MRI sites reveals some minor deviations. This is shown in Fig. 2 which plots the LOESS-smoothed progression of the QA values over time together with the overall confidence bands [5]. Smoothed curves are very similar across sites with a slightly elevated curve for Sharpness in Berlin and slightly lower SNR in Augsburg.

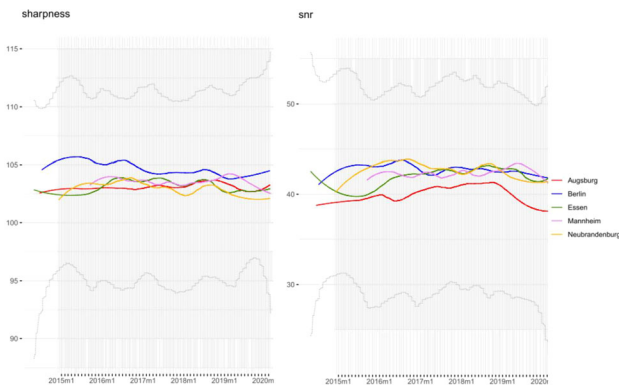


Figure 2: LOESS-smoothed time-course of the two QA values sharpness (left) and SNR (right) together with overall confidence intervals.

To group data points with the same underlying physical reason for image quality degradation, a clustering algorithm is used. Based on all estimated QA values, a principal component analysis is performed to reduce the complex data to two dimensions. Subsequent DBSCAN [6] clustering can then identify clusters with similar image quality characteristics, as seen in Fig. 3. In this case, the second (yellow) cluster correlates with partly inactive receiver coil elements.

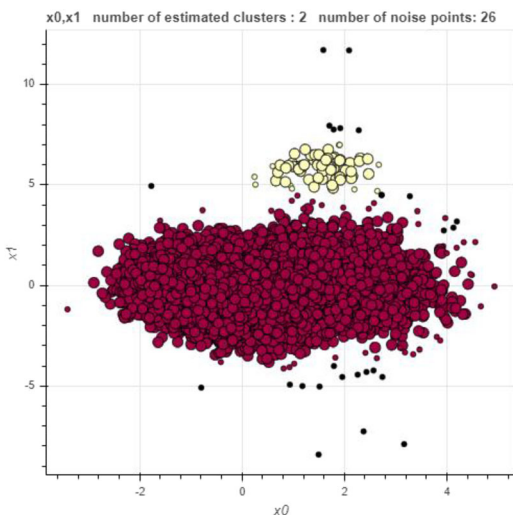


Figure 3: Cluster map based on all estimated QA values, after reducing the dimensions to two (PCA) and performing DBSCAN clustering. red: main cluster, yellow: second cluster, black: undefined noise.

Automatic image quality assessment was used to report the long-time stability of study data and characterize deviating data clusters. The presented material reports very stable image quality over the time course of 6 years, 5 contributing centers, and more than 30,000 observed subjects, mainly driven by the standardized characteristics of the study.

References: [1] German National Cohort Consortium. *Eur J Epidemiol* 2014;29(5):371-82

[2] Bamberg et al. *Radiology* 2015;277(1):206-20

[3] Hirsch et al. *ISMRM* 2017:4458

[4] Schmidt et al. *Stud Health Technol Inform* 2017;235:549-53

[5] Cleveland et al. *J Econom* 1988;37(1):87-114

[6] Ester et al. *KDD* 1996:226-231

Acknowledgements:

The NAKO study is funded (01ER1301A, 01ER1801B) by the German Ministry for Education and Research (BMBF), the Federal States, and the Helmholtz Association.

L01.125

Quantitative MRI performed under dynamic conditions to reveal the biomechanical nature of the Nucleus Pulposus in a fissured intervertebral disc, a proof of concept study

J.-P. Deneuille¹, M. Yushchenko², T. Vandeuve¹, G. Arnaud¹, M. Billot¹, M. Roulaud¹, M. Sarracanie², P. Rigoard¹, N. Salameh²

¹PRISMATICS Lab (Predictive Research in Spine/Neuromodulation Management and Thoracic Innovation/Cardiac Surgery), Poitiers University Hospital, Poitiers, France., Poitiers, France, ²Center for Adaptable MRI Technology (AMT Center), University of Basel, Department of Biomedical Engineering, Allschwil, Switzerland

Introduction: Low back pain (LBP) has become the leading cause of disability worldwide¹. LBP is complex though, and could result from multiple factors that make its etiology and diagnosis non-trivial, even today. In a recent study, Manchikanti et al. reported that 39% of LBP was due to discogenic pain associated with a radial fissure in the disc's Annulus Fibrosus (AF). While gold-standard techniques (i.e. CT-scan or X-ray contrast-agent discography) to uncover discogenic pain are accurate, they are also invasive and lead to an increased risk of disc degeneration³. Further, they require static condition and hence fail to assess the potential dynamic nature of discogenic pain⁴. The proposed proof of concept study aims to establish a protocol for dynamic assessment of the intervertebral disc in the presence and absence of radial fissure via quantitative MRI (T_1 and T_2 mapping).

Subjects/Methods: We used a fresh, *ex-vivo* lamb specimen (3 vertebrae, 2 discs) conditioned for mechanical testing (hydration and axial load control according to guidelines)⁵. Bending load was applied with a custom MRI-compatible system to scan a non-fissured disc under neutral (baseline), flexion and extension conditions. Subsequently, the disc was teared with a puncture needle in the anterior AF part, and MR scans were repeated for each loading condition. MRI consisted in T_2 -w images (2D TSE, $0.31 \times 0.31 \times 1$ mm³), quantitative T_1 (TSE IR, $0.52 \times 0.52 \times 2$ mm³, 8 TIs ranging from 30 ms to 5.8 s) and T_2 data (SE, $0.52 \times 0.52 \times 2$ mm³, 32 echoes evenly spaced between 30 ms and 360 ms) acquired at 3 T. Displacement and strain of the nucleus pulposus (NP) were assessed, as well as its migration within the AF following the radial fissure.

Results/Discussion: Nucleus displacement and strain during flexion or extension are visible on each type of images (T_1 and T_2 maps and T_2 -w images) when compared to baseline scans (fig 1 & 2). The migration of NP into the anterior fissure is confirmed by T_1 and T_2 maps (fig 2), allowing the calculation of mechanical parameters (fig 3). The anterior fissure impacted the nucleus' mechanical behavior as predicted: strain and displacement of the fissured disc's NP seem to depend on both the bending load and the radial fissure directions.

Our study shows the dynamic nature of a fissured disc with predictable NP migration following the direction of the load and fissure. Our study provides insights for new discogenic pain assessment in physiological and pathological conditions, which could ultimately be an alternative to invasive and ionizing discographies. Supplementary studies will be needed to confirm our findings in a larger cohort of cadaveric specimens and further *in vivo*.

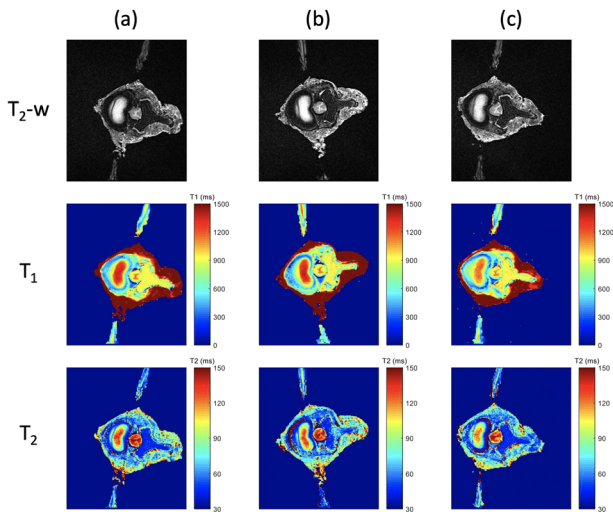


Fig 1: MR images for each mechanical loading state of the intact specimen, (a) Neutral, (b) Flexion, (c) Extension. First row: T₂-weighted images, second row: T₁ maps, third row: T₂ maps.

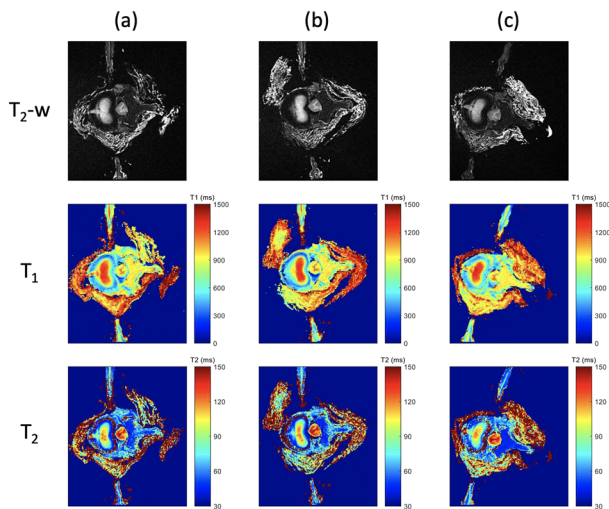
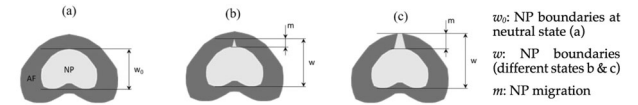


Fig 2: MR images for each mechanical loading state of the specimen with radial tear, (a) Neutral, (b) Flexion, (c) Extension. First row: T₂-weighted images, second row: T₁ maps, third row: T₂ maps.



Mechanical states	Angle (°)	NP strain (mm)	NP global (mm)	NP boundaries (mm)	NP migration (%)
Intact	Neutral	4.7	-	-	-
	Flexion	-8.8	-5.6	-2.20	0
	Extension	10.4	-6.1	-0.95	2.22
Fissure	Extension	11.1	21.1	3.70	5.0
	Flexion	-8.9	-3.1	-1.60	-0.6
	Neutral	8.7	20.8	1.55	4.5

Fig 3: Axial strain & bending angle variation vs mechanical state. NP strain: $s=(w-w_0)/w_0$. NP boundaries: distance between each nucleus boundary, w_0 at neutral state (a), w at various states (b & c). m : ratio of NP displacement & AF thickness.

References: 1 Vos 2015 The Lancet
 2 Manchikanti 2018 Pain Physician
 3 Carragee 2009 Spine
 4 Laslett 2005 The Spine Journal
 5 Adams 1995 Spine

Electronic Posters

P01.01

Automatic wrist cartilage segmentation in MR images by a patch-based convolutional neural network

E. Brui¹, A. Y. Efimtcev², V. A. Fokin², R. Fernandez³, A. G. Levchuk², A. C. Ogier⁴, J. P. Mattei⁴, D. Bendahan⁵, A. Andreychenko⁶

¹ITMO University, Department of Physics and Engineering, Saint-Petersburg, Russian Federation, ²Federal Almazov North-West Medical Research Center, Saint-Petersburg, Russian Federation, ³APHM, Service de Radiologie, Hôpital de la Conception, Marseille, France, ⁴Aix-Marseille Université, CNRS, Centre de Résonance Magnétique Biologique et Médicale, Marseille, FRANCE, ⁵Aix-Marseille Université, CNRS, Centre de Résonance Magnétique Biologique et Médicale, Marseille, Russian Federation, ⁶Department of Health Care of Moscow, Research and Practical Clinical Center of Diagnostics and Telemedicine Technologies, Moscow, Russian Federation

Introduction: Measuring of knee cartilage volume by segmentation from 3D MR images is a routine procedure. The most promising techniques are based on convolutional neural networks (CNNs) with the Dice similarity coefficient (DSC) achieving 0.88¹ with respect to the manual labels. At the same time, only a few methods have been developed for wrists². The automatic segmentation of wrist cartilage could facilitate research of novel imaging biomarkers of wrist osteoarthritis. In this work, we propose a method based on dedicated CNN and investigate its performance in comparison with manual and state-of-the-art CNN-based¹ methods.

Subjects/Methods: 8 healthy volunteers and 3 patients were enrolled in the study. The same wrist was scanned twice with two RF coils (conventional and homemade) providing a different signal-to-noise ratio (SNR). 20 3D VIBE images were acquired at 1.5 T. Wrist cartilage was first manually segmented by a radiologist (O1) in 300 coronal slices (260 for training and 260 for testing the CNN, and 20 for developing its architecture). 20 medial coronal slices (validation set) were manually segmented twice by R1 and once by two other radiologists (O2, O3) in order to study the variability of the manual procedure.

Planar network architecture with a small number of trainable parameters and a patch-based (PB) training approach (with a patch of 28x28 pixels) were utilized. The network parameters were optimized by a grid search. To assess the PB-CNN sensitivity to the anatomical heterogeneity of the training data, several PB-CNN variants were trained using different training subsets. The robustness of manual and PB-CNN approaches to the SNR of the images was also studied. Performances of PB-CNN and image-based U-Net were compared. For each CNN, the performance was evaluated by comparing CNN-based and manual labels using DSC values.

Results/Discussion: The averaged DSC for the CNN-based segmentation of the validation set was comparable with the interobserver DSC (Table 1) and with the one reported on knee cartilage³.

Study	O1 - O1 (manual)	O1 - O2 (manual)	O1 - O3 (manual)	O1 - PB-CNN for VS	O1 - IB-CNN	O1 - PB-CNN for DS
DSC	0.90±0.04	0.88±0.04	0.78±0.06	0.81±0.05	0.64±0.08	0.86±0.05
Segmentation rate s/slice	180 (O1)	180 (O2)	180 (O3)	15 (PB-CNN)	0.75 (IB-U-Net)	15 (PB-CNN)

Table 1. Statistics for the validation of segmentation methods. IB - image based, VS - validation set, DS - development set. Manual method was validated on VS. IB-U-Net was tested on a DS. Our PB-CNN was tested on both VS and DS

The segmentation accuracy was not influenced (paired t-test, $p > .05$) by the coil selection (Fig. 1a). In the sensitivity analysis (Fig. 1b), the DSC value increased continuously and did not reach saturation. The training dataset should be further enlarged by the data

of new volunteers and patients. PB-CNN did not demonstrate robustness regarding some anatomical structures that have appearances similar to cartilage (Fig. 2). The major improvement may come from exploiting 3D peculiarities of cartilage by expanding the network architecture into 3D. Image-based U-Net showed a significantly lower performance (Table 1). Segmentation rates for all cases are summarized in Table 1. Overall, our PB-CNN provided a fast and reliable segmentation of wrist cartilage.

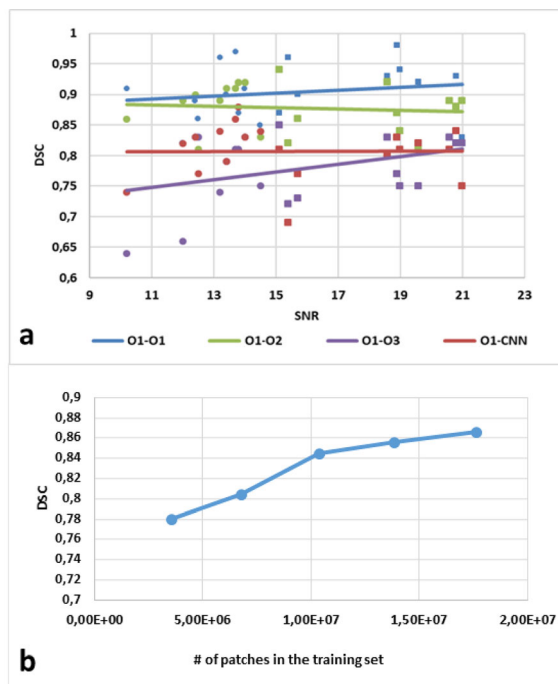


Fig. 1. DSC vs SNR of cartilage tissue for intraobserver, interobserver and intermethod studies (circles correspond to the images obtained with a conventional coil, rectangles - with a home-built coil). Sensitivity analysis results (b)

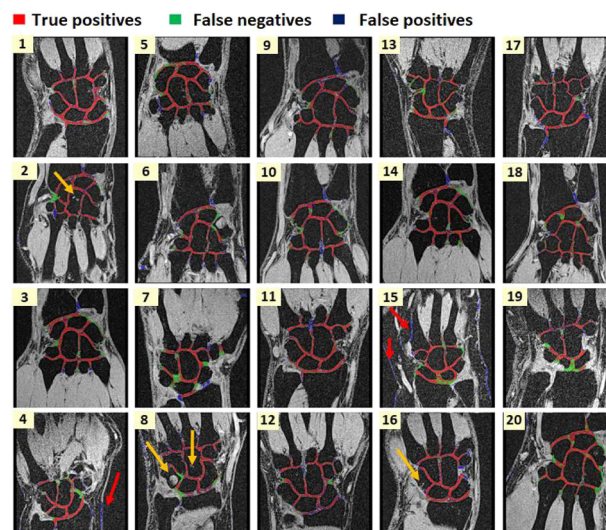


Fig. 2. PB-CNN performance on the validation dataset. The arrows point at areas, which had a similar structure and contrast as cartilage and were correctly recognized as a background (yellow) or mistakely recognized as cartilage (red).

References: ¹Norman et al., Radiology. 2018;288(1)
²Zink et al., World J Orthop 2015; 6(8)
³Shim et al., Radiology. 2009;251(2)

P01.02

Under-sampled golden-angle radial data reconstruction using convolutional neural network

T. Aslam¹, H. Shahzad², H. Omer¹

¹COMSATS University Islamabad, Islamabad Pakistan, Electrical and Computer Engineering, Islamabad, Pakistan, ²National Center for Physics, Islamabad, Pakistan

Introduction: Golden-angle radial trajectory¹ has been recently proposed in literature to acquire under-sampled data to reduce the MRI scan time but it introduces aliasing in the resulting image. This work proposes a new Convolution Neural Network (CNN) based framework to reconstruct the MR image from the under-sampled golden-angle radial data. The results are compared with the state-of-the-art CG-SENSE² reconstruction method. Artifact Power (AP), Signal-to-Noise Ratio (SNR) and computation time are used to quantify the results.

Subjects/Methods: To reconstruct MR images from the under-sampled data, a CNN architecture is proposed that trains itself by estimating the weights using multiple convolution layers. Figure-1 shows the main steps of this work. Training is performed using 1400 images obtained from an open-source database³ and the test data contains 430 images. The label images are first converted into golden angle radial *k*-space data using golden-angle¹ (111.25°) radial sampling and retrospectively under-sampled with AF=2 and 4 for the training and testing purposes. The under-sampled golden-angle radial *k*-space data is first gridded with GRAPPA Operator Gridding (GROG) to get Cartesian *k*-space; inverse FFT (iFFT) of the gridded data provides MR images that contain aliasing artifacts. The proposed CNN is trained with the aliased and label MR images. The trained network is used to reconstruct MR images from the under-sampled golden-angle radial data (test images).

Figure-2 shows architecture of the proposed CNN, where 18 convolution layers are used to estimate the weights; Rectified linear unit (ReLU) is used as an activation function and Batch Normalization (BN) is used to avoid over-fitting. The last layer is regression layer that is used to provide the final image. The number of layers is selected empirically; fewer number of layers provide less accurate image and no significant improvement was achieved in the output image with more than 18 layers.



Figure 1: Flow chart of the proposed work

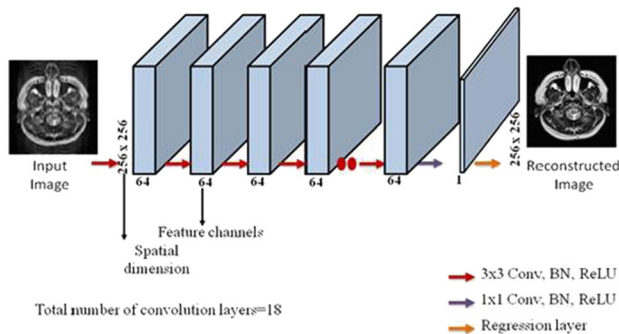


Figure 2: Architecture of the Convolution Neural Network (Proposed method)

Results/Discussion: Figure-3 and Figure-4 show the results of the reconstructed human head images using the CNN (proposed method)

and CG-SENSE² method at AF=2 and 4 respectively. Table-1 shows a comparison of the computation time between the proposed method and the CG-SENSE method.

The results demonstrate that the proposed method has almost similar reconstruction quality (though it can be further improved with better training) as of CG-SENSE method. However, our proposed method shows 84% improvement in computation time as compared to CG-SENSE (Table-1). Furthermore, the receiver coil sensitivity information⁴ is required in the CG-SENSE method to reconstruct the MR image which may be difficult to estimate in some applications; however our proposed method does not require any such information⁴.

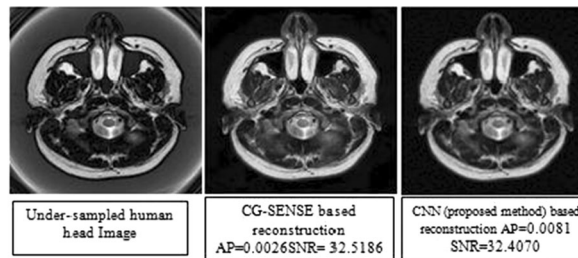


Figure 3: Reconstruction of under-sampled golden-angle radial data with CG-SENSE method and CNN (proposed method) for AF=2 for human head data set

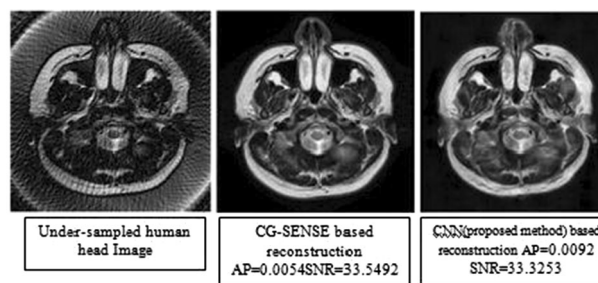


Figure 4: Reconstruction of under-sampled golden-angle radial data with CG-SENSE algorithm and the CNN (proposed method) for AF=4 for human head data set

Acceleration factor (AF)	CNN (proposed method)	CG-SENSE algorithm	Improvement (%)
AF=2	18.187 sec	135.070 sec	86.5%
AF=4	18.082 sec	118.452 sec	84.7%

Table 1: Comparison of computation time for the CNN (proposed method) and CG-SENSE method for golden-angle radial human head data for AF=2 and 4

References: 1. S. Winkelmann et.al. IEEE 2007
 2. KP Pruessmann et.al. MRM 2001
 3. Loizou et.al. IEEE 2011
 4. A.Irfan et.al. APMR 2016

P01.03**Aberrant resting-state functional connectivity in cognitively unimpaired patients with Parkinson's disease and freezing of gait**

A. Martín-Bastida^{1, 2}, M. Delgado-Alvarado³,
I. Navalpotro-Gómez⁴, C. Caballero-Gaudes⁵, M. Carreiras⁵,
M. C. Rodríguez-Oroz²

¹Clinica Universidad de Navarra, Neurology, Madrid, Spain, ²Clinica Universidad de Navarra, Neurology, Pamplona-Madrid, Spain, ³Hospital Sierrallana, Neurology, Torrelavega, Spain, ⁴Biodonostia Health Research Institute, Neurology, San Sebastian, Spain, ⁵Basque Center on Cognition, Brain and Language, Neuroimaging, San Sebastian, Spain

Introduction: Freezing of gait (FOG) is of the most debilitating symptoms in Parkinson's disease (PD), being an important cause of falls and disability. Previous studies have showed reduced functional connectivity in executive and visual networks, however, cognitive dysfunction acted as an important confounding factor. In the present study we analysed brain functional connectivity with resting state functional MRI in patients with PD and FOG without cognitive impairment.

Subjects/Methods: Forty-three PD patients (seventeen with FOG (FOG+) and twenty-six without FOG (FOG-)) without cognitive impairment and twenty-four age-matched controls underwent resting-state fMRI. Seed-based correlation analysis from locomotor neural areas involved in FOG was performed using subthalamic nucleus (STN), pedunculopontine nucleus (PPN), supplementary motor area (SMA) and cerebellar locomotor region (CLR). Pairwise t-test between PD patients with and without FOG and controls was performed in order to obtain whole-brain connectivity analysis with threshold-free cluster enhancement statistics with $p < 0.05$ corrected for multiple comparisons.

Results/Discussion: In PD patients with FOG vs controls, we observed reduced functional connectivity between the right SMA and the bilateral sensorimotor, parietal and insular cortices and ipsilateral caudate. Additional reductions in functional connectivity in patients with FOG vs controls were showed between the left STN (in less degree in FOG-) and middle frontal premotor area, cuneus/precuneus, anterior cingulate cortex, cerebellum and basal ganglia. Functional hypoconnectivity was observed in right STN in FOG+ vs controls with cuneus, fusiform gyrus and sensorimotor cortex (in less degree in FOG-). Finally, reduced functional connectivity was showed between left PPN and bilateral lingual gyrus in PD patients FOG+ vs FOG-.

References: Our findings suggest a resting state functional connectivity disruption of STN and right SMA in PD patients with FOG (and less degree in FOG-) vs controls with cortical and subcortical regions involved with attention, response inhibition and conflict resolution in absence of cognitive impairment. In addition further hypoconnectivity of left PPN in PD FOG+ vs FOG- were observed with cortical regions associated with visual processing.

P01.04**Classifying liver lesions using distributions of intravoxel incoherent motion (IVIM) MRI attributes with machine learning algorithms (MLA)**

O. Hatipoglu, A. Kus, A. Özcan

Acibadem Mehmet Ali Aydinlar Univ., Istanbul, Turkey

Introduction: Hepatocellular carcinoma (HCC) is the most common malignant primary hepatic tumor worldwide¹ difficult to discriminate from malignant liver metastases and benign hemangiomas². IVIM³ might be favorable by its characterization of diffusion and perfusion without contrast agent with 3 attributes: true diffusion coefficient D_r

perfusion-related incoherent microcirculation coefficient D_p and the micro vascular volume fraction fp . However, this dimensionality causes inter- and intra-observer variability. Herein, MLAs are tested for their potential of resolving this issue objectively.

Subjects/Methods: In this IRB approved study, out of 62 consecutive patients with informed consent, IVIM data from 43 patients (mean age 56.42 ± 13.56 years, with full data set), 13 hemangiomas, 20 liver metastases and 10 HCC cases were analyzed. Data collection was on a 3T SiemensTM Magnetom SkyraTM, 18 channel body coil, TE/TR = 56/7300 ms, $b = [0, 10, 15, 20, 30, 50, 80, 100, 200, 400, 600, 800, 1000]$ s/mm², slice thickness 6.5mm with motion correction. IVIM model $S(b) = s_0(1 - f_p e^{-bD_r} + f_p e^{-bD_p})$ was used to estimate D_r , D_p and f_p using non-linear least squares.

Lesions were demarcated manually with MIPAV⁴. Mean, standard deviation and, 60, 90 and 120 bin histograms were calculated. The distributions were vectorized and normalized. New feature vectors were created by concatenating each attribute's distribution consecutively. All of these features used as inputs to 22 MATLAB MLAs using disease types as labels. Execution variations consisted of using leave-one-out to 30-fold cross validation, with PCA retaining 98% variance, retaining 5 components and without PCA. Three group classification and pairwise discrimination was tested.

Results/Discussion: Using mean values and single parameter distributions as features resulted in poor outcomes equivalent to coin toss. For metastasis-hemangioma pairwise discrimination logistic regression with concatenated 60 bin distributions, 5 component retaining PCA resulted in the best 66.7% accuracy.

For classifying the three subtypes, support vector machine (SVM) algorithm with 5 component PCA retention obtained 59.5% accuracy as the best score.

The results indicate that IVIM attributes are insufficient for accurate classification of hepatic pathologies and further features derived from IVIM and/or collected from other MRI modalities need to be included in future research.

References: 1. Bray, F. *et al. CA: A Cancer Journal for Clinicians* **68**, 394-424

2. Jang, H.-J. *et al. American Journal of Roentgenology* **180**, 135-141, 3. Le Bihan, D. *NeuroImage* **187**, 56-67,

4. McAuliffe, M. MIPAV (Medical Image Processing, Analysis, and Visualization), <https://mipav.cit.nih.gov/>

P01.05**Correlation between clinical and diagnostic imaging findings in patients with Crohn's disease**

M. Nowakowska¹, M. Kuczyńska¹, M. Grzegorzczak¹, K. Siejka¹, W. Cyranka¹, M. Zbroja¹, M. Piekarska¹, A. Drellich-Zbroja¹, P. Furtak²

¹Medical University of Lublin, Department of Interventional Radiology and Neuroradiology, Medical University of Lublin, Poland, Lublin, Poland, ²Medical University of Lublin, Department of Gastroenterology with the Endoscopic Laboratory, Independent Public Teaching Hospital No. 4 in Lublin, Poland, Lublin, Poland

Introduction: Crohn's disease (CD) is a chronic inflammatory disease of the gastrointestinal tract. It usually affects younger people, with the peak of illness between the age of 15 and 25. MR enterography (MRE) is a proven and reliable modality in the evaluation of the lesion extent within this group of patients. The purpose of the study was to compare MRE findings with clinical index of the disease activity - CDAI score, in order to verify the utility of magnetic resonance enterography in the precise assessment of disease severity (grade of activity).

Subjects/Methods: 46 consecutive patients (25 females and 21 males, mean age of 39) underwent MRE on a 1.5T scanner according to a standard protocol, including dynamic contrast-enhanced

sequences. All studies were performed in prone position, using manitol as a positive oral contrast agent. The MRE severity grading was performed according to the consensus recommendations proposed by Bruining et al. CDAI score was assessed prior to examination by a specialist in the field of gastroenterology. MRE findings were verified with endoscopy whenever necessary.

Results/Discussion: 32 patients had multifocal lesions, with the majority (N=23) localized within both small and large intestine. 14 patients presented with unilocular lesions (13 involving the ileocecal valve and terminal ileum, and 1 with large intestinal disease). 14 patients (30.4%) had a history of previous bowel resection due to disease complications. Penetrating disease was diagnosed in 15 subjects (32.6%). The results indicate for good correlation between MRE and CDAI assessment in groups of patients with moderate and severe clinical symptoms. However, there is a significant discrepancy in MRE findings in the group of patients with mild disease activity according to CDAI. Out of 23 patients with clinically mild symptoms, 1 exhibited MRE characteristics of severe, 9 of moderate and 7 of mild inflammatory intestinal lesions. No active lesions according to MRE criteria were found in 6 subjects from this subgroup. Patients in whom severe and moderate inflammation was observed in MRE underwent further verification by means of endoscopy; enterography results were confirmed in 7 cases.

MRE is a useful tool in evaluating patients with Crohn's disease. There is good accordance between MRE and clinical findings in patients with prominent disease symptoms, indicating that MR enterography might be a promising modality in terms of lesion activity grading. Nonetheless, there exist a significant group of patients with mild disease symptoms, in whom MRE tends to show full spectrum of disease severity. This, however, might be associated with individual response to treatment, and temporal difference between clinical and MRE symptom resolution.

References: 1. Consensus Recommendations for Evaluation, Interpretation, and Utilization of CT and MRE in Patients With Small Bowel Crohn's Disease. D.H. Bruining et al. *Radiology* 2018 Mar; 286(3): 776-799

P01.06

Atlas based segmentation of mouse basal ganglia sections using 9.4T MRI

S.-J. Im¹, H.-M. Baek²

¹Gachon University, Department of Health Sciences and Technology, Incheon, South Korea, ²Gachon University, Department of Molecular Medicine, Lee Gil Ya Cancer and Diabetes Institute, Incheon, South Korea

Introduction: The combination of image registration methods and voxel-based statistical parametric mapping techniques has been used to identify phenotypic differences between disease and control animals¹. Atlas-based segmentation of the mouse brain has evolved quickly in recent years, becoming a capable methodology for automatic parcellation of structural images. However, few studies have applied these methods to preclinical research². In this study, unlike manual hand-drawn approaches, we present a method for automatically segmenting visual areas, of the mouse brain, particularly the basal ganglia.

Subjects/Methods: This study was conducted on a 9.4T Bruker scanner. All experiments were performed on C57BL/6N ex-vivo mouse brain (N = 1, male, 1 year old). The pulse sequence used for this acquisition was 3D TurboRARE T2 and 2D EPI-Diffusion tensor. Basal ganglia structures were processed using ANTx^{3,4,5} and FSL⁶. First, we acquired brain extracted images from whole-head input data and created masks based on Allen anatomical regions using ANTx. Subsequently, we registered the basal ganglia masks obtained using ANTx to our native mouse brain using FSL's FLIRT tool. Second, we acquired fiber reconstruction data using FSL.

Results/Discussion: The acquired MR data comprised of T2 and DTI of a mouse as shown in **Figure 1A**. **Figure 1B** shows our segmentations of the basal ganglia⁷. Visualization was done by partitioning the striatal and pallidal structures in relation to anatomical landmarks (**Figure 1C**).

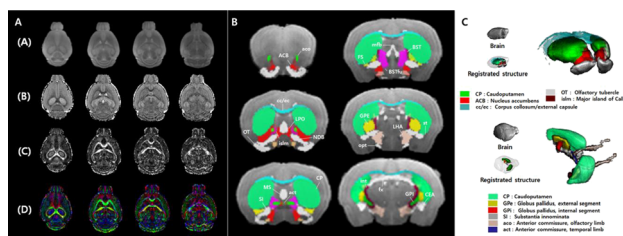


Figure 1 (A) Brain extracted MRI T2 images, (B) ADC maps, (C) FA maps and (D) FA maps displayed with color overlays. (E) Segmentation of the striatum and pallidum on representative T2/DTI minimum deformation images. (F) 3D volume rendering image.

Figure 2 shows the name and abbreviation of the regions segmented in our study. For each structure, the name and abbreviation were acquired from previous study⁸ as well as from Allen reference atlas⁹. The name and color code of the Workplace template used to create this segmentation are shown in **Figure 2**.

The Mouse Brain in Stereotaxic Coordinates (Barta, Paxinos, G., et al. 2005)				The Allen Reference Atlas (Our study)	
Region	Structure Names	Abbreviations	Color Code	Abbreviations	Structure Names
Subpallidum					
Striatum					
Corpus striatum					
	Amygdalostratial transition area	ASr		CP	Caudoputamen
	Caudate putamen	CPu			
	Lateral striatal stripe	LSS			
Accumbens					
	Accumbens nucleus core	AcbC		ACB	Nucleus accumbens
	Accumbens nucleus shell	AcbSh			
	Accumbens nucleus shell, lateral part	LAcbSh			
Olfactory tubercle		Tu		OT	Olfactory tubercle
Pallidum					
	Globus pallidus	GP		GPE	Globus pallidus, external segment
	Ventral pallidum	VP		SI	Substantia innominata
	Major island of callosa	ICM		Idm	Major island of callosa
	Entopeduncular nucleus	EP		GPI	Globus pallidus, internal segment
Red nucleus of the stria terminalis					
	Red nucleus of stria terminalis	ST		BST	Red nucleus of stria terminalis
	Red nucleus of stria terminalis, fusiform part	Fu		BSTfu	Red nucleus of the stria terminalis, anterior division, fusiform nucleus
Diagonal domain					
	Nucleus of the horizontal limb of the diagonal band	HDB			
	Lateral nucleus of the horizontal limb of the diagonal band	LDB		NDB	Diagonal band nucleus
	Nucleus of the vertical limb of the diagonal band	VDB			
	Basal nucleus (Meynert)	B		SI	Substantia innominata
	Substantia innominata part B	SIB			
Associated structures					
	Central amygdaloid nucleus	Ce		CEA	Central amygdala nucleus
	Extension of the amygdala	EA			
	Lateral hypothalamus	LH		LHA	Lateral hypothalamic area
	Interstitial nucleus of the posterior limb of the anterior commissure	IPAC		FB	Fundus of the striatum
	Lateral preoptic area	LPO		LPO	Lateral preoptic area
	Medial septal nucleus	MS		MS	Medial septal nucleus
Fiber groups					
	Anterior limb of anterior commissure	aca		aoa	Anterior commissure, olfactory limb
	Posterior limb of posterior commissure	apc		act	Anterior commissure, temporal limb
	Corpus callosum/external capsule	cc/cx		cc/cx	Corpus callosum/external capsule
	Forix	f		fx	Forix
	Internal capsule	ic		int	Internal capsule
	Medial forebrain bundle	mfb		mfb	Medial forebrain bundle
	Optic tract	opt		opt	Optic tract
	Stria terminalis	st		st	Stria terminalis

Figure 2 Segmentation of mouse basal ganglia and associated structures using the Allen Reference Atlas on T2/DTI.

Segmented using Allen labels				Ref#13 Jeremy F. P. Ullmann et al. 2014					
Structure	Volume (mm ³)	Intensity (%)	ADC	FA	Structure	Volume (mm ³)	Intensity (%)	ADC	FA
CP	24,583	92.674	2.44E ⁻⁴	2.12E ⁻¹	ASI	0.305	72.89	2.75E ⁻⁴	1.91E ⁻¹
ACB	4,863	88.370	2.34E ⁻⁴	1.95E ⁻¹	CPu	20,298	64.757	2.71E ⁻⁴	2.04E ⁻¹
OT	3,848	82.802	2.22E ⁻⁴	2.50E ⁻¹	LSS	0.101	68.147	2.52E ⁻⁴	1.52E ⁻¹
GPE	1,657	81.248	2.40E ⁻⁴	2.61E ⁻¹	AcBc	1,447	70.611	2.55E ⁻⁴	1.73E ⁻¹
SI	2,960	77.995	2.29E ⁻⁴	2.21E ⁻¹	AcBsh	1,351	70.318	2.54E ⁻⁴	1.79E ⁻¹
lsh	0.014	59.988	2.31E ⁻⁴	1.38E ⁻¹	LAcBsh	0.959	68.604	2.83E ⁻⁴	1.87E ⁻¹
GPI	0.265	74.526	2.16E ⁻⁴	4.16E ⁻¹	Tu	2,737	65.913	2.44E ⁻⁴	2.12E ⁻¹
BST	1,546	79.738	2.04E ⁻⁴	2.53E ⁻¹	GP	2,109	56.874	2.48E ⁻⁴	1.58E ⁻¹
BSTfu	0.010	63.913	1.47E ⁻⁴	3.61E ⁻¹	VP	1,087	62.767	2.39E ⁻⁴	1.22E ⁻¹
NDB	1,013	79.443	2.04E ⁻⁴	2.40E ⁻¹	ICJM	0.059	73.733	2.47E ⁻⁴	1.90E ⁻¹
SI	2,960	77.995	2.29E ⁻⁴	2.21E ⁻¹	EP	0.236	59.353	2.44E ⁻⁴	2.68E ⁻¹
CEA	1,164	81.713	2.45E ⁻⁴	1.99E ⁻¹	ST	0.436	58.942	2.74E ⁻⁴	1.89E ⁻¹
LHA	3,402	84.893	1.95E ⁻⁴	3.76E ⁻¹	Fu	0.003	68.511	2.22E ⁻⁴	1.98E ⁻¹
FS	0.267	70.808	2.59E ⁻⁴	1.61E ⁻¹	HDB	0.373	60.942	2.65E ⁻⁴	1.67E ⁻¹
LPO	0.894	75.073	1.98E ⁻⁴	2.24E ⁻¹	LDB	0.144	60.158	1.95E ⁻⁴	9.71E ⁻²
MS	0.604	84.571	2.17E ⁻⁴	2.83E ⁻¹	VDB	0.33	63.116	1.38E ⁻⁵	8.43E ⁻³
aco	0.766	69.753	2.31E ⁻⁴	2.36E ⁻¹	B	0.007	60.883	2.97E ⁻⁴	2.13E ⁻¹
act	0.657	58.927	2.40E ⁻⁴	1.63E ⁻¹	SIB	0.137	63.436	2.24E ⁻⁴	2.23E ⁻¹
cc.ec	4,310	67.160	2.30E ⁻⁴	2.70E ⁻¹	Ce	0.817	71.162	2.60E ⁻⁴	2.19E ⁻¹
fx	2,957	73.389	2.14E ⁻⁴	4.22E ⁻¹	EA	0.644	63.81	2.72E ⁻⁴	1.91E ⁻¹
int	2,386	72.499	1.97E ⁻⁴	4.62E ⁻¹	LH	0.485	60.223	2.79E ⁻⁴	1.65E ⁻¹
mb	4,367	71.478	2.14E ⁻⁴	4.08E ⁻¹	IPAC	0.721	69.388	2.49E ⁻⁴	1.33E ⁻¹
opt	0.591	69.286	1.83E ⁻⁴	3.47E ⁻¹	LPO	0.063	64.577	2.25E ⁻⁴	1.69E ⁻¹
st	0.432	66.681	1.97E ⁻⁴	4.16E ⁻¹	MS	0.149	58.17	8.80E ⁻⁵	5.73E ⁻²
					aca	0.446	46.314	7.51E ⁻⁵	5.22E ⁻²
					act	0.242	55.943	2.00E ⁻⁴	1.06E ⁻¹
					cc.ec	5,555	50.586	2.68E ⁻⁴	2.13E ⁻¹
					f	0.259	52.044	2.12E ⁻⁴	2.11E ⁻¹
					ic	2.024	44.186	2.53E ⁻⁴	1.53E ⁻¹
					mb	0.946	61.426	2.43E ⁻⁴	2.25E ⁻¹
					opt	0.825	39.594	2.84E ⁻⁴	2.34E ⁻¹
					st	0.784	73.430	2.42E ⁻⁴	2.35E ⁻¹

Table 1 Comparison of segmented basal ganglia structure volume, intensity, FA value and ADC value between Allen mask registration data and Jeremy F. P. Ullmann et al. 2014 data.

Table 1 displays the volume, intensity, ADC and FA value of our segmented structures as well as those of a previous study's segmentations for comparison⁷. We performed segmentation and visualization using Allen anatomical regions. 24 striatal, pallidal and basal ganglia-related structures were segmented in our study⁹. We compared the volume, intensity, ADC and FA values of our study with those of a previous study, with results shown in **Table 1**. Comparison with a similar study completed indicates that volume and intensity were not very consistent, but ADC and FA value were approximately similar⁷. In this study, we were able to utilize automatic segmentation to study anatomical and functional information about the mouse brain.

References: [1] JFP Ullmann et al. *NeuroImage* (2013) [2] D Ma et al. *PLOS ONE* (2014) [3] Koch et al. *JCBFM* (2017) [4] Hübner et al. *NeuroImage* (2017) [5] Lein et al. *Nature* (2006) [6] M Jenkinson et al. *NeuroImage* (2005) [7] JFP Ullmann et al. *Brain Structure and Function* (2014) [8] G Paxinos et al. *Academic Press* (2004) [9] HW Dong et al. *John Wiley & Sons Inc* (2008)

P01.07

Chronic cancer-induced bone pain in rats shows reorganization of resting-state networks in brain

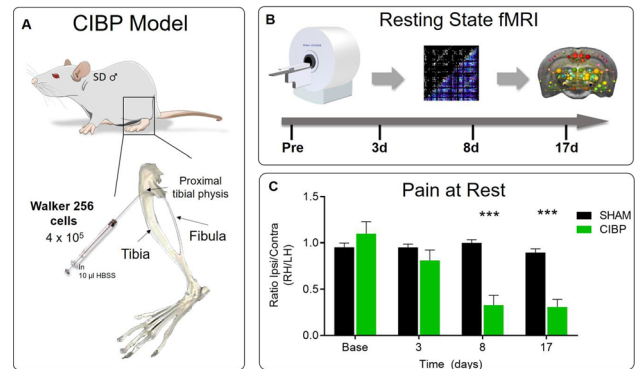
B. Pradier¹, D. Segelcke², L. Wachsmuth¹, S. Kreitz³, A. Hess³, C. Faber¹, E. Pogatzki-Zahn²

¹University Hospital Münster, Department of Clinical Radiology, Translational Research Imaging Center, Münster, Germany,

²University Hospital Münster, Department of Anesthesiology, Intensive Care and Pain Medicine, Münster, Germany, ³University of Erlangen-Nuremberg, Erlangen, Germany, Institute of Experimental and Clinical Pharmacology and Toxicology, Emil Fischer Center, Erlangen, Germany

Introduction: Initiation and maintenance of chronic pain have complex pathophysiology and high clinical relevance and are also pain entity-specific. Despite extensive progress in the field, the mechanisms leading to chronification of pain remain poorly under-

stood. Longitudinal neuroimaging studies have been proven to be well suited to investigate changes in brain circuitry during the initiation and maintenance phase of chronic pain but are still rare. We therefore performed longitudinal resting-state MRI experiments to probe changes in brain network dynamics during chronic cancer-induced bone pain (CIBP) [1].



(A) Diagram of the chronic cancer-induced bone pain (CIBP) model. (B) CIBP or sham animals were tested before and at three time points after injection of cells. (C) CIBP animals showed significantly increased pain at rest at exp. day 8 and 17.

Subjects/Methods: Male SD rats received an injection of potent Walker 256 cells or heat-killed cells (sham, n=4) into the proximal tibia to initiate CIBP (or a sham condition, n=5, Fig. 1a). We performed longitudinal resting state (RS) MRI 1 week before (baseline), and at 3 time points (day 3, 8, and 17) after inoculation followed by graph theory-based brain network analysis (Fig. 1B). MRI measurements were conducted as recently published [2] on a 9.4 T Bruker Biospec 94/20 small animal scanner (Bruker Biospin GmbH, Ettlingen, Germany) using a rat surface array coil (Bruker). During acquisition, anesthesia was switched from isoflurane to medetomidine. Body temperature was maintained at 36-37°C over the entire experiment. Functional MR acquisition was started 40 min after stopping isoflurane. fMRI scans were acquired with a GE-EPI sequence (TR/TE:1000/18ms, 16 slices, 1.2mm thick slices, FOV 28x26mm², Matrix 80x80, 600 repetitions). MRI analyses were correlated with behavioral data, which monitors pain at rest in the same animals before MRI scans (ratio of ipsi- to contralateral hind-paw print area, Fig. 1c).

Results/Discussion: Our preliminary resting-state network analysis shows a strengthening of functional connections between sensory and thalamic brain regions combined with a decreased path length in CIBP rats (Fig. 2a+b). While network size and density were not affected (Fig. 2c), we detected increased modularity, indicative of enhanced information flow (Fig. 2d). Further, we observe a significantly increased functional connectivity between brain regions of the sensory, thalamic, sensorimotor, and limbic system starting at day 8 that further strongly increased towards day 17 ($p_{FWE} < 0.05$, calculated using permutation testing, Fig. 2e). Global longitudinal changes in network parameters, especially altered functional connectivity in thalamic, sensorimotor and limbic regions provide new insights into the initiation and chronification of cancer-induced bone pain.

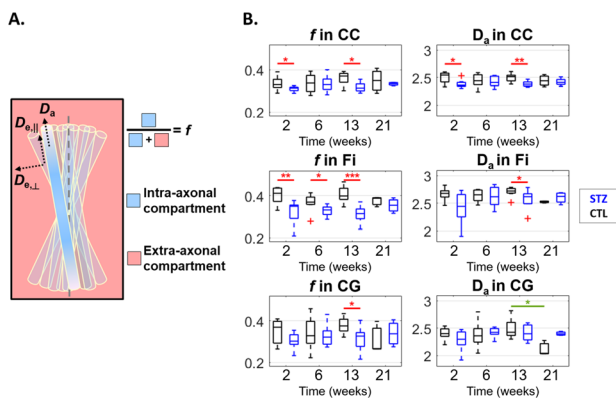


Figure 3: A) Schematics of the WMTI-Watson biophysical model, which accounts for two non-exchanging compartments: the intra and extra-axonal spaces. The intra-axonal space is described by a signal fraction f and the parallel intra-axonal diffusivity D_a . The extra-axonal space is characterized by parallel $D_{e||}$ and perpendicular $D_{e\perp}$ diffusivities. The axons' orientations are modeled by a Watson distribution. B) WMTI-Watson model estimates in the corpus callosum (CC, top), fimbria (Fi, middle) and cingulum (CG, bottom). Two-tailed Mann-Whitney U-test was used for inter-group comparison and one-way ANOVA with Tukey-Cramer correction for within-group comparison across time ($\alpha=0.05$). This model provided more specific characterization of WM integrity than DTI and DKI. Similar to f , STZ rats displayed a nonmonotonic trend with partial recovery at 6 weeks post-injection and reduced f and D_a at 2 and 13 weeks. These alterations are indicative of acute intra-axonal injury and demyelination, respectively.

Results/Discussion: STZ rats showed altered f and intra-axonal damage in regions typical of AD, in a temporal pattern of acute injury, transient recovery and chronic degeneration – also reported in behavioral studies³.

These nonmonotonic trends suggest a compensatory mechanism, possibly recruiting ketone bodies, that enables temporary repair of brain structure and function⁶ in spite of glucose hypometabolism. Regions with reduced FDG uptake at 6 weeks later showed altered f , supporting the manifestation of a chronic stage.

Thus, early acute phase could be a therapeutic window to prevent/delay degeneration.

This work highlights the signature of brain insulin resistance and proposes potent MRI biomarkers translatable to human AD and diabetes.

References: ¹Hölscher, C. *Front. Aging Neurosci.* 2019

²Nitsch, R.; Hoyer, S. *Neurosci. Lett.* 1991

³Knezovic, A. et al. *J. Neural Transm.* 2015

⁴Diao, Y. et al. *Phys Q-Bio* 2020

⁵Jespersen, S. N. et al. *NeuroImage* 2018

⁶Yang, H. et al. *Front. Neurol.* 2019

P01.09

Time-course characterisation of brain metabolites using ¹H-MRS at 9.4 T in the R6/2 and zQ175 mouse models of Huntington’s disease

L. Riggall¹, E. Demetriou², M. Arridge², E. Danby¹, B. Taxy¹, B. Siow³, G. P. Bates¹, X. Goley²

¹University College London, HD Centre, Dept. of Neurodegenerative Disease & UK Dementia Research Institute, London, UK, ²University College London, Dept. of Brain Repair & Rehabilitation, London, UK, ³The Francis Crick Institute, MRI Unit, London, UK

Introduction: Huntington’s disease (HD) is a lethal genetic disorder caused by a CAG repeat expansion in the huntingtin (*HTT*) gene. It results in widespread brain atrophy and severe movement disorders, as well as cognitive and psychiatric disturbances from an early age. To better track disease onset and progression for effective therapeutic intervention, biomarkers that precede structural changes are needed. Brain metabolites detectable by proton magnetic resonance spectroscopy (¹H-MRS) may provide such biomarkers, but need in-depth characterisation in HD-like mouse models to improve their clinical translatability.

Subjects/Methods: Here, single voxel ¹H-MRS was applied *in vivo* to two of the most widely used HD mouse models: the R6/2 [1] and zQ175Δneo knock-in [2-4]. To undertake a comprehensive time-course analysis of metabolites in the HD brain, ¹H-MRS was acquired in selected brain regions (striatum, cortex, hippocampus and thalamus) using PRESS (TR/TE = 5000/7.5 ms). Acquisition was performed on Bruker and Agilent 9.4 T preclinical MRI systems in zQ175 (~200 CAGs) and R6/2 (~180 CAGs) mice, plus wild-type littermate controls, respectively. Timepoints ranged from pre-symptomatic to late-stage and included 4, 8 and 12 weeks (R6/2 mice) and 2, 12 and 16 months (zQ175 mice) (n ≥ 9 across all groups). The concentrations of eleven metabolites were derived from brain regions using LCModel [5] by fitting a simulated basis set of metabolite signals to the acquired spectra.

Results/Discussion: Significant time-course changes in metabolite concentrations were found, including global increases in total creatine (creatine + phosphocreatine, tCr), glutamine + glutamate and taurine (Taur), as well as reductions in total N-acetylaspartate (NAA + N-acetylaspartylglutamate, tNAA) in both zQ175 and R6/2 mice compared to controls. Significant increases in total choline (glycerophosphorylcholine + phosphocholine) and myo-inositol were also found in R6/2 and zQ175 mice respectively. Figure 1 shows examples from the striatum of late-stage mice, a region that selectively degenerates in patients. These results suggest diminished neuronal integrity, disrupted energy metabolism and glial cell alterations. Furthermore, many changes, including increases in tCr and Taur, occurred before late-stage was reached. Regions also exhibited specific metabolic profiles, indicating regional changes occur to differing extents throughout HD progression. Therefore, this study has revealed in detail the metabolic consequences of HD in two commonly used mouse models. Our findings also provide potential biomarkers that may have clinical applicability.

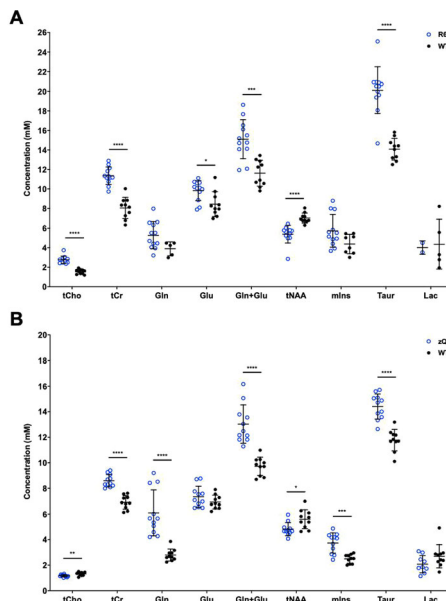


Figure 1: Quantification of striatal metabolites in 12-week-old R6/2 (A) and 16-month-old zQ175 (B) mice using ¹H-MRS at 9.4 T. At late-stage both mouse models present with significant alterations in striatal metabolite concentrations compared to their WT littermate controls. Abbreviations: tCho, total choline; tCr, total creatine; Gln, glutamine; Glu, glutamate; Gln+Glu, glutamine + glutamate; tNAA, total N-acetylaspartate; mIns, myo-inositol; Taur, taurine; Lac, lactate. Data are presented as mean ± SD, where $p < 0.05^*$, $p < 0.01^{**}$, $p < 0.001^{***}$ and $p < 0.0001^{****}$ (R6/2, n = 12 [n = 2, Lac]; WT, n ≥ 5 and zQ175, n ≥ 9; WT, n = 10).

References: [1] Mangiarini, L. et al., 1996. *Cell.* 87(3): 493-506
 [2] Menalled, L. B. et al., 2012. *PLoS One.* 7(12): e49838
 [3] Heikkinen, T. et al., 2012. *PLoS One.* 7(12): e50717
 [4] Franich, N. R. et al., 2019. *J Neurosci Res.* 97(12): 1590-1605
 [5] Provencher, S.W., 1993. *Magn Reson Med.* 30(6): 672-9

P01.10**A visual comparison of ASL and DSC perfusion MRI for brain tumour surveillance**

W. Teunissen¹, A. Lavrova², C. Flies³, T. Snijders³, J. W. Dankbaar⁴, C. Vladimir², E. Warnert¹, M. Smits¹

¹Erasmus MC, Radiology and Nuclear Medicine, Rotterdam, The Netherlands, ²Saint Petersburg State University Hospital, Radiology and Nuclear Medicine, Saint Petersburg, Russian Federation, ³UMC Utrecht, Brain Center, Utrecht, The Netherlands, ⁴UMC Utrecht, Radiology and Nuclear Medicine, Utrecht, The Netherlands

Introduction: Perfusion MRI (pMRI) is increasingly used as an advanced MRI technique to assess treatment response in brain tumour patients [1]. Different pMRI techniques are available and all come with their own advantages and disadvantages [2]. DSC perfusion is the most commonly used technique and estimates relative cerebral blood volume (rCBV). It is widely available, cheap and fast. Disadvantages are the use of contrast, the relatively high sensitivity to artefacts, such as susceptibility, and the difficult post-processing and interpretation. ASL perfusion measure cerebral blood flow (CBF) via radio-frequency labelling of inflowing blood and therefore does not require contrast agent [3]. The aim of this study is to visually compare ASL with DSC in brain tumour patients and to evaluate the usability of visual interpretation without extensive post-processing for coregistration and quantification.

Subjects/Methods: We identified a retrospective cohort of 122 patients who underwent both DSC and ASL perfusion MRI during the same session in 2019 for surveillance of any intra-axial brain tumour. All patients were scanned at 3T (GE). ASL derived CBF maps ('ASL-CBF') were calculated with AW Server (GE), DSC derived rCBV (without leakage correction: 'DSC-rCBV') maps were calculated with IntelliSpace Portal (Philips Healthcare). Lesions were identified on T1w post-contrast, T2w or T2-FLAIR and classified as enhancing or non-enhancing. Each lesion was scored on each perfusion map as "low perfusion" if the lesion showed signal intensity lower than normal cortex and "high perfusion" if signal intensity was as intense as or more intense than normal cortex.

Results/Discussion: Table 1 shows patient characteristics. Of the 122 analysed scans, 63 scans showed at least one enhancing lesion and 9 had non-enhancing, mostly T2w-hyperintense lesions. 51 scans did not show any lesions.

Characteristic	Value
Mean age (yr, range)	54 (22-81)
Gender	86 male 36 female
Tumour type	
Glioma (all types)	86
Metastasis	15
Lymphoma	8
Other / unknown	13

Table 2 shows perfusion signals per lesion.

	ASL-CBF high	ASL-CBF low
DSC-rCBV high	25	8
DSC-rCBV low	5	34

Of these 72 lesions, 25 showed high signal both on ASL-CBF and DSC-rCBV and 34 showed low signal both on ASL-CBF and DSC-rCBV. All 8 scans which showed low ASL-CBF and high DSC-rCBV signal, showed susceptibility artefacts or contrast leakage on DSC-rCBV. All 5 scans which showed high ASL-CBF and low DSC-rCBV signals, showed a cortical localisation or localisation near the skull base. There was a relatively high concordance between ASL-CBF and DSC-rCBV upon visual assessment. Thirteen scans showed discrepancies which can all be attributed to limitations of DSC.

Future work, to be concluded at the time of the congress, will include an assessment of diagnostic accuracy after the ongoing 6 months' follow-up to confirm either the diagnosis of tumour progression or an alternative diagnosis.

References: 1. Chuang, M.T. et al, Plos One 2016, PMID: **26741961**
2. Jahng, G.H., et al, Korean Journal of Radiology, 2014, PMID: **25246817**
3. Grade, M., et al. Neuroradiology 2015, PMID: **26351201**

P01.11**Hypoxia alters posterior cingulate cortex metabolism during a memory task: a ¹H fMRS study**

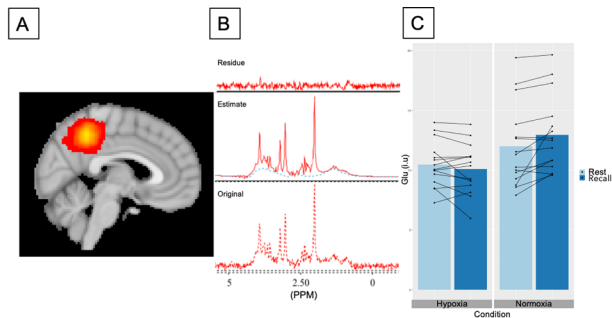
M. Rogan¹, A. Friend², S. Oliver², J. Macdonald², G. Rossetti², R. Edden³, M. Mikkelsen³, P. Mullins¹

¹Bangor University, Bangor Imaging Unit, School of Psychology, Bangor, UK, ²Bangor University, Extremes Research Group, School of Sport Health and Exercise Sciences, Bangor, UK, ³The Johns Hopkins University School of Medicine, Department of Radiology and Radiological Science, Baltimore, USA

Introduction: The brain is reliant on a supply of oxygen to meet neural metabolic demand via a relationship known as neurovascular coupling. Exposure to hypoxia such as that at high-altitude challenges this tightly coupled relationship. As arterial oxygen saturation falls, cerebral blood flow (CBF) increases to maintain oxygen delivery to mitigate any threat of decoupling between oxygen supply and demand. We have shown that the posterior cingulate cortex (PCC) has an unexpected decrease in CBF during acute hypoxia^(1,2). Furthermore, during a memory recall task, hypoxia reversed the task evoked BOLD signal within the PCC⁽²⁾. These findings suggest that hypoxia causes a regionally specific reversal of neurovascular coupling; however, the inherent vascular dependence of the BOLD signal means it cannot distinguish between vascular and metabolic alterations that may underlie this observation. This study utilised functional MRS (fMRS) to measure the metabolite dynamics within the PCC during a memory recall task during hypoxia. It was hypothesised that glutamate concentration within the PCC will increase in response to a memory recall task during normoxia and that hypoxia will not change this task induced glutamate response.

Subjects/Methods: In a repeated-measures crossover design 15 participants were exposed to 3.5 hours of normoxia (fraction of inspired oxygen (FiO₂) = 20.9%) and a procedurally matched poikilocapnic hypoxia (FiO₂ = 12.0%). After 2 hours resting, participants were

scanned at 3T whilst remaining in the respective condition. Event related fMRS (PRESS, TE = 40ms, TR = 2 s, voxel size $20 \times 20 \times 20 \text{ mm}^3$) allowed the probing of the dynamic alterations in metabolites during rest and memory recall in both conditions. Metabolite concentrations were estimated using QUEST (jMRUI), referencing to an unsuppressed water peak for absolute concentration estimations. A 2×2 repeated measures ANOVA was used to assess differences in metabolite concentrations between rest and task in both conditions.



A) Mean voxel location across participants and conditions. B) Example spectrum. C) Graph representing glutamate ANOVA results. Lines represent within condition rest to recall change in individual participants. Bars represent the group mean.

Results/Discussion: There was a significant main effect of task and condition for glutamate. In hypoxia, glutamate was observed to be lower during rest (10.5 ± 1.9 vs 12.0 ± 3.5 [i.u], $P = 0.07$) and memory recall (10.1 ± 2.1 vs 13.0 ± 3.2 , $P = 0.001$) compared to normoxia. Glutamate increased between rest and memory recall in normoxia, ($P = 0.01$), but this task induced increase was not present in hypoxia ($P > 0.05$). Glucose concentration in hypoxia was significantly lower during rest (0.83 ± 0.26 vs 0.65 ± 0.24 , $P = 0.01$) and recall (0.86 ± 0.24 vs 0.63 ± 0.25 , $P = 0.01$). No other measured metabolite was found to change.

Loss of task induced increases in glutamate during hypoxia suggest oxidative metabolism is altered within the PCC. However, the reduction in glucose seen during hypoxia would suggest the PCC is still metabolically active, but this may be sustained by non-oxidative means.

References: 1) Lawley J, et al (2017). *J. Physiology*. 2) Rossetti G, et al (2020). *JCBFM*

P01.12 Investigating distal ADC distribution for radiogenomic classification of gliomas via machine learning

F. K. Aras¹, H. Halilibrahimoglu², N. Renkli¹, A. Kaykayoglu¹, K. Ozduman¹, E. Ozturk-isik², N. Pamir¹, A. Dincer¹, A. Özcan¹

¹Acibadem Mehmet Ali Aydinlar Univ., Istanbul, Turkey, ²Bogazici University, Istanbul, Turkey

Introduction: Characterizing glioma infiltration in peritumoral normal-appearing white matter (pNAWM) might be relevant to the nature of the newly introduced genomic WHO 2016¹ classifications for identifying different disease subtypes. Microstructural changes inferred by the apparent diffusion coefficient (ADC) within the pNAWM distal to the tumor can be used as an infiltration measure. Herein, features of the ADC distributions of pNAWM bands with increasing distal thickness to the tumor boundary were used in machine learning algorithms (MLA) for classifying IDH and TERT mutations.

Subjects/Methods: In this IRB approved study, 24 patients (11F/13M, and 42.58 ± 16.74 years of age) with full data sets and written informed consent were analyzed. A 3T Siemens TrioTrimTM was used for collecting DW (EPI, TE/TR=114/4600ms, b=0, 2000s/mm², 20 slices) and T2W (TSE, TE/TR=107/3470ms, 20 slices) images. IDH and TERT mutation data were obtained using Sanger sequencing with an Applied BiosystemsTM 3500 Series Genetic Analyzer, and defined 4 molecular

subgroups: [double negative (-), IDH only (+-), TERT only (-+), double positive (++)] with 2, 10, 6 and 6 patients respectively.

ADC images were co-registered onto T2W images using symmetric diffeomorphic registration in ANTs² software. NAWM masks and whole tumor masks were semi-automatically delineated on T2W images^{3,4}

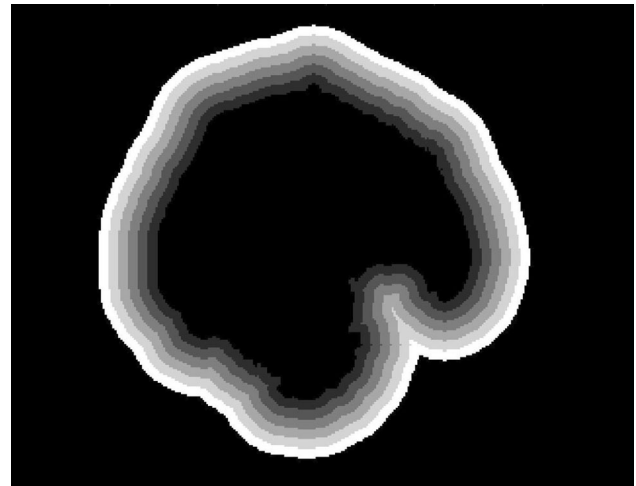


Fig. 1: Six peritumoral bands were obtained by dilating the tumor boundary (shown with gray levels).

In-house MATLAB[®] software created 1.28mm dilations of whole tumor masks at 6 peritumoral bands (Fig.1) and calculated a $6 \times 9 = 54$ -dimensional feature vector from mean, standard deviation, mode, kurtosis, skewness; 10th, 25th, 75th and 90th percentile points from each band's ADC distribution.

Using molecular subgroups as labels, MLAs in MATLAB package were run with leave-one-out cross-validation with 1) Principle Component Analysis (PCA) retaining 98% of the variance 2) retaining 3 components 3) without PCA.

Results/Discussion:

Classification Group	PCA Status	Accuracy	Sensitivity	Specificity	Precision
double negative (-), IDH only (+-), TERT only (-+), double positive (++)	OFF	50.0%	40.0%	82.0%	51.7%
IDH	Retaining 3 numerical components	79.2%	77.5%	77.5%	58.3%
TERT	Retaining 3 numerical components	66.7%	66.7%	66.7%	66.7%

Table 1: Best MLA Results from MATLAB Statistics and Machine Learning Toolbox Routines

ADC distribution features of pNAWM bands showed low to medium accuracy for classifying the genetic mutations of the tumors (Table 1), which raises the question whether different modes of infiltration are involved. Gliomas are known to infiltrate through blood vessels along with WM tracts⁵. Therefore, multimodal imaging studies creating a higher dimensional feature space may be more descriptive for characterizing the infiltration. Furthermore, performance of MLAs is influenced by sample size and label distributions⁶. More samples balancing cohort's group distribution might be useful for increasing MLA performance and effectiveness. Funding: TUBITAK-1003-216S432

References: 1 Louis, D. N. et al. *Acta Neuropathol* 131, 803-820. 2 Avants, B. B., et. al. *Medical Image Analysis* 12, 26-41, 3 Bazin, P.-L. et al. *Journal of neuroscience methods* 165, 111-121 4 Yushkevich, P. A., et. al. *Conf Proc IEEE Eng Med Biol Soc* 2016, 3342-3345 5 Scherer, H. J. *The American Journal of Cancer* 34, 333-351 6 Vabalas, A., et. al. *PLOS ONE* 14, e0224365

P01.13**Characterization of ventricular function in infarcted myocardium and its border zones by cardiac tagged MRI**

I. Del-Canto^{1, 2, 3}, M. P. López-Lereu⁴, J. V. Monmeneu⁴, S. Ruiz-España³, V. Bodi¹, F. J. Chorro¹, D. Moratal³

¹Health Research Institute INCLIVA, Valencia, Spain, ²Universitat Politècnica de València, Electronic Engineering, Valencia, Spain, ³Universitat Politècnica de València, Center for Biomaterials and Tissue Engineering, Valencia, Spain, ⁴Eresa, Unidad de Imagen Cardíaca, Valencia, Spain

Introduction: Quantification of regional myocardial function is a valuable non-invasive tool for the risk assessment of patients with myocardial infarction (MI) [1]. Myocardial deformation mechanisms, including regional strain and rotation, have been introduced as clinical markers of myocardial function and can be assessed by tagged MR imaging [2]. The aim of this study is to determine LV deformation parameters at different distances from MI by the combination of tagged MRI and late gadolinium enhancement (LGE) images in order to assess function in the infarcted ventricle and its border zones. **Subjects/Methods:** Cardiac tagged images and LGE images were acquired from 14 patients with previous MI. The deformation was measured from short-axis tagged images using an algorithm based on sine wave modeling [3]. Circumferential and radial strain (CS, RS) and local rotation were determined in 16 LV segments. Then, peak strain and time to peak (TTP) were measured. Infarct extent was determined from LGE images analysis [4] and the percentage of scar tissue area in the segment was used to classify it into 4 regions: infarct (> 25%), border zone (< 25% and immediately contiguous to the infarcted region), adjacent (without scar tissue and adjacent to those in the infarct or border regions) and remote (without scar tissue and located outside the adjacent region) (Figure 1). A one-way ANOVA test was used. Significance: $p < 0.05$.

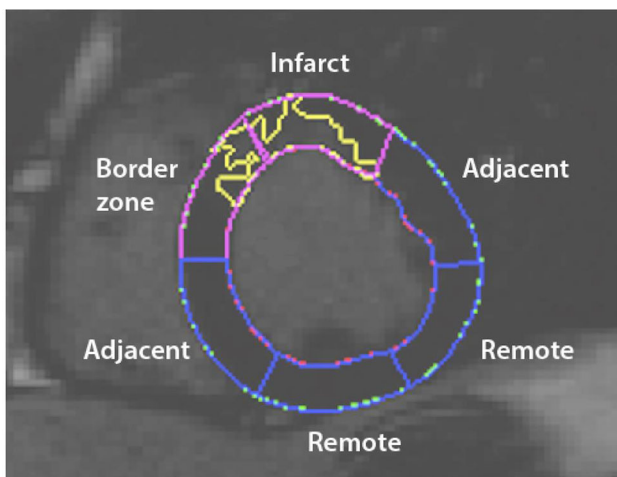


Figure 1. Classification of myocardial segments based on LGE transmuralty.

Results/Discussion: Based on the transmuralty and location of LGE, a total of 224 myocardial segments were divided into 97 remote, 62 adjacent, 23 border zone and 42 infarct. Peak CS for the remote ($p < 0.001$) and border zone ($p < 0.01$) areas was significantly greater than for the infarct areas; and peak RS was also greater for the remote ($p < 0.01$) and border ($p < 0.05$) segments than for infarct segments. Maximum apical rotation was found at the border zone segments ($p < 0.01$), and we observed that infarct zone presented similar values than adjacent and remote myocardium. There was no significant difference in the basal rotation values among the four regions (Figure 2). TTP CS and the TTP RS were significantly shorter for the remote ($p < 0.01$) and border zone ($p < 0.05$) than for infarct segments (Figure 3).

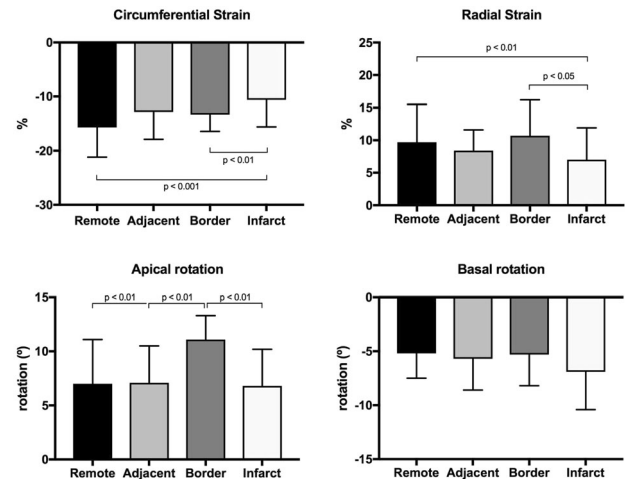


Figure 2. Peak strain and rotation values for infarct, border, adjacent and remote regions.

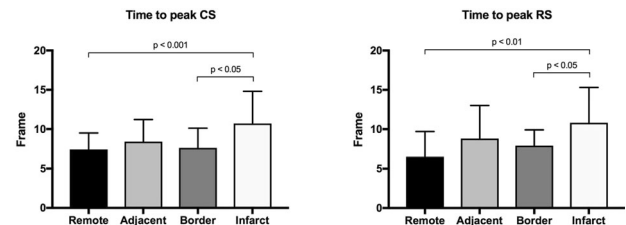


Figure 3. Time to peak strain values for infarct, border, adjacent and remote regions.

Quantitative assessment of LV strain and rotation by combining tagged MRI with LGE images provides mechanical characteristics of infarct and peri-infarct areas in patients with myocardial infarction, showing a correlation between contractile dysfunction and location at different distances from the infarct. Moreover, maximum apical rotation and earlier time to peak strain obtained in the peri-infarct region could be related with ventricular arrhythmias in post-MI patients.

- References:** 1. Wang N, et al. *Eur Heart J* 2016;37:466–472. 2. Chitboi T, Axel L. *J Magn Reson Imaging* 2017;46:1263–1280. 3. Arts T, et al. *IEEE Trans Med Imaging* 2010;29:1114–1123. 4. Kim RJ, et al. *N Engl J Med* 2000;343:1445–1453.

P01.14**MRI reveals brain ventricle expansion in pediatric patients with acute disseminated encephalomyelitis**

J. Millward¹, L. Bramé¹, K. Rostásy², M. Baumann³, T. Niendorf¹, S. Waiczies¹

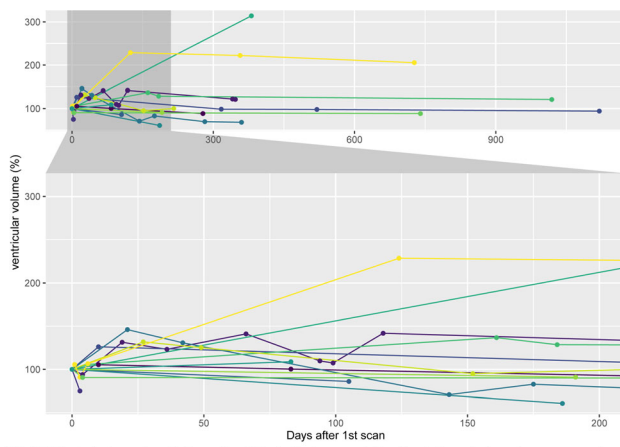
¹Max Delbrück Center for Molecular Medicine, Berlin Ultrahigh Field Facility, Berlin, Germany, ²Witten/Herdecke University, Department of Paediatric Neurology, Children's Hospital Datteln, Datteln, Germany, ³Medical University of Innsbruck, Division of Paediatric Neurology, Department of Paediatrics I, Innsbruck, Austria

Introduction: Pediatric patients with neuroinflammatory disease such as acute disseminated encephalomyelitis (ADEM) are at risk of impaired brain growth, with profound long-term neuropsychiatric consequences. ADEM patients have reduced brain volume and increased ventricle volume (VV) compared to age-matched controls.¹

In this study we examined VV changes in ADEM, investigating longitudinal MRI scans of pediatric ADEM patients, to distinguish temporary VV expansions (reflecting acute disease activity) from persistent ones (reflecting brain atrophy).

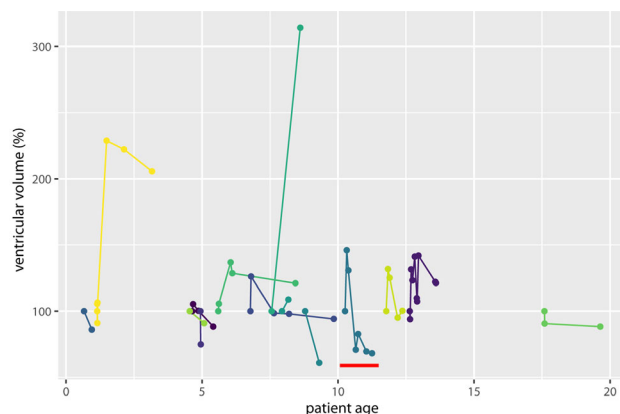
Subjects/Methods: Scans from patients with confirmed ADEM were obtained from 7 neurology clinics in Germany and Austria: n=14; 8/14 female; mean age=7.2 years (range 0.7-17.6). Brain VV was obtained from routine native T1-weighted scans (using FreeSurfer v6.0⁴ for scans with 1mm-isotropic resolution; for lower resolution scans using FMRIB Software Library FSL v5.0⁵ with manual correction. The same method was used for all scans of the same patient, to allow for consistent intra-individual comparisons.

Results/Discussion: Brain VV of ADEM patients showed a heterogeneous mixture of expansion and contraction, which generally stabilized over the long-term follow-up period (Fig1).



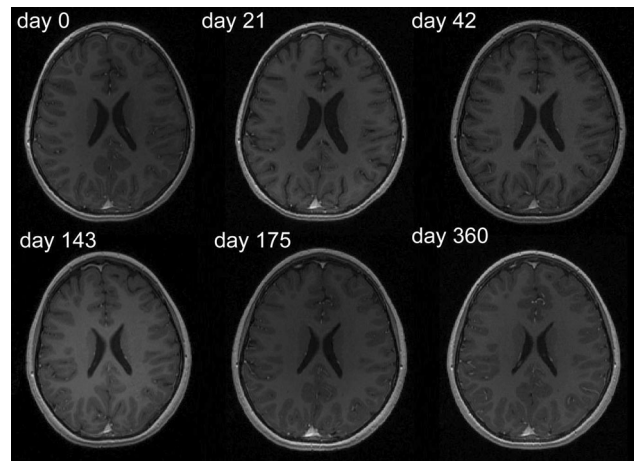
VV in ADEM patients change dynamically over time. VV is depicted as percent of baseline. In the acute phase, there was a complex mixture of VV contraction, expansion, and oscillation, which had generally stabilized in the long-term phase.

The majority of patients (11/14) showed VV contractions $\geq 10\%$; 3/14 patients showed exclusively expansion of VV (including one patient with $>300\%$ increase), although these three patients had only one follow-up scan. VV changes occurred in different age groups, and indicate that VV did not merely increase monotonically over time (Fig2).



VV changes plotted with respect to patient age. Dynamic VV changes occur across all ages in the cohort. Images from the patient marked in red are shown in Fig3.

Images from a representative patient show VV expanded beyond the initial level by the second timepoint, and subsequently contracted, reaching a value lower than baseline after 1y follow-up (Fig3).



Images from a representative patient show that VV had increased by d21 compared to baseline, and decreased by d143. At 1y follow-up VV was lower than at baseline, suggesting that the initial VV represented an expansion over the physiological volume.

The expectation for pediatric patients is that VV increases over time, with normal brain growth. In fact, the majority of these patients showed decreases in VV, either directly following the initial clinical event, or following subsequent VV expansion – often stabilizing during long-term follow-up. This suggests that, in some patients, the VV expansion was not a consequence of irreversible brain atrophy, but rather likely reflected some process associated with acute disease. In one notable case, the VV expanded during the course of the investigation, but did not return to baseline levels during the follow-up period, suggesting neurodegeneration and permanent brain damage. Monitoring VV could be a crucial marker to differentiate between transient processes and permanent damage, and plan treatment strategies accordingly.

- References:** 1. Baumgartner, B., et al. *Neuropediatrics* 50, S1-S55 (2019).
 2. Lepore, S., et al. *PloS one* 8, e72841 (2013).
 3. Millward, J.M., et al. *ISMRM Montreal, Canada* (2019).
 4. Fischl, B. *NeuroImage* 62, 774-781 (2012).
 5. Smith, S.M., et al. *NeuroImage* 23 Suppl 1, S208-219 (2004).

P01.15

Low-rank plus sparse compressed sensing for accelerated pulmonary imaging

K.-j. Chao, E. Ilicak, J. Zapp, L. Schad, F. Zöllner

Computer Assisted Clinical Medicine, Medical Faculty Mannheim, Heidelberg University, Mannheim, Germany

Introduction: Imaging of pulmonary function is of significant clinical value for diagnosis and follow-up investigations. To this end, Fourier Decomposition (FD) MRI was demonstrated to be a viable method for obtaining functional ventilation and perfusion maps during free-breathing [1]. However, this method critically depends on various acquisition parameters, including temporal resolution [2]. In a previous study, low-rank (L) plus sparse (S) matrix decomposition has been proven to be helpful to accelerate the dynamic cardiac MRI

while maintaining image quality [3]. Inspired by this work, we propose a novel reconstruction approach on this idea for free-breathing pulmonary imaging to improve the scan efficiency.

Subjects/Methods: In vivo acquisitions of a healthy volunteer (female, 29 years old) during free-breathing was obtained using a 1.5 T scanner (Avanto, Siemens Healthineers, Erlangen, Germany). 210 images were acquired using a 2D balanced steady-state free precession sequence with 0.1s pause between measurements, TR/TE = 1.88/0.80 ms, total acquisition time was 49 s. The scanner reconstructed images were then registered via a stand-alone non-rigid registration software. This dataset was then treated as the reference data [4]. The dataset was retrospectively undersampled in the phase encoding direction to yield acceleration rates (R) = 2-5 via variable-density random sampling. The reconstructions were obtained by solving an optimization problem (see Figure 1). At each iteration, the data were separated into L and S components, followed by temporal total variation (TV) and wavelet sparsity enforced on S part. To measure reconstruction quality, root mean square error (RMSE), peak signal-to-noise ratio (PSNR) and structural similarity index metric (SSIM) were calculated with the respect to the reference data for each R .

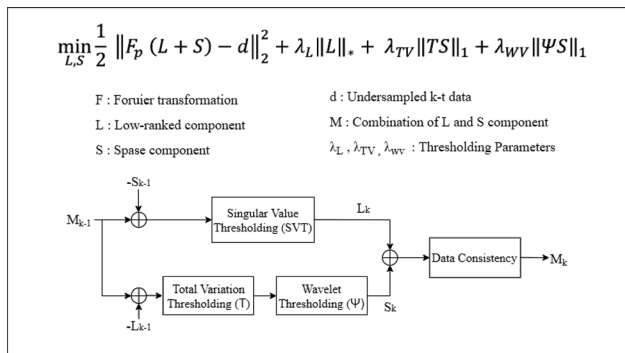


Figure 1: The formulated optimization problem and the flow chart of the reconstruction process. At each iteration, SVT and sparsity projections are used together with prior iteration solutions to minimize aliasing artifacts.

Results/Discussion: Figure 2 and Figure 3 show reconstructions for a representative cross-section and the quality performance across different R s, respectively. Our method is able to maintain image quality even at $R = 5$, without compromising tissue depiction. Quantitative assessments also reflect this observation, yielding an average PSNR > 43.2, RMSE < 0.008, SSIM > 98.98, for all R s.

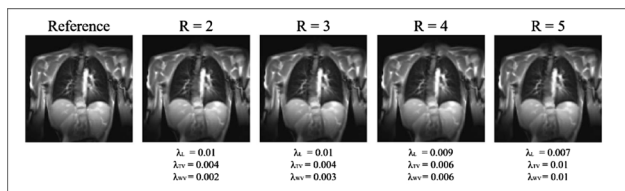


Figure 2: Representative reconstructions of a cross-section across $R = 2-5$. λ_L, λ_{TV} and λ_{WV} denote the thresholding parameters for singular value thresholding, total variation and wavelet denoising method, respectively.

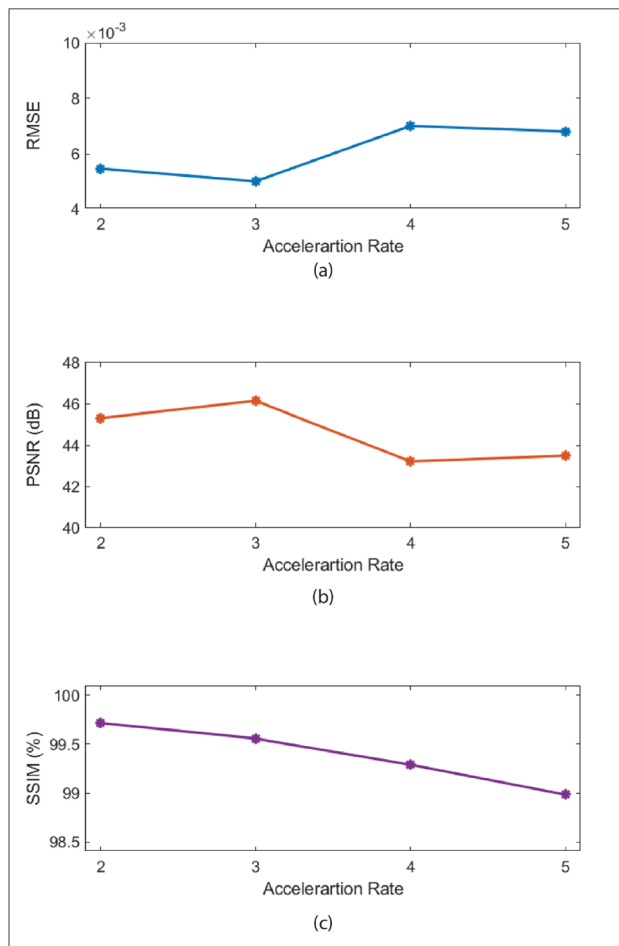


Figure 3: Image quality was measured using (a) RMSE, (b) PSNR and (c) SSIM

In this work, we have focused on the overall reconstruction quality, which does not necessarily represent the functional image quality. Although evaluation of function maps and studies with more subjects are warranted; our preliminary results indicate promising results for reconstructing undersampled acquisitions.

References: 1. Bauman, G., et al., *Magn Reson Med.* 2009;**62**(3): p.656–664
 2. Kjørstad, Å., et al. *MAGMA.*, 2014. **27**(6): p. 467-476.
 3. Otazo, R., et al., *Magn Reson Med.*, 2015. **73**(3): p. 1125-1136.
 4. Ched'hotel, C., et al., *Proc. Intl. Symp. Biomed. Imag.* 2002.
 The first two authors contributed equally to the work

P01.16
Combination of AlignedSENSE and groupwise motion-compensated compressed sense for cardiac cine MRI reconstruction

A. Godino-Moya¹, R. M. Menchón-Lara¹, M. Martín-Fernández¹, C. Prieto², C. Alberola-López¹

¹Universidad de Valladolid, Image Processing Lab, Valladolid, Spain, ²King's College London, School of Biomedical Engineering and Imaging Sciences, London, UK

Introduction: Motion is the major source of artifacts in MRI, especially in those modalities that require long scan times or when imaging moving organs. Previous approaches rely on retrospectively binning the acquired k-space data in different motion states and

reconstructing the corresponding images¹; motion compensation can also be added to improve image quality^{2–3}. Such approaches involve high computational cost and the binning process causes that scarce data are available for each motion state, especially when high acceleration factors are considered; the reconstruction problem is worse posed and, consequently, more difficult to solve. Aligned-SENSE⁴ (AS), however, obtains directly a motion-free image and a set of spatial transformations without the need of additional images. It relies on the idea that motion can be described with fewer parameters than the images themselves, resulting in a better posed reconstruction problem.

In this work a methodology that combines AS and a groupwise motion-compensated compressed sensing^{2–3} (GWCS) strategy for reconstructing cardiac cine MRI is proposed.

Subjects/Methods: The proposed method consists of two phases. In the first one, a reconstruction based on the AS algorithm was performed. This approach was originally formulated for rigid deformations; therefore, we carried out an extension to non-rigid deformation; spatio-temporal regularization terms were also included. Afterwards, the resulting output was fed to the GWCS phase.

Fully sampled 2D Cartesian breath-hold cine cardiac acquisitions with 32 coils from 7 volunteers were retrospectively subsampled and reconstructed for different acceleration factors to validate the proposed method. SER and HFSE⁵ were calculated as image quality measurements. Due to the lack of a reliable ground truth, fully sampled images and reconstructions as well were registered to adjacent frames to compare the resulting displacement fields; RMSE between them was used as measurement of the motion quality.

The proposed integrated method has been compared with GRASP¹, GWCS² and the original AS⁴.

Results/Discussion: Fig.1 shows temporal profiles for a representative case where differences appear depending on motion direction; Fig.2 shows the effect of acceleration factor. The proposed method presents less blurred edges in endocardium and papillary muscles; movement seems more faithful in AS and MIX than the other, but AS introduces some tremor. This is coherent with results provided in Fig.3; the proposed method gives rise to higher SER and HFSE; RMSE values point out that general movement in the image is also better preserved.

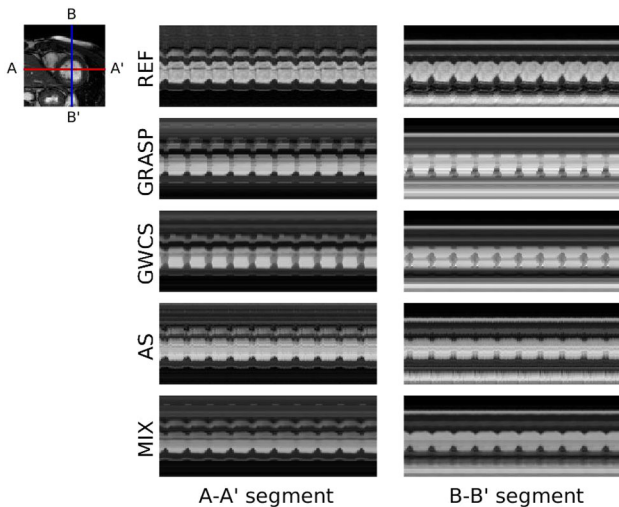


Fig 1. Temporal profiles for a representative case (acceleration factor 18) in different directions. REF: reference image; GRASP: GRASP method; GWCS: Groupwise motion-compensated compressed sensing; AS: AlignedSENSE; MIX: proposed integrated method.

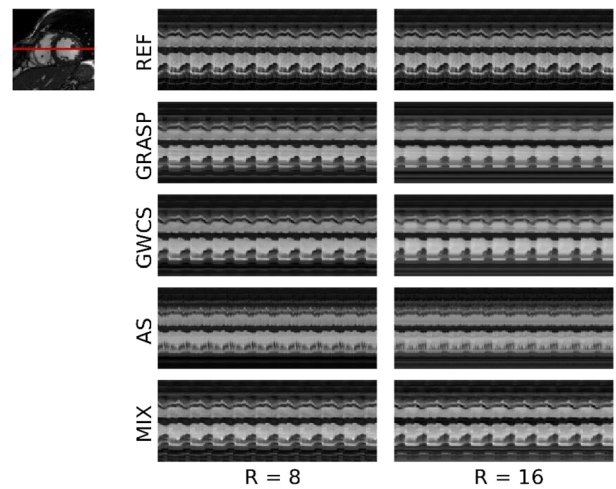


Fig2. Temporal profiles for acceleration factors of R=8 (left) and R=16 (right). REF: reference image; GRASP: GRASP method; GWCS: Groupwise motion-compensated compressed sensing; AS: AlignedSENSE; MIX: proposed integrated method.

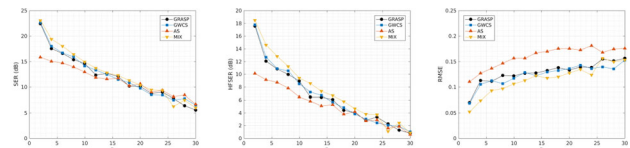


Fig3. SER (left), HFSE (center) values between reconstructions and reference images for different acceleration factors (R). RMSE values between displacement fields derived from fully sampled images and reconstructions are shown on the right.

References: ¹ Feng, L. et al. (2014) doi:10.1002/mrm.24980
² Royuela-del-Val, J. et al. (2017) doi:10.1002/mrm.26198
³ Menchón-Lara, RM et al. (2017) doi:10.1007/978-3-319-67564-0_14
⁴ Cordero-Grande, L. et al. (2016) doi:10.1109/TCI.2016.2557069
⁵ Godino-Moya, A. et al. (2019) doi:10.1016/j.mri.2019.01.005

P01.17

Water T2 relaxometry in fat-containing tissues using a T2-prepared Dixon-TSE sequence

Y. Zhao¹, S. Ruschke¹, D. Weidlich¹, M. Wu¹, C. Held¹, M. Doneva², M. R. Makowski¹, B. Menze³, D. C. Karampinos¹

¹Department of Radiology, Klinikum rechts der Isar, School of Medicine, Technical University of Munich, Munich, Germany, ²Philips Research Europe, Hamburg, Germany, ³Department of Computer Science, Technical University of Munich, Garching, Germany

Introduction: Quantitative water T2 (T2w) mapping is a promising tool for assessing edema, tumors and iron deposition.¹ However, the quantification of T2w becomes challenging in fat-containing tissues like bone marrow, fatty liver, fatty muscle, soft tissue tumors and brown adipose tissue (BAT). Accurate T2w mapping requires to either fully suppress the fat component or to separate the water signal from the fat signal.² The present study aims to theoretically compare and validate three signal modeling strategies for T2w mapping using a T2-prepared (T2prep) Dixon-Turbo-Spin-Echo (dTSE) sequence and apply the methods in the human supraclavicular fossa.

Subjects/Methods: *Signal model*

Three models were defined and implemented based on a general signal formulation³ and extended as follows (Fig1a): Model A comprises a simple 2-step approach, model B uses a single-step approach with positive-constrained T2 and model C extends model B

with a T2prep specific pre-calibrated fat model. Models A and B use a 10-peak triglyceride model⁴ calibrated for human subcutaneous tissue (ndb:2.88, nmdb:0.70, CL:17.48)⁵. T2* relaxation was neglected.

For models A and B, theoretical T2w model biases were simulated (reference: model C) for varying T2w and PDFF. Cramér-Rao lower bound (CRLB) and Monte Carlo (MC) analyses were performed for the estimation of T2w.³

Sequence and measurements

A BIR4-based T2prep 3D dTSE sequence (Fig1b) was acquired in the cervical region of 3 healthy volunteers with TEs of -0.2/0.6/1.4ms and effective T2prep-weighting of 13.6/20.4/27.2ms, resolution:2x2x2mm³, FOV:400x120x20mm³, TR:1450ms, TSEfactor:30, echo spacing:6.1ms, 16-channel anterior coil & 12-channel posterior coil scan duration:7:54min. Fatty tissue in the supraclavicular fossa (BAT depot) was manually segmented based on proton density fat fraction (PDFF) maps and defined as the region of interest (ROI).

The pre-calibrated fat model (model C) was determined in an oil phantom using the identical T2prep module with a STEAM MRS (TR/TE/TM:5000/10/16ms) readout (Fig1b). Scans were performed on a 3T scanner (Ingenia Elition, Philips).

a) Model formulation

Model A: Step 1: $S(TE) = \sum_{m=1}^M \rho_m e^{i\phi_m} e^{i2\pi w_m TE}$ Step 2: $S(TE_{prep}) = \rho_{water} e^{-\frac{TE_{prep}}{T_{2water}}}$

Two-step approach

Model B: $S(TE, TE_{prep}) = \sum_{m=1}^M \rho_m e^{i\phi_m} e^{i2\pi w_m TE} e^{-\frac{TE_{prep}}{e^{\tau_{2m}}}}$

Single-step approach with positive-constrained T₂

Model C: $S(TE, TE_{prep}) = \sum_{m=1}^M \rho_m \theta_m TE_{prep} e^{i\phi_m} e^{i2\pi w_m TE} e^{-\frac{TE_{prep}}{e^{\tau_{2m}}}}$

Single-step approach with positive-constrained T₂ and pre-calibrated fat model

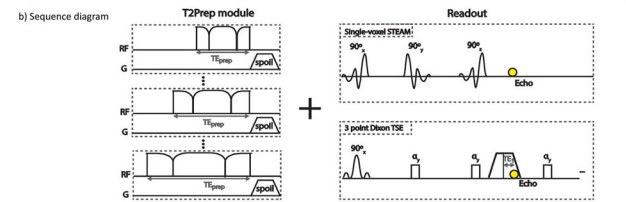
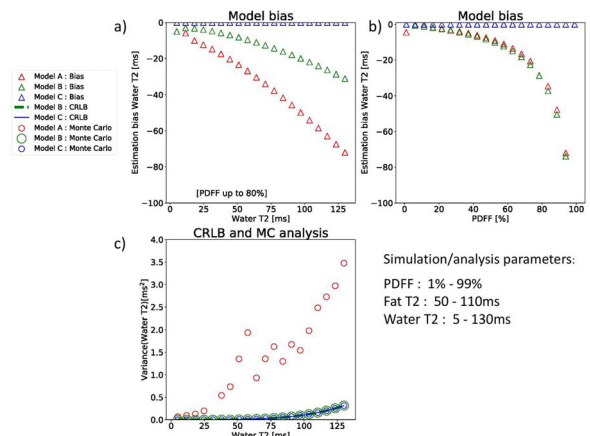


Fig1. a) quantification models: A, 2-step model, B single-step model w/ positive-constrained T2, C single-step model w/ positive-constrained T2 and pre-calibrated fat model. b) sequence: T2prep module combined with single-voxel STEAM or Dixon-TSE readout

Results/Discussion: For models A and B, the T2w model bias analysis (Fig2ab) yielded an underestimation of T2w with increasing true T2w and PDFF. In the CRLB and MC analysis (Fig2c), model A showed the largest parameter variances; models B and C showed comparable variances. All three models showed increasing variances with increasing true T2w. Theoretical trends were confirmed in the in vivo measurements (Fig3): Models A and B obtained lower median T2w values in BAT.

The present study demonstrated that quantitative T2w mapping in fat-containing tissues based on T2prep dTSE depends on the underlying quantification strategy and that a T2prep specific pre-calibrated fat model prevents a potential underestimation of T2w.



Notice: Displayed values represent the largest bias/variance in the simulated/analyzed parameter space

Fig2. Models A, B tend to underestimate water T2 in the error simulation(model C as true model)for varying a) water T2 and b) PDFF. c) CRLB and MC analysis for the estimation of water T2 yielded higher variances for model A compared to models B and C

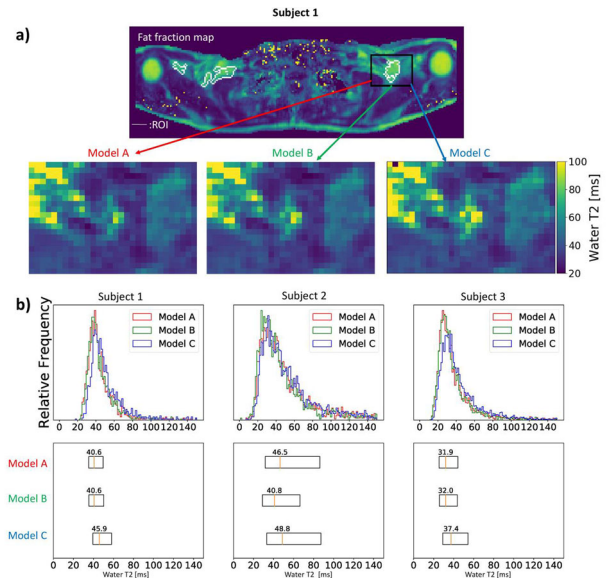


Fig3. In vivo results: a) example ROI (single slice) and water T2 maps in one of the subjects. b) ROI histograms and boxplots (median & quartiles) of water T2 in three subjects. Models A and B estimated lower water T2 values compared to model C.

References: 1. Cheng, *JMRI*, 2012
 2. Bojorquez, *MRI*, 2017
 3. Diefenbach, *QIMS*, 2020
 4. Berglund, *MRM*, 2012
 5. Bydder, *MRI*, 2011

P01.18**Vessel distance mapping**H. Mattern¹, O. Speck²

¹Otto-von-Guericke-University, Magdeburg, Biomedical Magnetic Resonance, Magdeburg, Germany, ²Otto-von-Guericke-Universität, Magdeburg, Biomedical Magnetic Resonance, Magdeburg, Germany

Introduction: Recently vessel atlases have been introduced^{1,2} to enable voxel-based morphometry of the vasculature. These atlases are built by co-registering the vasculature of all subjects non-linearly. While the major vessels are consistent between subjects, the vascular inter-subject variability increases with decreasing vessel size. Thus, registration and assessment of these variable small vessel patterns is challenging. Vascular pattern analysis is aggravated further by the routine uses of dimensionality-reducing techniques such as intensity projections for visual inspection and ROI-summarized metric for quantitative interpretation.

We propose vessel distance mapping (VDM) to overcome these challenges. After vessel segmentation, the distance to the closest vessel is computed for each non-vessel voxel. This so-called distance transform interpolates the sparse vessel data and is tested for high resolution arterial and venous data acquired at 7T.

Subjects/Methods: Six subject consented to this study (approved by the local ethics committee) and were scanned at 7T (Siemens Healthineers, Erlangen, Germany) with a 32 channel head coil (Nova Medical, Wilmington, USA).

Arteries and veins were depicted with Time-of-Flight (ToF) angiography and Quantitative Susceptibility Mapping (QSM), respectively. MSDI was used for QSM reconstructions³. All images were upsampled from at 0.3 x 0.3 x 1 mm to 0.3 mm isotropic resolution and non-linearly co-registered using ANTs⁴.

Vessels were segmented in the images using a Frangi vesselness filter⁵, followed by thresholding. Afterwards, Euclidian distance transform⁶ was applied to interpolate the sparse vessel information and generate VDMs (see Fig.1). Arterial and venous VDMs for each subject and the group average are shown in Fig.2.

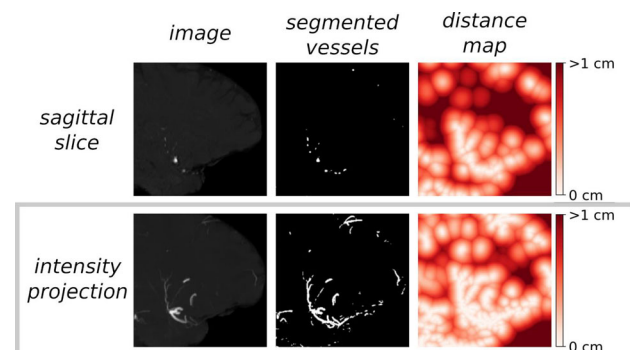


Figure 1: From the image data vessels are extracted using a vesselness filter and thresholding. Afterwards, a distance transform is applied to interpolate the sparse vessel information. Additionally, intensity projections are shown.

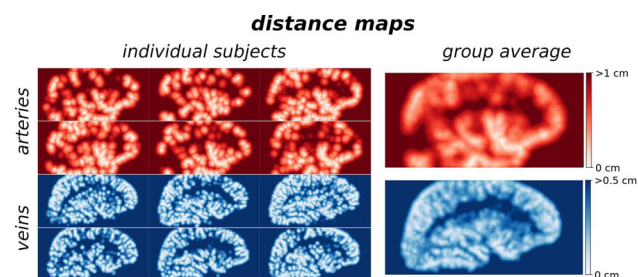


Figure 2: Arterial and venous distance maps for six subjects and their group average. While bright voxels represent vessels, non-vessel voxels with more than 1cm distance to an artery or 0.5cm to a vein are shown in dark red and blue, respectively.

Results/Discussion: The computed maps are plausible, as distances are lower in gray than white matter and resemble perfusion maps to some extent (see Fig.2). Compared with vessel probability maps, distance maps interpolate the sparse vessel images (see Fig.3) This could have several advantages: 1) A single 2D slice provides information about the nearby 3D proximity without using a projection; 2) The vasculature is assessed with respect to non-vessel voxels. Thus, a potential tool to link vasculature and structure quantitatively is provided. 3) Machine-based interpretation and non-linear registrations might benefit from the non-sparse distance maps compared to sparse vessel images.

Like other vessel morphometry pipelines, VDM results depend on the image resolution. By varying the sensitivity of the vesselness filter, VDM can be computed at multiple scales to study this dependency in the future.

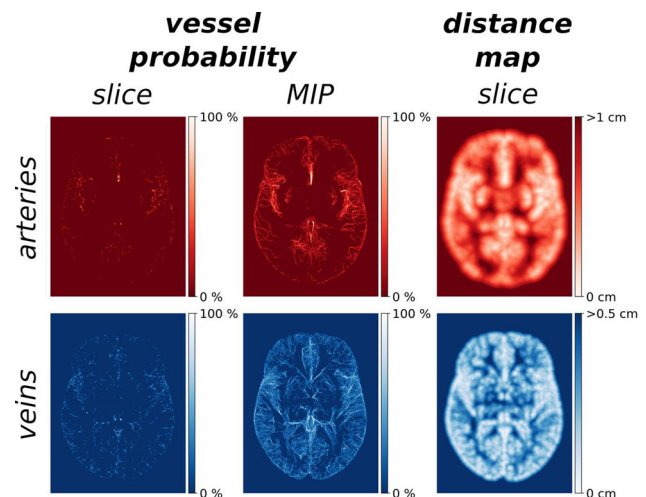


Figure 3: Comparison of vessel probability and distance maps for arterial and venous vasculature, respectively. Unlike vessel probability maps, a single 2D distance map provides an intuition about the 3D distribution of the vasculature.

Acknowledgment

This work was funded by the DFG-MA 9235/1-1.

References: ¹ Huck et al. Brain Struct Funct. 2019

² Bernier et al. HBM. 2018

³ Acosta-Cabronero et al. NeuroImage. 2018

⁴ Avants et al. Medical Image Analysis. 2008

⁵ Frangi et al. MICCAI. 1998

⁶ Maurer et al. IEEE. 2003

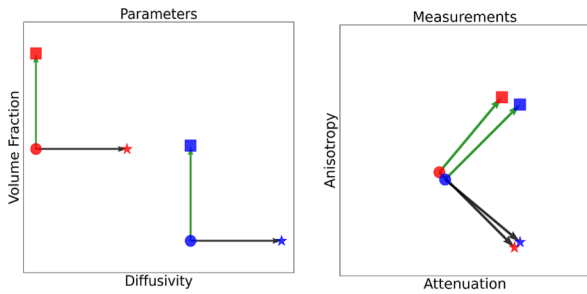
P01.19**Inversion-free identification of microstructural changes in diffusion MRI**

H. Rafipoor, S. Jbabdi, M. Cottaar

University of Oxford, Wellcome Centre for Integrative Neuroimaging, Nuffield Department of Clinical Neuroscience, Oxford, UK

Introduction: Diffusion MRI data is sensitive to a wide variety of changes in microstructural tissue properties. This means that any realistic microstructural model has many more parameters than can be estimated from the data and thus cannot be inverted. To circumvent this, the common practice is fixing some parameters of the model and estimate the rest. Any change in the diffusion MRI data between subjects will be explained by these pre-selected free parameters even if they are caused by something else. Here we present a novel approach that asks the question “given a change in diffusion data, what is the best microstructural parameter(s) that can explain the

change?” This question can be answered without explicitly inverting the forward model.



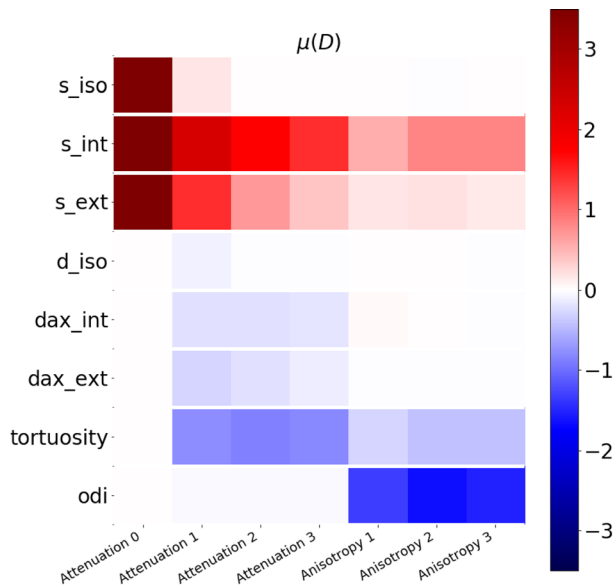
Samples in parameter space and their corresponding measurements. Distinct parameter settings may produce identical measurements. Yet, we can identify the altered parameter(arrows) without knowing actual parameter values by directly modeling changes.

Subjects/Methods: As we are only interested in the microstructural parameters, our input data is a vector D with the rotation-invariant mean and anisotropy of the diffusion data in each shell. Given some model of diffusion, we aim to compute how well each subset of model parameters ($S = \{p_1, \dots, p_k\}$) explains an observed change in the data ΔD due to e.g., disease or aging. To this end, we estimate the posterior probability of which parameters are in the subset: $P(SID, \Delta D) \sim P(\Delta DID, S) * P(SID)$

We assume no prior preference, i.e. $P(SID)=1$. Consequently, our main goal is to calculate the likelihood probability, $P(\Delta DID, S)$, by integrating over all possible values of the change in parameters presented in the set (Δv):

$$P(\Delta DID, S) = \int P(\Delta DID, \Delta v) P(\Delta v) d\Delta v$$

We efficiently solve this equation by approximating $P(\Delta DID, \Delta v)$ as a Gaussian, whose mean and variance can be computed offline using the forward model before looking at any actual data.

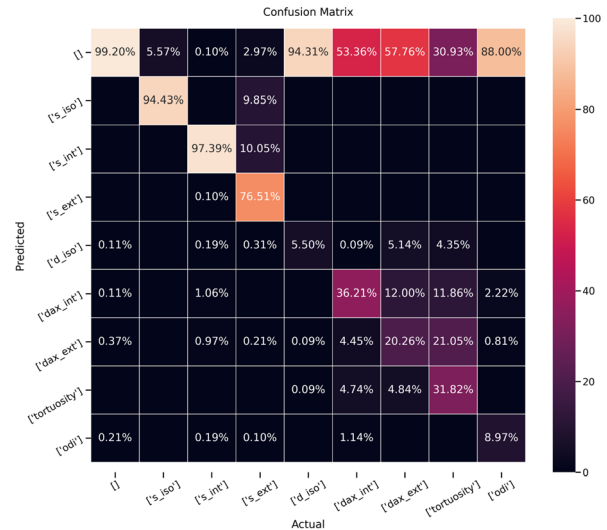


Estimated mean patterns of change in measurements for a sample data as a result of altering each of the parameters in the presumed model (Watson-NODDI). Measurements are represented by attenuation and anisotropy in three b-shells (b=0,1,2,3 ms/μm²).

Results/Discussion: For a Watson-NODDI model [1] we estimate how we expect the data to change for each parameter ($P(\Delta DID, \Delta v)$) (fig. 2). Note that the original NODDI model fixes all but 3 free parameters. Here we keep all possible parameters free to change (total=8 parameters), which means the model cannot be inverted. We

simulated a dataset with 3 shells (b=0, 1, 2 & 3) containing pairs of measurements with a single changed parameter using the same forward model. We then tested whether our approach was able to successfully identify which parameter changed (fig. 3).

The proposed algorithm can successfully identify the correct change in most cases, although our model predicts no change (i.e. the empty set) when the change in the data was small enough to be explained by noise. This is especially apparent for parameters that the data is less sensitive to (e.g., d_{iso}). Also, we observe confusion between the diffusivity parameters, as they have similar effects on the measured signals. Altogether, the presented approach shows that we can identify true changes in a highly overparametrized forward model without inversion.



The confusion matrix shows high precision in identifying the actual change for signal fraction parameters, while changes in diffusivity parameters mostly attributed to noise (no parameter change) or confused with each other.

References: 1- Zhang, Hui, et al. 2012 *Neuroimage* 61 (4): 1000-16.

P01.20

Relations between functional brain connectivity and intelligence using functional MRI and graph techniques

V. Ghibaudo¹, A. Stadler², B. Barile², F. Nusbaum³, S. Mouchet-Mages⁴, D. Sappey-Marini⁵

¹Université de Lyon, CREATIS, UMR5220 & U1206 INSERM, Centre Hospitalier Le Vinatier, Lyon, France, ²Université de Lyon, CREATIS, UMR5220 & U1206 INSERM, Lyon, France, ³Université de Lyon, Laboratoire P2S, Lyon, France, ⁴Centre Hospitalier Le Vinatier, Laboratoire P2S, Bron, France, ⁵Université de Lyon, CREATIS, UMR5220 & U1206 INSERM, CERMEP-Imagerie du vivant, Lyon, France

Introduction: Neuroscientists have investigated the neural substrate of intelligence using the most recent neuroimaging techniques such as functional MRI (fMRI) and diffusion tensor imaging (DTI). More recently, theory of graph has been used to model the cerebral connectivity measured by MRI and search for correlations with intelligence indices (1). A previous teamwork has shown that high intelligence quotient (IQ) of children had a more uniform topology of functional brain networks (2). Therefore, we aimed in this work to investigate such issues in adults.

Subjects/Methods: 60 men (aged from 20 to 60 years old) underwent resting-state fMRI acquisitions using an EPI BOLD sequence with a

multiband factor of 6 (700 scans, TR = 750 ms, TE = 30 ms, voxel size = 2.2 x 2.2 x 2.2 mm, FOV = 211 x 211 mm). Then, they were tested using the Wechsler Adult Intelligence Scale Fourth version (WAIS-IV) to assess their IQ. Three main indices were measured: Full Scale Intelligence Quotient (FSIQ), Verbal Comprehension Index (VCI), and Perceptual Reasoning Index (PRI). After data pre-processing, we calculated different global and local metrics using graph techniques, based on the functional connectivity matrices obtained in each subject. Correlations between graph metrics and IQ scores were then statistically analyzed.

Results/Discussion: Several global and local graph metrics were significantly correlated with different intelligence indices. Only one global metric, the Transitivity, was significantly negatively correlated to the PRI of the subjects. From the local analysis, six cerebral nodes were correlated with intelligence indices: bilateral caudal anterior cingulate, left paracentral lobule, left putamen, left accumbens, and left thalamus (Table 1). Degree measures the number of connections of one node with others while Betweenness Centrality (BC) measures the fraction of shortest paths passing through a given node. Both are related to the integration of a node into a network. Thus, the increased degree and BC with IQ highlight the role of the anterior cingulate, related to risk and decision management, in intelligence as well as accumbens and putamen, two striatal nuclei, also implicated in reward system and decision-making.

Table 1: Linear significant correlations between local metrics of network and Full-Scale Intelligence Quotient (FSIQ), Verbal Comprehension Index (VCI), Perceptual Reasoning Index (PRI).

Index	Hemisphere	Degree			Betweenness Centrality		
		FSIQ	VCI	PRI	FSIQ	VCI	PRI
Caudal Anterior Cingulate	Left	ns	ns	ns	0.04*	ns	0.04**
	Right	0.44**	0.43*	0.34*	0.03*	ns	ns
Paracentral	Left	0.68***	0.55*	0.66***	0.05*	0.06*	ns
Accumbens	Left	-0.46*	ns	-0.46*	-0.02**	ns	ns
Putamen	Left	ns	-0.59**	ns	ns	ns	ns
Thalamus	Left	-0.26*	-0.05*	ns	-0.04*	ns	ns
	Right	ns	ns	ns	ns	ns	0.02*

*p-value<0.05, **p-value<0.01, ***p-value<0.001, ns = non-significant

In conclusion, our study showed in men adults, a relationship between intelligence and the homogeneity of the functional brain connectivity, particularly in limbic systems. These findings obtained in adults confirmed those found previously in a children population.

References: (1) Song et al.(2008). Brain spontaneous functional connectivity and intelligence. *NeuroImage* 41, 1168–1176

(2) Kocevar et al. (2019). Brain structural connectivity correlates with fluid intelligence in children: A DTI graph analysis. *Intelligence* 72, 67–75

(3) Suprano et al. (2019). Topological Modification of Brain Networks Organization in Children With High Intelligence Quotient: A Resting-State fMRI Study. *Front. Hum. Neurosci.*

P01.21

Somatotopy mapping of the sensory thalamic nucleus at 7T

O. Mougín, O. Adeyemi, P. Gowland, R. Sanchez Panchuelo

University of Nottingham, Sir Peter Mansfield Imaging Centre, Nottingham, UK

Introduction: Maladaptive reorganization of the somatosensory system may originate at the level of the thalamic nuclei in the

pathway to the cerebral cortex. However, the reliable localization of thalamic nuclei with MRI has been difficult. Ultra-high field (7T) MRI offers improved SNR and contrast mechanisms to visualize intra-thalamic nuclei [1]. Here, we use structural MRI to localize the sensory ventro-posterior lateral (VPL) nuclei of the thalamus in-vivo and functional MRI using a motor task paradigm to characterize the hand/foot and finer D2/D5 somatotopy within the VPL nucleus.

Subjects/Methods: Two subjects participated in two separate (Hand/Foot and D2/D5) fMRI mapping sessions at 7T. The paradigm was a block (12s ON, 16s OFF) design consisting of 8 blocks alternating between movement (ball squeezing) of the right hand and of the right foot (session 1) or a button press alternating between D2 and D5 (session 2). Eight fMRI runs were performed in each session. fMRI data was acquired using GE-EPI (TE=22ms, TR=2s, 26 coronal slices, 1.5mm isotropic resolution) and analyzed using a GLM. Z-statistical maps (after FDR correction for multiple comparison) are displayed at $z > 3.08$. High spatial resolution MP2RAGE (0.4 x 0.4 x 1 mm³, T11/T12 = 0.7/1.9 s, TRshot = 5s) and cardiac gated FLASH (0.3 x 0.3 x 1.2 mm³, TE = 25ms) data were acquired in a separate anatomical scan session. The first MP2RAGE volume was used with a multi-atlas segmentation method [2] to delineate the VPL nucleus, and the FLASH data was used to provide a vein mask. The location of activations in the thalamus were spatially compared with the subject's VPL structural boundaries.

Results/Discussion: The anatomically derived VPL segmentation (magenta, Fig.A) partially overlaps with the BOLD activations for hand and foot locations in contralateral thalamus (Fig.Bi), with representation of the hand (yellow) found medially with respect to the foot representation (cyan). Within the hand region, the representations for D2 (green) and D5 (red) largely overlap (Fig.Bii) in subject 1, but in subject 2 D5 extends posterior-laterally with respect to D2.

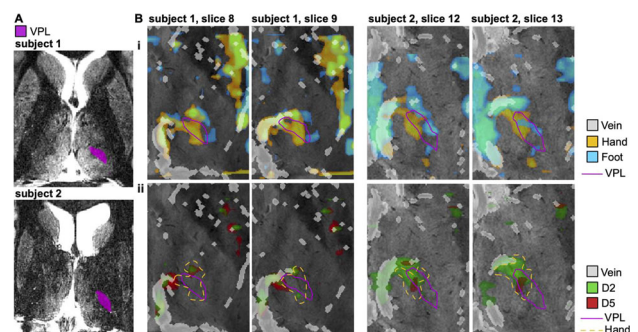


Figure 1: (A) VPL segmentation (magenta) over MP2RAGE first volume. (B) Activation maps for (i) hand (yellow), foot (cyan), (ii) D2 (green) and D5 (red), over FLASH data. White region: veins. Magenta line: VPL boundary. Yellow line: hand area.

Discussion: We show correspondence of the hand and foot activations (which overlap medially and laterally respectively) with the subject specific anatomically defined VPL. The observed hand/foot somatotopy is consistent with the medial to lateral organization within the VPL for digits-arm-leg described from direct electric stimulation in humans [3]. Although in subject 2 the D2-D5 somatotopy also seems to follow the expected somatotopy, more subjects are needed to corroborate this finding.

References: [1] Tordias et al (2014). *NeuroImage*, 84:534-45.

[2] Su et al (2019). *NeuroImage*, 194:272-82.

[3] Lenz et al (1988). *J Neurophys*, 59:299-316.

P01.22**A feasibility study of an automatic detection method of the stationary period of the coronary artery using the convolutional neural network (CNN)**

R. Kasai, Y. Endo, H. Shibo, M. Amanuma, K. Kobayashi, S. Kuhara

Department of Medical Radiological Technology, Faculty of Health Sciences, Kyorin University, Mitaka-shi, Tokyo, Japan

Introduction: Magnetic resonance imaging (MRI) of the coronary arteries requires acquisition of data during the stationary period of the coronary arteries. Therefore, it is important to know the stationary period accurately. However, detection of the stationary period of the coronary arteries is currently time-consuming and operator-dependent because it is visually determined by the operator from cine images. As a method of automatically extracting the stationary period, a template-matching method has been developed for tracking the position of the coronary arteries [1]. However, because the shape of the coronary arteries changes during the cardiac phase, it is difficult to detect its position for all cardiac periods using a single template for each coronary, even more difficult for both sides. Template methods can also suffer from individual patient diversity. In addition, some ROI setting operations make it difficult to be fully automated. To solve this problem, we developed an automatic detection method for the stationary period of coronary arteries using the convolutional neural network (CNN) and investigated the feasibility of this method.

Subjects/Methods: Steady-state free precession cine images (4ch, 31–63 phases, total of 125 images) of healthy volunteers were obtained using 3T MRI (Vantage Titan 3T, Canon Medical Systems). We proposed a method to detect the coronary artery position on the four-chamber-view cine images of each cardiac phase using the CNN. A single-shot multi-box detector [2] was used as the CNN, and the 4ch and right and left coronary arteries were labeled on each of the 94 cine images and used for the fine tuning of transfer learning. Thirty-one resting images were used for testing. The centroid of each detected region of interest (ROI) box was calculated, and the amount of movement of temporally adjacent ROIs was then calculated on each cine image. The curve of the coronary artery movement was then drawn, and the stationary period of coronary artery was estimated. A comparison of the proposed method and template method was also performed.

Results/Discussion: Using the proposed CNN-based method, a higher degree of coronary artery detectability was possible in all phases without any manual operation compared to that using the template method. Moreover, it was possible to detect both coronary arteries simultaneously in all phases (Figure 1). Figure 2 shows the case of RCA. Based on the coronary artery movement curve, the stationary period was estimated to occur from the 19th to the 26th frames of the cine images, which was in agreement with the visual assessment by the operators. The proposed method is expected to contribute to improving the accuracy of coronary artery stationary period determination, shortening the examination time, reducing operator dependence.

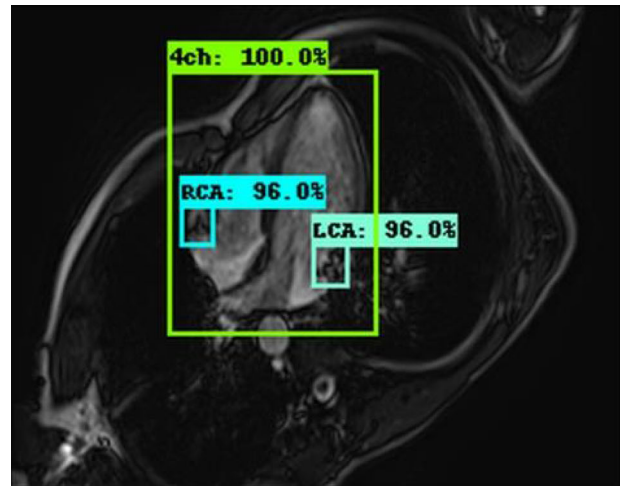


Figure 1. Detection result for the 4ch, RCA and LCA

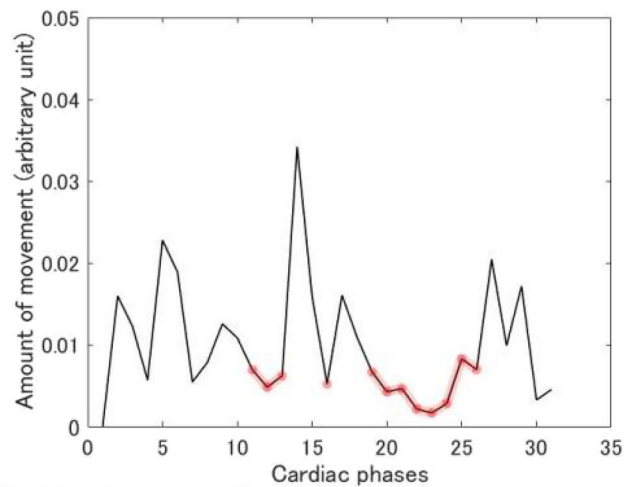


Figure 2. Curve of coronary movement (in case of RCA)

References: [1] A. Ninomiya, et al. JCMR 2010, 12(Suppl 1):P34
[2] W. Liu., et al. In ECCV, 21–37, 2016

P01.23**A radiomics-based approach to predict therapy response in advanced melanoma patients treated with immunotherapy**

A. Liebgott¹, T. Haueise², S. Gatidis¹, V. C. Vu¹, B. Yang²

¹University Hospital of Tuebingen, Diagnostic and Interventional Radiology, Tuebingen, Germany, ²University of Stuttgart, Institute of Signal Processing and System Theory, Stuttgart, Germany

Introduction: Using immunotherapy on patients with malignant melanoma is a promising approach to treat advanced stages of the disease¹. However, the therapy can cause serious side effects and not every patient responds to it, which means crucial time may be wasted by an ineffective treatment. Assessment of the possible therapy

response is hence an important research issue. The work presented in this study focuses on the investigation of the potential of medical imaging and machine learning to solve this task. To this end, we extracted Radiomics² features from multi-modal images and trained a classifier to differentiate non-responsive patients from responsive ones.

Subjects/Methods: Our data set consists of 3D PET/MR images (Fig. 1) from 24 patients acquired at three times over the course of treatment. As our cohort of patients is small and we did not want individual physiological traits to influence our results too much, we conducted our experiments on the livers only. This organ has been selected because it exhibits limited variability between individuals and is related to the immune system³. The organs have been segmented by an experienced radiologists on the MR images, the resulting VOIs have then been transferred to the corresponding PET and diffusion weighted images.

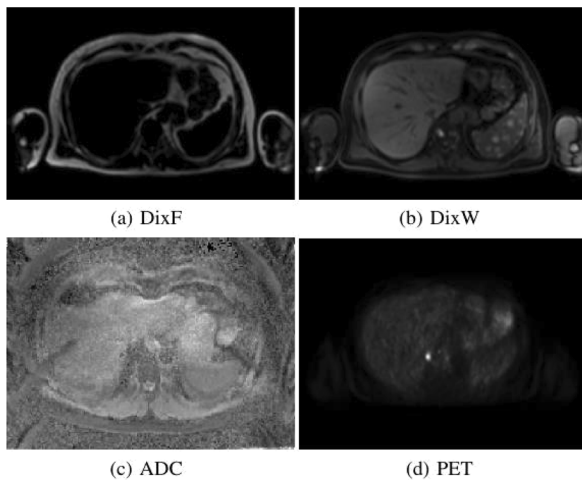


Fig. 1: Example images of the liver region from our multi-modal data set containing fat- and water-weighted Dixon MR images (a, b), ADC maps (c) and PET images (d). The Radiomics features were extracted from the segmented liver only.

We extracted 810 Radiomics features⁴ (Fig. 2). In addition, we used metrics derived directly from the imaging modalities (ADC mean, SUV max, SUV mean, organ volume, fat percentage). We then employed AFS⁵ and Concrete autoencoders (CAE)⁶ to select the most meaningful subset of features. A support vector machine (SVM) and a random forest (RF) were trained with the reduced feature sets using 5-fold cross-validation (70% of patients for training and 30% for testing). The mean balanced classification accuracy (A_b) was used as final result to compare our methods.

Feature group	# of features
Intensity	7
Histogram	6
Gradient	81
Gray-level co-occurrence matrix	672
Gray-level run length	44
Total	810

Fig. 2: List of features based on gray-level variation we extracted using the toolbox ImFEATbox4 from each patient's liver for all modalities. Adding the modality-derived metrics, this leads to a total of $810 \cdot 4 + 5 = 3245$ features per patient.

Results/Discussion: Fig. 3 shows the results of our experiments. The best performance ($A_b=94.4\%$) could be achieved using CAE for feature selection and RF for classification. Our preliminary study indicates the potential of using Radiomics-based classification to differentiate between responsive and non-responsive patients based

on radiological images. However, our findings need to be validated on a larger patient cohort, which we aim to do in the future.

Classifier	Feature selection	A_b
RF	AFS	73.33 %
RF	CAE	94.40 %
SVM	AFS	88.90 %
SVM	CAE	91.11 %

Fig. 3: The mean resulting A_b for each combination of classifier and feature selection. Using AFS, SVM clearly outperformed RF. However, CAE worked better for both RF and SVM, leading to the best overall result in combination with RF.

- References:** [1] Lugowska et al.: “Immunotherapy of melanoma.” Contemporary Oncology, 2018
 [2] Gillies et al.: “Radiomics: Images are more than pictures, they are data.” Radiology, 2016
 [3] Robinson et al.: „Liver immunology and its role in inflammation and homeostasis.“ Cell Mol Immunol, 2016
 [4] Liebgott et al.: “ImFEATbox: a toolbox for extraction and analysis of medical image features”, IJCARS 2018
 [5] Gui et al.: “Afs: An attention-based mechanism for supervised featureselection” arXiv 2019
 [6] Abid et al.: “Concrete autoencoders for differentiable feature selection and reconstruction”, arXiv 2019

P01.24

Accelerated fat-fraction mapping using signal profile asymmetries for robust multi-compartment quantification (SPARCQ)

A. L. C. Mackowiak¹, T. Hilbert², G. M. C. Rossi¹, T. Kober², J. A. M. Bastiaansen¹

¹Lausanne University Hospital (CHUV), Radiology, Lausanne, Switzerland, ²Advanced Clinical Imaging Technology, Siemens Healthcare AG, Lausanne, Switzerland

Introduction: Abnormal fat content in the liver, the heart or the pancreas can be an indicator of pathology^{1–6}. SPARCQ is a novel MRI acquisition and post-processing framework based on phase-cycled bSSFP⁷ which is capable of mapping water-fat fraction. Early developments provided reliable fat-fraction maps of the human knee, but at the cost of long acquisition times (TA) and using low-resolution imaging (>20min for (2mm)³). This work focused on the clinical translation of SPARCQ by shortening the TA and increasing the spatial resolution.

Subjects/Methods: Prototype framework: N bSSFP acquisitions are performed with an increment of the RF pulse phase $\varphi_j=2\pi j/(N-1)$ with $j=0, \dots, N-1$. Data is concatenated in a bSSFP profile, i.e. the complex transverse magnetization as a function of φ . A dictionary of single-compartment profiles with fixed TR, TE and RF pulse angle α (matching the acquisition), but varying off-resonance df and relaxation time ratio $\Lambda=TI/T2$, is generated with Bloch simulations. Profiles are estimated as weighted sums of dictionary entries using a Laplacian-regularized non-negative least squares fitting algorithm. A df spectrum is extracted, from which parameters are estimated (FIG1&2).

Acceleration: Parallel imaging (GRAPPA⁸) is used to accelerate individual acquisitions. By reducing N, the TA is shortened which leaves time to increase the spatial resolution. However, reducing N may render the fitting algorithm ill-conditioned and bias the estimation.

The robustness of SPARCQ to reducing N was tested using numerical simulations, a fat phantom with various concentrations of peanut oil⁷ and *in vivo* human knee data (n=4) acquired at 3T on a clinical scanner (MAGNETOM Prisma^{fit}, Siemens Healthcare, Erlangen, Germany).

The mean and standard deviation of the estimated fat fraction was computed in ROIs in phantoms and in volunteers for a decreasing number of sample points N.

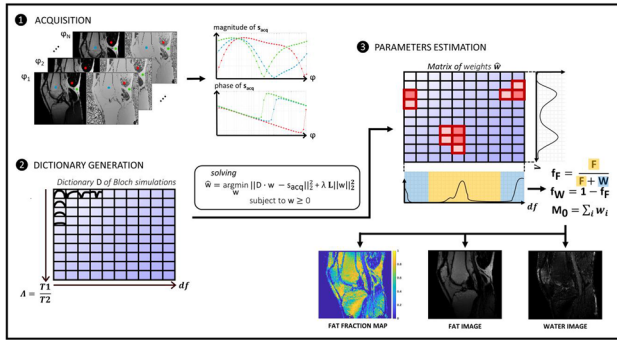


FIG1: 1 Acquisition of N bSSFP images with a varying RF phase. 2 bSSFP profiles are generated with Bloch simulations. 3 Dictionary fitting and estimation of fat-fraction FF, water-fraction FW, and equilibrium magnetization M0.

Results/Discussion: Simulations suggest that for SNR>30, a reduction to N in [6;17] maintains the mean fat quantification error below 5%, which is corroborated by phantom experiments (FIG2). In volunteers, fat estimation in various tissues (FIG3) show that using up to N=14 phase cycles yields an average error of 5% with respect to the fully sampled profile.

With N=16, maps of resolution (1.25mm)³ could be obtained in 7:12min. An estimation bias can be seen in tissue boundaries (FIG3, red arrows) or in the presence of B₀ inhomogeneities (FIG3, purple arrows), a limitation of SPARCQ currently under investigation. In said regions, image quality degrades with acceleration. In the rest of the FOV, image quality is maintained with N=16.

The impact of the size and resolution of the dictionary, as well as the profile sampling pattern, remains to be investigated.

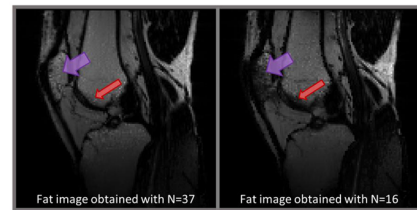
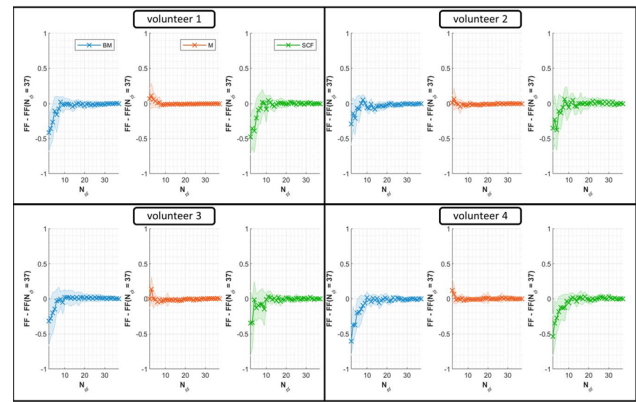


FIG3: Top: Mean error (w.r.t N=37) and standard deviation of estimated fat fraction as function of N. ROIs of 125 voxels in bone marrow BM, muscle M, sub-cutaneous fat SCF. Bottom: Fat images reconstructed with N=37 and N=16 phase cy

References: ¹10.1002/jmri.1880050311
²10.1056/NEJMr011775
³10.1023/A:1006304626233
⁴10.1148/radiol.2241010986
⁵10.2337/diabetes.49.3.399
⁶10.1073/pnas.91.23.10878
⁷arXiv:2005.09734
⁸10.1002/mrm.10171

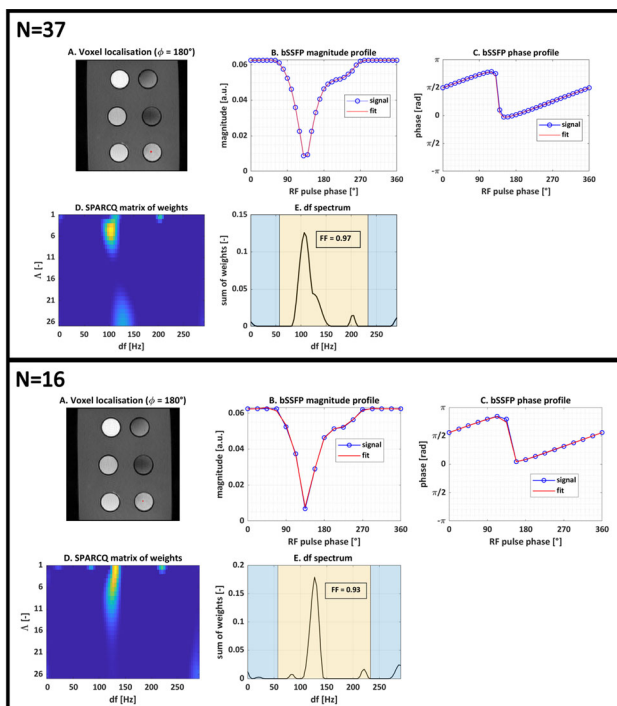


FIG2: SPARCQ applied in a voxel containing pure peanut oil. Gold standard fat fraction measurements of all vials were obtained with MR spectroscopy at 9.4T. Pure peanut oil contained 91% of fat, compared with a SPARCQ estimation of 93% (N=16).

P01.25

Automated multimodal segmentation of paraspinal muscles based on chemical shift encoding-based water/fat-separated images

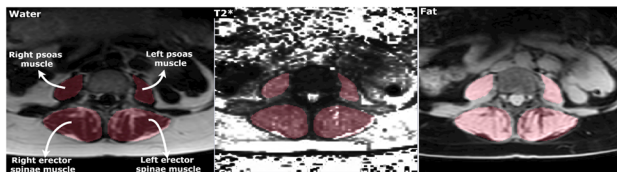
Y. Al Khalil¹, C. Lorenz², T. Baum³, J. Weese², M. Breeuwer¹

¹Eindhoven University of Technology, Biomedical Engineering, Eindhoven, The Netherlands, ²Philips Research Laboratories, Hamburg, Germany, ³Klinikum rechts der Isar, Technical University of Munich, Munich, Germany

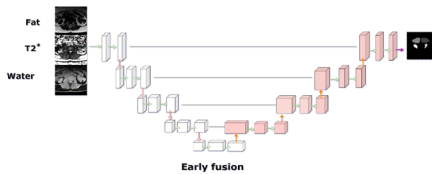
Introduction: Chronic lower back pain (LBP) is the most prevalent musculoskeletal disorder among adults [1,2]. Research suggests paraspinal muscle atrophy and fatty infiltration as accurate indicators of LBP, which can be determined through extraction of proton density fat fraction (PDFF) maps from chemical shift encoding-based water-fat MRI [3,4]. However, the use of water-fat MRI in clinical routines is limited due to the lack of an accurate segmentation procedure of muscle compartments. In this work, we utilize water-fat MRI and deep learning (DL) to automate paraspinal muscle segmentation and explore how to use multimodal data more effectively in DL.

Subjects/Methods: We utilize 54 MRI datasets of healthy volunteers acquired from a 3T Philips Ingenia system containing axial water, fat and T2* [5]. Manual segmentations of right/left erector spinae and psoas muscles were obtained from axial PDFF maps by a board-certified radiologist. Use of convolutional neural networks for paraspinal muscle segmentation is challenging due to unclear boundaries, variable muscle shape and complex background [6], which can be addressed by contrast variation and better data

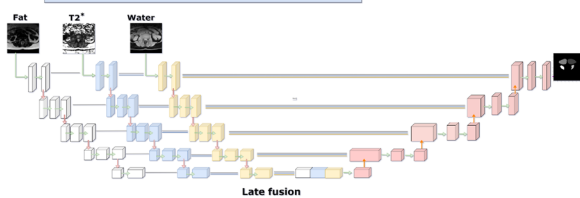
representation in water-fat MR. However, effective integration and extraction of features that fully leverage information in multimodal data is still unexplored. We employ a 3D U-Net on water-fat and T2* images (Fig.1a) by fusing them into three channels at the input (early fusion) and compare it to the late fusion approach of three encoder paths fused at the bottleneck of the U-Net (Fig.1b) to better handle multimodal data complexity.



(a) Representative slices from one of the multimodal MRI volumes in the training set, containing water, T2* and fat images, with manually segmented target muscle compartments. All data is normalized to zero mean and unit standard deviation.



Legend for Figure 1(b):
 - Convolution + Batch normalization + Leaky ReLU (green arrow)
 - Max pooling (red arrow)
 - Up-sampling (orange arrow)
 - Softmax (purple arrow)



(b) Early and late fusion architectures used in the paper. Both networks are trained under the same settings, using the sum of cross-entropy and dice loss and Adam optimizer with the starting learning rate of 10^{-4} and weight decay of 10^{-4} . Both networks converge after 180 epochs.

Method	Erector Spinae (L)	Erector Spinae (R)	PSOAS (L)	PSOAS (R)
Early fusion 3D U-Net	0.859	0.867	0.835	0.853
Late fusion multi-pathway 3D U-net	0.869	0.872	0.851	0.862
Literature [7]	0.90	0.89	0.77	0.83

(c) Segmentation performance of early and late fusion 3D U-Net-based networks on the task of paraspinial muscle segmentation on water-fat MR images with comparison to the results reported in the literature [8]. All reported scores are mean Dice coefficients per each test case. Both networks are trained on 40 images and tested on the remaining 14 multimodal MR images.

Figure 1: Details and results of the proposed work.

Details and results of the proposed work.

Results/Discussion: Obtained results (Fig.1c) demonstrate that both multimodal data and late fusion improve paraspinial muscle segmentation, despite the mentioned challenges and data limitations. Compared to the early fusion approach, late fusion solves the problem of significant overestimation of the erector spinae muscles and improves the generalization to poor contrast. To conclude, this study suggests that DL-based segmentation significantly benefits from multimodal data, where feature extraction from different modalities at separate stages outperforms early data merging.

References: [1] Al-Kafri et al. IEEE Access, 43487–43501, 2019

[2] Panagopoulos et al. AJNR 38(9), 1826-1832, 2017

[3] Beneck et al. Archives-PMR, 93(2), 300-306, 2012

[4] Baum et al. EJR, 85(8), 1512-1518, 2016

[5] Burian et al. BMC MD, 20(1), 152, 2019

[6] Li et al. Sensors, 19(12), 2650, 2019

[7] Baum et al. ER Exp, 2(1), 1-5, 2018

P01.26

Can deep learning-based feature selection improve results in radiomics? A study on the example of gleason score prediction

T. Hauaise¹, A. Liebgott¹, S. Gatidis², T. Hepp², B. Yang¹

¹University of Stuttgart, Institute of Signal Processing and System Theory, Stuttgart, Germany, ²University Hospital of Tuebingen, Department of Diagnostic and Interventional Radiology, Tuebingen, Germany

Introduction: In Radiomics¹, large amounts of features are extracted from medical images to perform complex image analysis tasks. Choosing relevant features is crucial for classification performance, especially due to the imbalance between the number of possible features and the limited number of subjects in most clinical applications. Feature selection (FS) additionally reduces the model complexity and thus the computational costs and strengthens the understanding of the underlying scientific problem.

This work applies four deep learning (DL)-based FS techniques to Gleason score prediction, comparing the results to a previous study² using conventional methods.

Subjects/Methods: The MR data set consists of data from prostate cancer patients with Gleason score labels. A total number of $N_F=6852$ features (Fig. 1) are extracted using ImFEATbox³. 6 subsets F_N are derived from the complete feature set F (Fig. 1).

Feature set	N_F	Extracted features	Best A_B in [2]	Best A_B
F	6852	Intensity, histogram, SVD, gradient-based, GLCM, run length, fractal dimension, form factor, Fourier transform, Hankel transform, distance transform, top-hat transform, skeletonization, unitary transform, Hough transform, Gabor filter, Zemike moments, Hu moments, affine moments, local binary pattern, MSER, salient region, quadtree decomposition, connectivity, sector decomposition, Harris, LAW, Laplacian of Gaussian, Gilles, SURF, LOSIB	0.82	0.96
F ₁	810	intensity, histogram, gradient-based, GLCM, run length	0.71	0.89
F ₂	4358	intensity, histogram, SVD, GLCM, Gabor filter	0.8	0.88
F ₃	945	intensity, histogram, SVD, gradient-based, GLCM, run length, fractal dimension, form factor	0.85	0.88
F ₄	4553	Fourier transform, Hankel transform, distance transform, top-hat transform, skeletonization, unitary transform, Hough transform, Gabor filter	0.79	0.9
F ₅	106	Zemike moments, Hu moments, affine moments	0.72	0.78
F ₆	1248	local binary pattern, MSER, salient region, quadtree decomposition, connectivity, sector decomposition, Harris, LAW, Laplacian of Gaussian, Gilles, SURF, LOSIB	0.73	0.58

Fig. 1: Considered feature sets. For each feature set, its size and the contained features are given, as well as a comparison of the best results achieved with conventional methods in [2] and with DL-based FS in this study.

DL-based FS applies concepts from general DL research to the problem of FS. The methods investigated in this study are: Attention-based feature selection (AFS)⁴, Concrete auto encoders (CAE)⁵, Auto encoder-inspired feature selection (AEFS)⁶, Teacher-student feature selection (TSFS)⁷.

Each method is used to select feature subsets of different sizes from all sets F_N . The selected features are used to train a support vector machine (SVM) employing 5-fold cross-validation. The performance of the FS methods is compared in terms of the mean balanced classification accuracy (A_B).

Results/Discussion: Fig. 2 shows the A_B over N_F for the complete feature set F using the aforementioned FS methods.

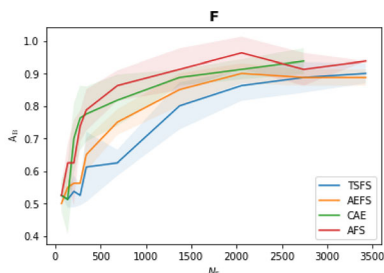


Fig. 2: Mean A_B and standard deviation (shaded area) for different FS algorithms over the number of used features N_F . The best result is achieved using AFS ($A_B=0.96$). CAE could not be used with more than 2741 features due to excess memory usage.

The results for F_{1-6} are given in Fig. 3.

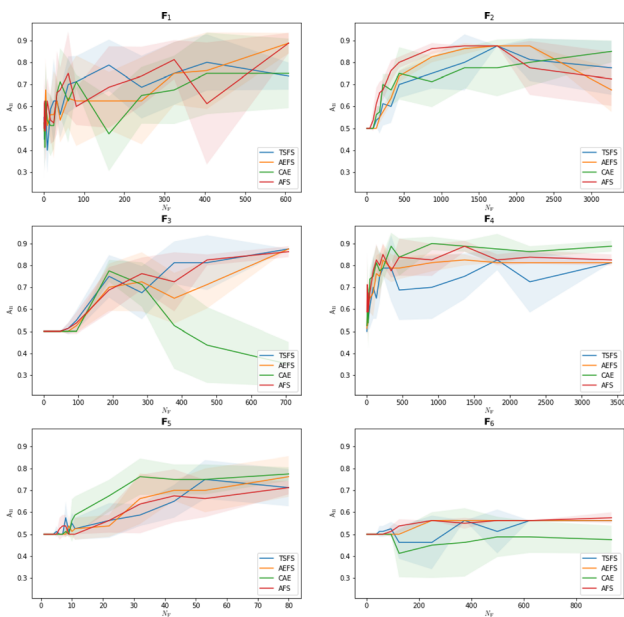


Fig. 3: Mean A_B and standard deviation (shaded area) using different FS algorithms on the feature subsets F_{1-6} . The best overall performance ($A_B=0.90$) is achieved with CAE on F_4 .

In all cases, the feature dimensionality of the best results in [2] is significantly smaller compared to our results, facilitating easier interpretation. However, most methods in this study lead to a higher performance (Fig. 1), improving the A_B by 14 % on F. The A_B on the

best set F_3 in [2] is improved by 3 %. The best result ($A_B=0.90$) is achieved using CAE on F_4 .

Overall, our results show that DL-based FS has the potential to significantly improve performance in Radiomics-based classification compared to conventional methods.

References: [1] Gillies et al.: “Radiomics: Images are more than pictures, they are data.” *Radiology*, 2016
 [2] Liebgott et al.: “Feature Reduction and Selection: a Study on their Importance in the Context of Radiomics”, *ISMRM 2019*
 [3] Liebgott et al.: “ImFEATbox: a toolbox for extraction and analysis of medical image features”, *IJCARS 2018*
 [4] Gui et al.: “Afs: An attention-based mechanism for supervised featureselection” *arXiv 2019*
 [5] Abid et al.: “Concrete autoencoders for differentiable feature selection and reconstruction”, *arXiv 2019*
 [6] Han et al.: “Autoencoder inspired unsupervised feature selection”, *arXiv 2017*
 [7] Mirzaei et al.: “Deep feature selection using a teacher-student network”, *arXiv 2019*

P01.27

Classification of brain tissue using multiparametric MRI

Z. Shawa¹, J. Hutter¹, P. Slator²

¹King’s College London, Biomedical Engineering, London, UK,

²University College London, Computer Science, London, UK

Introduction: Combined diffusion relaxation MRI has the potential to measure tissue properties that are obscured in single contrast scans. This project developed computational techniques for analysing such data. Specifically, we modified diffusion microstructure MRI models to include relaxation phenomena, and developed data-driven software to learn signatures of different brain tissues.

Subjects/Methods: In total, 5 combined diffusion relaxation MRI scans acquired using the ZEBRA [1] protocol were used. ZEBRA simultaneously varies echo times (TE), inversion times and diffusion weightings to measure T_1 , T_2^* , and diffusivity whilst accounting for correlations.

A T_1 - T_2^* extended diffusion tensor model (Equation 1) was fitted to the voxel signatures of each dataset. From the model, T_1 , T_2^* , mean diffusivity (MD) and fractional anisotropy (FA) maps of the brain volume were produced.

$$S = |S_0 \exp(-TE/T_2^*) \times [1 - I \exp(-TI/T_1) + \exp(-TR/T_1)] \times \exp(-bgTDg)|$$

Equation 1

Furthermore, Random Forest Classifiers were trained to create probabilistic segmentations of WM, GM and CSF on each dataset and the feature importances were examined.

Experiments on three datasets were used to determine if a combined T_1 - T_2^* -diffusion scan (i.e. ZEBRA) performs better than separate T_1 , T_2^* , diffusion scans:

1. Full-combined: the entire ZEBRA acquisition and therefore all 1296 parameter sets.

2. Separate: 86 parameter sets simulating data acquired from separate T_1 , T_2^* and diffusion MRI scans.

3. Short-Combined: Consists of 100 trials in the modelling component and 50 trials in the Random Forest component. Each trial has 86 parameter sets chosen at random, which is the same size as the Separate dataset, from the full ZEBRA acquisition.

Results/Discussion: The maps produced from the fit of the extended diffusion tensor model qualitatively and quantitatively matched literature results (Fig. 1).

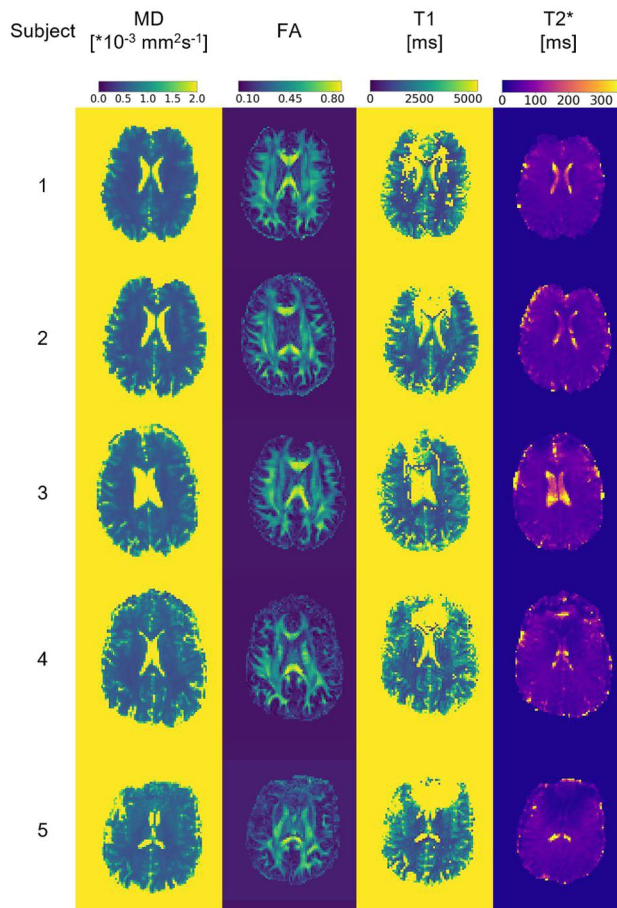


Figure 1 – Modelling of MD, FA, T1 and T2* maps of the same slice (z=33) for all 5 scans using the Full-Combined dataset.

The average segmentation map accuracies of each dataset was $97.5 \pm 2\%$ for the Full-Combined (Fig. 2), $98.14 \pm 2.2\%$ for the Separate, and $98.04 \pm 0.3\%$ for the Short-Combined. Therefore, the Short-Combined dataset was found to perform as well as the Separate dataset and all datasets were highly accurate. All selected important features had an echo time of 80 ms. Thus, the data obtained with $TE > 80$ ms may be redundant due to the loss of signal.

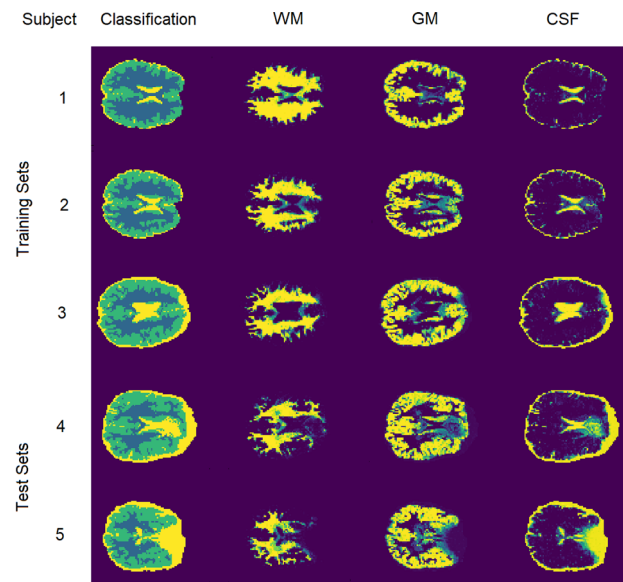


Figure 2 - Random Forest automatic segmentation results using the entire ZEBRA acquisition (z=33). The first column contains the predicted segmentation, while the last 3 columns contain the probabilistic segmentation for each tissue type.

Overall, the results show that the ZEBRA acquisition can provide multi-dimensional detailed tissue information and has the potential to be refined and used in clinical settings. Future work involves performing similar analysis on other unique tissue voxel signatures at the sub-voxel level.

References: 1. Hutter J, Slatore PJ, et al. Integrated and efficient diffusion-relaxometry using ZEBRA. *Scientific Reports* 2018 10/11;8(1):15138.

P01.28

Fully automatic analysis of residual tumor volumes relating to MGMT-methylation in a subset of patients from the EORTC CENTRIC and CORE trials

K. A. van Garderen¹, A. Alafandi¹, S. Klein¹, S. R. van der Voort¹, M. Weller², J. C. Tonn³, T. Gorlia⁴, M. Smits¹

¹Erasmus MC, Radiology and Nuclear Medicine, Rotterdam, The Netherlands, ²University Hospital and University of Zurich, Department of Neurology, Zurich, Switzerland, ³Ludwig-Maximilians-University Munich, Department of Neurosurgery, Munich, Germany, ⁴EORTC HO, Brussels, Belgium

Introduction: Glioblastoma (GBM) is the most common primary malignant brain tumor and has a poor prognosis, with a median survival of 1 year [1]. Surgical resection is the standard therapy for GBM and larger extent of resection, and smaller residual tumor volume, are related to a longer survival [2]. The MGMT promoter methylation status is an important genetic biomarker and tumors with this methylation also have better prognosis. The aim of this study is to test the correlation between residual volume and MGMT promoter methylation status. This is an initial analysis leading up to our final goal of establishing whether the relation between residual tumor volume and prognosis is independent of MGMT status.

Subjects/Methods: Patients were selected from the EORTC CENTRIC and CORE trials, with imaging available within 7 days of surgery. Processing of the images was performed with minimal human intervention. DICOM files were uploaded to an XNAT system to be automatically sorted [3], in order to select the input sequences for segmentation with HD-GLIO [4,5,6]. For this initial analysis, the results were checked for issues in the processing and selection. The resulting volumes were used to test the relation between MGMT status and post-operative tumor volume (enhancing volume, non-enhancing T2-weighted hyperintensities and the combination of both) using a Mann-Whitney U test.

Results/Discussion: From the two trials, 318 MRI datasets were available, of which 153 patients were excluded for various reasons (Figure 1). The resulting segmentations of 166 tumors (111 MGMT-methylated) were used for statistical testing, which showed no significant correlation between MGMT status and residual volume. The median (IQR) were 1.5 (0.4–5.6) cm³ for enhancing tumor volume (met 1.4 (0.3–5.1) cm³, unmet 2.0 (0.5–6.0) cm³, $p = 0.18$), 49 (28–77) cm³ (met 49 (25–79) cm³, unmet 50 (33–76) cm³, $p = 0.28$) for the non-enhancing T2-weighted hyperintensities and 52 (31–82) cm³ for whole tumor volume (met 56 (29–82) cm³, unmet 51 (38–81) cm³, $p = 0.29$) (Figure 2).

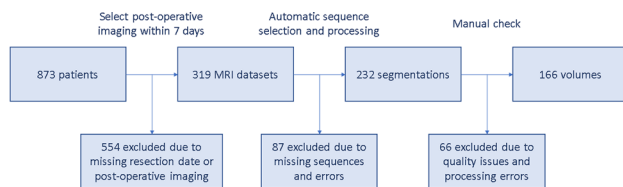


Figure 1: Flowchart and patient numbers of the inclusion.

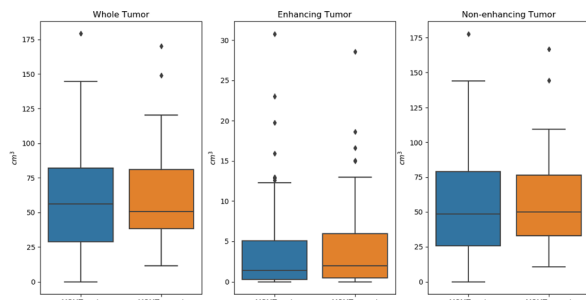


Figure 2: Boxplot of volumes for the three regions of interest, separated in MGMT-methylated and -unmethylated tumors.

In this study, a fully automatic pipeline was used to delineate tumor volumes on post-operative imaging. No significant relation was found between post-operative residual tumor volume and MGMT promoter methylation status, indicating that their relation to survival could be independent. However, the delineations were only evaluated for clear processing errors, excluding a large part of the population as a result, and may still include small errors. We aim to present at the congress the next step in this research, including a thorough check of resulting volumes, inclusion of more patients, and correlation with survival.

- References:** 1. Ostrom *et al.* *Jama Oncol.* 4(9) (2018)
 2. Chaichana *et al.* *Neuro Oncol* 16(1) (2014)
 3. van der Voort *et al.* *Neuroinformatics* (2020)
 4. Kickingeder *et al.* *Lancet Oncol.* 20(5)(2019)
 5. Isensee *et al.* *arXiv preprint* (2019)
 6. Isensee *et al.* *Hum Brain Mapp.* 40(17) (2019)

P01.29

Improving longitudinal cerebral atrophy quantification in brain magnetic resonance imaging using FSL-SIENA through retrospective intensity standardisation

E. E. Carvajal Camelo¹, J. Bernal², M. Trujillo¹

¹Universidad del Valle, Valle del Cauca, Cali, Colombia, ²University of Edinburgh, Edinburgh, Edinburgh, UK

Introduction: The loss of neurons and axons in the human brain comes with ageing, but also with neurodegenerative diseases. The quantification of the magnitude and speed at which such a loss happens is essential for understanding the nature of brain pathologies, diagnosing and monitoring diseases, and assessing treatment effectiveness. These assessments can be carried out by measuring alterations in brain volume between magnetic resonance images, taken at different time points. Many of these studies have used a fully automated method called SIENA. However, such analyses are compromised by intensity non-standardness, even if the same patient is scanned during the same session using the same scanner and the same acquisition protocol. In this work, we study whether retrospective intensity standardisation in longitudinal assessments leads to significantly better estimates compared to when omitted.

Subjects/Methods: We assessed the effect of intensity standardisation by examining whether it improved the SIENA robustness against subtle imaging variations (scan-rescan tests) and its ability to produce different atrophy values for groups of patients undergoing different pathologies over time (power analysis). For that, we used 166 T1-w scans from 123 subjects from the OASIS dataset (63 dementia vs 60 control) and 43 subjects from the ADNI dataset (24 Alzheimer's disease vs 19 control). We studied the applicability of seven intensity standardisation techniques comprising the z-score (subtract mean and divide by standard deviation), three segmentation-based white matter peak normalisation strategies (segment brain tissues, identify white matter peak, and divide all image intensities by it), two algorithms based on the so-called white stripe (find white matter in the image histogram, estimate mean and variance of that region, perform z-score normalisation) and piece-wise linear histogram matching [1].

Results/Discussion: In scan-rescan assessments, we used the one-sided Wilcoxon signed-rank test to examine whether the scan-rescan error yielded after applying intensity standardisation was lower compared to when omitted. We observed that none of the seven intensity standardisation schemes led to significant improvements in this regard (p -values > 0.05). In power analysis, we compared the Cohen's d statistics obtained before and after including intensity standardisation in the SIENA pipeline, assuming 80% power, 25% treatment effect, and 5% significance level. We noticed that intensity standardisation led to a reduction in the sample size of up to 56%. Segmentation based approximations performed consistently well compared to the other four schemes (>30% reduction). Overall, our

research evinces the need for intensity standardisation in longitudinal brain atrophy quantification using SIENA.

OASIS (n=123)	Baseline	Z-score	Fuzzy c-means	Gaussian mixture model	Kernel density estimation	Histogram matching	White stripe	RAVEL
Median	-0.644 (-)	-1.207 (-)	-1.296 (-)	-1.350 (-)	-1.300 (-)	-0.641 (-)	-1.081 (-)	-0.922 (-)
(IQR) Demanded, %	1.350, -0.225)	2.253, -0.442)	2.202, -0.431)	2.280, -0.447)	2.210, -0.431)	1.087, -0.305)	1.867, -0.377)	1.838, -0.397)
Median (IQR) Control, %	-0.274 (-0.470, -0.001)	-0.408 (-0.671, -0.013)	-0.411 (-0.699, -0.008)	-0.358 (-0.711, -0.012)	-0.411 (-0.700, -0.009)	-0.284 (-0.433, -0.070)	-0.343 (-0.612, -0.014)	-0.342 (-0.641, -0.050)
Sample size, n	371	256	260	246	260	309	274	332
Sample size improvement, %	-	30.997	29.919	33.693	29.919	16.712	26.146	10.512
ADNI (n=43)								
Median (IQR) AD, %	-0.635 (-0.927, -0.358)	-1.523 (-2.18, -0.692)	-0.976 (-2.18, -0.633)	-1.052 (-2.410, -0.671)	-0.975 (-2.180, -0.630)	-0.621 (-0.995, -0.389)	-6.420 (-15.330, 0.117)	-1.144 (-2.430, 0.574)
Median (IQR) Control, %	-0.222 (-0.358)	-0.283 (-2.070, 1.241)	-0.049 (-1.070, 0.599)	-0.283 (-1.140, 0.931)	-0.047 (-1.070, 0.600)	-0.207 (-0.500, 0.186)	-3.510 (-7.070, 2.438)	-0.472 (-1.980, 0.419)
Sample size, n	648	722	392	392	392	288	1800	1800
Sample size improvement, %	-	-	39.506	39.506	39.506	55.556	-	-

Sample size per arm for SIENA before and after intensity standardisation. AD: Alzheimer's disease. IQR: Interquartile range. RAVEL: Removal of artificial voxel effect by linear regression.

Methods	Median	IQR
Baseline	0.210	[0.073, 0.482]
Z-score	0.317	[0.103, 0.706]
Fuzzy c-means	0.307	[0.105, 0.721]
Gaussian mixture model	0.305	[0.113, 0.716]
Kernel density estimation	0.303	[0.105, 0.720]
Histogram matching	0.254	[0.077, 0.496]
White stripe	0.257	[0.094, 0.597]
RAVEL	0.417	[0.168, 0.818]

Error as the absolute percentage of brain volume change obtained between scans acquired in the same visit. RAVEL: Removal of artificial voxel effect by linear regression.

References: Nyúl LG, Udupa JK, Zhang X. New variants of a method of MRI scale standardization. *IEEE T MED IMAGING*. 2000;19(2):143–150.

P01.30

Investigating multi-compartment T2 estimation of knee cartilage with MSE sequences and a dictionary-based Non-Negative Least Squares (NNLS) fitting method

A. C. Freitas¹, J. M. Coelho², L. Nogueira², R. G. Nunes¹

¹Instituto Superior Técnico, Universidade de Lisboa, Institute for Systems and Robotics/LARSyS, Department of Bioengineering, Lisbon, Portugal, ²Escola Superior de Saúde do Politécnico do Porto, Oporto, Portugal

Introduction: Loss of collagen integrity and increased water content in cartilage osteoarthritis (OA) results in T2 increase [1]. T2 mapping enables early-OA detection[2] and is often performed with multi spin-echo (MSE) and mono-exponential fitting. However, this is hampered by inaccurate T2 estimation [3]. Dictionary-based methods improve T2 estimation, as shown in hip cartilage considering a single compartment [4]. As different cartilage components (proteoglycans, free and collagen-bound water) present distinct T2s, a multi-compartment model may be more suitable[5]. The non-negative least squares (NNLS) algorithm has been suggested, allowing to fit MSE data to computed echo modulation curves (EMC) with no previous assumptions. We explore the application of a T2 multi-compartment NNLS

toolbox [6], developed for brain myelin mapping, to characterize cartilage and the impact of using refocusing pulses < 180° on identifying T2 components.

Subjects/Methods: A single-voxel two-compartment signal was simulated: short/long components (7/45 ms), such that $EMC(t) = F_s \times EMCT2s + F_l \times EMCT2l$, where F_s/F_l are their fraction weights ($F_s + F_l = 1$) [5], and $EMCT2s$ and $EMCT2l$ the corresponding signal curves. This was implemented using Extended Phase Graph (EPG) [7] and considering: 90° excitation pulse, 12 echoes (echo-spacing=5.8 ms) and $T1=1s$ [3]. T2 values and corresponding F_s/F_l were estimated using the NNLS. Minimum energy regularization was used (empirically set at 0.01). Estimation of varying F_s/F_l was investigated. The refocusing flip angle (FA) varied from [90,100:5:140,180]°. Monte Carlo experiments were undertaken with 5000 noise instances (SNR=100).

Results/Discussion:

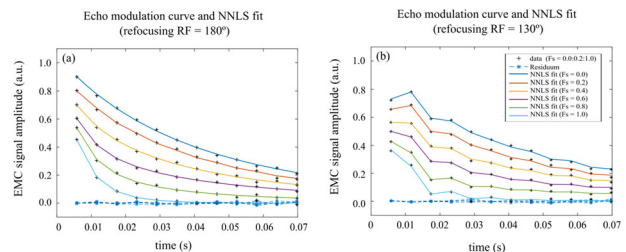


Fig 1: Simulated EMC data points, corresponding NNLS fit and residual. (a-b) EMC amplitude if refocusing FA=180° or 130°. If nominal FA=180°, T2 decay is accurately described by an exponential model (a) but that is no longer true for a smaller FA (b).

As expected, if a nominal refocusing 180° is applied, EMCs resemble an exponential curve (Fig. 1 a). If using smaller refocusing FAs, EMCs start to deviate further from this (Fig. 1 b).

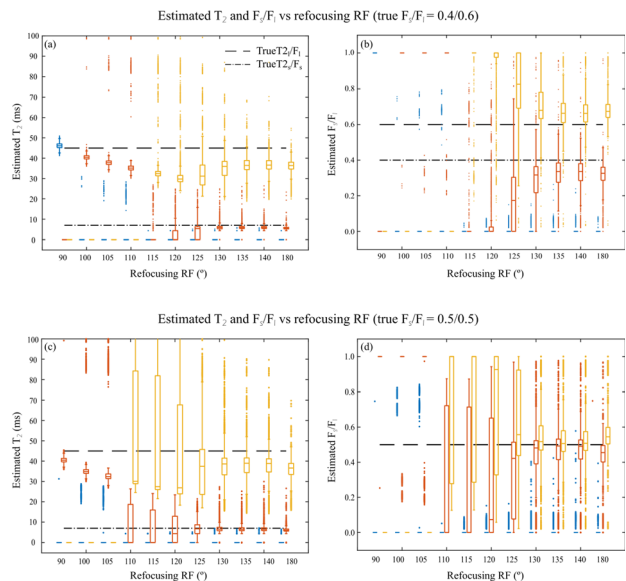


Fig2: Estimated T2 and F_s/F_l vs refocusing RF with true F_s/F_l of 0.4/0.6 and 0.5/0.5. Larger FAs (>130°) allow for closer T2 and F_s/F_l distribution to ground truth (no visible difference to 180°). Residual component (blue) was also identified by NNLS.

Fig2 shows estimated T2 and F_s/F_l distribution for different refocusing FAs. Each colour represents one signal component NNLS-identified. An inflexion point appears to occur at 130°: above this, parameters are closely estimated, while for smaller FAs, the NNLS identifies erroneous values.

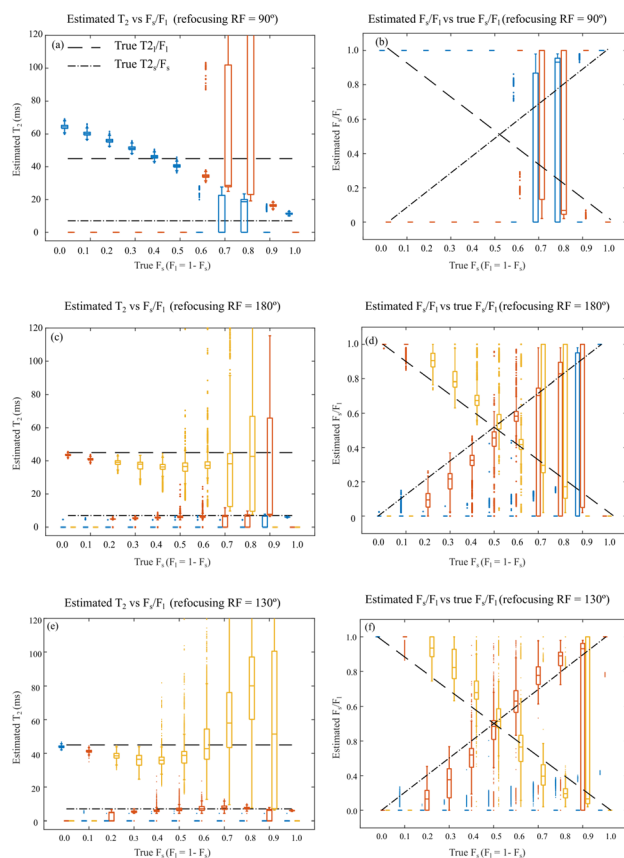


Fig3: Estimated T_2 and F_2/F_1 vs true F_2/F_1 with refocusing FA=90°/180°/130°. Erroneous estimation when FA=90° but more accurate estimations were observed with 180° (except if $F_2 > 0.7$). Similar results to the nominal 180° can be obtained with FA=130°.

Considering an optimal FA=130°, accurate F_2/F_1 estimation was possible, except if $F_2=0.9$ (Fig3 f). Although T_2 could be estimated when $F_2 < 0.6$, estimation starts to deteriorate as F_2 increases (Fig3 e). In summary, multi-compartment T_2 and F_2/F_1 estimations were possible. We concluded that a lower refocusing of 130° enables accurate parameter estimation. As expected, EMCs mainly composed of the short component were harder to estimate. Future work will focus on applying the optimized protocol in a cartilage-OA patient cohort.

- References:** [1]Joseph. *Osteo Cart.* 2012;20(7):727-735
 [2]Baum. *Arthritis Care Res.* 2012;64(2):248-255
 [3]Ben-Eliezer. *MRM.* 2015;73(2):809–817
 [4]Ben-Eliezer. *Cartilage.* 2019
 [5]Sharafi. *JMRI.* 2017;47:809-819
 [6]Prasloski. *MRM.* 2012;67:1803-1814
 [7]Weigel. *JMRI.* 2015;41:266-295

P01.31

Measurement of ^{23}Na point-spread function (PSF) in ultrashort TE (UTE) acquisitions in a 3D printed resolution phantom

P. Polak¹, R. Schulte², M. Noseworthy¹

¹McMaster University, School of Biomedical Engineering, Hamilton, ON, CANADA, ²GE Global Research, Munich, Germany

Introduction: In vivo ^{23}Na MRI is desirable due to sodium's ubiquity in human metabolism. Unfortunately, ^{23}Na MRI suffers from inherent technical challenges, including low gyromagnetic ratio, rapid T_2 relaxation, low signal and henceforth long acquisitions. Ultrashort TE (UTE) pulse sequences are preferred, the most common of these being 3D radial projections (3DRP), and Fermat looped

orthogonally encoded trajectories (FLORET) [1,2]. This work examines the point-spread functions (PSF) from ^{23}Na MRI UTE pulse sequences.

Subjects/Methods: Imaging was conducted using a GE 3T MR750 (General Electric, Milwaukee, WI) using a custom built single-tune birdcage head coil (frequency 33.8 MHz). A phantom was 3D printed and filled with different sodium concentrations – 15 mM ^{23}Na with 8% agar, 13 mM and 60 mM ^{23}Na in prepared gelatin, before being imaged in the coronal plane.

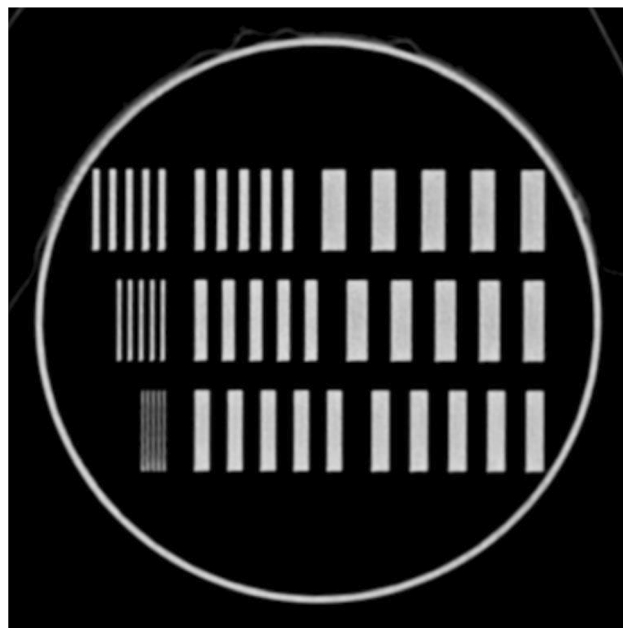


Figure 1: Computed Tomography (CT) image of phantom. Resolutions are split into 9 areas with positive and negative contrasts ranging from 1 to 9 mm. Top row, left to right: 3.4 9 mm, middle, 2.5 8 mm, bottom, 1.6 7 mm.

Pulse sequences used the GE MNS Research Pack (v. 2018-07-18). Center-out, 3DRP trajectories (TR: 24 ms, 13500 spokes, 2 averages) and FLORET (TR: 24.3 ms, 3 hubs, 150 interleaves/hub, 64 averages) used a field of view (FOV) of 240 mm, flip angle 70°, and isotropic resolution of 3.2 mm. Transmit gain and frequency calibrations were performed using the Bloch-Siegert shift [3]. Each concentration was scanned with 3DRP and FLORET for a total of 6 acquisitions.

Reconstructions were performed offline using the BART toolbox [4], and converting images into NIFTIs (240³, 1 mm³ isotropic). Regions of interest (ROI) were created with FSL, and the data were used to create modulation transfer functions (MTF) using the methods described by Gonzalez-Lopez [5]. MTFs were interpolated on to a 1D grid, before calculating normalized PSFs. The MTFs and PSFs were assumed to be Gaussian for fitting purposes. Signal to noise ratios (SNR) and R^2 values for the MTF interpolation were calculated.

Results/Discussion:

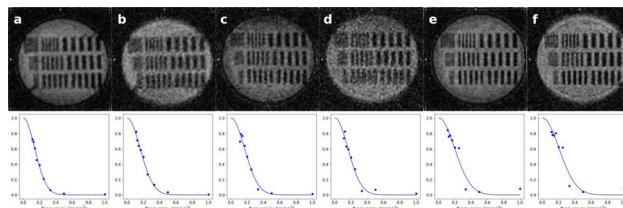


Figure 2: (a-f) ^{23}Na image (top) and calculated MTF (below). All images 240x240, individually windowed. (a) 15 mM agar 3DRP (b) 15 mM agar, FLORET (c) 13 mM gelatin 3DRP (d) 13 mM gelatin FLORET (e) 60 mM gelatin 3DRP (f) 60 mM gelatin FLORET.

	3DRP SNR	3DRP FWHM	3DRP R2	FLORET SNR	FLORET FWHM	FLORET R2
15 mM agar	18,4	2,6	0,99	16,0	2,3	0,99
13 mM gelatin	11,4	2,2	0,97	10,9	2,3	0,97
60 mM gelatin	16,1	1,9	0,93	13,3	1,8	0,93

Table 1. 3DRP: 3D radial projections; FLORET: Fermat looped orthogonally encoded trajectories; FWHM: full-width, half-maximum; R2: modulation transfer function R-squared fit; SNR: signal to noise ratio

Figure 2 shows the MTFs and representative images from each acquisition. The 3DRP images have qualitatively sharper edges and apparent superior image quality over the FLORET images, although this is not indicated in either the MTFs or FWHM from the PSFs in Table 1.

SNR does not scale predictably in gelatin compared to the agar phantom – ^{23}Na being less bound in gelatin due to lowered pH [6,7], and thus having T_1/T_2 properties more akin to saline.

FLORET covers k-space more efficiently than 3DRP [2], which is indicated by the increased averages required in order to attain a similar acquisition time. However, performance is approximately equal between the sequences, demonstrating that ^{23}Na MRI is SNR limited regardless of the chosen acquisition schema.

References: 1.Nagel AM. MRM 2009;62.

2.Pipe JG. MRM 2011; 66:1303.

3.Schulte RF. NMR in Bio. 2011;24.

4.Uecker M. Proc Intl Soc Mag Reson Med; 2015.

5.González-López A. Med Phys 2016; 43:5653.

6.Cole CGB. Gelatin. Enc of Food Sci and Tech, 2nd ed. NY, 2000.

7.Reddi BA. Int J Med Sci 2013;10(6).

P01.32

Multiclass texture-based PI-RADS classification in multiparametric MRI: performance evaluation of the DWI sequence

J. M. Jaén-Lorites¹, S. Ruiz-España¹, T. Piñero-Vidal², I. Del-Canto¹, J. M. Santabàrbara², D. Moratal¹

¹Universitat Politècnica de València, Center for Biomaterials and Tissue Engineering, Valencia, Spain, ²ASCIREs-Grupo Biomédico, Valencia, Spain

Introduction: One of the key aspects of prostate cancer (PCa) is its early detection. However, tests for detection are often invasive. A non-invasive alternative is PI-RADS classification from multiparametric MRI (mpMRI). This study aims to find biomarkers to classify prostate lesions from mpMRI on the PI-RADS scale using a radiomics approach. It is also intended to analyze the performance offered by the diffusion-weighted imaging (DWI) series.

Subjects/Methods: A total of 97 subjects (27 with PI-RADS 2, 37 with PI-RADS 3 and 33 with PI-RADS 4 and 5) underwent T2-weighted images, DWI (90 cases with $b = 800 \text{ s/mm}^2$, and 7 with $b = 1500 \text{ s/mm}^2$) and apparent diffusion coefficient (ADC) maps. These series have been co-registered, and the segmentation of the PCa has been performed.

A first radiomics study has been carried out with the T2W and ADC series. As a first step, image normalization has been performed and quantization of gray-levels has been applied to improve the signal-to-noise ratio of the texture outcome. Different gray-level quantizations have been evaluated (16, 32, 64, 128, 256). Afterward, 86 features have been extracted by gray-level quantization, with 5 statistical methods [1]. Two feature selection (FS) methods have been compared

to see the optimal number of features, and 8 predictive models have been studied. The performance of the models has been evaluated from the area under the ROC curve (AUC).

A second study has been carried out, including the DWI series (43 additional features of each number of gray-levels, 129 in total). Since there were 2 different b-values, it has been evaluated with the Mann-Whitney-Wilcoxon test if there were statistically significant differences in the textures. Textures with statistically significant differences have been eliminated.

Results/Discussion: The best results of each study are shown in Table 1. Additionally, profiles of the best models (Table 1) are presented in Figure 1, where the AUC values are shown according to the number of textures used.

Study	Ng	Model	FS method	# of textures	AUC ($\mu \pm \sigma$)
1	128	SVM	SVM-RFE	25	0,7128 \pm 0,0876
1	32	RF	SVM-RFE	84	0,7039 \pm 0,0942
1	32	RF	ReliefF	84	0,7034 \pm 0,0954
2	256	SVM	ReliefF	46	0,7503 \pm 0,0692
2	256	AdaBoost	ReliefF	67	0,7428 \pm 0,0780
2	32	RF	ReliefF	110	0,7422 \pm 0,0818

Table 1. Results of the studies, The number of gray-levels (Ng), the model, the FS method, the number of features and the AUC as mean \pm standard deviation are shown.

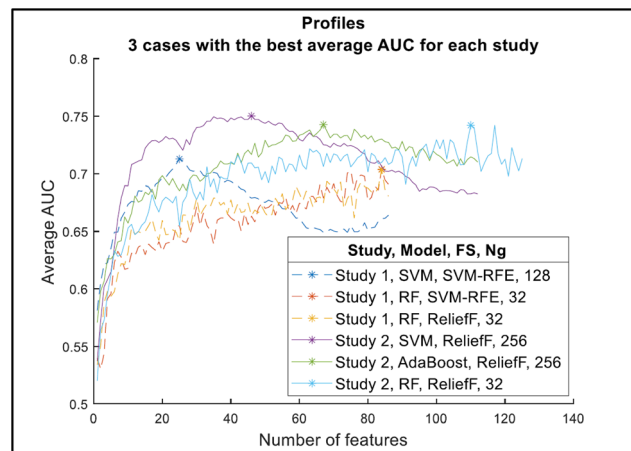


Figure 1. Profile graph. The AUC is shown as a function of the number of textures. The legend indicates the study it came from and the model, FS method and number of gray-levels used.

For the first study, the best results have been obtained with the Random Forest (RF) and Support Vector Machine (SVM) models (AUC > 0.7). The highest AUC has been 0.7128 ± 0.0876 , with SVM, 128 gray-levels and the 25 best textures according to the SVM-RFE FS method.

In the second study there were 48 DWI textures corresponding to different numbers of gray-levels with statistically significant differences, which have been excluded from the study. The best results have provided AUC values higher than 0.74, a 5% improvement. The highest AUC has been again obtained with the SVM model (AUC = 0.7503 ± 0.0692), with 256 gray-levels and the 46 best textures according to the ReliefF FS method.

Good results have been achieved in classifying PCa. This methodology could be used as an aid to PCa diagnosis. In addition, the DWI series have been improved the results obtained.

References: [1] Vallières M. et al. Phys Med Biol 2015;60,5471–96.

P01.33

Multimodal medical image fusion in stereotactic electroencephalography

J. A. Pérez Hinestroza¹, C. Mazo², M. Trujillo¹, A. Herrera³

¹Universidad del Valle, Cali, Colombia, ²University College Dublin, Dublin, Ireland, ³Centro Médico Imbanaco, Cali, Colombia

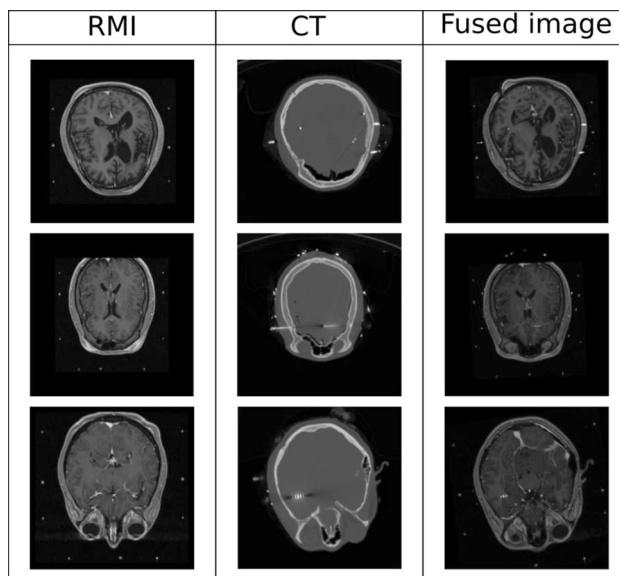
Introduction: Epilepsy is one of the most frequent neurological disorders, with a global prevalence of 0.8% to 1.2% and significant social and economical burden. The main treatment for epilepsy uses anti-epileptic drugs (AED). However, 20% to 30% of epilepsy cases cannot be controlled using AED. A reliable treatment for these cases is a surgical intervention to remove the epileptogenic tissue. One of the two methods for invasive evaluation to detect the epileptogenic tissue is the stereo electroencephalography (SEEG). The SEEG is a procedure that uses depth electrodes and neuroimaging to monitoring the electromagnetic signals during ictal seizures in the brain, mapping de cortical functions; and thereby define the tissue to resect to obtain seizure freedom or control. The SEEG uses two different modalities of medical images, Computed Tomography (CT) and Magnetic Resonance Image (MRI), to obtain the anatomical location of the contacts of electrodes. The localization of electrodes in the SEEG can be done using image fusion, which is a technique in computational vision that combines two or more images. However, there is not development, in image fusion methods, which consider external elements. In this work, we present a method to fuse CT and MRI considering the presence of electrodes.

Subjects/Methods: We propose a three-fold fusion procedure: Initially, the registration of a postsurgical CT with a presurgical MRI is done; then, electrodes from the CT are segmented; finally, the segmented electrodes and the registered RMI are fused superposing the segmented image with the registered image. Since the registration is the hardest part, we compare five different registration methods for selecting the registration method to use: Euler, Affine, versor, similarity, and scale versor.

Results/Discussion: For the comparison, we used 10 pairs of CT and MRI images and the performance was measure using four metrics: Root Mean Square Error (RMSE), Peak Signal to Noise Ratio (PSNR), Structural Similarity Index (SSIM), and Mutual Information (MI). The results of registration, of a postsurgical CT with a presurgical MRI, by the Euler method produced the better performance among the five methods, and also the minimum RMSE and PSNR (see Table 1). However, the Affine and the ScaleVersor methods produced a better MI, of 0.43, since MI is a more significant metric to evaluate multimodal image fusion.

TRANSFORM	MSE	RMSE	PSNR	SSIM	MI
Euler	15798,84	125,69	128,73	0,31	0,41
Affine	15991,97	126,45	128,67	0,31	0,43
Versor	15971,50	126,37	128,68	0,31	0,42
Similarity	15909,43	126,13	128,70	0,31	0,42
ScaleVersor	15974,86	126,39	128,68	0,31	0,43

Table 1: Average metrics results of registration evaluation.



a) Original MRI; b) Original CT; c) Fused image

References: Dogra A, Goyal B, Agrawal S. From Multi-Scale Decomposition to Non-Multi-Scale Decomposition Methods: A Comprehensive Survey of Image Fusion Techniques and Its Applications, IEEE Access, 2017

H. B. Mitchell, Image Fusion: Theories, Techniques, and Applications. Berlin Heidelberg: Springer-Verlag, 2010.

P01.34

The effect of noise in measurement of the ²³Na modulation transfer function (MTF): a simulation study

P. Polak, M. Noseworthy

McMaster University, School of Biomedical Engineering, Hamilton, ON, Canada

Introduction: Imaging systems can be described with the use of the point-spread function (PSF) and the modulation transfer function (MTF). Measurement of these functions are usually performed in a low noise environment in order to reduce interference on the MTF. However, the effect of noise in some contexts, such as with ²³Na MRI, cannot be avoided since these have inherently low SNR [1]. This work will examine the performance MTF quantification under varying noise conditions in a Monte-Carlo simulation study.

Subjects/Methods: MTF calculation methods:

1. Direction Modulation (DM): $= (I_{max} - I_{min}) / (I_{max} + I_{min})$,

I_{max} and I_{min} are the maximum and minimum intensities across the profile.

2. Fourier Harmonic (FH): $= |F_{1,f} / G_1|$,

$F_{1,f}$ and G_1 denote the first odd harmonics of the Fourier transforms for the output and ideal output [2].

A simulated bar phantom was created with 25 combs of differing resolutions (200 to 10 pixels). This binary phantom had values (100 and 0), representing signal / empty, created to a size of 3360x3360 (Fig. 1a).

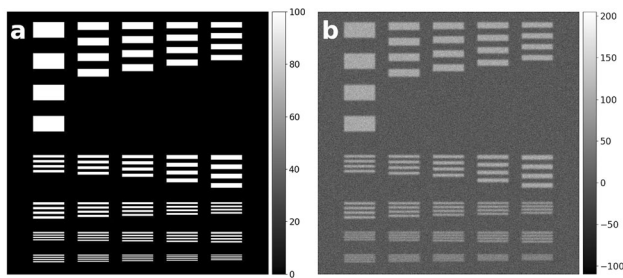


Figure 1: (a) Noise-free phantom (3360x3360), 25 comb widths, measuring 200 to 10 pixels. Values of 0 are black and 100 white. (b) Data after application of 2D Gaussian PSF (width 9 pixels), downsampling (factor 4), and addition of noise (0.25).
 To represent the effects of a PSF the phantom was convolved with a rotationally symmetric Gaussian kernel width $\sigma=9$ pixels, then downsampled by a factor of 4 (Fig. 1b). Each region of interest (ROI) spanned one period, and each had a width of 28 pixels - with the mean data being used in the MTF calculations.

Normally distributed noise, mean of 0 and σ_n values of 0.05,0.1,0.15,0.2,0.25,0.3, were scaled and added to the phantom. Simulations were performed for 2500 trials at each noise level, and DM and FH MTFs were created from the ROIs. Means and variances were calculated across the trials for each noise level and comb frequency.

Results/Discussion:

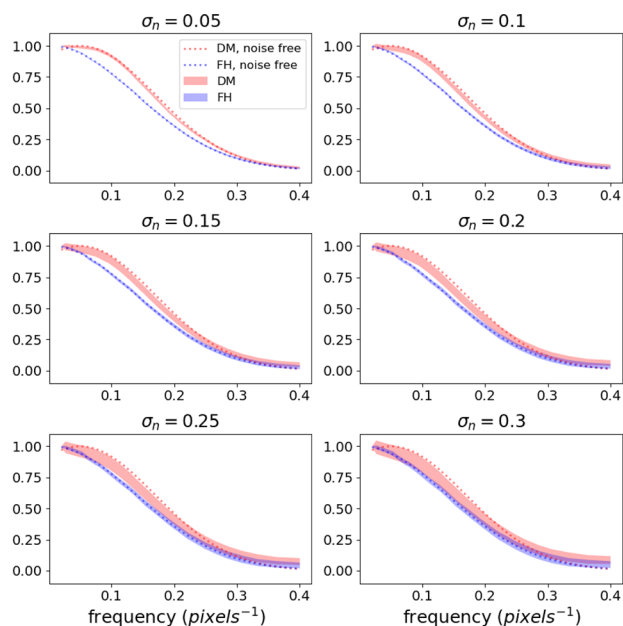


Figure 2: MTF curves for DM (red) and FH (blue) methods for all simulated noise levels. Dotted lines are derived from the noise-free data. Solid fills represent the mean +/- standard deviation across all trials for each noise level and frequency.

The noise-free MTFs (dotted) indicate that the DM method has a better MTF at low frequencies, but it degrades as σ_n increases. In particular, the mean (center of the red fill) reduces compared to the noise-free curve. Conversely, the FH method is centered on the noise-free curve at all noise levels. This indicates the FH is more robust and consistent in noisy experiments, and demonstrates a linear dependence on frequency and σ_n as predicted in [3].

Figure 3 exhibits the effect of noise on the variance of the calculated MTFs.

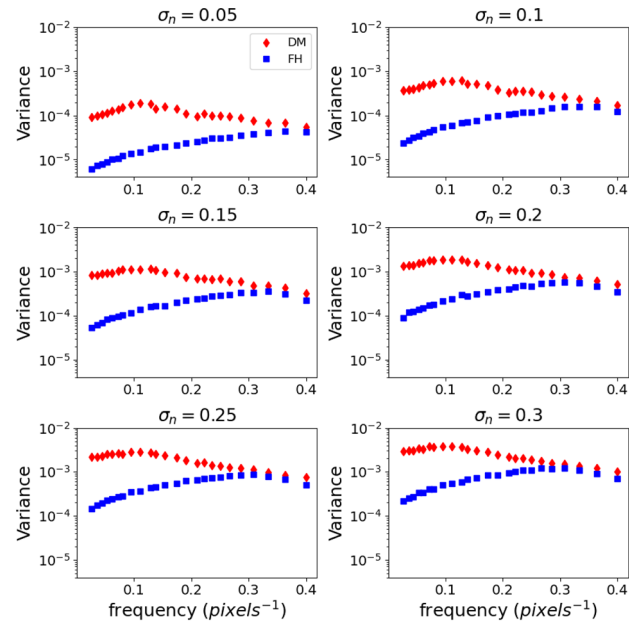


Figure 3: Simulated MTF variances versus frequency data for DM (red diamonds) and FH (blue squares) methods for all simulated noise levels.

Although both methods have increased variance as σ_n increases, the FH method demonstrates a lower overall variance across frequencies. At higher noise levels and/or frequencies, the variances are approximately equal, possibly due to low SNR in the relevant ROIs, and the Gaussian assumption of noise no longer applying [4]. For frequencies with SNR in the ROI, the MTF data is unreliable and heuristically may be set to 0.

This work demonstrates the effects of noise on MTF calculations, and provides a guide to their utilization in ^{23}Na MRI.

- References:** 1.Madelin G et al. JMRI 2013;38.
 2.González-López A et al. Med Phys 2016;43.
 3.González-López A. Med Phys 2018;45.
 4.Gudbjartsson H et al. MRM 1995;34.

P01.35

Free breathing simultaneous T_1 , T_2 and T_2^* quantification using gradient echo readouts in the myocardium

I. Hermann¹, P. Kellman², L. Schad³, S. Weingärtner¹

¹Magnetic Resonance Systems Lab, Department of Imaging Physics, University of Technology, Delft, The Netherlands, ²National Heart, Lung, and Blood Institute, National Institutes of Health, DHHS, Bethesda, USA, ³Computer Assisted Clinical Medicine, Medical Faculty Mannheim, Univeristy Heidelberg, Mannheim, Germany

Introduction: Quantitative mapping in the myocardium has received major clinical interest, as markers related to myocardial relaxation time yield promising sensitivity to a broad spectrum of cardiomyopathies. T_1 , T_2 and T_2^* mapping are routinely used in advanced CMR centers for, among others, the assessment of fibrosis, edema and iron overload. However, no method has been proposed to reliably quantify all three relevant markers, necessitating separate scans. This hampers the evaluation and leads to long scan protocols. In this study we sought to implement a navigator gated free breathing sequence for robust, joint quantification of T_1 , T_2 and T_2^* using gradient echo readouts.

Subjects/Methods: Figure 1 shows the sequence diagram of the proposed Saturation And T_2 prepared Relaxometry using Navigator (SATURN) sequence. The sequence is based on a multi gradient echo

with various saturation and T_2 -preparations to generate T_1 and T_2 weightings. A six parameter fit was used for the estimation of the relaxation times.

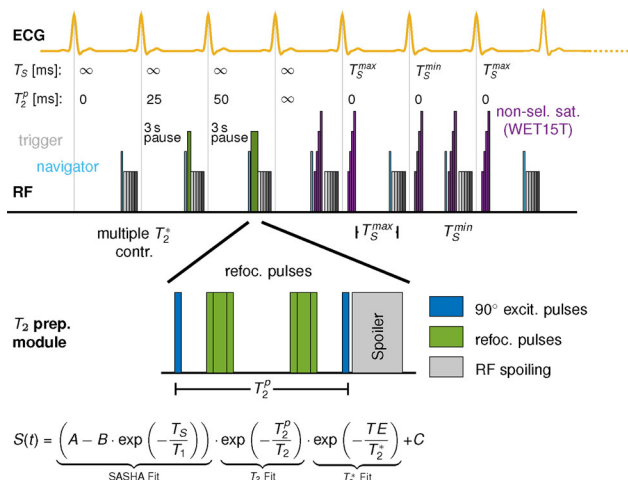


Figure 1: Sequence diagram for the proposed T_1 , T_2 and T_2^* mapping technique. Navigator pulses (brightblue) are played before the readouts. Five different multi gradient echoes per imaging block are generated.

Inter-scan motion was reduced by using rigid registration. Bloch simulations were performed to visualize the magnetization evolution throughout the sequence and to validate the fit-model.

Simultaneous T_1 , T_2 and T_2^* measurements were performed in a phantom and 9 healthy volunteers (23-29 years old, 6 male) at 3T.

Sequence parameter were TE = 1.5-10 ms forming 5 echos, centric reordering, FOV = 384x288 mm, base resolution = 192x144, slice thickness = 8 mm, flip angle = 20, partial Fourier 6/8 and GRAPPA factor = 3. All measurements were compared with the reference methods SASHA T_1 [1], cardiac T_2 -Map [2] and GRE T_2^* [3].

Results/Discussion: The simulation (Figure 2 A) shows the longitudinal magnetization evolution throughout the sequence. Accurate multi-parameter quantification for T_1 , T_2 and T_2^* across the relevant in vivo range was achieved in simulations (<1% deviation).

Phantom measurements (Figure 2 B) showed good agreement to reference methods with deviations of less than 5%. Improved T_2 accuracy was achieved in comparison to clinically used single-parameter methods [4].

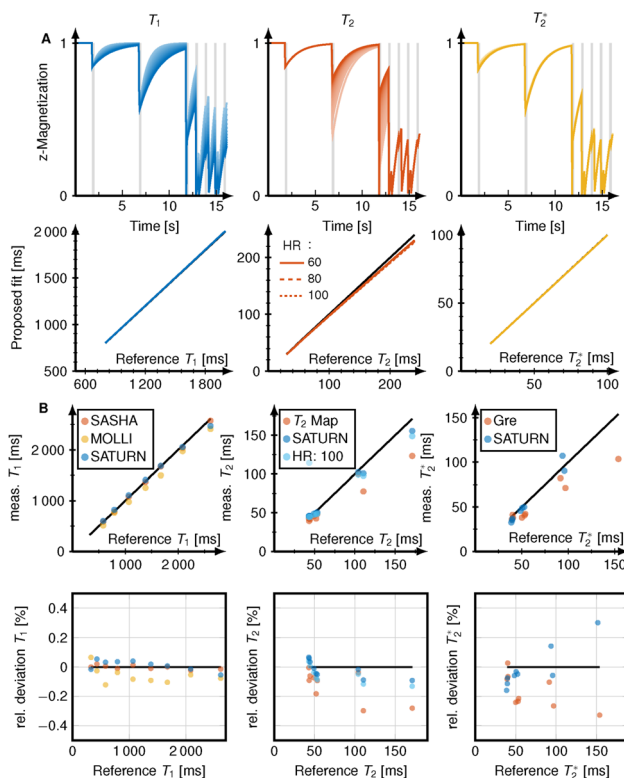


Figure 2: A) Simulated magnetization of the proposed sequence for varying T_1 , T_2 and T_2^* on the top. Increasing relaxation times are depicted as increasing brightness. Bottom panel shows the deviations of the pro

Example parameter maps are shown in Figure 3 for three healthy subject. The relaxation times in the healthy myocardium measured with SATURN (Figure 3) were $T_1 = 1565 \pm 41$ ms, $T_2 = 38 \pm 3$ ms and comparable to the conventional methods. T_2^* obtained with SATURN was 26 ± 3 ms, this was 20% increased compared the conventional method, which, however, suffered from major artifacts.

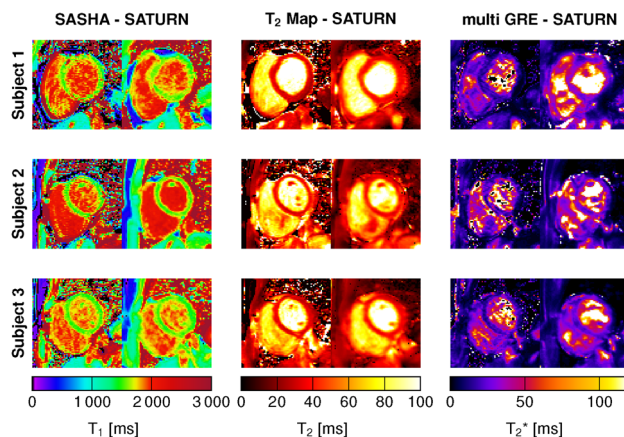


Figure 3: In vivo measurement of T_1 , T_2 and T_2^* for the proposed SATURN sequence (right) for three healthy subjects compared to reference methods (left).

SATURN enables joint quantification of the most relevant clinical relaxation times, T_1 , T_2 and T_2^* , with robust image quality. Good quantification accuracy was demonstrated in a phantom. In vivo free breathing imaging yielded high visual image quality.

References: [1] K. Chow et al., Magn Reson Med 71, 2082-2095, 2014.

[2] T. Huang et al., Magn Reson Med 57, 960-966, 2007.

[3] M. Westwood et al., *JMRI* 18, 33-39, 2003.

[4] C. Roy et al. *Magn Reson Med* 73, 1741-1753.

P01.36

Lipid and water separation through an SMS-like approach in 7T brain EPI

A. Seginer¹, E. Furman-Haran², I. Godberg³, R. Schmidt⁴

¹Siemens Healthcare Ltd, Rosh Haayin, Israel, ²Weizmann Institute of Science, Life Sciences Core Facilities, Rehovot, Israel, ³Wolfson medical center, Neurology, Holon, Israel, ⁴Weizmann Institute of Science, Neurobiology, Rehovot, Israel

Introduction: Functional MRI (fMRI) is based on the well-known gradient-echo echo-planar imaging (GRE-EPI), offering ultrafast acquisition. However, EPI is also noted for its low effective bandwidth along the phase encoding (PE) direction¹. One consequence of this low bandwidth is a large apparent spatial shift of the lipids due to the chemical shift between the lipids and water signals, resulting in artifacts in the image. The shift artifact is commonly removed by prepending an RF pulse to suppress the lipid signal. In this study, we examine the potential to significantly reduce the SAR by circumventing the fat-suppression pulse. To compensate for the removal of the fat-suppression pulse we utilized a reconstruction based on parallel imaging to separate the lipid and water images. An EPI implementation without fat suppression can offer fMRI studies greater flexibility to reduce the SAR, shorten the repetition time, and/or increase the volume coverage.

Subjects/Methods: Separate lipid and water images can be recovered by considering the acquisition as a simultaneous multi slice (SMS) problem with a built in CAIPRINHA shift – due to the chemical shift – as was demonstrated in Ref.² The substantial lipid-water spatial shift at 7T, for commonly used scan parameters, allows for a reliable separation. In this study we implemented a reconstruction method for three parallel imaging aspects: (i) in-plane PE acceleration, (ii) SMS acceleration, and (iii) lipid-water separation. We used BART³ with L1 norm to reconstruct the final images. The scans in this study were performed on a 7T MRI system (MAGNETOM Terra, Siemens Healthcare, Erlangen) using a commercial 1Tx/32Rx head coil (Nova Medical, Wilmington, MA).

Results/Discussion: Figure 1 compares the lipid-water separation with standard SMS=2. The same slice is reconstructed in both cases, and the g-factor maps for this slice are compared. The average and standard deviation of the g-factor is 1.06 ± 0.12 for lipid-water separation and 1.01 ± 0.08 for SMS=2. The low g-factor for SMS=2 is due to the CAIPRINHA implementation. The SNR of the image without fat suppression was estimated to be x1.3 higher than with fat suppression. Figure 2 demonstrates human imaging of two representative slices out of 30 acquired, with in-plane and slice accelerations of factor 3 and 2, respectively. The scan parameters are summarized in the figure. The SAR levels were 97% with fat suppression and only 33% without.

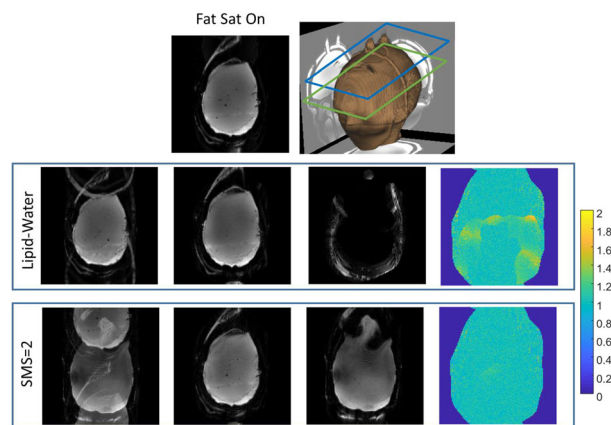


Fig. 1-Top-with fat suppression and 3D image with slices (green, blue). Mid- fat separation: standard reconstruction, water and lipid images, and g-factor of water. Bottom- SMS=2: standard reconstruction, two slices and g-factor of the first slice

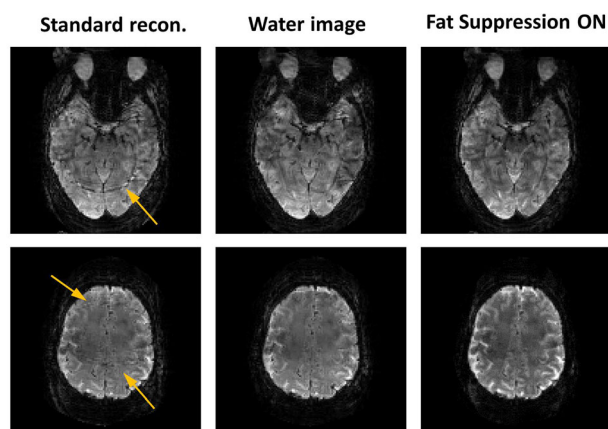


Fig. 2- Left to right: standard reconstruction, fat separation and fat suppression. Arrows point to artifacts. Scan parameters: FOV 220x220 mm², resolution 1.7x1.7 mm², slice thick. 1.7 mm, TR/TE 1500/22 ms, in-plane acceleration x3, and SMS=2

In this study, we demonstrated a method that allows to avoid fat suppression in EPI in 7T brain imaging. In such a case the GRE-EPI SAR can be reduced by more than a factor of two. A robust reconstruction based on SMS-like parallel imaging was demonstrated to separate the water and lipid images. fMRI scans at 7T can benefit extensively from avoiding the fat suppression.

References: 1) Schmitt F. et al., (1998), 2) Uecker M ISMRM 2012, 2490, 3) <https://mricon.github.io/bart>

P01.37

Correlation of artifact size of medical implants at different field strength – a simulation based study

T. Spronk¹, O. Kraff¹, J. Kreutner², G. Schaeffers³, H. Quick¹

¹University of Duisburg-Essen, Erwin L. Hahn Institute for MR Imaging, Essen, Germany, ²MRI-STaR Magnetic Resonance Institute for Safety, Technology and Research GmbH, Gelsenkirchen, Germany, ³MR: comp GmbH, Testing Services for MR Safety & Compatibility, Gelsenkirchen, Germany

Introduction: For scanning patients with medical implants it is essential to know the influence of the implants on the MR imaging

process. The procedure of testing MR image artifacts from passive medical implants is described in the standard ASTM F2119. Based on the increasing relevance of MR scans at higher field strengths (3T and 7T), a potential challenge is that the artifact size of older implants remains to be tested at 1.5T only. Within this study, the goal was to analyze the correlation of artifact size at different field strengths based on numerical simulations.

Subjects/Methods: The simulations were performed with a self-developed and validated framework [1] using JEMRIS [2], a numerical simulation tool, which is based on the Bloch equation.

A voxel model of a cubic phantom was defined and three test objects (TO) of simplified passive implants (Fig. 1) were placed in the center of the phantom. Additionally, three kinds of materials (titanium, stainless steel, and platinum) were used for each TO. The longitudinal axis for each TO was aligned parallel, vertically and horizontally to the static magnetic field and images were acquired in three orthogonal slice orientations at the center of the phantom with a gradient echo sequence as specified in ASTM F2119. An artifact is defined as all pixels with signal change of more than 30% compared to a reference image without the TO.

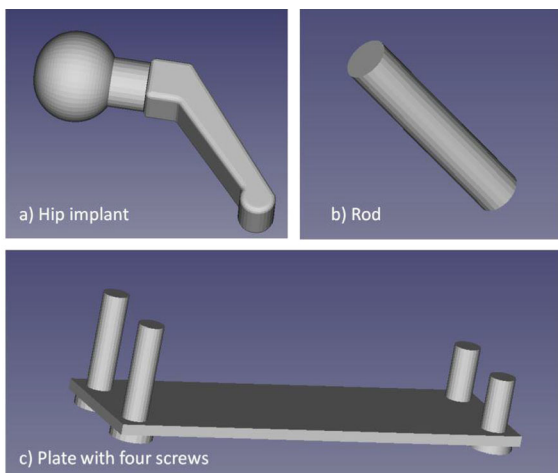


Fig. 1. Test objects that were simulated in this study. a) Simplified hip implant; b) simple rod; c) simplified orthopedic plate with four screws

Results/Discussion: The artifact area (Fig. 2) of all simulations was determined and compared to the same scan configuration at different field strength. As shown in Fig 3 a strong linear correlation between the artifact areas of the different field strengths is demonstrated by a linear fit. Furthermore the slope of the trend line and the result of $\sqrt{(B_{0, higher}/B_{0, lower})}$ of all three field strengths comparisons have a low deviation.

This study shows that an estimation of the artifact area between different field strengths is possible by using a scaling factor, which can be calculated with a simple equation. This equation could be used as a rule of thumb, which can help clinical personnel to estimate an artifact area based on the reference measurement of the medical implant at lower field strength. The equation is limited to susceptibility dominated implants such as orthopedic plates, screws or joint implants. In the future this project will confirm with MR scans.

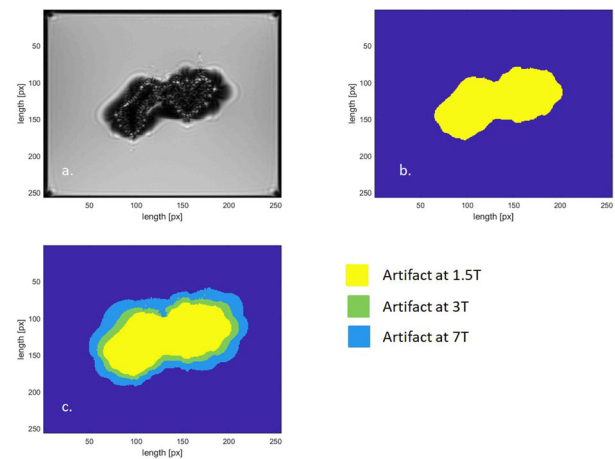


Fig 2. a) simulated artifact image of the simplified hip implant at 1.5T b) calculated artifact size mask, which highlights all pixels with a signal change of more than 30%; c) color-coded comparison of three artifact masks at 1.5T, 3T and 7T.

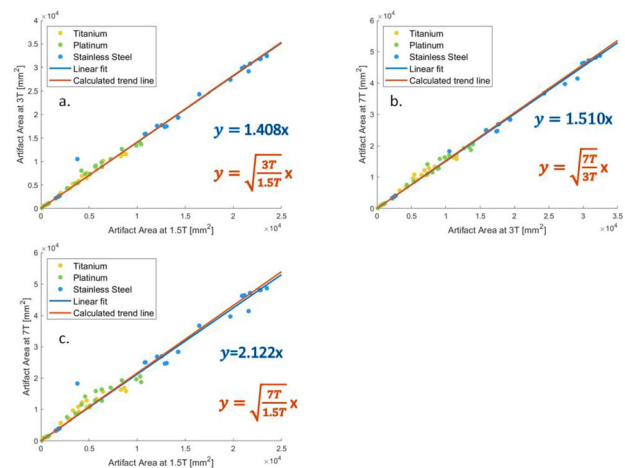


Fig. 3 Visualization of the different field strengths, each compared to another field strength. Trend line describes the linear correlation and calculated trend line based on the rule of thumb.

References: [1] T. Spronk, A. Chinnaiyan, J. Kreutner, and G. Schaefer, ‘Validation of the numerical simulation of susceptibility artifacts and consequences for artifact size calculation in the ASTM standard F2119-07(2013)’, ISMRM-ESMRMB, Paris, 2018.

[2] T. Stöcker, K. Vahedipour, D. Pflugfelder, and N. J. Shah, ‘High-performance computing MRI simulations’, *Magnetic Resonance in Medicine*, vol. 64, no. 1, pp. 186–193, Jul. 2010.

P01.38

A target field approach for designing quadrature RF coils for low field Halbach array MR systems

B. de Vos¹, T. O’Reilly¹, R. Remis², A. Webb¹

¹Leiden University Medical Center, C.J. Gorter Center for High Field MRI, Leiden, The Netherlands, ²Delft University of Technology, Circuits and Systems, Delft, The Netherlands

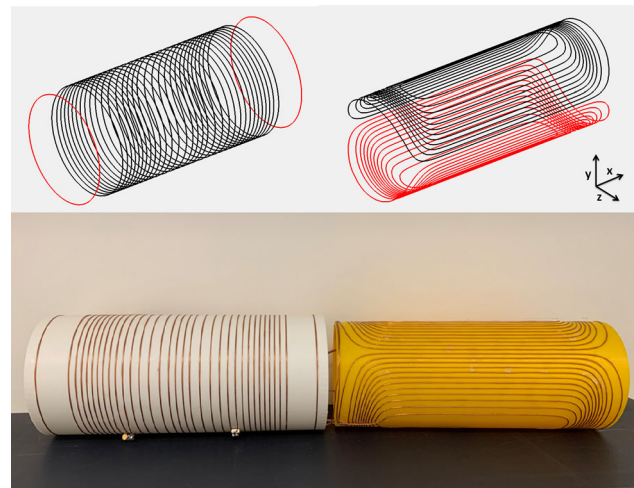
Introduction: Quadrature transmit coils, usually a birdcage configuration, are the standard radio frequency (RF) body coils in clinical MR systems. Most low field Halbach systems, in contrast, use a linear solenoidal coil due to the axial direction of the main magnetic field. Quadrature hemispherical head coils for Halbach systems have been designed¹. This work however, focuses on the design and construction

of clear bore cylindrical coils for a Halbach permanent magnet array MR system. In addition, we use a target field method² (usually used for gradient coil design, but here used for a frequency of 2.15 MHz which corresponds to a good approximation to a quasi-static system) and rewrite them in order to prescribe a uniform transverse field rather than a linear gradient field³. The dimensions and current patterns of the coils are designed to produce two coils with equal sensitivity (B_1 per squared root watt) and to maximize the volume where the combined polarization is circular. The coils are constructed using 3D printed molds which fix the wires in the correct position. The quadrature coils have been tested on a 50.2 mT system⁴.

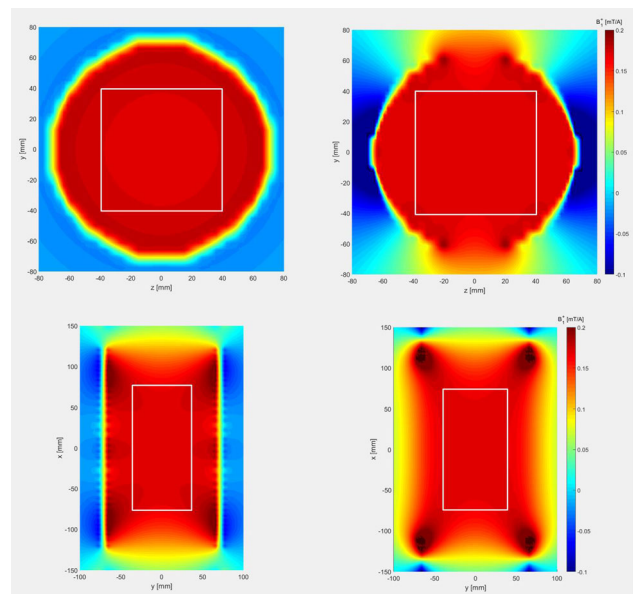
Subjects/Methods: Uniform orthogonal target fields are prescribed for a volume of 15x8x8 cm (x,y,z). The inverse source problem is solved resulting in surface current densities for each coil. Using stream functions, wire patterns are obtained. The sensitivities of both coils are then matched by varying the number of turns. The B_1 field from the resulting wire patterns are simulated using a quasi-static solver in CST Microwave studio (Darmstadt, Germany). Experimentally, the coils are wound on a 3D printed cylinder former, using 1mm diameter enameled copper wire. Both coils are tuned to 2.15 MHz. The sensitivities of the constructed coils are compared by measuring the power required to obtain a 90-degree flip angle.

Results/Discussion: The wire patterns produced by the target field method are shown in Figure 1. The radii are 71 and 66 mm for the solenoid and saddle coil, respectively. Both coils have a simulated sensitivity of $17 \text{ uT}/\sqrt{\text{W}}$. Figures 2 and 3 show that the simulated results produce the prescribed fields. Moreover, full circular polarization can be obtained within almost the entire target region. Measurements done using an apple with a diameter of 6 cm reveal that 0.91 and 1.3 W is required to obtain a 90-degree flip angle for the solenoid and saddle coil, respectively. In terms of sensitivity this results in $25.7 \text{ uT}/\sqrt{\text{W}}$ for the saddle coil and $30.8 \text{ uT}/\sqrt{\text{W}}$ for the solenoid. Driving the coils in quadrature would lead to an increase in transmit efficiency of 28%.

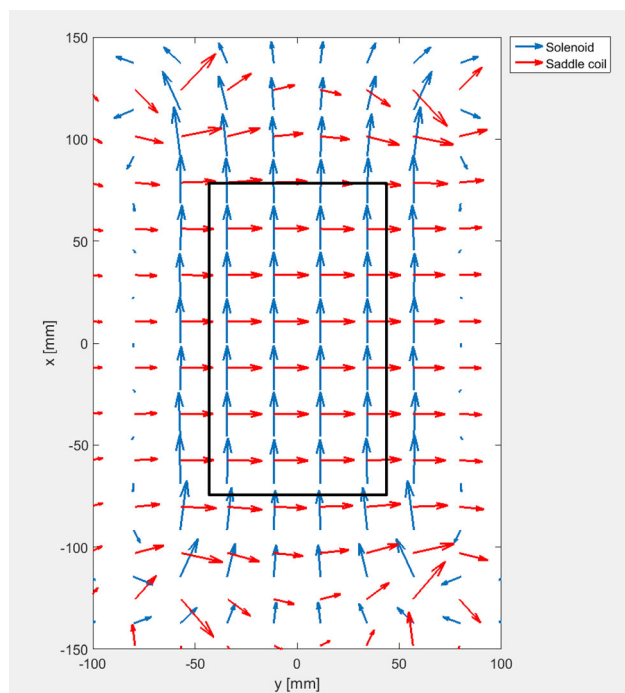
References: [1]N. Koonjoo, et al. *enc-conference* (abstract)
[2]B. de Vos, et al. *IEEE Transactions on Magnetics*, vol. 56, no. 3, pp. 1-8
[3]R. Turner, *Journal of Physics* 1986; vol. 19, no. 8.
[4]T. O'Reilly, et al. *J Magn Reson.* 2019; 307



Wire patterns resulting from the target field method, colors represent current direction. Left) solenoid creating a uniform field in the x-direction. Right) Saddle coil creating a uniform field in the y-direction.



Simulated fields of the x-component of the solenoid (left) and y-component of the saddle coil (right). White squares denote the targeted region.



Showing the amount of circular polarization by presenting the individual contributions of the solenoid and saddle coils. The square shows the targeted region.

P01.39

Characterization of a realistic head-shaped phantom with brain-mimicking metabolites for 7 Tesla spectroscopic imaging

G. Jona¹, E. Furman-Haran¹, R. Schmidt²

¹Weizmann Institute of Science, Life Sciences Core Facilities, Rehovot, Israel, ²Weizmann Institute of Science, Neurobiology, Rehovot, Israel

Introduction: In this study, we report on the development and characterization of a realistic head-shaped phantom with brain-mimicking metabolites for spectroscopic imaging in 7T MRI. For this purpose, a 3D head-shaped container and agar-based suspension were planned. The objectives included similar to human brain B_0 and B_1 distribution, representing *in-vivo* T_1/T_2 values, a brain-mimicking metabolite composition and lipid compartment.

Subjects/Methods: The 3D container in this work was based on the Martinos Center's "MGH Angel 001"^{1,2}. Nylon powder was used as the printing material to improve robustness and waterproofing. Our design includes three screw caps for easy refill³. The phantom was designed to include three sub-sections – mimicking brain, muscle and lipid tissues. The inner compartment was filled with a brain-mimicking mixture. The outer compartment was divided into two sections – the bottom one mimics muscle tissue, and the top one the lipid precranial layer. The metabolite phantom included 10mM L-Glutamic acid, 10mM Creatine 8mM myo-Inositol, 2mM GABA, 2mM Choline chloride, 5mM Sodium lactate 12.5mM NAA, 0.1mM GdDTPA and 2.5% agarose for similar T_1/T_2 to the human brain white matter, 5.5 gr/L NaCl (as in the fBIRN phantom⁴). Potassium dihydrogen orthophosphate was used as a buffer to achieve pH of ~ 7 . Peanut oil was used to mimic lipid tissue⁵.

Results/Discussion: The comparison of human and phantom B_0 and B_1 maps is shown in Fig.1. Images of the B_0 maximal deviation projection emphasize the main inhomogeneous areas – demonstrating high values near nasal, eye and ear regions, similar to human brain results. The range of the maximal deviations in the human and in phantom reached 250 Hz and 200 Hz, respectively. The human B_1 coefficient of variation was 37% and 28% for sagittal and axial scans, respectively, and that of the phantom was 23% and 18%, respectively. T_1 and T_2 relaxation times of the "brain" compartment were estimated in the central area (144 pixels) as 1160 ± 35 ms and 57 ± 2 ms, respectively; those of the "lipid" compartment were estimated as 426 ± 1 ms and 145 ± 1 ms, respectively.

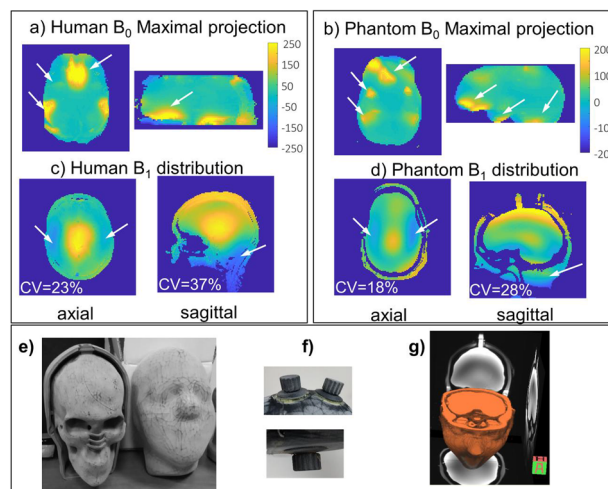


Fig. 1- Maximal absolute B_0 projection for human (a) and phantom (b). B_1 distribution of the human (c) and phantom (d). Photos of the 3D container (e) and screw caps (f). g) 3D image. Arrows point to the main B_0 high and B_1 low areas.

Figure 2 shows the spectroscopic imaging that was performed using EPSI. Single voxel was also acquired and fitted with LCMODEL. Measured concentrations were estimated for the main peaks, with deviations of 14% for NAA, 28% for Cr+PCr, 13% for Cho, 15% for Glu, 2% for mI, 4.5% for Lac, 0.5% for GABA.

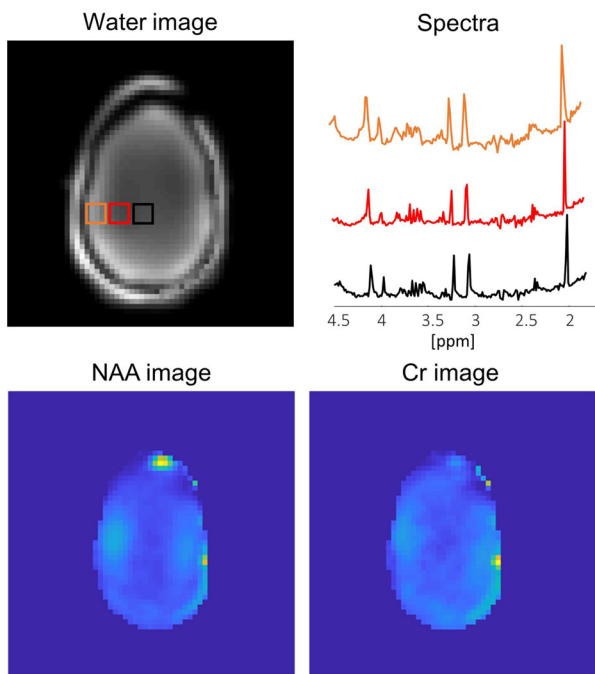


Fig. 2. 1H MRSI with EPSI, including water, NAA and Cr images and spectra for three shown regions. Scan parameters: TR/TE 2000/18 ms, FOV 300x300 mm³, resolution 4.3x4.3 mm², slice thick. 20 mm, echo spacing 0.52ms, SW 960 Hz, scan duration 2.20 min.

The B_0 and B_1 distribution measured in the phantom “brain” were in good agreement with human brain distribution, which is an important feature for the practical usage of the phantom. MRSI was demonstrated using EPSI. The ability to exploit such a phantom to examine MRSI parameters can be extremely valuable, especially with lipid mimicking compartment.

References: [1] Guérin, B., (2016) MRM 76, [2], <https://phantoms.martinos.org>, [3] <https://github.com/RitaSchmidt>, [4], Glover (2012) JMRI 36, [5] Hines C (2009) JMRI 30.

P01.40

Design and experimental characterization of a strong prepolarized magnet for high resolution MRI

J. P. Rigla Pérez¹, C. Gramaner², R. Iturbe³, E. Pallas², D. Grau-Ruiz¹, J. M. González¹, J. Alonso², A. Ríos¹, J. M. Benlloch²

¹Tesoro Imaging S.L., Valencia, Spain, ²Institute for Instrumentation for Molecular Imaging (i3M), Spanish National Research Council (CSIC), Valencia, Spain, ³ANTEC Magnets S.L.U., Portugaete, Spain

Introduction: One of the objectives of the HISTO-MRI project [1] is to develop a prepolarizing magnetic technology for a low field system. In this work, we present the Prepolarized Magnet (PM) design and its experimental characterization for a home-made special-purpose scanner (0.26 T) developed by Tesoro Imaging S.L. and i3M[2].

Subjects/Methods: The PM is a water-cooled solenoid consisting of 20 layers, where each layer has a spiral configuration with 16 turns. The PM has an inner and external diameter of 35 and 99.21 mm respectively and a length of 90.37 mm. The resistance and inductance of the PM are 74.44 mΩ and 0.6 mH, respectively. Each two layers are electrically connected in series and the water cooling paths are connected in parallel for heat removal efficiency. It is manufactured out of OF-OK Copper hollow tube (4x3 mm² copper section and an

inner hole of 2 mm in diameter where the coolant circulates). A picture of the PM is shown in



Picture of the Prepolarized Magnet

The PM is designed to generate magnetic pulses with an intensity >0.5 T and a duration > 1s over a field of view of 20 mm. For generating the pulse current we will use a battery bank (16 batteries in parallel) with a switch (IPM-16P)[3] and SMC HRS6060 cooling system. A diagram of the power supply system is shown in

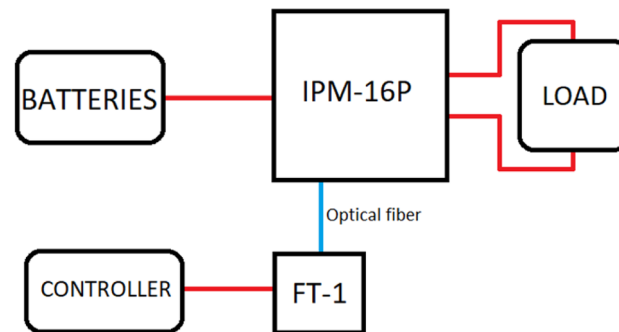
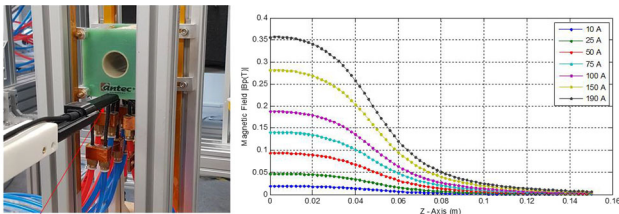


Diagram of the control and power supply system

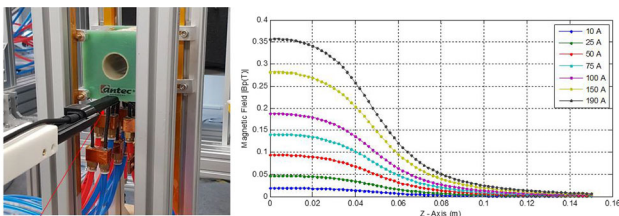
In the meantime, the experimental characterization of the prepolarizer magnet was carried out in continuous mode using a Danfysik 9100 Unipolar Power Supply (maximum current of 200A). The magnetic characterization was performed with a hall probe (Metrolab THM1176-MF) attached to a 3D positioning system (Left).



Hall Sensor
(Left) Picture of the Prepolarizer magnet during the experimental characterization at MRILab (3M) and (Right) X - axis distribution of the magnetic field $[B_p(z)]$ for different currents

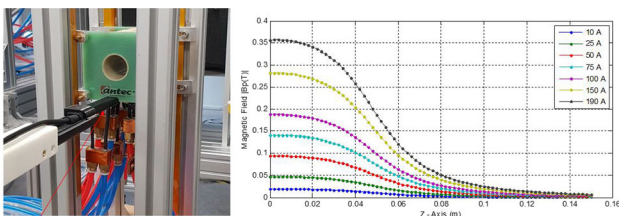
The hydraulic and thermal characterization was made using a flowmeter (SMC PF3W704-F03) located at the exit of each loop.

Results/Discussion: The magnetic field generated by the PM was measured along the X - axis of the magnet over a range of 160 mm (in steps of 2 mm) and for currents between 10 and 190 A, see



Hall Sensor
(Left) Picture of the Prepolarizer magnet during the experimental characterization at MRILab (3M) and (Right) X - axis distribution of the magnetic field $[B_p(z)]$ for different currents

. For a moderate maximum current of 190 A, the magnetic field reached >0.35 T in dc mode. The heat power dissipated in the system with these settings is around 5.4 kW. Once we integrate the PM in the scanner, we will drive pulses of up to 280 A (0.50 T) from the batteries, and expect a power dissipation of 5.8 kW with a 50 % duty cycle. Each loop was independently characterized both thermally and hydraulically by means of a flowmeter at the output of each loop. The flow in each loop was approx. 6 l/min and the thermal jump to the maximum current was around 12.5 degrees. These values are in agreement with the results obtained in the simulations (not shown in Right).



Hall Sensor
(Left) Picture of the Prepolarizer magnet during the experimental characterization at MRILab (3M) and (Right) X - axis distribution of the magnetic field $[B_p(z)]$ for different currents

References: [1] HISTO-MRI Project (European Commission under Grant 737180), <http://www.histo-mri.i3m.upv.es/>
[2] J.M. Algarin et al, Simultaneous Imaging of hard and soft biological tissues in a low-field dental MRI scanner, arXiv:2005.01462.
[3] IPM-16P, <https://www.eagleharbortech.com/>

P01.41

Experimental validation of B_1 for remote excitation at 3 T

F. Vazquez¹, R. Martin¹, S. Solis-Najera¹, O. Marrufo²,
A. Rodriguez³

¹Universidad Nacional Autonoma de Mexico, Departamento de Fisica, Facultad de Ciencias, Mexico City, 04510, Mexico, ²National Institute of Neurology and Neurosurgery MVS, Department of Neuroimaging, Mexico City, 14269, Mexico, ³Universidad Autonoma Metropolitana Iztapalapa, Department of Electrical Engineering, Mexico City, 09340, Mexico

Introduction: Traveling wave MRI is an alternative to overcome the B_1 inhomogeneities and the use of coil arrays with larger number of elements for human applications at UHF MRI [1-2]. We performed experimental B_1 mapping of a parallel-plate waveguide (PPWG), using a surface coil for transmission and a coil array for reception to validate electromagnetic simulations at 3T. Imaging experiments were performed on a commercial MR imager.

Subjects/Methods: The finite element method (FEM) was used to numerically compute the principal mode with propagation along the z-direction and the B_1^+ field with COMSOL MULTIPHYSICS (V. 3.2, Comsol, Burlington, MA, USA) at 128 MHz [2-3]. A PPWG was build as reported in [3]. A loop coil coil was used for transmission and a coil array was for reception, as shown in Fig. 1. T_1 -weighted images of a solution-filled cylindrical phantom (30 cm in diameter and 40 cm long with $\epsilon = 75$) were acquired using gradient echo sequences (TR/TE = 1500/7.6 ms, FOV = 240 mm x 240 mm, matrix size = 288 x 224, slice thickness = 5 mm, NEX = 1). The flip angle was swept from 15° to 90° with a 15° step and images were digitally processed to compute the B_1^+ map [4]. All electromagnetic simulations and imaging experiments were carried out using the setup in Fig. 1, and on a 3T GE Signa imager (GE Healthcare, Milwaukee, WI, USA).

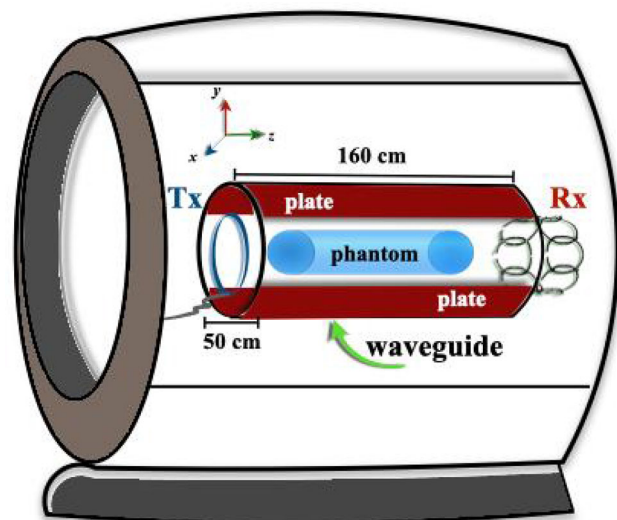


Figure 1. Schematic of experimental and simulation setup.

Results/Discussion: Fig. 2.b) and c) show simulated bi-dimensional maps of B_1 and phantom images obtained. Fig. 2.a) shows a comparison profile of the experimental and simulated B_1 data. This plot shows an excellent agreement between experiment and simulation. The experimental measurement of B_1^+ field serves as validation of the electromagnetic simulations. This work demonstrates that B_1^+ simulations are a reliable tool to study the remote excitation MRI at

high field. Numerical simulations of B_1^+ can be used for a priori study on the feasibility to conduct imaging experiments with a PPWG for traveling wave MRI. No modifications were done to the MR imager and standard pulse sequences were used, this approach can be implemented in other preclinical and clinical MR imagers. It has been demonstrated that a simple method together with a simple technique to map the B_1^+ field can provide the means to develop the traveling wave MRI approach for applications at higher fields.

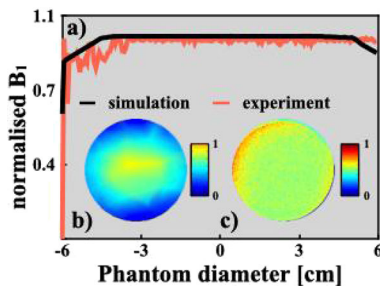


Figure 2. a). Comparison profile of simulation and theory, b) bi-dimensional B_1 maps and phantom image (c).

- References:** 1. Brunner et.al. Nature 457, 994, 2008.
2. Vazquez et. al. ISMRM-ESMRMB, 6484, 2010.
3. Vazquez et. al. J. Appl Phys, 114, 064906, 2013.
4. Vazquez et. al. 28th ESMRMB, 589, 2011.

P01.42

Numerical estimation of SAR for a circular slot surface coil at 11.7 T

S. Solis-Najera¹, F. Vazquez¹, R. Martin¹, O. Marrufo², A. Rodriguez³

¹Universidad Nacional Autonoma de Mexico, Departamento de Fisica, Facultad de Ciencias, Mexico City, 04510, Mexico, ²National Institute of Neurology and Neurosurgery MVS, Department of Neuroimaging, Mexico City, 14269, Mexico, ³Universidad Autonoma Metropolitana Iztapalapa, Department of Electrical Engineering, Mexico City, 09340, Mexico

Introduction: We have recently proved that the slotted surface coil is able to produce high quality images at 11.7 T [1]. Additionally, we have shown that this coil design can produce a reduced SAR at 300 MHz [2]. We investigated the SAR as a function of the number of slots via numerical evaluation at 500 MHz, using a phantom filled with a solution mimicking gray matter for small animal MRI.

Subjects/Methods: Numerical simulations of SAR for the slotted surface coil varying the number of slots were done using the finite integration method and CST Microwave Studio (CST MICROWAVE STUDIO, CST GmbH, Darmstadt, Germany). SAR simulations were computed assuming configurations above and grey matter ($\epsilon = 57$ at 500 MHz [2], $\mu = 1$, $\rho = 1030 \text{ kg/m}^3$, and $\sigma = 0.527133 \text{ S/m}$) in a sphere phantom (radius = 10 mm). The coil diameter was 20 mm and each slots had a 2 mm diameter. All SAR predictions were computed assuming 1 g averaging. The slotted coil was excited by feeding the port in the coil at the 6 o'clock position, and was iteratively tuned to a resonant frequency of 500 MHz for all simulations. An illustration of the coil with a six circular slot configuration showing capacitors and trimmers and the simulation setup is in Fig. 1.

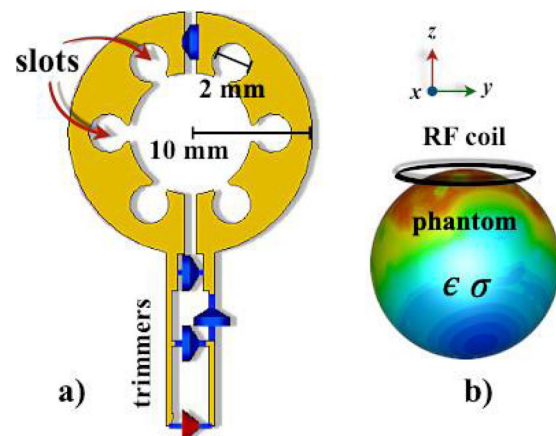


Figure 1. a) Schematic of slotted coil showing dimensions and components, b) Simulation setup.

Results/Discussion: Fig. 2.a)-c) shows bi-dimensional maps of SAR for the circular slot coil varying the number of slots at 500 MHz. Comparison plots were also computed and shown in Fig. 2.d)-e). Profiles for each case were computed along the black and red lines as indicated in the figure. The SAR bi-dimensional maps show the usual pattern produced by a surface coil, where the higher intensity of SAR is within the vicinity of the coil plane for maps in Fig. 2.a)-c). This is in good concordance with results reported in [1,3]. There is a considerable increment on the SAR compared to results obtained at 300 MHz, however it is practically the same pattern and values regardless the number of slots used in the coil configuration as shown in Fig. 2.d). Profiles of Fig. 2.e) show the characteristic pattern of SAR, where higher values of SAR can be appreciated towards the extremes of the plot, and moving towards the centre, all values drastically decrease compared to both ends. These numerical results exhibit that the number of slots do not affect the SAR produced by this coil design at UHF MRI.

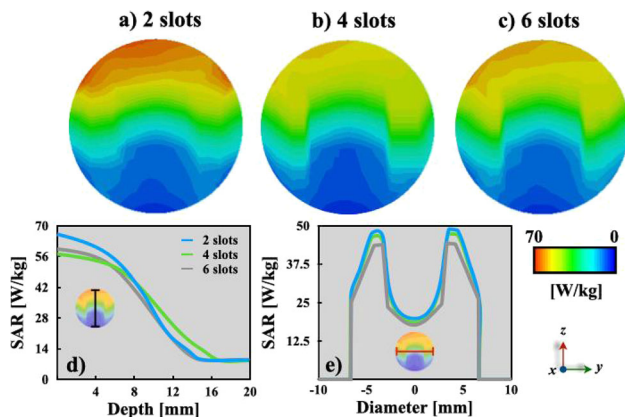


Figure 2. Bi-dimensional maps of SAR varying the number of slots (a-c). SAR comparison plots for two orientations (d-e).

- References:** 1. Solis-Najera, et. al. 2018, Abs. # 1746 ISMRM. <http://archive.ismrm.org/2018/1746.html>.
 2. Solis-Najera, et. al. 2015, Magn. Reson. Mater. Phys. **28** 599. <https://doi.org/10.1007/s10334-015-0501-8>.
 3. Prock et. al. 2002, Phys. Med. Biol. **47** 1805. <https://doi.org/10.1088/0031-9155/47/10/314>.

P01.43

Slotted end ring coil sensitivity experimentally validated at 4 T

S. Solis-Najera¹, D. Tomasi², A. Rodriguez³

¹Universidad Nacional Autonoma de Mexico, Departamento de Fisica, Facultad de Ciencias, Mexico City, 04510, Mexico, ²National Institutes of Health, National Institute of Alcohol Abuse and Alcoholism, Laboratory of Neuroimaging, Bethesda, MD 20892-1013, USA, ³Universidad Autonoma Metropolitana Iztapalapa, Department of Electrical Engineering, Mexico City, 09340, Mexico

Introduction: There is an important difference between the end rings in a standard birdcage coil and the cavity resonator developed by Mansfield et. al. [1]. To investigate the effect of the squared-slot end rings, we derived a B_1 expression for a low pass cavity resonator and built a volumen coil prototype. We acquired phantom images and compared these theoretical and experimental results.

Subjects/Methods: To investigate the effect of the squared-slot end rings, we used the formalisms reported in [1-2]:

$$B_{cav} = 2i_{cav}(l^2 + 2d^2)d^{-1}(l^2 + d^2)^{-3/2}$$

where l (length) and d (diameter). A prototype of the 4 leg cavity resonator coil was built using wide copper (12 cm long/10 cm diameter) and the 4 circular cavities (2 cm diameter) [1], see Fig. 1. This coil was tuned to 170.29 MHz and 50 Ohm matched and it was designed as a transceiver in the quadrature-drive mode. All MR in vitro (sample phantom filled with a water-based 0.1 M CuSO_4 solution) images were acquired with TR/TE = 900/20 ms, number of slices = 25, FOV = 8 cm x 8 cm, matrix size = 256 x 256, slice thickness = 2 mm, NEX = 1, and were performed with a 4-Tesla MRI scanner driven by a Varian INOVA Varian, Inc, Palo Alto, CA) console with shielded whole-body SONATA-Siemens gradient set.

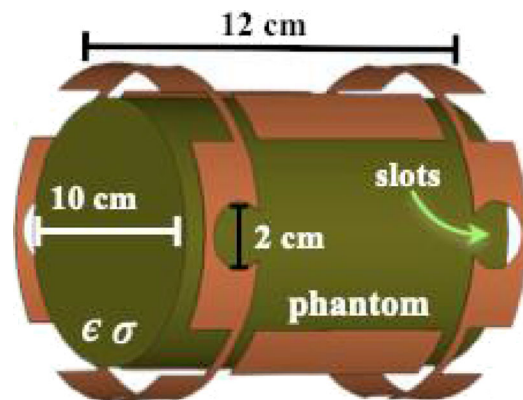


Figure 1. Schematic of coil prototype showing dimension.

Results/Discussion: Axial phantom T_1 -weighted images were acquired with our coil (Fig. 2.a). A sensitivity plot was computed using image data and the equation above and shown in Fig. 2.b). An excellent correspondence can be observed between experiment and theory. This paves the way to experimentally develop volume coils using Mansfield's cavity resonator principles and the Biot-Savart law.

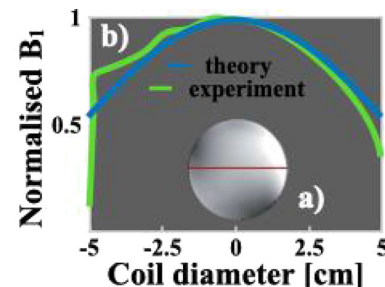


Figure 2. a) Phantom image, and b) comparison profiles of theory and experiment.

- References:** 1. Mansfield et. al. Meas. Sci. Technol. **1** (1990) 1052-1059. iopscience.iop.org/0957-0233/1/10/010.
 2. Vaughan, J.T. and Griffiths, J.R. eds., 2012. RF coils for MRI. John Wiley & Sons.

P01.44

Towards high sensitivity ^{13}C MR spectroscopy of human brain glycogen at 7T

E. Serés Roig, R. Gruetter

Laboratory of Functional and Metabolic Imaging (LIFMET) - Ecole Polytechnique Federale de Lausanne (EPFL), Lausanne, Switzerland

Introduction: Although accepted as the main energy storage in the central nervous system, the role of glycogen in the conscious human brain is largely unknown. Carbon-13 magnetic resonance spectroscopy (^{13}C -MRS) allows the non-invasive detection of human brain glycogen *in-vivo* [1,2], which is typically done via ^{13}C -glucose infusion labelled at the C_1 -carbon to enhance the sensitivity giving rise to three C_1 -resonances (glycogen, glucose- β , and glucose- α). To further improve both sensitivity and spectral resolution, the use of high magnetic field (i.e. 7T) has the clear advantage of separating the resonances to better facilitate their quantification. In this context, the aim of this study was to explore the advantage of ^{13}C -MRS at 7T in conjunction with broadband ^1H -decoupling while adjusting the decoupling scheme parameters towards optimal sensitivity and simultaneous detection of glycogen and glucose.

Subjects/Methods: *In-vitro* ^1H -decoupled ^{13}C -MRS measurements were performed on a 7T human-scanner (Siemens Erlangen/Germany) using a home-built ^{13}C -linear/ ^1H -quadrature RF-surface-coil. A pulse-acquire sequence for ^{13}C -MRS using broadband ^1H -decoupling was implemented using the WALTZ-16 scheme [3]. All *in-vitro* measurements were performed using a two-compartment phantom containing 1) 800mM natural abundance of glycogen and 2) 8mM of glucose- C_1 labelled, while all spectra were acquired using uniform adiabatic ^{13}C -excitation [4] placing the carrier frequency at the glucose- β resonance (96.6ppm). The performance of the decoupling scheme was investigated by increasing successively the number of WALTZ-cycles from 1 to 8 (i.e. 4 WALTZ-cycles corresponds to the WALTZ-16 scheme), while adjusting in each case the decoupling duration accordingly to the FID ($\sim 96\text{ms}$).

Results/Discussion: *In-vitro* ^1H -decoupled ^{13}C -MRS at 7T revealed three well resolved C_1 -resonances including glycogen (100.5ppm), glucose- β (96.6ppm) and glucose- α (92.8ppm), as by comparing spectra without and with decoupling using the WALTZ-16 scheme (Figure1-left). The signal intensities of glucose- β and - α increased or decreased whether and odd or even number of WALTZ-cycles was applied (Figure1-Figure2A), and this could be attributed to the fact that the ^1H -spin ended up either down (Figure1/green-arrows) or up (Figure1/red-arrows), respectively. In contrast, no such effect was observed for glycogen in which the signal intensity remained fairly constant (Figure2A). The slight decrease of the glucose- β slope (Figure2A) could be attributed either to the presence of sidebands (Figure1-bottom/ocher-arrows) and/or to the proximity of glucose- β to water (Figure2B). Overall, the use of 3 versus 4 WALTZ-cycles (Figure1/top-right) may be advantageous in terms of optimal sensitivity and lower ^1H -power for *in-vivo* measurements.

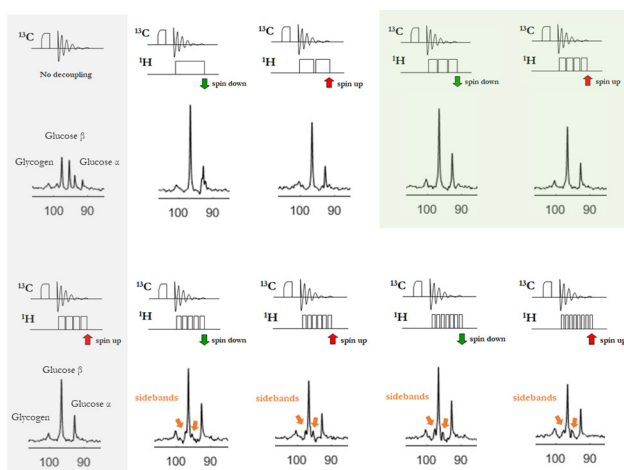


Figure1. *In vitro* ^{13}C spectra of natural abundance of glycogen and glucose- C_1 labeled. From left to right, ^1H -decoupling was applied by increasing successively the number of WALTZ cycles while adjusting the decoupling duration accordingly to the FID.

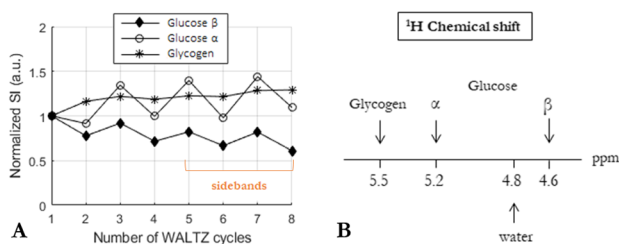


Figure2. A) Representative curves of spectra from Figure1. The data points correspond to the maximum signal intensity of each metabolite as a function of the number of WALTZ cycles. B) Scheme illustrating the ^1H -chemical shift of each metabolite.

References: [1] Gruetter R. JNR.2003;74(2):179-83

[2] Oz G. NInt.2003;43:323-9

[3] Shaka AJ.JMR.1983;52:335-338

[4] Serés Roig E. NMR Biomed.2019

P01.45

Blood clotting process monitoring by T_2 : setup and analysis strategies

M. Stolz¹, T. Bakchoul¹, F. Schick²

¹University Hospital Tübingen, Transfusion Medicine, Tübingen, Germany, ²University Hospital Tübingen, Section on Experimental Radiology, Tübingen, Germany

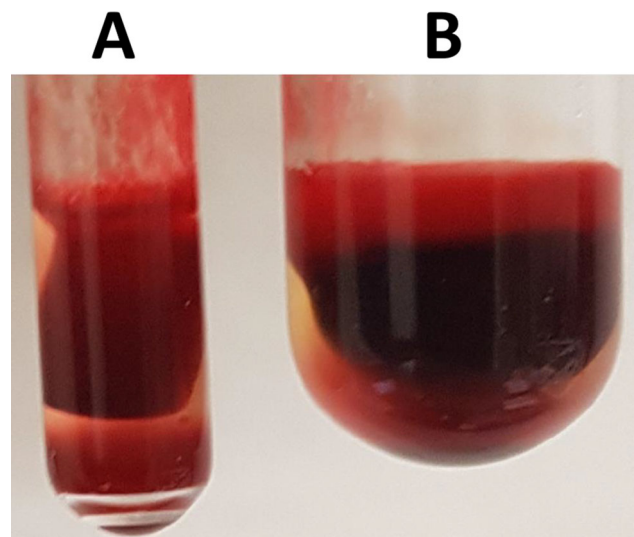
Introduction: During clotting blood, a suspension of cells and plasma, becomes a sponge-like structure. The framework is formed by the protein fibrin: Inside are cells and serum., outside the network serum is dominant. Applying a magnetic field in a typical NMR setup makes the water molecules experience different magnetic field inhomogeneities depending on their position. These distinct populations can be monitored by a T_2 measurement. A typical CPMG for a blood sample can be conducted in several seconds, so a continuous monitoring is possible.

Published work conducted the measurement on an optimized relaxometer at 0.5 T with 40 μL sample volume heated to 37°C [1,2]. The water molecules in the serum outside of the clot exhibited a T_2 value of about 1000 ms in contrast to the population inside of about 200 ms. Promising results were achieved compared to the gold-standard light-transmission-aggregometry. We investigated the method on another device: What experimental setup is required for stable and reproducible measurements? What challenges are faced during data analysis?

Subjects/Methods: 340 μL blood (healthy donors) with citrate-anticoagulant were recalcified with CaCl_2 and activated with recombinant tissue factor in a 10 mm tube. Continuous CPMG measurements were performed every 15 s for 60 min on a 0.5 T research NMR device (Magspec, Pure Devices GmbH, Germany), operating at 30°C.

Results/Discussion: Similar curves to Skewis and Cuker were produced and we observed the following points:

The tube geometry influences the clot shape, which affects the sensitivity, best seen when compared to a tube with half diameter (fig1A vs fig1B).

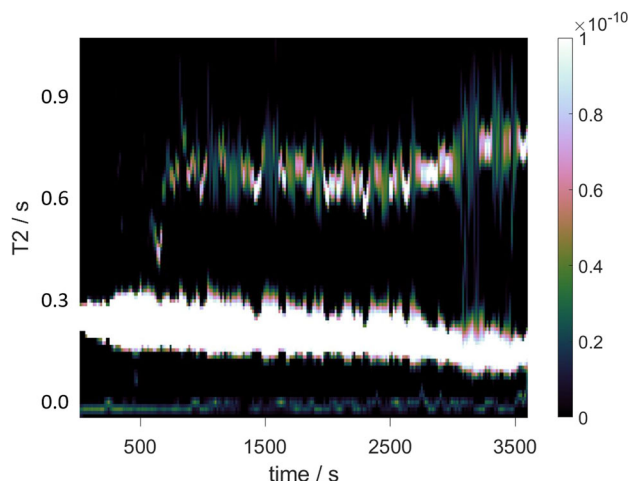


Shapes of clotted blood vs tube geometry: (A) Tube with 5 mm diameter, (B) 10 mm tube (default size for NMR device)

Biological processes are best observed at 37°C, the reaction kinetics is slower at lower temperatures, so the splitting was observed later within the series, but with comparable magnitude.

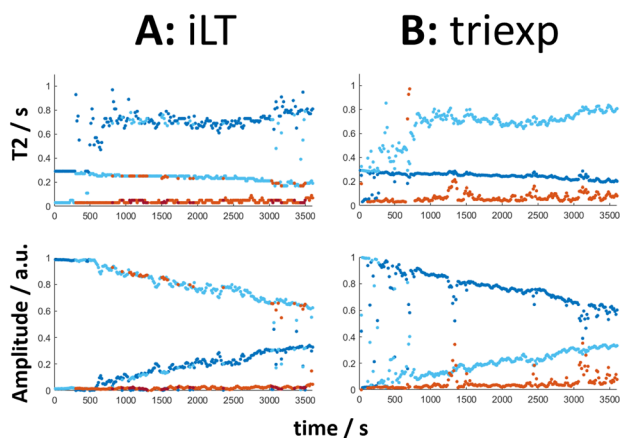
A moving average filter and a Savitzky-Golay filter optimized to simulated data with the same SNR were applied.

There are two wide-spread approaches for multiexponential fitting: The inverse Laplace transformation (iLT) and a direct non-linear least-squares fit, if the number of components is known.



T2 distribution generated by inverse Laplace transformation. CPMG data of a clotting blood sample.

The iLT (fig2) is ill-posed and requires regularization to result in reproducible solutions [3]. Artefacts need to be carefully identified. We are currently testing other options to force a continuous overall solution. A “new” continuous contribution starting at 50 ms and raising over time to about 80 ms was observed. The T_2 distribution can be converted to a dot plot (fig3A).



Dot plots of a clotting process: (A) is the plot generated from the T_2 distribution. (B) is directly obtained after triexponential fitting.

Prior knowledge allowed modelling by a triexponential, where the parameters are then sorted by rationality (fig3B). Properties like water content or clot consistence can be derived. We like to motivate further steps to stabilize the method on common devices.

References: [1] Skewis et al., 2014, DOI: 10.1373/clinchem.2014.223735

[2] Cuker et al., 2016, DOI: 10.1093/ajcp/aqw189

[3] Zou et al., 2016, DOI: 10.1007/s12182-016-0093-6

P01.46

Paramagnetic metals in human brain tissue: a preliminary EPR study at variable temperature.

F. Otsuka¹, M. C. G. Otaduy², H. Heinsen³, J. F. de Lima⁴, O. R. Nascimento⁴, C. E. G. Salmon¹

¹Department of Physics, University of São Paulo, Ribeirão Preto, SP, Brazil, ²Medical School, University of São Paulo, São Paulo, SP, Brazil, ³University of Würzburg, Würzburg, Germany, ⁴Institute of Physics, University of São Paulo, São Carlos, SP, Brazil

Introduction: Study of iron content in human brain tissue has gained a lot of attention over the years, supported by the observed relationship between iron accumulation and neurodegenerative diseases. A full understanding of paramagnetic species present in the human brain tissue is still needed. On this work, an Electron Paramagnetic Resonance (EPR) analysis of brain tissue with variable temperature is presented for three samples from one post-mortem subject.

Subjects/Methods: This study was approved by the ethical committee in research of the Medical School of the University of São Paulo (FMUSP). Fixed brain tissue samples from a post-mortem subject (959 days after death) without neurological or neurodegenerative diseases were acquired at the FMUSP. Samples from Substantia Nigra (SN), Globus Pallidus (GP) and Locus Coeruleus (LC) were frozen-dried and turned into pellets.

EPR data were acquired in a temperature range from 5K to 293K using a X-Band spectrometer (9.11 GHz). Following acquisition parameters were used: sweep range 25 - 675mT, microwave power 0.5mW, sweep time of 120s, modulation frequency of 100kHz, modulation amplitude of 0.8mT, and 4 reads per sample (8 reads for LC sample). Recorded spectra were normalized by dry mass and processed/simulated using OriginLab 8.5/EasySpin toolbox (Matlab).

Results/Discussion: Three main peaks were observed for all the samples: high-spin iron (Fe_{hs}) at $g=4.28$, copper (Cu) at $g_1=2.06$ and $g_2=2.28$, and a broader iron peak associated to ferritin (Ft) at $g=2.0$ [2] (Figure 1).

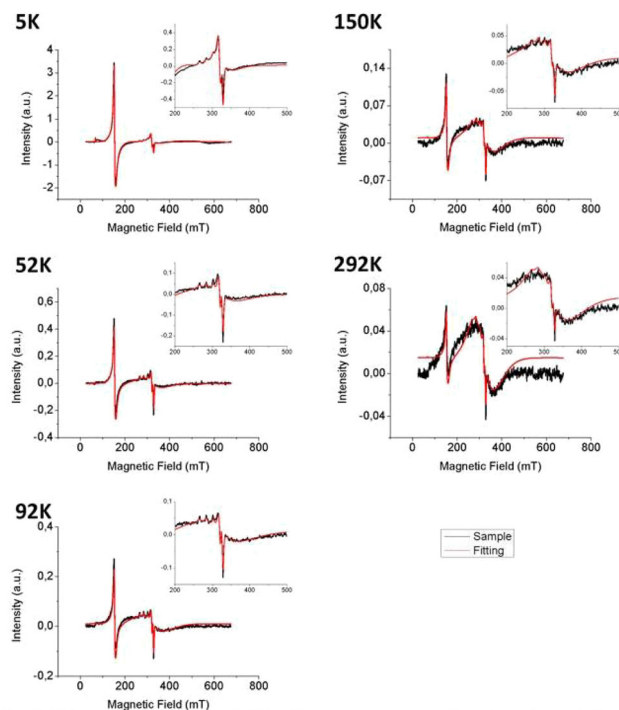


Figure 1 - EPR spectra and the fitting of GP sample at different temperatures. Inserts represent the spectrum region around $g=2$.

Fe_hs and Cu peaks showed a Curie-Weiss behavior, while Ft seems to have contributions from different magnetic species, exhibiting a superparamagnetic and antiferromagnetic behavior, in accordance to previous findings [1-4], with a phase transition occurring near 100 K (Figure 2).

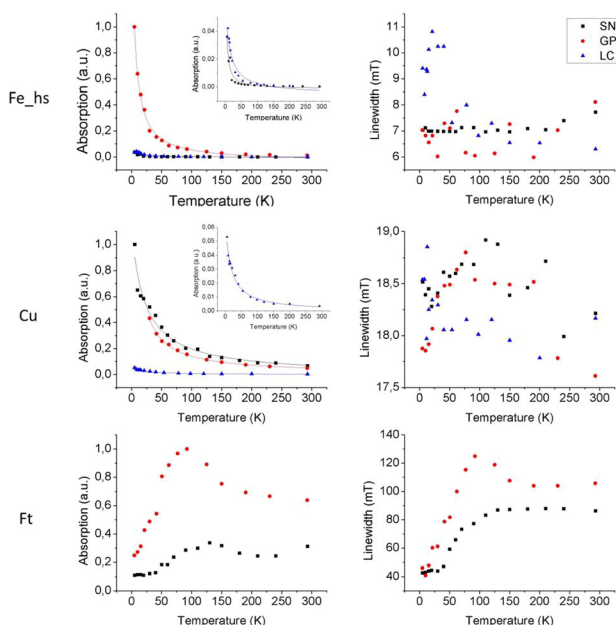


Figure 2 - Second integral and linewidth as a function of temperature for each peak (Fe_hs, Cu, Ft) and sample (SN, GP, LC).

By other hand, additional peaks around 190mT at T < 70K and 260mT at T > 70K in LC sample made it difficult to obtain a good fitting of Ft peak (Figure 3-a). These peaks are not the same as the one found in GP and SN for Ft (Figure 3-b), suggesting that it could be related to iron or another paramagnetic ion in another chemical state [1].

Our preliminary result suggests another paramagnetic site in the LC, not observed on SN and GP. Additionally, Ft peaks showed a temperature behavior with multiple contributions indicating the existence of different iron compounds [3].

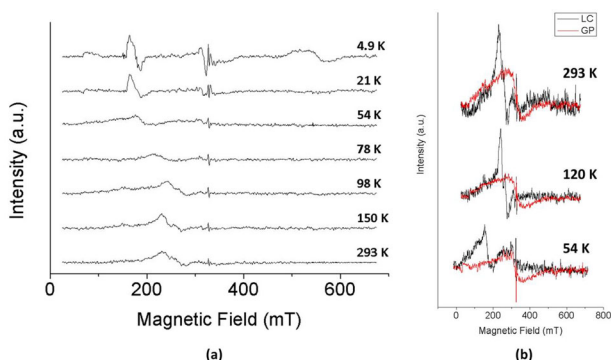


Figure 3 - (a) LC sample after subtraction of Fe_hs and Cu peaks at different temperatures. (b) LC and GP spectra after Fe_hs and Cu subtraction at three temperatures.

- References:** [1] Aime S, et al. *Bioc et Biop Acta* (1361), 1997.
 [2] Weir M, et al. *Bioc et Biop Acta* (828), 1985.
 [3] Galvez N, et al. *JACS* (130), 2008.
 [4] Kumar P., et al. *Sci Rep*, 2016.

P01.47
Visualizing tree-ring structures of waterlogged wood using Super-Resolution Convolutional Neural Network

M. Mori¹, R. Kasai², K. Kobayashi³, S. Suzuki⁴, S. Kuhara³

¹Juntendo University, Department of Radiological Technology, Faculty of Health Science, Tokyo, Japan, ²Kyorin University, Graduate School of Health Sciences, Tokyo, Japan, ³Kyorin University, Department of Medical Radiological Technology, Faculty of Health Sciences, Tokyo, Japan, ⁴Tokyo Metropolitan Archaeological Center, Tokyo, Japan

Introduction: Recently, nondestructive imaging by CT and MRI has contributed to the progress of dendroarchaeology. MRI is particularly suitable for waterlogged wood owing to its high spatial resolution imaging at 50 μm [1]. However, obtaining high-resolution images requires a long acquisition time that must be reduced.

Super-resolution convolutional neural network (SRCNN) is a technology that can generate high-resolution images from unknown low-resolution input images after training with low-resolution input and high-resolution teacher images [2]. Data acquisition for a low-resolution image requires less data acquisition time than that for a high-resolution image. Therefore, if a high-resolution image can be obtained from a low-resolution image, the acquisition time can be reduced.

In this study, we performed high-resolution MRI using SRCNN on waterlogged wood and investigated whether the acquisition time could be reduced.

Subjects/Methods: First, high-resolution images (matrix size: 768 × 768, res: 50 μm, acquisition time: 2 h 20 m) of simulated excavated wooden artifacts were acquired as teacher images using uHR-T2WI [1].

Next, low-resolution images (matrix size: 384 × 384, res: 100 μm) were created based on these images. The low-resolution and high-resolution teacher images were then used to train the SRCNN. As reference images, linearly interpolated (LI) images were created from the low-resolution input images with the same matrix size as the original high-resolution images.

We compared the results of the SRCNN trained only with natural images and that trained by adding high-resolution MR images of tree rings (sample number: 11) to the natural images. Furthermore, PSNR was calculated for all the images and the results of the LI and SRCNN images were compared.

Results/Discussion:

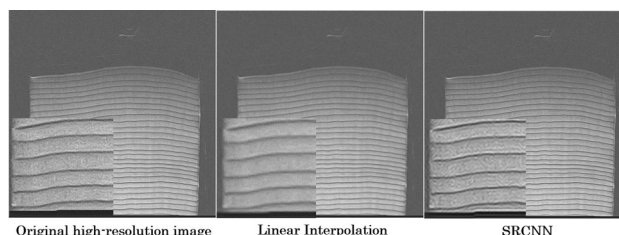


Fig.1. Comparisons between Linear Interpolation and SRCNN.

For the SRCNN trained with only natural images, the PSNR was 26.3 dB and 28.4 dB for LI and SRCNN images respectively. When high-resolution tree-ring MR images were added and used for training, the PSNR improved from 28.4 dB to 29.2 dB for SRCNN images (Fig.1).

The improvement of PSNR when training with added high-resolution tree-ring MR images is considered to be the result of using training images similar to the object tree-ring images. Regarding this point, further study should be needed with more data.

This study shows that SRCNN can reconstruct high-resolution tree-ring images from low resolution input images. Therefore, SRCNN can be used to reduce the data acquisition volume and shorten the data acquisition time.

References: [1] Mika Mori. et al.,2019, Dendrochronologia 57, 125630

[2] Chao Dong. et al., 2015, IEEE TPAMI 32, 295–307

Clinical Review Posters

P02.01

ASL perfusion MRI in the follow-up of pediatric brain tumors

S. Verschuren¹, J. Petr², H. J. Mutsaerts³, S. Plasschaert⁴, J. Wijnen¹, M. Lequin¹, E. Wiegens¹

¹University Medical Center Utrecht, Radiology, Utrecht, The Netherlands, ²Helmholtz-Zentrum Dresden-Rossendorf, Institute for Radiopharmaceutical Cancer Research, Dresden, Germany, ³Amsterdam Neuroscience, Amsterdam University Medical Center, Location VUmc, Radiology and Nuclear Medicine, Amsterdam, The Netherlands, ⁴Princess Máxima Center for Pediatric Oncology, Utrecht, The Netherlands

Introduction: Arterial spin labeling (ASL) perfusion MRI has already been successfully applied for pediatric brain tumor classification, tumor grading and lesion differentiation [1-3]. ASL is, due to its non-invasiveness, an appealing option to image perfusion in the pediatric population. However, its value during follow-up of children with brain tumors, e.g., detecting recurrent lesions, cerebral metastases or radiation necrosis, is largely unknown. Here we show five clinical cases which illustrate the clinical value of ASL MRI in the follow-up of pediatric brain tumors.

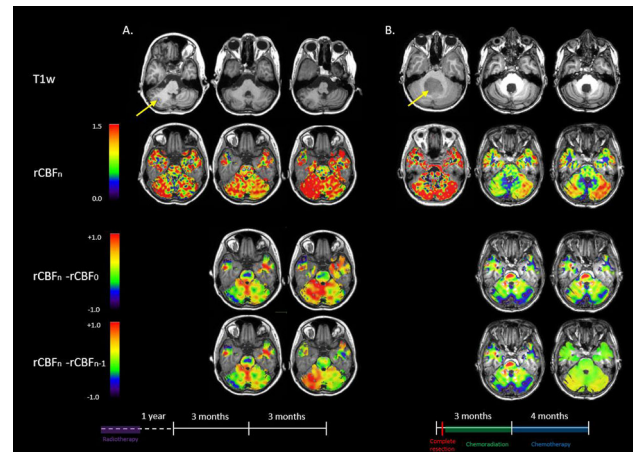
Subjects/Methods: We included the ASL MRI data of five clinical pediatric cases: a recurrent medulloblastoma, a medulloblastoma in complete remission, a pineoblastoma with leptomeningeal metastases, a diffuse intrinsic pontine glioma (DIPG) and a pleomorphic xanthoastrocytoma (PXA).

2D EPI pCASL MRI data were acquired during routine clinical scanning at 1.5T and 3.0T (Philips Healthcare). The initial post-labeling delay was set to 1800 and 1525 ms for 1.5T and 3.0T respectively, while the labeling duration was set to 1800 ms. Additionally, background suppression was used.

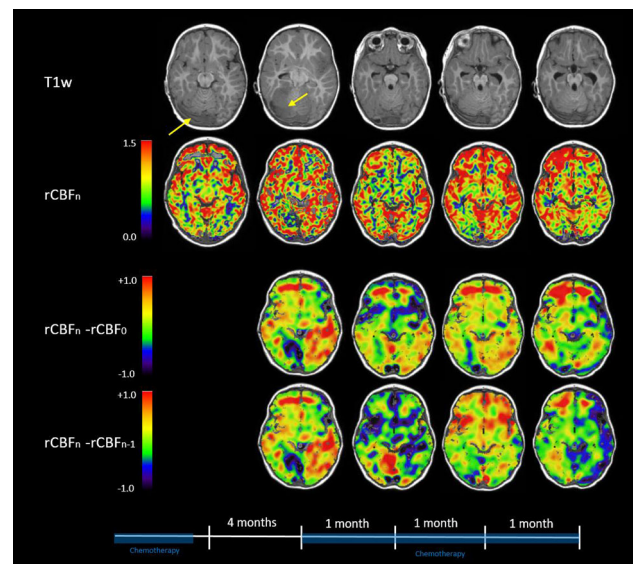
ASL data were processed using the ExploreASL toolbox [4], adjusted for usage on the pediatric population. Whole brain cerebral blood flow (CBF) was quantified per scan session and normalized to the healthy-appearing gray matter CBF ($rCBF_n$). Gaussian smoothing with a standard deviation of 2.5 voxels was then applied, after which image subtraction was performed between successive co-registered ASL follow-up scans ($rCBF_n - rCBF_{n-1}$). Furthermore, $rCBF$ was compared per timepoint to the first available ASL MRI scan ($rCBF_0$).

Results/Discussion: Figure 1, 2 and 3 show the $rCBF$ data of the 5 clinical cases, demonstrating the potential of ASL to provide valuable information in the follow-up of pediatric brain tumors. $rCBF$ maps, especially when evaluated over time, may aid to discriminate between recurrent and remissive medulloblastoma (fig 1), may be of added value in the follow-up of metastasis (fig 2) and may indicate therapy response by a decrease in tumor $rCBF$ over time (fig 3).

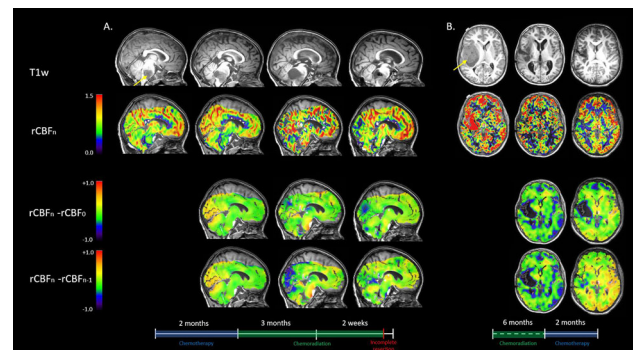
In summary, ASL may provide complementary information to standard clinical MRI protocols, especially regarding the differentiation between active tumor and tumor-like lesions. These findings encourage future longitudinal studies to evaluate the added value of ASL perfusion MRI in a cohort of pediatric brain tumor patients during follow-up.



A: Boy (13y) with a medulloblastoma. The tumor has progressed over time, which is accompanied by an increase in $rCBF$ in the tumor region. B: Girl (12y) with a medulloblastoma, no recurrence after therapy and $rCBF$ is stable over time



$rCBF$ of a girl (2y) with a pineoblastoma and leptomeningeal metastases. In sessions 2 and 4, left-occipital metastasis progression is accompanied with an increase of local $rCBF$. A partly necrotic lesion in session 2 yields local $rCBF$ decrease.



A: Girl (3y) with a DIPG. After initial tumor progression, the tumor remained stable resulting in a stable $rCBF$ pattern over time. B: Boy (15y) with a PXA. Tumor $rCBF$ decreases over time, in accordance with good therapy response.

References: [1] Dangouloff-Ros et al., Radiology 2016 281:553–566
[2] Yeom et al., AJNR Am J Neuroradiol.2014 Feb;35(2):395-401.

- [3] Keil et al., *Pediatr Radiol.* 2019 Feb;49(2):245-253.
 [4] Mutsaerts., et al. *Neuroimage.* 2020;117031

P02.02

CEST: challenges and opportunities in clinical neurology

S. Derks¹, E. Warnert², Y. Wu², L. Knutsson³, X. Golay⁴, M. Van den Bent⁵, A. Van der Veldt⁶, M. Smits²

¹Erasmus Medical Center, Oncology, Radiology and Nuclear Medicine, Neuro-oncology, Rotterdam, The Netherlands, ²Erasmus Medical Center, Radiology and Nuclear Medicine, Rotterdam, The Netherlands, ³Lund University, Department of Radiation Physics, Lund, Sweden, ⁴University College London, Institute of Neurology, London, UK, ⁵Erasmus Medical Center, Neuro-oncology, Rotterdam, The Netherlands, ⁶Erasmus Medical Center, Oncology, Radiology and Nuclear Medicine, Rotterdam, The Netherlands

Introduction: Objectives

- Understanding CEST and its challenges for clinical translation
- Presenting neurological applications of CEST
- Introducing CEST into clinical workflow

Introduction

Some neurological diseases are still poorly understood, for which advanced imaging modalities are warranted. Chemical exchange saturation transfer (CEST) MRI allows the detection of small, physiological (millimolar) concentrations of molecules containing exchangeable protons. Clinical implementation poses several challenges, e.g. reduced signal-to-noise ratio and accurate detection of fast exchanging protons due to coalescence of the exchangeable proton peaks with the water peak. In addition, reduced RF duty cycle on clinical scanners leads to the need for shorter saturation times, also hampering CEST effect.(1, 2) However, aspiring to overcome these challenges is rewarding, because CEST shows promise in clinical practice, especially in brain diseases.

Subjects/Methods: Clinical applications in neurology

Brain tumors – Due to elevated protein concentrations and altered glucose metabolism in tumor, respectively amide-weighted CEST (or APT CEST) and glucoCEST can be useful in brain tumor detection, grading, assessment of tumor recurrence vs. treatment effect, and identification of tumor genetic markers. In the future, CEST may be guiding local brain therapies.(2)

Stroke – Decreased cerebral blood flow creates anaerobic metabolism, causing a pH drop. Decreased pH is a first marker of ischemia, occurring even before apparent diffusion coefficient or perfusion MRI abnormalities show.(3) CEST is sensitive to pH alterations, which can be used to discriminate between brain tissue at risk (penumbra) and areas with oligemia (core), relevant in acute stroke therapies.(1, 2)

Other – CEST can detect altered signals in brain of multiple sclerosis, Parkinson's disease, Alzheimer's disease and traumatic brain injury patients.(1, 2)

Results/Discussion: CEST shows promising in vitro and early clinical results, indicating its potential added value in neurological practice. In this exhibit, we will share our early experience of CEST in brain tumor patients, in whom imaging still faces many challenges for detection and follow-up of tumors and treatment effects. CEST could provide complementary information on tumor proteasome and/

or metabolism. We aim to explore this through assessing glucoCEST, setting up a series of phantom, volunteer and patient studies.

- References:** 1. Jones et al. PMID 28792646
 2. Zhou et al. PMID 30663162
 3. Leigh et al. PMID 28345479

P02.03

Characterization of superior longitudinal fasciculus by diffusion tensor imaging

M. M. Ribeiro¹, B. E. Alves², C. R. Madeira³

¹Polytechnic Institute of Lisbon - School of Health Technology, Medical Imaging - H&TRC (Health and Technology Research Centre), Lisbon, Portugal, ²SAMS - Medical Assurance of Banker's Hospital, Medical Imaging, Lisbon, Portugal, ³3DXi - Medical Imaging Center and Faculty of Dental Medicine of Lisbon, Medical Imaging, Lisbon, Portugal

Introduction: The diffusion tensor¹ is used in Magnetic Resonance Imaging (MRI) to characterize the architecture of the neuronal tissue. The tractography^{2,3} provides the path of the neural fibers of the white matter. This study aimed to evaluate the integrity of the superior longitudinal fasciculus (SLF) in the left hemisphere, since it is directly correlated with language's disorders. In this study, we compared the clinical cases with and without pathology to well highlight the differences founded in SLF fibers using the same acquisition protocol.

Subjects/Methods:

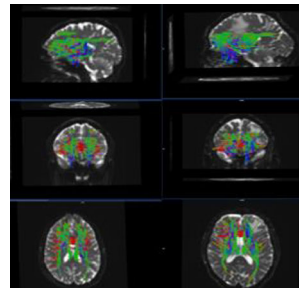


Figure1-MPR mode of fibers. Images of sag., coronal and axial projections (top to bottom, respectively), using Angle Threshold of 30°, FA Threshold=0.2 and length of 25-400mm, in one case without pathology(left) and the case with pathology(right).

A 3 Tesla, MAGNETOM Skyra (Siemens Healthineers, Erlangen, Germany) with Gradient of 45mT/m and Slewrate of 200T/m/s, it was used.

Using SyngoVia(VB20A version, February 2017), the analysis was performed based on diffusion-weighted sequence through 3 phases, varying the post-processing parameters. Different images of fiber tract of SLF were obtained changing the Fractional Anisotropy Threshold(FAT), the Angle Threshold(AT) and the Tract Length(TL). Firstly, the minimum TL was tested followed by the FAT and it was proved an increase in the fiber lateralization. After that, the AT(20°,30°,45°) was varied, and revealed that when the angle increases, the signal intensity increases too. In the pathological cases were visualize a loss of fibers transmission (left-right direction), in the images of high density, in any of applied values.(Fig.1) <https://por->

tal.smart-abstract.com/esmrm2020/submission/abstractimages/17984/3194/get.html

Results/Discussion: Concluding, there are changes in the fiber tracts representation by changing the selected parameters. It was demonstrated that an increasing in the FAT values provides more definition and sharpness in the images, since a higher AT growth the number of fibers displayed. FAT is the parameter that most influences the fibers distribution, having a pronounced impact on the amount and density of the tracts. knowing the higher number of softwares and techniques to process the data of DTI we recommend a standardization and guidelines production, to allow comparisons between studies and may to reveal the real disease. Otherwise, these procedures including a lot of manipulation of parameters, decreases reliability and have a weak contribution in clinical decisions.

References: 1. Kollias S. Parcelation of the White Matter Using DTI: Insights into the Functional Connectivity of the Brain. *Neuroradiol J* [Internet]. 2009 Sep [cited 2019 Jan 14];22(1_suppl):74–84. 2. Richter M, et.al. Evaluation of Diffusion-Tensor Imaging-Based Global Search and Tractography for Tumor Surgery Close to the Language System. Draganski B, editor. *PLoS One* [Internet]. 2013 Jan 7 [cited 2019 Jan 14];8(1):e50132. Available from: <https://www.ncbi.nlm.nih.gov/pubmed/23308093> 3. Kamali A, et al. Tracing Superior Longitudinal Fasciculus Connectivity in the Human Brain using High Resolution Diffusion Tensor Tractography.

P02.04

Magnetic resonance imaging to determine the reactions of Cerebro-Spinal Fluid Volume to different methods of dehydration

A. Spicer, E. Marcham, J. Freeman, M. Newton, R. Morris

Nottingham Trent University, Physics, Clifton, UK

Introduction: In both contact sports and a night on the town, traumatic brain injuries are commonly seen from relatively minor impacts and can have serious repercussions. Due to its shock absorbing properties it has been postulated that Cerebro-Spinal Fluid (CSF) volume correlates to negative outcomes after head impact¹. There is little agreement in the literature regarding the effect of dehydration on CSF volume^{2–4}. This study not only looks at the effect of dehydration on CSF volume, but also at the effect of the mechanism for dehydration.

Subjects/Methods: Thirteen participants were scanned using both a TrueFISP and TSE sequence at 1.5T (Avanto, Siemens). Participants underwent 4 separate scanning sessions: one before and one after a training session of their choice and the other time such that they occurred before and after an evening where the participants would be consuming alcohol. At each session a participant's mass was obtained using 3 separate scales (Exzact EX9360 digital scales, ActiveERA BS01 digital bathroom scales, Salter Ultimate Accuracy Electronic Bathroom Scale) to later be used as a measure of dehydration. Volumetric measurements of the CSF were determined using a custom produced MATLAB (Mathworks, 2018b) script which thresholded the images such that only signal from CSF (within the skull, spinal canal CSF is excluded) and eyes remained. The number of pixels was summed and converted to approximate volume using the voxel dimensions.

Results/Discussion:

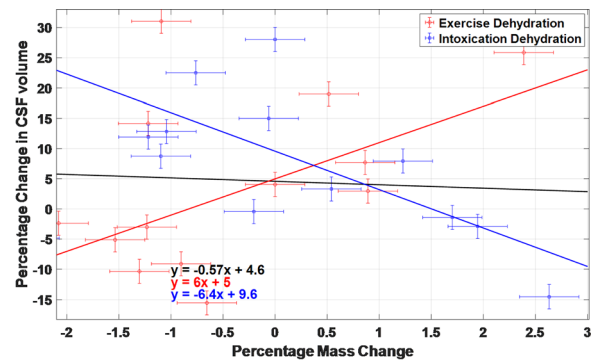


Fig. 1 Percentage change in mass against percentage loss of CSF.

It can be seen in figure 1 that the method of dehydration has significant impact on the correlation between dehydration and CSF volume. With the results from exercise showing a loss of CSF volume as the participants dehydrate, whilst intoxicated participants gained CSF as they dehydrated. It is postulated that during exercise the body is losing water much faster than it is replenished and so the rate of CSF production is decreased too much and so the total volume starts to decrease. However, as a person becomes intoxicated, although they are becoming dehydrated, they are still consuming fluids and so there may be a panic response in the brain that causes it to increase production to protect the person from injury.

References: 1. Cerebrospinal Fluid (CSF). National Multiple Sclerosis Society. 2017 [https://www.nationalmssociety.org/Symptoms-Diagnosis/Diagnosing-Tools/Cerebrospinal-Fluid-\(CSF\)](https://www.nationalmssociety.org/Symptoms-Diagnosis/Diagnosing-Tools/Cerebrospinal-Fluid-(CSF)). Accessed November 1, 2018. 2. Dickson, J.M. et al. *Int J Sports Med*. 2005 Jul-Aug;26(6):481-5. 3. Curran-Sill, G. *Sports Med Open*. 2018 Jan 12;4(1):6. doi: 10.1186/s40798-018-0119-2. 4. Kempton, M.J. et al. *Hum Brain Mapp*. 2009 Jan;30(1):291-8.

P02.05

Microbleeds show a characteristic distribution in cerebral fat embolism

B. Balogh¹, O. Giyab², P. Bogner², G. Orsi³, A. Tóth²

¹University of Pécs, Department of Medical Imaging, Pécs, Hungary, ²University of Pécs, Pécs, Hungary, ³HAS-PTE Clinical Neuroscience MR Research Group, Pécs, Hungary

Introduction: Cerebral fat embolism is part of fat embolism syndrome (FES), which is caused by intravascular clogging of fat globules. FES often occurs after long bone fractures, orthopedic surgeries, or following liposuction, or in conditions like sickle cell anemia. (1)

Subjects/Methods: Our study was aimed to review the hypothesis that microbleeds detected by MRI are common and show a characteristic pattern in cerebral fat embolism (CFE). Based on a systematic literature search up to 31. 01. 2020, 84 papers presenting MR imaging in 140 CFE patients were eligible for this review. An additional case was added from our hospital records. Patient data were individually scrutinized to extract

epidemiological, clinical and imaging variables. Characteristic CFE microbleed pattern resembling a “walnut kernel” (WK) was defined as punctuate hypointensities of monotonous size diffusely located in the subcortical white matter, the internal capsule and the corpus callosum, with mostly spared corona radiata and non-subcortical centrum semiovale, detected by susceptibility- or T2* weighted imaging. The rate of the presence of this pattern and other, previously described MRI markers of CFE, such as the starfield pattern (SF) and further diffusion abnormalities, were recorded and statistically compared.

Results/Discussion: The rate of the presence of microbleeds of any pattern, the WK, diffusion abnormality of any pattern and the SF was found in 98.1%, 89.74%, 87.94% and 68.5% of cases, respectively. The rate of the presence WK was significantly ($p < 0.05$) different from that of the SF. Since the clinical diagnosis of CFE is often difficult to establish, imaging could provide significant help. We hypothesized that the increasingly described microbleeds and their particular distribution, the WK, comprising of diffuse uniform punctiform microbleeds located in the subcortical region, the corpus callosum, and in the internal capsule, may be an important marker for CFE. Reviewing the literature and our database, it can be concluded that the WK appears to be indeed very common in CFE, observed in 89.74% of the cases. Recognizing this specific pattern could be of utmost importance, as microbleeds in other distributions can be associated with other, possibly coinciding pathologies such as diffuse axonal injury (DAI) or sepsis, but they are also common in cardiovascular diseases. Microbleeds are very common and mostly occur in a characteristic pattern resembling a “walnut kernel” as reported in the CFE MRI literature. Microbleeds of this pattern in SWI or T2* MRI, along with the starfield pattern in diffusion imaging, appear to be the most important imaging markers of CFE, and may aid the differential diagnosis in clinically equivocal cases.

References: 1 Parizel PM, Demey HE, Veeckmans G, et al (2001) Early diagnosis of cerebral fat embolism syndrome by diffusion-weighted MRI (starfield pattern). *Stroke* 32:2942–4

P02.06

PET/MRI hybrid imaging in the management of CNS tumors: educational exhibit of the usability and advantages shown by a clinical series of diffuse midline glioma (DMG) patients treated with [⁸⁹Zr]Zr-bevacizumab

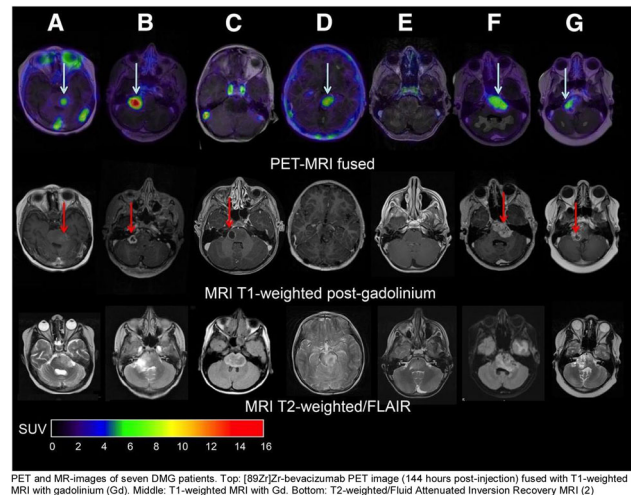
I. Pruis¹, M. Jansen², G. van Dongen³, G.-J. Kaspers², M. Smits¹, S. Veldhuijzen van Zanten¹

¹Erasmus MC, Radiology and Nuclear Medicine, Rotterdam, The Netherlands, ²Princess Máxima Center for Pediatric Oncology, Utrecht, The Netherlands, ³VU University Medical Center, Radiology and Nuclear Medicine, Amsterdam, The Netherlands

Introduction: PET/MRI combines exquisite structural characterization with non-invasive quantification of target expression and target binding, which can be used to study the potential of drugs to reach (parts of) a tumor, or to determine organs potentially at risk for toxicity (1). To this end, PET/MRI can be used for the selection of the most effective drugs and their most optimal dosage and administration route, and for the selection of patients most likely to benefit from treatment. In this educational exhibit of the first drug imaging study in pediatric brain tumor patients we illustrate the potential of PET/MRI for optimizing the management of tumors located in the brain and nervous system (2).

Subjects/Methods: Seven DMG patients (aged 6-17) received [⁸⁹Zr]Zr-labeled bevacizumab at 0.1 mg/kg; 0.9 MBq/kg. Biodistribution analyses, quantified by standardized uptake values (SUVs), showed both inter-

and intratumoral heterogeneity of [⁸⁹Zr]Zr-bevacizumab uptake in 5/7 patients (white arrows). In 4/5 patients (A/B/F/G) uptake corresponded with Gadolinium (Gd)-enhancement on MRI, i.e., sites of blood-brain barrier disruption (red arrows). In 2/7 patients (C/E) bevacizumab did not reach the tumor, despite signs of blood-brain barrier disruption. Highest organ uptake (i.e., risk of toxicity) was seen in liver.



PET and MR-images of seven DMG patients. Top: [⁸⁹Zr]Zr-bevacizumab PET image (144 hours post-injection) fused with T1-weighted MRI with gadolinium (Gd). Middle: T1-weighted MRI with Gd. Bottom: T2-weighted/Fluid Attenuated Inversion Recovery MRI (2)

Results/Discussion: The ability of PET/MRI to study drug-tumor targeting (i.e., treatment efficacy) and toxicity *in vivo* holds great promise for improving personalized patient care, and is also attractive for pharma companies as it will increase the success rates in drug development, shorten the time to market, reduce the number of patients needed in clinical trials, and therefore will reduce health-care system costs. PET/MRI studies also enable exploration of the potentially beneficial effect of targeted drugs labeled with radionuclides, to additionally induce localized radiation therapy.

References: 1. Pruis IJ, van Dongen GAMS, Veldhuijzen van Zanten SEM. Added value of Diagnostic and Theranostic PET Imaging for the Treatment of CNS Tumors. *Int. J. Mol. Sci.* 2020;21(3):1029. 2. Veldhuijzen van Zanten SEM, Jansen MHA, van Vuurden DG, Huisman MC, Vugts DJ, Hoekstra OS, van Dongen GAMS, Kaspers GJL. Molecular drug imaging: ⁸⁹Zr-bevacizumab PET in children with diffuse intrinsic pontine glioma. *J. Nucl. Med.* 2017;58(5):711–6.

P02.07

Visualization of Nigrosome 1 at 3T MRI and ¹⁸F-DOPA PET for the diagnosis of Parkinson’s disease

A. Martín-Bastida^{1, 2}, V. Suárez-Vega³, P. Domínguez-Echavarrí³, F. Guillén-Valderrama⁴, I. Avilés-Olmos², J. Arbizu⁴, M. C. Rodríguez-Oroz²

¹Clinica Universidad de Navarra, Neurology, Madrid, Spain, ²Clinica Universidad de Navarra, Neurology, Pamplona-Madrid, Spain, ³Clinica Universidad de Navarra, Radiology, Pamplona-Madrid, Spain, ⁴Clinica Universidad de Navarra, Nuclear Medicine, Pamplona-Madrid, Spain

Introduction: Differential diagnosis of Parkinson’s disease (PD) is often challenging, with rate of approximately 30% of misdiagnosis especially at early stages. In the current study, we aimed to evaluate and compare whether visual analyses of nigrosome 1 (N1) imaging using susceptibility weighted imaging (SWI) 3T MRI in the substantia

nigra and striatal 6-18F-fluoro-L-dopa (^{18}F -FDOPA) are useful for the diagnosis of PD. The objective of the present work is to determine and compare the utility of Nigrosome 1 at 3T MRI and ^{18}F -DOPA PET for the diagnosis of Parkinson's disease.

Subjects/Methods: Twenty-eight patients with PD according to the UK Brain Bank Criteria and 31 patients with other non-PD diagnoses such as essential tremor underwent both 3T SWI MRI and ^{18}F -DOPA PET imaging techniques. Two independent raters evaluated both imaging techniques twice in one month. N1 signals in the SN and striatal ^{18}F -DOPA uptake were visually evaluated using a 4-point ordinal scale (normal, non-diagnostic, unilateral and bilateral diagnostic scans).

Results/Discussion: Absolute inter and intra-rater agreements for ^{18}F -DOPA PET and SWI-MRI were 93.44% ($\kappa=0.891$, $p<0.001$) and 54.11% ($\kappa=0.310$, $p<0.001$) respectively. 29/31 non-PD and 26/28 PD subjects were correctly diagnosed with ^{18}F -DOPA PET. In addition 18/31 non-PD and 13/28 were correctly diagnosed with SWI-MRI with additional 9 subjects (5 PD and 4 non-PD) scored as non-diagnostic. The diagnostic sensitivity/specificity was 92.9% and 93.5% for ^{18}F -DOPA PET and 53.6% and 58.1% for SWI-MRI respectively.

References: Not applicable

P02.08

Efficient diagnosis of prostate cancer using a robotic MRI-in bore targeted biopsies.

A. Parals, S. Sala, M. Planas, A. Pérez de Tudela, M. Rodrigo, J. Barceló, **J. C. Vilanova**

Ressonància Girona, Magnetic Resonance, Girona, Spain

Introduction: To show the innovative MRI-in bore robotic remote controlled manipulator to perform efficient target biopsies to detect prostate cancer.

Subjects/Methods: The robotic MRI compatible remote controlled device was performed on a 1.5T MRI (GE Healthcare) with an eight channel pelvic coil. Written informed consent was obtained from all patients. The procedure was performed without local anesthesia. Fast imaging employing steady-state acquisition (FIESTA) sequence was used for fast control imaging to align with the MR transrectal visible needle guide (tilted axial and oblique sagittal), and after the desired target was selected, the motion of the robot was remotely activated. T2-weighted and DWI with ADC images were also acquired to localize the lesion. The patient was then removed from the scanner bore. A biopsy sample with two cores were taken with a standard compatible biopsy gun.

Results/Discussion: Thirty patients with a single cancer suspicious lesion interpreted on MRI using PI-RADSv2.1 category ≥ 3 underwent the robotic MRI biopsy procedure. The overall cancer detection rate (CDR) for any cancer was 73% (22/30). It was 86% (19/22) for significant tumors (Gleason score of more than 3 or maximum cancer core length greater than 3 mm) and 77% (17/22) for tumors with Gleason > 6 . CDR for cancer for biopsy-naïve patients was 89% (16/18) and 50% (6/12) for patients with prior negative transrectal ultrasound-guided biopsies. The CDR for PI-RADS > 3 was 92% (22/24). All the lesions ($n = 30$) were reachable with the robotic MRI device. A self-limited rectal hemorrhagic complication was reported.

A robotic MRI-guided transrectal biopsy is a useful, efficient, safe and feasible procedure in the new paradigm to diagnose significant prostate cancer

References: Matthias Barral, Arnaud Lefevre, Philippe Camparo, Martijn Hoogenboom, Thibaut Pierre, Philippe Soyer, François Cornud. In-Bore Transrectal MRI-Guided Biopsy With Robotic Assistance in the Diagnosis of Prostate Cancer: An Analysis of 57 Patients. *AJR*:213, October 2019 9

Nicolas Linder, Alexander Schaudinn, Tim-Ole Petersen, Nikolaos Bailis, Patrick Stumpp, Lars-Christian Horn, Jens-Uwe Stolzenburg, Thomas Kahn, Michael Moche, Harald Busse. *Magnetic Resonance Materials in Physics, Biology and Medicine* (2019) 32:599–605

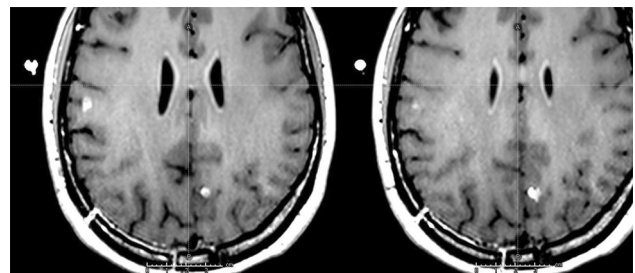
P02.09

External markers reproduction artifact in SPACE parallel imaging sequences

F. Crop¹, R. Mouttet-Audouard², X. Mirabel², T. Lacomberie¹

¹Centre Oscar Lambret, Medical physics, Lille, France, ²Centre Oscar Lambret, Academic radiotherapy department, Lille, France

Introduction: MR imaging is becoming standard for radiotherapy (RT) treatments. In order to improve image fusion and tumor contouring, patients are positioned using radiotherapy immobilization devices and markers are applied for MR-only treatment planning. MR for RT comes with several caveats concerning the sequences: distortions, respiration phases... Here we present a specific artifact occurring with the combination of parallel imaging and external markers. The markers are sometimes multiplied inside the patient volume, which can be interpreted as a metastasis (Figure 1)). In the case of 3D SPACE CAIPIRINHA with acceleration in phase and slice direction, the artifact can be more difficult to interpret as it does not appear in the same slice or rectilinear direction.

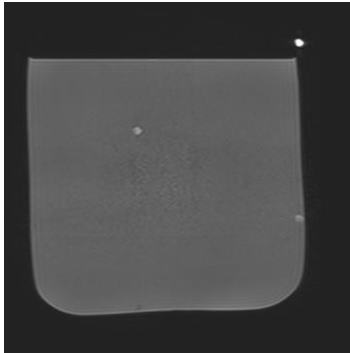


There are both an artifact and a metastasis in the image. Native 3D SPACE sagittal acquisition. The artifact is created on another axial/sagittal slice.

Subjects/Methods: MR imaging was performed on a 1.5T Sola (Siemens). Intracranial and Head & Neck imaging was performed in treatment position using a thermoplastic mask and the Omniboard positioning system. Antennas used were Body12 + Body 6 posterior. The 3D SPACE sequence (Mugler, 2014) uses a GRAPPA/CAIPIRINHA acceleration and is preferred as it has a better CNR for metastasis and gliomas (Danieli et al., 2019) than MPRAGE and has less distortions for radiotherapy planning.

Artifact reconstruction errors were tested on a low intensity silicone oil phantom, representing typical brain signal intensity.

Results/Discussion: The controlled aliasing fails with high intensity signals outside the patient. The aliased high signal intensity is during reconstruction interpreted as belonging inside the brain. Sometimes the inverse happens: the signal of the brain is interpreted as part of the marker and a hyposignal is left inside the brain. As the external markers are not perfect spheres, the erroneous reconstruction could be interpreted as a metastasis and subsequently treated.



External marker multiplication. One can also see part of a hyposignal at the bottom of the phantom. Axial slice represented in order to show the artifact, native sagittal SPACE acquisition CAIPIRINHA 2/2.

The artefact is more probable with the proximity of the markers to the antennas. Using only GRAPPA acceleration in phase encoding reduces the artifact and simplifies the interpretation, but does not eliminate it. When performing the SPACE CAIPIRINHA sequence in native axial direction (3D phase in head-feet direction), the controlled aliasing of this artifact arrives more likely in “dead space” and is thus not incorrectly reconstructed or even seen. We aim to verify this issue with the Compressed Sensing SPACE.

Finally, users should be warned that any high intensity signal at the skin could be susceptible for this erroneous reproduction and it is more difficult to interpret in CAIPIRINHA accelerated sequences. In the case of melanoma metastasis, the pre-contrast image will not show a difference either.

References: Danieli et al *American Journal of Neuroradiology*, 40(7), 1140–1148.

Mugler et al *Journal of Magnetic Resonance Imaging*, 39(4), 745–767.

P02.10

Is there a future for novel MR magnet in collagen imaging techniques in assessing the anterior cruciate ligament?

D. Khodatars¹, K. Chappell², C. Gupte³, M. Ristic³, D. Amiras¹

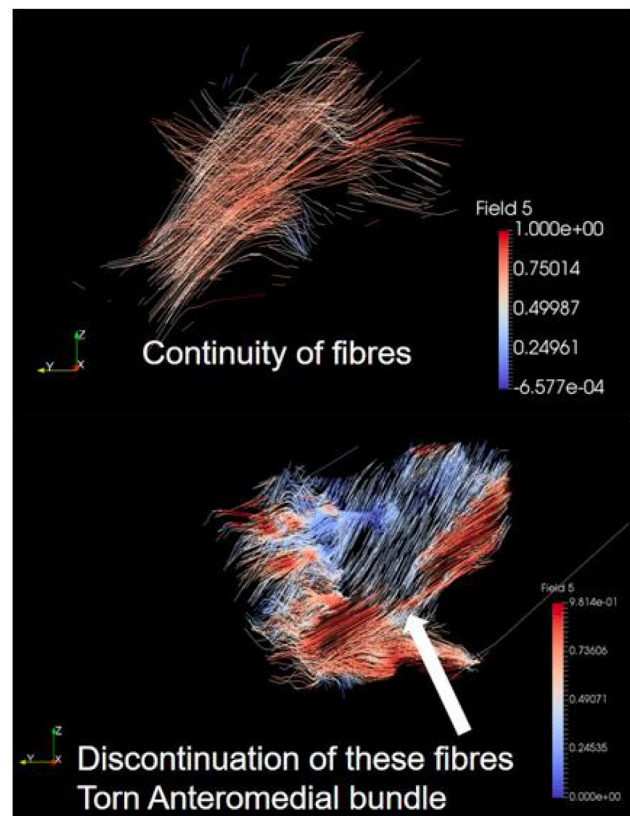
¹Imperial College Healthcare NHS Trust, Radiology, London, UK,

²Imperial College London, Honorary Research Associate- department of Orthopaedic surgery, London, UK, ³Imperial College London, London, UK

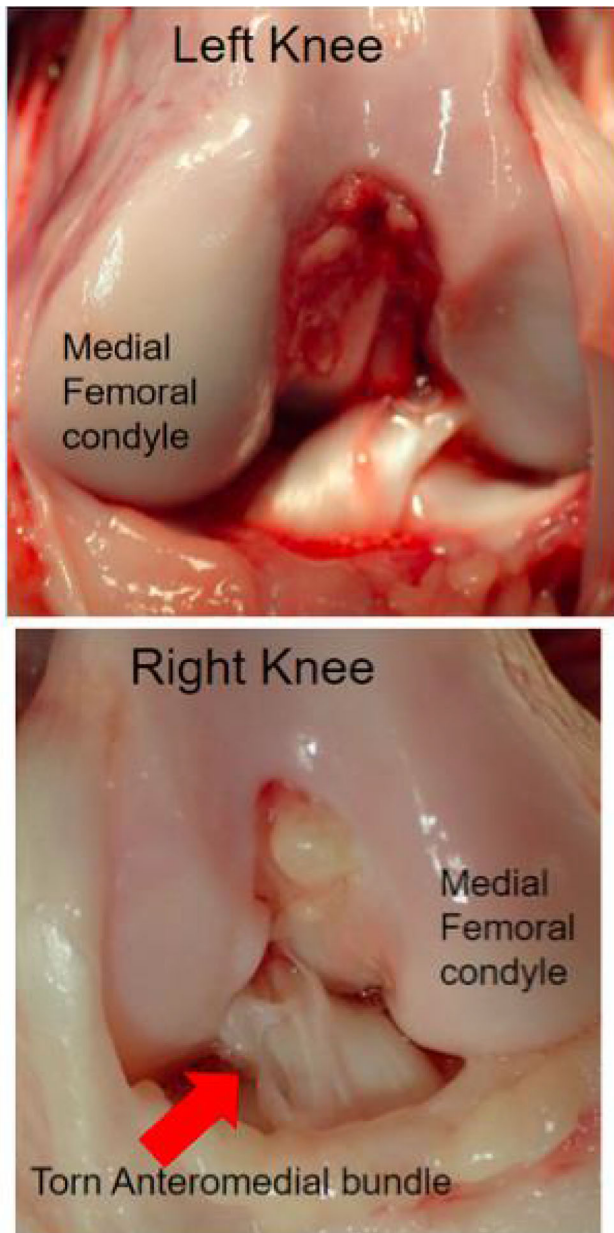
Introduction: The anterior cruciate ligament (ACL) is an important knee structure that stabilises the knee joint by resisting anterior tibial translational and rotational forces. Its ultra-structural organisation of densely packed collagen in healthy individuals is considered the prin-

ciple property that allows it to withstand multiaxial stresses and varying tensile strengths (properties crucial to high performing athletes). In vitro studies have demonstrated that in the ageing population and following high-grade injuries, the ACL collagen density and alignment is altered morphologically. Whilst current conventional MR imaging techniques have a high sensitivity and specificity for diagnosing acute ACL injuries, they have a limited role in assessing chronic ACL injuries.

Subjects/Methods: Potential MRI methods to determine tissue microstructure based on anisotropies include diffusion and susceptibility tensor imaging (DTI and STI), dipolar anisotropy fibre imaging, (DAFI) and magic angle directional imaging (MADI). Whilst research into DTI and STI have shown these techniques can map collagen 3D structures and quantify anisotropy artefact, one of the limitations has been low spatial resolution and signal to noise ratio. Improving this by harnessing the magic angle effect, as employed by the MADI technique, can deduce the microstructure with a high spatial resolution and signal to noise ratio (1,2). Thus far MADI has been researched on cadavers in a fixed magnet field (B₀) by rotating the limb to various angles to B₀. A novel reorientable magnet that allows a fixed patient position combined with a moving B₀ creating magic angle effects at different angles would be required for clinical use. Our work has shown these modified MRI machines are potentially cost effective, easy to install, operate and would complement conventional whole body MRI.

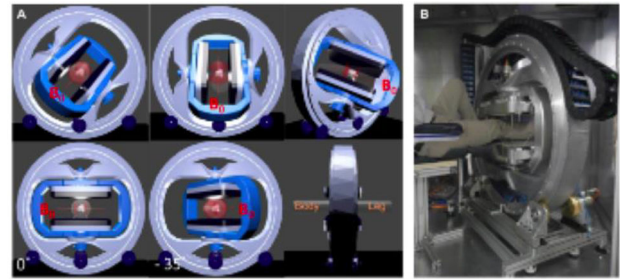


ParaView streamline visualisation of ACL.



Dissection photographs of ACL

Results/Discussion: A novel MR rotating magnet combined with the MADI technique provide a new and potentially better way to characterise ACL injuries when compared to the current imaging techniques. This will especially be useful in the context of patients suffering from knee joint instability following chronic ACL injuries where current conventional MR imaging is of limited use. Additionally there may be a vital role for novel collagen imaging techniques in guiding injury management in sport medicine.



Novel scanner

- References:** 1. Wei H, Gibbs E, Zhao P, Wang N, Cofer GP, Zhang Y, Johnson GA, Liu C. Susceptibility Tensor Imaging and Tractography of Collagen Fibrils in the Articular Cartilage. *Magnetic Resonance in Medicine*. 2017; 78:1683-1690.
2. Chu CR, Williams AA, West RV, Qian Y, Fu FH, Do BH, Bruno S. Quantitative Magnetic Resonance Imaging UTE-T2 Mapping of Cartilage and Meniscus Healing After Anatomic Anterior Cruciate Ligament Reconstruction. *The American Journal of Sports Medicine*. 2014; 42:1847-1856.

P02.11

Myocardial perfusion associates with extracellular volume, but not with rotating frame relaxation times or steady state

S. a. Mirmojarabian¹, E. Liukkonen¹, M. J. Nissi², L. Ahvenjärvi¹, J. Junttila¹, T. Liimatainen¹

¹University of Oulu, faculty of medicine, Oulu, Finland, ²University of Eastern Finland, Department of Applied Physics, Kuopio, Finland

Introduction: Longitudinal relaxation time in rotating frame ($T_{1\rho}$) and Relaxation along a Fictitious Field (RAFF) [1], including rotating frames with rank n (RAFF $_n$) [2] have been associated with increased extracellular volume (ECV) in infarcted myocardium [3]. Both $T_{1\rho}$, RAFF $_n$ relaxation time (T_{RAFFn}) and RAFF $_n$ steady state (SS_{RAFFn}) have been shown to assess myocardial infarct accurately [3, 4]. In the current work, we investigated the role of myocardial perfusion to explain differences between infarct and remote area T_{RAFFn} , SS_{RAFFn} , and ECV.

Subjects/Methods: Study participants ($n=8$) were recruited from a group of patients who have coronary artery disease and myocardial infarction. Gadoteridol was injected and 50 frames were acquired over a minute with shallow breathing and electrocardiograph gating to obtain image time series to calculate up-slope perfusion [5]. For RAFF $_2$ and RAFF $_3$, the pulse duration was set to 2.83 ms and the maximum pulse amplitudes (γB_1) were 500 Hz and 418 Hz, respectively, similarly as in [4]. Before calculating the relaxation times, all data was motion corrected either with standard Siemens protocols (T_1) or using Matlab (MathWorks Inc., MA, USA) (RAFF $_2$ and RAFF $_3$). Regions-of-interest were located on infarct scar and remote area based on high and low ECV values. Up-slope perfusion map was calculated as fraction of myocardial slope and slope from LV blood. Up-slope perfusion, ECV, relaxation times (T_{RAFF2} , T_{RAFF3}) and steady state (SS) fractions for RAFF $_2$ and RAFF $_3$ (SS_{RAFF2} and SS_{RAFF3} , respectively), were averaged over the regions-of-interests. A non-rigid registration was used to align up-slope perfusion to SS_{RAFF3} , T_{RAFF3} and ECV maps of the patient with largest infarction area. Spearman Correlation was used to evaluate association between up-slope perfusion and $SS_{RAFF2/3}$, $T_{RAFF2/3}$ and ECV maps.

Results/Discussion: Previous studies demonstrated significant difference between infarct and remote areas in $T_{RAFF2/4}$ [4] and steady state $SS_{RAFF2/3}$ [3]. In addition, strong correlation between $SS_{RAFF2/3}$ and ECV were observed [3]. In this study we found non-significant

association between the RAFFn parameters $T_{RAFF2/4}$, $SS_{RAFF2/4}$ and up-slope perfusion indicating other than perfusion as a source of RAFFn contrast between infarct and remote myocardium. Reasons behind the association differences between up-slope perfusion and ECV, and between up-slope perfusion and rotating frame relaxations is still unclear.

References: [1] T. Liimatainen, D.J. Sorce, R. Connell, M. Garwood, S. Michaeli, MRI Contrast from Relaxation along a Fictitious Field (RAFF). *Magn Reson Med*, 2010 64 983-994.

[2] T. Liimatainen, H. Hakkarainen, S. Mangia, J.M. Huttunen, C. Storino, D. Idiyatullin, D. Sorce, M. Garwood, S. Michaeli, MRI contrasts in high rank rotating frames. *Magn Reson Med*, 2015 73 254-262.

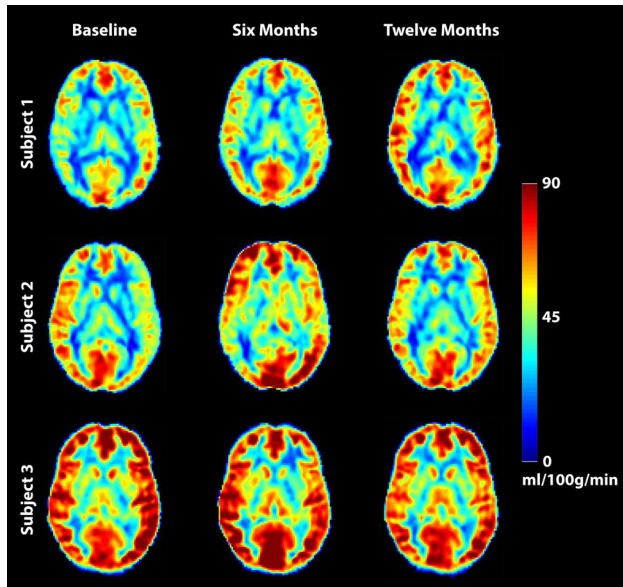


Figure 1: Estimated CBF maps of three example subjects at baseline, 6 months, and 12 months.

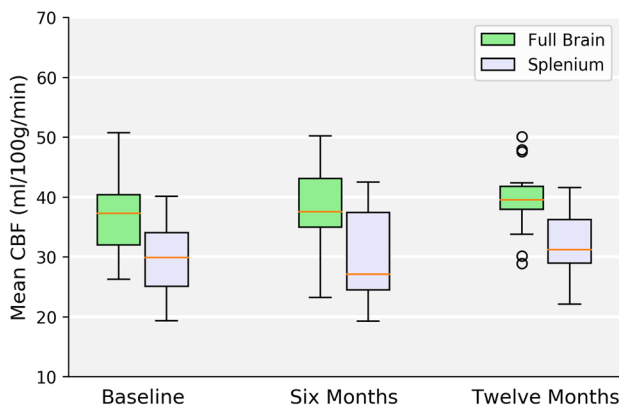


Figure 2: Mean perfusion of the full brain and splenium of all patients. No significant CBF differences were identified.

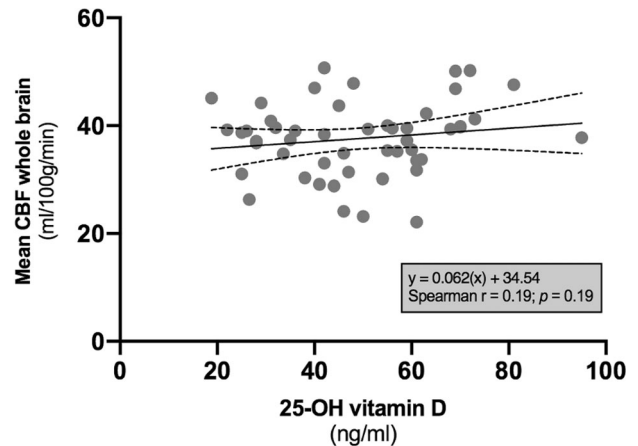


Figure 3: Correlation between CBF and vitamin D after 12 months. A weak correlation was found.

- References:** 1 Van Haren, et al, *Neurology*, vol. 2013
 2 Lauer, et al, *Brain J. Neurol.*, 2017
 3 Chappell, et al, *IEEE Trans. Signal Process*, 2009
 4 Jenkinson, et al, *NeuroImage*, 2002

Software Exhibits

SWE01.01

LAYNII: a software suite for layer-fMRI

R. Huber¹, B. Poser¹, P. Bandettini², K. Arora¹, K. Wagstyl³, A. C.⁴, J. Goense⁵, R. Goebel⁶, O. F. Gulban⁷

¹MR-Methods group, MBIC, Uni Maastricht, Faculty of Psychology and Neuroscience, Maastricht, The Netherlands, ²NIMH, SFIM, Bethesda, USA, ³UCL, London, UK, ⁴Uni Minneapolis, Uni Glasgow, NIMH, NIH, Washington, USA, ⁵University of Glasgow, Glasgow, UK, ⁶MBIC, Uni Maastricht, Faculty of Psychology and Neuroscience, Maastricht, The Netherlands, ⁷Brain Innovation, Maastricht, The Netherlands

Introduction: High-resolution fMRI in the sub-millimeter regime allows researchers to resolve brain activity across cortical layers and columns non-invasively (Koopmanns 2010, de Martino 2015, Huber 2017). While these high-resolution data make it possible to address novel questions of directional information flow within and across brain circuits, the corresponding data analyses are challenged by MRI artifacts, including image blurring, image distortions, low SNR, and restricted coverage (Kemper 2018, Polimeni 2018). These challenges often result in insufficient performance accuracy of conventional analysis pipelines. Here we introduce a new software suite that is specifically designed for layer-specific functional MRI: LAYNII. It is a non-commercial software. It's name is pronounced: lei-nee.

Subjects/Methods: This toolbox is a collection of command-line executable programs written in C++ and is distributed open-source and as pre-compiled binaries for Linux, Windows, and macOS. LAYNII is designed for layer-fMRI data that suffer from SNR and

coverage constraints and thus cannot be straightforwardly analysed in alternative software packages. Some of the most popular programs of LAYNII contain ‘layerification’ and columnarization in the native voxel space of functional data as well as many other layer-fMRI specific analysis tasks: layer-specific smoothing, vein-removal of GE-BOLD data, quality assessment of artifact dominated sub-millimeter fMRI, as well as analyses of VASO data.

Results/Discussion: Figures 1-3 exemplify the features of LAYNIIs most popular functionalities:

Fig. 1: Assigning layer values to each voxel across the cortical depth. a.k.a. Layerification.

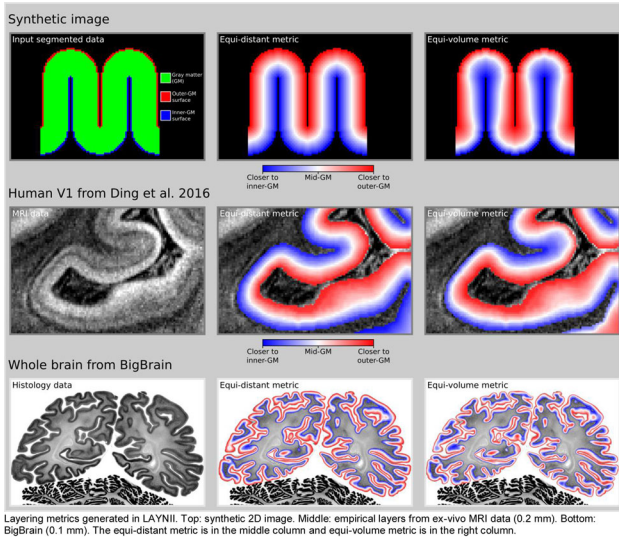


Fig. 2: Column assignment for topographical layer analyses.

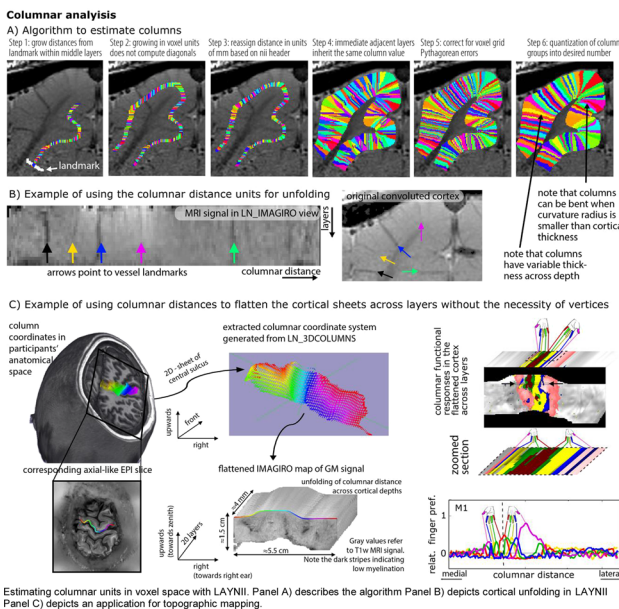
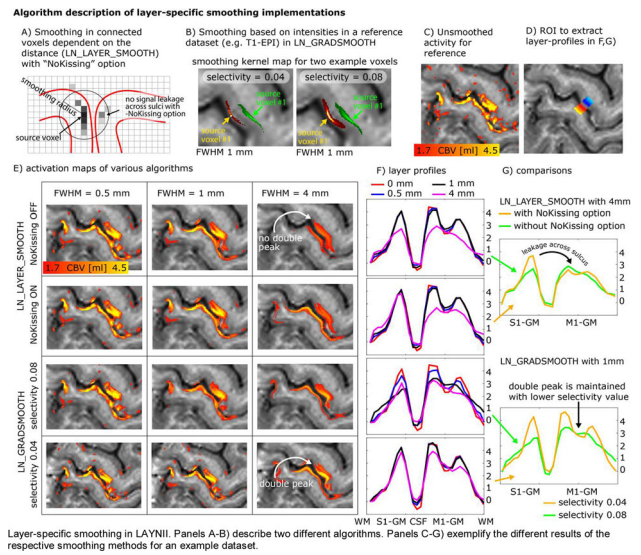


Fig. 3: Layer specific smoothing similar to (Blazejewska 2019).



Example data, source code, binary executables, installation instructions, installer packages can be found here: <https://doi.org/10.5281/zenodo.3514298>

Also see LAYNII repository: <https://github.com/layerfMRI/LAYNII>.

While the current functionality largely focuses on applications where the challenges of layer-fMRI data do not allow the application of standard analysis pipelines of the major software packages (AFNI, Brain Voyager, SPM, FreeSurfer, Nighres, CBStools etc.), we hope that the flexible and modular framework encourages contribution of new tools, stimulates collaboration, and accelerates progress in the promising field of layer-fMRI neuroimaging.

Acknowledgements: 016.Veni.198.032, ZIA-MH002783, R01MH/111444, ERC-2010-AdG, FP7-ICT-2013-FET-F/604102, 16.Vidi.178.052

References: Blazejewska, Neuroimage. 2019; <https://doi.org/10.1016/j.neuroimage.2019.01.054>
 De Martino, PNAS. 2015; <https://doi.org/10.1073/pnas.1507552112>
 Huber, Neuron. 2017; <https://doi.org/10.1016/j.neuron.2017.11.005>
 Kemper, Neuroimage. 2018; <https://doi.org/10.1016/j.neuroimage.2017.03.058>
 Koopmans, HBM. 2010; <https://doi.org/10.1002/hbm.20936>
 Polimeni, Neuroimage. 2018; <https://doi.org/10.1016/j.neuroimage.2017.04.053>

SWE01.02
XNAT-PIC: expanding XNAT to preclinical imaging centers

S. Zullino¹, A. Paglialonga¹, W. Dastrù¹, S. Aime¹, D. L. Longo²

¹University of Torino, Department of Molecular Biotechnology and Health Sciences, Torino, Italy, ²Italian National Research Council (CNR), Institute of Biostructures and Bioimaging (IBB), Torino, Italy

Introduction: Preclinical research generates a large amount of diverse biomedical imagery, such as Magnetic Resonance Imaging (MRI), Positron Emission Tomography (PET), Computed Tomography (CT), or Ultrasound (US), with an increasing need of standard tools for managing image data. XNAT is a widely used open-source platform for archiving, accessing and processing medical images [1]. However, tools for importing preclinical images and pipelines for processing large image datasets are not yet available. To overcome

these limitations, we have developed several tools in XNAT devoted to Preclinical Imaging Centers (XNAT-PIC).

Subjects/Methods: The Molecular Imaging Center (CIM) has developed an XNAT installation for preclinical imaging (<http://cim-xnat.unito.it>) [1]. This instance is running on XNAT 1.7.5, using Apache Tomcat 7, Oracle JDK 8, PostgreSQL 9.5.14 and Ubuntu 16.04.6 LTS Operative System.

XNAT-PIC consists of a set of tools built in Python 3.7.6 and based on the workflow in Fig. 1:

- XNAT-PIC Uploader to import large, multimodal imaging studies in DICOM standard to XNAT
- XNAT-PIC MRI2DICOM, a ParaVision® (Bruker-Biospin Inc. Billerica, MA) to DICOM standard converter
- XNAT-PIC pipelines for image processing based on tailor-made Python and MATLAB scripts.

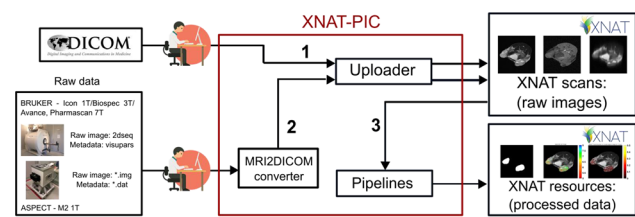


Fig. 1: Schematic workflow for image archiving and processing.

Results/Discussion: In XNAT-PIC, users can convert raw images to DICOM or upload them to XNAT (Fig. 2A). The DICOM Uploader requires the XNAT web address and the login credentials (Fig. 2B). The communication with XNAT uses the xnatpy Python library. Users can create a new project or select an existing one among the list (Fig. 2C). Then, they can browse to the directory and type the number of custom variables for longitudinal studies (Fig. 2D).

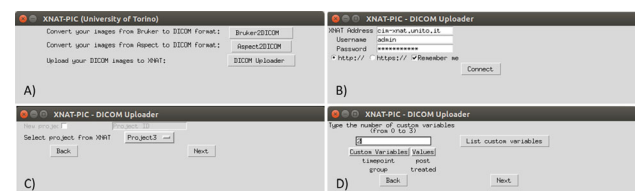


Fig. 2: Screenshots of XNAT-PIC. A) User selection, B) Login to XNAT, C) Select XNAT project, D) custom variables.

Mri2dicom Converter is based on the Python libraries Numpy 1.18.1 and Pydicom 1.4.2, and compatible with ParaVision® 5.1, 6.0.1 and 360.1.1. It reads the image binary file and parses the acquisition parameters into the DICOM attributes.

XNAT-PIC pipelines are project level pipelines that can be launched from any subject in the project to loop over all its subjects. In-house MATLAB R2015b (The MathWorks, Inc., US) codes have been wrapped in Python scripts and implemented as XNAT pipelines to process different types of MR images, including T1/T2 mapping, Diffusion Weighted Imaging (DWI), and to apply a mask to parametric map computing simple statistics in the region of interest (Fig. 3).

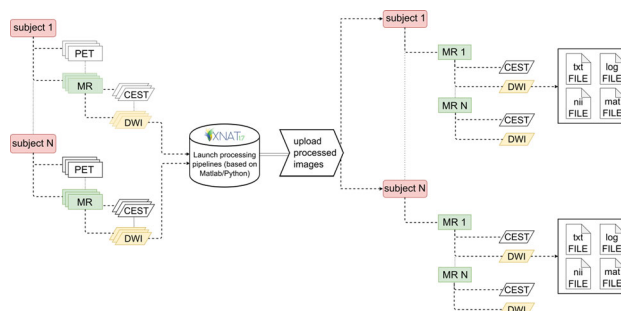


Fig. 3: Schema of an XNAT pipeline retrieving, downloading and processing all the DWI scans in a project. The output files (.txt/log file, NIFTI file, MATLAB workspace) are then uploaded back to XNAT under the corresponding subject.

While the default XNAT installation provides a platform for securely hosting and processing clinical imaging studies, XNAT-PIC broaden its functionalities to support preclinical imaging facilities. To our knowledge, XNAT-PIC is the first tool developed for integrating preclinical imaging in XNAT.

This work has been funded by EU H2020 projects: EOSC-Life (No 824087), CORBEL (No 654248), GLINT (No 667510) and by Compagnia San Paolo (Regione Piemonte, grant #CSTO165925).

References: [1] Marcus et al, Neuroinformatics, 2007.

SWE01.03

Kmaps: a flexible, open source MITK framework for dynamic contrast enhanced MRI analysis

D. Villano¹, W. Dastrù¹, S. Zullino¹, A. Anemone¹, A. Corrado¹, D. Longo²

¹University of Turin, Molecular Biotechnology and Health Sciences, Turin, Italy, ²Italian National Research Council (CNR), Institute of Biostructures and Bioimaging (IBB), Turin, Italy

Introduction: DCE-MRI is a popular method to characterize pathology and evaluate treatment response, especially in cancer¹. Several tools for DCE-MRI data analysis have been developed so far, but many of them require a long time for the analysis, show poor data flexibility, are difficult to use by an inexperienced user or are not suitable for preclinical use^{2,3}.

Kmaps is a flexible, user friendly, open source software for the analysis of DCE-MRI data exploiting different methods from the Medical Imaging Interaction Toolkit (MITK⁴). A dedicated GUI and a simple and guided workflow for DCE-MRI quantifications have been implemented. Moreover, it allows to directly import MRI datasets from several preclinical vendors (Bruker and Aspect raw data).

Subjects/Methods: The analysis workflow is articulated in:

- Data loading.
- Background segmentation.
- Images registration to correct motion artifacts.

-T₁ mapping via Variable Flip Angle, Saturation Recovery or Inversion Recovery acquisitions fitting. Initial values and constraints can be imposed on the parameters to exclude unrealistic values.

-Automatic or manual AIF detection and fitting. Different fitting models (Single Exp., Double Exp., Orton Double Exp., Polynomial) and parameter constraints can be selected.

-Intensities conversion to contrast agent Concentration. The analytic conversion can be executed exploiting the T₁ pre-contrast map and calculating the ΔR₁ time series³ or by means of the signal difference method (ΔSignal)⁵.

-ΔR₁/ΔSignal fitting by the Extended Tofts/Semiquantitative model. Initial values and constraints can be imposed on the model parameters to avoid unrealistic values and to limit the search space (Fig.1).

-Generation of parametric permeability maps and R² map.

Thanks to its integration into MITK, Kmaps offers easy data image viewing and time series plotting, loading and/or manual definition of regions of interest (ROI), calculation of ROI-based descriptive statistics. Moreover, C++ language implementation ensures very fast computation.

Results/Discussion: Kmaps robustness to provide reliable fits was demonstrated on simulated data. As shown by error and SSIM maps, simulated and fitted values were in good accordance (Fig.2). Its applicability for in vivo studies was tested using a murine tumor model DCE-MRI data set acquired at 7 T (Fig.3).

In summary, Kmaps has proven to compete with other existing tools for DCE-MRI analysis due to its good data flexibility, highly automatized and feature rich workflow, good accuracy, integration into a global image processing platform, and its open source nature.

Acknowledgments:

Funding from Associazione Italiana Ricerca Cancro (AIRC MFAG 2017, project #20153) and from PON R&I 2014-2020 (project #ARS01_00144).

References: 1 Türkbey B et al; Diagn Interv Radiol 2010,16, 86

2 Debus C et al; BMC Bioinformatics 2019,20,31

3 Smith D et al; PeerJ 2015,3,e909

4 <http://www.mitk.org/>.

5 Wang P et al; Magn Reson Imaging 2015,33,166

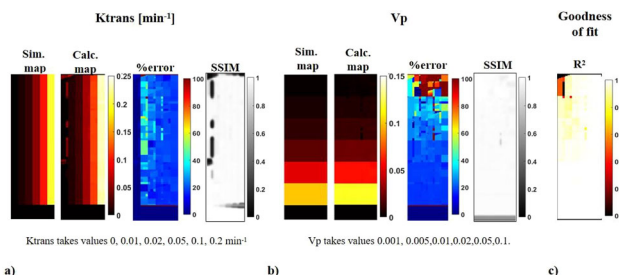


Figure 2: Kmaps validation. Simulated and calculated parametric maps, %error and SSIM maps for Ktrans(a) and Vp(b). For both the parameters a small deviations between fit and ground truth is obtained. The fit quality is showed as R2 map(c).

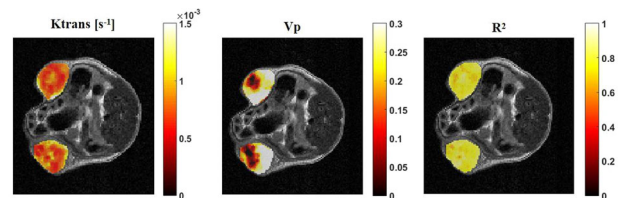


Figure 3: Representative calculated parametric maps for Ktrans, Vp and R2 maps overlaid on T2w anatomical images for a tumor murine model.

SWE01.04

Machine LEARNING in BART – implementation of a deep learning method for segmentation

M. Schilling, M. Blumenthal, M. Uecker

University Medicine Goettingen, Diagnostic and Interventional Radiology, Goettingen, Germany

Introduction: The Berkeley Advanced Reconstruction Toolbox (BART) features multiple techniques for MR image reconstruction, e.g. Nonlinear Inverse Reconstruction (NLINV)[1] for calibration-less reconstruction and ESPIRiT for auto-calibrating parallel MRI [2]. The combination of image reconstruction and segmentation into a unified deep neural network has shown to be beneficial for both tasks, as they positively reinforce each other [3]. Therefore, implementing machine learning methods into BART could also benefit the reconstruction of undersampled k-space data. As a first step, this presentation features the implementation of a deep learning method for segmentation as an example for machine learning in BART.

Subjects/Methods: A convolutional neural network based on the U-Net structure[4] is implemented in BART for image segmentation of fully reconstructed cardiac MR images. The Sunnybrook Cardiac Data[5] is used for training and validation. It features cine-MR images from a mix of patients and pathologies: healthy, hypertrophy, heart failure with infarction and heart failure without infarction. It consists of 86 training and 47 validation images of the left ventricle in short-axis view with contours of epicardium, endocardium and papillary muscles. These contours have been used to create segmentation masks for the myocardium and the two papillary muscles of the left ventricle.

Elastic deformations have been used for data augmentation as they help to simulate realistic deformations efficiently and compensate the little amount of training data.

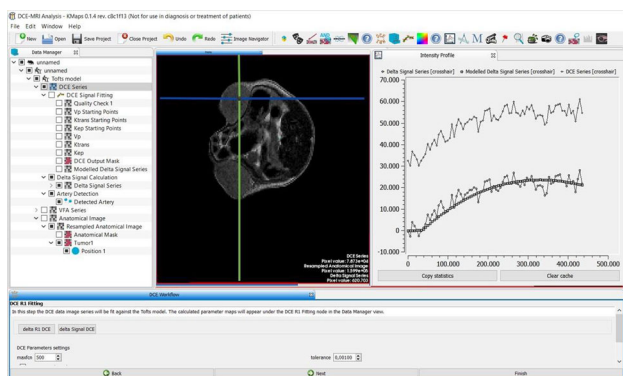
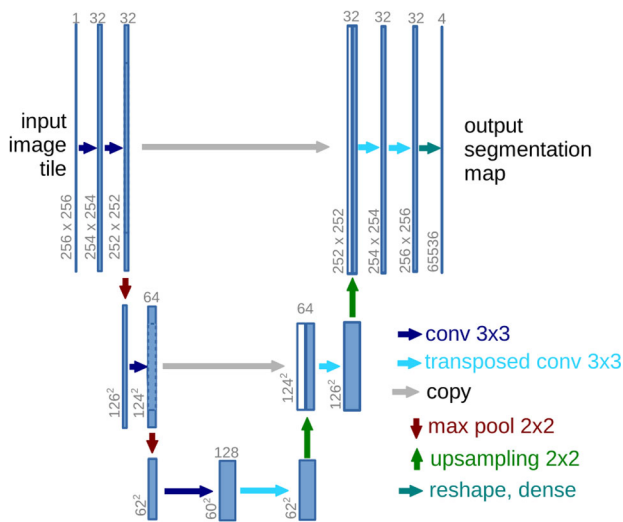


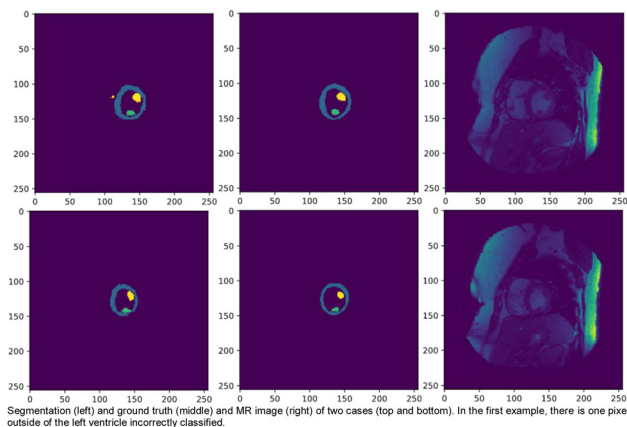
Figure 1: Kmaps application on a tumor murine model: results of the ΔSignal fitting step.



Neural network based on U-Net architecture. A network with similar structure and five max pooling layers was used for training.

Results/Discussion: Basic neural network layers are successfully implemented in BART using its existing framework. A variety of neural networks are based on U-Net architecture so future networks can benefit from its implementation.

Besides small deviations, segmentation of validation images produces promising results for further development of deep learning methods and unification of image reconstruction and tissue classification.



References: [1] Uecker, M., Hohage, T., Block, T., & Frahm, J. (2008). Image reconstruction by regularized nonlinear inversion - Joint estimation of coil sensitivities and image content. *Magnetic Resonance in Medicine*, 60:674–682.

[2] Uecker, M., Peng, L., Murphy, M.J., Virtue, P., Elad, M., Pauly, J.M., Vasanawala, S.S., & Lustig, M. (2013). ESPIRiT—an eigenvalue approach to autocalibrating parallel MRI: Where SENSE meets GRAPPA. *Magnetic Resonance in Medicine*, 71:990-1001.

[3] Sun, L., Fan, Z., Huang, Y., Ding, X., & Paisley, J. (2019). Joint CS-MRI Reconstruction and Segmentation with a Unified Deep Network. LNCS Vol. 11492

[4] Ronneberger, O., Fischer, P., & Brox, T. (2015). U-Net: Convolutional Networks for Biomedical Image Segmentation. *Med Image Comput Comput Assist Interv* Vol. 9351 of *Lect Notes Comput Sci.*, 234–241

[5] Sunnybrook Cardiac Data, <http://www.cardiacatlas.org/studies/sunnybrook-cardiac-data/>.

Publisher’s Note Springer Nature remains neutral with regard to jurisdictional claims in published maps and institutional affiliations.